Advances in Modelling and Numerical Simulation of Sediment Transport in Shallow Water Flows

THOMAS SIMON LEACROFT ROWAN

How to cite:

ROWAN, THOMAS SIMON LEACROFT (2019) Advances in Modelling and Numerical Simulation of Sediment Transport in Shallow Water Flows. Doctoral thesis, Durham University.

Advances in Modelling and Numerical Simulation of Sediment Transport in Shallow Water Flows

Thomas S. L. Rowan

A Thesis presented for the degree of
Doctor of Philosophy

Department of Engineering
University of Durham
England

October 2018

Dedicated to

My loving family.

Advances in Modelling and Numerical Simulation of Sediment Transport in Shallow Water Flows

Thomas S. L. Rowan

Submitted for the degree of Doctor of Philosophy
October 2018

Abstract

A class of novel models for sediment transport, for which multilayer fluid models are combined with a multi-sediment method, is developed and analysed. Turbulent effects in both water flow and sediment transport are also accounted for in the presented models. The aim of this thesis is to advance fast and accurate techniques that overcome some of the assumptions limiting current sediment transport models of this type. To the best knowledge of the author, this is the first time a two-dimensional multilayer model has been used for modelling and simulation of sediment transport. Sediment transport methods using the Shallow Water Equations (SWEs) are reviewed and some of the limiting assumptions are highlighted. Fast methods for modelling sediment transport with multiple sediments are developed in both one space dimension (1D) and two space dimensions (2D). A new formulation for multilayer SWEs is expanded in 1D and 2D to also include sediment transport. Turbulence modelling with the well-established k-ϵ model is also evolved to deal with a multilayer formulation. Each development is tested by itself to quantify its effects and then combined with all the other developments to create the final model. Two second-order accurate solvers are in this thesis: namely a Roe-type solver and a novel Eulerian-Lagrangian formulation. The latter is favoured and is used to solve the complete model, including turbulence and multiple sediment types. This creates a fast and easy-to-implement method that can handle complex flows and irregular bed topographies. The methods are compared to other shallow water systems along with Navier-Stokes results and data obtained from experiments performed in the Department of Engineering at Durham University. Overall, this thesis provides interesting and highly applicable results that add a new avenue of applications to sediment transport in shallow water flows.

Keywords: Sediment transport, Multilayer shallow water equations, Multi-sediments, Turbulence modelling, Eulerian-Lagrangian method, Dam-break problems.

Declaration

The work in this thesis is based on research carried out at the Mechanics Research Group in the Department of Engineering, UK. No part of this thesis has been submitted elsewhere for any other degree or qualification and it is all my own work unless referenced to the contrary in the text.

Acknowledgements

With many thanks to my outstanding supervisor, Dr. M. Seaid, for his guidance and never-ending patience. Thank you also to all the technicians in the Mechanics and Civil Laboratories, for their invaluable expertise. Alex Holdsworth deserves a huge thank you for his untiring sense of humour and his help with experiments. Thanks are also due to my friends and family, for helping proof and edit this thesis.

Nomenclature

Latin

b_ϱ	Bed height (of the ϱth sediment)	L	m
B	Bed height	L	m
c	Depth-averaged concentration	-	-
c_B	Near bed depth averaged concentration	-	-
C_B	Coefficient of bed friction	-	-
C_D	Coefficient of drag	-	-
C_{wi}	Coefficient of wind induced shear stress	-	-
d	Sediment diameter	L	m
d_{50}	Sediment diameter of 50th fraction	L	m
d_*	Dimensionless sediment diameter	L	m
D	Deposition rate	LT^{-1}	m/s
E	Erosion rate	LT^{-1}	m/s
f_c	Coriolis parameter	-	-
f_f	Darcy-Weisbach friction factor	-	-
Fr	Froude number	-	-
g	Gravitational acceleration	LT^{-2}	m/s^2
h_α	Water height of the αth layer	L	m
H	Water height	L	m
k	Turbulent kinetic energy	$\mathrm{L}^2\mathrm{T}^{-2}$	m^2/s^2
p	Pressure	$\mathrm{ML}^{-1}\mathrm{T}^{-2}$	kg/ms^2
P_R	Rouse number	-	-
q_T	Solid transport rate	MT^{-1}	kg/s
q_s	Suspended sediment load	MT^{-1}	kg/s
q_b	Bedload	MT^{-1}	kg/s
Q	Volumetric flow rate	$\mathrm{L}^3\mathrm{T}^{-1}$	m^3/s

n_m	Manning's roughness coefficient	$TL^{-1/3}$	$s/m^{1/3}$
Re	Reynolds number	-	-
Re_p	Particle Reynolds number	-	-
sg	Submerged specific gravity	-	-
t	Time	T	s
u, v, w	Rectangular velocity components	LT^{-1}	m/s
$u_{*,cr}$	Critical velocity for the initiation of motion	LT^{-1}	m/s
U_p	Characteristic particle speed	LT^{-1}	m/s
U_{wi}	Wind speed	LT^{-1}	m/s
U_*	Friction/Shear speed (1D)	LT^{-1}	m/s

Greek

ϑ	Perturbation in water height	M	m
γ	Sediment diffusion coefficient	-	-
ϵ	Turbulent energy dissipation rate	$\mathrm{L}^2\mathrm{T}^{-3}$	m^2/s^3
ε_c	Vertical sediment diffusion coefficient	$\mathrm{L}^2\mathrm{T}^{-1}$	m^2/s
κ_{vK}	von Karman constant	-	-
μ	Viscosity	$\mathrm{ML}^{-1}\mathrm{T}^{-1}$	$kg/m \cdot s$
μ_t	Turbulent viscosity	$\mathrm{ML}^{-1}\mathrm{T}^{-1}$	$kg/m \cdot s$
φ	Erosion coefficient	-	-
Ψ	Porosity	-	-
ρ	Density	ML^{-3}	kg/m^3
ρ_s	Density of sediment	ML^{-3}	kg/m^3
ρ_w	Density of water	ML^{-3}	kg/m^3
ρ_0	Density of bed (saturated)	ML^{-3}	kg/m^3
τ	Shear stress	$\mathrm{ML}^{-1}\mathrm{T}^{-2}$	$kg/m \cdot s^2$
τ_{ij}	Shear stress on the ij plane	$\mathrm{ML}^{-1}\mathrm{T}^{-2}$	$kg/m \cdot s^2$
τ_{cr}	Critical shear stress	$\mathrm{ML}^{-1}\mathrm{T}^{-2}$	$kg/m \cdot s^2$
τ_*	Dimensionless shear stress	-	-
ν	Kinematic viscosity	$\mathrm{L}^2\mathrm{T}^{-1}$	m^2/s
ν_H	Effective horizontal kinematic viscosity	$\mathrm{L}^2\mathrm{T}^{-1}$	m^2/s
ν_{mol}	Molecular kinematic viscosity	$\mathrm{L}^2\mathrm{T}^{-1}$	m^2/s
ν_t	Turbulent kinematic viscosity	$\mathrm{L}^2\mathrm{T}^{-1}$	m^2/s
ν_v	Effective vertical kinematic viscosity	$\mathrm{L}^2\mathrm{T}^{-1}$	m^2/s

ω	Settling velocity	LT^{-}1	m/s
ω_s	Hindered settling velocity	LT^{-}1	m/s
$\omega_{s,i}$	Impact law settling velocity	LT^{-}1	m/s
Ω_s	Angular velocity of the earth	-	-

Acronyms

1D	One Dimensional
2D	Two Dimensional
3D	Three Dimensional
CFL	Courant-Friedrichs-Lewy
DNS	Direct Numerical Simulation
ELFV	Eulerian-Lagrangian Finite Volume
FDM	Finite Difference Method
FEM	Finite Element Method
FVM	Finite Volume Method
HLL	Harten-Lax-van Leer
HLLC	Harten-Lax-van Leer-Contact
LES	Large Eddy Simulation
MoC	Method of Characteristics
PDE	Partial Differential Equation
RaNS	Reynolds-averaged Navier-Stokes
SWE	Shallow Water Equation
TVD	Total Variation Diminishing

Contents

List of Figures

List of Tables

Chapter 1

CH1 Introduction

1.1 Project background

The boundaries of water and land have determined the location of settlements for millennia. Coastal and river systems were vital to ancient civilisations, generating wealth and prosperity, and industry, agriculture, and transportation have historically been dependant on these systems [195]. However, they are not a static resource: the borders are constantly changing as a result of sedimentation and erosion. The limited supply of viable locations for development has forced modern civilisation to encroach more and more upon natural waterways. The past century has seen rapid increases in the habitation of flood prone-areas and the creation of artificial waterways and dams [71]. This has allowed for much greater expansion but it has come with huge risks [95].

Globally, flooding has become the most common and destructive natural hazard in high-risk areas with under-engineered infrastructure, and climate change has significantly raised the probability of these hazards becoming catastrophes [130]. From 1975 to the turn of the century more than $170,000$ people lost their lives due to floods [91]. Between 1980 and 2012 the global economy has averaged a loss of over \$23 billion per annum as a result of flood damage [98]. Climate change and further socio-economic development may see the number of extreme floods double by 2050 [97]. Strategic development and improvement of coastal and river systems has been proven to minimise the risks whilst allowing use of their boundaries to be maximised, for example [99]. Techniques such as sea walls, diversion spillways, and bank reinforcement are just a few of the methods employed to mitigate danger [156]. These methods are dependent on understanding the impact of the interaction of water with soil. Historically, trial and error has been used to produce rudimentary formulae for insight into waterworks [72]. The advent of modern scientific techniques, combined with the more recent advances in computing has led to mathematical modelling replacing trial and error.

Mathematical models are simplifications of real world situations that enable future events to be predicted. Water is a fluid medium, making it computationally expensive to model accurately over long time periods as multiple iterations are required. High computing power requirements combined with limited data availability make such analyses a trade-off between accuracy and expense. Coarse analysis, whilst useful in certain situations, often neglects sedimentary effects (such as erosion, deposition and transport) which can fundamentally change the course of the water and the landscape around it. These hydrogeomorphic changes can occur over long time frames, making them extremely computationally expensive and difficult to model [7]. They are, however, increasingly important to understand given the ever-ambitious projects of the modern age. The Three Gorges Dam is one of the most notable examples of coarse analysis failing [216]. The dam, completed in 2008, altered the sedimentation pattern of the Yangtze river which carries 520 million tons of silt annually. With much of the silt trapped behind the dam, the cleaner water flowed faster scouring the river bed downstream and lowering it by more than 2 m between Hubei and Hunan, whilst washing away around 150 million cubic metres of sand. This caused riverbank collapses downstream, increasing the flooding hazards and forcing further investments in bank reinforcements and flood defences.

One of the most commonly used models in hydrodynamics is a set of partial differential equations, called the Navier-Stokes equations, which detail the movement of water in three dimensions (3D). This study will look at the Shallow Water Equations (SWEs) - derivatives of the Navier-Stokes equations - in their one (1D) and two-dimensional (2D) forms. The 2D form will be developed to capture 3D effects using a multilayer approximation. The effects of turbulence are also modelled in this work for the first time in a multilayer formulation. The 1D SWEs are used to test and verify novel methods (multilayer sediment transport, multilayer diffusion and multi-sediment handling). These advances in sediment modelling are then used in conjunction with advances in shallow water modelling to create a more complete approach to complex sediment flow interaction.

There are many different sediment transport models. Varying types of sediments are treated with different formulae depending on their characteristics. Challenges exist in successfully integrating these relations with the SWEs, as they introduce further instabilities and complications to the system. The current generation of sediment transport models are specialised for specific types of scenarios and lack universal applicability, as they do not overcome limiting assumptions. One of the objectives of the current work is to create a fast and modular method for sediment transport modelling that can be easily optimised for specific problems.

1.2 Sediment transport modelling

Water moving over an erodible bed in either steady or unsteady conditions can scour particles off the bed and transport them some distance [87]. These particles can either travel as bedload, where sediment tumbles across the bottom of the bed, or as suspended sediment which is immersed in the flow of water itself. Approximately $20-22$ trillion tonnes of sediments a year are discharged into the oceans (75% from Asian mainland rivers) [170], thus understanding this process has been a subject of great importance as it effects everything from harbour sedimentation to irrigation system design, causing congestion and channel narrowing due to deposition of sediment. Many methods and models for sediment transport exist in the literature and according to [84] these can be split into four categories: empirical, conceptual, physically-based, and hybrid models.

Empirical models use existing data either in further analysis or in equilibrium based modelling, see for example [34,163,204]. In equilibrium based models, a balancing equation is formed that takes into account all relevant variables. When the user changes a variable, the sedimentation rates (and therein the bathymetry) are altered to compensate. Data analysis uses historical trends or sediment-based predictions to enable the forecast of sedimentary rates. Empirical models predicate other classes of models and are typically used to make morphological predictions over long time periods, with an annual temporal scale. Their relative simplicity makes them efficient and widely employed, though they require data on the area to be collected and are often coarse in their results with poor capture of small scale effects.

Conceptual models are the step between empirical and physically-based models, combining a statistical approach with a sediment continuity equation, see for example [96, 101, 118, 211]. They are mainly used to predict sediment yield through the calibration of variables against measured data. This class of model tends to consider general trends in catchment areas and watersheds without examining specific flow interactions. This factor, combined with the problems of identifiability of their parameter values, limits their abilities especially when considering more complex structure interactions and effects. This type of model can be easily scaled in complexity to best capture the problem at hand and typically has a daily time-scale.

Physically-based models, in which hydrodynamic modelling (such as SWEs) are coupled with sediment transport equations, can be used to simulate a wide range of situations including waves, shocks and steady flows [55, 58, 139, 205]. This work concentrates on examining this category of models, specifically focussing on how best to integrate sediment transport and morphological bathymetry equations into the SWEs. Physically-based models are most suited to small scale, short-term simulations. These models are ideal for capturing relatively small effects like structure interaction (such as bridge and pier foundations). Historically, in comparison to empirical models, they are extremely computationally expensive for long-term simulations. Thus one of the key features in their development is the creation of more efficient methods, which this body of work will concentrate on.

Hybrid is the final category of model, in which elements of the previous classes are combined to make the most practical approach for modelling some long-term problems [93,123,124]. This method normally uses a variety of 1D and 2D hydrodynamic models, together with a statistical or rules-based approach. This class of model can vary widely depending on formulation, but suffers all of the issues of the classes of models that it utilises. The time-scale for this type of model can vary depending on formulation. It has the advantage though of being the most flexible, and can incorporate different features as pertinent to the situation under review.

It should be mentioned that of the four categories, physically-based sediment transport models are comparatively underdeveloped due to their reliance on computationally expensive modelling, progress on which has only really begun in the last few decades. The trade off between accuracy and computational power has meant that overly simplistic models are often employed, and these fail to predict real-world events accurately. Sediment is generally defined by density, shape, size (including distribution and/or diameter), and cohesiveness. Though much work has been done to gain experimental data, there are still large numbers of untested conditions and sediments. Due to the size of the required experiments and the limitations of measurement equipment, testing under ideal conditions is expensive and complex, though in recent decades a good number of benchmark tests have developed and become standard in the field.

1.3 Project objectives

The primary objective of this project is to develop techniques to remove limiting assumptions from SWE sediment transport models without substantially increasing computational cost. In order to realise this goal, it is necessary to develop a number of 1D and 2D methods for sediment transport. The individual effects of each modification are developed separately, so that their impact on the model can be quantified. This will be achieved by a critical assessment of current sediment transport models and three developments: multi-sediment handling, a multilayer shallow water formulation and turbulence modelling. The multi-sediment handling tackled in this work enables multiple sediment types to be considered in both homogeneous and heterogeneously formed beds. This removes the homogeneous assumption that limits other models in this field. A multilayer shallow water formulation is also developed in this work, enabling the capture of 3D effects by treating fluid bodies as a series of vertically stacked fluid layers that interact with each other. This formulation enables a more accurate capture of 3D effects which is crucial to accurate modelling of sediment transport. Finally, the introduction of turbulence modelling enables complex flow features to be better captured and complex situations further understood. This work is, to the knowledge of the author, the first time that turbulence has been combined with a multilayer formulation. The specific goals of this study are:

- To give a critical assessment of current physically-based sediment transport models and their limitations.
- To create and validate a multi-sediment bed model that is capable of tracking and mixing sediments in both one and two space dimensions.
- To develop a multilayered (in flow) method for sediment transport in order to deliver vertically stratified velocity advantages.
- To create a 2D multilayer method for flow which includes exchange between the layers.
- To devise and test a SWE formulation for a multilayered flow in 2D which incorporates turbulence modelling.
- To combine all the previously detailed advances into a single sediment transport model.

Each of the specific goals are developed separately to ensure that their effects on the models are fully understood. The goal is to create a modular system whereby features can be included as required. As is seen in the previous section, the creation of tools for multi-sediment handling or turbulence may not always be required and can add un-necessary complexity. Consequently, sediment transport models are adjusted for different situations to ensure the best return on computational expenditure.

1.4 Thesis structure

This thesis is structured as follows:

- **Chapter 1** introduces the subject matter and sets out the objectives of the thesis. It details the motivation for the work conducted and the historical and current significance of the problems encountered. A brief overview of the classes of techniques available is given. The objectives of this study area are also listed with a brief explanation of the advances made. Finally, the structure of this thesis is detailed with the advances and contributions highlighted.

- **Chapter 2** reviews current literature, evaluating different models within the physically-based class as well as overviewing the mathematics and methods used to solve the problems arising. First, the SWEs are detailed with major features and additions listed. A brief derivation is also given in order to expound the basis for some of the limiting assumptions. Sediment transport in physically-bases models is then reviewed from basic principals to current studies. The assumptions made and the reliance on empirically gained entrainment functions are expounded, with the principal models reviewed. The third section reviews the numerical methods used to solve this class of problem. The Finite Volume Method (FVM), which is used in this work, is covered. Next, the various approximation methods used to solve this class of problems are highlighted, with relative advantages and disadvantages discussed. Finally, a range of existing sediment transport models (mostly in the physically-based class) are reviewed, with interesting developments and features discussed. This chapter provides all the background material and details the research conducted to enable the developments of this study.

- **Chapter 3** develops the multi-sediment model, determining its potential and verifying it against benchmark tests. As there is no homogeneous bed in the natural world, it is important to be able to capture and collate the effects of the various sediment types. A novel technique is developed from base principles (similar to the Saint-Venant-Hirano model) incorporating a fully discretised bed capable of modelling both vertically and horizontally stratified bed layers for the first time. Computation is kept minimal by considering the sediment in suspension as an averaged value for the hydrodynamic parts of the model and as separate fractions for the entrainment functions. This novel formulation is found to be conservative and is tested against two benchmark simulations, presenting accurate and interesting results as new features like sediment tracking are possible.

- **Chapter 4** investigates a novel multi-layered 1D model for sediment transport, testing it against its single-layer counterpart and showcasing its adaptability. This multilayered model is able to capture vertically stratified flow speeds which helps in the computation of erosion and suspended load, as the slower moving highly concentrated bedload can now be modelled as part of the flow. Combined with a fast finite volume of characteristics solver, this method does not incur the usual increase in computational expense associated with adding a dimension. The method is found to be fast and accurate and reduces the over-scouring problem usually found in simulations of this nature. It also allows for new problems (such as recirculation) to be simulated that previously were not within the ability of shallow water sediment transport modelling.

- **Chapter 5** presents a 2D multi-sediment model, using multiple methods for sediment handling. The model is trialled against complex high-shear situations, including experimental data. Building on the work presented in Chapter 3, this chapter details the projection method used to solve the 2D model, as part of the conservative Eulerian-Lagrangian method. This work is the first time that a 2D model has been formulated capable of handling the multi-layered bed simulations. The effects of various bed assumptions are detailed and the performance of the model is evaluated against experimental data from the Université de Louvain. Overall this method is found to be consistent, though experimental data to assess the multi-sediment abilities of this formulation does not yet exist.

- **Chapter 6** introduces the 2D multilayered model without sediment transport, evolving the method into 3D. This is tested against specially developed scenarios. The model presented is a significant advancement, in that it is the first to solve a multi-layer shallow water system with exchange terms. This is achieved by using a projection FVM for the Eulerian stage and a method of characteristics to approximate the numerical fluxes for the Lagrangian stage. The multilayer shallow water formulation is capable of delivering vertically stratified velocities, creating 3D results with a level of computational expense usually associated with two dimensions. This method is tested against Navier Stokes formulations and found to provide excellent results.

- **Chapter 7** extends the 2D multilayered model for flow to include turbulence modelling without sediment transport. The model is tested against experimental data as well as 3D Navier-Stokes simulations. Through the adaptation of the popular k-ϵ model, the model developed in Chapter 6 is enhanced to give better resolution to some of the most complex situations, including the back-step and partial dam-break problems. This is the first time to the knowledge of the author that turbulence has been incorporated in this way. The presented model offers a deeper insight into flow structures and is significantly faster than comparable 3D formulations.

- **Chapter 8** combines the work of all the previous chapters, in order to build a 2D multilayer model for sediment transport that includes heterogeneous sediments and turbulence modelling. This model is tested against experimental data and 3D Navier-Stokes simulations. It is found to be fast, well-balanced and stable. The model is also tested against some new experimental data gathered as part of this study (at the Engineering Department in Durham University) to assess the vertical distribution of sediment in 1D dam-break flows. This is the first time data of this nature has been collected and it offers a new method of assessment for models of this type. The presented model is found to have good agreement with the experimental data. The model is also used to compute the horizontally packed composite bed partial dam-break problem - a problem that has, to the knowledge of the author, never been simulated before. Overall this model successful combines all the previous work to create an advanced sediment transport modelling tool.

- **Chapter 9**, concludes the thesis, evaluating the limitations and benefits of the models that have been developed. A brief summary of each of the developments is given, outlining the work completed and the various merits and costs of this class of models. It goes on to outline further areas of interest and highlights possible new fields of interest, based on the research conducted. Four areas of possible development for this work are briefly mentioned: differential sediment transport rates for bedload and sediment types, wet-dry fronts, steady state optimisation, and asymptotic analysis.

Each chapter is designed to be as self-contained as possible. Although a general background to the work presented in each chapter is given in Chapter 2, each subsequent chapter also contains a more specific background and explanation of the motivation behind the work conducted in it. This structure is adopted to ensure that the relevant information and review is as close as possible to the work that builds on it. The chapters are further structured to detail the presented models and any numerical techniques developed for the presented work, though for the sake of brevity any repeated material is excluded.

Chapter 2

Literature review

This chapter is divided into five sections, each assessing an area upon which this thesis builds, together with a summary. The first section examines the shallow water equations, and covers some of the associated notations and useful modifications (such as the Exner equation, the k-ϵ turbulence model, etc.) that are used in conjunction with the shallow water equations. The second section delineates the work done to date on sediment transport, focusing on the variety of methods used to solve this problem with a physically-based approach. The third section of this chapter discusses numerical methods used to solve the shallow water equations. The fourth section provides an overview of flux estimation approaches. Finally, in the fifth section, a few of the existing sediment transport models are reviewed.

2.1 Shallow water equations

This section deals with the Shallow Water Equations (SWEs) and alternative fluid concepts, with attention focussing on the characteristics and categorization of one-dimensional (1D) and two-dimensional (2D) forms of the equations. This lays out the mathematical base for the thesis. Ideally all simulations would use an un-approximated system, like the three-dimensional (3D) Navier-Stokes equations. The most detailed solution is the Direct Numerical Simulation (DNS) [132], which captures the smallest flow features using a very fine mesh, however it is highly computationally expensive. Cheaper approaches can be used: Large Eddy Simulations (LES) [59], where only large eddies and flow features are captured and Reynolds-averaged Navier-Stokes (RaNS) simulations [141], where the equations are time averaged, *i.e.* instantaneous quantities are split into averaged and fluctuating quantities. The RaNS and LES models save considerable amounts of computational time compared to DNS models. The SWEs however, are able to produce larger computational savings by further simplifying the governing equations. The SWEs were first derived by Saint-Venant in 1871 [154]. They are the simplest form of equations that can be used to model the flow of water and other incompressible or near incompressible fluids. The SWEs enable both gravitational and rotational accelerations to be modelled (Coriolis effect, etc.). Derivations can be drawn from many different sources including the Navier-Stokes equations.

2.1.1 Derivation of 2D shallow water equations

The Navier-Stokes equations are a system of five partial differential equations that can be used to relate the density, velocity and temperature fields of a fluid to each other. At the turn of the 19^{th} century, M. Navier and G. Stokes originally derived these from the Euler equations to incorporate viscosity effects. They form the basis for most Computational Fluid Dynamics (CFD) models and are used in various forms. In this derivation of the SWEs, the following assumptions are made:

- The fluid is incompressible such that the fluid density is constant in all directions.
- Viscosity and thermal conductivity are uniform across the fluid it is also considered a Newtonian fluid.
- The fluid is isothermal, decoupling the velocity field from energy conservation.

These initial assumptions reduce the Navier-Stokes equations from a 5-equation system to the following 4-equation system

$$\frac{\partial u}{\partial t} + u\frac{\partial u}{\partial x} + v\frac{\partial u}{\partial y} + w\frac{\partial u}{\partial z} = -\frac{1}{\rho}\frac{\partial p}{\partial x} + \frac{\partial \tau_{xx}}{\partial x} + \frac{\partial \tau_{xy}}{\partial y} + \frac{\partial \tau_{xz}}{\partial z}, \tag{2.1.1a}$$

$$\frac{\partial v}{\partial t} + u\frac{\partial v}{\partial x} + v\frac{\partial v}{\partial y} + w\frac{\partial v}{\partial z} = -\frac{1}{\rho}\frac{\partial p}{\partial y} + \frac{\partial \tau_{xy}}{\partial x} + \frac{\partial \tau_{yy}}{\partial y} + \frac{\partial \tau_{yz}}{\partial z}, \tag{2.1.1b}$$

$$\frac{\partial w}{\partial t} + u\frac{\partial w}{\partial x} + v\frac{\partial w}{\partial y} + w\frac{\partial w}{\partial z} = -\frac{1}{\rho_{av}}\frac{\partial p}{\partial z} - \frac{g\rho}{\rho_{av}} + \frac{\partial \tau_{xz}}{\partial x} + \frac{\partial \tau_{yz}}{\partial y} + \frac{\partial \tau_{zz}}{\partial z}, \tag{2.1.1c}$$

$$\frac{\partial u}{\partial x} + \frac{\partial v}{\partial y} + \frac{\partial w}{\partial z} = 0, \tag{2.1.1d}$$

where (u, v, w) are velocities in the x, y, and z directions, p is pressure, ρ is the density of the fluid, ρ_{av} is the average density of the fluid, g is acceleration due to gravity, and $\tau_i j$ is the shear stress on the ijth plane. There are four main steps to the derivation of the SWEs.

1. The hydrostatic balance reaction must be incorporated.
2. The boundary conditions at the top and bottom of the water column are specified.
3. The depth-averaged integration is determined.
4. The specified boundary conditions must be applied to the integrated equations.

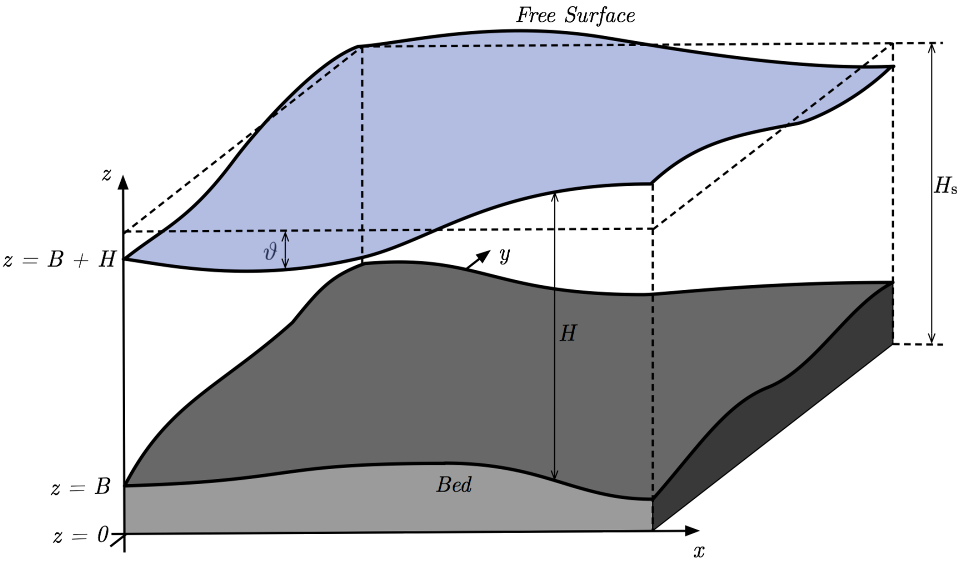

Figure 2.1: Typical water column over a non-flat bathymetry.

Let us consider the water column shown in Figure 2.1. It is bounded by the surface $z = B$ and the free-surface $z = B + H$. Here, $\vartheta(t, x, y)$ is the perturbation in the water surface, and H_s is a water datum height, with $H(t, x, y)$ being the total depth $H = H_s - \vartheta - B$. Two methods of notation for water height exist, both shown in Figure 2.1. Either the more standard notation H, or the less common ϑ, is used in the derivation. Thus (2.1.1c) reduces to

$$0 = -\frac{1}{\rho_{av}}\frac{\partial p}{\partial z} - g.$$

As the fluid is incompressible it is assumed that the density is constant $\rho = \rho_{av}$ and hence

$$\rho g = \frac{\partial p}{\partial z},$$

this may be integrated along the vertical to show

$$p = \rho g z + cte.$$

where *cte* is an (integration) constant. This is the hydrostatic pressure distribution. The following boundary conditions are developed based on the parameters of the free-surface and of the topography. As in [175] at the interface of the bed with the bottom of the water column, the following conditions are considered:

- No-slip in either direction

$$u = v = 0.$$

- There is no normal flow
$$u\frac{\partial B}{\partial x}+v\frac{\partial B}{\partial y}+w=0.$$

- The bottom shear stress is expressed as
$$\tau_{\mathrm{B},x}=\tau_{xx}\frac{\partial B}{\partial x}+\tau_{xy}\frac{\partial B}{\partial y}+\tau_{xy}.$$

At the free-surface (where $z=B+H$) the following boundary conditions apply:

- No relative normal flow
$$\frac{\partial\vartheta}{\partial t}+u\frac{\partial\vartheta}{\partial x}+v\frac{\partial\vartheta}{\partial y}+w=0.$$

- Pressure is assumed to be atmospheric only *i.e.*
$$p=0.$$

- Surface shear stress is defined by
$$\tau_{fs,x}=-\tau_{xx}\frac{\partial\vartheta}{\partial x}-\tau_{xy}\frac{\partial\vartheta}{\partial y}+\tau_{xy}.$$

The next step is to integrate the continuity equation (2.1.1d) from the bed to the free-surface. Using Leibniz's integral rule the following is attained

$$\begin{aligned}
0 &= \int_{z=B}^{z=H+B}\left(\frac{\partial u}{\partial x}+\frac{\partial v}{\partial y}+\frac{\partial w}{\partial z}\right)dz,\\
&= \int_{z=B}^{z=H+B}\left(\frac{\partial u}{\partial x}+\frac{\partial v}{\partial y}\right)dz+w\Big|_{z=H+B}-w\Big|_{z=B},\\
&= \frac{\partial}{\partial x}\int_{z=B}^{z=H+B}u\ dz+\frac{\partial}{\partial y}\int_{z=B}^{z=H+B}v\ dz-\left(u\Big|_{z=H+B}\frac{\partial\vartheta}{\partial x}+u\Big|_{z=B}\frac{\partial B}{\partial x}\right)\\
&\quad -\left(v\Big|_{z=H+B}\frac{\partial\vartheta}{\partial x}+v\Big|_{z=B}\frac{\partial B}{\partial x}\right)+w\Big|_{z=H+B}-w\Big|_{z=B}. \qquad (2.1.2)
\end{aligned}$$

We also define the depth-averaged velocities as

$$\bar{u}=\frac{1}{H}\int_{z=B}^{z=H+B}u\ dz, \qquad \bar{v}=\frac{1}{H}\int_{z=B}^{z=H+B}v\ dz.$$

Applying the boundary conditions and substituting in the depth-averaged velocities into (2.1.2), the following is gained

$$\frac{\partial H}{\partial t} + \frac{\partial (H\bar{u})}{\partial x} + \frac{\partial (H\bar{v})}{\partial y} = s_1.$$

Integration of the x and y momentum equations (2.1.1a) and (2.1.1b) over depth yields

$$\begin{aligned}
\int_{z=B}^{z=H+B} \left(\frac{\partial u}{\partial t} + u\frac{\partial u}{\partial x} + v\frac{\partial u}{\partial y} + w\frac{\partial u}{\partial z} \right) dz &= \int_{z=B}^{z=H+B} \left(-\frac{1}{\rho_{av}}\frac{\partial p}{\partial x} + \frac{\partial \tau_{xx}}{\partial x} + \frac{\partial \tau_{xy}}{\partial y} + \frac{\partial \tau_{xz}}{\partial z} \right) dz, \\
\int_{z=B}^{z=H+B} \left(\frac{\partial v}{\partial t} + u\frac{\partial v}{\partial x} + v\frac{\partial v}{\partial y} + w\frac{\partial v}{\partial z} \right) dz &= \int_{z=B}^{z=H+B} \left(-\frac{1}{\rho_{av}}\frac{\partial p}{\partial y} + \frac{\partial \tau_{xy}}{\partial x} + \frac{\partial \tau_{yy}}{\partial y} + \frac{\partial \tau_{yz}}{\partial z} \right) dz.
\end{aligned}$$

After applying the boundary conditions and substituting in the equations for depth-averaged velocity, we obtain

$$\begin{aligned}
\frac{\partial (H\bar{u})}{\partial t} + \frac{\partial}{\partial x}\left(H\bar{u}^2 + \frac{1}{2}gH^2 \right) + \frac{\partial}{\partial y}\left(H\bar{u}\bar{v} \right) &= -gH\frac{\partial B}{\partial x} + \frac{1}{\rho_{av}}\left[\tau_{sx} - \tau_{bx} + \frac{\partial}{\partial x}\int_{z=B}^{z=H+B} \tau_{xx}\, dz \right. \\
&\quad \left. + \frac{\partial}{\partial x}\int_{z=B}^{z=H+B} \tau_{xy}\, dz \right], \\
\frac{\partial (H\bar{v})}{\partial t} + \frac{\partial}{\partial x}\left(H\bar{u}\bar{v} \right) + \frac{\partial}{\partial y}\left(H\bar{v}^2 + \frac{1}{2}gH^2 \right) &= -gH\frac{\partial B}{\partial y} + \frac{1}{\rho_{av}}\left[\tau_{sy} - \tau_{by} + \frac{\partial}{\partial x}\int_{z=B}^{z=H+B} \tau_{xy}\, dz \right. \\
&\quad \left. + \frac{\partial}{\partial y}\int_{z=B}^{z=H+B} \tau_{yy}\, dz \right].
\end{aligned}$$

We further simplify the source terms by equating:

$$\frac{\boldsymbol{\tau}_b}{\rho} = gH\mathbf{S}_f, \qquad \frac{\boldsymbol{\tau}_s}{\rho_{av}} = \boldsymbol{\tau}_{wi},$$

$$\begin{pmatrix} \dfrac{1}{\rho_{av}}\left[\dfrac{\partial}{\partial x}\displaystyle\int_{z=B}^{z=H+B} \tau_{xx}\, dz + \dfrac{\partial}{\partial y}\displaystyle\int_{z=B}^{z=H+B} \tau_{xy}\, dz \right] \\ \dfrac{1}{\rho_{av}}\left[\dfrac{\partial}{\partial x}\displaystyle\int_{z=B}^{z=H+B} \tau_{xy}\, dz + \dfrac{\partial}{\partial y}\displaystyle\int_{z=B}^{z=H+B} \tau_{yy}\, dz \right] \end{pmatrix} = \begin{pmatrix} BF_x \\ \\ BF_y \end{pmatrix}.$$

Where $\mathbf{S}_f$ is the horizontal bed friction and BF_x, BF_y are used to include body forces on a case appropriate basis. For ease in further notation the bars over the u and v are neglected and from this point on they are assumed to be the depth-averaged velocities. Here, s_1, s_2, and s_3 are all source terms and vary on a case-to-case basis. This brief derivation encompasses all of the basic assumptions (negligible depth scale, averaged velocities, incompressibility, and an homogeneous fluid at constant temperature). The SWEs may be rewritten in a vector form as

$$\frac{\partial \mathbf{W}}{\partial t} + \frac{\partial \mathbf{F}(\mathbf{W})}{\partial x} + \frac{\partial \mathbf{G}(\mathbf{W})}{\partial y} = \mathbf{S}, \tag{2.1.3}$$

where

$$\mathbf{W} = \begin{pmatrix} H \\ \\ Hu \\ \\ Hv \end{pmatrix}, \quad \mathbf{F(W)} = \begin{pmatrix} Hu \\ \\ Hu^2 + \dfrac{1}{2}gH^2 \\ \\ Huv \end{pmatrix}, \quad \mathbf{G(W)} = \begin{pmatrix} Hv \\ \\ Huv \\ \\ Hv^2 + \dfrac{1}{2}gH^2 \end{pmatrix},$$

$$\mathbf{S} = \begin{pmatrix} s_1 \\ \\ s_2 \\ \\ s_3 \end{pmatrix} = \begin{pmatrix} 0 \\ \\ -gH\dfrac{\partial B}{\partial x} - gHS_{fx} + \tau_{wi,x} + BF_x \\ \\ -gH\dfrac{\partial B}{\partial y} - gHS_{fy} + \tau_{wi,y} + BF_y \end{pmatrix}. \tag{2.1.4}$$

Here the vector of conserved variables is $\mathbf{W}$, $\mathbf{F(W)}$ and $\mathbf{G(W)}$ are the flux vectors in the x- and y-directions and $\mathbf{S}$ is the source vector. The conserved variables are employed when formulating a numerical scheme (as shown above) as they are inherently conservative with physical and meaningful quantities being used throughout. In this formulation of the source terms, only the effects of bottom topography in the x and y direction are shown.

Various initial conditions and boundary conditions must next be added to this formulation. Initial conditions require the assignment of water height, bed height and velocities (as well as concentration and turbulence variables in more complex formulations). Boundary conditions are tackled through the use of ghost cells, as in [193]. There are four main types of boundary conditions used in this work: (i) inlet conditions, where the volumetric rate of inlet flow is defined through the manipulation of water height and velocities, (ii) outlet conditions, where the gradient of conserved variables in the outflow direction is set to zero, (iii) physical boundary conditions, where a wall is defined in a direction and there is no flow perpendicular to it, walls can be slip or non-slip (with tangential velocities either allowed or set to zero), and (iv) symmetric conditions, where all variables are mirrored by the ghost cells. A major disadvantage of these configurations is the lack of stratified velocities. As a result, faster moving flow at the top of the water column is assumed to be consistent with the slower flow at the bottom. In reality, sediment species travel through different modes and at different speeds. This is one of the main challenges when modelling sediment transport using the SWEs. This work tackles this problem, through the use of multilayer formulations, developed in later chapters, which provide a more accurate description of the flow.

2.1.2 Derivation of the source terms

There are five other main effects on the momentum equations that should be considered when using sediment transport with movable beds. This section examines the first four namely: bed geometry, bed friction, wind, and the Coriolis effect. The effects of the concentration and movable beds will be introduced later alongside their governing equations. Hence the momentum parts of vector **S** can be rewritten

$$\begin{pmatrix} s_2 \\ \\ s_3 \end{pmatrix} = -gH\nabla B - gH\mathbf{S}_f + f_c H \wedge \mathbf{u} + \boldsymbol{\tau}_{wi},$$

where $\mathbf{S}_f$ is the horizontal bed friction, f_c is the Coriolis parameter, $\wedge$ is the exterior product, the horizontal velocity components are denoted by $\mathbf{u} = (u, v)^T$, and τ_{wi} is the force due to wind.

Bed geometry: Simulations involving sediment transport rarely consider flat beds. This undulating topography affects the momentum as shown in equation (2.1.5). It is important to note that these undulations may change during the course of the simulation, as the beds are often movable. Hence,

$$-gH\nabla B = \begin{pmatrix} -gH\dfrac{\partial B}{\partial x} \\ \\ -gH\dfrac{\partial B}{\partial y} \end{pmatrix}. \tag{2.1.5}$$

Bed friction: Bed friction generally uses the Manning's roughness coefficient n_m whose values range from $0.075 - 0.009\ m^{-1/3}s$ (describing the typical variants from a heavy bush scrub on a flood plain to a smooth plastic pipe). The equation for bed friction may be expressed as [119]

$$\mathbf{S}_f = C_B \mathbf{u}|\mathbf{u}|,$$

where

$$C_B = {n_m}^2 H^{-4/3},$$

where n_m is the Manning coefficient. Other friction relations include the Chezy coefficient, the Manning-Strickler formula [173], and the White-Colebrook (Thysse) equation [51].

Wind effects: Wind can apply a shear stress at its interface with water, creating currents. Over large bodies of water this interaction can build into waves; however, at wind speeds less than 10 m/s, it can be assumed to be a constant force. The effect of wind is [94]

$$\boldsymbol{\tau}_{wi} = \begin{pmatrix} \tau_{wi,x} \\ \\ \tau_{wi,y} \end{pmatrix} = \begin{pmatrix} C_{wi} U_{wi}^2 \cos\theta \\ \\ C_{wi} U_{wi}^2 \sin\theta \end{pmatrix},$$

where U_{wi} is the wind speed, θ is the angle between direction of flow of the wind and the x-axis, and C_{wind} is the wind friction coefficient typically of order 0.001.

Coriolis effect: Coriolis effects are the forces exerted by the rotation of the earth on a free body (in this case bodies of water on the surface of the earth). As the reference frame is moving, a force is exerted, and on earth this force is calculated using latitude such that

$$f_c H \wedge \mathbf{u} = \begin{pmatrix} -f_c H v \\ \\ -f_c H u \end{pmatrix},$$

where $f_c = 2\Omega_s \sin(\phi)$, Ω_s is the angular velocity of the Earth, and ϕ is the latitude. This term is only included to demonstrate that the model and numerical method can handle body forces. It is generally neglected in any flow considered in this field.

2.1.3 Models for turbulence effects

When considering any fluid motion it is important to make accurate assumptions about the flow. It is often appropriate to assume that the turbulent features of the flow may be neglected. This is the basis for the standard three-equation model of the SWEs. However, many shallow water flows have prominent turbulent features that require modelling in order to simulate the flow accurately. The quantity of chaotic variation of velocity and pressure within a fluid is caused by excess kinetic energy in the fluid that overcomes its viscosity. It is difficult to model as it occurs on many length scales and, with the exception of the DNS model, a quantity of turbulent flow features are not captured by the simulation. This produces a closure problem, which is arrived at by time-averaging the Navier-Stokes equations to produce the RaNS equations [141]. As the fluctuating velocities (known as Reynolds stresses) are still present in the formulation, a method of modelling the Reynolds stress is required. In 1877 Boussinesq proposed the first solution to this problem by devising eddy viscosity which relates the Reynolds (turbulent) stresses to the mean velocity. This concept has enabled over 200 RaNS models to be created and these can be categorized by the number of equations that they add to the system:

- **Zero-equation/algebraic models**: (for example Baldwin-Lomax model [15]). This category of models is simple and ideal for start-up flow and basic situations. They are of limited use however, as they only consider instantaneous turbulence production, rather than the evolution of turbulence through diffusion and convection.

- **One-equation models**: (for example Spalart-Allmaras [168], k-model). These models were widely used in the early development of turbulence modelling. The issue with these models is that one-equation is not sufficient to compute the eddy viscosity.
- **Two-equation models**: (for example k-ϵ [108], k-ω). Still actively developed to this day, the two-equation models allow the user to quantify both the turbulent kinetic energy k and a second value that defines the scale (length or time) of the turbulence.

It should be noted that other more complex models (like the k-ϵ-A and the v^2-f [109]) with more than two equations do exist. In this study, the k-ϵ model is adopted as it has the most research behind it and offers reasonable execution times.

Table 2.1: Coefficients used in the k-ϵ as in [205].

C_μ	$C_{\epsilon 1}$	$C_{\epsilon 2}$	σ_k	σ_ϵ	$C_{\epsilon\Gamma}$
0.09	1.44	1.92	1.0	1.3	1.8

The k-ϵ model

The standard k-ϵ model, that was first proposed by [108] in 1974, overcomes some of the difficulties of the exact k-ϵ equations. Developed to improve upon the mixing-length model, it adds two transport variables to the system, namely k the turbulent kinetic energy and ϵ the rate of dissipation of turbulent kinetic energy. This method requires the use of wall functions to reconcile the boundary conditions imposed on a system by solid walls. If we consider the Reynolds stresses, which are neglected in the derivations of the standard SWEs outlined in Section 2.1.1, we gain

$$-\overline{u_i' u_j'} = \mu_t \left(\frac{\partial \bar{u}_i}{\partial x_j} + \frac{\partial \bar{u}_j}{\partial x_i} \right) - \frac{2}{3} k \delta_{ij}, \qquad i, j = 1, 2, 3.$$

The quantification of these stresses, as they contain the fluctuating terms $\bar{u}_i \bar{u}_j$, has provided many solutions. Two-equation models have prevailed as they allow for the accounting of turbulent kinetic energy k and its dissipation rate ϵ in both the current time step and historically. The k-ϵ model was designed to improve on the mixing length for exactly this purpose. By defining

$$k = \frac{1}{2} \left| \boldsymbol{u}' \right| \qquad \epsilon = \frac{\nu_{mol}}{2} \langle \left| \nabla \boldsymbol{u}' + (\nabla \boldsymbol{u}')^T \right|^2 \rangle,$$

where ν_{mol} is the molecular viscosity; the turbulent viscosity may be equated thus

$$\mu_t = \frac{\rho C_\mu k^2}{\epsilon},$$

where, as with many parts of this model, C_μ is dependent on the case and formulation under consideration.

2.1.4 The k-ϵ model for depth-averaged flow

Turbulence modelling was largely designed for 3D flows and turbulence modelling in shallow water flow has developed slowly as often its effects are less pertinent than other assumptions made when using Shallow Water models. There are generally two types of flow effect that are important to consider in shallow water flow. Firstly the vertical effects of turbulence, caused by shear at the top and bottom of the fluid column. Secondly the horizontal effects of flow mixing and boundary effects.

The development of turbulence modelling in shallow water has required the adaptation of the k-ϵ model, notably [62, 128, 198]. This normally involves flow mixing and boundary effects. Unfortunately any vertical effects of turbulence for depth-averaged flow is hard to approximate due to the lack of vertically stratified velocities.

The Vertical effects of flow are well accounted for in the k-ϵ model developed by [108]. The vertical flow effects are usually neglected because in most shallow water flows there is only one velocity considered within the depth of the column. Both the extended [48] and RNG [209] based k-ϵ models only consider these vertical effects Though in recent times there have been some noticeable developments including the WAQUA model developed recently in [75]. Which uses a multiple stacked shallow water layers to provide vertically-stratified velocity data. This is along the lines of the approach adopted in this thesis, though the work here will include transport of quantities between the layers.

The k-ϵ model has been implemented for sediment transport in [205] with great success. The depth-averaged k-ϵ equations read

$$\begin{aligned}
\frac{\partial(Hk)}{\partial t} + \frac{\partial}{\partial x}(Hku) + \frac{\partial}{\partial y}(Hkv) &= \frac{\partial}{\partial x}\left(\frac{H(\nu_t+\nu)}{\sigma_k}\frac{\partial k}{\partial x}\right) + \frac{\partial}{\partial y}\left(\frac{H(\nu_t+\nu)}{\sigma_k}\frac{\partial k}{\partial y}\right) + P_h, \\
\frac{\partial(H\epsilon)}{\partial t} + \frac{\partial}{\partial x}(H\epsilon u) + \frac{\partial}{\partial y}(H\epsilon v) &= \frac{\partial}{\partial x}\left(\frac{H(\nu_t+\nu)}{\sigma_\epsilon}\frac{\partial \epsilon}{\partial x}\right) + \frac{\partial}{\partial y}\left(\frac{H(\nu_t+\nu)}{\sigma_\epsilon}\frac{\partial \epsilon}{\partial y}\right) + P_\epsilon,
\end{aligned}$$

where ν is kinematic viscosity, and P_h and P_ϵ are the source terms which depend on the model formulation and are generally expressed as

$$\begin{aligned} P_h &= P_k + C_B^{-1/2} U_*^3 - H\epsilon, \\ P_\epsilon &= C_{\epsilon 1} \frac{\epsilon}{k} P_k + \frac{1}{H} \left(C_{\epsilon\Gamma} C_{\epsilon 2} C_\mu^{1/2} C_B^{-3/4} U_*^4 \right) - C_{\epsilon 2} H \frac{\epsilon^2}{k}, \end{aligned}$$

where

$$P_k = H\nu_t \left(2 \left(\frac{\partial u}{\partial x} \right)^2 + 2 \left(\frac{\partial v}{\partial y} \right)^2 + \left(\frac{\partial u}{\partial y} + \frac{\partial v}{\partial x} \right)^2 \right),$$

and ν_t is the effective turbulent kinematic viscosity, and U_* is the bed friction velocity which is defined as

$$\nu_t = C_\mu \frac{k^2}{\epsilon}, \qquad U_* = \sqrt{C_B(u^2 + v^2)}.$$

This model relies on several empirical parameters and these are given in Table 2.1.

2.2 Sediment transport in shallow water flows

Sediment can be both eroded and deposited by flowing water. Sediment transport is the process of movement between these two actions. This process alters the morphology of sediment beds. In this body of work concentration is placed on physically-based (numerical rather than statistical) models and the advances made in this area, especially in terms of computational speed. Due to the long-term modelling required for many projects (for example forecasting the scour around a bridge foundations over its lifetime or the silting of an estuary between dredges), any savings in computational speed are to be welcomed.

2.2.1 The characteristics of sediments

Sediments can be categorised as cohesive or non-cohesive, but all have the same general characteristics: diameter (mean diameter) d across the particle, grading (the size distribution) often summarised with d_{10}, d_{90} (where d_{10} represents the diameter of the 10^{th} percentile), density ρ, and porosity Ψ (when in a packed bed). Cohesive sediment is defined as having a significant proportion of clays (or other organic matter) whose electromagnetic properties cause the sediment to bind together and act as a putty, rather than as sand. This category includes silt, clay, and any other organic matter that has gelatinous properties. Cohesive sediments are also able to adsorb pollutants, such as heavy metals and organic chemicals. This characteristic is useful when tracking contamination spills from tailings (mining waste) and other harmful chemical pools. Non-cohesive sediment, which does not have electromagnetic properties, is primarily

---

[1] `https://sites.agu.org/`

Table 2.2: A classification of particles according to the American Geophysical Union[1].

Type of particle	Grading	Cohesive	Diameter d [mm]
Gravel	Very coarse	No	64-32
	Coarse	No	32-16
	Medium	No	16-8
	Fine	No	8-4
	Very fine	No	4-2
Sand	Very coarse	No	2-1
	Coarse	No	1.0-0.5
	Medium	No	0.5-0.25
	Fine	No	0.25-0.125
	Very fine	No	0.125-0.062
Silt	Coarse	No	0.062-0.031
	Medium	No	0.031-0.016
	Fine	No	0.016-0.008
	Very fine	No	0.008-0.004
Clay	Coarse	Yes	0.004-0.002
	Medium	Yes	0.002-0.001
	Fine	Yes	0.0010-0.0005
	Very fine	Yes	0.0050-0.00024

made up of fine and medium grade sands. Table 2.2 shows the classification of soils by size (according to the American Geophysical Union). Particle size is one of the most important characteristics in sediment transport as it directly affects the erosion, deposition, and transport rates. In most models diameter d is used in calculations and is approximated to d_{50}, this helps classify sediments as shown in in Table 2.2. Sediments are classified as follows:

Gravel: is comprised of unconsolidated rock fragments that may or may not have been smoothed by the flow of water or ice. It can be divided into granular (very fine) at $2-4$ mm and pebble gravel $4-64$ mm, as shown in Table 2.2. Two types of gravel are of particular interest:- (i) bank gravel which is found mixed into the sand or clay of river and estuary beds and (ii) creek rock which is found on the bed surface of streams and rivers. This becomes important when studying phenomena like armouring. Note that a typical density for gravel is ~ 1800 kg/m^3.

Sand: is a granular material made up of finely divided rock and/or mineral particles. It is usually composed of silica in the form of quartz or calcium carbonate (aragonite). Sand is normally produced from the grinding down of larger parts, such as gravel, and is typically between $2-0.062$ mm as shown in Table 2.2. Particles of older sand tend to be more spherical in shape, while geologically newer sand is more irregular.

Silt: is also a granular material originating from mineral quartz and feldspar. It is often mixed in with sand and/or clay and it is typically more spherical in shape. Though its size range

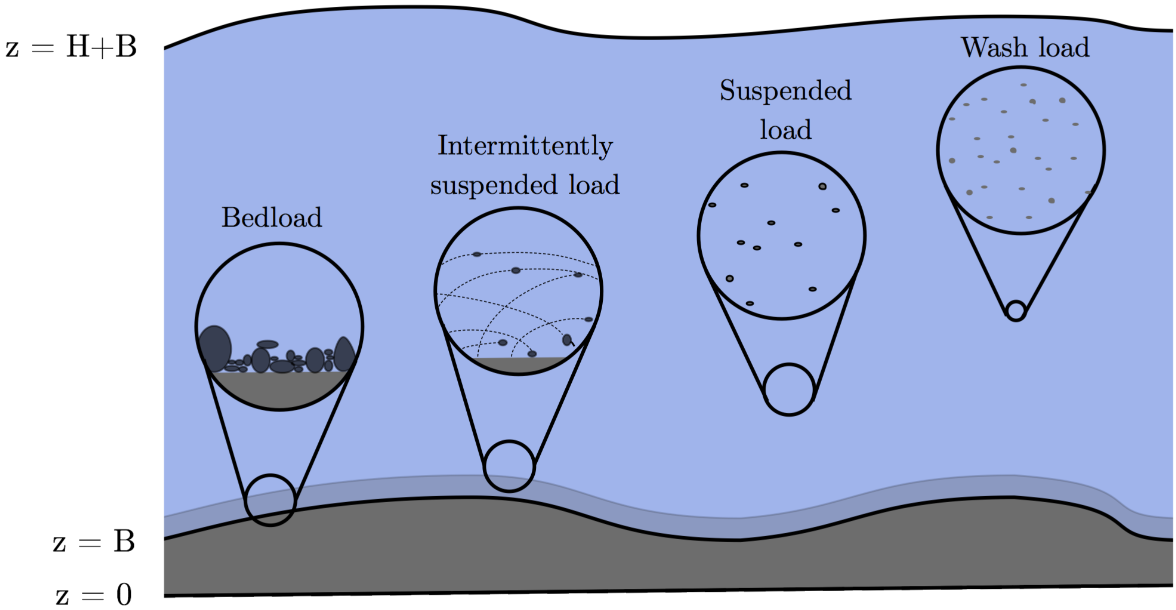

Figure 2.2: Illustration of the four principal modes of sediment transport.

may overlap with clay, according to the Udden-Wentworth scale, it is known not to be cohesive.

Clay: is a very fine-grained natural rock that combines clay minerals with metal oxides and organic matter. This unique composition gives rise to cohesive properties, whereby the clay will become sticky due to the electromagnetic forces between its particles. The clay minerals are the crucial distinguisher between clay and silt. This, together with its water content, gives rise to the plastic nature of clay. Any grain with a composition smaller than 0.004 mm, as in Table 2.2, and with a cohesive mineral make-up is considered clay.

Often in sediment transport modelling, the material being transported is generalised to a single equivalent quantity which does not take into account the sediment mix (or even natural sediment layers). This often causes models to over-estimate erosion and fail to display the correct characteristics of these sediment types. Multi-sediment handling is one of the advances developed in this work. With a better ability to model the complex mixes and properties of sediment, the accuracy of the sediment transport model will be increased.

2.2.2 Modes of sediment transport

In sediment transport, sediment moves in one of four possible ways as shown in Figure 2.2. Each transport category has different interactions with the water causing a diverse range of behaviour.

Wash load: Particles are held in suspension by Brownian motion, which is a random agitation at a molecular level. Wash load particles are impossible to distinguish from the rest of the suspended load with current sampling methods. Wash load is normally uniformly distributed

Table 2.3: Modes of sediment transport and their Rouse numbers [150].

Mode of Transport	Rouse Number
Initiation of motion	$P_R > 7.5$
Bedload	$2.5 < P_R < 7.5$
Intermittently suspended load (50 % suspended)	$1.2 < P_R < 2.5$
Suspended Load	$0.8 < P_R < 1.2$
Wash Load	$P_R < 0.8$

throughout the fluid.

Suspended load: Suspended sediments (mainly silt and sand) are kept in suspension by localised turbulence. Maintaining suspension requires the turbulent (or upward) currents to exceed the settling velocity of the particle. The diameter and concentration of particles tends to vary logarithmically with the height above the bed. Generally, larger sediments cluster at bed height, while finer sediments are more evenly distributed through the water column. This is the most commonly modelled type of sediment transport and is often simulated with erosion and deposition equations. Here, the erosion is characterised with a critical shear stress and deposition with a critical settling velocity.

Intermittently suspended load: This is a subclass between bed and suspended load: partially supported by the bed and partially supported by the fluid. This type of transport is rarely modelled as it can usually be approximated by the in-bedload calculations. However, it is of use in recognising turbulence as, particles too large for suspended load are excited and lifted by turbulent currents and settle slowly.

Bedload: Here, particles tumble along the bed floor and are entirely supported by it. As a rule, bedload is made up of the largest sediments (sand and gravel) that can be mobilised by shear stress acting on the bed. Bedload is often modelled by capacity-limiting sediment transport equations. It can be computed by examining excess shear stress, discharge or stream power.

Rouse Number: is a dimensionless variable used to determine which mode of transport an entrained sediment particle is most likely to be carried in. The Rouse number P_R is defined as [150]

$$P_R = \frac{w_s}{\kappa_{vK} U_*},$$

where w_s is the settling velocity of the sediment (which will be discussed later in this section), the von Karman constant $\kappa_{vK} = 0.4$, and U_* is the bed shear velocity. Table 2.3 shows the approximate Rouse numbers for each mode of transport. In real world situations the exact mode will vary due to turbulence and sediment-to-sediment contact.

2.2.3 Modelling erosion in sediment transport problems

Erosion is the process by which bed material is stripped away by a fluid moving over the surface of the bed. A unifying formulation of both erosion and deposition has still not been found. As a result, various different models exist. The analysis performed by White [202] gives a simplistic view of erosion which assumes that particles will move when their submerged weight is exceeded by a force. Examination of the top particle is shown in Figure 2.3.

The critical shear stress τ_{cr} for this example is assumed to be

$$\tau_{cr} = \frac{\eta_p}{\tan\phi} g(\rho_s - \rho_w)d,$$

where $\eta_p = n_s d^2$ is the packing coefficient, n_s is the number of particles per unit area, ρ_s is the density of the sediment, ρ_w is the density of the water, d is the diameter of the particle, and ϕ is the contact angle. This approach is useful for a basic understanding but it greatly oversimplifies the problem as other forces are considered. The principal forces acting to lift the sediment particles are:

1. **Shear Stress:** the force (τ/n_s) as applied by the water to the particles at rest. This is considered the most important force acting on the particles of sediment as, from a mechanical standpoint, it approximates many of the others.

2. **Impact Forces:** the transfer of momentum from the column of water upstream to the particles. This force is nearly impossible to calculate as it depends on the mean speed of the water, the area presented by the particles and the density of the fluid, though it has been investigated in [133]. It is one of the principal causes of disparity between theoretical approaches and experimental data.

3. **Lift Forces:** these are mainly comprised of three effects: (i) buoyancy, (ii) vertical velocity-gradient pressure forces (as shown in Figure 2.4) caused by the pressure of arrested water creating a pressure gradient at the base of the particles, and (iii) upward turbulence (eddying forces) formed by the profile of the grains creating eddies behind the particles and effectively lifting them.

Opposing the erosion of the particles are many forces and effects that add to the inertia of the sediment. The prominent ones are:

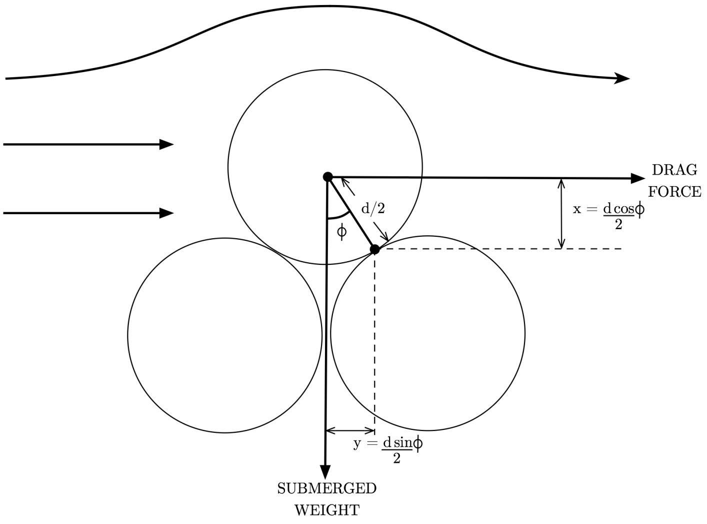

Figure 2.3: A typical sediment particle under water flow considered in [202].

1. **Submerged weight of the grain:** generally considered the most important factor in erosion and deposition.

2. **Armouring:** as real world sediments are non-uniform in size there is a size distribution in the bed. Larger sediments left on bed surface require greater fluid velocities in order to be moved and consequently protect smaller sediments under them from scour. These larger sediments build up at the surface of the bed over time.

3. **Packing:** frictional forces caused by well-packed beds where voids between larger particles are filled with smaller particles. This packing is not accounted for in the analysis conducted by White, but is considered by Shields later in this section.

4. **Grain fabric effects:** over time particles will organise themselves into interlocking structures. This is caused by the non-spherical nature of most sediment types, where odd and elongated shapes come together to form an imbrication pattern. This configuration of particles makes them hard to shift.

5. **Adhesion forces:** (cohesive sediments only) these are the electromagnetic effects that are seen in clay-based beds, where particles are attracted to each other and thereby less mobile.

6. **Organic mats:** algae or slime that build up over time in conditions of low flow can be hard to break down as they are comprised of interlocking cells and organic chains. This organic matter can also cause particles to bind together when in the flow.

These extra forces and effects add too much complexity for models to quantify from basic

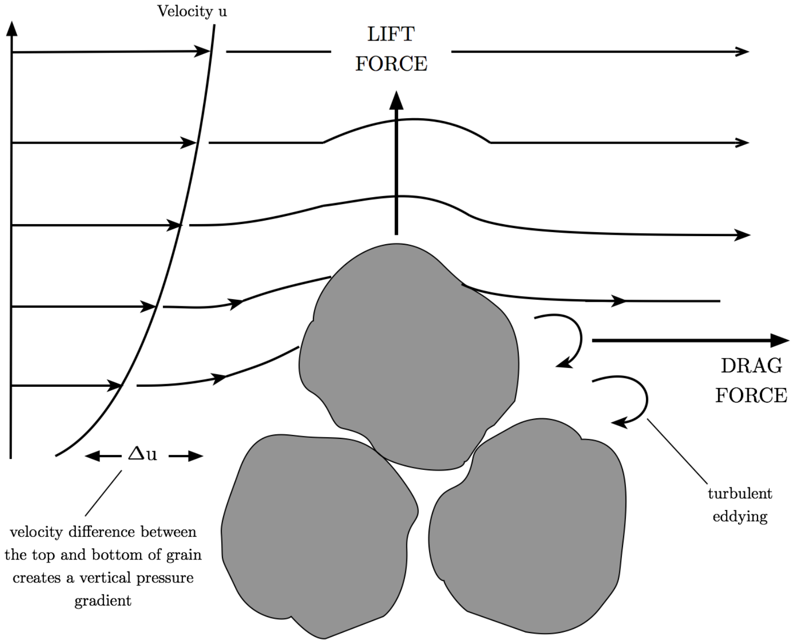

Figure 2.4: Typical sediment particles under water flow.

principles. Thus, a semi-empirical approach is almost always adopted. The most common semi-theoretical analysis for the initiation of motion is the Shields criterion. Proposed in 1936 and reported in [160], it was the first use of semi-theoretical analysis in sediment transport. Shields related the dimensionless shear stress τ_* to the critical shear stress τ_{cr}

$$\tau_* = \frac{\tau_{cr}}{g(\rho_s - \rho_w)d},$$

to the dimensionless particle Reynolds number (originally attributed to [171])

$$Re_p = \frac{U_p d}{\nu},$$

where U_p is the characteristic particle velocity, and ν is the kinematic viscosity. This allowed Shields to generate one of the earliest sediment motion graphs, shown in Figure 2.5, which is still in use today. This plot, whilst very useful, has a number of limitations as it only covered grains of small sizes over a limited range of Reynolds numbers. Shields also noted that the initiation of motion was not always full entrainment but often merely the formation of ripples. As a consequence, further work was required to refine the relationships. This has been studied in [32, 135, 186] amongst others. These, together with many other bodies of work over the years, have refined and modified the Shields diagram as shown in Figure 2.6.

---

[2] `https://ascelibrary.org/doi/book/10.1061/9780784408230`

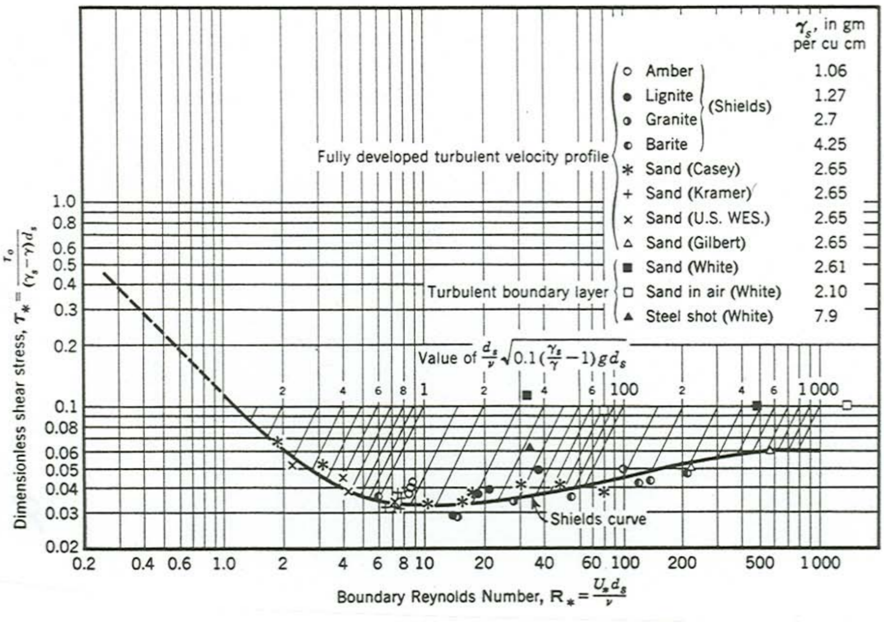

Figure 2.5: A Shields diagram courtesy of the American Society of Civil Engineers[2] [190].

While the modified Shields parameter is very useful for predicting sediment entrainment, it still does not accurately predict real world situations. Consequently, the Shields parameter is often used in combination with other empirical formulae to model a more realistic erosion function that compensates for varying soil properties.

2.2.4 Modelling deposition in sediment transport problems

Deposition occurs when a flow of water transporting sediment no longer has the required conditions (turbulence and/or velocity) to maintain the particles in suspension or motion. Sediment will then move to the bottom of the water column and settle on the bed. Whilst deposition is less complex to model than erosion, simulating this phenomenon still presents challenges. The settling velocity, the terminal speed at which a particle will settle in water, is used in most empirical formulae that deal with deposition. Assuming a spherical particle, the settling velocity ω is calculated as

$$\omega = \frac{g(\rho_s - \rho_w)}{\mu} d^2,$$

where μ is the viscosity, ρ_w is the density of the water, ρ_s is the density of the particle, g is acceleration due to gravity, and d is the diameter of the particle. This formula, presented in [151], is useful but fails to take into account fluid speed around the particle. A hindered

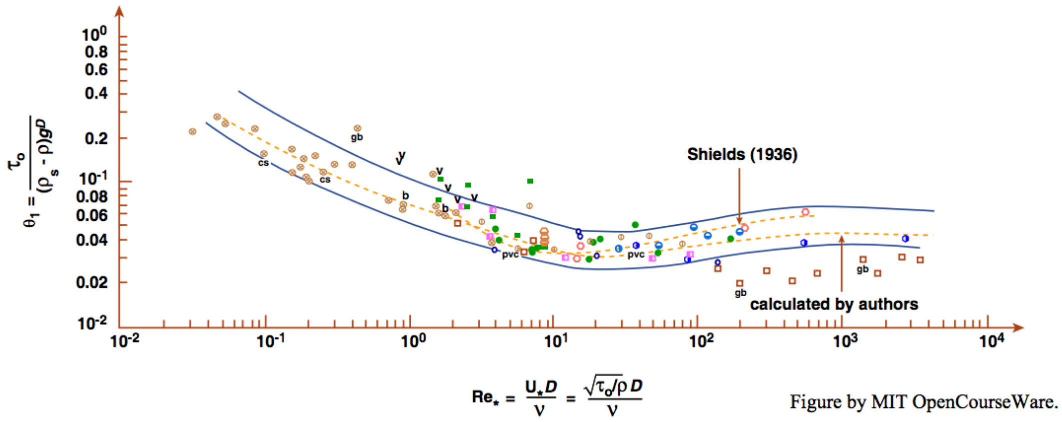

Figure by MIT OpenCourseWare.

Figure 2.6: Updated Shields diagram courtesy of Michigan Institute of Technology[3].

settling velocity ω_s can be calculated using

$$\omega_s = \frac{\sqrt{\frac{2}{3} g \rho_w (\rho_s - \rho_w) d^3 + 36\mu^2} - 6\mu}{\rho_w d}. \tag{2.2.6}$$

This considers the friction between the sediment particle and the fluid, but does not allow for the partial momentum exchange that occurs as the fluid deviates around the particle. The impact law settling velocity $\omega_{s,i}$ presents a solution for this

$$\omega_{s,i} = \sqrt{\frac{4}{3} \frac{1}{C_D} g d \left(\frac{\rho_s - \rho_w}{\rho_w} \right)},$$

where C_D is the drag coefficient. A lack of experimental data has resulted in equation (2.2.6) becoming a common formula for erosion and deposition. However, its limited scope does not allow for other effects, such as cohesive sediment flocculation (where two or more clay particles combine spontaneously due to their electromagnetic attraction) forming a larger particle or floc. Thus, when possible experimental data is used to define the settling velocity.

2.2.5 Equations for sediment transport

Recent work has focussed on developing methods and models for sediment transport, producing an array of techniques. Consequently, there is now a variety of spatial and temporal permutations in 1D, 2D, and 3D models. For a 2D shallow water model a species conservation equation is generally employed

$$\frac{\partial (Hc)}{\partial t} + \frac{\partial (Huc)}{\partial x} + \frac{\partial (Hvc)}{\partial y} = E - D, \tag{2.2.7}$$

---

[3] `https://doi.org/10.1111/j.1365-3091.1977.tb00136.x`

Table 2.4: Some of the explicit empirical equations for the Shields diagram.

Reference	Equations developed
Brownlie [32]	$\tau_{cr} = 0.22{R_b}^{-0.6} + 0.06\exp(-17.77{R_b}^{-0.6})$ where $R_d = \dfrac{d(\Delta g d)^{0.5}}{\nu}$
Van Rijn [186]	$\tau_c(D_* \leqslant 4) = 0.24/D_*$ $\tau_{cr}(4 < D_* \leqslant 10) = 0.14/D_*^{0.64}$ $\tau_{cr}(10 < D_* \leqslant 20) = 0.04/D_*^{0.1}$ $\tau_{cr}(20 < D_* \leqslant 150) = 0.013/D_*^{0.29}$ $\tau_{cr}(D_* > 150) = 0.055$ where $D_* = d\left(\dfrac{\Delta g}{\nu^2}\right)^{1/3}$
Soulsby and Whitehouse [167]	$\tau_{cr} = 0.24/D_* + 0.055[1 - \exp(-0.02D_*)]$
Paphitis [135]	$\tau_{cr}(10^{-2} < R_* \leqslant 10^4) = 0.273/(1 + 1.2D_*)$ $+0.046[1 - 0.57\exp(-0.02D_*)]$

where erosion rate is denoted as E, the deposition rate as D, and where c is the depth-averaged concentration, such that

$$c = \frac{\rho - \rho_w}{\rho_s - \rho},$$

where ρ is the mixture density, ρ_s is the sediment density, and ρ_w is the density of water. This approach does not consider bedload separately. The following source terms are added to the SWE equations to account for the effects of the entrained sediment.

$$\begin{pmatrix} \dfrac{E - D}{1 - \varPsi} \\ -\dfrac{(\rho_s - \rho_w)gH^2}{2\rho}\dfrac{\partial c}{\partial x} - \dfrac{(\rho_0 - \rho)(E - D)u}{\rho(1 - \varPsi)} \\ -\dfrac{(\rho_s - \rho_w)gH^2}{2\rho}\dfrac{\partial c}{\partial y} - \dfrac{(\rho_0 - \rho)(E - D)v}{\rho(1 - \varPsi)} \end{pmatrix},$$

where $\varPsi$ is the porosity of the sediment. Methods and notation for describing the modes of transport vary in the literature. Total sediment transport can be represented as q_T, this solid transport rate can also be divided further into

$$q_{\mathrm{T}} = q_s + q_b,$$

where q_s is the suspended sediment load and q_b is the bedload. The need for multiple modes of sediment transport stems from the SWEs formulation that gives only one value for fluid speed. This formulation cannot take into account the slower moving bed level flow. This study is addresses this problem with a multilayer formulation that can simulate the bedload and the suspended sediment by having multiple vertically stratified fluid speeds. Sediment entrainment models (of which some verge on transport models) are categorised helpfully into two types: empirical and hybrid models [134].

Empiric equations for entrainment: empirically derived models for entrainment rates can be effective, however their scope is limited to simulation of the conditions and sediment types they were based on. For the sake of brevity only a few of these are detailed below, for a more complete list we refer to [134].

du Boys formula [61] : this early sediment flux model was detailed by du Boys in 1879. Although now largely out-dated, features of the formula are still prevalent in later models. This method is notable as it divides the upper stream into layers by depth h, with M being the number of layers. Balancing the shear stress in each layer of the stream produces

$$M = \frac{\tau_l}{\tau_u},$$

where τ_l is the shear stress at the lower side and τ_u is the shear stress on the upper side. The velocity field decreases with depth, and setting $u^* = \max(u)$ gives

$$q_{\mathrm{T}} = \left(\frac{hu^*}{2\tau_u^2}\right)\tau_l(\tau_l - \tau_u).$$

Exner model [105]: in 1925, Exner simplified his original conservation sediment equation, with the following observations: (i) the mass flow rate is constant (ii) the waves are lower than the water level and (iii) the fluid flux is less than fluid velocity. Thus the Exner bed equation model becomes only a function of bed slope

$$(1 - \Psi)\frac{\partial B}{\partial t} + \frac{\partial Q(B)}{\partial x} = 0,$$

where

$$Q(B) = \frac{\alpha H u}{H - B},$$

where α is the ratio between fluid speed and sediment speed. Further simplifying the equation, using a non-dimensional seabed slope, produces $\bar{B} = \frac{B}{D_0}$, where D_0 is the typical length of the water scale, thus

$$\frac{\partial \bar{B}}{\partial t} + C_c \frac{\partial (\bar{B})}{\partial x} = 0,$$

where C_c ia a non-dimensional migration speed for the bed

$$C_c = \frac{m}{(1 - \bar{n}_m)^{m+1}} \frac{A_s^*}{1 - \Psi} Fr \ ,$$

where A_s^* and m are problem dependant variables, V_0 is a velocity-scale, n_m is the Mannings coefficient, Ψ is the porosity, and Fr is the Froude number expressed as

$$Fr = \frac{V_0}{\sqrt{g D_0}}.$$

One of the limitations is the use of A_s^* and m, which are difficult to determine and often lead to error when not correctly calibrated. This method is still used as it is simple to implement and accurate for some cases.

Meyer-Peter-Muller (MPM) model [122]: in 1948, following extensive experimentation, Meyer-Peter and Muller devised the follow relation between sediment flux and shear stress

$$q_b = \sqrt{\left(\frac{\rho_s - \rho}{\rho}\right) g \ d_{50}^3} \ 8 \ \mathrm{sgn}(u) \big(\tau - \tau_{cr}\big)^{3/2},$$

where τ is the bed level non-dimensional shear stress, and τ_{cr} is the critical bed level non-dimensional shear stress. Designed for use in rivers with abundant creek rock, it is still used today for calculating bedload (though improvements have been added over the years). However, if modelling sediment in suspension, it still requires two modes for sediment transport.

Grass model [78] : develops relations for both suspended and bedloads (q_s and q_b), using a non-linear expression for q_s

$$q_s = \beta u^m \ ,$$

where β and m are empirical coefficients. The model does not use Shields theory for the bedload relation such that

$$q_b = A_g \frac{Q}{H} \left|\left|\frac{Q}{H}\right|\right|^{m_g - 1} ,$$

where A_g and m_g are experimentally determined coefficients, and Q is the volumetric flow rate. This relation is interesting as it also contains both an exponent and a linear coefficient, that can easily be used with experimentation to model sediment entrainment. This model was largely designed for sands, for which it provides good results, beyond that it requires further modification.

Semi-theoretical equations for entrainment: hybrid models expand on empirical models by including theoretical elements. This decreases the limitations placed on the simulations by the original data. One of the main advantages is the separation of sediment transport as an individual function.

Einstein model [64]: proposed a new approach to sediment transport, using probabilities based on work from the Mississippi basin. This probabilistic approach means that the bed and suspended loads are considered as one. Avoiding Shields theory, it considers the ratio between particles entering and leaving a domain, the chance of them settling, and the probabilities that sediment transport is initiated. Thus

$$q_{\mathrm{T}} = \Phi' \frac{I_s}{I_b} \rho_s g \sqrt{\left(\frac{\rho_s - \rho}{\rho}\right) g\ d_{50}^3}\ . \tag{2.2.8}$$

The author uses various relations to form his method, key amongst them is the term Φ', which is supposed to be constant for a given particle size (graphs of 'transport-intensity functions' are produced to find the required values). In equation (2.2.8), I_s is the portion of particles d_i which passes over the area considered, and I_b is the percentage of particles detaching from it. This approach is still used for discrete sediment grain sizes, under the assumption that each particle moves independently.

Engelund-Hansen model [65]: this formula was derived from energy balance equations and is designed to look at tidal and wave currents. It is expressed as

$$q_{\mathrm{T}} = 0.05 \hat{u} C_\tau \frac{\tau_{\mathrm{B},c}^2}{\left(\frac{\rho_s}{\rho} - 1\right)^2 d_{50} \rho^2 g^{5/2}} \left(1 + \frac{1}{2}\left(\xi \frac{U_{wave}}{\hat{u}}\right)^2\right),$$

where C_τ is the linear coefficient relating shear stress and the square of velocity, the average velocity of the water is $\hat{u}$, U_{wave} is the velocity of the waves, shear stress due only to current effect is $\tau_{\mathrm{B},c}$, and ξ is a dampening coefficient. The shear stress due to current and wave effect is

$$\tau_{\mathrm{B},wc} = \tau_{\mathrm{B},c} \left(1 + \frac{1}{2}\left(\xi \frac{U_{wave}}{\hat{u}}\right)^2\right).$$

While this relation is useful due to the reliance on wave factors, it goes beyond the purview of this investigation.

Bijker model [27]: this formula also uses a probabilistic approach, though sediment load is divided into bed and suspended load. It is designed for coastal regions with coefficients for wave structures and shapes. Hence

$$q_b = A d_{50} \frac{\bar{u}}{C_\tau} \sqrt{g} \exp \left(\frac{-0.27(\frac{\rho_s}{\rho} - 1) d_{50} \rho g}{\beta_{wave} \tau_{\mathrm{B},wc}} \right),$$

where A and β_{wave} are coefficients depending on waves type, and β_w is conditional on wave type and sediment properties [18]. The bedload is assumed to be a thin layer resting on the bed surface with a constant concentration. The suspended sediment may be expressed using Einstein integrals I_1 and I_2 as

$$q_s = 1.83 q_b \left(I_1 \ln \left(\frac{33H}{\kappa_r} \right) + I_2 \right),$$

where κ_r is a bed roughness coefficient.

Van Rijn model [185,187,188]: as one of the most popular models for sediment transport, the Van Rijn model includes the Shields parameter such that

$$q_b = \sqrt{\left(\frac{\rho_s}{\rho} \right) g d_{50}^3} \frac{0.005}{\beta_d^{1.7}} \left(\frac{d_{50}}{H} \right)^{0.2} \left(\sqrt{\tau} - \sqrt{\tau_{cr}} \right)^{2.4} \sqrt{\tau},$$

where β_d is an empirically calibrated value. This formulation is easy to implement and has been proven to be accurate [18, 41]. Suspended sediment can be expressed as

$$q_s = c u_{av} H F,$$

where u_{av} is a mean velocity in the field, c is the depth-averaged concentration, and F is an empirical coefficient [33]. These are some of the most popular formulae for sediment transport. Although they consider the velocity of the fluid flow, as shown, the lack of stratified velocities does lead to the need for a bedload calculation which is inefficient and makes it less accurate than some 3D formulations. This problem is addressed by vertically stratified horizontal velocities used later in this study.

2.3 Overview of numerical methods for hyperbolic systems of conservation laws

Numerical methods for the solution of Partial Differential Equations (PDEs) including the SWEs, have been extensively studied, going back to Euler [67] and his system for ordinary differential equations. Many methods exist for the solution of PDEs, including the extensive work done by [52, 74]. Such developments have been aided by the advent of modern computing, leading to a wide range of numerical solutions for PDEs. The systems used in this thesis are hyperbolic (unless otherwise stated) and the solutions of hyperbolic equations are wave-like. If there is a perturbation in a system, it will incur a delay in its transmission effects, *i.e.* there is a transmission speed (in the SWEs, this is wave speed). This attribute distinguishes hyperbolic systems from elliptic and parabolic systems.

A set of equations is said to be strictly hyperbolic if the Jacobian of its system has a number of distinct real eigenvalues and is diagonalizable. There are two crucial properties of a hyperbolic system [175] that any accurate numerical scheme should capture: first, there is an inherent direction of wave propagation and, secondly, there can be discontinuities in the solutions.

2.3.1 Well-established approximate methods

There are many methods for solving PDEs, five of the principal ones are detailed here. The differences outlined below show why the proposed method is chosen to solve the SWEs.

Finite Difference Method (FDM): The FDM approximates the PDEs and then solves them [79]. The domain is regularly discretised into a grid (with the appropriate number of dimensions). The partial derivatives are approximated using Taylor expansions. It can be solved implicitly, explicitly, or using a Crank-Nicolson scheme. This method is very quick to set up and simple to run (with a lower computational expense than other methods), though the requirement for a regular grid makes it unsuitable for many real world domains (due to the complications incurred when modelling complex geometry). As it approximates the differential equations, the formulation is not conservative, often making it unsuitable for problems in CFD (it is however often used in astrology and meteorology).

Finite Element Method (FEM): The FEM formulates the problem into a set of algebraic equations, and yields approximate values of the unknowns of the system at a number of points over the domain [220]. When solving, the problem is divided into simpler parts called finite elements. The simplified equations are then assembled into larger systems of sparse matrix equations that model the entire system. The FEM works well for diffusion systems and is generally stable. It is usually convergent, as the variational forms are normally consistent with the governing equations, and widely used for mechanical problems. Although it is often use complications arise when considering domains with irregular boundaries. It can be made conservative, but these formulations are often unstable. Despite this there has been some very powerful code developed in this area including TELEMAC[4]. Discontinuous Galerkin methods

---

[4] `www.opentelemac.org/index.php/publications`

have also been adapted to offer new advantages to FEM models.

Finite Volume Method (FVM): The FVM breaks the domain down into cells on a structured or unstructured mesh [126]. The FVM integrates the PDEs over the small volume of each cell in the mesh. Divergence terms are evaluated as fluxes on the surfaces of each cell and, as the flux exiting one cell into the adjacent is identical, the method is conservative. The FVM is quick to implement and simple to program, like the FDM, but it is also more efficient than the FEM. Its major strength is that it only needs to evaluate fluxes for the cell boundaries; this is very advantageous for non-linear problems (e.g. conservation laws in transport problems). The FVM is now widely used for CFD problems, due to its simplicity, accuracy, ability to compute irregular boundaries, and conservative nature.

Method of Characteristics (MoC): The MoC reduces PDEs to a group of ordinary differential equations [53]. Combined with the solution, it can be integrated on a suitable hyper surface. This method requires the original problem to be stated analytically. The MoC suffers from slow convergence and is often cumbersome in capturing shock waves in complex flows. Consequently, the MoC has largely been superseded by other methods, like the FVM. That said, it is used by some in the predictor stages of more complex solutions as it is suitable for obtaining an initial predictor stage solutions. Due to its slow nature, lack of conservation and complications around boundary conditions, this method is rarely used in CFD.

Spectral Methods: Spectral Methods are very similar to FEM, in that they break the differential (or partial differential) equations into a set of basis functions that approximate the governing equations [214]. This is often achieved with a Fourier series and consequently uses a set of trigonometric functions. The main difference between this method and FEM is that the functions used are non-zero over the whole domain, rather than only small areas. The Spectral Method has the advantage of being quick, especially when utilising the fast Fourier transform, but the transformation and multiplication can cause aliasing problems. It is also difficult to apply to non-linear problems with complex boundary conditions or geometries. For these reasons (lack of conservation, poor shock capture and model limitations), it is infrequently used in CFD.

2.3.2 Hyperbolic systems of conservation laws

As shown, the SWEs (and additional governing equations for concentration, turbulence modelling and bed morphology) are conservation laws and fall into the class of hyperbolic PDEs that can be written as

$$\frac{\partial \mathbf{W}}{\partial t} + \nabla \cdot \mathbf{H}(\mathbf{W}) = 0, \tag{2.3.9}$$

where $\mathbf{W}$ is a set of conserved quantities, where $\mathbf{H}(\mathbf{W})$ is a vector containing the fluxes of the system such that $\mathbf{H}(\mathbf{W}) = (\mathbf{F}_1(\mathbf{W}), \ldots, (\mathbf{F}_R(\mathbf{W}))$ and where there are R number of dimensions in the system. $\mathbf{F}_\alpha(\mathbf{W})$ is the physical fluxes of the conserved quantities in the αth dimension (where $\alpha \in (1, \ldots, R)$). Equation (2.3.9) is a conservation law defined by the arbitrary domain Ω with smooth boundary $\partial\Omega$, it is possible to derive the integral of the equation using divergence theorem which is

$$\frac{d}{dt}\int_{\Omega} \mathbf{W}\, dA + \int_{\partial\Omega} \mathbf{H}(\mathbf{W})\mathbf{n}\, d\sigma = 0, \tag{2.3.10}$$

where $\mathbf{n}$ is a vector of the unit normal vectors to the boundaries $\partial\Omega$. The equation (2.3.10) states that the variation in time of the conserved quantities is solely dependant on the flux at the boundaries. It is worth noting that equation (2.3.9) has no source terms as, due to the nature of source terms, these can and often are treated in a separate step or part of the solver in order to accelerate simulations.

Both equations represent the conservation laws; the difference lies in the solutions they can exhibit. The equation (2.3.9) is known as the strong form, and equation (2.3.10) is the integral form of the conservation law. This form is able to capture discontinuities; these discontinuities give rise to the Riemann problem and can exist in the global sense as shock or rarefaction waves in the solution or, in the case of the FVM, more locally at the interfaces between cells.

2.3.3 Definition of the Riemann problem

The Riemann problem exists in hyperbolic PDEs where there is piecewise data. For conservation laws in 1D with initial piecewise data, the problem can be expressed as

$$\begin{aligned} \frac{\partial \mathbf{W}}{\partial t} + \frac{\partial \mathbf{F}(\mathbf{W})}{\partial x} &= 0, \\ \mathbf{W}(0,x) &= \begin{cases} \mathbf{W}^l, & \text{if } x\ > 0, \\ \mathbf{W}^r, & \text{if } x\ < 0, \end{cases} \end{aligned}$$

where $\mathbf{W}^l$ is the left-hand state and $\mathbf{W}^r$ is the right-hand state of conserved variables about the point $x = 0$. This problem exists in a local manner in the FVM, as the FVM gives one value over the entire cell, meaning there is a jump or discontinuity between it and the neighbouring cells. As fluid may be moving at different speeds and in different directions, this discontinuity causes problems when calculating fluxes between two cells and estimating the values at the interface.

The Riemann problem is one of the main sources of complication in the FVM [126], and much work is being done to solve it either exactly or approximately [179]. Three types of Riemann problems exist: shocks, rarefactions, and contact discontinuities. These discontinuities

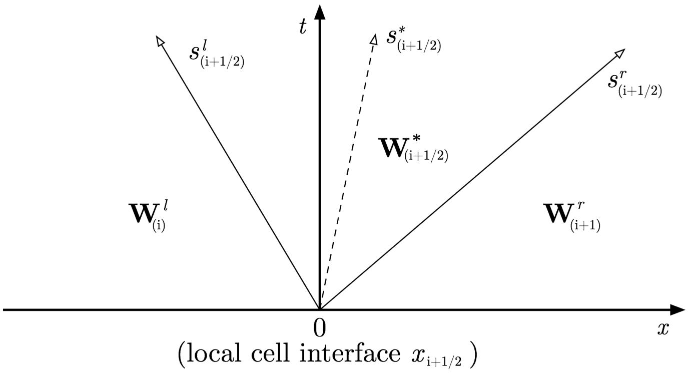

Figure 2.7: Wave diagram for the structure of the Riemann problem.

are normally seen in fluids as variations of pressure and velocity. A shock wave is where density increases and velocity decreases very suddenly. For a fluid with a free-surface, similar to the SWEs, this can be a variation in height. A rarefaction wave occurs when a fluid moves faster and becomes less dense. Contact discontinuities are interfaces that separate zones of different densities or heights, but there is no flow across these interfaces.

This problem can have three quantifiable waves as shown in Figure 2.7. The left and right waves are either shocks or rarefaction waves, while the middle wave is always a contact discontinuity. All three must be considered when selecting the correct method to estimate interface values. In this type of study, the Riemann problem is usually solved with either a Roe approximate Riemann solver [147] or the Harten-Lax-van Leer-Contact (HLLC) [86] type approximate Riemann solver.

2.3.4 Formulation of finite volume methods

In this section, the FVM is outlined and some of the characteristics that arise from its use are discussed. The important steps that are required to build a FVM formulation are detailed in this section.

Space discretisation: The first step is to discretise the domain into a number of cells (control volumes) which can be in the form of either structured or unstructured grids. Structured grids have a discernible pattern that is indexable: neighbouring cells can be found by adding or subtracting one from the index. Unstructured grids, however, have no indexable pattern and therefore when, implementing them in a code, pointers containing neighbouring cell numbers must be stored. This makes unstructured grids slower to compute, as the index of structured grids makes for faster algorithms. For simple problems like aerofoils or isolated wings, structured grids are generally more accurate, but for more complex flows the adaptivity of unstructured grids allows for greater accuracy. Crucially, unstructured girds allow for more complex geometry

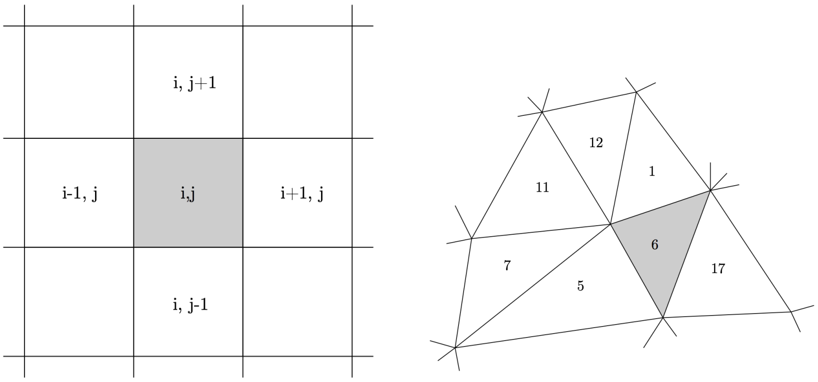

Figure 2.8: Examples of structured and unstructured meshes: a 2D Cartesian structured mesh (left) and a 2D triangular unstructured mesh (right).

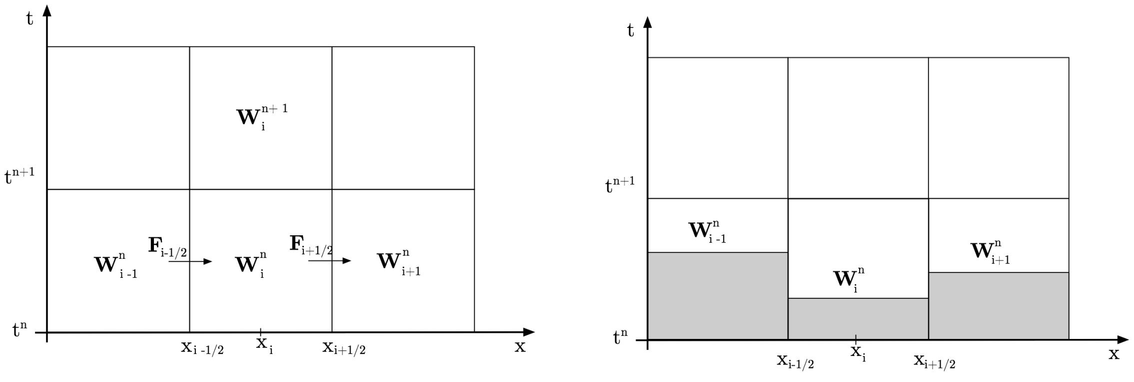

Figure 2.9: A typical 1D grid of cells showing fluxes (left) and a depiction of the 1D local Riemann problem (right).

and are consequently more useful for real world problems, where the domain can rarely be divided accurately into a structured grid. Figure 2.8 depicts example meshes, where the indexing problem for unstructured grids can be seen. Element 6 is surrounded by elements $1, 5, 17$, while in the structured grid any element like i, j can easily index to its neighbours. A Cartesian grid is not the only type of structured mesh, indeed elements do not have to be of regular size to be structured (though this does introduce further complications when implementing the method). Rectilinear and curvilinear grids can also be used to produce structured meshes. It is also possible to have vertex centred cells, where the control volume is centred around a vertex point rather than the centre of a volume bounded by vertex to vertex points. This method has more complicated volume shapes during calculation but can ease post-processing visualisation techniques.

Time discretisation: The FVM requires the discretisation of time into discrete time-steps. This is relatively straight forward, but it should be noted that various methods of calculation (as seen later when schemes are discussed) use different approaches to achieve the solution at time t^{n+1}, given time t^n. Time is divided into these discrete time-steps (t^{n+1} and t^n) such that $\Delta t = t^{n+1} - t^n$. Time-stepping schemes can either be explicit (using only date from the current time-step to solve for the next) or implicit (where data from both the next and current time-step are used to compute the next time-step) [79]. In this work only explicit time-steps are used, as they are easy to implement and parallelize, and have a lower computational cost per time-step. Implicit schemes are avoided as they have higher computational cost and are hard to parallelize. One of the great challenges for explicit schemes is steady state or stationary flows. Thus this is one of the standard tests used to evaluate the solvers in this study.

Integrating the conservation equations

Once the basic discretisation has been defined, we are able to integrate the system under study. We begin by integrating our system using the discretisation shown in Figure 2.9. The governing equations may be written as

$$\frac{\partial \mathbf{W}}{\partial t} + \frac{\partial \mathbf{F}(\mathbf{W})}{\partial x} = 0 \ . \tag{2.3.11}$$

In Figure 2.9, $x_{i-1/2} = i\Delta x$ and $x_i = (i + 1/2)\Delta x$ is the centre of the control volume, such that we can define the cell average as

$$\mathbf{W}_i^n = \frac{1}{\Delta x} \int_{x_{i-1/2}}^{x_{i+1/2}} \mathbf{W}(t^n x) \ dx \ . \tag{2.3.12}$$

In this way an average for the cell is obtained. If it is assumed that the cell average of the conserved variables $\mathbf{W}_i^n$ at time-step t^n are known, then the conservation equations can be integrated in space and time over the domain $[x_{i-1/2}, x_{i+1/2}] \ \times \ [t^n, t^{n+1}]$, thus

$$\int_{t^n}^{t^{n+1}} \int_{x_{i-1/2}}^{x_{i+1/2}} \frac{\partial \mathbf{W}}{\partial t} \ dxdt + \int_{t^n}^{t^{n+1}} \int_{x_{i-1/2}}^{x_{i+1/2}} \frac{\partial \mathbf{F}(\mathbf{W})}{\partial x} \ dxdt = 0 \ .$$

This yields

$$\mathbf{W}_i^{n+1} - \mathbf{W}_i^n + \frac{1}{\Delta x} \left[\int_{t^n}^{t^{n+1}} \mathbf{F}\big(\mathbf{W}(x_{i+1/2}, t)\big) \ dt - \int_{t^n}^{t^{n+1}} \mathbf{F}\big(\mathbf{W}(x_{i-1/2}, t)\big) \ dt \right] = 0 \ .$$

As the cell averages defined in (2.3.12) create a Riemann problem at the interface, making the evaluation of $\mathbf{W}(x_{i\pm,1/2}, t)$ complex. Thus we define an approximation for the average flux along $x = x_{i-1/2}$ such that

$$\boldsymbol{\mathcal{F}}_{i-1/2}(t) \approx \mathbf{F}\big(\mathbf{W}(x_{i-1/2}, t)\big) \ dt.$$

As the time integration in (2.3.13) still poses a problem, we require a method of time-stepping. This can either be implicit (requiring only values from the current time-step) or explicit (where values from the next time-step are required). If we employ the first-order accurate forward Euler method, where fluxes are estimated using the initial state $\mathbf{W}^n$, we achieve

$$\mathbf{W}_i^{n+1} = \mathbf{W}_i^n - \frac{\Delta t}{\Delta x}\left(\boldsymbol{\mathcal{F}}_{i+1/2}(t^n) - \boldsymbol{\mathcal{F}}_{i-1/2}(t^n)\right) .$$

In the field of shallow water flow, a second-order accuracy is generally a minimum.

Higher order time-stepping procedures for FVM

One of the more complex time-stepping procedures is the MUSCL-Hancock scheme [184], which is second-order accurate in time and uses a two-step predictor-corrector method. Again we consider the 1D domain shown in Figure 2.9. The non-conservative predictor step uses a intermediate value at $t^{n+1/2} = t^n + \frac{1}{2}\Delta t$, such that

$$\mathbf{W}^{n+1/2} = \mathbf{W}^n - \frac{\Delta t}{2}\left(\boldsymbol{\mathcal{F}}_{i+1/2}(t^n) - \boldsymbol{\mathcal{F}}_{i+1/2}(t^n)\right),$$

this step allows us to calculated the left and right-hand Riemann states $\mathbf{W}^{l,n+1/2}$ and $\mathbf{W}^{r,n+1/2}$. Thus we are able to create a Riemann solver such that

$$\mathbf{W}^{n+1} = \mathbf{W}^n - \Delta t\left(\boldsymbol{\mathcal{F}}_{i+1/2}^{MUSCL} - \boldsymbol{\mathcal{F}}_{i-1/2}^{MUSCL}\right),$$

where the fluxes are calculated using the approximation

$$\boldsymbol{\mathcal{F}}_{i+1/2}^{MUSCL} = \boldsymbol{\mathcal{F}}\left(\mathbf{W}_{i+1/2}^{l,n+1/2}, \mathbf{W}_{i+1/2}^{r,n+1/2}\right).$$

Another popular group of time-stepping schemes are the Runge-Kutta family [107, 152]. The second-order two-step scheme can be written as

$$\begin{aligned}
\mathbf{W}^* &= \mathbf{W}^n + \Delta t\boldsymbol{\mathcal{L}}(\mathbf{W}^n), \\
\mathbf{W}^{n+1} &= \frac{1}{2}\mathbf{W}^n + \frac{1}{2}\mathbf{W}^* + \frac{\Delta t}{2}\boldsymbol{\mathcal{L}}(\mathbf{W}^*),
\end{aligned}$$

where $\boldsymbol{\mathcal{L}}(\mathbf{W}^n)$ is an operator including flux and source terms. For our approximated 1D system (2.3.11) this means that

$$\boldsymbol{\mathcal{L}}(\mathbf{W}^n) = \frac{1}{\Delta x}\left(\boldsymbol{\mathcal{F}}_{i+1/2}(t^n) - \boldsymbol{\mathcal{F}}_{i+1/2}(t^n)\right).$$

This two-stage method is second-order accurate, but is prone to the creation of spurious oscillations (*i.e.* it is not Total Variation Diminishing). Thus we wish to expand this method to create a strong stability preserving Runge-Kutta method which is

$$\begin{aligned}
\mathbf{W}^{*} &= \mathbf{W}^{n} + \Delta t \boldsymbol{\mathcal{L}}(\mathbf{W}^{n}), \\
\mathbf{W}^{**} &= \frac{3}{4}\mathbf{W}^{n} + \frac{1}{4}\mathbf{W}^{*} + \frac{\Delta t}{4}\boldsymbol{\mathcal{L}}(\mathbf{W}^{*}), \\
\mathbf{W}^{n+1} &= \frac{1}{2}\mathbf{W}^{n} + \frac{2}{3}\mathbf{W}^{**} + \frac{2\Delta t}{3}\boldsymbol{\mathcal{L}}(\mathbf{W}^{**}).
\end{aligned}$$

This method requires the three steps shown, but is stable and does not produce spurious oscillations. The explicit Runge-Kutta method used here is stable, so long as the simulation remains within the stability region for the method [158]. Which in the case of the explicit Runge-Kutta method is expressed in a polynomial function. The Runge-Kutta family of methods is popular for modelling of SWEs due to its accuracy and speed.

2.3.5 Reconstruction of numerical fluxes

This discontinuity at each cell interface creates the local Riemann problem. The main complication for solving the FVM is estimating the fluxes across cell boundaries. As shown in Figure 2.9, the local Riemann problem must be solved at each cell interface. The solution presented in [74] is to equate

$$\boldsymbol{\mathcal{F}}_{i+1/2}^{n} \approx \frac{1}{\Delta t}\int_{t^n}^{t^{n+1}} \mathbf{F}(\mathbf{W}(x_{i+1/2}, t))\ dt\ .$$

Centring the grid about the boundary, for example $x_{i+1/2}$, and choosing a suitably small time-step ensures that waves from different boundaries do not interact. The solution to the Riemann problem can be defined as $\overline{\mathbf{W}}_i(x,t)$. We relate

$$\xi = \frac{x - x_{i+1/2}}{t - t^n},$$

thus $\overline{\mathbf{W}}_i(x,t)$ can be written as a function of ξ, $\overline{\mathbf{W}}_i(\xi)$ such that

$$\overline{\mathbf{W}}_i(x,t) = \overline{\mathbf{W}}_i\left(\frac{x - x_{i+1/2}}{t - t^n}\right),$$

which means that the solution is constant when ξ is constant. When $\xi = 0$ at the cell interface, the flux across the interface may be given as

$$\mathbf{F}\left(\mathbf{W}(x_{i+1/2}, t)\right) = \mathbf{F}\left(\overline{\mathbf{W}}_i(0)\right). \tag{2.3.13}$$

The function $\overline{\mathbf{W}}_i\left(\xi\right)$ is either continuous or discontinuous when $\xi = 0$. When the former case occurs we gain

$$\mathbf{F}\left(\overline{\mathbf{W}}_i(0^+)\right) = \mathbf{F}\left(\overline{\mathbf{W}}_i(0^-)\right).$$

When $\overline{\mathbf{W}}_i$ is discontinuous at $\xi = 0$, a stationary shock occurs at the cell interface. The discontinuity must satisfy the Rankine-Hugoniot condition (detailed in [17]), enabling us obtain the following

$$\mathbf{F}\left(\overline{\mathbf{W}}_i(0^+)\right) - \mathbf{F}\left(\overline{\mathbf{W}}_i(0^-)\right) = 0 \cdot \left(\overline{\mathbf{W}}_i(0^+) - \overline{\mathbf{W}}_i(0^-)\right) = 0.$$

It should be noted that (2.3.13) also holds in this case. Thus the term $\mathbf{F}\left(\overline{\mathbf{W}}_i(0)\right)$ is well defined and the edge-centred flux value can be described as

$$\boldsymbol{\mathcal{F}}^n_{i+1/2} := \mathbf{F}\left(\overline{\mathbf{W}}_i(0^+)\right) = \mathbf{F}\left(\overline{\mathbf{W}}_i(0^-)\right).$$

Thus the approximate flux may be explicitly computed, as it is constant in time

$$\begin{aligned}\overline{\boldsymbol{\mathcal{F}}}^n_{i+1/2} &= \frac{1}{\Delta t}\int_{t^n}^{t^{n+1}} \mathbf{F}(\mathbf{W}(x_{i+1/2},t))\; dt,\\ &= \boldsymbol{\mathcal{F}}^n_{i+1/2}.\end{aligned}$$

Finally, this FVM scheme can be rearranged to

$$\mathbf{W}^{n+1}_i = \mathbf{W}^n_i - \frac{\Delta t}{\Delta x}\Big(\boldsymbol{\mathcal{F}}^n_{i+1/2} + \boldsymbol{\mathcal{F}}^n_{i-1/2}\Big). \tag{2.3.14}$$

The next stage is to estimate the numerical flux. Various possible schemes can be implemented for the approximation of fluxes.

2.4 Approximate Riemann solvers

The most high profile methods are reviewed in [6] with a brief discussion of benefits and shortcomings. In broad terms, Riemann solvers fall into one of two categories: linearized systems or Harten-Lax-van Leer (HLL) type schemes [112]. Specifically, interest is focused on how the schemes handle the solution of the Riemann problem and how they estimate numerical flux.

Godunov solver [112]: Godunov flux can be written as

$$\boldsymbol{\mathcal{F}}^n_{i+1/2} = \boldsymbol{\mathcal{F}}^{Godu}(\mathbf{W}^n_i, \mathbf{W}^n_{i+1}) = \begin{cases} \displaystyle\min_{\mathbf{W}^n_i \le \theta \le \mathbf{W}^n_{i+1}} \mathbf{F}(\theta), & \text{if} \quad \mathbf{W}^n_i \le \mathbf{W}^n_{i+1}, \\ \\ \displaystyle\max_{\mathbf{W}^n_{i+1} \le \theta \le \mathbf{W}^n_i} \mathbf{F}(\theta), & \text{if} \quad \mathbf{W}^n_i > \mathbf{W}^n_{i+1}. \end{cases}$$

When this is combined with a FVM formulation (equation (2.3.14)), it results in a Godunov scheme. That said, it has a number of other drawbacks as it relies on explicit formula for the solution of the Riemann problem, and these are rarely available for scalar conservation laws (especially for more complicated systems). Furthermore, the method is fairly computationally expensive. This difficulty is compounded when more elaborate multi-dimensional systems with a greater number of unknowns are involved, as a complex optimisation problem must then be solved.

Linearized Roe solvers [147]: The Roe approximate Riemann solver, developed in 1981, is an approximate method based on the Godunov scheme. It enables the user to find the flux between two cells, $\mathbf{W}_i$ and $\mathbf{W}_{i+1}$, in some space and time discretised domain. The non-conservative form of the system (2.3.11) can be written as

$$\frac{\partial \mathbf{W}}{\partial t} + \mathbf{A}(\mathbf{W})\frac{\partial \mathbf{W}}{\partial x} = 0,$$

where

$$\mathbf{A}(\mathbf{W}) = \frac{\partial \mathbf{F}}{\partial \mathbf{W}}$$

is the Jacobian matrix of the flux vector $\mathbf{F}(\mathbf{W})$. This is calculated using the derivatives of the system. An approximation matrix $\boldsymbol{\mathcal{A}}(\mathbf{W})$ is utilised that can be approximated from $\mathbf{A}(\mathbf{W})$ but must satisfy the following conditions:

- The eigenvalues are real and Jacobian diagonalizable, ensuring that the approximated system is truly hyperbolic.

- It must be consistent with the exact Jacobian matrix, thus when $\mathbf{W}^l, \mathbf{W}^r \to \mathbf{W}$ then

$$\boldsymbol{\mathcal{A}}\left(\mathbf{W}^l, \mathbf{W}^r\right) = \mathbf{A}(\mathbf{W}).$$

- It satisfies the following condition

$$\mathbf{F}^l - \mathbf{F}^r = \boldsymbol{\mathcal{A}}\left(\mathbf{W}^l - \mathbf{W}^r\right).$$

A way to linearize the system is achieved by

$$\mathbf{F}(\mathbf{W}) = \mathbf{F}'(\mathbf{W})\mathbf{W} \approx \mathcal{A}(\mathbf{W})\mathbf{W},$$

where $\boldsymbol{\mathcal{A}} \approx \mathbf{F}'$. Through the use of a Roe average, when $\mathcal{A}(\mathbf{W})$ is applied to the local Riemann problem (2.3.11), we obtain

$$\boldsymbol{\mathcal{A}}(\mathbf{W}) = \begin{cases} \dfrac{\mathbf{F}(\mathbf{W}^r) - \mathbf{F}(\mathbf{W}^l)}{\mathbf{W}^r - \mathbf{W}^l}, & \text{if } \mathbf{W}^r \neq \mathbf{W}^l, \\ \mathbf{F}'(\mathbf{W}^l), & \text{if } \mathbf{W}^r = \mathbf{W}^l. \end{cases} \tag{2.4.15}$$

Using an explicit time-step we can write the fluxes as

$$\boldsymbol{\mathcal{F}}^n_{i+1/2} = \boldsymbol{\mathcal{F}}^{Roe}(\mathbf{W}^n_i, \mathbf{W}^n_{i+1}) = \begin{cases} \mathbf{F}(\mathbf{W}^n_i), & \text{if } \boldsymbol{\mathcal{A}}(\mathbf{W}^n_{i+1/2}) \geq 0, \\ \\ \mathbf{F}(\mathbf{W}^n_{i+1}), & \text{if } \boldsymbol{\mathcal{A}}(\mathbf{W}^n_{i+1/2}) < 0. \end{cases}$$

The Roe solver is effective in capturing shocks but it is poor in resolving rarefaction waves. Consequently, they are only used for limited flow problems.

2.4.1 Central finite volume schemes

As Roe solvers fail in solving rarefactions (where two waves move in different directions), a new approach must be adopted. This problem is highlighted in Figure 2.7. The solution of the local Riemann problem can be expressed as

$$\mathbf{W}(t,x) = \begin{cases} \mathbf{W}^n_i, & \text{if } \dfrac{\Delta x}{\Delta t} < s^l_{i+1/2}, \\ \\ \mathbf{W}^*_{i+1/2}, & \text{if } s^l_{i+1/2} < \dfrac{\Delta x}{\Delta t} < s^r_{i+1/2}, \\ \\ \mathbf{W}^n_{i+1}, & \text{if } \dfrac{\Delta x}{\Delta t} > s^r_{i+1/2}. \end{cases}$$

This method is the basis of many schemes including Engquist-Osher [66], the second order Lax-Wendroff [111], and some two-step methods like Richtmyer-Morton method [142] and MacCormack [120]. This review examines two schemes that estimate wave speed differently: the Lax-Friedrichs method and the Rusanov method.

Lax-Friedrichs scheme [110]: This method was first proposed in 1954. It has many uses including the approximation of scalar conservation laws. It has provided a good baseline for comparison of more evolved schemes and can be expressed as

$$\boldsymbol{\mathcal{F}}^{LaxFri}_{i+1/2} = \frac{1}{2}\left(\mathbf{F}(\mathbf{W}^n_i) + \mathbf{F}(\mathbf{W}^n_{i+1})\right) - \frac{\Delta x}{2\Delta t}\left(\mathbf{W}^n_i + \mathbf{W}^n_{i+1}\right).$$

It is often seen as an introductory method as it does not involve the solution of the Riemann problem, only using flux evaluations. The scheme is consistent, conservative and monotone, consequently it is also Total Variation Diminishing (TVD). Thus it captures sharp shocks neglecting any spurious oscillations. The downside of the Lax-Friedrichs method is its diffusive nature. It is often prone to numerical diffusion, which distorts waves making them unrecognisable (lost peaks, smoothed functions etc.). This is likely to be due to the choice of wave speeds. These are set at maximums and do not necessarily take into account the speed of propagation of the problem at hand.

Rusanov scheme: the Rusanov scheme improves on the Lax-Friedrichs scheme by more correctly estimating the propagation speed of the left and right shock waves such

$$s^r_{i+1/2} = s_{i+1/2} \ , \qquad\qquad s^l_{i+1/2} = -s_{i+1/2} \ ,$$

where

$$s_{i+1/2} = \max\big(|\mathbf{A}'(\mathbf{W}^n_i)|,\ |\mathbf{A}'(\mathbf{W}^n_{i+1})|\big).$$

Thus, the scheme reduces to

$$\boldsymbol{\mathcal{F}}^{Rus}_{i+1/2} = \frac{1}{2}\big(\mathbf{F}(\mathbf{W}^n_i) + \mathbf{F}(\mathbf{W}^n_{i+1})\big) - \frac{s_{i+1/2}}{2}\left(\mathbf{W}^n_{i+1} + \mathbf{W}^n_i\right).$$

This scheme is sometimes called the local Lax-Friedrichs scheme, as it takes into account local variations in wave speed. It offers significant improvement over the Lax-Friedrichs method in both accuracy and numerical diffusion.

Harten-Lax-van Leer (HLL) scheme [85]: The HLL method falls into the second category of schemes, as it does not linearise the flux terms. This solver is designed to resolve the intermediate state problem presented in Figure 2.7. Instead of linearisation, the solution is assumed to be made of two discontinuities moving respectively at speeds $s^l_{i+1/2}$ and $s^r_{i+1/2}$ that separate the left and right state of the Riemann problem. Thus for a boundary where $x_{i+1/2} = 0$ it estimates the states thus

$$\mathbf{W}(t,x) = \begin{cases} \mathbf{W}_i, & \text{if } 0 \le s^l_{i+1/2}, \\ \mathbf{W}^{HLL}, & \text{if } s^l_{i+1/2} \le 0 \le s^r_{i+1/2}, \\ \mathbf{W}_{i+1}, & \text{if } 0 \ge s^r_{i+1/2}. \end{cases}$$

Given estimates for $s^l_{i+1/2}$, $s^r_{i+1/2}$, the Rankine-Hugoniot conditions can be written across the

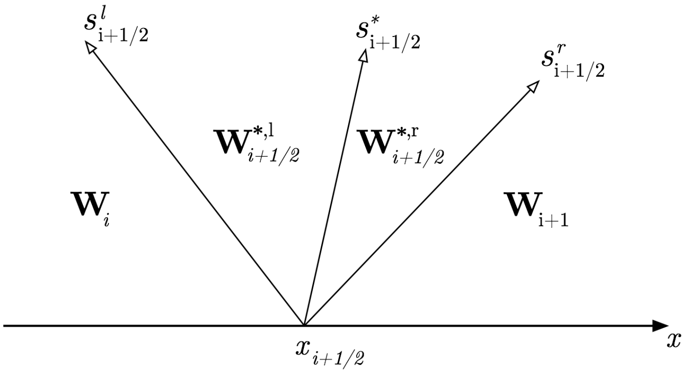

Figure 2.10: Riemann problem showing the intermediary stage split into two regions as in the HLLC scheme.

two waves, which yield

$$\boldsymbol{\mathcal{F}}^{HLL}_{i+1/2} = \mathbf{F}(\mathbf{W}_i) + (\mathbf{W}^{HLL} - \mathbf{W}_i)s^l_{i+1/2}, \qquad \boldsymbol{\mathcal{F}}^{HLL}_{i+1/2} = \mathbf{F}(\mathbf{W}_{i+1}) + (\mathbf{W}^{HLL} - \mathbf{W}_{i+1})s^r_{i+1/2}.$$

Using these two relations it is possible to describe the HLL flux as

$$\boldsymbol{\mathcal{F}}^{HLL}_{i+1/2} = \begin{cases} \mathbf{F}(\mathbf{W}_i), & \text{if } 0 \leq s^l_{i+1/2}, \\ \dfrac{s^r\mathbf{F}(\mathbf{W}_i) - s^l\mathbf{F}(\mathbf{W}_{i+1}) + s^l s^r\left(\mathbf{F}(\mathbf{W}_i) - \mathbf{F}(\mathbf{W}_{i+1})\right)}{s^r - s^l}, & \text{if } s^l_{i+1/2} \leq 0 \leq s^r_{i+1/2}, \\ \mathbf{F}(\mathbf{W}_{i+1}), & \text{if } 0 \geq s^r_{i+1/2}. \end{cases}$$

This method is useful but is prone to errors if there is any form of intermediate wave.

Harten-Lax-van Leer Centred (HLLC) scheme [180]: The HLLC scheme is an extension of the HLL scheme and is designed to restore the missing contact and shear waves (from the Euler Equations) not captured by the HLL scheme. The innovation here is the estimation of the Riemann problem with three wave-speeds $s^l_{i+1/2}$, $s^r_{i+1/2}$, and $s^*_{i+1/2}$. This means that the star region is divided into two parts, $\mathbf{W}^{l*}_{i+1/2}$, and $\mathbf{W}^{l*}_{i+1/2}$, as shown in Figure 2.10. By integrating as before we obtain

$$\begin{aligned} \mathbf{F}^{*,l}(\mathbf{W}) &= \mathbf{F}(\mathbf{W}_i) + s^l_{i+1/2}\left(\mathbf{W}_i - \mathbf{W}^{*,l}\right), \\ \mathbf{F}^{*,r}(\mathbf{W}) &= \begin{cases} \mathbf{F}(\mathbf{W}^{*,l}) + s^*_{i+1/2}\left(\mathbf{W}^{*,r} - \mathbf{W}^{*,l}\right), \\ \mathbf{F}(\mathbf{W}_{i+1}) + s^r_{i+1/2}\left(\mathbf{W}^{*,r} - \mathbf{W}_{i+1}\right). \end{cases} \end{aligned}$$

These equations hold four unknowns and the switch condition for the second one is case dependant. Using these two relations it is possible to solve for the values of $\mathbf{F}^*$ such that, the HLL flux can be calculated as

$$\boldsymbol{\mathcal{F}}^{HLL}_{i+1/2} = \begin{cases} \mathbf{F}(\mathbf{W}_i), & \text{if } 0 \leq s^l_{i+1/2}, \\ \mathbf{F}^{*,l}(\mathbf{W}), & \text{if } s^l_{i+1/2} \leq 0 \leq s^*_{i+1/2}, \\ \mathbf{F}^{*,r}(\mathbf{W}), & \text{if } s^*_{i+1/2} \leq 0 \leq s^r_{i+1/2}, \\ \mathbf{F}(\mathbf{W}_{i+1}), & \text{if } 0 \geq s^r_{i+1/2}. \end{cases}$$

Both the HLL and HLLC schemes require wave speed estimations to be made, and many methods exist for doing this. One of the most popular is the direct wave speed estimate, the most simple of which was devised in [57], though a range of methods exists including [147].

2.4.2 Upwind finite volume schemes

So far attention has been focused on centred schemes, where the method is symmetric around the point of interest, *i.e.* information for the solution comes equally from both the left and the right of the cell being solved. As hyperbolic systems have waves that propagate in certain directions (different directions and speeds for different waves), it is possible to formulate a different family of schemes: the Upwind scheme, where information comes from the direction of propagation of the wave. Upwind schemes may be preferable to centred ones in order to ensure stability and for the capture of the correct wave propagation speed. These upwind schemes were originally designed for other applications in 1952 [54], but were later adapted for SWEs in studies like [25, 210]. The first-order formulation of the upwind-method can be expressed as

$$\mathbf{F}_{i+1/2} = u^l \mathbf{W}^n_i + u^r \mathbf{W}^r_i,$$

where u^l and u^r are the speeds of the fluid wave in question defined by

$$u^l = \min(u_{i+1/2}, 0), \qquad u^r = \max(u_{i+1/2}, 0).$$

For the solution of complex systems of equations, where information may be coming from both directions, a characteristic decomposition is typically implemented to select which information to use from each side of the boundary.

2.4.3 High resolution finite volume schemes

High-resolution schemes are used when high accuracy is needed, especially around shocks and discontinuities. They achieve a minimum of second-order accuracy. Once again, a considerable amount of work has been undertaken to create these schemes see [179], among others.

Lax-Wendroff scheme [111]: One of the first second-order schemes is based on the Taylor expansion of the linear system ($\mathbf{q}_t + \mathbf{A}\mathbf{q}_x = 0$) thus

$$\mathbf{q}(x, t_{n+1}) = \mathbf{q}(x, t_n) + \Delta t \mathbf{q}_t(x, t_n) + \frac{1}{2}(\Delta t)^2 \mathbf{q}_{tt}(x, t_n) + \dots$$

Keeping only the first three terms of the expansion, and using a central finite difference approach, the following is obtained

$$\mathbf{W}_i^{n+1} = \mathbf{W}_i^n - \frac{1}{2}\left(\frac{\Delta t}{\Delta x}\right)\mathbf{A}\Big(\mathbf{W}_{i-1}^n - \mathbf{W}_{i+1}^n\Big) + \frac{1}{2}\left(\frac{\Delta t}{\Delta x}\right)^2 \mathbf{A}^2\Big(\mathbf{W}_{i-1}^n - 2\mathbf{W}_i^n + \mathbf{W}_{i+1}^n\Big).$$

This is a finite difference interpretation but it can be re-interpreted to give a FVM with a flux function given by

$$\boldsymbol{\mathcal{F}}_{i+1/2}^{LaxWen} = \frac{1}{2}\mathbf{A}\Big(\mathbf{W}_i^n + \mathbf{W}_{i+1}^n\Big) + \frac{1}{2}\frac{\Delta t}{\Delta x}\mathbf{A}^2\Big(\mathbf{W}_{i+1}^n - \mathbf{W}_i^n\Big).$$

This method is still in use today as it offers a good trade-off between speed and accuracy.

Beam-Warming scheme [19]: The above is a three-point centred scheme. By manipulating the derivatives used, and assuming the eigenvalues of $\mathbf{A}$ are positive, it is possible to generate an upwind scheme. Replacing the cell centred scheme for derivatives enables

$$\mathbf{q}_x(x_i, t_n) = \frac{1}{2\Delta x}\Big(3\mathbf{q}(x_i, t_n) - 4\mathbf{q}(x_{i-1}, t_n) + \mathbf{q}(x_{i-2}, t_n)\Big),$$

$$\mathbf{q}_{xx}(x_i, t_n) = \frac{1}{\Delta x^2}\Big(\mathbf{q}(x_i, t_n) - 2\mathbf{q}(x_{i-1}, t_n) + \mathbf{q}(x_{i-2}, t_n)\Big).$$

Thus, the approximation used for the characteristics becomes

$$\mathbf{W}_i^{n+1} = \mathbf{W}_i^n - \frac{\Delta t}{2\Delta x}\mathbf{A}\Big(3\mathbf{W}_i^n - 4\mathbf{W}_{i-1}^n + \mathbf{W}_{i-2}^n\Big) + \frac{1}{2}\left(\frac{\Delta t}{\Delta x}\right)^2 \mathbf{A}^2\Big(\mathbf{W}_i^n - 2\mathbf{W}_{i-1}^n + \mathbf{W}_{i-2}^n\Big).$$

This allows the extraction of the Beam-Warming flux differencing FVM

$$\boldsymbol{\mathcal{F}}_{i-1/2}^{Beam} = \mathbf{A}\mathbf{W}_{i-1}^n + \frac{1}{2}\mathbf{A}\left(1 - \frac{\Delta t}{\Delta x}\mathbf{A}\right)(\mathbf{W}_{i-1}^n - \mathbf{W}_{i-2}^n).$$

Both the Lax-Wendroff and Beam-Warming methods entail poor shock capture and often produce spurious oscillations around shocks. They are second or higher order accurate in smooth regions but do not present acceptable results around discontinuities. As a result, limiters are often utilised.

Total Variation Diminishing (TVD) property: the aim of most schemes is to reduce the spurious oscillations found around discontinuities especially in high-order schemes. To measure this effect, a mathematical notion called total variation is implemented, producing

$$TV(\mathbf{W}) = \sum_{i=-\infty}^{\infty} |\mathbf{W}_i - \mathbf{W}_{i-1}|.$$

For the simple solution of a wave propagating at a set speed without distortion, the total variation will remain constant; if some diffusion is included, the total variation will decrease. Only when the solver introduces spurious oscillations does the total variation increase. Accordingly solvers are employed to reduce it such that

$$TV(\mathbf{W}^{n+1}) \leq TV(\mathbf{W}^n).$$

This is called the Total Variation Diminishing (TVD) property [85], which is a standard measure of the stability and accuracy of a scheme. The TVD property is a very desirable feature (if not a requirement) in calculations of this nature.

2.4.4 Flux and slope limiters for numerical schemes

Limiters combine the first order accuracy around shocks with a higher order accuracy scheme for smooth regions. This is achieved by calculating both a high order and low order flux, then placing limits on their contribution to the flux solution (where the limits sum to one). This method was first introduced by Harten and Zwas [86] (and Boris and Book a year later [28]). Two types of limiters exist: slope limiters, where the limit is applied based on the slope of the solution, and flux limiters.

Slope limiters: the slope limiter differs from the flux limiter in that (based on the slope) it will adjust the value of a certain cell (or cells) in order to prevent oscillations and overshoot. This is achieved in piecewise linear schemes like that of the advection equation, for the numerical flux we have

$$\begin{aligned} \boldsymbol{\mathcal{F}}^n_{i-1/2} &= \frac{1}{\Delta t}\int_{t^n}^{t^{n+1}} u\mathbf{W}^n_{i-1/2}\, dt \\ &= u\mathbf{W}^n_{i-1} + \frac{1}{2}u\left(\Delta x - u\Delta t\right)\sigma^n_{i-1} \end{aligned}$$

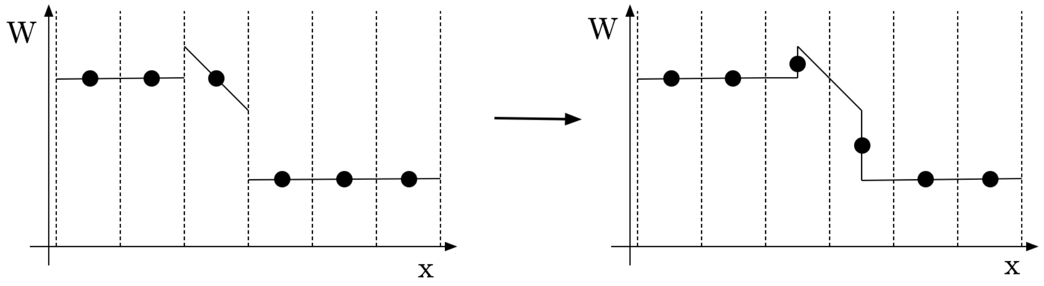

Figure 2.11: The problem of overshoot in piecewise solutions of continuous systems.

which combined with equation (2.3.14) gives

$$\mathbf{W}_i^{n+1} = \mathbf{W}_i^n - \frac{u\Delta t}{\Delta x}\Big(\mathbf{W}_i^{n+1} - \mathbf{W}_{i-1}^n\Big) - \frac{u\Delta t}{\Delta x}\frac{1}{2}\Big(\sigma_i^n - \sigma_{i-1}^n\Big)\Big(\Delta x - u\Delta t\Big). \tag{2.4.16}$$

where u is the wave speed. The choice of slope σ_i^n is crucial. Three popular methods are

$$\begin{aligned}
\text{Centred slope:} \quad \sigma_i^n &= \frac{\mathbf{W}_{i+1}^n - \mathbf{W}_{i-1}^n}{2\Delta x}, && \text{Froom method,}\\
\text{Upwind slope:} \quad \sigma_i^n &= \frac{\mathbf{W}_i^n - \mathbf{W}_{i-1}^n}{\Delta x}, && \text{Beam-Warming method,}\\
\text{Downwind slope:} \quad \sigma_i^n &= \frac{\mathbf{W}_{i+1}^n - \mathbf{W}_i^n}{\Delta x}, && \text{Lax-Wendroff method.}
\end{aligned}$$

All of these slope calculation options supply second-order accurate results. This is ideal for smoothing linear solutions, but for non-linear high order methods, where overshoot can be a problem, a new choice of slope is required. Consider Figure 2.11, as the solution progresses the nodes are forced to overshoot realistic values thus causing spurious oscillations. This can be countered by utilising slope limiter methods. When the slope limiter method is applied to high order schemes, the slope parameters are modified to avoid this overshoot problem. Three of the most commonly used are the minmod slope, the super bee and the MC slope limiters. The minimum of the modulus (minmod) selects the lesser of two slopes thus

$$\sigma_i^n = \text{minmod}\left(\frac{\mathbf{W}_i^n - \mathbf{W}_{i-1}^n}{\Delta x}, \frac{\mathbf{W}_{i+1}^n - \mathbf{W}_i^n}{\Delta x}\right),$$

where

$$\text{minmod(a,b)} = \begin{cases} a, & \text{if } |a| < |b| \text{ and } ab > 0,\\ b, & \text{if } |b| < |a| \text{ and } ab > 0,\\ 0, & \text{if } ab \leq 0. \end{cases}$$

The superbee limiter was introduced by Roe in 1985 [148]. The limiter compares the slopes to twice the slope on the other side of the node in question, selecting the smaller. It then chooses the maximum of those two slopes. It is implemented thus

$$\begin{aligned}\sigma_i^n &= \max\left(\sigma_i^{(1)}, \sigma_i^{(2)}\right),\\ \sigma_i^{(1)} &= \operatorname{minmod}\left(\frac{\mathbf{W}_i^n - \mathbf{W}_{i-1}^n}{\Delta x}, 2\frac{\mathbf{W}_{i+1}^n - \mathbf{W}_i^n}{\Delta x}\right),\\ \sigma_i^{(2)} &= \operatorname{minmod}\left(2\frac{\mathbf{W}_i^n - \mathbf{W}_{i-1}^n}{\Delta x}, \frac{\mathbf{W}_{i+1}^n - \mathbf{W}_i^n}{\Delta x}\right).\end{aligned}$$

The superbee limiter has better shock capturing (it holds vertical wave-fronts in SWE calculations more precisely) but can 'harden' or steepen some wave-fronts. One of the most popular limiters is the Monotonized Central-difference limiter (MC Limiter) scheme. Proposed by van Leer [183], it aims to avoid the steepening of the superbee and the rounding of the minmod. It achieves this with the following slope selection

$$\sigma_i^n = \operatorname{minmod}\left(\frac{\mathbf{W}_{i+1}^n - \mathbf{W}_i^n}{\Delta x}, 2\frac{\mathbf{W}_i^n - \mathbf{W}_{i-1}^n}{\Delta x}, 2\frac{\mathbf{W}_{i+1}^n - \mathbf{W}_i^n}{\Delta x}\right).$$

Flux limiters: the second class of limiters is the flux limiter. In this method the flux is altered according to gradient of the slope, rather than the quantity. This is implemented using

$$\boldsymbol{\mathcal{F}}_{i-1/2}^n = \boldsymbol{\mathcal{F}}^L + \phi_{i-1/2}^n(\boldsymbol{\mathcal{F}}^L - \boldsymbol{\mathcal{F}}^H).$$

The limiting functions have evolved steadily and though many limiters exist, including (HQUICK [218], Koren [103], Osher [43] and Sweby [174]), the four most commonly used are:

$$\begin{aligned}\text{minmod:}\quad \phi(\theta) &= \operatorname{minmod}(1, \theta),\\ \text{superbee:}\quad \phi(\theta) &= \max(0, \min(1, 2\theta), \min(2, \theta)),\\ \text{MC:}\quad \phi(\theta) &= \max(0, \min((1+\theta)/2, 2, 2\theta)),\\ \text{van Leer:}\quad \phi(\theta) &= \frac{\theta + |\theta|}{1 + |\theta|},\end{aligned}$$

where

$$\theta_{i-1/2}^n = \begin{cases}\dfrac{\Delta\mathbf{W}_{i-3/2}^n}{\Delta\mathbf{W}_{i-1/2}^n}, & \text{if } u > 0,\\[2ex] \dfrac{\Delta\mathbf{W}_{i+1/2}^n}{\Delta\mathbf{W}_{i-1/2}^n}, & \text{if } u < 0.\end{cases}$$

Where $\Delta\mathbf{W}^n_{i-1/2}$ is the jump in $\mathbf{W}$ observed at $x_{i-1/2}$, as shown in Figure 2.11.

$$\Delta\mathbf{W}^n_{i-1/2} = \mathbf{W}^n_i - \mathbf{W}^n_{i-1}.$$

2.5 Existing shallow water sediment transport models

The usual classification of models is based on their number of dimensions. It should be noted that partial dimensionality can occur in quasi-2D and 3D models. Early examples of 1D models can be found in [55,138,139,206] and 2D and 3D models can be found in [58,116,205]. A good general overview of sediment transport modelling is presented in [197], containing a good summary of 1D, 2D, and 3D methods is a very useful starting point. The report discusses many of the main considerations such as turbulence model closure, channel roughness, and non-equilibrium adaptations. Interestingly, it also outlines cohesive sediment transport equations which are often avoided. The report further details the various methods for real world applications, such as coupling with different dimensional models and multi-block equations. The following references are a few examples of sediment transport configured with erodible beds.

Analysis of wave, tidal, long-shore transport, total transport, and bed level change relations are all incorporated by the authors of [131] in their paper looking at dune formation on beaches. They solve real world situations over small domains and compare the results with experimental data over long time periods. They utilise the Proudman Oceanographic Laboratory Coastal Ocean Modelling System (POLCOMS)[5], which combines the effects of high frequency wind with a long-shore sediment transport model. They develop the 2D numerical tidal and wave relations to model the hydrodynamic forces that move sediment over long time-scales.

In [69] a paper modelling multilayer polydisperse sedimentation is presented; one of the only papers to date to deal with multiple sediment types in 1D using the Masliyah-Lockett-Bassoon (MLB) method. They devise a novel algorithm for dealing with the many complications presented by such a complex system. Utilising the fact that concentration is a scalar quantity in the hyperbolic system, they use a two-step predictor method in which a largely simplified system is solved. Then, the approximate concentrations are developed using an upwind scheme related to the concentration flux. The model can also handle multiple sediment types. Though no comparable experimental data exists, their results appear reasonable.

The paper [22] presents an interesting model of sediment transport in 1D based on a flux limiter method, utilising a non-homogeneous Riemann solver coupled with the Lax-Wendroff

---

[5] `http://cobs.noc.ac.uk/modl/polcoms/`

method and flux limiters. A two-step approach, using a discretisation of the gradient terms followed by the treatment of the source terms, provides a well-balanced conservative scheme. The methodology adheres well to benchmark tests and presents a fast and flexible solver. Notably, this model captures the hydraulic jump which is often lost with other models.

Advances in the field of bank failure are presented in [4], where the authors couple a 2D sediment transport model with a novel algorithm for bank failure. This is innovative, as failed material is not immediately discarded into the flow for transport. The algorithm compares each cell in the unstructured grid to an angle of repose for the bank. Any material that is not found to be at equilibrium is redistributed into lower cells. Their model achieves good results in comparison with experimental data in both 1D and 2D.

A classical dam-break over a movable bed is modelled in [208] using a Godunov upwind solver. Unusually, although their model is 1D in nature, they consider the other two dimensions and work in terms of volumetric discharge and bed area, rather than flow speed and bed height. The method is tested against the Taipei and Louvain experiments and returns reasonable results. The alterations to the formula presented by Van Rijn on equilibrium bedload transport appears to improve upon the work done in [38].

A detailed model for 2D sediment transport is developed in [162]. It includes features for both cohesive and non-cohesive sediment transport, utilising the FVM in the solver in combination with a Godunov-type method. This is enabled by the assumption that the left and right hand waves of the Riemann problem are rarefactions. The model also includes 2D concentration diffusion. Although it is only a single layer (and does not take into account bedload) it still has good agreement with benchmark dam-break problems. It also proposes novel uses for the model, including simulations of Tsunamis over erodible beds, and the creation and distortion of rills (small sediment ripples) in sedimentary flows.

Comparisons between coupled and un-coupled models for sediment transport are drawn in [37]. This paper highlights the need for coupled models. It concludes that decoupling sediment transport equations from bathymetric evolution equations can lead to substantial errors. The study presents the importance of not making these generalisations for the sake of deposition, though interestingly the standard simplifications do not cause inaccuracies in erosion. It is also shown that the asynchronous solution procedure has further ill effects on both erosion and deposition. They conclude that, for accurate results, a coupled and complete set of governing equations must be solved simultaneously.

A new method for calculating water depth and velocities in a shear wave is presented by [140]. This model, a Saint-Venant equation coupled with Grass's Exner equation [78] for concentration and bed evolution, is adequate for their applications. This novel method for approximating values on the shear wave includes the use of vertex values together with reconstructed values (from the predictor stage of the HLLC solver). Evaluated against several situations, including the Louvain set of tests, this model obtains very satisfactory results.

A classic 2D sediment transport and bed evolution model is created in [113]. They developed a model that can be utilised on both small-scale and large domains over a range of time periods. This model uses a standard upwind approximate Riemann solver for unstructured grids, and incorporates some useful features like linear reconstruction and slope limiting. The model is tested for accuracy in both dam-breaks (where it is compared with Louvain and Taipei experiments in 2D) and rainfall run-off experiments, for both it provides encouraging results.

A coupled sediment dynamic model for GEOtop is developed in [219]. GEOtop[6] is not strictly in the class of models being reviewed but their work provides a useful comparison for other methods of sediment transport. GEOtop solves the Richards equation to account for rain, surface run-off, infiltration, and saturation, as well as flow routing using water and energy balance equations.

A physical model which makes fewer assumptions about the flow, it is a good way to perform scaled calculations for complex 3D flows and structure interaction is detailed in [3]. The challenge with this class of model is correct scaling. The authors relax the Reynolds number but ensure the Froude scaling remained correct, resulting in a satisfactory undistorted model. The model is able to handle multiple-sized sediments making it fairly robust, though it does simplify the Shields criterion and the particle Reynolds number to enable larger particles to be moved. The authors also give a good review of physical modelling up to 2013, and discuss in depth some of the drawbacks of physical methods around scaling.

A notable set of experiments are written up in [45]. The authors use a flume filled with coloured fine gravels, from which they perform multiple bedload experiments enabling a comparison of a probabilistic model for bedload dispersion with a more novel dispersion. Their work shows very good results for the non-equilibrium dispersion model.

There are a wide variety of models with various advantages and shortcomings. One of the most apparent limitations for shallow water modelling is the reliance on depth-averaged velocities. Suitable for some applications, it adds complexity to entrainment and deposition functions for both suspended sediment and bedload transport. This is because near bed velocities must be estimated.

Another important constraint is that the effects of turbulence on sediment transport are overlooked in most models (with some notable exceptions). As shown in the previous section,

---

[6] http://geotopmodel.github.io/geotop/

this is a crucial factor in the initiation and continuation of sediment transport. Addressing both of these problems, as well as the single sediment assumption mentioned earlier, will be the contributions of the current work through the development of a multilayer formulation with turbulence and the inclusion of multi-sediment methods.

2.6 Summary

In this literature review, work relevant to the creation of sediment transport models is divided into five areas of study based on the different aspects of model and method creation. Attractive characteristics and implementation problems encountered in each area are considered. The first area of evaluation focuses on the Shallow Water Equations (SWEs) that are used for fast and stable simulations of systems which can be depth-averaged. A brief derivation from the Navier-Stokes equations is given, as well as some of the basic characteristics that are encountered. The limiting assumption of the basic shallow water derivation is the lack of stratified velocities and turbulent kinetic energy, which produces inaccuracies in the model. Solutions to both of these problems are developed in later chapters of this study. Specifically a multilayer formulation for flow is developed for the first time for sediment transport incorporating a novel approach to turbulence modelling. The second section details sediment transport modelling methods. The basic processes of erosion and deposition are also expanded upon. Particular attention is given to the many assumptions required in sediment transport equations, and the fact that they lead to large inaccuracies. One particular assumption highlighted: the requirement for the use of a single sediment type in almost all simulations, which reduces the accuracy of these models, as the effects of varying sediment types and sizes can have profound effects on the bed-forms produced. It is particularly difficult to demonstrate the effects of armouring when modelling an homogeneous sediment. In this study, this assumption is removed through the use of a multi-sediment formulation in both the fluid and the bed. This formulation enables the user to not only gain more detailed results but also to track sediment types, without significant increases in computational speed.

The numerical methods used to solve the SWEs are overviewed in the third section. The SWEs are classified and their general properties are briefly detailed. An overview of approximate methods used to solve the SWEs is then given, with a brief analysis of the advantages and disadvantages of each. The Finite Volume Method (FVM) is chosen and a synopsis of the formulation of the FVM is detailed in order to explain its limiting assumptions. Crucially, the Riemann problem is examined both in general and local terms with reference to the FVM. The particular problems around the basic solutions to the SWEs and how they relate to sediment transport are also highlighted. The fourth section summaries the approximate Riemann solvers. It underlines the complexity of many of these solvers and mentions some of the methods required to improve stability. Through the review of central, upwind and high order schemes a baseline for complexity is set. This baseline will be used to assess a new scheme that enables the multilayer SWEs to be developed. A new method, presented in later chapters, allows problems to be computed with a greater speed and comparable accuracy to three-dimensional Navier-Stokes, simulations even with a multi-layer formulation.

Finally, in the fifth section, current sediment transport models are briefly reviewed. Models of particular interest are highlighted in order to establish the essential qualities required by the model developed in this study. This section also looks at models outside the physically-based approach to underline advantages that physically-based models should aspire to. This section elucidates the problems found in previous sections: lack of stratified velocities, single sediment assumptions and the rarity of turbulence modelling in shallow water sediment transport. All of these problems will be addressed in this study. Overall, this chapter produces an overview of previous works that is vital to the understanding of shallow water and sediment transport simulations. It details the fundamental ideas and their positive and negative attributes that this thesis hopes to develop in order to produce a superior method for SWE sediment transport modelling.

Chapter 3

Modelling and numerical simulation of shallow water flows over multi-sediment beds in one space dimension

In this chapter, the first limiting assumption of sediment transport modelling in shallow water is tackled, namely the single sediment assumption. The aim is to develop a method for handling multiple sediments in the model without significantly increasing its computational expense. In order to achieve this, the standard governing equations for such a model must not be radically expanded. The model consists of the one-dimensional shallow water equations for the flow, a species conservation equation for suspended sediments, and a bed Exner-type equation. The model also comprises a set of empirical equations for erosion and deposition terms. Multilayer beds composed of different erodible soils and the exchange conditions between them are considered in this chapter. The coupled system employs a non-homogeneous Riemann solver equipped with interface-tracking tools to resolve discontinuous soil properties in the bed. The accuracy of the model is verified against several test examples in evolving and steady-state flow domains. The results demonstrate the ability of the method to preserve the conservation property whilst avoiding numerical oscillations and dissipation in the approximated solutions.

This chapter is organized as follows: Section 3.1 gives background and explains the motivation for the work conducted in greater depth than in the previous chapter. In Section 3.2, the governing equations for shallow water flows over sedimentary topography are presented. Modelling exchange terms between multilayer beds is discussed in Section 3.3. In Section 3.4, the Riemann solver for both the discretisation of gradient fluxes and the treatment of source terms is formulated. Numerical results and examples are presented in Section 3.5. Finally, Section 3.6 summarizes the chapter.

3.1 Motivation for modelling multiple sediments in shallow water flow

The primary intention of sediment transport analysis is to determine the evolution of bed levels for hydrodynamic systems such as rivers, estuaries, bays, and other near-shore regions where water flows interact with the bed topography. Examples of engineering applications include: beach profile changes due to severe wave actions, seabed response to dredging procedures or imposed structures, and harbour siltation [3, 36, 113, 215]. In general, suspended sediments and bedload transport in shallow water flows are determined by the characteristics of the hydraulic flow and the properties of the suspended sediments. Dynamics of the water flow and dynamics of the sediments must be studied using a mathematical model formed of at least three different but dependent model variables:

- A set of hydraulic variables defining the dynamics of the water flow.
- A sediment variable defining the transport and dispersion of the sediments.
- A topography variable defining the dynamics of the bedload.

Most existing models for this class of problems consider either the three-dimensional (3D) Navier-Stokes equations or Shallow Water Equations (SWE)s for the hydrodynamics, coupled to equations for sediment transport and/or bed morphology [1, 39, 177]. The difficulties in the first approach are seen by the re-meshing required to deal with moving boundaries for free-surface and bottom topography, due to the hydrostatic pressure and erosion/deposition forces. Because of its high computational cost, this approach is rarely used in practical applications. Thus, a more simple SWE model is often used as it is less computational expensive and is easily adaptable to most situations. One of the main advantages of this approach is that no re-meshing is required, as the SWE mesh has no vertical component. The drawback in the second approach lies in the failure of the coupled SWE and sediment equations to capture vertical effects in soil-superposed packed beds as an homogeneous assumption about the bed is often made (due to the nature of model and inherent complications of adding multiple sediment types).

Understanding morphological evolution due to shallow water flows is crucial to the development of river defences and flood control [102, 192]. The ability to simulate a range of situations accurately, from near steady-state bed degradation to dam-break conditions, is important to the design and maintenance of hydro-infrastructure [3]. Precise modelling of entrainment and deposition rates allows for a good understanding of the interaction between water flows and movable beds. A set of formulae for entrainment was first proposed in [160]. Although good

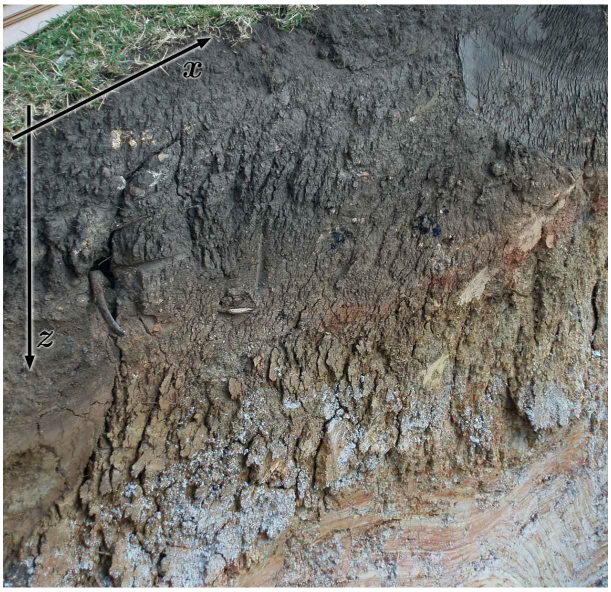

Figure 3.1: A photograph of natural soil layers courtesy of Science Stock Photos[1].

categorizations have been introduced, a unified theory has yet to be found [32, 135]. For modelling morphodynamics in shallow water flows, the three most popular models are the Grass model [78], the Meyer-Peter & Muller model [122] and the Van-Rijn model [186]. In this chapter, the erosion and deposition formulae proposed in [36, 186] are used, as they are best suited to the problems considered. One of the most complicated aspects of simulating sediment transport is the accurate modelling of the bed given the assumptions required; these include the levels of armouring, vegetation, composition, and compaction. They often lead to a large disconnect between laboratory simulations and real-world events. Recently, corrections have been investigated in [47, 155, 196] to improve these assumptions. However, homogeneous assumptions on the erodible beds are one of the severe limitations in these models, as there is no real-world situation where the bed is truly homogeneous.

In the current study, a new-coupled model for hydraulics over multilayer erodible beds is presented. The bed is assumed to be heterogeneous and formed with multiple layers of different soil, similar to that shown in Figure 3.1. The structure of soil-superposed packed beds and the total number of layers to be considered in the analysis are fixed a priori. The governing equations consist of a coupled system of SWEs for the hydraulics, a transport equation for suspended sediments, an Exner-type equation for the bed, and a series of exchange terms for the mass transfer between the bed layers due to erosion and/or deposition effects. These equations form a non-linear hyperbolic system of conservation laws with source terms to be solved for the time interval, the horizontal space coordinate, and the vertical bed depth. Such practical coupled

---

[1] `http://www.sciencestockphotos.com/free/geology/soil_layers.jpg`

hydrodynamic and morphodynamic problems are not trivial to simulate, since the soil deposition can be irregular. It should be pointed out that other mathematical models for sediment transport have also been studied in [104], among others. In these systems, the SWEs have been coupled to an Exner-type equation for the bedload, which does not account for suspended sediments as shown in the current study. In this chapter, a fully coupled model for shallow water flows over multilayer and mixed sediment erodible beds is presented. The Exner equation for the bed is modified to allow for inter-cellular flux in the vertical discretisation of the bed depth. The bed layers can be assumed to be heterogeneous and composed of multiple layers of different sediment mixtures. The structure of the soil-superposed packed beds is known, along with the number of layers in the model. Combined with the sediment handling tools and a two-dimensional (2D) discretised bed, multiple sediments can be eroded, deposited or remain stationary within the same cell, depending on the properties of the studied sediments.

The novelty of this work lies in the bed discretisation and bed flux function building on methods, like the Saint-Venant-Hirano model [169] to deliver a model capable of handling discretely layered beds. Crucially, the approach is designed to impact the complexity of the model as little as possible and therein the computational expense. The development and design of numerical methods that are able to predict the hydraulics over multilayer erodible beds have clear real -world applications. Effort has been put into the implementation of numerical schemes for sediment transport models capable of resolving all hydrodynamics and morphodynamics scales. A class of Riemann solvers is proposed for the numerical simulation of transient flows involving erosion and deposition of sediments in the multilayer beds. The method consists of a predictor stage, where the numerical fluxes are constructed, and a corrector stage, to recover the conservation equations within the framework of finite volume methods. The sign of the Jacobian matrix is used in the reconstruction of the numerical fluxes. Most of these techniques have been recently investigated in [22] for solving sediment transport models, but do not resolve erosion and deposition effects within the bed. The current work presents an extension of this method to transient flows over erodible beds that are subject to erosion and deposition of sediments as well as the exchange between the bed layers. The proposed method also satisfies the well-established C-property by balancing the discretisation of flux gradients and source terms in the system. This allows for the comparison of initial sediment assumptions, as shown in this chapter. To analyse the effectiveness of the proposed techniques, the computational results of the model are first compared to experimental data for the test examples of a dam-break flow over an erodible bed as reported in [39], and for the degradation of a dyke studied in [81]. Next, similar flow problems over erodible multilayer beds are simulated and the performance of the proposed techniques is examined using different numbers of layers in the sediment topography. These examples also highlight the ability of the method to handle multiple sediment erosion and deposition equations. Results presented in this chapter demonstrate the high resolution of the proposed method, and confirm its ability to provide accurate and efficient simulations for sediment transport by water flows including erosion and deposition effects in heterogeneous beds.

3.2 A model for multi-sediment handling in one space dimension

The conventional governing equations of sediment transport in shallow water flows are obtained by balancing the net inflow of mass, momentum, and species, through boundaries of a control volume. This is achieved during an infinitesimal time interval while accounting for the accumulation of mass, resultant forces, and species within the control volume [1, 35]. These equations can be formulated in a conservative form as

$$\begin{aligned}
\frac{\partial H}{\partial t}+\frac{\partial (Hu)}{\partial x} &= \frac{E-D}{1-\Psi},\\
\frac{\partial (Hu)}{\partial t}+\frac{\partial}{\partial x}\left(Hu^2+\frac{1}{2}gH^2\right) &= -gH\frac{\partial B}{\partial x}-\frac{(\rho_s-\rho_w)}{2\rho}gH^2\frac{\partial c}{\partial x}-\\
&\qquad \frac{(\rho_0-\rho)(E-D)u}{\rho(1-\Psi)}-gHS_f,\\
\frac{\partial (Hc)}{\partial t}+\frac{\partial}{\partial x}\Big(Huc\Big) &= E-D,\\
\frac{\partial B}{\partial t} &= -\frac{E-D}{1-\Psi},
\end{aligned}\tag{3.2.1}$$

where $u(t,x)$ is the depth-averaged water velocity, $H(t,x)$ the water depth, $B(t,x)$ the bottom topography, $\rho(t,x)$ is the density of the water sediment mixture, $\rho_0(t,x)$ is the density of the saturated bed, g the gravitational acceleration, Ψ the porosity of the sediment, ρ_w the water density, ρ_s the sediment density, and $E(t,x)$ and $D(t,x)$ represent the total entrainment and deposition terms in upward and downward directions, respectively. The density of the water-sediment mixture $\rho(t,x)$ and the density of the saturated bed $\rho_0(t,x)$ are defined as

$$\rho=\rho_w(1-c)+\rho_s c, \qquad \rho_0=\rho_w\Psi+\rho_s(1-\Psi).$$

The depth-averaged concentration of the suspended sediment $c(t,x)$ is defined as

$$c=\frac{\rho-\rho_w}{\rho_s-\rho}.$$

Here, S_f is the friction slope defined as

$$S_f=\frac{n_m^2 u|u|}{H^{4/3}},$$

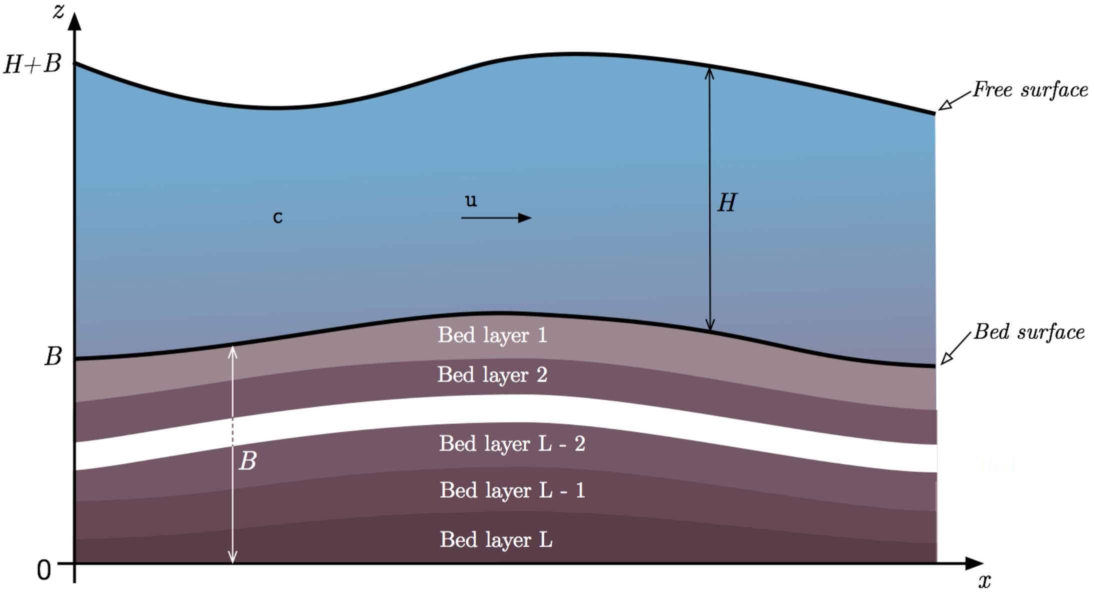

Figure 3.2: A system of shallow-water flow over a multilayer bed.

where n_m is the Manning roughness coefficient. Notice that equations (3.2.1) have been widely used to model sediment transport [1,22,38,90]. These equations can be rewritten in a canonical vector form as

$$\frac{\partial \mathbf{W}}{\partial t} + \frac{\partial \mathbf{F}(\mathbf{W})}{\partial x} = \mathbf{S}(\mathbf{W}) + \mathbf{Q}(\mathbf{W}), \tag{3.2.2}$$

where

$$\mathbf{W} = \begin{pmatrix} H \\ Hu \\ Hc \\ B \end{pmatrix}, \qquad \mathbf{F}(\mathbf{W}) = \begin{pmatrix} Hu \\ Hu^2 + \frac{1}{2}gH^2 \\ Huc \\ 0 \end{pmatrix},$$

$$\mathbf{S}(\mathbf{W}) = \begin{pmatrix} 0 \\ -gH\frac{\partial B}{\partial x} - \frac{(\rho_s - \rho_w)}{2\rho} gH^2 \frac{\partial c}{\partial x} \\ 0 \\ 0 \end{pmatrix}, \qquad \mathbf{Q}(\mathbf{W}) = \begin{pmatrix} \frac{E - D}{1 - \Psi} \\ -\frac{(\rho_0 - \rho)(E - D)u}{\rho(1 - \Psi)} - gHS_f \\ E - D \\ -\frac{E - D}{1 - \Psi} \end{pmatrix}.$$

The system (3.2.1) can also be rearranged in a non-conservative form as

$$\frac{\partial \mathbf{W}}{\partial t} + \boldsymbol{\mathcal{A}}(\mathbf{W})\frac{\partial \mathbf{W}}{\partial x} = \mathbf{S}(\mathbf{W}) + \mathbf{Q}(\mathbf{W}), \tag{3.2.3}$$

where

$$\boldsymbol{\mathcal{A}}(\mathbf{W}) = \begin{pmatrix} 0 & 1 & 0 & 0 \\ gH - u^2 - \dfrac{(\rho_s - \rho_w)}{2\rho} gHc & 2u & \dfrac{(\rho_s - \rho_w)}{2\rho} gH & gH \\ -uc & c & u & 0 \\ 0 & 0 & 0 & 0 \end{pmatrix}.$$

It is easy to verify that the system (3.2.1) is hyperbolic in nature with four real and distinct eigenvalues, as found in [22], of the matrix $\boldsymbol{\mathcal{A}}$ given by

$$\lambda_1 = 0, \qquad \lambda_2 = u, \qquad \lambda_3 = u - \sqrt{gH}, \qquad \lambda_4 = u + \sqrt{gH}, \tag{3.2.4}$$

and their corresponding eigenvectors are

$$\boldsymbol{e}_1 = \begin{pmatrix} -gH \\ 0 \\ -gHc \\ gH - u^2 \end{pmatrix}, \quad \boldsymbol{e}_2 = \begin{pmatrix} \dfrac{\rho_s - \rho_w}{2\rho} \\ \dfrac{\rho_s - \rho_w}{2\rho} u \\ \dfrac{\rho_s - \rho_w}{2\rho} c - 1 \\ 0 \end{pmatrix}, \quad \boldsymbol{e}_3 = \begin{pmatrix} 1 \\ u - \sqrt{gH} \\ c \\ 0 \end{pmatrix}, \quad \boldsymbol{e}_4 = \begin{pmatrix} 1 \\ u + \sqrt{gH} \\ c \\ 0 \end{pmatrix}.$$

Note that in all the studies cited above, the sediment transport system (3.2.2) is solved for homogeneous beds formed of a single type of soil. However, for many realistic applications in sediment transport by shallow water flows the topography is composed of multiple soils and in many cases superposed in layers. Therefore, situations of shallow water flows over multilayer beds as shown in Figure 3.2 are of interest in the current study. Thus, the bed topography depends also on the vertical direction z. In this work, a system is considered where multiple species of sediments ($\varrho = 1, 2, \ldots, N$) exist in a number of layers ($l = 1, 2, \ldots, L$), where N and L refer to the total number of sediment species and the total number of layers in the bed, respectively. Note that two layers may contain the same sediment species, or a single layer may

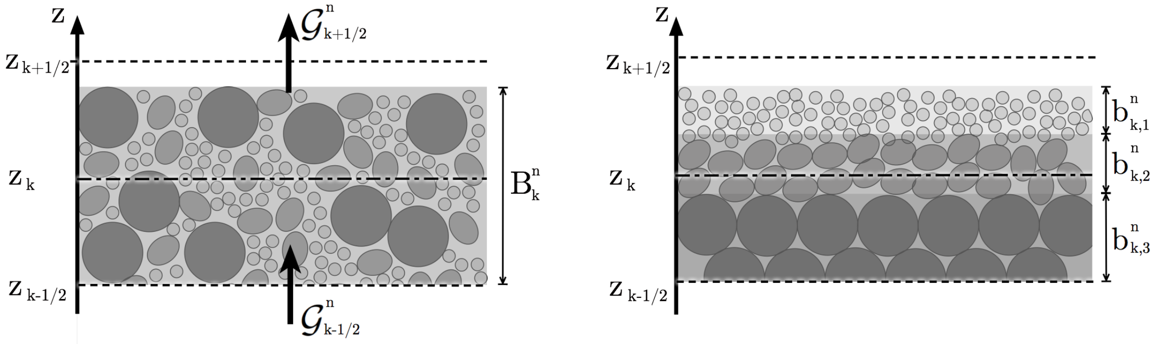

Figure 3.3: Vertical discretisation of the bed into control volumes $\left[z_{k+1/2}, z_{k-1/2}\right]$.

contain multiple sediment species. For simplicity, the cumulative sediment concentration is used

$$\overline{c} = \sum_{\varrho=1}^{N} c_\varrho.$$

Subsequently, the averaged variables are also introduced

$$\overline{\rho}_s = \sum_{\varrho=1}^{N} \frac{c_\varrho}{\overline{c}} \rho_{s,\varrho}, \qquad \overline{\rho} = \rho_w(1-\overline{c}) + \sum_{\varrho=1}^{N} \frac{c_\varrho}{\overline{c}} \rho_{s,\varrho}, \qquad \overline{D} = \sum_{\varrho=1}^{N} \frac{c_\varrho}{\overline{c}} D_\varrho.$$

For the remaining variables $\overline{\rho}_0$, $\overline{E}$, and $\overline{p}$, the equivalent averaging is used with respect to sediments in the bed associated with the active cell. The active cell is defined as the cell that contains sediment and is in contact with the water (*i.e.* contains the bed surface). To ascertain the composition of the bed, it is discretised in the vertical direction into a set of control volumes $\left[z_{k-1/2}, z_{k+1/2}\right]$ $(k = 1, 2, \ldots, K)$ with uniform size Δz. In this study the size is kept uniform to enable us to accurately assess the effects of the bed discretisation. When modelling real world situations where the bed layers are known a priori it is a simple adjustment to modify the bed cell heights to most accurately capture any discrete layers present. Each control volume may contain a variety of sediment species. The active top cell has a height B_k, formed of three sediments with effective height in the cell of $b_{k,1}$, $b_{k,2}$, and $b_{k,3}$, respectively. The bed-dependent variables are then calculated using the weighted averaging procedure [177] as

$$\overline{\Psi} = \sum_{\varrho=1}^{N} \frac{b_{k,\varrho}}{B_k} \Psi_\varrho, \qquad \overline{\rho}_0 = \rho_w(1-\overline{\Psi}) + \sum_{\varrho=1}^{N} \frac{b_{k,\varrho}}{B_k} \rho_{s,\varrho}, \Psi_\varrho, \qquad \overline{E} = \sum_{\varrho=1}^{N} \frac{b_{k,\varrho}}{B_k} E_\varrho.$$

Balancing the exchange forces in each control volume shown in Figure 3.3 the following bedload equation is obtained

$$\frac{\partial B}{\partial t} + \frac{\partial \mathcal{G}(B)}{\partial z} = -\frac{\overline{E} - \overline{D}}{1 - \overline{\Psi}},$$

where $\mathcal{G}(B)$ is a flux function which depends on the exchange terms between the bed cells as discussed below in Section 3.3. Note that each cell only interacts with its two neighbouring cells, whilst erosion and deposition only occur in the active top cell. Thus, the equations considered in the present study for modelling shallow water flows over multilayer beds read

$$\begin{aligned}
\frac{\partial H}{\partial t}+\frac{\partial (Hu)}{\partial x} &= \frac{\overline{E}-\overline{D}}{1-\overline{\Psi}},\\
\frac{\partial (Hu)}{\partial t}+\frac{\partial}{\partial x}\left(Hu^2+\frac{1}{2}gH^2\right) &= -gH\frac{\partial B}{\partial x}-\frac{(\overline{\rho}_s-\rho_w)}{2\overline{\rho}}gH^2\frac{\partial \overline{c}}{\partial x}-\\
&\qquad \frac{(\overline{\rho}_0-\overline{\rho})(\overline{E}-\overline{D})u}{\overline{\rho}(1-\overline{\Psi})}-gH\overline{S}_f, \qquad (3.2.5)\\
\frac{\partial (H\overline{c})}{\partial t}+\frac{\partial}{\partial x}\Big(Hu\overline{c}\Big) &= \overline{E}-\overline{D},\\
\frac{\partial B}{\partial t}+\frac{\partial \mathcal{G}(B)}{\partial z} &= -\frac{\overline{E}-\overline{D}}{1-\overline{\Psi}}.
\end{aligned}$$

Next, a description of the equations used to model the erosion terms E_ϱ and the deposition terms D_ϱ is given. Most formulae for models of suspended sediments obtained from experiments are empirical to differing extents, and detailed discussions on the mathematical and physical aspects of the considered sediment formulae are given in [36,37,162]. To determine the entrainment and deposition terms in the above equations, the empirical relations reported in [35,113] are used. Thus, for a given sediment

$$D_\varrho=\omega_{s,\varrho}(1-c_{B,\varrho})^2c_{B,\varrho}, \qquad \varrho=1,2,\ldots,N, \qquad (3.2.6)$$

where $c_{B,\varrho}$ is a coefficient larger than unity to ensure that the near-bed concentration does not exceed the value of $(1-\overline{\Psi})$. Here, the coefficient $c_{B,\varrho}$ is computed as in [38] by the relation

$$c_{B,\varrho}=\min\left(2,\frac{1-\overline{\Psi}}{c_\varrho}\right), \qquad \varrho=1,2,\ldots,N.$$

In equation (3.2.6), $\omega_{s,\varrho}$ is the settling velocity of a single particle in tranquil water defined as

$$\omega_{s,\varrho}=\frac{\sqrt{\left(\dfrac{36\nu}{d_\varrho}\right)^2+7.5\rho_{s,\varrho}gd_\varrho}-36\left(\dfrac{\nu}{d_\varrho}\right)}{2.8}, \qquad \varrho=1,2,\ldots,N,$$

where ν is the kinematic viscosity of the water and d_ϱ is the average diameter of the sediment particles. For the erosion term E_ϱ, the equations proposed in [36] are employed

$$E_\varrho = \begin{cases} \varphi_\varrho \dfrac{\tau_\varrho - \tau_{cr,\varrho}}{H} u d_\varrho^{-0.2}, & \text{if} \quad \tau_\varrho \geq \tau_{cr,\varrho}, \\ 0, & \text{otherwise}, \end{cases} \qquad \varrho = 1, 2, \ldots, N, \tag{3.2.7}$$

where φ_ϱ is a coefficient to control the erosion forces, $\tau_{cr,\varrho}$ is a critical value of Shields parameter for the initiation of sediment motion, and τ_ϱ is the Shields coefficient defined by

$$\tau_\varrho = \frac{u_{*,\varrho}^2}{sg_\varrho g d_\varrho}, \qquad \varrho = 1, 2, \ldots, N,$$

the submerged specific gravity of sediment sg_ϱ is calculated by $sg_\varrho = \rho_{s,\varrho}/\rho_w - 1$, and $u_{*,\varrho}$ is the friction velocity defined using the Darcy-Weisbach friction factor $f_{f,\varrho}$ as

$$u_{*,\varrho}^2 = \sqrt{\frac{f_{f,\varrho}}{8}} \, |u| \,, \qquad \varrho = 1, 2, \ldots, N.$$

It should be stressed that the erosion terms (3.2.7) are not suitable for problems with low shear sediment transport. In this case, the system can be assumed to be at equilibrium and the following erosion terms, as suggested in [186], are considered

$$E_\varrho = \begin{cases} 0.0033 \rho_{s,\varrho} \sqrt{\Delta g d_\varrho} d_{*,\varrho}^{0.3} \beta_{t,\varrho}^{1.5}, & \text{if} \quad u_{*,\varrho} > u_{*,cr,\varrho}, \\ 0, & \text{otherwise}, \end{cases} \qquad \varrho = 1, 2, \ldots, N, \tag{3.2.8}$$

where $d_{*,\varrho}$ is the dimensionless diameter of the particle and $\tau_{t,\varrho}$ is a transport-stage parameter defined as

$$d_{*,\varrho} = d_{50,\varrho} \left(\frac{\Delta g}{\nu^2} \right)^{1/3}, \qquad \beta_{t,a} = \frac{(u_{*,\varrho}^2) - (u_{*,cr,\varrho}^2)}{(u_{*,cr,\varrho}^2)}, \qquad \varrho = 1, 2, \ldots, N,$$

where $d_{50,\varrho}$ is the average size of sediment particle, and $u_{*,cr,\varrho}$ is the critical friction velocity for the initiation of motion. Note that the equations (3.2.5) can also be rearranged in the compact vector form (3.2.3), and other empirical formulae for the erosion and deposition terms can also be used in this analysis without major conceptual modifications. Since the flux function added in the bedload is only differentiated with respect to z, the hyperbolic parts in the system (3.2.5) are not changed from those appearing in its conventional counterpart (3.2.1). Therefore, the eigenvalues and eigenvectors associated with the system (3.2.5) are also given by the set of expressions (3.2.4), which enables us to use them to approximate the required time-steps in order to ensure stability.

3.3 Modelling the exchange terms for multilayer beds

The bottom topography is discretised into control volumes $[z_{k+1/2}, z_{k-1/2}]$ with same length Δz as shown in Figure 3.3. The time interval is also divided into subintervals $[t_n, t_{n+1}]$ with uniform size Δt. Here, $t_n = n\Delta t$, $z_{k+1/2} = k\Delta z$ and $z_k = (k-1/2)\Delta z$ is the centre of the control volume. Following the standard finite volume formulation, the bedload equation (3.2.5) is integrated with respect to time and space over the domain $[t_n, t_{n+1}] \times [z_{k+1/2}, z_{k-1/2}]$ to obtain the following discrete equation

$$B_k^{n+1} = B_k^n + \frac{\Delta t}{\Delta z}\left(\mathcal{G}_{k+1/2}^n - \mathcal{G}_{k-1/2}^n\right) + \Delta t \mathcal{P}_k^n, \tag{3.3.9}$$

where B_k^n is the space depth-averaged bed B in the control volume $[z_{k+1/2}, z_{k-1/2}]$ at time t_n,

$$B_k^n(x) = \frac{1}{\Delta z}\int_{z_{k-1/2}}^{z_{k+1/2}} B(t_n, x, z)\, dz,$$

and $\mathcal{G}_{k\pm 1/2}^n = G(B_{k\pm 1/2}^n)$ are the numerical fluxes at $z = z_{k\pm 1/2}$ and time t_n. Since erosion and deposition take place only in the top active cell, the source term in (3.3.9) is defined as

$$\mathcal{P}_k^n = \begin{cases} -\dfrac{\overline{E}_k^n - \overline{D}_k^n}{1-\overline{\Psi}_k}, & \text{if } \ z_{k+1/2} < B_k^n \leq z_{k-1/2}, \\ 0, & \text{elsewhere.} \end{cases}$$

It should be noted that, as $0 \leq B_k^n \leq \Delta z$, only four possible cases illustrated in Figure 3.4 may occur for erodible beds. These cases are:

1) **Cell growth:** where erosion and deposition rates in the cell do not exceed the cell bounds. The net movement of sediment together with the original amount of sediment remains within the bounds of the cell.

2) **Cell depletion:** where the cell is entirely eroded and the cell below becomes active. All sediment within the cell is removed so that the sediment in the cell below is now in contact with the water.

3) **Cell overfill:** where the cell is overfilled and the cell above becomes the active cell. The deposition of sediment plus the initial quantity of sediment is so great that the cell is no longer in direct contact with the water but the cell above it is now partially filled and consequently becomes the active cell.

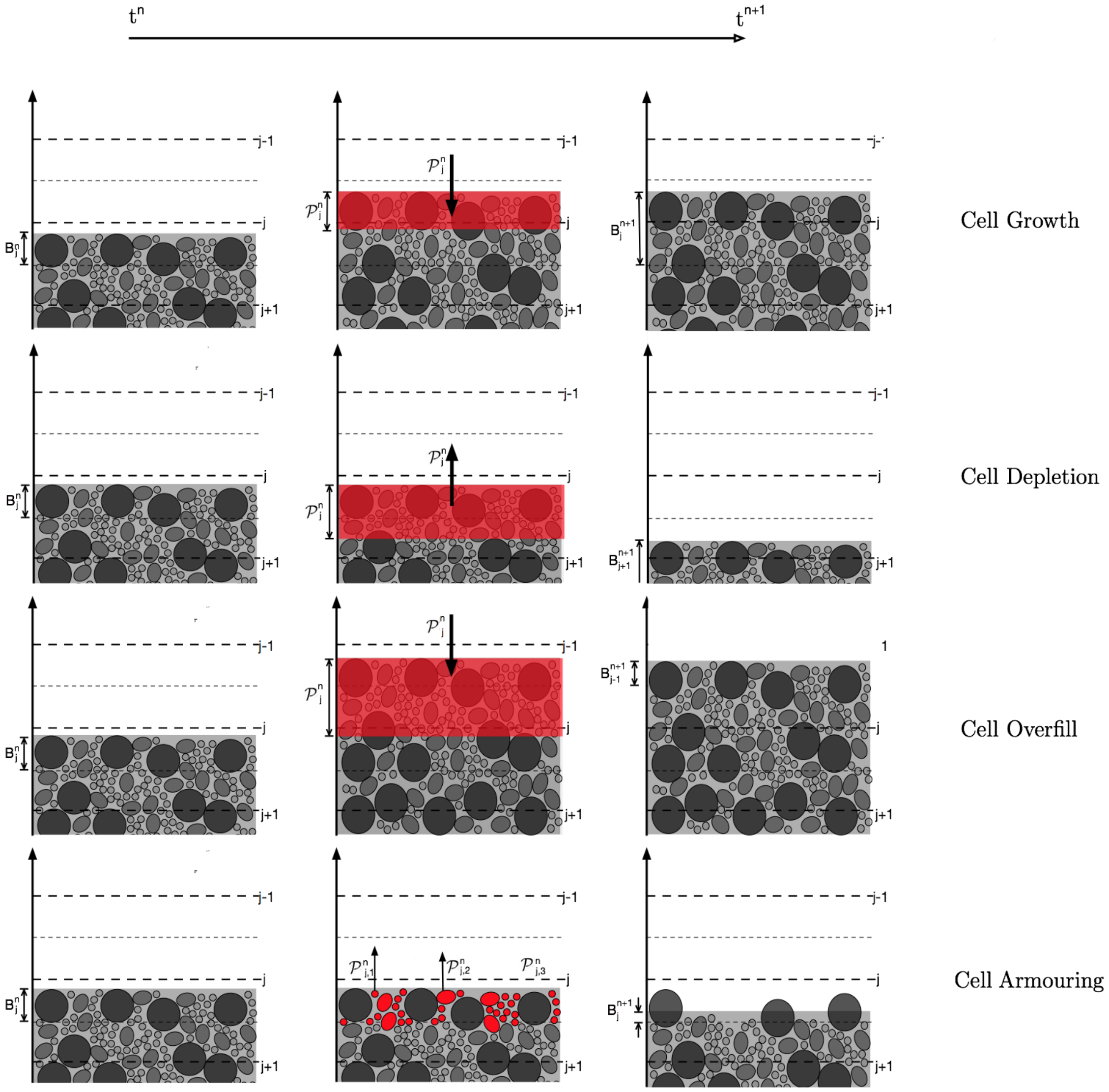

Figure 3.4: Illustration of different cell alterations for shallow water flows over erodible beds. Here the active cell - the one in which soil is eroded from or deposited into - is the jth cell.

4) **Cell armouring:** where the cell holds out against total erosion. One or more sediment types have been totally eroded from the cell, but one or more other sediment types remain in the cell protecting the cell beneath from contact with the water.

To derive the flux functions $\mathcal{G}^n_{k\pm1/2}$ in (3.3.9), the boundary conditions for the first three cases of homogeneous sediments are applied. For example, in the case of cell overfill, we have $B^{n+1}_k = \Delta z$ and $\mathcal{G}^n_{k+1/2} = 0$. Hence,

$$\Delta z = B^n_k + \frac{\Delta t}{\Delta z}\left(-\mathcal{G}^n_{k-1/2}\right) + \Delta t \mathcal{P}^n_k,$$

Algorithm 1: Reconstruction of the bed in the homogeneous multilayer model.

```
if $B_{*,k}^{n+1} > \Delta z$ then
    $B_k^{n+1} = \Delta z$
    $B_{k-1}^{n+1} = B_k^n - \Delta z - \Delta t \frac{E_k^n - D_k^n}{1 - \Psi_k}$
else if $B_{*,k}^{n+1} \leq 0$ then
    $B_k^{n+1} = 0$
    $B_{k+1}^{n+1} = B_k^n + \Delta z - \Delta t \frac{E_k^n - D_k^n}{1 - \Psi_k}$
else
    $B_k^{n+1} = B_{*,k}^{n+1}$
end
```

which can be rearranged as

$$\mathcal{G}_{k-1/2}^n = \frac{\Delta z}{\Delta t} \left(B_k^n - \Delta z - \Delta t \frac{\overline{E}_k^n - \overline{D}_k^n}{1 - \overline{\Psi}_k} \right). \tag{3.3.10}$$

For the case of cell depletion, we have $B_k^{n+1} = 0$ and $\mathcal{G}_{k-1/2}^n = 0$. Hence,

$$0 = B_k^n + \frac{\Delta t}{\Delta z} \left(\mathcal{G}_{k+1/2}^n \right) + \Delta t \; \mathcal{P}_k^n,$$

which can be rearranged as

$$\mathcal{G}_{k-1/2}^n = \frac{\Delta z}{\Delta t} \left(-B_{k-1}^n + \Delta t \frac{\overline{E}_{k-1}^n - \overline{D}_{k-1}^n}{1 - \Psi_{k-1}} \right).$$

For the case of cell growth, both upper and lower fluxes vanish, as the cell bounds are not exceeded, and

$$\mathcal{G}_{k-1/2}^n = \begin{cases} \dfrac{\Delta z}{\Delta t} \left(B_k^n - \Delta z - \Delta t \dfrac{\overline{E}_k^n - \overline{D}_k^n}{1 - \overline{\Psi}_k} \right), & \text{if} \quad B_k^n - \Delta t \dfrac{\overline{E}_k^n - \overline{D}_k^n}{1 - \Psi_k} > \Delta z, \\ \dfrac{\Delta z}{\Delta t} \left(-B_{k-1}^n + \Delta t \dfrac{\overline{E}_{k-1}^n - \overline{D}_{k-1}^n}{1 - \overline{\Psi}_{k-1}} \right), & \text{if} \quad B_k^n - \Delta t \dfrac{\overline{E}_{k-1}^n - \overline{D}_{k-1}^n}{1 - \overline{\Psi}_{k-1}} < 0, \\ 0, & \text{otherwise.} \end{cases}$$

Note, this approach requires only the evaluation of bed height in the three neighbouring cells and it can be implemented for homogeneous beds using the test bed height

$$B_{*,k}^{n+1} = B_k^n - \Delta t \frac{\overline{E}_k^n - \overline{D}_k^n}{1 - \overline{\Psi}_k}.$$

Given the bed B_k^n at time t_n, the bed B_k^{n+1} at time t_{n+1} is updated using Algorithm 1. This algorithm first checks for cell overfill by comparing the test bed height to the height of the cell. In the case of cell overfill, the cell is filled to its maximum bed height and the cell above it is filled with any excess, this second cell then becomes the active cell. If the conditions for cell overfill are not present, then the cell depletion is tested for. If the cell depletion has occurred then the active bed height is set to zero, and the cell beneath it is made the active cell and depleted as required. If neither of the first two cases have occurred then the cell growth is selected and the active bed height becomes the test bed height. For the cell armouring, the sediment mixes between the bed and the flow and, in order to handle this, it is assumed that the cell height can be expressed as the sum of the heights of sediments inside the cell, as shown in Figure 3.4. For this case, the proposed bed factional height $b_{*,k,\varrho}$ is calculated at each time-step as

$$b_{*,k,\varrho}^{n+1} = b_{k,\varrho}^n + \Delta b_{k,\varrho}^n = b_{k,\varrho}^n + \Delta t \left(\frac{E_{k,\varrho}^n - D_{k,\varrho}^n}{1 - \Psi_{k,\varrho}} \right), \qquad \varrho = 1, 2, \ldots, N,$$

where $b_{k,\varrho}$ are the corresponding heights of sediment contained within the cell. The $\Delta b_{*,k}^-$ and $\Delta b_{*,k}^+$ are defined as the sum of all the negative and all the positive $\Delta b_{k,\varrho}$ sediment height changes in the cell, respectively. The procedure to update the bed cell B_k^n to B_k^{n+1} for these cases is described by Algorithm 2, where the four options are evaluated and the correct flux outcome is chosen. This is achieved by first checking for overfill, if this has occurred each sediment is evaluated and the correct quantity of each sediment is assigned (allowing for varying erosion and deposition rates) to the active cell as the cell above it. Next, if overfill has not occurred then cell armouring is evaluated, so if any of the sediments have held out against erosion then they are preserved and all other cell sediment heights are set to zero. If neither of the previous two have been activated then the cell is checked for erosion; if it is found that this has place then the cell height is set to zero and the cell beneath it is depleted as required and becomes the active cell. Finally, if none of the first three options are chosen, then cell growth is activated and the sediment test bed heights become the sediment bed heights.

It should be stressed that the case of cell armouring, inappropriate discretisation of the bed may have a direct effect on the morphodynamic results. Hence, a lower limit on the vertical discretisation is set using the largest particle size for the ϱth sediment d_ϱ. Therefore, for multilayer discretisation, where armouring is possible, the following constraint is recommended

$$\Delta z \geq 10 \max_{\varrho=1,\ldots,N} (d_\varrho).$$

The composition of beds should be known in advance, but the number of discretised layers in

Algorithm 2: Reconstruction of the bed in the non-homogeneous multilayer model.

```
if $\sum_{\varrho=1}^{N} b_{*,k,\varrho}^{n+1} \geq \Delta z$ then
    for $\varrho = 1 : N$ do
        if $b_{*,k,\varrho} \geq 0$ then
            $b_{k,\varrho}^{n+1} = b_{k,\varrho}^{n} + (\Delta z - B_k^n - \Delta b_{*,k}^{-}) \frac{\Delta b_{*k,\varrho}^{n}}{\Delta b_{*,k}^{+} - \Delta b_{*,k}^{-}}$
            $b_{k-1,\varrho}^{n+1} = \Delta b_{*,k,\varrho}^{n+1} - (\Delta z - B_k^n - \Delta b_{*,k}^{-}) \frac{\Delta b_{*,k,\varrho}^{n}}{\Delta b_{*,k}^{+} - \Delta b_{*,k}^{-}}$
        else
            $b_{k,\varrho}^{n+1} = b_{*,k,\varrho}^{n+1}$
        end
    end
else if any $\varrho \in \{1, \ldots, N\}$ $b_{*,k,\varrho}^{n+1} \geq 0$ and $\sum_{\varrho=1}^{N} b_{*,k,\varrho}^{n+1} \leq 0$ then
    for $\varrho = 1 : N$ do
        if $b_{*,k,\varrho} > 0$ then
            $b_{k,\varrho}^{n+1} = b_{*,k,\varrho}^{n+1}$
        else
            $b_{k,\varrho}^{n+1} = 0$
            $\Delta b_{*,k,\varrho}^{n} = -b_{k,\varrho}^{n}$
        end
    end
else if all $b_{*,k,\varrho}^{n+1} \leq 0$ then
    for $\varrho = 1 : N$ do
        if $b_{*,k+1,\varrho}^{n+1} > 0$ then
            $b_{k+1,\varrho}^{n+1} = b_{k,\varrho}^{n} + b_{k+1,\varrho}^{n} - \Delta b_{*,k,\varrho}^{n}$
        else
            $\Delta b_{*,k,\varrho}^{n} = -b_{k,\varrho}^{n}$
        end
        $b_{k,\varrho}^{n+1} = 0$
    end
else
    for $\varrho = 1 : M$ do
        $b_{k,\varrho}^{n+1} = b_{*,k,\varrho}^{n+1}$
    end
end
```

the algorithm can be set by the user, and multiple layers may be formed with the same soil.

3.4 A Riemann solver for 1D multi-sediment model

For the finite volume discretisation of the system (3.2.1), the spatial domain is discretised into control volumes $[x_{i-1/2}, x_{i+1/2}]$ with uniform size Δx for sake of simplicity. This solver is adapted from the work presented in [22]. Here, $x_{i-1/2} = i\Delta x$ and $x_i = (i + 1/2)\Delta x$ defines the centre of the control volume. Integrating the system (3.2.5) with respect to time-space over the domain $[t_n, t_{n+1}] \times [x_{i-1/2}, x_{i+1/2}]$, the following discrete system is obtained

$$\mathbf{W}_i^{n+1} = \mathbf{W}_i^n - \frac{\Delta t}{\Delta x}\Big(\boldsymbol{\mathcal{F}}(\mathbf{W}_{i+1/2}^n) - \boldsymbol{\mathcal{F}}(\mathbf{W}_{i-1/2}^n)\Big) + \Delta t\mathbf{S}\left(\mathbf{W}_i^n\right) + \Delta t\mathbf{Q}\left(\mathbf{W}_i^n\right), \tag{3.4.11}$$

where $\mathbf{W}_i^n$ is the space averaged solution of $\mathbf{W}$ in the control volume $[x_{i-1/2}, x_{i+1/2}]$ at time t_n, defined as

$$\mathbf{W}_i^n = \frac{1}{\Delta x}\int_{x_{i-1/2}}^{x_{i+1/2}} \mathbf{W}(t_n, x)\, dx,$$

and $\mathbf{F}(\mathbf{W}_{i\pm1/2}^n)$ are the numerical fluxes at the interfaces $x = x_{i\pm1/2}$ and time t_n. The treatment of source terms $\mathbf{S}$ and $\mathbf{Q}$ in (3.4.11) is dealt with using the standard splitting procedure detailed in [179]

$$\begin{aligned} \mathbf{W}_i^* &= \mathbf{W}_i^n - \frac{\Delta t}{\Delta x}\Big(\boldsymbol{\mathcal{F}}(\mathbf{W}_{i+1/2}^n) - \boldsymbol{\mathcal{F}}(\mathbf{W}_{i-1/2}^n)\Big) + \Delta t\mathbf{S}\left(\mathbf{W}_i^n\right), \\ \mathbf{W}_i^{n+1} &= \mathbf{W}_i^* + \Delta t\mathbf{Q}\left(\mathbf{W}_i^*\right). \end{aligned} \tag{3.4.12}$$

To complete the spatial discretisation of the equations (3.4.12), a reconstruction of the numerical fluxes $\mathbf{F}(\mathbf{W}_{i\pm1/2}^n)$ and source term $\mathbf{S}\left(\mathbf{W}_i^n\right)$ must be selected. In general applications, this reconstruction requires a solution of Riemann problems at the interfaces $x_{i\pm1/2}$. Here, the self-similar solution to the Riemann problem, formed of the equation (3.2.2) and subject to the initial condition

$$\mathbf{W}(0, x) = \begin{cases} \mathbf{W}_L, & \text{if} \quad x < 0, \\ \mathbf{W}_R, & \text{if} \quad x > 0, \end{cases}$$

is given by

$$\mathbf{W}(t, x) = \mathbf{R}_s\left(\frac{x}{t}, \mathbf{W}_L, \mathbf{W}_R\right),$$

where $\mathbf{R}_s$ is the Riemann solution which can be evaluated analytically for the SWEs over fixed beds. Note, we refer to [8] for the exact expression of $\mathbf{R}_s$. Thus, the intermediate state $\mathbf{W}_{i+1/2}^n$

in equation (3.4.12) at the cell interface $x_{i+1/2}$ is defined as

$$\mathbf{W}_{i+1/2}^n = \mathbf{R}_s\left(0, \mathbf{W}_i^n, \mathbf{W}_{i+1}^n\right).$$

This procedure is computationally demanding, and it may restrict the applications where exact Riemann solvers are not available. Furthermore, the discretisation of the source terms in equation (3.4.11) may suffer from singular values raised from the Riemann solver at the interfaces. These difficulties are typical in the numerical solution of SWEs over erodible sediment beds and they will be retained for shallow water flows over sedimentary topography. In order to avoid these difficulties and reconstruct an approximation of $\mathbf{W}_{i+1/2}^n$, an adaptation of the finite volume non-homogeneous Riemann solver proposed in [153] is used in the present study.

The Riemann solver has also been extended in [22] for solving dam-break problems over homogeneous erodible beds. In the present work, the performance of the Riemann solver for solving shallow water flows over multilayer sedimentary beds is examined. In the splitting form (3.4.12), the Riemann solver results in a predictor-corrector scheme of the form

$$\begin{aligned}
\mathbf{W}_{i+1/2}^n &= \frac{1}{2}\left(\mathbf{W}_{i+1}^n + \mathbf{W}_i^n\right) - \frac{1}{2}\mathrm{sgn}\Big[\boldsymbol{\mathcal{A}}(\widehat{\mathbf{W}}_{i+1/2}^n)\Big]\left(\mathbf{W}_{i+1}^n - \mathbf{W}_i^n\right), \\
\mathbf{W}_i^{n+1} &= \mathbf{W}_i^n - \frac{\Delta t}{\Delta x}\bigg(\mathbf{F}\left(\mathbf{W}_{i+1/2}^n\right) - \mathbf{F}\left(\mathbf{W}_{i-1/2}^n\right)\bigg) + \Delta t\mathbf{S}\left(\mathbf{W}_i^n\right),
\end{aligned} \tag{3.4.13}$$

where the averaged state $\widehat{\mathbf{W}}_{i+1/2}^n$ is calculated as

$$\widehat{\mathbf{W}}_{i+1/2}^n = \begin{pmatrix} \dfrac{H_i^n + H_{i+1}^n}{2} \\ \dfrac{\sqrt{H_i^n}\,u_i^n + \sqrt{H_{i+1}^n}\,u_{i+1}^n}{\sqrt{H_i^n} + \sqrt{H_{i+1}^n}} \\ \dfrac{\sqrt{H_i^n}\,\bar{c}_i^n + \sqrt{H_{i+1}^n}\,\bar{c}_{i+1}^n}{\sqrt{H_i^n} + \sqrt{H_{i+1}^n}} \\ \dfrac{B_i^n + B_{i+1}^n}{2} \end{pmatrix}, \tag{3.4.14}$$

and the sign matrix in (3.4.13) is given by

$$\mathrm{sgn}\Big[\boldsymbol{\mathcal{A}}(\widehat{\mathbf{W}}_{i+1/2}^n))\Big] = \boldsymbol{\mathcal{R}}\left(\widehat{\mathbf{W}}_{i+\frac{1}{2}}^n\right)\left|\boldsymbol{\Lambda}\left(\widehat{\mathbf{W}}_{i+\frac{1}{2}}^n\right)\right|^{-1}\boldsymbol{\Lambda}\left(\widehat{\mathbf{W}}_{i+\frac{1}{2}}^n\right)\boldsymbol{\mathcal{R}}^{-1}\left(\widehat{\mathbf{W}}_{i+\frac{1}{2}}^n\right). \tag{3.4.15}$$

The determination of the sign matrix $\mathrm{sgn}\Big[\boldsymbol{\mathcal{A}}\left(\widehat{\mathbf{W}}\right)\Big]$ is carried out using the eigenvalues in (3.2.4) as

$$\mathrm{sgn}\Big[\boldsymbol{\mathcal{A}}\left(\widehat{\mathbf{W}}\right)\Big] = \boldsymbol{\mathcal{R}}\left(\widehat{\mathbf{W}}\right)\mathrm{sgn}\Big[\boldsymbol{\Lambda}\left(\widehat{\mathbf{W}}\right)\Big]\boldsymbol{\mathcal{R}}^{-1}\left(\widehat{\mathbf{W}}\right),$$

where

$$\operatorname{sgn}\left[\mathbf{\Lambda}\left(\widehat{\mathbf{W}}\right)\right] = \begin{pmatrix} \operatorname{sgn}\left(\widehat{\lambda}_1\right) & 0 & 0 & 0 \\ 0 & \operatorname{sgn}\left(\widehat{\lambda}_2\right) & 0 & 0 \\ 0 & 0 & \operatorname{sgn}\left(\widehat{\lambda}_3\right) & 0 \\ 0 & 0 & 0 & \operatorname{sgn}\left(\widehat{\lambda}_4\right) \end{pmatrix},$$

and $\widehat{\lambda}_k$ $(k = 1, 2, 3, 4)$ are the eigenvalues in (3.2.4) calculated at the averaged state (3.4.14). The right and left eigenvector matrices in (3.4.15) are defined by

$$\boldsymbol{\mathcal{R}}\left(\widehat{\mathbf{W}}\right) = \begin{pmatrix} -\widehat{s}^2 & \widehat{r} & 1 & 1 \\ 0 & \widehat{r}\widehat{u} & \widehat{\lambda}_3 & \widehat{\lambda}_4 \\ -\widehat{s}^2\widehat{c} & \widehat{r}\widehat{c} - 1 & \widehat{c} & \widehat{c} \\ -\widehat{\lambda}_3\widehat{\lambda}_4 & 0 & 0 & 0 \end{pmatrix},$$

$$\boldsymbol{\mathcal{R}}^{-1}\left(\widehat{\mathbf{W}}\right) = \begin{pmatrix} 0 & 0 & 0 & \dfrac{-1}{\widehat{\lambda}_3\widehat{\lambda}_4} \\ \widehat{c} & 0 & -1 & 0 \\ \dfrac{\widehat{\lambda}_4 - \widehat{c}\widehat{r}\widehat{s}}{2\widehat{s}} & \dfrac{-1}{2\widehat{s}} & \dfrac{\widehat{r}}{2} & \dfrac{-\widehat{s}}{2\widehat{\lambda}_3} \\ -\dfrac{\widehat{\lambda}_3 + \widehat{c}\widehat{r}\widehat{s}}{2\widehat{s}} & \dfrac{1}{2\widehat{s}} & \dfrac{\widehat{r}}{2} & \dfrac{\widehat{s}}{2\widehat{\lambda}_4} \end{pmatrix},$$

where $\widehat{s} = \sqrt{g\widehat{H}}$ is the wave speed and $\widehat{r} = \dfrac{\bar{\rho}_s - \rho_w}{2\widehat{\rho}}$ is a density ratio. Using the above matrices, the averaged state $\mathbf{W}^n_{i+1/2}$ can be easily obtained from the predictor stage in (3.4.13). Once these states are computed, the solution $\mathbf{W}^{n+1}_i$ is recovered using the corrector stage in (3.4.13).

For the discretisation of the source terms $\mathbf{S}$ and $\mathbf{Q}$ in (3.4.12) a well-balanced method is used as reported in [22]. Here, the discretisation of the source terms produces a scheme that is well-balanced with the discretisation of the flux gradients using the concept of C-property. Recall that a numerical scheme is said to satisfy the still-water equilibrium (C-property) for the equations (3.2.5) if the condition

$$\overline{E} - \overline{D} = 0, \qquad u = 0, \qquad B^n = \bar{B}(x), \qquad H + B = cte_1, \qquad \rho = cte_2, \tag{3.4.16}$$

holds for stationary flows at rest, cte_1 and cte_2 are non-negative constants. Therefore, the treatment of source terms in (3.4.13) is reconstructed such that the condition (3.4.16) is preserved at the discretised level. Note that, since the density is constant, the concentration is also a constant. By applying the conditions of zero velocity and a fixed bed to the system (3.2.5), results in

$$\frac{\partial}{\partial t}\begin{pmatrix} H \\ 0 \\ B \end{pmatrix} + \frac{\partial}{\partial x}\begin{pmatrix} 0 \\ \frac{1}{2}H^2 \\ 0 \end{pmatrix} = \begin{pmatrix} 0 \\ -gH\dfrac{\partial B}{\partial x} \\ 0 \end{pmatrix}. \tag{3.4.17}$$

The matrices $\boldsymbol{\mathcal{R}}^n_{i+1/2}, \boldsymbol{\Lambda}$ and $\left(\boldsymbol{\mathcal{R}}^n_{i+1/2}\right)^{-1}$, are expressed as

$$\boldsymbol{\mathcal{R}}^n_{i+1/2} = \begin{pmatrix} 1 & 1 & -\sigma^2 \\ -\sigma & \sigma & 0 \\ 0 & 0 & \sigma^2 \end{pmatrix}, \quad \boldsymbol{\Lambda}^n_{i+1/2} = \begin{pmatrix} -\sigma & 0 & 0 \\ 0 & \sigma & 0 \\ 0 & 0 & 0 \end{pmatrix}, \quad \left(\boldsymbol{\mathcal{R}}^n_{i+1/2}\right)^{-1} = \frac{1}{2}\begin{pmatrix} 1 & \frac{-1}{\sigma} & 1 \\ 1 & \frac{1}{\sigma} & 1 \\ 0 & 0 & \frac{2}{\sigma^2} \end{pmatrix},$$

where $\sigma = \sqrt{g\dfrac{H_i^n + H_{i+1}^n}{2}}$ is the wave speed at the cell interface. When applied to the predictor step of (3.4.13), the system (3.4.17) becomes

$$\mathbf{W}^n_{i+1/2} = \begin{pmatrix} \dfrac{H_i^n + H_{i+1}^n}{2} \\ -\dfrac{\sigma^n_{i+1/2}}{2}\left(H_i^n + B_i^n - H_{i+1}^n - H_{i+1}^n\right) \\ \dfrac{B_i^n + B_{i+1}^n}{2} \end{pmatrix}, \tag{3.4.18}$$

and the corrector stage updates to

$$\mathbf{W}_i^{n+1} = \mathbf{W}_i^n - g\frac{\Delta t}{2\Delta x}\begin{pmatrix} 0 \\ \left(H^n_{i+1/2}\right)^2 - \left(H^n_{i-1/2}\right)^2 \\ 0 \end{pmatrix} - \Delta t\begin{pmatrix} 0 \\ \left(gH\dfrac{\partial B}{\partial x}\right)_i^n \\ 0 \end{pmatrix}. \tag{3.4.19}$$

For the stationary solution $\mathbf{W}_i^{n+1} = \mathbf{W}_i^n$. Thus the discretised flux gradients and source terms in equation (3.4.19) should sum to zero, therefore

$$g\frac{1}{2\Delta x}\left(\left(H^n_{i-1/2}\right)^2 - \left(H^n_{i+1/2}\right)^2\right) = \left(gH\frac{\partial B}{\partial x}\right)_i^n. \tag{3.4.20}$$

Hence we combine $H^n_{i+1/2} = \dfrac{H_i^n + H_{i+1}^n}{2}$ and $H^n_{i+1} - H^n_{i-1} = B^n_{i+1} - B^n_{i-1}$, and thus equation (3.4.20) becomes

$$\left(gH\frac{\partial B}{\partial x}\right)_i^n = g\frac{H_{i+1/2}^n + H_{i-1/2}^n}{2}\frac{B_{i+1}^n - B_{i-1}^n}{2\Delta x}. \tag{3.4.21}$$

The source terms in the corrector stage of (3.4.13) are discretised as

$$\mathbf{S}\left(\mathbf{W}_i^n\right) = \begin{pmatrix} 0 \\ -g\dfrac{H_{i+1/2}^n + H_{i-1/2}^n}{2}\dfrac{B_{i+1}^n - B_{i-1}^n}{2\Delta x} - \dfrac{(\bar{\rho}_s - \rho_w)}{2\bar{\rho}_i^n}g\left(\dfrac{H_{i+1/2}^n + H_{i-1/2}^n}{2}\right)^2\dfrac{\bar{c}_{i+1}^n - \bar{c}_{i-1}^n}{2\Delta x} \\ 0 \\ 0 \end{pmatrix},$$

$$\mathbf{Q}\left(\mathbf{W}_i^n\right) = \begin{pmatrix} \dfrac{\overline{E}_i^n - \overline{D}_i^n}{1-\overline{\Psi}} \\ -\dfrac{\left(\bar{\rho}_0 - \bar{\rho}_i^n\right)\left(\overline{E}_i^n - \overline{D}_i^n\right)u_i^n}{\bar{\rho}_i^n\left(1-\overline{\Psi}\right)} - g\dfrac{H_{i+1/2}^n + H_{i-1/2}^n}{2}\overline{S}_f \\ \overline{E}_i^n - \overline{D}_i^n \\ -\dfrac{\overline{E}_i^n - \overline{D}_i^n}{1-\overline{\Psi}} \end{pmatrix}.$$

It should be stressed that well-balanced discretisation is key for accurate predictions of sediment transport by shallow water flows. In practice, if the C-property is not satisfied by the numerical method then non-physical oscillations may appear in its numerical solutions. Failure to capture shocks and the presence of instability problems may also occur if the discretisation of the flux gradients and the discretisation of the source terms are not adequately balanced. This method is implemented as shown in Figure 3.5.

3.5 Numerical results

This section considers test examples for evolving and steady-state simulations of homogeneous, non-homogeneous, and graded erodible sediment beds, using the sediment properties presented in Table 3.1. These parameters have been used in many sediment transport applications, see for example [151,189,207]. For all results presented in this section $\rho_w = 1000\ kg/m^3$, $g = 9.81\ m/s^2$ and $\nu = 1.2 \times 10^{-6}\ m^2/s$. The main goal here is to illustrate the performance of the proposed Riemann solver coupled with the discretised bed in modelling these situations. The later two simulations are first tested against experimental data for which only homogeneous single-layered beds are solved and then extended to show the effects of varying the bed composition. In all computations, the Courant number Cr = 0.7 is used to vary the time-step Δt according to the

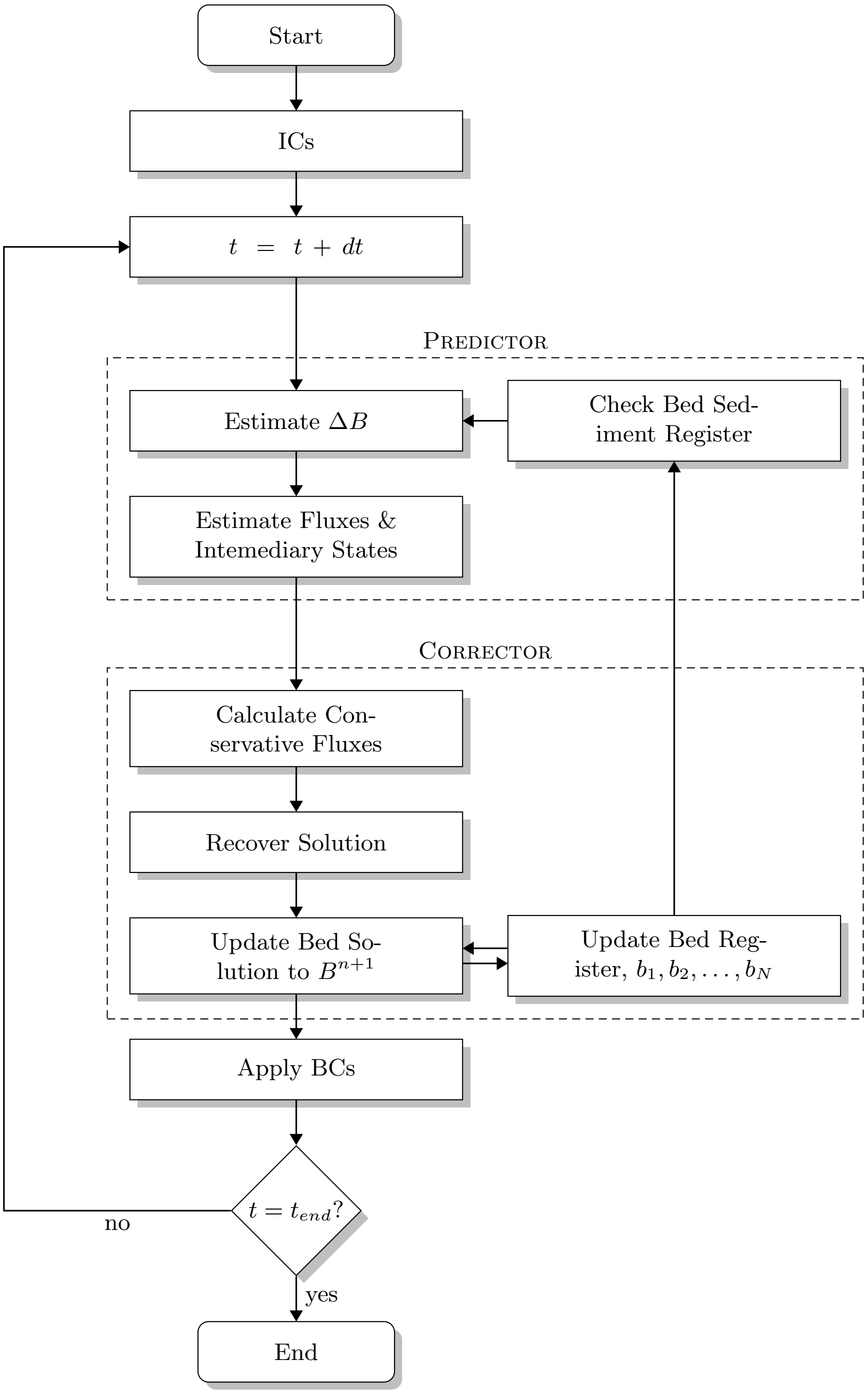

Figure 3.5: A flowchart demonstrating the Predictor Corrector steps in the proposed Riemann Solver. The bed register is highlighted.

Table 3.1: Sediment characteristics used in the present study [151, 189, 207].

Type	d $[mm]$	Ψ	φ	ω_s $[m/s]$	ρ_s $[kg/m^3]$	n_m $[s/m^{1/3}]$
Sand 1	0.0625	0.5	0.015	0.00014	1650	0.012
Sand 2	0.25	0.35	0.015	0.001	1650	0.013
Sand 3	0.20	0.4	0.015	0.0015	1600	0.013
Sand 4	0.16	0.4	0.075	0.019	2650	0.01
Sand 5	0.20	0.4	0.075	0.019	2700	0.01
Sand 6	0.25	0.4	0.075	0.020	2800	0.01
Sand 7	0.16	0.4	0.00004	0.5	1500	0.011
Sediment 1	0.5	0.42	0.00015	0.2	2630	0.01
Sediment 2	1.61	0.42	0.00015	0.2	2630	0.01
Sediment 3	2	0.42	0.00015	0.2	2630	0.01
Sediment 4	2	0.4	0.015	0.2	2650	0.011
Clay	0.07	0.51	0.012	0.0001	1200	0.010
Silt	0.016	0.55	0.01	0.0001	1250	0.010
Pearls	6.1	0.4	0.000015	0.0001	1048	0.025

stability condition

$$\Delta t = \mathrm{Cr} \min \left(\frac{\Delta x}{\max\limits_{k=1,2,3,4} (|\lambda_k^n|)} \right),$$

where λ_k $(k = 1, 2, 3, 4)$ are the four eigenvalues of the sediment transport system given in system (3.2.4). Lambdas are used here to enable the reader to track their evolution through chapters. Note that the above stability condition takes into account the rate of vertical changes and it ensures that the bed information never jumps more than one vertical cell as long as $\Delta z \leq \Delta x$. The sediment parameters for all sediments used in this work are listed in Table 3.1.

3.5.1 Verification of C-property

The lake at rest problem is one of the well-established tests for verifying the C-property. Introduced in [25], it requires that a flow at rest should remain at rest for a 1000 s over the uneven domain shown in Figure 3.6. A period of 1000 s is used as so long as the error remains within the machine precision, the simulation can be assumed to be indefinitely stable. The simulation is run with no sediment and over a fixed bed. The water was initially at rest and the free-surface height was set at 15 m (*i.e.* $H + B = 15$ m). As is shown in Figure 3.6, the errors from the simulation are equivalent to the machine precision. Therefore it can be concluded that the method is well-balanced and retains the C-property.

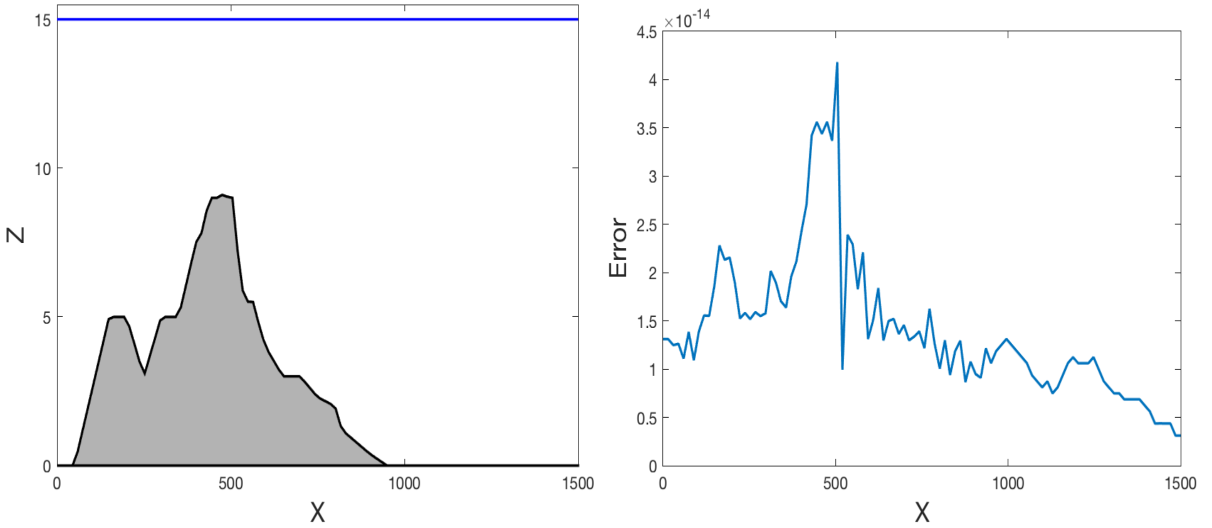

Figure 3.6: The free-surface of the lake at rest flow problem (left) and the associated error in the water free-surface (right) at $t = 1000\ s$.

3.5.2 Dam-break problems

Dam-break problems over erodible beds formed with homogeneous single-layered sand, heterogeneous three-layered sands, and gradually varying sand composition, are depicted in Figure 3.9 and considered in this section. For this evolving problem, the erosion term is given by the formula (3.2.7). Initially, the bottom topography is assumed to be flat ($i.e.$ $B(0, x) = 0$) and at $t = 0$ the dam breaks and the flow problem yields a shock wave travelling downstream and a rarefaction wave travelling upstream. To validate the numerical results obtained using the presented Riemann solver, the dam-break experiment detailed in [39] is considered. In this experiment, the channel is 1.2 m long and the bed is assumed to be homogeneously formed by spherical pearls with the sediment properties given in Table 3.1. The initial conditions used are

$$H(0,x) = \begin{cases} 0.1\ m, & \text{if} \quad x \leq 0, \\ 0.01\ m, & \text{if} \quad x > 0, \end{cases} \qquad B(0,x) = 0\ m, \qquad u(0,x) = 0\ m/s, \qquad c(0,x) = 0.$$

The spatial domain is discretised into 150 control volumes, and results for bed and free-surface are presented. Figure 3.7 shows a comparison of the computed results and measurements obtained for the bed and the water free-surface at time $t = 0.505\ s$. The agreement between the simulations and measurements is reasonably good. The erosion magnitude and wave-front location are well predicted by this Riemann solver. As expected an hydraulic jump is formed near the initial dam place ($x = 0\ m$) and propagates upstream along the channel. However, the location of the hydraulic jump is less accurately predicted by the numerical model. This may be attributed to the fact that 3D effects from the experimental set-up have not been accounted

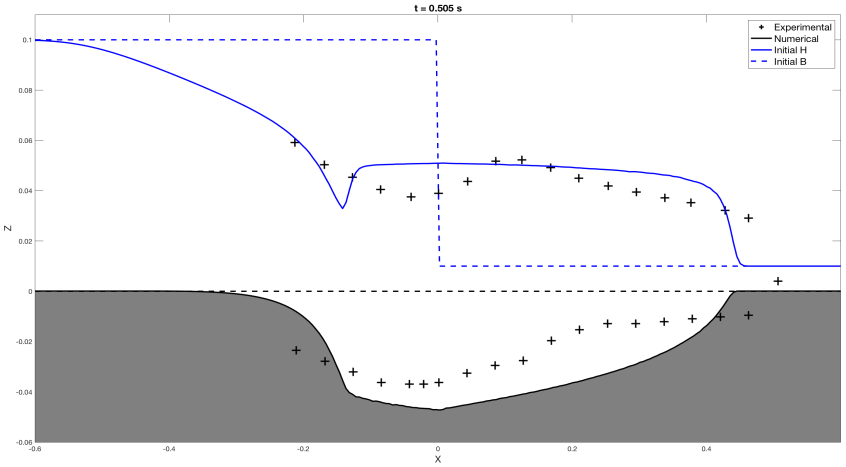

Figure 3.7: Comparison between numerical results and experimental data for a dam-break problem over a single-layered bed at time $t = 0.505\ s$.

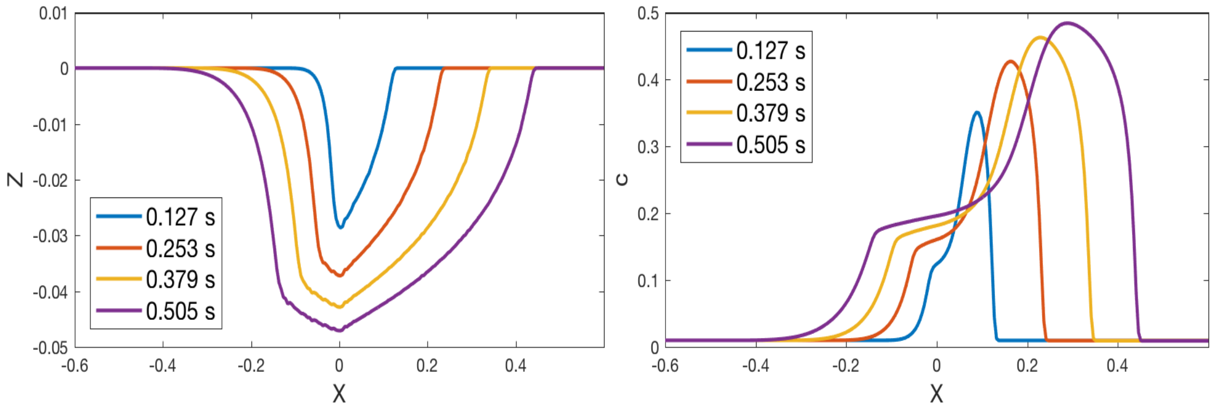

Figure 3.8: Time evolution of the bed profile (left) and the sediment concentration (right) for a dam-break problem over the single-layered Taipei experiment bed.

for in the simulation. Time evolutions of the bed profile and the sediment concentration are presented in Figure 3.8. As the time evolves, the erosion acts on an ever-growing portion of the bed and the eroded material contributes to the sediment concentration. The proposed Riemann solver performs very well for this dam-break problem since it does not diffuse the moving bed and no spurious oscillations have been observed when the water flows over the erodible bed. Furthermore, the results compare favourably with those reported in [38, 162] for the similar test problems of dam-break flows over erodible beds. Next, the model is tested with a dam-break problem in a rectangular channel with an heterogeneous bottom initially assumed to be flat. The channel length is 1000 m and the initial conditions are given by

$$H(0,x) = \begin{cases} 5\ m, & \text{if} \quad x \leq 500\ m, \\ 0.0001\ m, & \text{if} \quad x > 500\ m, \end{cases} \qquad B(0,x) = 0\ m, \quad u(0,x) = 0\ m/s, \quad c(0,x) = 0.0001.$$

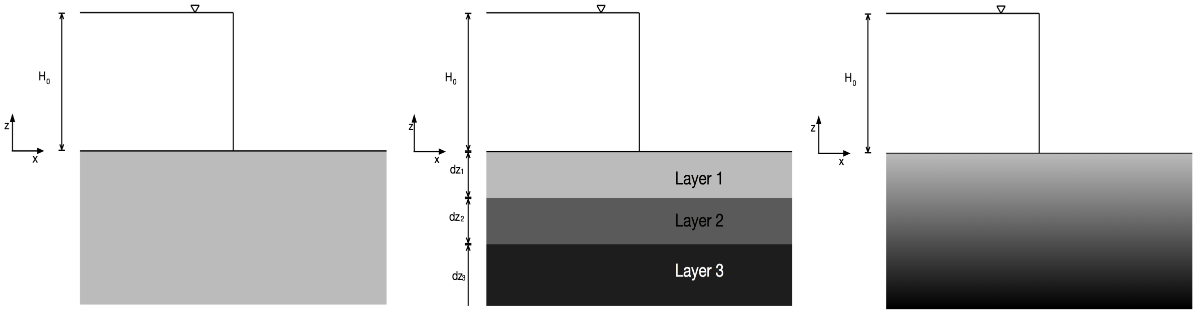

Figure 3.9: Illustration of a dam-break problem over a single-layered bed (left), a three-layered bed (middle) and a gradually varying bed (right), all three before discretisation.

Highlighting the effect of making different assumptions on the bed, three situations are modelled: (i) an homogeneous single-layer bed of Sand 2, (ii) an heterogeneous three-layered bed of Sand 1, Sand 2, and Sand 3, and (iii) a gradually varying bed from Sand 1 to Sand 3. The depth of the bed is 4 m and for the three-layered situation it is initially formed by

$$B(0,x,z) = \begin{cases} \text{Sand 1}, & \text{if } -1.25\,m \leq z < 0\,m, \\ \text{Sand 2}, & \text{if } -2.5\,m \leq z < -1.25\,m, \\ \text{Sand 3}, & \text{if } -4\,m \leq z < -2.5\,m. \end{cases}$$

For a gradually varying bed, the initial bed is formed by a gradual variation from Sand 1 to Sand 3 as

$$B(0,x,z) = \left(\frac{2.5+z}{2.5}\right)\text{Sand 1} + \left(\frac{z}{-2.5}\right)\text{Sand 3}.$$

First, a convergence study is performed for the spatial and bed discretisations in order to quantify the errors and to check the effectiveness of the proposed techniques. To this end, the dam-break problem over an homogeneous single-layered bed of Sand 2 is considered: this could be interpreted as an average between the two other situations considered in this test example. In order to quantify the errors in this example, a reference solution computed using a fine discretisation with $\Delta x = 2\ m$ and $\Delta z = 0.015\ m$ is used as an exact solution. The solutions are calculated at time $t = 20\ s$, using different spatial and bed discretisations.

Table 3.2 summarizes the errors in the concentration, the bed profiles, and the computational times for each discretisation combination $(\Delta x, \Delta z)$. As can be seen from the results presented in this table, increasing the number of control volumes in the horizontal spatial discretisation produces an increase in the accuracy and also in the computational cost of the Riemann solver. The largest numerical errors are produced by the coarse discretisation $(\Delta x = 3.33\ m, \Delta z = 0.12\ m)$. Table 3.2 shows that, when compared to the horizontal discretisation, the vertical

Table 3.2: CPU times, error in the concentration, and error in the minimum values of the bed profile using different spatial and bed discretisation steps Δx and Δz.

		Horizontal discretisation				
		$\Delta x = 3.33$ m	$\Delta x = 2.86\ m$	$\Delta x = 2.50\ m$	$\Delta x = 2.22\ m$	$\Delta x = 2.00\ m$
Vertical discretisation	$\Delta z = 0.12\ m$	203 s	262 s	346 s	438 s	540 s
		9.17 %	6.62 %	3.08 %	1.95 %	0.69 %
		1.79 %	1.27 %	0.92 %	0.52 %	0.17 %
	$\Delta z = 0.060\ m$	205 s	261 s	349 s	446 s	553 s
		9.57 %	6.32 %	5.15 %	2.16 %	0.26 %
		1.75 %	1.31 %	0.81 %	0.46 %	0.18 %
	$\Delta z = 0.030\ m$	205 s	268 s	351 s	455 s	567 s
		9.05 %	7.63 %	4.19 %	2.21 %	1.07 %
		1.79 %	1.23 %	0.84 %	0.52 %	0.17 %
	$\Delta z = 0.020\ m$	208 s	280 s	363 s	458 s	567 s
		7.96 %	6.40 %	4.11 %	1.76 %	0.71 %
		1.83 %	1.25 %	0.66 %	0.52 %	0.15 %
	$\Delta z = 0.015\ m$	208 s	280 s	365 s	461 s	571 s
		7.66 %	6.41 %	4.44 %	2.23 %	0.62 %
		1.83 %	1.28 %	0.82 %	0.51 %	0.17 %

discretisation has small effects on both efficiency and accuracy. For example, using ($\Delta x = 2.86\ m, \Delta z = 0.12\ m$) the computational time and the variance in the suspended load error are respectively 262 s and 1.10 %, whereas using ($\Delta x = 2.22\ m, \Delta z = 0.020\ m$) these results are 458 s and 0.34 %. A spatial convergence is clearly achieved in the proposed Riemann solver for both horizontal and vertical discretisations. For the considered flow and sediment conditions, a balance between accuracy and efficiency in this method favoured the discretisation using ($\Delta x = 2.22\ m, \Delta z = 0.020\ m$).

The performance of the model in situations of dam-break flows over heterogeneous multilayer beds is assessed. The Riemann solver is run for the three-layered beds, and the gradually varying beds, using ($\Delta x = 2.22\ m, \Delta z = 0.020\ m$). Other multilayer simulations with higher number of layers can also be computed using this model. Figure 3.10 presents water heights, bed profiles and sediment concentrations for the dam-break problem over a three-layered bed at four different instants $t = 5$, 10, 15 and 20 s. Those results obtained for the dam-break problem over a gradually varying bed are presented in Figure 3.11. Dark and light colours in this figure are used for the bed of Sand 3 and Sand 1, respectively. As can be observed from these results, the dam-break flow over the movable bed can build up a heavily concentrated wave-front which

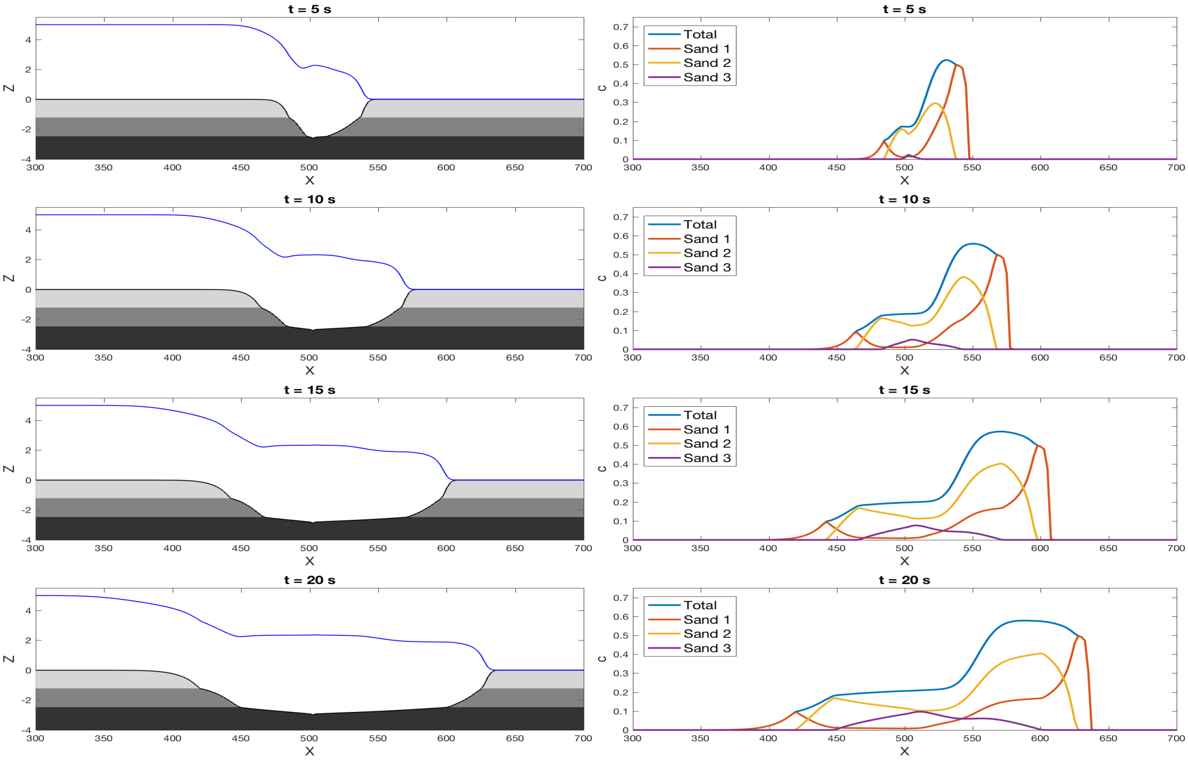

Figure 3.10: Water heights and bed profiles (left) and sediment concentrations (right) for a dam-break problem over a three-layered bed at four different instants.

is bounded by the wave forefront and a contact discontinuity of the sediment transport, and it depresses over the course of the simulation. The bed mobility can strongly modify the water free-surface profiles and may have considerable implications for flood predictions. As in the previous simulations, an hydraulic jump in the water free-surface is initially formed around the dam site, it depresses progressively as it propagates upstream and eventually disappears. It is evident that the movable bed can be significantly scoured and the dimensions of the scour hole are of a similar order of magnitude to those of the water flow itself. Therefore, the rate of bed deformation is not negligible compared to that of the flow change, characterizing the need for coupled modelling of the strongly interacting flow-sediment-morphology system, as considered in the present work. From the presented results it can be concluded that the proposed Riemann solver performs very well for this dam-break problem, since it does not diffuse the moving water-fronts and no spurious oscillations have been detected when the dam breaks over the sedimentary bed. Finally, Figure 3.12 shows a comparison of the bed profiles obtained, using the three bed configurations. It is interesting to note that while all of these cases are approximations of the same situation, very different final bed profiles are developed. Unfortunately, there is no experimental data to validate these results, but the proposed method captures the morphodynamic features accurately.

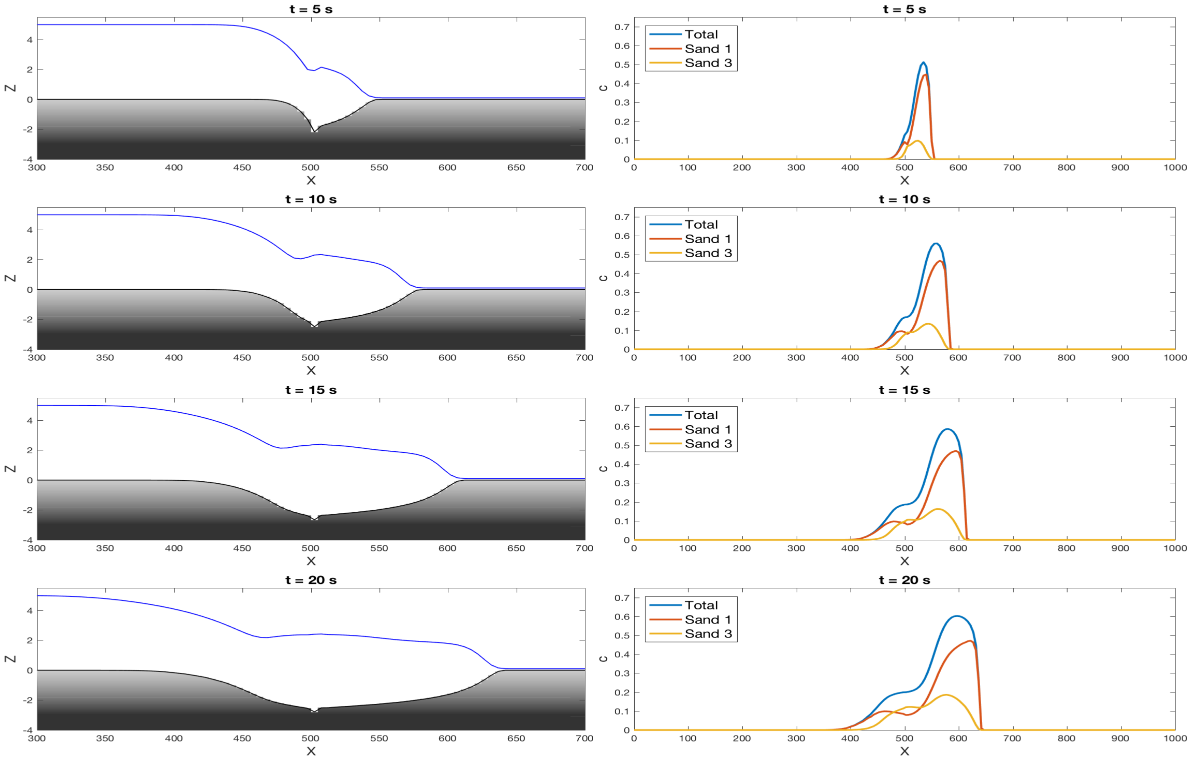

Figure 3.11: Water heights and bed profiles (left) and sediment concentrations (right) for a dam-break problem over a gradually varying bed at $t = 5\ s, 10\ s, 15\ s,$ and $20\ s$.

3.5.3 Stream-flow problems

The performance of the proposed numerical techniques for stream-flow problems over erodible beds is then examined, and the numerical results are validated against measurements for single-layered homogeneous beds. The problem of a stream-flow over a dyke studied in the Delft hydraulics laboratory [81] is a similar test example. Here, the experiment is carried out in a channel with sides of a 1:10 slope, as sketched in the left plot of Figure 3.13. The bed is assumed to be single-layered formed with Sand 4, the sediment properties of which are listed in Table 3.1. Initially the flow is at rest with a water height $H(0, x) = 0.39\ m$, and a velocity of $u(t, x) = 0.51\ m/s$ is set as an upstream boundary condition. For this steady-state problem the erosion term is given by the formula (3.2.8).

As in the previous example, a study of mesh convergence is performed. Table 3.3 summarizes the minimum value of the bed profile B, the location (x, z) where this minimum is reached, and the computational cost obtained at simulation time $t = 27000\ s$. For this steady-state problem, the mean velocity is slow compared to the previous test example and therefore longer simulation times are required to obtain well-developed morphodynamics. It is clear from the obtained results that using fine grids yields larger CPU times. Based on the results shown in Table 3.3, a spatial discretisation with $\Delta x = 0.2\ m$ is considered for this test example, as the differences in

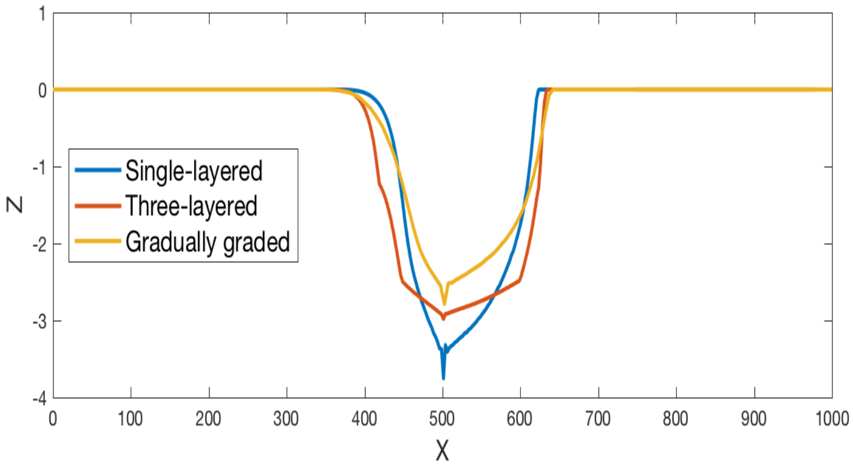

Figure 3.12: Comparison of bed profiles obtained for a dam-break problem over single-layered, three-layered and gradually varying bed at time $t = 20\ s$.

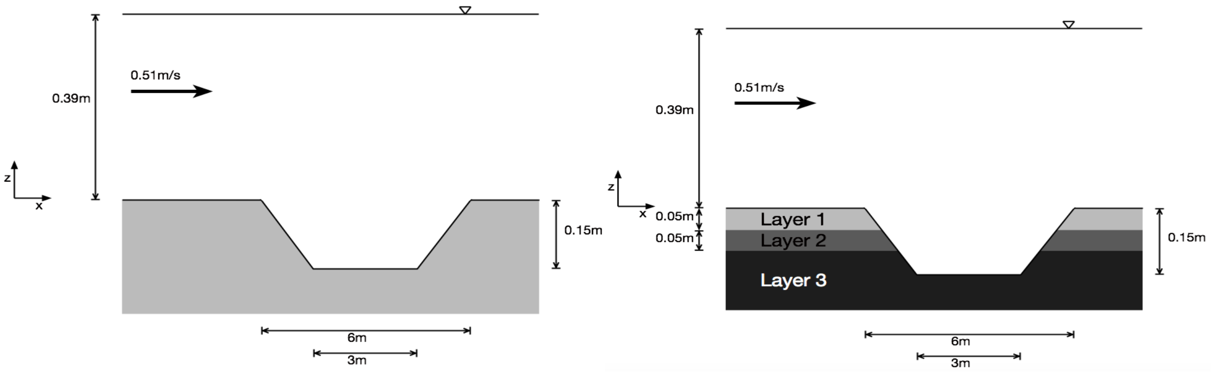

Figure 3.13: Schematic description of the stream-flow problem over a single-layered dyke (left) and a three-layered dyke (right).

the accuracy between this discretisation and the refined ones using $\Delta x = 0.15\ m$ or $\Delta x = 0.1\ m$ are very small, but the difference in the computational cost is substantial. A comparison between the computational results and experimental data has also been carried out for this test problem. Figure 3.14 compares the numerical results for the bed profile at time $t = 27000\ s$ to measurements reported in [81]. In this figure, the initial bed profile is also

Table 3.3: Convergence results for the stream-flow problem over single-layered dyke.

Discretisation Δx $[m]$	Minimum B $[m]$	Location of the minimum B $[m, m]$	CPU time $[min]$
0.6	-0.1250	(16.15,-0.1250)	126
0.5	-0.1173	(16.36,-0.1173)	254
0.2	-0.1103	(16.38,-0.1103)	928
0.15	-0.109	(16.38,-0.1090)	1736
0.1	-0.1083	(16.39,-0.1083)	3774

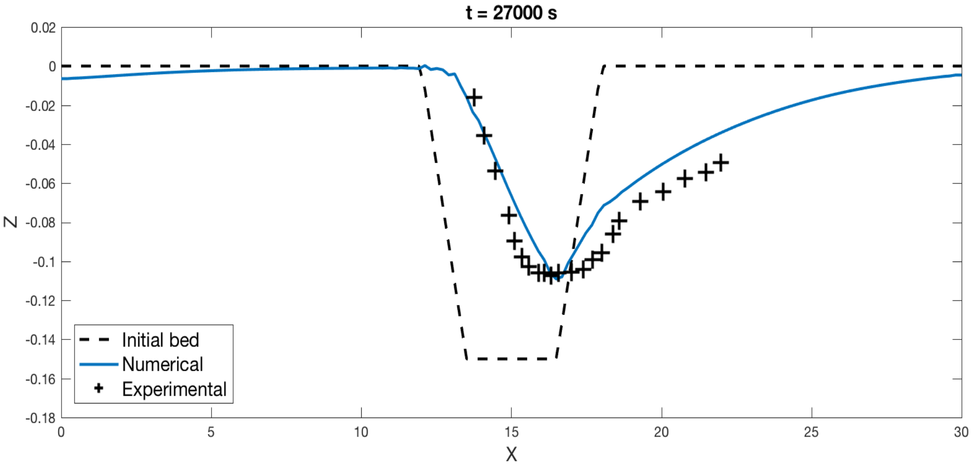

Figure 3.14: Comparison between numerical results and experimental data for the stream-flow problem over a single-layered dyke at time $t = 27000$ s.

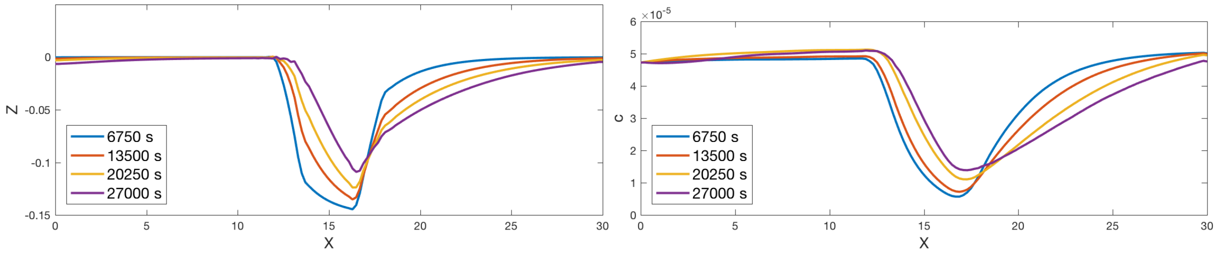

Figure 3.15: Time evolution of bed profile (left) and sediment concentration (right) for the stream-flow problem over a single-layered dyke.

included for comparison reasons. It is clear that the numerical and experimental results demonstrate similar morphodynamic patterns, and the presented Riemann solver is capable of accurately capturing both hydrodynamic and morphodynamic features. Both erosion and deposition effects have been numerically resolved using this approach without introducing excessive numerical diffusion or non-physical oscillations. These effects can be clearly seen in the time evolution of the bed profile and the sediment concentration shown in Figure 3.15. The minimum

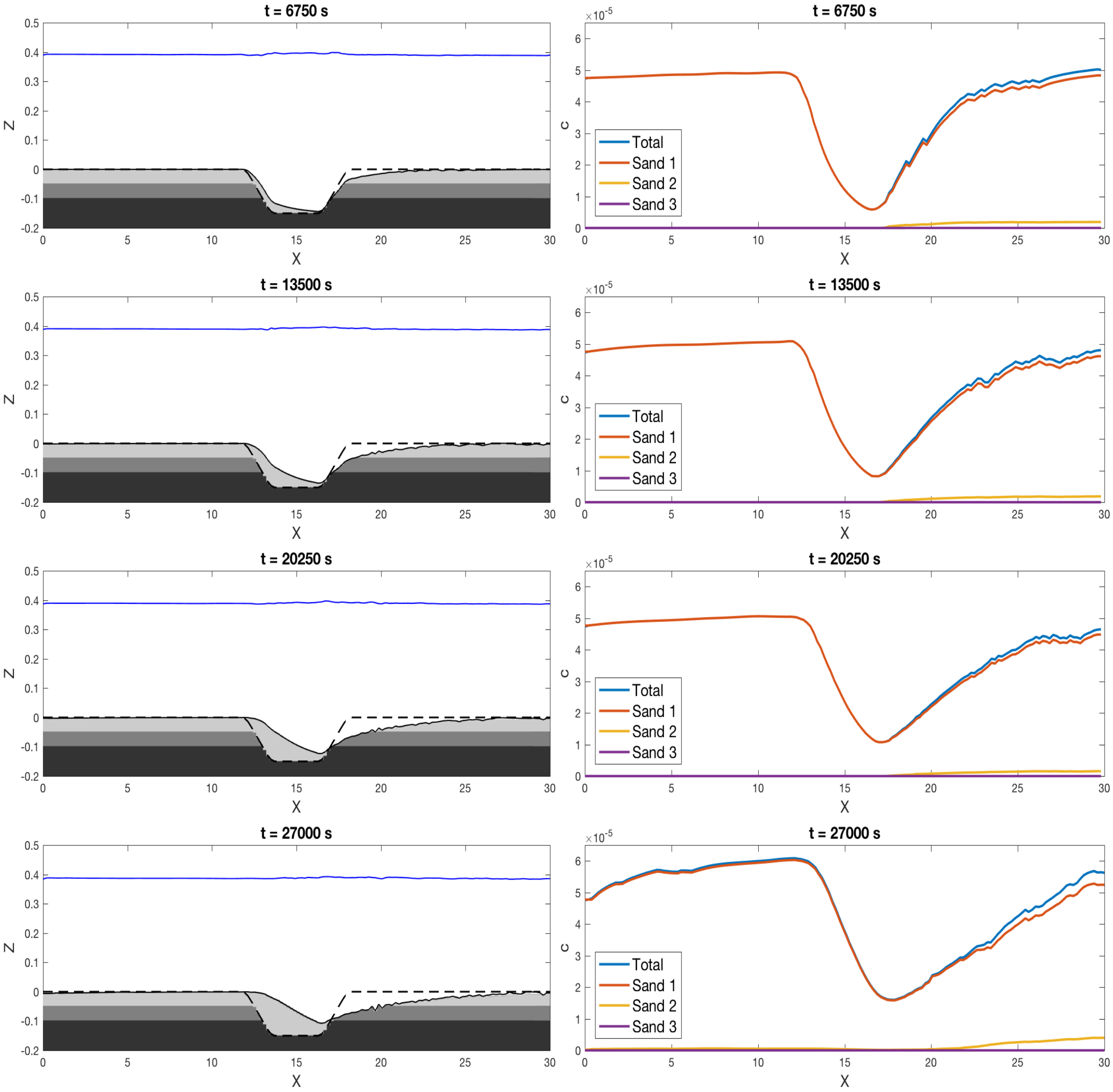

Figure 3.16: Bed profiles (left) and sediment concentrations (right) for the stream-flow problem over a three-layered dyke at four instants $t = 6750\ s$, $13500\ s$, $20250\ s$, and $27000\ s$. The blue and dashed lines in the left plots refer to the water free-surface and the initial bed profile, respectively.

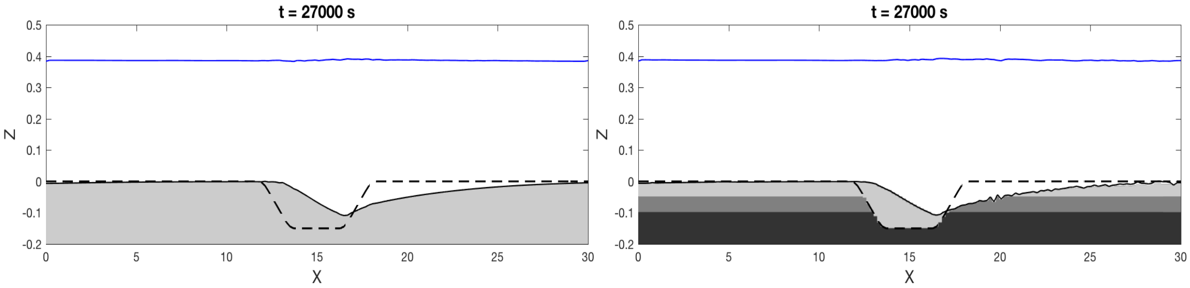

Figure 3.17: Bed profiles at time $t = 27000\ s$ obtained using a single-layered bed (left) and a three-layered bed (right). The blue and dashed lines in the left plots refer to the water free-surface and the initial bed profile, respectively.

values of the bed profiles and their locations obtained using the proposed Riemann solver, are shown to be similar to the measurements.

It should also be pointed out that in the previous test examples of large-scale dam-break problems the obtained results do not demonstrate large amounts of deposition, mainly due to their high levels of scouring. Therefore, the aim of this test example is to demonstrate the effects of deposition and showcase the phenomenon of armouring. Hence, a new test case is devised using three discrete sediment layers, The computed results for the bed profiles and sediment concentrations are illustrated in Figure 3.16 at four different instants $t = 6750$, 13500, 20250, and 27000 s, using a spatial discretisation with $(\Delta x = 0.2\ m, \Delta z = 0.002\ m)$. The bed layers are defined as

$$B(0,x,z) = \begin{cases} \text{Sand 4,} & \text{if} \quad -0.05\ m \ \leq z < \ 0\ m, \\ \text{Sand 5,} & \text{if} \quad -0.1\ m \ \leq z < \ -0.05\ m, \\ \text{Sand 6,} & \text{if} \quad -0.2\ m \ \leq z < \ -0.1\ m, \end{cases}$$

where the associated sediment properties for Sand 4, Sand 5 and Sand 6 are summarised in Table 3.1. The deposition effects on the dyke are clearly visible over the time frame. The variation of the bed sediments creates a very active sediment exchange between the water flow and the bed. This produces a sharp spatial gradient of sediment concentration presented in Figure 3.16. As can also be seen, the water free-surface remains almost constant during the simulation times. It seems that, for the considered sediment conditions, erosion effects are more pronounced for the first layer of Sand 4 than for the second layer of Sand 5 and third layer of Sand 6. Figure 3.17 presents a comparison between simulations for the single-layer bed (using Sand 4 only) and the three-layered bed (using Sand 4, Sand 5, and Sand 6) at time $t = 27000\ s$. This clearly shows the effects of armouring, as ripples of sediment are created behind the dyke. This effect varies greatly with the discretisation of the bed and sediment selected, the key lies not in the individual rills but the area that they cover which was found to be consistent. It is interesting to see how this finely tuned setup can be altered by the smallest change in the sediment distribution properties. Again, for the considered sediment properties, both simulations deliver similar top bed profiles, but using the single-layer bed would not reveal the intermediate profiles for sedimentary beds.

3.6 Concluding remarks

A model for handling the sediment transport of multiple particle types from multilayered and heterogeneously mixed soil beds is presented. The governing equations consist of the shallow water system for the water flow, a transport equation for the sediments, and a bed Exner-type equation for the bed. The model avoids a complicated expansion of the governing equations by treating the sediment as an average for flow calculations, whilst at the same time handling each sediment separately when considering erosion and deposition. To model erosion and deposition, empirical equations for high and low shear conditions are used. The vertical exchanges between the bed layers have been accounted for using a balance law for the bed elevation. The proposed model is fully coupled and can handle an arbitrary number of layers within the bed topography. In addition, the governing equations can be formulated as an hyperbolic system of conservation laws with source terms.

A finite volume Riemann solver has been proposed for the numerical solution of shallow water flows over multilayer beds. The numerical method uses a class of predictor-corrector procedures for which the numerical fluxes are reconstructed in the predictor stage using the Jacobian matrix of the fluxes in the system, followed by a corrector stage to update the solution. A conservative vertical discretisation of finite volume type for the multilayer bed is considered to allow for different soil properties. The combined techniques offer an accurate and stable numerical solver with a well-balanced discretisation of the flux gradient and the source term.

The numerical performance of the proposed solver is examined for several test examples, including the lake at rest problem, which verifies the well-balanced property of the method. Then, a dam-break flow problem over homogeneous, heterogeneously mixed and multilayer erodible beds is simulated. Next, a stream-flow problem over homogeneous and multilayer erodible dykes is considered. This test case is first validated using experimental data and then used to demonstrate the effects of armouring. In these later two problems the model is tested against experimental data, and found to have good agreement. In all presented results, the proposed solver has exhibited accurate predictions of both the water free-surface and the bed topography, with correct conservation properties and stable representations of free-surface response to the multilayer erodible beds. The advantages of this method is that they do not expand the number of partial differential equations to be solved, meaning it is very efficient whilst at the same time offering substantial new features and capabilities for the modeller.

Chapter 4

Modelling and simulation of multilayer shallow water flows over erodible beds in one space dimension

This chapter extends the work of one-dimensional methods for sedimentary models to quasi-two-dimensional. It introduces the Eulerian-Lagrangian Finite Volume (ELFV) method which is the focus of this thesis. The aim is to develop a fast and accurate numerical method for multilayer shallow water flows with mass exchange and an erodible bed. The governing equations consist of the multilayer shallow water equations for the hydraulic variables, a set of transport equations for the suspended sediments in each layer, a bed Exner-type equation and empirical equations for erosion and deposition terms. Mass exchange terms between layers account for both fluid flow and suspended sediment inter-layer exchange. The coupled model for each layer has been reformulated as a single system of conservation laws with source terms, and a simple two-step Eulerian-Lagrangian method is presented for its numerical solution. In the first step, the governing equations are rewritten in a non-conservative form and the numerical fluxes are calculated using the methods of characteristics. In the second step, the numerical solutions are updated in a conservative form. Numerical results are presented for a multilayer dam-break problem over an erodible bed and for a wind-driven recirculation problem over an erodible non-flat bed. The obtained results for these test examples demonstrate the capabilities of the combined multilayer flow model and ELFV method to accurately simulate shallow water flows, including suspended sediments, over erodible beds.

This chapter is structured as follows: Section 4.1 details the background to the sediment transport limiting assumption tackled in this chapter. In Section 4.2, the model for multilayer shallow water flows over erodible beds is presented. The ELFV method for solving the governing equations is formulated in Section 4.3, together with the reconstruction of numerical fluxes using the modified method of characteristics and the discretisation of the source terms in the model.

The novel experimental method used to obtain data for a one-dimensional dam-break is detailed in Section 4.4. Section 4.5 examines the numerical performance of the proposed model using two test examples. The numerical results for both a dam-break flow and a wind-driven flow over erodible beds are then presented. Finally, a summary of this chapter is given in Section 4.6.

4.1 Modelling sediment transport flows using the multilayer approach

Due to their three-dimensional (3D) nature and algorithmic complexity, most free-surface flows in real-world domains with complex and movable geometry require huge computational expenditure [116]. If the vertical scale of these problems is much smaller than the two horizontal scales, it can be averaged out to form the Shallow Water Equations (SWEs). These can be derived from the non-stationary 3D incompressible Navier-Stokes equations. This method allows for the modelling of many real-world flows (channels, rivers, estuaries, reservoirs, and coastal regions, together with a variety of wave and steady flow conditions). The depth-averaged velocity assumptions have been a limiting factor to wider adoption of the SWEs. Thus, two classes of multilayer models have been developed over the last two decades: one in which the layers of separate fluids are immiscible, see for example [29, 82], whilst the other is based on a single fluid and allows for fluid exchange, examples of this can be found in [13, 70]. The advantage of both methods is that they avoid highly computationally expensive Navier-Stokes formulations and, at the same time, obtain vertically stratified horizontal velocities. The modelling of the sediments along with the water flows that transport them is a non-trivial problem: their interaction and spacing in a fluid is not accurately represented by the single-layer SWEs. For most entrainment and deposition equations a bed level concentration factor is used. By contrast, this study presents a model which, through the calculation of multiple fluid layers, allows for sediment concentration to vary with depth. Although much work has been done on vertical diffusion [92, 164], this study differs in that different layers are able to capture different concentrations without relying on vertical velocities. There are four main modes of sediment transport: (i) bedload, which is completely supported by the bed; (ii) intermittently suspended load, where the bed and water support the weight of the sediment; (iii) suspended sediment, where the fluid completely supports the sediment, and (iv) wash load, which is kept suspended by the Brownian motion of the fluid. One of the more complex challenges in sediment transport modelling is correctly accounting for these different modes of transport, especially the bedload and suspended load as they form a multi-scale problem due to their differences in characteristic speeds. This is tackled by the multilayer method through the use of different speeds for different layers, combined with a vertical distribution of sediment.

A large amount of work has been done on the effects of flows on sediment beds, see for example [177,192]. Almost all models rely on the experimental data for sediments that form the basis of an empirical formula, such as those reported in [151] among others. Many methods of modelling sediment transport exist: from particle tracking [63] to sediment balance models such as ESTMORPH [199]. In this chapter, a suspended load flux is calculated by empirical erosion and deposition formulae. The formulae employ flow characteristics and sediment properties to calculate erosion and deposition separately. An increasing number of models use both bedload, and suspended load equations. The presented model does not require this, as it considers multiple fluid layers and can easily model the bedload in the slower moving bottom layer. Over the years many sediment transport functions have been developed [64, 105]. Over time, three of these have become popular: (i) the Grass model [78], (ii) the Meyer-Peter and Muller model [122] and (iii) the Van Rijn model [186]. In this chapter, the Van Rijn style relations are used. This set of expressions are selected because of the accurate results they provide for various test cases, as well as the fact that they are easily able to be modified for different sediment types. The accuracy of the model is verified against several test examples in evolving and steady-state flow domains and a comparison to new experimental data for a dam-break problem in one space dimension.

The goal of this chapter is to extend [12] to include sediment transport. For the predictor stage, the SWEs are rewritten in a non-conservative form and then integrated along the characteristic curves. From here it is possible to reconstruct the fluxes required for the second stage which is reached by integrating the governing equations (including an Exner-type equation for the bed) in Eulerian time and space. This forms the conservative corrector stage in the Eulerian-Lagrangian Finite Volume (ELFV) method.

4.2 Multilayer shallow water flows with sediment transport

Multilayer flow systems are usually obtained through the simplifications of 3D Navier-Stokes equations which include the shallow water assumptions, compare [12–14] among others. This study presents a one-dimensional (1D) version of the SWE model for each of the layers of fluid, including species conservation for sediment transport. A bed Exner-type equation is added to model the bed. The system includes terms for both mass exchange between the layers, and between the erodible bed and the water flow. This derivation is based on work conducted in [11], but developed to include exchange terms for sediment and a moveable bed. In order to derive this model we begin with the incompressible form of the Navier-Stokes equations (2.1.1) (in

Chapter 2 on page 10), for which we then remove the y-dimension as

$$\begin{aligned}
\frac{\partial u}{\partial x}+\frac{\partial w}{\partial z} &= 0,\\
\frac{\partial u}{\partial t}+u\frac{\partial u}{\partial x}+w\frac{\partial u}{\partial z}+\frac{\partial p}{\partial x} &= \frac{\partial \Sigma_{xx}}{\partial x}+\frac{\partial \Sigma_{xz}}{\partial z},\\
\frac{\partial w}{\partial t}+u\frac{\partial w}{\partial x}+w\frac{\partial w}{\partial z}+\frac{\partial p}{\partial z} &= -g+\frac{\partial \Sigma_{zx}}{\partial x}+\frac{\partial \Sigma_{zz}}{\partial z},
\end{aligned} \tag{4.2.1}$$

where p denotes pressure and g is acceleration due to gravity. The chosen form of the viscosity tensor is symmetric and defined by

$$\Sigma_{xx}=2\nu\frac{\partial u}{\partial x}, \qquad \Sigma_{zz}=2\nu\frac{\partial w}{\partial z}, \qquad \Sigma_{xz}=\Sigma_{zx}=\nu\left(\frac{\partial u}{\partial z}+\frac{\partial w}{\partial x}\right),$$

where ν is the viscosity coefficient. The kinematic boundary condition at the water surface can be written thus

$$\frac{\partial \vartheta}{\partial t}+u_{fs}\frac{\partial \vartheta}{\partial x}-w_{fs}=0, \tag{4.2.2}$$

where u_{fs} and w_{fs} are the velocity components at the surface. As we are modelling a sedimentary system, erosion and deposition can occur, and therefore we consider the bed level kinematic boundary condition to be

$$\frac{\partial B}{\partial t}+u_B\frac{\partial B}{\partial x}-w_B=0, \tag{4.2.3}$$

where u_B and w_B are the velocity components at bed level and B is the bed height. Next, we consider the boundaries of the flow domain: we define $\mathbf{n}_{fs}$ as the unit normal to the surface and $\mathbf{n}_B$ as the unit normal to the bed by

$$\mathbf{n}_{fs}=\frac{1}{\sqrt{1+\left(\frac{\partial \vartheta}{\partial x}\right)^2}}\begin{pmatrix}-\frac{\partial \vartheta}{\partial x}\\ \\ 1\end{pmatrix}, \qquad \mathbf{n}_B=\frac{1}{\sqrt{1+\left(\frac{\partial B}{\partial x}\right)^2}}\begin{pmatrix}-\frac{\partial B}{\partial x}\\ \\ 1\end{pmatrix}.$$

We also use Σ_T to denote the total stress tensor

$$\Sigma_T=-p\mathbf{I}_d+\begin{pmatrix}\Sigma_{xx} & \Sigma_{xz}\\ \\ \Sigma_{zx} & \Sigma_{zz}\end{pmatrix}.$$

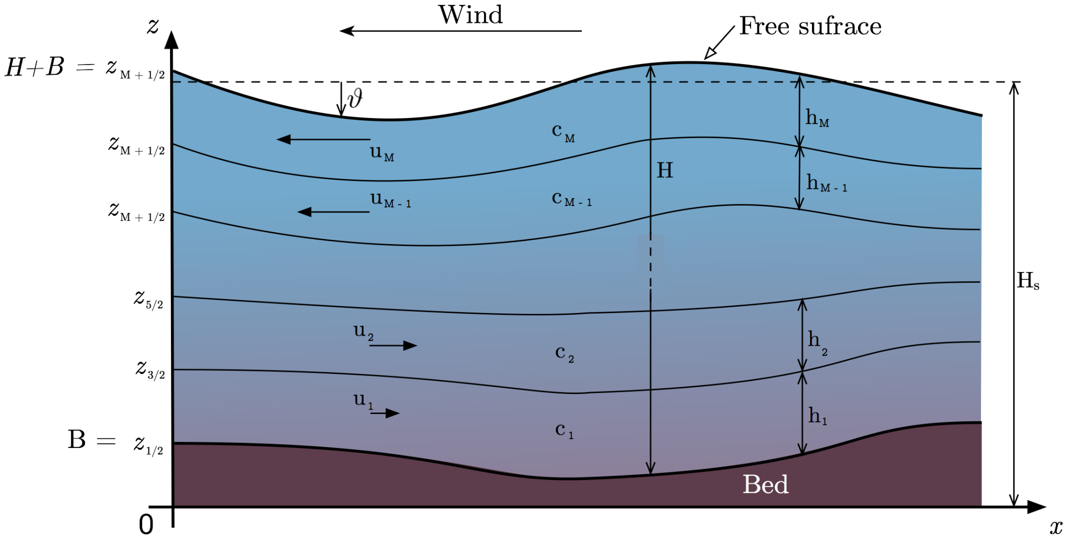

Figure 4.1: A simple illustration of multilayer shallow water flows over erodible beds.

Including the effects of wind, we describe the stresses at the free-surface boundary as

$$\Sigma_T \mathbf{n}_{fs} = -p^a \mathbf{n}_{fs}, \tag{4.2.4}$$

where $p^a = p^a(t, x)$ is the atmospheric pressure function. Thus,

$$\mathbf{n}_{fs} \cdot \Sigma_T \mathbf{n}_{fs} = -p^a, \qquad\qquad \mathbf{t}_{fs} \cdot \Sigma_T \mathbf{n}_{fs} = 0,$$

where $\mathbf{t}_{fs}$ is orthogonal to $\mathbf{n}_{fs}$. For the fluid stresses at the bed we consider a wall law in the form

$$\Sigma_T \mathbf{n}_B - (\mathbf{n}_B \cdot \Sigma_T \mathbf{n}_B)\mathbf{n}_B = \kappa(\mathbf{v}_B, H)\mathbf{v}_B, \tag{4.2.5}$$

where

$$\mathbf{v}_B = \mathbf{u}_B - \begin{pmatrix} 0 \\ \\ \dfrac{\partial B}{\partial t} \end{pmatrix},$$

is the relative velocity between the bed and the bottom of the fluid. Thus

$$\kappa(\mathbf{v}_B, H) = \kappa_l + \kappa_t H |\mathbf{v}_B|,$$

where κ_l is the laminar and κ_t is the turbulent friction coefficient. As a result of thermomechanical considerations we denote $\kappa(\mathbf{v}_B, H) \geq 0$ and we denote $\kappa(\mathbf{v}_B, H) = \kappa$. As with the surface boundary condition, the bed surface conditions are

$$\mathbf{t}_B \cdot \Sigma_T \mathbf{n}_B = \kappa \mathbf{v}_B \cdot \mathbf{t}_B, \qquad \mathbf{v}_B \cdot \mathbf{n}_B = 0.$$

Next, we rescale the system using the quantities h and Λ as the characteristic dimensions along the z and x dimensions. We denote a_{fs} as the typical wave amplitude, a_B as the typical bed variation, and $C = \sqrt{gh}$ as the typical horizontal wave speed. Two basic relations for our system are created

$$\varepsilon = \frac{h}{\lambda}, \qquad \delta = \frac{a_{fs}}{h}.$$

For the bathymetry we find $\frac{a_B}{h} = \mathcal{O}(0)$. For the shallow water system we are considering, we also use the characteristic quantities $\lambda = TC$ for speed, $W = \frac{a_{fs}}{T} = \varepsilon\delta C$ for the vertical velocity, $U = \frac{W}{\varepsilon} = \delta C$ for the horizontal velocity, and $P_P = C^2$ for pressure. From there, we obtain the following dimensionless quantities

$$\tilde{x} = \frac{x}{\Lambda}, \quad \tilde{z} = \frac{z}{h}, \quad \tilde{\vartheta} = \frac{\vartheta}{a_{fs}}, \quad \tilde{t} = \frac{t}{T}, \quad \tilde{p} = \frac{p}{P}, \quad \tilde{u} = \frac{u}{U}, \quad \tilde{w} = \frac{w}{W}. \tag{4.2.6}$$

It is important to note that from this it can be implied that $\delta = \frac{U}{C}$ so δ corresponds to the Froude number. If $\delta = \mathcal{O}(1)$, then $U \approx C$ and the classic rescaling used for the shallow water system is gained. For the bed height B we consider $B(t, x) = Z_B(x) + z_B(t)$, from this the following dimensionless quantities are also produced

$$\tilde{B} = \frac{Z_B}{h}, \quad \tilde{z_B} = \frac{z_B}{a_B}.$$

Thus,

$$\frac{\partial B}{\partial t} = \varepsilon\delta C \frac{\partial \tilde{z_B}}{\partial \tilde{t}}, \qquad \frac{\partial B}{\partial x} = \varepsilon \frac{\partial \tilde{B}}{\partial \tilde{x}}.$$

Further we use

$$\tilde{\nu} = \frac{\nu}{\lambda C}, \qquad \tilde{\kappa} = \frac{\kappa}{C}.$$

It is also assumed that the regime is asymptotic and therefore

$$\kappa\nu = \varepsilon\kappa_0, \qquad \tilde{\nu} = \varepsilon\nu_0,$$

where

$$\kappa_0 = \kappa_{l,0} + \varepsilon\kappa_{t,0}(\tilde{\mathbf{v}}_B, \tilde{H}),$$

where $\kappa_{l,0}$ is constant. When the non-dimensional relations are applied to Navier-Stokes system in (4.2.1) we gain

$$\begin{aligned}
\frac{\partial \tilde{u}}{\partial \tilde{x}} + \frac{\partial \tilde{w}}{\partial \tilde{z}} &= 0, && (4.2.7a)\\
\varepsilon\delta\frac{\partial \tilde{u}}{\partial \tilde{t}} + \varepsilon\delta^2\frac{\partial \tilde{u}^2}{\partial \tilde{x}} + \varepsilon\delta^2\frac{\partial (\tilde{u}\tilde{w})}{\partial \tilde{z}} + \varepsilon\frac{\partial \tilde{p}}{\partial \tilde{x}} &= \varepsilon^2\delta\frac{\partial}{\partial \tilde{x}}\left(2\nu_0\frac{\partial \tilde{u}}{\partial \tilde{x}}\right) + \frac{\partial}{\partial \tilde{z}}\left(\delta\nu_0\frac{\partial \tilde{u}}{\partial \tilde{z}} + \varepsilon^2\delta\nu_0\frac{\partial \tilde{w}}{\partial \tilde{x}}\right), && (4.2.7b)\\
\varepsilon^2\delta\left(\frac{\partial \tilde{w}}{\partial \tilde{t}} + \delta\frac{\partial (\tilde{u}\tilde{w})}{\partial \tilde{x}} + \delta\frac{\partial \tilde{w}^2}{\partial \tilde{z}}\right) + \frac{\partial \tilde{p}}{\partial \tilde{z}} &= -1 + \varepsilon\delta\nu_0\frac{\partial}{\partial \tilde{x}}\left(\frac{\partial \tilde{u}}{\partial \tilde{z}} + \varepsilon\frac{\partial \tilde{w}}{\partial \tilde{x}}\right) + \varepsilon\delta\frac{\partial}{\partial \tilde{z}}\left(2\nu_0\frac{\partial \tilde{w}}{\partial \tilde{z}}\right). && (4.2.7c)
\end{aligned}$$

Now by applying the divergence free condition, we can re-write equations (4.2.7b) and (4.2.7c) and applying the boundary conditions (4.2.2) - (4.2.5) we gain

$$\begin{aligned}
\frac{\partial \tilde{\vartheta}}{\partial \tilde{t}} + \delta\tilde{u}_{fs}\frac{\partial \tilde{\vartheta}}{\partial \tilde{x}} - \tilde{w}_{fs} &= 0, && (4.2.8a)\\
2\varepsilon\delta\nu_0 \left.\frac{\partial \tilde{w}}{\partial \tilde{z}}\right|_{fs} - \tilde{p}_{fs} - \varepsilon\delta^2\nu_0\frac{\partial \tilde{\vartheta}}{\partial \tilde{x}}\left(\left.\frac{\partial \tilde{u}}{\partial \tilde{z}}\right|_{fs} + \varepsilon^2 \left.\frac{\partial \tilde{w}}{\partial \tilde{x}}\right|_{fs}\right) &= -\delta\tilde{p}^a, && (4.2.8b)\\
\delta\nu_0\left(\left.\frac{\partial \tilde{u}}{\partial \tilde{z}}\right|_{fs} + \varepsilon^2 \left.\frac{\partial \tilde{w}}{\partial \tilde{x}}\right|_{fs}\right) - \varepsilon\delta\frac{\partial \tilde{\vartheta}}{\partial \tilde{x}}\left(2\varepsilon\delta\nu_0 \left.\frac{\partial \tilde{u}}{\partial \tilde{x}}\right|_{fs} - \tilde{p}_{fs}\right) &= \varepsilon\delta^2\frac{\partial \tilde{\vartheta}}{\partial \tilde{x}}\tilde{p}^a, && (4.2.8c)\\
\frac{\partial \tilde{z}_B}{\partial \tilde{t}} + \tilde{u}_B\frac{\partial \tilde{B}}{\partial \tilde{x}} - \tilde{w}_B &= 0, && (4.2.8d)\\
\delta\nu_0\left(\varepsilon^2 \left.\frac{\partial \tilde{w}}{\partial \tilde{x}}\right|_B + \left.\frac{\partial \tilde{u}}{\partial \tilde{z}}\right|_B\right) - \varepsilon\frac{\partial \tilde{B}}{\partial \tilde{x}}\left(2\varepsilon\delta\nu_0 \left.\frac{\partial \tilde{u}}{\partial \tilde{x}}\right|_B - p_B\right) + {}&\\
\varepsilon\frac{\partial \tilde{B}}{\partial \tilde{x}}\left(2\varepsilon\delta\nu_0 \left.\frac{\partial \tilde{w}}{\partial \tilde{z}}\right|_B - p_B - \varepsilon\nu_0\frac{\partial \tilde{B}}{\partial \tilde{z}}\left(\delta\left.\frac{\partial \tilde{u}}{\partial \tilde{z}}\right|_B + \varepsilon^2\delta \left.\frac{\partial \tilde{w}}{\partial \tilde{x}}\right|_B\right)\right) &= \\
\varepsilon\delta\kappa_0\sqrt{1 + \varepsilon^2\left(\frac{\partial \tilde{B}}{\partial \tilde{x}}\right)^2}\left(\tilde{u}_B\varepsilon^2\frac{\partial \tilde{B}}{\partial \tilde{x}}\left(\tilde{w}_B - \frac{\partial \tilde{z}_B}{\partial \tilde{t}}\right)\right)&. && (4.2.8e)
\end{aligned}$$

At this point, some of the viscosity tensor terms are very small and can be neglected. At this stage we also drop the " ˜ " notation. By only preserving high order terms we arrive at

$$\begin{aligned}
\frac{\partial u}{\partial x} + \frac{\partial w}{\partial z} &= 0, && (4.2.9a)\\
\varepsilon\delta\frac{\partial u}{\partial t} + \varepsilon\delta^2\frac{\partial u^2}{\partial x} + \varepsilon\delta^2\frac{\partial (uw)}{\partial z} + \varepsilon\frac{\partial p}{\partial x} &= \varepsilon^2\delta\frac{\partial}{\partial x}\left(2\nu_0\frac{\partial u}{\partial x}\right) + \frac{\partial}{\partial z}\left(\delta\nu_0\frac{\partial u}{\partial z}\right), && (4.2.9b)\\
\varepsilon^2\delta\left(\frac{\partial w}{\partial t} + \delta\frac{\partial (uw)}{\partial x} + \delta\frac{\partial w^2}{\partial z}\right) + \frac{\partial p}{\partial z} &= -1 + \frac{\partial}{\partial x}\left(\varepsilon\delta\nu_0\frac{\partial u}{\partial z}\right) + \frac{\partial}{\partial z}\left(2\varepsilon\delta\nu_0\frac{\partial w}{\partial z}\right). && (4.2.9c)
\end{aligned}$$

Thus it is possible to neglect the $\varepsilon^2 \dfrac{\partial w}{\partial x}$ term. By only considering high-order terms and the same boundary conditions we arrive at

$$
\begin{aligned}
\frac{\partial \vartheta}{\partial t} + \delta u_{fs} \frac{\partial \vartheta}{\partial x} - w_{fs} &= 0, && \text{(4.2.10a)}\\
2\varepsilon\delta\nu_0 \left.\frac{\partial w}{\partial z}\right|_{fs} - p_{fs} - \varepsilon\delta^2 \nu_0 \frac{\partial \vartheta}{\partial x} \left.\frac{\partial u}{\partial z}\right|_{fs} &= -\delta p^a, && \text{(4.2.10b)}\\
\delta\nu_0 \left.\frac{\partial u}{\partial z}\right|_{fs} - \varepsilon\delta \frac{\partial \vartheta}{\partial x} \left(2\varepsilon\delta\nu_0 \left.\frac{\partial u}{\partial x}\right|_{fs} - p_{fs} \right) &= \varepsilon\delta^2 \frac{\partial \vartheta}{\partial x} p^a, && \text{(4.2.10c)}\\
\frac{\partial B}{\partial t} + u_B \frac{\partial B}{\partial x} - w_B &= 0, && \text{(4.2.10d)}\\
\delta\nu_0 \left.\frac{\partial u}{\partial z}\right|_B - \varepsilon \frac{\partial B}{\partial x} \left(2\varepsilon\delta\nu_0 \left.\frac{\partial u}{\partial x}\right|_B - p_B \right) + \varepsilon \frac{\partial B}{\partial x} \left(2\varepsilon\delta\, \nu_0 \left.\frac{\partial w}{\partial z}\right|_B - p_B - \varepsilon\delta\nu_0 \frac{\partial Z_B}{\partial x} \left.\frac{\partial u}{\partial z}\right|_B \right) & \\
= \varepsilon\delta\kappa_0 \left(1 + \varepsilon^2 \left(\frac{\partial B}{\partial x} \right)^2 \right)^{3/2} u_B. && \text{(4.2.10e)}
\end{aligned}
$$

Next, our focus turns to the hydrostatic and non-hydrostatic pressure terms. The integration of equation (4.2.10d) from z to $\partial\vartheta$ gives

$$
\begin{aligned}
\varepsilon^2\delta \int_z^{\delta\vartheta} \left(\frac{\partial w}{\partial t} + \delta \frac{\partial (uw)}{\partial x} \right) dz + \varepsilon^2\delta^2 (w_{fs}^2 - w^2) + p_{fs} - p \;=\; z - \delta\vartheta + \varepsilon\delta \int_z^{\delta\vartheta} \frac{\partial}{\partial x} \left(\nu_0 \frac{\partial u}{\partial z} \right) dz \,- \\
2\varepsilon\delta\nu_0 \frac{\partial w}{\partial z} + 2\varepsilon\delta\nu_0 \left.\frac{\partial w}{\partial z}\right|_{fs}. \qquad \text{(4.2.11)}
\end{aligned}
$$

By combining equations (4.2.8b) and (4.2.8c) we arrive at

$$
\left.\frac{\partial u}{\partial z}\right|_{fs} = \mathcal{O}(\varepsilon^2),
$$

then (4.2.8b) yields

$$
p_{fs} = \delta p^a + 2\varepsilon\delta \left.\frac{\partial w}{\partial z}\right|_{fs} + \mathcal{O}(\varepsilon^3\delta^2). \tag{4.2.12}
$$

By combining the boundary condition (4.2.8a) with (4.2.11) we arrive at

$$
\begin{aligned}
\varepsilon^2\delta \left(\frac{\partial}{\partial z} \int_z^{\delta\vartheta} w \; dz + \delta \frac{\partial}{\partial x} \int_z^{\delta\vartheta} (uw) \; dz \right) - \varepsilon^2\delta^2 w^2 + \delta p^a - p \;&=\; \varepsilon\delta \int_z^{\delta\vartheta} \frac{\partial}{\partial x} \left(\nu_0 \frac{\partial u}{\partial z} \right) \; dz \,+ \\
& \qquad 2\varepsilon\delta\nu_0 \frac{\partial w}{\partial z} + \mathcal{O}(\varepsilon^3\delta) - (\delta\vartheta - z).
\end{aligned}
$$

We also use the classical relation used in [11]

$$
\frac{\partial u_{fs}}{\partial x} = \left.\frac{\partial u}{\partial x}\right|_{fs} + \delta \frac{\partial \vartheta}{\partial x} \left.\frac{\partial u}{\partial z}\right|_{fs} = \left.\frac{\partial u}{\partial x}\right|_{fs} + \mathcal{O}(\varepsilon^2\delta). \tag{4.2.13}
$$

By combining (4.2.9a) and (4.2.13) and using the Leibniz rule we obtain

$$\varepsilon\delta \int_{z}^{\delta\vartheta} \frac{\partial}{\partial x}\left(\nu_0 \frac{\partial u}{\partial z}\right) dz - 2\varepsilon\delta\nu_0 \frac{\partial w}{\partial z} = \varepsilon\delta\nu_0 \frac{\partial u}{\partial x} + \varepsilon\delta\nu_0 \left.\frac{\partial u}{\partial x}\right|_{fs} + \mathcal{O}(\varepsilon^3\delta).$$

Thus, the pressure can be expressed as

$$p = p_h + p_{nh} + \mathcal{O}(\varepsilon^3\delta).$$

As we are considering a shallow water system, we have a hydrostatic pressure assumption

$$p = p_h + \mathcal{O}(\varepsilon^2\delta), \tag{4.2.14}$$

where the hydrostatic pressure is given by

$$p_h = \delta p^a + (\delta\vartheta - z) - 2\varepsilon\delta\nu_0 \frac{\partial u}{\partial x}. \tag{4.2.15}$$

By considering (4.2.8c), (4.2.8e) and (4.2.12) we arrive at

$$\left.\frac{\partial u}{\partial z}\right|_{fs} = \mathcal{O}(\varepsilon^2), \qquad \left.\frac{\partial u}{\partial z}\right|_{B} = \mathcal{O}(\varepsilon). \tag{4.2.16}$$

By combining (4.2.15) and (4.2.14), we gain

$$\frac{\partial p}{\partial x} = \mathcal{O}(\delta),$$

and this combined with (4.2.9b) yields

$$\nu_0 \frac{\partial^2 u}{\partial z^2} = \mathcal{O}(\varepsilon).$$

Combining the equation (4.2.16) with the above relation leads to

$$u(x, z, t) = u(x, 0, t) + \mathcal{O}(\varepsilon).$$

Next we define an averaged velocity and water height

$$\bar{u} = \frac{1}{\delta\vartheta - B} \int_{B}^{\delta\vartheta} u \, dz, \qquad H = \vartheta - B.$$

This allows us to form the following relation in which the system (4.2.9) with the hydrostatic pressure (4.2.14) and (4.2.15) results in

$$\begin{aligned} \frac{\partial H}{\partial t}+\frac{\partial (H\bar{u})}{\partial x} &= 0, \qquad (4.2.17a)\\ \frac{\partial (H\bar{u})}{\partial t}+\frac{\partial (H\bar{u}^2)}{\partial x}+\frac{1}{2}g\frac{\partial H^2}{\partial x} &= -H\frac{\partial p^a}{\partial x}-gH\frac{\partial B}{\partial x}+\frac{\partial}{\partial x}\left(4\nu H\frac{\partial \bar{u}}{\partial x}\right)-\frac{\kappa(\bar{\mathbf{v}}H)}{1+\dfrac{\kappa(\bar{\mathbf{v}},H)}{3\nu}H}\bar{u}. \end{aligned}$$

The fluid layer is then divided into M vertically stacked layers, where each layer has a height h_α. Where

$$h_\alpha = Hl_\alpha,$$

and l_α is the proportional height of the αth layer. Thus, we need a new notation for u, and we therefore relate

$$u^{mc}(x,z,\{z_\alpha\},t)=\sum_{\alpha=1}^{\mathrm{M}} 1_{[z_{\alpha-1/2},z_{\alpha+1/2}]}(z)u_\alpha(x,t),$$

where u_α, $\alpha \in \{1,\dots,\mathrm{M}\}$ are the velocities of each layer as shown in Figure 4.1. Next, it is important to quantify the error between u and the piecewise approximation u^{mc}. By considering (4.2.16) we arrive at

$$\frac{\partial u}{\partial z}=\mathcal{O}(\varepsilon^2), \quad \text{for } z \geq z_{3/2}.$$

Thus, for all layers where $\alpha > 1$

$$u(w,z,t)-u_\alpha(x,t)=\mathcal{O}(\varepsilon^2). \qquad (4.2.18)$$

For $\alpha = 1$ we have

$$u(w,z,t)-u_1(x,t)=\mathcal{O}(\varepsilon).$$

Through a parabolic correction it can be shown [31, 73] that we obtain a good approximation for velocity with

$$u=\left(1+\frac{\varepsilon\kappa_0}{\nu_0}\left(z-B-\frac{(z-B)^2}{2H}-\frac{H}{3}\right)\right)u_1+\mathcal{O}(\varepsilon^2). \qquad (4.2.19)$$

Next, we consider the horizontal velocity equation (4.2.9b) and integrate it over the vertical dimension in the interval $[z_{\alpha-1/2}, z_{\alpha+1/2}]$, and using approximations along the lines of (4.2.19) we can obtain

$$\frac{1}{h_\alpha}\int_{z_\alpha-1/2}^{z_\alpha+1/2} u^2(x,z,t)\ dz = u_\alpha^2+\mathcal{O}(\varepsilon^2). \qquad (4.2.20)$$

We can also consider the gravitational part of the pressure as

$$\int_{z_\alpha-1/2}^{z_\alpha+1/2} \frac{\partial}{\partial x}(\delta\vartheta - z)\, dz = \frac{1}{2l_\alpha}\frac{\partial h_\alpha^2}{\partial x} + \frac{h_\alpha}{l_\alpha}\frac{\partial B}{\partial x}, \tag{4.2.21}$$

and the viscous part of pressure leads to

$$\int_{z_\alpha-1/2}^{z_\alpha+1/2} \frac{\partial}{\partial x}\left(2\nu\frac{\partial u}{\partial x}\right) dz = \frac{\partial}{\partial x}\left(2\nu h_\alpha \frac{\partial u_\alpha}{\partial x}\right) + 2\nu\left[\frac{\partial z_j}{\partial x}\frac{\partial u_j}{\partial x}\right]_{j=\alpha-1/2}^{j=\alpha+1/2} + \mathcal{O}(\varepsilon^2\delta). \tag{4.2.22}$$

Finally, we must account for the viscous terms of the right hand side of the equation (4.2.9b) which gives us

$$\begin{aligned}\int_{z_\alpha-1/2}^{z_\alpha+1/2} \frac{\partial}{\partial z}\left(\nu_0\frac{\partial u}{\partial z}\right) dz &= \nu_0\left.\frac{\partial u}{\partial z}\right|_{z_{\alpha+1/2}} - \nu_0\left.\frac{\partial u}{\partial z}\right|_{z_{\alpha-1/2}},\\ &\approx 2\nu\frac{u_{\alpha+1}-u_\alpha}{h_{\alpha+1}+h_\alpha} - 2\nu\frac{u_\alpha - u_{\alpha-1}}{h_\alpha + h_{\alpha-1}}.\end{aligned} \tag{4.2.23}$$

Thus, by combining (4.2.18)-(4.2.23) with the system (4.2.9) we gain the system

$$\begin{aligned}
\frac{\partial H}{\partial t} + \sum_{\alpha=1}^{\mathrm{M}}\frac{\partial(h_\alpha u_\alpha)}{\partial x} &= 0,\\
\frac{\partial(h_1u_1)}{\partial t} + \frac{\partial(h_1u_1^2)}{\partial x} + \frac{1}{2}\frac{g}{l_1}\frac{\partial h_1^2}{\partial x} &= -h_1\frac{\partial p^a}{\partial x} - gh_1\frac{\partial B}{\partial x} + u_{3/2}\mathcal{E}_{3/2}^x + \frac{\partial}{\partial x}\left(4\nu h_1\frac{\partial u_1}{\partial x}\right) -\\
&\quad 4\nu\frac{\partial z_{3/2}}{\partial x}\frac{\partial u_{3/2}}{\partial x} + 2\nu\frac{u_2-u_1}{h_2+h_1} - \kappa(\bar{\mathbf{v}},H)u_1,\\
\frac{\partial(h_\alpha u_\alpha)}{\partial t} + \frac{\partial(h_\alpha u_\alpha^2)}{\partial x} + \frac{1}{2}\frac{g}{l_\alpha}\frac{\partial h_\alpha^2}{\partial x} &= -h_\alpha\frac{\partial p^a}{\partial x} - gh_\alpha\frac{\partial B}{\partial x} + u_{\alpha+1/2}\mathcal{E}_{\alpha+1/2}^x - u_{\alpha-1/2}\mathcal{E}_{\alpha-1/2}^x +\\
2\nu\left(\frac{\partial}{\partial x}\left(2h_\alpha\frac{\partial u_\alpha}{\partial x}\right) + \frac{u_{\alpha+1}-u_\alpha}{h_{\alpha+1}+h_\alpha}\right.&\left. -\frac{u_\alpha-u_{\alpha-1}}{h_\alpha+h_{\alpha-1}} - 2\left[\frac{\partial z_j}{\partial x}\frac{\partial u_j}{\partial x}\right]_{j=\alpha-1/2}^{j=\alpha+1/2}\right), \qquad \alpha = 2,\ldots,\mathrm{M}-1,\\
\frac{\partial(h_{\mathrm{M}}u_{\mathrm{M}})}{\partial t} + \frac{\partial(h_{\mathrm{M}}u_{\mathrm{M}}^2)}{\partial x} + \frac{1}{2}\frac{g}{l_{\mathrm{M}}}\frac{\partial h_{\mathrm{M}}^2}{\partial x} &= -h_{\mathrm{M}}\frac{\partial p^a}{\partial x} - gh_{\mathrm{M}}\frac{\partial B}{\partial x} - u_{\mathrm{M}-1/2}\mathcal{E}_{\mathrm{M}-1/2}^x + \frac{\partial}{\partial x}\left(4\nu h_{\mathrm{M}}\frac{\partial u_{\mathrm{M}}}{\partial x}\right) +\\
&\quad 4\nu\frac{\partial z_{\mathrm{M}-1/2}}{\partial x}\frac{\partial u_{\mathrm{M}-1/2}}{\partial x} - 2\nu\frac{u_{\mathrm{M}}-u_{\mathrm{M}-1}}{h_{\mathrm{M}}+h_{\mathrm{M}-1}}.
\end{aligned}$$

Note that we have also dropped the $\mathcal{O}(\varepsilon^2\delta)$ terms, neglected horizontal viscosity and set $p^a = 0$. We combine the equations above into the simplified system

$$\begin{aligned}
\frac{\partial h_\alpha}{\partial t} + \frac{\partial\left(h_\alpha u_\alpha\right)}{\partial x} &= \mathcal{E}_{\alpha+1/2}^x - \mathcal{E}_{\alpha-1/2}^x,\\
\frac{\partial\left(h_\alpha u_\alpha\right)}{\partial t} + \frac{\partial}{\partial x}\left(h_\alpha u_\alpha^2 + \frac{1}{2l_\alpha}gh_\alpha^2\right) &= -gh_\alpha\frac{\partial B}{\partial x} + F_\alpha.
\end{aligned} \tag{4.2.24}$$

In (4.2.24), F_α includes the inter-layer forces as defined below and $\mathcal{E}^x_{\alpha\pm1/2}$ are mass exchange terms between the layers, including erosion and deposition in the lower layer, as

$$\mathcal{E}^x_{\alpha-1/2} = \begin{cases} -\dfrac{E_1 - D_1}{1-\Psi}, & \text{if} \quad \alpha = 1, \\[2ex] \displaystyle\sum_{\beta=1}^{\alpha}\left(\frac{\partial(h_\beta u_\beta)}{\partial x} - l_\beta \sum_{\gamma=1}^{\mathrm{M}} \frac{\partial(h_\gamma u_\gamma)}{\partial x}\right), & \text{if} \quad \alpha = 2,\dots,\mathrm{M}, \\[2ex] 0, & \text{if} \quad \alpha > \mathrm{M}, \end{cases}$$

where Ψ is the porosity and E_1 and D_1 represent the entrainment and deposition terms between the flow and bottom layer. This chapter considers both bedload and suspended sediments as one variable within the multilayer shallow water system (4.2.24). This is reasonable as the bedload is accounted for in the bottom layer moving at a different speed to the main fluid flow. To this end, the depth-averaged concentration c_α for the αth layer is defined as

$$c_\alpha = \frac{\rho_\alpha - \rho_w}{\rho_s - \rho_\alpha},$$

where ρ_α is the density of the fluid-sediment mixture in the αth layer. Hence, the governing equations considered are

$$\begin{aligned} \frac{\partial H}{\partial t} + \sum_{\alpha=1}^{\mathrm{M}} \frac{\partial(h_\alpha u_\alpha)}{\partial x} &= \frac{E_1 - D_1}{1-\Psi}, \\ \frac{\partial\left(h_\alpha u_\alpha\right)}{\partial t} + \frac{\partial}{\partial x}\left(h_\alpha u_\alpha^2 + \frac{1}{2} g h_\alpha H\right) &= -g h_\alpha \frac{\partial B}{\partial x} - \frac{(\rho_s - \rho_w)}{2\rho_\alpha} g h_\alpha^2 \frac{\partial c_\alpha}{\partial x} + F_\alpha, \\ \frac{\partial(h_\alpha c_\alpha)}{\partial t} + \frac{\partial}{\partial x}\Big(h_\alpha u_\alpha c_\alpha\Big) &= E_\alpha - D_\alpha + c_{\alpha+1/2}\mathcal{E}^x_{\alpha+1/2} - c_{\alpha-1/2}\mathcal{E}^x_{\alpha-1/2} + \\ &\qquad \varepsilon_c \left(\frac{\partial^2 c_{\Delta,\alpha-1/2}}{\partial z^2} - \frac{\partial^2 c_{\Delta,\alpha+1/2}}{\partial z^2}\right), \\ \frac{\partial B}{\partial t} &= -\frac{E_1 - D_1}{1-\Psi}, \end{aligned} \tag{4.2.25}$$

where the external force F_α acting on the αth layer accounting for friction and momentum exchange effects, is

$$F_\alpha = F_\alpha^{(u)} + F_\alpha^{(b)} + F_\alpha^{(w)} + F_\alpha^{(\mu)}, \tag{4.2.26}$$

with $F_\alpha^{(u)}$ related to the momentum exchanges between the layers. Extra momentum correction terms are applied to account for the movement of sediment between the bed and the layers.

$$
\begin{aligned}
F_\alpha^{(u)} &= u_{\alpha+1/2}\mathcal{E}^x_{\alpha+1/2} - u_{\alpha-1/2}\mathcal{E}^x_{\alpha-1/2} - \frac{1}{l_\alpha}\frac{(\rho_0-\rho_\alpha)(E_\alpha-D_\alpha)u_\alpha}{\rho_\alpha(1-\varPsi)} - \\
&\qquad \frac{(\rho_s-\rho_w)}{2\rho_\alpha}gh_\alpha^2\left(\varepsilon_c\frac{\partial^2 c_{\Delta,\alpha-1/2}}{\partial z^2} - \varepsilon_c\frac{\partial^2 c_{\Delta,\alpha+1/2}}{\partial z^2} + c_{\alpha+1/2}\mathcal{E}^x_{\alpha+1/2} - c_{\alpha-1/2}\mathcal{E}^x_{\alpha-1/2}\right),
\end{aligned}
$$

where ρ_0 is the density of the saturated bed related to the porosity as

$$
\rho_0 = \rho_w\varPsi + \rho_s(1-\varPsi),
$$

and the intermediate velocity $u_{\alpha+1/2}$ and concentration $c_{\alpha+1/2}$ is reconstructed using an upwind method based on the sign of the mass exchange term as

$$
u_{\alpha+1/2} = \begin{cases} u_\alpha, & \text{if} \quad \mathcal{E}^x_{\alpha+1/2} \geq 0, \\ \\ u_{\alpha+1}, & \text{otherwise}, \end{cases} \qquad c_{\alpha+1/2} = \begin{cases} c_\alpha, & \text{if} \quad \mathcal{E}^x_{\alpha+1/2} \geq 0, \\ \\ c_{\alpha+1}, & \text{otherwise}. \end{cases}
$$

It should be stressed that another method used in [14]

$$
u_{\alpha+1/2} = \frac{u_{\alpha+1}+u_\alpha}{2},
$$

is also possible. The vertical kinematic eddy viscosity term $F_\alpha^{(\mu)}$ in (4.2.26) takes into account the friction between neighbouring layers as

$$
F_\alpha^{(\mu)} = \begin{cases} -2\nu\dfrac{u_{\alpha-1}-u_\alpha}{(l_{\alpha-1}+l_\alpha)H}, & \text{if} \quad \alpha = \mathrm{M}, \\ 2\nu\dfrac{u_{\alpha+1}-u_\alpha}{(l_{\alpha+1}+l_\alpha)H} - 2\nu\dfrac{u_{l-1}-u_\alpha}{(l_{\alpha-1}+l_\alpha)H}, & \text{if} \quad \alpha = 2,\ldots,\mathrm{M}-1, \\ 2\nu\dfrac{u_{l+1}-u_\alpha}{(l_{\alpha+1}+l_\alpha)H}, & \text{if} \quad \alpha = 1, \end{cases}
$$

where ν is the eddy viscosity. The external bed friction term $F_\alpha^{(b)}$ in (4.2.26) is given as

$$
F_\alpha^{(b)} = \begin{cases} -\dfrac{gn_m^2}{H^{1/3}}u_1|u_1|, & \text{if} \quad \alpha = 1, \\ \\ 0, & \text{otherwise}, \end{cases}
$$

where n_m is the Manning roughness coefficient. The surface wind force $F_\alpha^{(w)}$ in (4.2.26) is defined as

$$F_{\alpha}^{(w)} = \begin{cases} -\dfrac{\sigma^2 \rho_a}{H}(U_{wi} - u_{\mathrm{M}})|(U_{wi} - u_{\mathrm{M}})|, & \text{if} \quad \alpha = \mathrm{M}, \\ 0, & \text{otherwise,} \end{cases}$$

where U_{wi} is the wind velocity at 10 m above the water surface and σ is the wind stress coefficient. Note that for the bottom layer an equation that relates the effects of an erodible bed is included in the model (4.2.25). These equations are presented in a general form such that appropriate erosion and deposition equations can be substituted with ease. Thus, to determine the entrainment and deposition terms in (4.2.25), the empirical relations reported in [35] are used

$$D_{\alpha} = \begin{cases} w_s(1 - c_B)^2 c_B, & \text{if} \quad \alpha = 1, \\ 0, & \text{otherwise,} \end{cases}$$

where w_s is the settling velocity of the sediment and c_B is a near bed concentration factor as used in the previous chapter. For the entrainment of the material, the following relation is used

$$E_{\alpha} = \begin{cases} \varphi \dfrac{\tau - \tau_{cr}}{h_1} u_1 d^{-0.2}, & \text{if} \quad \tau \geq \tau_{cr} \quad \text{and} \quad \alpha = 1, \\ 0, & \text{otherwise,} \end{cases}$$

where the erosion coefficient is denoted by φ, τ_{cr} is the critical shear stress and d is the diameter of the sediment particle. Note that these equations for the entrainment and depositions have been widely used in the literature for the conventional single-layer shallow water flows over erodible beds, see [22] and further references therein.

No vertical velocities are calculated in this model, but vertical sediment diffusion is a major problem for a formulation of this type. Thus, a sediment diffusion coefficient ε_c is introduced in this study. Research has been undertaken to both measure [191] and compute [83, 92] the vertical diffusion of sediment in flows. Figure 4.2 shows a typical sediment distribution in a water flow. As the shape, size, and precise sediment distribution for various sediments types has been categorised, a simplistic method for vertical distribution is proposed. Calculating the diffusion for each cell boundary is computationally expensive, consequently a distribution curve for the quantity of diffusion is implemented. The curve is calculated by comparing the sediment to be diffused to the portion that should be diffused, for example $C_0 = \dfrac{1}{z}$. Then, by applying the limits for each layer, the curve yields

$$C_{0,\alpha} = \left(\frac{\ln(z_{\alpha+\frac{1}{2}}) - \ln(z_{\alpha-\frac{1}{2}})}{\ln(h + \lambda_c) - \ln(h_{0.05} + \lambda_c)} \right) \sum_{\alpha=1}^{\mathrm{M}} \left(c_{\alpha} h_{\alpha}\right),$$

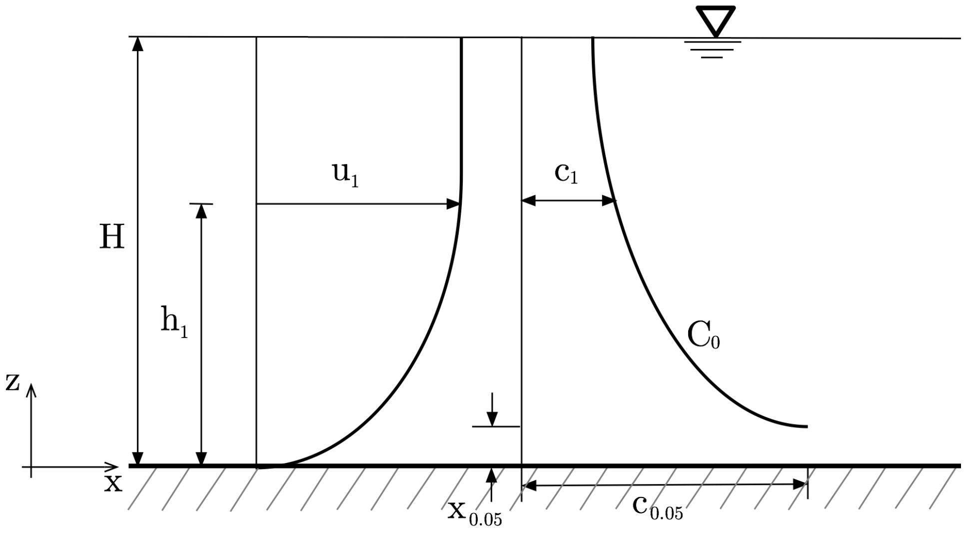

Figure 4.2: Typical sediment distribution in a water flow [115].

where z_α is the height of the αth layer, $h_{0.05}$ is the effective bottom (*i.e.* where bedload takes over) and λ_c is a empirically measured coefficient used to describe the concentration curve. The quantity of diffusible material at each layer interface is defined as

$$\frac{\partial^2 c_{\Delta,\alpha+\frac{1}{2}}}{\partial z^2} = \begin{cases} 0, & \text{if } \alpha \leq 0. \\ \dfrac{1}{h_\alpha}\left(C_{0,\alpha+1} - c_{\alpha+1}h_{\alpha+1} - C_{0,\alpha} + c_\alpha h_\alpha\right), & \text{if } \alpha = 1, \dots, \mathrm{M}-1 \\ 0, & \text{if } \alpha \geq \mathrm{M}. \end{cases}$$

Note that this method is easily adaptable to any sediment distribution curve and, as the distribution curve can be calculated in advance of any time-stepping procedure, it is efficient. For ease of presentation, the above equations are re-arranged into a compact vector form as

$$\frac{\partial \mathbf{W}}{\partial t} + \frac{\partial \mathbf{F}(\mathbf{W})}{\partial x} = \mathbf{Q}(\mathbf{W}) + \mathbf{R}(\mathbf{W}), \tag{4.2.27}$$

where $\mathbf{W}$ is the vector of conserved variables, $\mathbf{F}(\mathbf{W})$ is the vector of flux functions, $\mathbf{Q}(\mathbf{W})$ and

$\mathbf{R}(\mathbf{W})$ are the vectors of source terms.

$$\mathbf{W} = \begin{pmatrix} H \\ Hu_1 \\ Hc_1 \\ Hu_2 \\ Hc_2 \\ \vdots \\ Hu_{\mathrm{M}} \\ Hc_{\mathrm{M}} \\ B \end{pmatrix}, \ \mathbf{F}(\mathbf{W}) = \begin{pmatrix} \sum\limits_{\alpha=1}^{\mathrm{M}} l_\alpha H u_\alpha \\ Hu_1^2 + \frac{1}{2}gH^2 \\ Hu_1c_1 \\ Hu_2^2 + \frac{1}{2}gH^2 \\ Hu_2c_2 \\ \vdots \\ Hu_{\mathrm{M}}^2 + \frac{1}{2}gH^2 \\ Hu_{\mathrm{M}}c_{\mathrm{M}} \\ 0 \end{pmatrix}, \ \mathbf{Q}(\mathbf{W}) = \begin{pmatrix} 0 \\ -gH\frac{\partial B}{\partial x} - \frac{(\rho_s - \rho_w)}{2\rho_1} g l_1 H^2 \frac{\partial c_1}{\partial x} \\ 0 \\ -gH\frac{\partial B}{\partial x} - \frac{(\rho_s - \rho_w)}{2\rho_2} g l_2 H^2 \frac{\partial c_2}{\partial x} \\ 0 \\ \vdots \\ -gH\frac{\partial B}{\partial x} - \frac{(\rho_s - \rho_w)}{2\rho_{\mathrm{M}}} g l_M H^2 \frac{\partial c_{\mathrm{M}}}{\partial x} \\ 0 \\ 0 \end{pmatrix},$$

$$\mathbf{R}(\mathrm{W}) = \begin{pmatrix} \frac{E_1 - D_1}{1 - \Psi} \\ -\frac{1}{l_1}\left(F_1^{(u)} + F_1^{(b)} + F_1^{(\mu)}\right) \\ E_1 - D_1 - \mathcal{E}^x_{3/2}c_{3/2} - \varepsilon_c \frac{\partial^2 c_{\Delta,3/2}}{\partial z^2} \\ -\frac{1}{l_2}\left(F_2^{(u)} + F_2^{(\mu)}\right) \\ +\mathcal{E}^x_{5/2}c_{5/2} - \mathcal{E}^x_{3/2}c_{3/2} + \varepsilon_c \frac{\partial^2 c_{\Delta,3/2}}{\partial z^2} - \varepsilon_c \frac{\partial^2 c_{\Delta,5/2}}{\partial z^2} \\ \vdots \\ -\frac{1}{l_{\mathrm{M}}}\left(F_{\mathrm{M}}^{(u)} + F_{\mathrm{M}}^{(w)} + F_{\mathrm{M}}^{(\mu)}\right) \\ -\mathcal{E}^x_{M-1/2}c_{M-1/2} + \varepsilon_c \frac{\partial^2 c_{\Delta,M-1/2}}{\partial z^2} \\ -\frac{E_1 - D_1}{1 - \Psi} \end{pmatrix}.$$

The novelty of this formulation as compared to previous models is the inclusion of a moveable bed and exchange terms between layers. This is done in order to accurately capture and predict the distribution of sediment in the fluid flow. It should be stressed that the source term **Q** contains the first-order differential terms, while the remaining forces are included in the source term **R**. This structure is useful as it allows for a time splitting operator in (4.2.27), for which the source terms **Q** and **R** are treated separately in different stages of the splitting.

4.3 Eulerian-Lagrangian finite volume method for the multi-layer system

To integrate the system (4.2.27) in time, the time domain is divided into subintervals $[t_n, t_{n+1}]$ with length $\Delta t = t_{n+1} - t_n$ and the notation $\mathbf{W}^n$ is used to denote the value of a generic function $\mathbf{W}$ at time t_n. Here, a second-order splitting procedure, reported in [172] is considered and carried out in three stages as:

Stage 1: Solve for $\mathbf{W}^*$

$$\begin{aligned} \frac{\partial \mathbf{W}^*}{\partial t} &= \mathbf{R}(\mathbf{W}^*), \qquad t \in (t_n, t_{n+1/2}], \\ \mathbf{W}^*(t_n) &= \mathbf{W}(t_n). \end{aligned} \tag{4.3.28}$$

Stage 2: Solve for $\mathbf{W}^{**}$

$$\begin{aligned} \frac{\partial \mathbf{W}^{**}}{\partial t} + \frac{\partial \mathbf{F}(\mathbf{W}^{**})}{\partial x} &= \mathbf{Q}(\mathbf{W}^{**}), \qquad t \in (t_n, t_{n+1}], \\ \mathbf{W}^{**}(t_n) &= \mathbf{W}^*(t_{n+1/2}). \end{aligned} \tag{4.3.29}$$

Stage 3: Solve for $\mathbf{W}^{***}$

$$\begin{aligned} \frac{\partial \mathbf{W}^{***}}{\partial t} &= \mathbf{R}(\mathbf{W}^{***}), \qquad t \in (t_{n+1/2}, t_{n+1}], \\ \mathbf{W}^{***}(t_{n+1/2}) &= \mathbf{W}^{**}(t_{n+1}). \end{aligned} \tag{4.3.30}$$

To complete the time integration the explicit third-order Runge-Kutta method [161] is used. This is to ensure that only the space interpolation in the Method of Characteristics (which is 1st or 2nd depending on whether linear or quadratic interpolation is used) is the limiting factor. By going an order of accuracy further with the time integration we ensure this.

For example, to advance the solution of (4.3.28) from time t_n to time t_{n+1} the following is used

$$\begin{aligned} \mathcal{W}^{(1)} &= \mathbf{W}^n + \Delta t \mathbf{R}\left(\mathbf{W}^n\right), \\ \mathcal{W}^{(2)} &= \frac{3}{4}\mathbf{W}^n + \frac{1}{4}\mathcal{W}^{(1)} + \frac{1}{4}\Delta t \mathbf{R}\left(\mathcal{W}^{(1)}\right), \\ \mathbf{W}^{n+1} &= \frac{1}{3}\mathbf{W}^n + \frac{2}{3}\mathcal{W}^{(2)} + \frac{2}{3}\Delta t \mathbf{R}\left(\mathcal{W}^{(2)}\right). \end{aligned} \tag{4.3.31}$$

The asterisk is dropped off the vectors of conserved variables for ease in the notation. The method is stable under the usual Courant-Friedrichs-Lewy (CFL) condition using the eigenvalues of the system under study.

Explicit expressions of the eigenvalues for the system (4.2.27) are not trivial to find and, as with multilayer SWEs over fixed beds, complex eigenvalues can occur. In these cases, the multilayer system (4.2.27) ceases to be hyperbolic and yields to the so-called Kelvin-Helmholtz instabilities at the interfaces between the flow layers. As a consequence, most FVMs based on Riemann solvers would fail to resolve the multilayer SWEs over erodible beds. The present study considers the ELFV method introduced in [24]. In this section, the Eulerian-Lagrangian formulation for the system (4.2.27) is described.

The spatial domain is discretised into control volumes $[x_{i-1/2}, x_{i+1/2}]$ centred at x_i with a step size Δx. For the space discretisation of the equations (4.2.27), the following notations are used

$$\mathbf{W}_{i\pm\frac{1}{2}}(t) = \mathbf{W}(t, x_{i\pm\frac{1}{2}}), \qquad \mathbf{W}_i(t) = \frac{1}{\Delta x}\int_{x_{i-\frac{1}{2}}}^{x_{i+\frac{1}{2}}} \mathbf{W}(t,x)\; dx,$$

to denote the point-values and the approximate cell-average of the variable $\mathbf{W}$ at the gridpoint $(t, x_{i\pm\frac{1}{2}})$ and (t, x_i), respectively. Integrating the equations (4.3.29) with respect to space over the control volume, the following semi-discrete equations are obtained

$$\frac{d\mathbf{W}_i}{dt} + \frac{\boldsymbol{\mathcal{F}}_{i+1/2} - \boldsymbol{\mathcal{F}}_{i-1/2}}{\Delta x} = \mathbf{Q}_i, \tag{4.3.32}$$

where $\boldsymbol{\mathcal{F}}_{i\pm1/2} = \mathbf{F}(\mathbf{W}_{i\pm1/2})$ are the numerical fluxes at the cell interfaces $x = x_{i\pm1/2}$. In equation (4.3.32), $\mathbf{Q}_i$ is a consistent discretisation of the source term $\mathbf{Q}$ in (4.2.27). In order to reconstruct the numerical fluxes $\boldsymbol{\mathcal{F}}^n_{i\mp1/2}$, the Method of Characteristics (MoC) is applied to the advective components of the system shown in stage (4.3.29). In order to reconstruct the fluxes $\boldsymbol{\mathcal{F}}^n_{i\mp1/2}$, the MoC is applied to the advective form of the system. Without accounting for the source term $\mathbf{R}(\mathbf{W})$, the equations in (4.2.25) are reformulated into advective form,

$$\begin{aligned}
\frac{\partial H}{\partial t} + \left(\sum_{\alpha=1}^{M} l_\alpha u_\alpha\right)\frac{\partial H}{\partial x} &= -\sum_{\alpha=1}^{M} l_\alpha H \frac{\partial u_\alpha}{\partial x},\\
\frac{\partial (Hu_\alpha)}{\partial t} + u_\alpha \frac{\partial (Hu_\alpha)}{\partial x} &= -Hu_\alpha \frac{\partial u_\alpha}{\partial x} - gH\frac{\partial (H+B)}{\partial x} - \frac{(\rho_s - \rho_w)}{2\rho_\alpha} g l_\alpha H^2 \frac{\partial c_\alpha}{\partial x},\\
\frac{\partial (Hc_\alpha)}{\partial t} + u_\alpha \frac{\partial (Hc_\alpha)}{\partial x} &= -H\frac{\partial (u_\alpha c_\alpha)}{\partial x}.
\end{aligned} \tag{4.3.33}$$

The proposed ELFV method does not require the calculation of the eigenvalues for the multilayer system, and the selection of time-steps can be carried out using the eigenvalues associated with the single-layer shallow water counterparts defined as

$$\lambda_\alpha^\pm = u_\alpha \pm \sqrt{gH}, \qquad \alpha = 1, 2 \ldots, M.$$

This is because the eigenvalues estimate the maximum wave speed thus ensuring that shock-waves do not cross cell boundaries. As each individual layer's wave speed is effected by its neighbours during the second step of the calculation this assumption is found to be reasonable The maximum stable step size, as with all explicit time-stepping methods, is dictated by the CFL condition using the equivalent eigenvalues

$$\Delta t = \mathrm{Cr}\frac{\Delta x}{\max\limits_{\alpha=1,\ldots,M}\left(|\lambda_\alpha^n|\right)},$$

where Cr is the Courant number (to be chosen less than unity).

4.3.1 Discretisation of the flux gradients

In order to reconstruct the fluxes $\boldsymbol{\mathcal{F}}_{i\mp1/2}^n$, the Method of Characteristics (MoC) is applied to the advective version of the system, as in [12]. Note that the fourth governing equation in (4.2.25) is not advective and therefore is not accounted for in the advective form. System (4.3.33) can be rearranged to

$$\begin{aligned}
\frac{DH}{Dt} &= -\sum_{\alpha=1}^{M} l_\alpha H \frac{\partial u_\alpha}{\partial x},\\
\frac{D(Hu_\alpha)}{Dt} &= -Hu_\alpha\frac{\partial u_\alpha}{\partial x} - gH\frac{\partial(H+B)}{\partial x} - \frac{(\rho_s-\rho_w)}{2\rho_\alpha} g l_\alpha H^2 \frac{\partial c_\alpha}{\partial x},\\
\frac{D(Hc_\alpha)}{Dt} &= -H\frac{\partial(u_\alpha c_\alpha)}{\partial x},
\end{aligned}$$

where $\frac{D}{Dt}$ is the total derivative defined by

$$\frac{D}{Dt} = \frac{\partial}{\partial t} + \mathcal{U}_\beta \frac{\partial}{\partial x},$$

$$\mathcal{U}_\beta = \begin{cases} \sum\limits_{\gamma=1}^{M} l_\gamma u_\gamma, & \text{if} \quad \beta = 0,\\ u_\beta, & \text{if} \quad \beta = 1, 3, 5, 7, \ldots\ ,\\ u_{\beta-1}, & \text{if} \quad \beta = 2, 4, 6, 8, \ldots\ . \end{cases}$$

The aim of the MoC is to impose a new grid at the next time level t_{n+1} by interpolating from

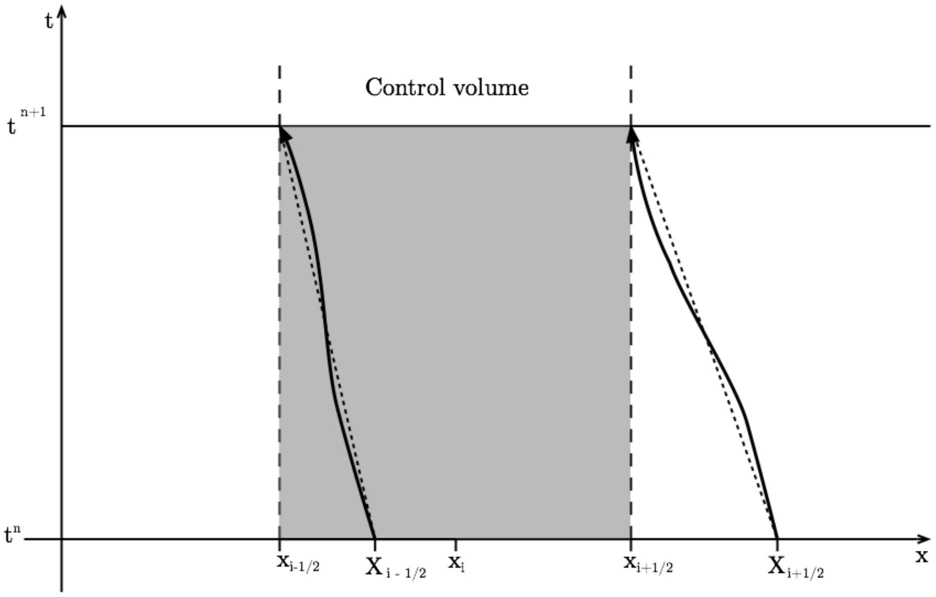

Figure 4.3: A schematic of the quantities used in the calculation of the departure points. The dotted lines show the interpolated trajectory, while the solid lines show the actual trajectory. Here, an Eulerian gridpoint $x_{i+1/2}$ is traced back in time to $X_{i+1/2}$ where the intermediate solution $\widetilde{\mathbf{W}}^n_{i+1/2}$ is interpolated.

t_n. This enables the evaluation of the characteristic curves shown in Figure 4.3

$$\frac{dX_{\alpha,i+1/2}(s)}{ds} = \mathcal{U}_{\alpha,i+1/2}(s, X_{\alpha,i+1/2}(s)), \qquad s \in [t_n, t_{n+1}].$$

Integrating with respect to t the following is gained

$$\begin{aligned} X_{\alpha,i+1/2}(t_n) &= x_{i+1/2} - \int_{t_n}^{t_{n+1}} \mathcal{U}_{\alpha,i+1/2}(s, X_{\alpha,i+1/2}(s))ds, \\ &= x_{i+1/2} - \delta_{\alpha,i+1/2}. \end{aligned} \tag{4.3.34}$$

To facilitate the integral in (4.3.34) the method proposed in [23] is used. Figure 4.3 tells us that

$$\delta_{\alpha,i+1/2} = x_{i+1/2} - X_{\alpha i+1/2}(t_n).$$

Through the use of the mid-point rule, equation (4.3.34) becomes

$$\delta_{\alpha,i+1/2} = \frac{\Delta t}{2} \mathcal{U}_{\alpha,i+1/2}\left(t_{n+1}, X_{\alpha i+1/2}(t_n+1)\right). \tag{4.3.35}$$

Via second-order extrapolation we obtain

$$\mathcal{U}_{\alpha,i+1/2}(t_{n+1}, x_{i+1/2}) = \frac{3}{2}\mathcal{U}_{\alpha,i+1/2}\left(t_n, x_{i+1/2}\right) - \frac{1}{2}\mathcal{U}_{\alpha,i+1/2}\left(t_{n-1}, x_{i+1/2}\right), \tag{4.3.36}$$

which can be approximated

$$X_{\alpha,i+1/2}(t_{n+1}) = x_{i+1/2} - \frac{1}{2}\delta_{\alpha,i+1/2}.$$

Thus an implicit formula for $\delta_{\alpha,i+1/2}$ is obtained

$$\delta_{\alpha,i+1/2} = \frac{\Delta t}{2}\left[\frac{3}{2}\mathcal{U}_{\alpha,i+1/2}\left(t_n, x_{\alpha i+1/2} - \frac{1}{2}\delta_{\alpha,i+1/2}\right) - \frac{1}{2}\mathcal{U}_{\alpha,i+1/2}\left(t_{n-1}, x_{i+1/2} - \frac{1}{2}\delta_{\alpha,i+1/2}\right)\right].$$

In order to solve for $\delta_{\alpha,i+1/2}$, a successive iteration procedure is used

$$\begin{aligned}
\delta^{(0)}_{\alpha,i+1/2} &= \frac{\Delta t}{2}\left[\frac{3}{2}\mathcal{U}_{\alpha,i+1/2}\left(t_n, x_{\alpha i+1/2}\right) - \frac{1}{2}\mathcal{U}_{\alpha,i+1/2}\left(t_{n-1}, x_{i+1/2}\right)\right], \\
\delta^{(k)}_{\alpha,i+1/2} &= \frac{\Delta t}{2}\left[\frac{3}{2}\mathcal{U}_{\alpha,i+1/2}\left(t_n, x_{\alpha i+1/2}\frac{1}{2}\delta^{(k-1)}_{\alpha,i+1/2}\right)\right] - \\
&\qquad \frac{\Delta t}{2}\left[\frac{3}{2}\mathcal{U}_{\alpha,i+1/2}\left(t_{n-1}, x_{\alpha i+1/2}\frac{1}{2}\delta^{(k-1)}_{\alpha,i+1/2}\right)\right], \quad k = 1, 2\ldots
\end{aligned} \tag{4.3.37}$$

The iterative procedure in (4.3.37) are terminated when

$$\frac{||\delta^{(k)}_{\alpha} - \delta^{(k-1)}_{\alpha}||}{||\delta^{(k-1)}_{\alpha}||} \leq tol,$$

where *tol* is a given tolerance. Thus the convergence of iterations (4.3.37) is sufficient when it satisfies

$$\max_{\alpha=0,1,\ldots,2M}\left|\frac{\partial \mathcal{U}_{\alpha}}{\partial x}\right|\frac{\Delta t}{4} \leq 1. \tag{4.3.38}$$

Once the characteristic curves $X_{\alpha,i+1/2}(t_n)$ are known, the solution

$$\mathbf{U}^{n+1/2}_{\alpha,i+1/2} = \begin{pmatrix} H^{n+1}_{i+1/2} \\ \\ (Hu)^{n+1}_{\alpha,i+1/2} \\ \\ (Hc)^{n+1}_{\alpha,i+1/2} \end{pmatrix}$$

is reconstructed as

$$\mathbf{U}^{n+1/2}_{\alpha,i+1/2} = \mathbf{U}_{\alpha}(t_{n+1}, x_{i+1/2}) = \widetilde{\mathbf{U}}_{\alpha}\left(t_n, X_{\alpha,i+1/2}(t_n)\right),$$

where $\widetilde{\mathbf{U}}_\alpha\left(t_n, X_{\alpha,i+1/2}(t_n)\right)$ is the solution found through interpolation from the previous time-step

$$\widetilde{\mathbf{U}}_\alpha(t_n, X_{\alpha,i+1/2}(t_n)) = \mathcal{P}\left(\mathbf{U}_\alpha(t_n, X_{\alpha,i+1/2}(t_n))\right),$$

where $\mathcal{P}$ is the interpolating polynomial. Many different polynomials are possible (including hermite, spine, and cubic) see [12]. The solutions at the characteristic foot $X_{\alpha,i+1/2}$ are computed by interpolation from the departure points $X_{\alpha,i+1/2}(t_n)$ and the numerical fluxes $\boldsymbol{\mathcal{F}}_{i\pm1/2}$ are calculated from the intermediate states of the predictor stage. The characteristic solutions are

$$\begin{aligned}
H_{i+1/2}^{n+1} &= \widetilde{H}_{i+1/2}^{n+1} - \frac{\Delta t}{\Delta x}\widetilde{H}_{i+1/2}^{n+1}\sum_{\alpha=1}^{M} l_\alpha\left(u_{\alpha,i+1}^{n+1} - u_{\alpha,i}^{n+1}\right),\\
(Hu_\alpha)_{i+1/2}^{n+1} &= \widetilde{(Hu_\alpha)}_{i+1/2}^{n+1} - \frac{\Delta t}{\Delta x}\left(\widetilde{(Hu_\alpha)}_{i+1/2}^{n+1}\left(u_{\alpha,i+1}^{n+1} - u_{\alpha,i}^{n+1}\right) + \right.\\
&\qquad g\widetilde{H}_{i+1/2}^{n+1}\left(\left(H_{i+1}^{n+1} + B_{i+1}^{n}\right) - \left(H_i^{n+1} + B_i^{n}\right)\right) +\\
&\qquad \left.\frac{(\rho_s - \rho_w)}{2\rho_\alpha} gH^2\left(c_{\alpha,i+1}^{n+1} - c_i^{\alpha,n+1}\right)\right),\\
(Hc_\alpha)_{i+1/2}^{n+1} &= \widetilde{(Hc_\alpha)}_{i+1/2}^{n+1} - \frac{\Delta t}{\Delta x}\widetilde{H}_{i+1/2}^{n+1}\left((uc)_{\alpha,i+1}^{n+1} - (uc)_{\alpha,i}^{n+1}\right),
\end{aligned}$$

where

$$\widetilde{H}_{i+1/2}^{n+1} = H(t_n, X_{0,i+1/2}(t_n)), \qquad \widetilde{(Hu_\alpha)}_{i+1/2}^{n+1} = (Hu_\alpha)(t_n, X_{0,i+1/2}(t_n)),$$
$$\widetilde{(Hc_\alpha)}_{i+1/2}^{n+1} = (Hc_\alpha)(t_n, X_{0,i+1/2}(t_n)).$$

Thus, the corrector stage reduces to

$$\begin{aligned}
H_i^{n+1} &= H_i^n - \frac{\Delta t}{\Delta x}\sum_{\alpha=1}^{M}\left((l_\alpha Hu_\alpha)_{i+1/2}^{n+1}) - (l_\alpha Hu_\alpha)_{i-1/2}^{n+1}\right),\\
(Hu_\alpha)_i^{n+1} &= (Hu_\alpha)_i^n - \frac{\Delta t}{\Delta x}\left(\left(Hu_\alpha + \frac{1}{2}gH^2\right)_{i+1/2}^{n+1} - \left(Hu_\alpha + \frac{1}{2}gH^2\right)_{i-1/2}^{n+1}\right) -\\
&\qquad \frac{\Delta t}{\Delta x} g\widehat{H}_i^{n+1}(B_{i+1}^n - B_{i-1}^n) + \frac{(\rho_s - \rho_w)}{2\rho_\alpha} g\left(\widehat{H}_i^{n+1}\right)^2 (c_{\alpha,i+1}^{n+1} - c_{\alpha,i-1}^{n+1}),\\
(Hc_\alpha)_{\alpha,i}^{n+1} &= (Hc_\alpha)_i^n - \frac{\Delta t}{\Delta x}\left((Hu_\alpha c_\alpha)_{i+1/2}^{n+1} - (Hu_\alpha c_\alpha)_{i-1/2}^{n+1}\right).
\end{aligned}$$

Note that, in order to satisfy the c-property and as in the previous chapter (3.4.21), the source terms are discretised

$$\widehat{H}_i^{n+1} = \frac{H_{i+1}^{n+1} + 2H_i^{n+1} + H_{i-1}^{n+1}}{4}.$$

This discretisation ensures the ELFV method satisfies the C-property. This procedure is implemented as shown in Figure 4.4.

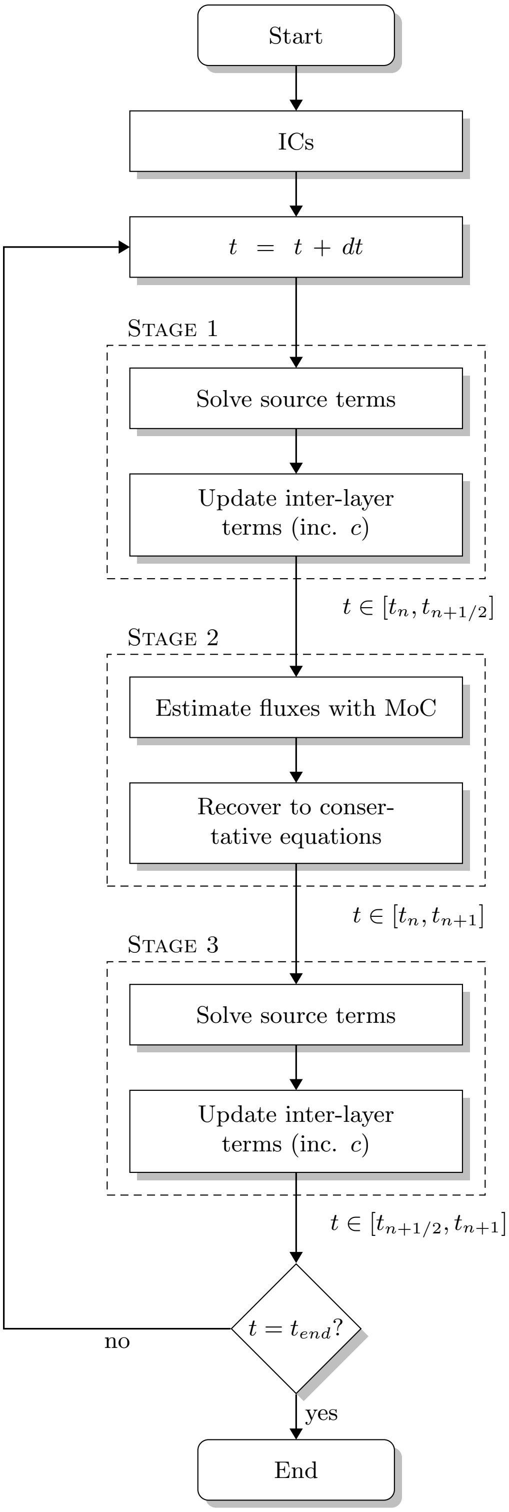

Figure 4.4: A flowchart demonstrating the stages in the proposed Eulerian-Lagrangian procedure.

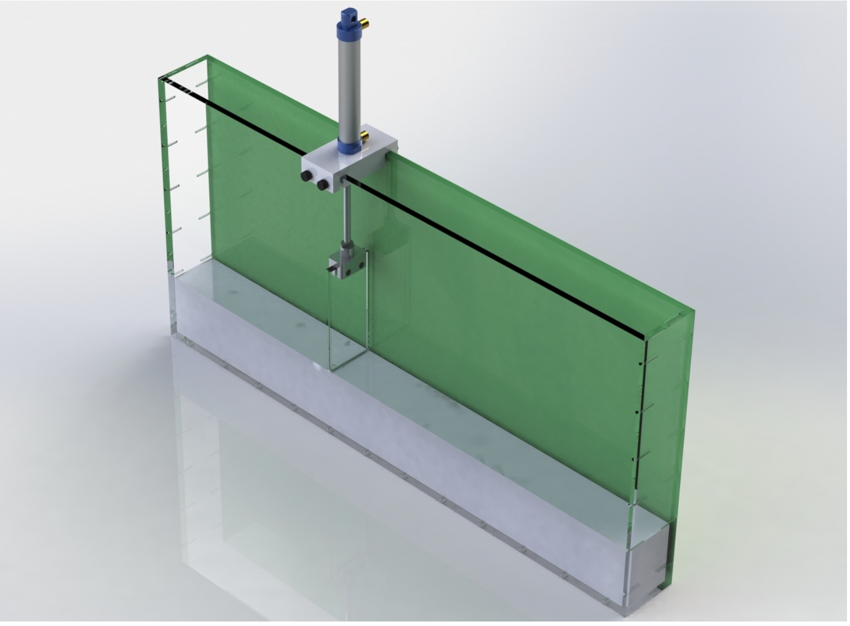

Figure 4.5: A picture of the design of the experimental rig showing a fixed bed.

4.4 One-dimensional dam-break experimental method

This section details the experimental method, namely the physical methods used to create a 1D dam-break flow over an erodible bed, as well as the digital methods used to extract the data. This section also discusses the design process and how parts are developed to improve the accuracy of results. MATLAB is used, as this provides a good basic image toolbox that can be quickly customized to the required method. Beyond the constraints of the possible, great care must be taken when deciding the size of the experiment to be undertaken. Many small-scale 1D dam-breaks have been carried out at various length scales, from the Taipei experiment at 1.2 m [39] to the Hanyang University experiments at 6 m [140]. Longer sedimentary experiments have also been performed, including the 30 m Delft trench experiment [27]. The camera has a 1080 p resolution at a frame rate of 100 fps, and the aim is to achieve a 0.5 mm to pixel precision. The well-graded soil has a range from 1 mm to 0.16 mm with an average particle size $d = 0.25$ mm, thus the domain is set at 900 mm in length. For easy access and to minimize edge effects, the width of the domain is set at 75 mm. The height of the dam-break was originally set at 100 mm; after testing it was revised to 120 mm to maximize erosion. The mechanism is designed for a dam-break to take less than 0.02 s. To reduce human error and increase opening time, an electronic valve is utilized. The line pressure available is 20 bar and initially a small tracking cylinder was thought advisable. A variety of designs were trialled, and eventually a directly mounted linear actuator (in its simplest configuration) was found to be the fastest and most repeatable, offering an average opening time of 0.011 s. In order to seal the edges (and

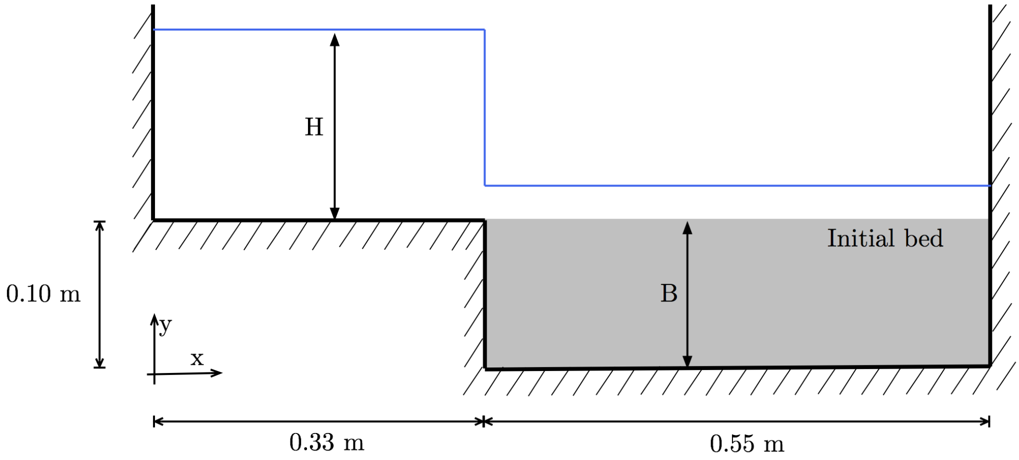

Figure 4.6: A sketch of the scour after an apron domain.

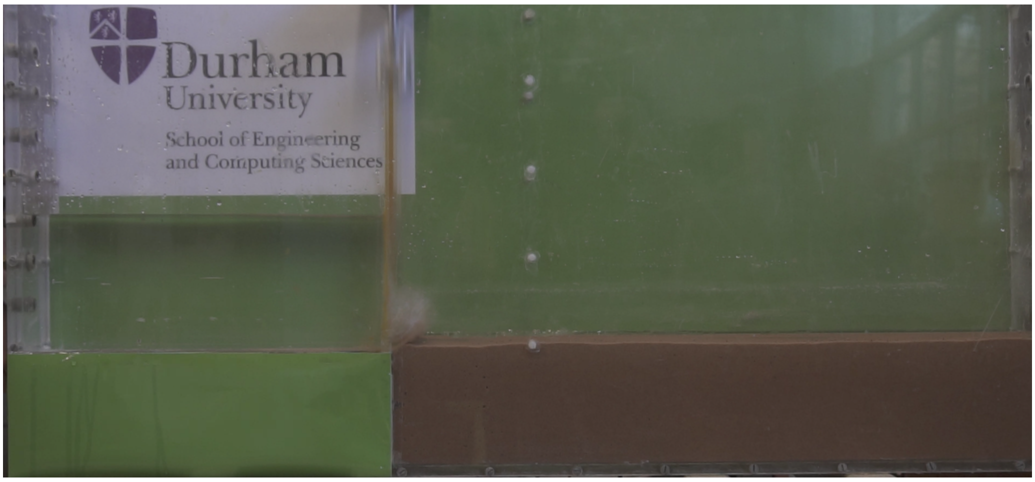

Figure 4.7: A photo of the experimental domain

without effecting the flow) a bead of sealant is added to the grove on the side of the dam break. This reduces the average opening speed to 0.018 s which is still within the target. One fact that became obvious during the simulation runs is that, even if compacted, the bed seeps. A variety of tests performed from pearls at 6 mm to fine sand at 0.25 mm are undermined by seepage under the dam before a differential height of 100 mm is reached. Thus, a solid apron as shown in Figure 4.6 is adopted, providing a solid seal. Due to the requirement of specialized high intensity lighting, a high-sided tank with fixed ends is used. This differs from the standard open ended or re-circulating tanks normally used in experiments of this type. In order to maximize the dam-break run time, the dam is located at 330 mm from the left hand side, leaving 640 mm for it to run over. The design is as shown in Figure 4.5. It offers a 0.42 s dam-break run without sediment (on a low slip surface) and 0.48 s dam-break run over the higher friction of a sand bed. The camera available is able to correct for photographic concerns such as white balance, and

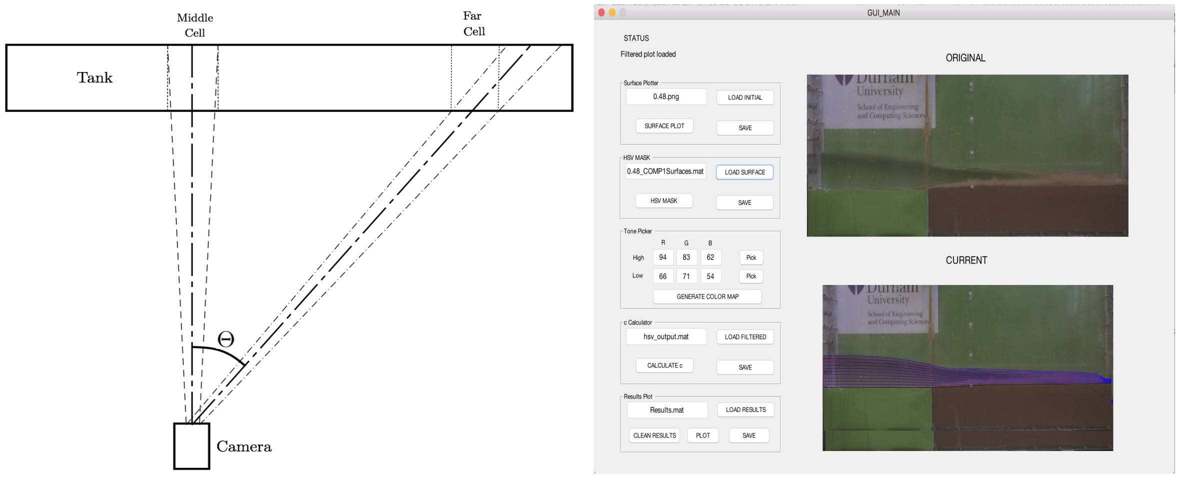

STATUS
Filtered plot loaded

Surface Plotter: 0.48.png
HSV MASK: 0.48_COMP1Surfaces.mat

	R	G	B
High	94	83	62
Low	66	71	54

c Calculator: hsv_output.mat
Results Plot: Results.mat

Figure 4.8: A sketch detailing the problem of parallax error (left) and a screen-shot of the automated program (right).

these factors are checked (and modified if required) during post processing. Beyond that, all conditions were kept as identical as possible. As the camera produces an image from one point of view, the first step in post-processing is to calibrate the image. The first issue is that of parallax error, as shown in Figure 4.4: the greater the angle of Θ from the normal, the less accurate the camera is in capturing the sediment. Three steps are taken to reduce this: firstly, a tele-centric lens is used which reduces parallax error; secondly, the camera is centred at 450 mm, not at the dam-break; finally, a simple calculation is performed to average across neighbouring cells. This error also occurs in the vertical dimension, though to a lesser extent than in the horizontal dimension. Since the water is at a maximum of 120 mm above the camera, it has the added problem of bed interference. Mapping pixels of the bed into the image would inadvertently increase the measured concentration. It is also important not to remove bedload, which is hard to separate from the bed, and this poses a complex problem. Two steps are taken to eliminate this, while retaining any bedload in the measurement. Firstly, the camera is placed on a level with the bed and, as erosion is minimal, this nearly removes the error. Secondly, the bed is measured at the light change with user inspection; as bedload is less disperse than packed bed, there is a noticeable light change. Algorithms trialled to perform this were found to be less accurate and more time consuming than doing it manually. It should be noted that vertical averaging is not used, as the angles in the sedimentary flow (often only 50 mm in height) are not considered necessary.

Once the images are captured and the timing assessed, the following procedures are followed in order to address these problems in turn:

1. Correct the white balance by ensuring that background colour and exposure is consistent in every frame.

2. Map the bed and water surfaces using a point-click and interpolation algorithm and compute scales and parallax error.

3. Remove irrelevant background colours and correct for lighting using multiple HSI masks.

4. Create a colour chart for sediment using known high and low sediment areas (*i.*e. bed and zero sediment cell)

5. Cut the image down into sub-cells and calculate the depth-averaged concentration by comparison of the pixel average to the colour chart.

6. Normalize according to quantity of erosion. This step also allows for an error measure to be taken.

This procedure was coded into a 5-step program where step 1 and step 6 could be fully automated. A screen-shot of this simple program is shown in Figure 4.4.

4.5 Numerical results

In this section, the results obtained for two case studies are presented. Here we present results for a standard dam-break situation (an erosion-based problem) and a more complex recirculation situation (a deposition based problem). In order to compare the rates of erosion, a comparison is made between the average speed (across the layers) in a multilayer dam with just the bottom layer. The dam-break situation is also computed with a varying number of fluid layers in order to investigate the effect of adding layers. It is expected that more layers will yield a decreased bottom layer velocity and therein less erosion. The effects of the inter-layer exchange terms are also investigated for the dam-break simulation to highlight their necessity. The vertical sediment diffusion coefficient $\varepsilon_c = 0.01 \ m^2/s$. Vertical velocities are reconstructed from the results of the simulations, using the method outlined in [12, 13]. In order to recover the vertical velocity components w, methods similar to those used in [12, 13] are employed. Hence, the vertical velocity w is recovered from the divergence-free condition

$$\frac{\partial u}{\partial x} + \frac{\partial w}{\partial z} = 0. \tag{4.5.39}$$

Integrating the equation (4.5.39) over a control volume yields

$$w^n_{\alpha+1,i,j} = w^n_{\alpha,i,j} + \Delta z \left(\frac{u^n_{\alpha,i+1/2,j} - u^n_{\alpha,i-1/2,j}}{\Delta x} \right), \tag{4.5.40}$$

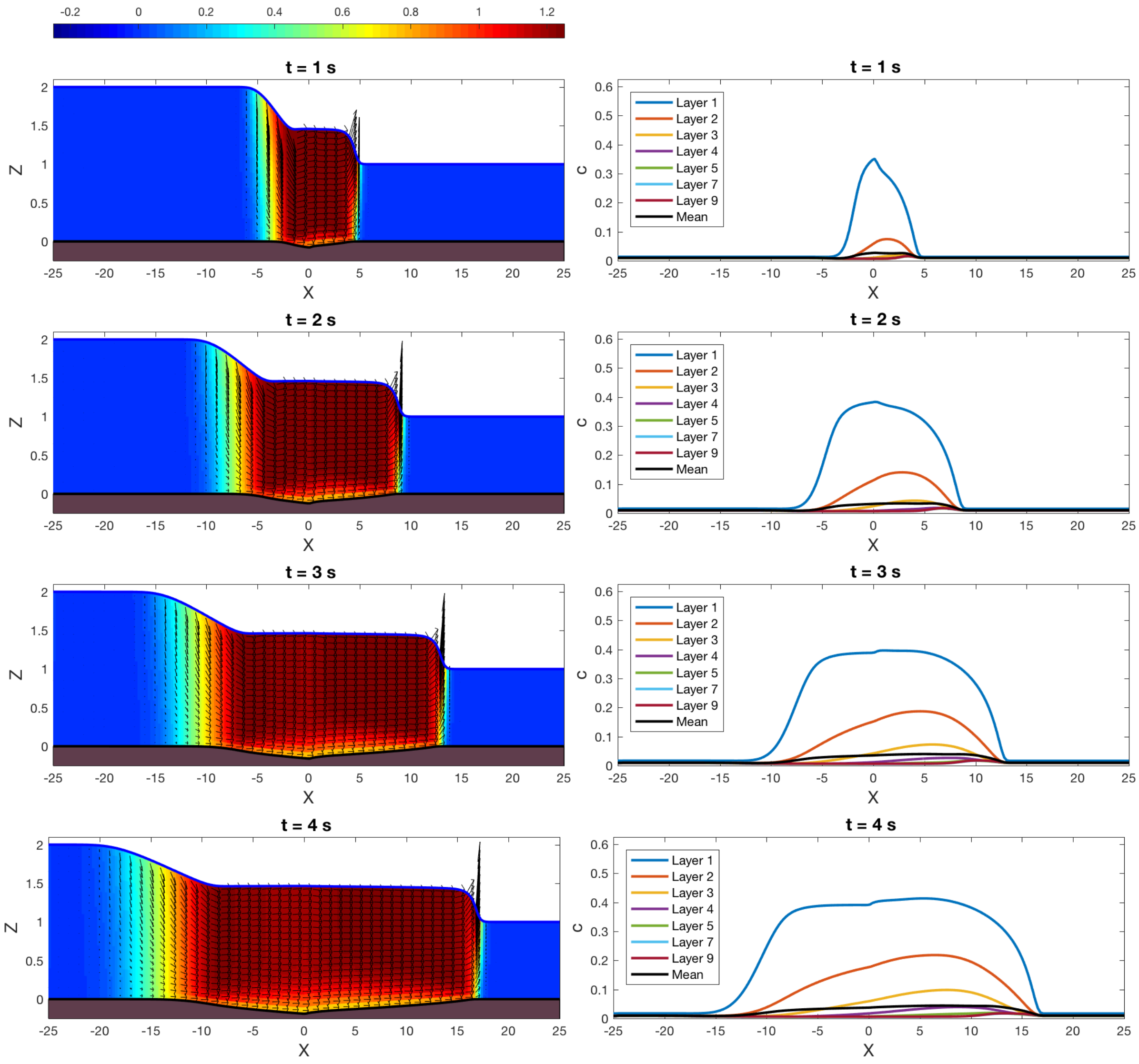

Figure 4.9: Results from a 20-layer dam-break simulation: velocity (left) and concentration (right) plots.

where $\Delta z = \dfrac{h_{\alpha+1} + h_\alpha}{2}$. The bed is assumed to be impenetrable (for these calculations) as in [70].

4.5.1 Dam-break simulations

In the dam-break situation, the domain is 50 m long and has a flat bottom. The initial conditions are

$$H(0,x) = \begin{cases} 2\ m, & x < 0, \\ 1\ m, & x \geq 0, \end{cases} \qquad c(0,x) = 0.01 \quad u(0,x,y) = 0\ m/s\ .$$

The dam-break is considered to be instantaneous and the resultant wave is allowed to develop for 4 s. The bed material is a non-cohesive sand (Sand 2 from Table 3.1). Prior to running experiments it is important to compare the effects of discretisation in both the x-dimension and

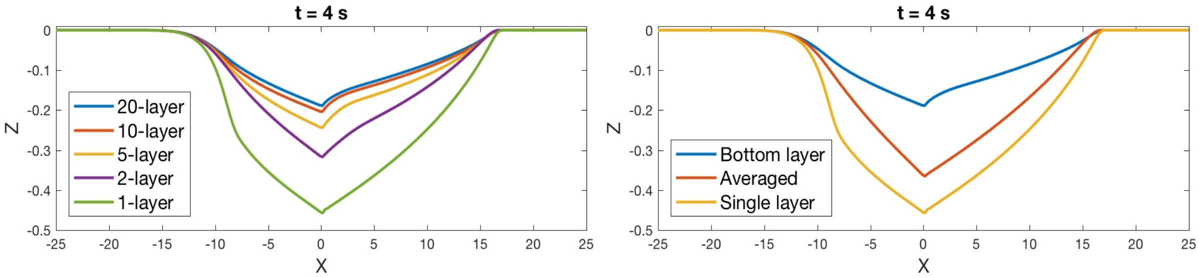

Figure 4.10: Comparison of sediment transport velocity functions for a multilayer dam-break simulation, with varying numbers of layers (left) and a comparison of averaged and bottom layered velocity in calculating erosion (right).

the number of layers used in the z-dimension. The results are displayed in Table 4.1 for the calculation of suspended sediment results; the y-dimension of the domain is assumed to be 1 m.

The results show that the number of fluid layers has a profound effect on the bathymetry and total suspended sediment. For example, if a 2-layer simulation with 200 gridpoints is considered the total suspended sediment is 3.792 m^3 and the deepest point of the bed is -0.3174 m. Whereas in a 20-layer simulation, the total suspended sediment drops to 1.899 m^3 and the deepest point rises to -0.1877 m. This underlines the importance of correctly selecting the number of layers and, although the CPU time rises from 1.003 s to 7.231 s, this appears a worthwhile trade off. As postulated in [11] if an infinite number of layers is used then the solution should recover to a 3D form, but as with all simulations of this nature it does become a question of CPU expenditure and complexity in post-processing. Thus to realised the benefit it is proposed that the user increase the number of layers used until no meaningful resolution or flow features are realised. The number of gridpoints also has an effect: if a 20-layer model is used, but only 50 gridpoints, then 1.964 m^3 is the total suspended sediment and the deepest point is increased to -0.1900 m. By including 400 gridpoints, the total suspended sediment drops to 1.900 m^3 and the deepest point of the bed becomes -0.1881 m, but there is a much higher computational time increase of 17.15 s as compared to 1.037 s. Thus, it can be concluded that 20-layer model is a worthwhile cost, but that only 200-gridpoints are required for this problem. These values are adopted for this section. Figure 4.5 shows the progression of the dam-break simulation at different times. The concentration profile and velocity profiles are displayed at the four stages. It is interesting to note how the flow develops from its initial position, as can be seen in Figure 4.5. The multilayer formulation used allows for variation in flow velocities and thus the bed-level velocities calculated are more realistic. Figure 4.10 shows the comparison between 1, 5, 10, and 20-layer simulations. It is interesting to note the wide disparities between these simulations. As expected, multiple layers reduce the bottom velocity and lower the quantity of erosion shown. This highlights the importance of selecting the most appropriate number of fluid

Table 4.1: Results for maximum bed depth, maximum bottom layer velocity, total volume of entrained sediment and CPU times for varying numbers of fluid layers and domain discretisations.

No. of layers	No. of gridpoints	Max bed depth $[m]$	Max bed depth x-coordinate $[m]$	Max speed (u_1) $[m/s]$	Volume of sediment $[m^3]$	CPU Time $[s]$
2	50	-0.3132	0.4902	1.084	3.551	1.003
	100	-0.3167	0.2475	1.097	3.660	1.916
	200	-0.3174	0.1244	1.104	3.792	3.762
	400	-0.3172	0.0623	1.110	3.770	9.812
5	50	-0.2402	0.4902	1.020	2.744	1.094
	100	-0.2433	0.2475	1.034	2.797	1.903
	200	-0.2439	0.1244	1.046	2.827	4.921
	400	-0.2435	0.0623	1.071	2.849	11.94
10	50	-0.2009	0.4902	0.9510	2.271	0.873
	100	-0.2033	0.2475	0.9714	2.290	1.894
	200	-0.2038	0.1244	0.9861	2.302	6.546
	400	-0.2036	0.0623	1.036	2.310	14.95
20	50	-0.1900	0.4902	0.9007	1.964	1.037
	100	-0.1892	0.2475	0.9180	1.902	2.579
	200	-0.1877	0.1244	0.9353	1.899	7.231
	400	-0.1881	0.0623	0.9864	1.900	17.15

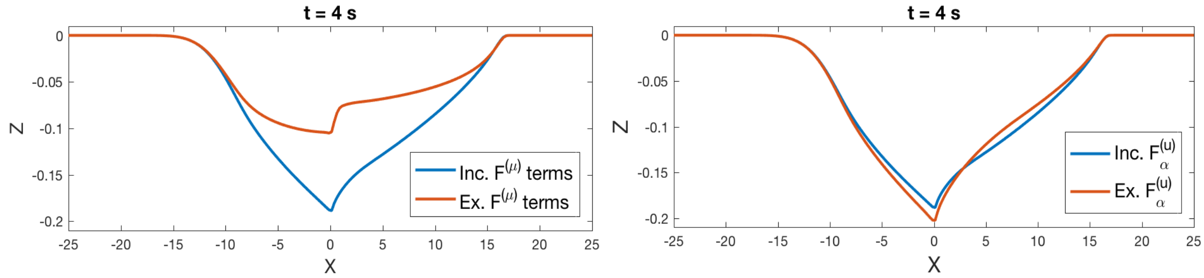

Figure 4.11: Comparison of the effect of inter-layer force terms on a dam-break simulation showing the effects of viscosity (left) and the effects of exchange terms (right).

layers for this type of simulation. Figure 4.10 highlights the advantages of the model presented in (4.2.25).

Figure 4.10 shows the comparison of 20-layer bed profile results, where only bottom layer velocity is used in the calculation of bed flux, and where an average of all the layers is computed. As expected the simulation using the average shows a substantial increase in erosion. This adds to the conclusions that are drawn from Figure 4.10, underlining the importance of choosing the correct bed interface velocities. As shown in the dam-break flows demonstrated here, bottom layer velocities can become greatly stratified. The effects of the exchange terms between the layers are then compared. The exchange terms are shown to have a varied effect on the bottom layer velocities and the morphologic results, as shown in Figure 4.11. This demonstrates the importance of the exchange terms $F_\alpha^{(u)}$ in this sediment transport model. It is interesting to

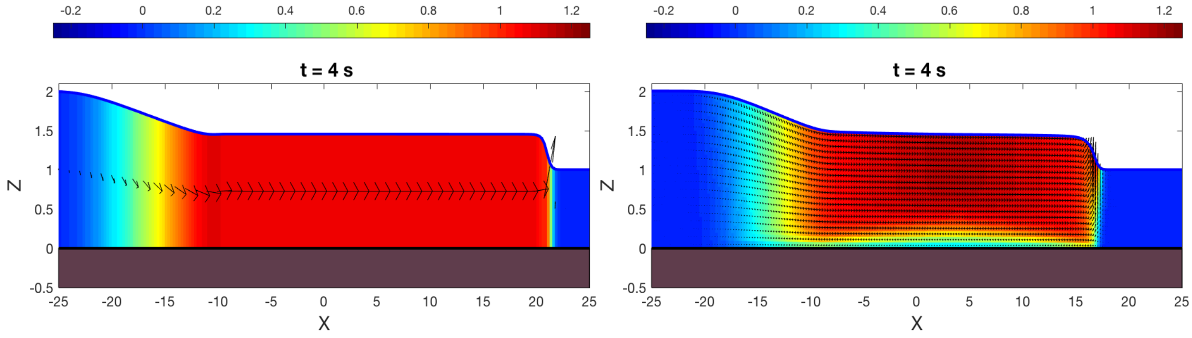

Figure 4.12: Comparison of dam-break simulations on a fixed bed, using a single layer (left) and 20 layers (right).

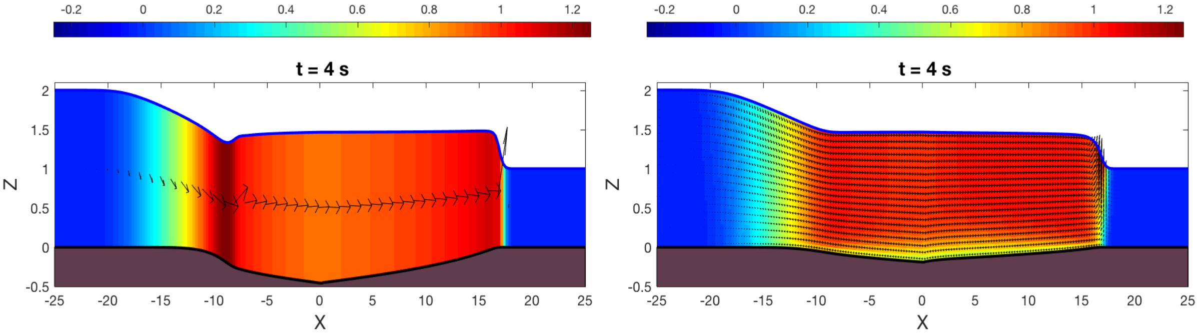

Figure 4.13: Comparison of dam-break simulations on an erodible bed, using a single layer (left) and 20 layers (right).

note the subtle effects of these terms; the viscosity term $F_\alpha^{(\mu)}$ for example greatly increases the bottom velocity, leading to a far greater quantity of erosion, as seen in Figure 4.11. Variations in the exchange terms have a smaller impact; this is due to the effects of slower moving sediment and loss of momentum to other layers, as also shown in Figure 4.11. To underline the advantages of the new model, Figure 4.12 and Figure 4.13 compare the single layer to 20-layer velocity plots on erodible and fixed beds. Figure 4.12 shows the results of fixing the bed in order to isolate the impact of varying erosion rates from the morphological effects of multiple layers. Figure 4.12 and Figure 4.13 clearly show the advantage of the stratified velocities gained using the multilayer system, and demonstrate in detail the effect this has on the bed. Figure 4.12 shows that the multilayer formulation causes a decrease in distance travelled, but a more stratified (in the x-direction) velocity profile. It is further interesting to note that in Figure 4.13 an hydraulic jump is seen in the single layer formulation. Therefore it is assumed that this not an increase in accuracy but a feature of the evolving bed. As can clearly be seen in Figure 4.13, the single layer model noticeably increases the quantity of material scoured away. This is the classic over-prediction of scour seen in a lot of simulations of this type. This run of simulations has clearly shown the advantages and features of the multilayer formulation presented .

4.5.2 Dam-break downstream of an apron problem

The next test is conducted on a dam-break beyond an apron, and is chosen as it is possible to test in the laboratories at Durham University. Details on the experimental method used are given in Section 4.4, and the domain is shown in Figure 4.6. The aim is to assess the ability of the model to capture sediment distribution in both the x and z-dimensions.

The domain size ($0.9\ m$ in length) is selected to enable a high speed, ultra high definition camera to capture the vertical sediment distribution as well as the evolving bed at high speed ($100\ fps$). This small domain provides around $0.4 - 0.5\ s$ of capture-able footage of the dam-break. This is enabled by a high pressure pneumatic linear actuator for the dam-break which achieves a dam-break opening of $0.02\ s$. This is ideal, as the dam-break is modelled to be near instantaneous, and the characteristics of the sediment used (Sand 7) are detailed in Table 3.1. Although arguably the most developed sediment transport tool in OpenFOAM, sedFOAM is not equipped for a free-surface and consequently cannot be used for this domain. Therefore, a dam-break over a fixed bed is considered before sediment is added to the domain. The IcoFOAM solver with the k-ϵ turbulence model disabled is utilized and the simulation parameters are set up as

$$v(0,x,y,z) = 0\ m/s \qquad u(0,x,y,z) = 0\ m/s, \qquad \overline{c}(0,x,y,z) = 0.0001 \qquad B(0,x,y) = 0.005\ m,$$

$$H(0,x,y) = \begin{cases} 0.10\ m, & \text{if } x \ \leq \ 0.33\ m, \\ 0.016\ m, & \text{if } x \ > \ 0.33\ m. \end{cases}$$

The simulation is allowed to run to $t = 0.42\ s$ time and the results are presented in Figure 4.14. As shown in the Figure 4.14, the OpenFOAM solver demonstrates a large degree of wall effect, as well as oscillations downstream of the dam-break. This is likely to be due to its considerations of two-phase flow, which create more turbulence and demonstrate more complex features.

The aim of adding sediment to this domain is to demonstrate the presented method's accuracy in capturing sediment distribution. To this end, the sediment distribution and depth-averaged concentration are captured by considering each frame in both the Hue Saturation and Intensity (HSI) and Red Blue Green (RGB) colour domains. In the HSI domain, it is easy to

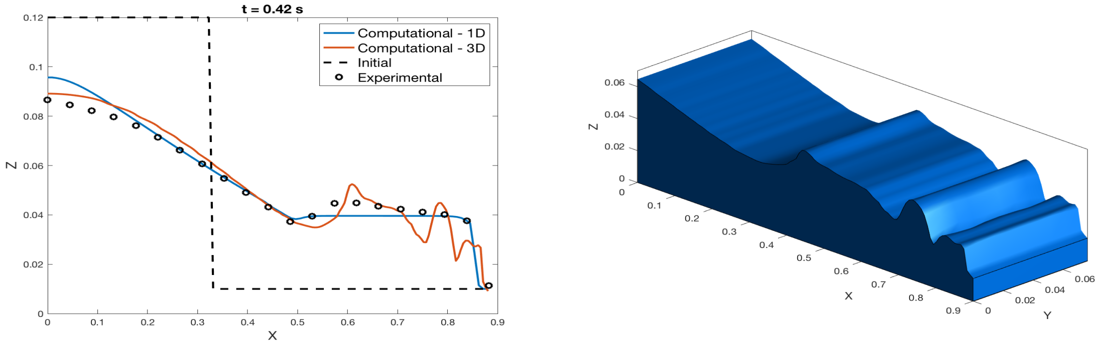

Figure 4.14: Comparison between the OpenFOAM simulation and the presented model (left) and waveform produced by the OpenFOAM simulation (right) at $t = 0.42\ s$.

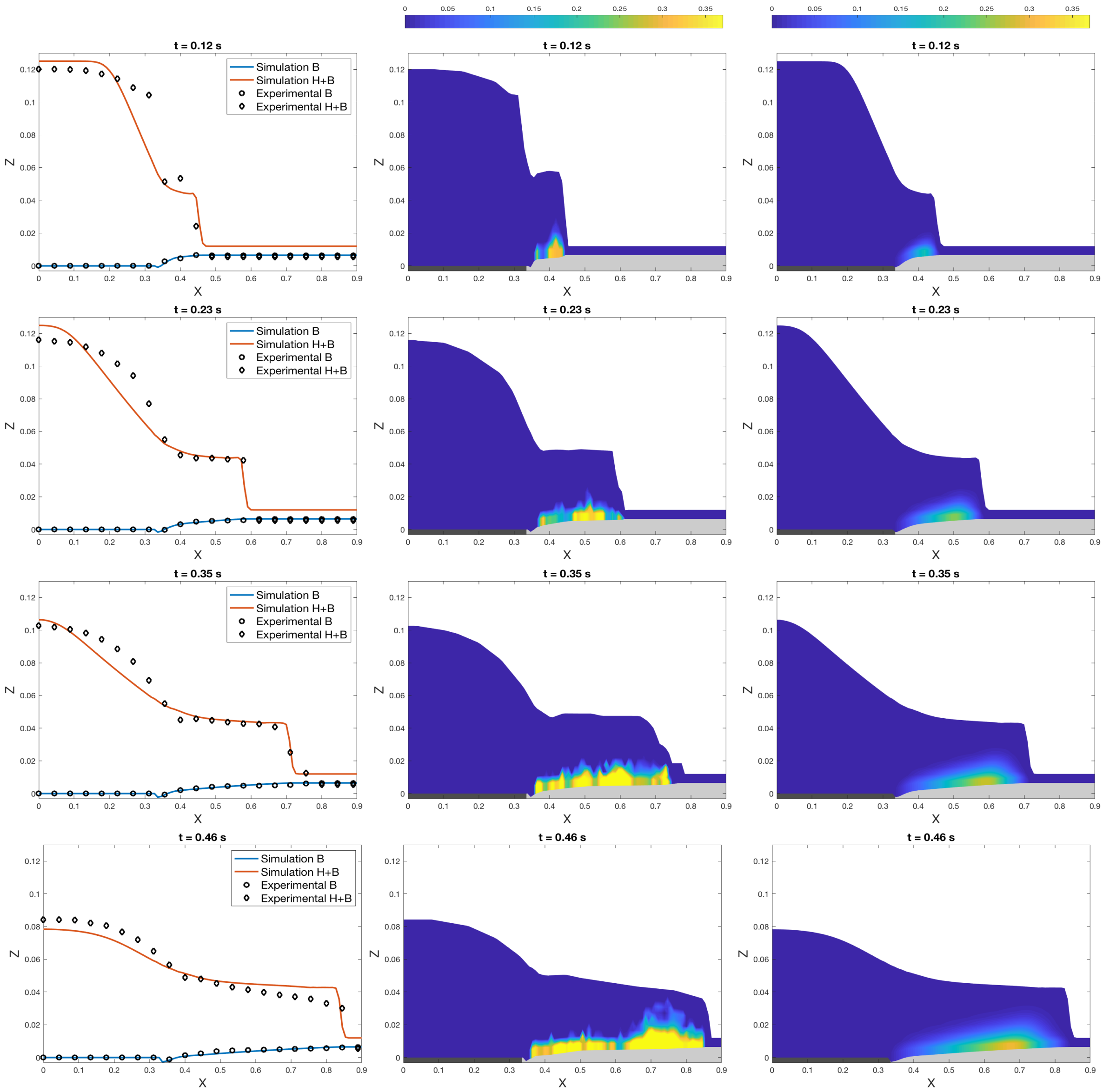

Figure 4.15: Comparison of waveforms (left) and concentrations for the simulation (right) and the experimental data (middle) at $t = 0.12\ s, 0.24\ s, 0.35\ s$ and $0.46\ s$.

Table 4.2: Comparison of errors in H, B, and $\bar{c}$ between 10-layer and 1-layer simulations and the experimental data, for $t = 0.12\ s,\ 0.24\ s,\ 0.35\ s$ and $0.46\ s$.

10-Layer Simulation

	B		H		c	
Time $[s]$	L^∞-error	L^2-error	L^∞-error	L^2-error	L^∞-error	L^2-error
0.12	1.314E-06	1.060E-04	2.081E-03	3.042E-02	1.328E-02	8.885E-02
0.24	4.741E-06	9.660E-04	1.426E-03	1.592E-02	9.626E-02	1.807E-01
0.35	7.854E-06	1.309E-03	9.674E-04	8.287E-03	1.656E-01	2.143E-01
0.46	1.371E-05	2.027E-03	1.077E-03	1.276E-02	5.118E-01	2.234E-01

1-Layer Simulation

	B		H		c	
Time $[s]$	L^∞-error	L^2-error	L^∞-error	L^2-error	L^∞-error	L^2-error
0.12	2.896E-07	6.913E-05	3.278E-02	1.376E-02	8.887E-01	1.798E+00
0.24	4.687E-04	3.157E-05	1.983E-02	1.605E-02	9.225E-01	3.859E+00
0.35	8.699E-04	2.834E-05	1.267E-02	1.807E-02	1.472E+00	9.924E+00
0.46	1.904E-03	5.054E-05	8.043E-03	2.645E-02	1.146E+00	1.651E+01

rid the picture entirely of green pixels, with the result that only the sediment dominated pixels are left. The remaining pixels are considered using the R and B scales from known quantities to deliver the distributions shown in Figure 4.15.

As shown in Figure 4.15, the simulation has slightly more acceleration than the experimental data. At $t = 0.12\ s$ the model does not capture the up motion of the dam being removed, as seen in the small peak at $x = 0.32\ m$. This, along with the complex near wall effects which may be underestimated, results in an over acceleration of flow by the simulation. Beyond this, the progression of the simulated wave-front is accurate and the bed deformation is also reasonable.

Figure 4.15 and Table 4.2 show that the simulation offers a good agreement with the experimental concentration data. These simulations were conducted on a grid of 200×10 control volumes. Here the multilayer simulation is compared to a single-layer simulation, and the results show that the multilayer simulation is more accurate, capturing features not possible with the single-layer simulation. This is because the results for the 10-layer simulations are generally an order of magnitude smaller. This demonstrates that the model is able to account for sediment erosion correctly, in that the L^∞ and L^2 errors in concentration grow only slightly from 0.0133 and 0.5118 to 0.0889 and 0.234. The high level of initial error, when compared to the growth in error over the time period, indicates that the errors are largely caused during the initial $0.12\ s$. Furthermore it is not unreasonable to suppose that some of this error is caused by suction and viscous forces, as the dam-break occurs in those initial $0.018\ s$. Overall, this is seen to be a very positive result for the proposed model, as it (in line with all other models in circulation to the knowledge of the author) does not consider the physical effects of the dam breaking. Also shown

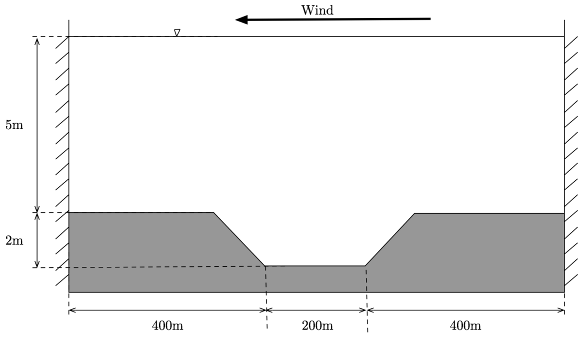

Figure 4.16: Recirculation flow problem over a dyke.

in Table 4.2 the differences in accuracy are small yet noticeable, with the L^2 and L^∞-errors in the bed B rising respectively from 8.747E-06 and 1.581E-03 to 1.371E-05 and 2.027E-03 at $t = 0.46$ s, when turbulence modelling is removed. The current simulation demonstrates the accuracy of the proposed method.

This is the first time, to the knowledge of the author, that sediment distribution has been compared to a simulation in both the vertical and the horizontal planes. There is a relatively low level of error in these simulations, which is encouraging for the model.

4.5.3 Recirculation flow problem over a dyke

As no recirculation problems with erosion and deposition have yet been published, to the best knowledge of the author, a novel situation is developed and designed to show the flexibility and features of the presented formulation. It is not normally possible to simulate this problem with SWEs (or software packages available to this study). Thus unfortunately it is not possible to provide a reference solution. The problem is detailed in Figure 4.16 and bounded in a domain of 1 km created with a 5 m - 7 m depth and 200 m long trench in the middle, the sides of the trench are banked with gradients of 0.02 and -0.02 respectively. A wind speed of 10 m/s is applied to the top of the water. Initially, there is a section of dirty water with a concentration of 0.4 of suspended sediment between 400 $m < x \leq 600$ m and between depths of -2 $m < z \leq 1.5$ m. This uses the same sediment as the bed, with the same characteristics as the previous experiment. The simulation was run with a Cr = 0.5 for 30 000 s. 100 nodes are used along the x-axis of the domain with 10 and 20-layers. The results of the simulations are shown in Figures 4.17 and Figure 4.19. It is interesting to note that two routes of recirculation are developed in this simulation. A dominant inner layer of recirculation occurs, this is likely to be due to the topography which ranges between 300 m and 700 m. This inner recirculation is more graded than the outer, as it is less direct (in terms of inter-layer transfer) due to the boundary conditions. The results also demonstrate the diffusion of the back current, which is equal (in terms of

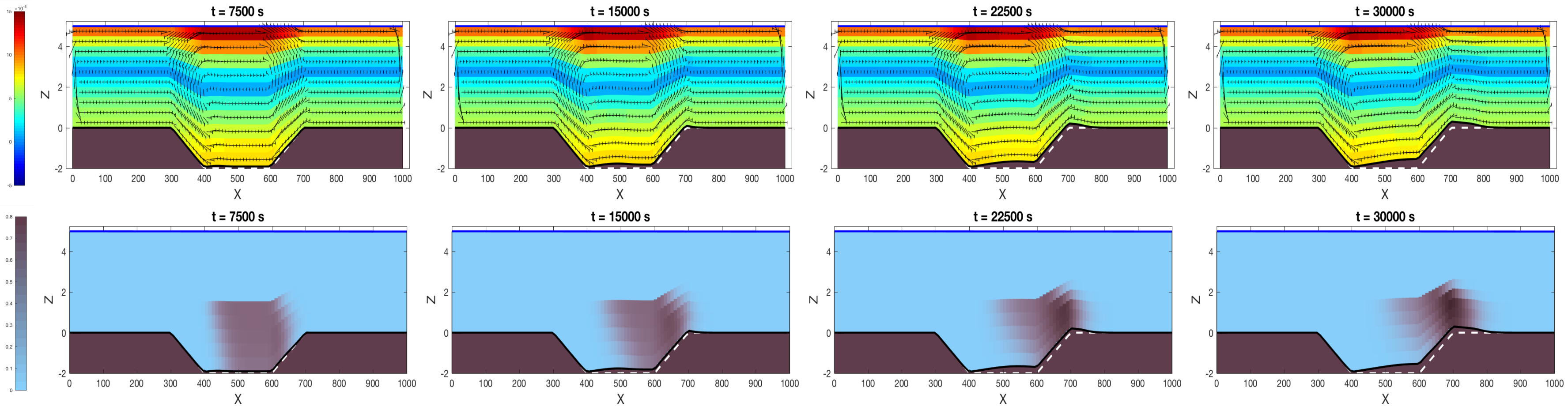

Figure 4.17: Results obtained from a 10-layer recirculation simulation: velocity plots (top) - here colour denotes the velocity magnitude, and concentration plots (bottom) - here colour denotes the sediment concentration.

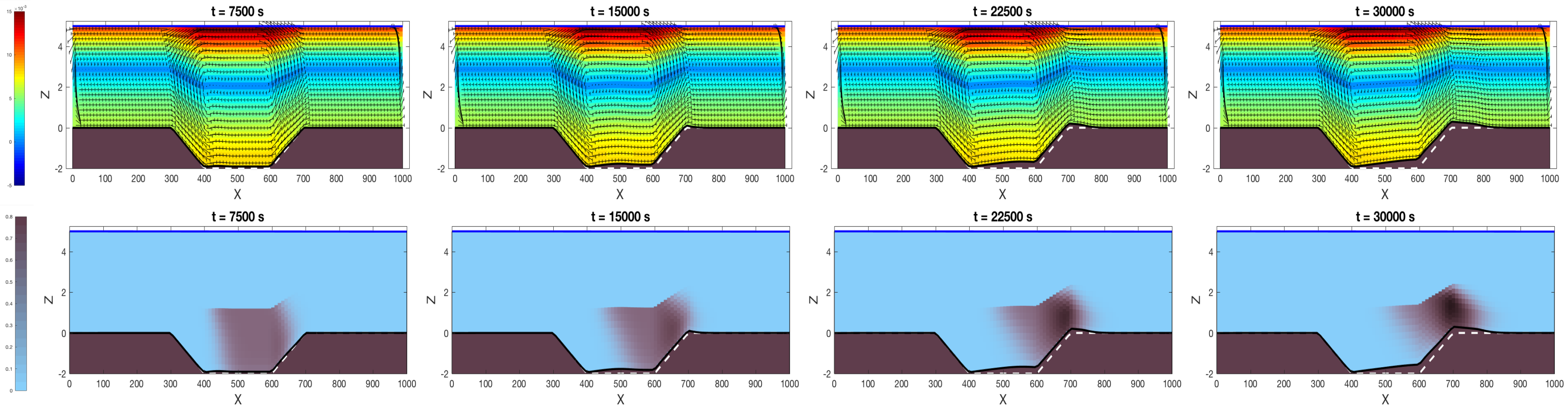

Figure 4.18: Results obtained from a 20-layer recirculation simulation: velocity plots (top) - here colour denotes the velocity magnitude, and concentration plots (bottom) - here colour denotes the sediment concentration.

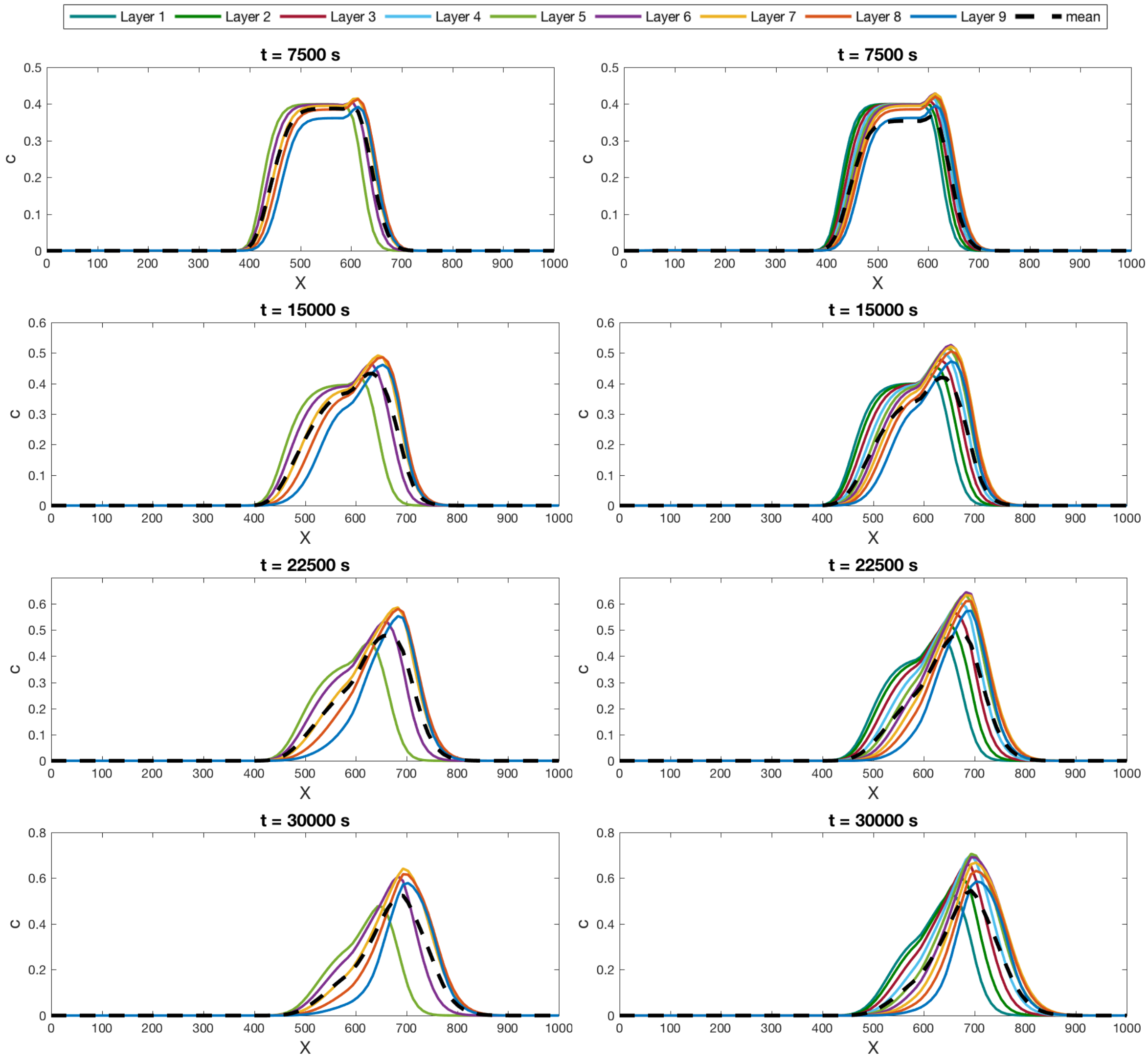

Figure 4.19: Recirculation over a dyke results: a comparison of 10 (left) and 20-layer (right) concentration profiles.

volumetric flow) to the current induced by the wind, though the back current is spread over more layers and therefore is comprised of lower velocities. This example demonstrates a deposition dominant test case, highlighting the ability of the model to handle complex and evolving topography. As shown in Figure 4.19, the inter-layer diffusion term is crucial to this model, as sediment is able to transit between layers and obtain a more natural distribution. The same simulation with 20-layers is run, as shown in Figure 4.18 and Figure 4.19. The differences are subtle beyond the higher resolution: the centre of rotation has migrated deeper in the fluid. No other large advantage is shown, thus it may be concluded that the 10-layer model is acceptable for this simulation.

4.6 Concluding remarks

This chapter presents a novel model that combines a one-dimensional multilayer flow model with sediment transport and bed morphodynamics. The derivation of a multilayer formulation of the shallow water equations is given. The new formulation is modified with the assignment of sediment variables to each layer in the formulation and the inclusion of their effects on the conservation of momentum equation. The model tackles the problem that arises from this formulation, namely the lack of vertical diffusion in the system, and this is overcome with the addition of capacity driven diffusion. This new model formulation is found to offer new insights into existing problems and even the solution of problems that are unsolvable with other shallow water equation formulations. This new model works without incurring large increases in the computational cost.

A novel experimental method is also detailed in this chapter and it is used to gather new experimental data on vertical stratification of suspended sediments. With a high-speed camera and a cellular post-processing method identifying sediment through image intensity and colour, it is possible to capture sediment concentrations in two space dimensions. It's low cost and simplistic nature make this experimental method robust and easily repeatable, and the data it provides is a new tool in the assessment of sediment transport models.

This model relies on a recently created Eulerian-Lagrangian finite volume method. This method uses a splitting approach: followed by a predictor to estimate the flow, and then a corrector stage to reconstruct the numerical fluxes. This method is able to provide stable results for both evolving and steady-state flows. The use of multilayer flow is of particular interest in the dam-break situation, which relies on bed-level velocities to predict erosion. Often other models overestimate these bed level velocities as they rely on a single depth-averaged speed. This is not the case with the presented multilayer model, as it produces a separate speed for the bottom layer. It should be noted that the number of layers used must be appropriately selected to represent a reasonable sediment load. The effects of the exchange terms included in this formulation are also examined. The inter-layer exchange terms are found to have a measurable and large effect on the results gained with this formulation. This demonstrates the huge importance of correct formulation in the model in order to capture the small effects of dividing the fluid column into multiple layers.

The second example presented shows the ability of the model to deal with uneven and developing bathymetry, as the floor of the bed develops under large amounts of deposition. It also demonstrates the ability to track sediment and (as relevant to both this and dam-break experiments) how sediment can move at differing speeds depending on its layer. This is a factor that is not captured by a single-layer formulation. Overall, this novel formulation for multilayer shallow water flows with sediment transport has been developed from the Navier-Stokes equations, and analysed for the new features it contains. It offers a more accurate method of capturing flow velocities while not incurring huge additional computational expense. It has been shown that these stratified vertical velocities offer a substantial advantage when modelling sediment transport.

Chapter 5

Modelling and numerical simulation of shallow water flows over multi-sediment beds in two space dimensions

This chapter extends the work conducted in Chapter 3 into two dimensions and tests the method against some novel and benchmark simulations. The same approach as Chapter 3 is adopted for the treatment of multiple sediment types, both in packed beds and suspended sediment. An interface tracking tool is developed and utilized on various different bed types in order to demonstrate its capabilities. The governing equations consist of the three two-dimensional shallow water equations for flow, a species conservation equation for suspended sediment, a bed Exner-type equation for evolving bathymetry, and empirical equations for sediment erosion and deposition. The Eulerian-Lagrangian finite volume method, detailed in Chapter 4, is extended from one-dimension to two-dimensions to handle the problems posed in this chapter. The aim of this chapter is twofold: Firstly, to develop a model that can handle multiple sediments in both the bed and the flow. Secondly, to implement a method for solving this new model that is both fast and accurate. In the current work, the bed is reformulated as a function of three-dimensional variables and its discretisation is carried out using control volumes. When interacting with the bed, the solver considers each sediment separately so that the entrainment and deposition accurately reflect the sediments being considered. In flow calculations are performed using the average values for the entrained sediment, this means that the equation system is not unnecessarily expanded. This simplicity is combined with a splitting method to ensure second-order accuracy with a fast implementation.

The chapter is organized as follows: Section 5.1 describes the background and gives an overview to the problem. Section 5.2 introduces the two-dimensional governing equations for shallow water flows over multilayer movable sedimentary beds. Modelling mass-exchange terms between multilayer beds is described in Section 5.3. In Section 5.4, the Eulerian-Lagrangian finite volume method is formulated for the numerical solution of the developed system. This includes the reconstruction of the numerical fluxes and the discretisation of source terms. Section 5.5 presents numerical results and examples. The performance of the proposed model for several examples of shallow water flows over multilayer movable beds, together with comparisons to experimental data, are also detailed here. A summary of the chapter is given in Section 5.6.

5.1 Overview of modelling multiple sediments in two space dimensions

Recently attention has turned to both the simulation of sediment transport in rivers [192], and the modelling and numerical simulation of sediment transport in coastal regions have also been subject of research in [27, 104]. Predictions for sediment transport, using the well-established Shallow Water Equations (SWEs) coupled with a species conservation equation and a bed Exner-type equation, have also been investigated in [30, 117, 166], among others. Until recently uncoupled models, for which the hydrodynamics were solved first and then the effects on the bed were calculated, were well established. However, the coupled approaches are more accurate for stronger and higher energy interactions between water flows and sediment transport, such as those in dam-break problems. The main limitation of the models referenced above lies in the number of assumptions needed for their validation, including the levels of armouring, vegetation, composition, and compaction. These assumptions often lead to a large disconnect between measurements and simulations when compared with real-world applications. Recently many corrections have been proposed to improve these problems [47, 196]. Nonetheless, the assumptions on the homogeneous nature of the beds remain a limitation of these models, as naturally deposited soils are mixed and incorporate multiple soil types. Modelling sediment sizes accurately in order to reflect the constituents of both anthropogenic and natural landscapes has been carried out in [3, 196]. Man-made banks, flood, and coastal defences are often layered with finely graded soils deposited on top of each other (due to geotechnical properties, permeability, fertility, cost, and other considerations). This leads to the complex case where the different sediment types have different erosion and deposition rates, creating intricate bed forms. Although the most modern models are able to deal with complex water flows, the area of complex sediments remains relatively unresolved, compare [104, 117]. In the present study, a new coupled model is proposed for two-dimensional (2D) shallow water flows over multilayer erodible beds. It is assumed that the bed is heterogeneous and made up of multiple layers of different sediment properties. The structure of the soil-superposed packed beds and the total number of layers to be considered in the analysis are fixed a priori. To the best knowledge of the author, simulation of 2D shallow water flows over multilayer erodible beds is presented for the first time.

In the current work, the bed is reformulated as a function of three-dimensional (3D) variables and its discretisation is carried out using control volumes. A fill factor is assigned for each control volume, which can be either fully filled by a single-sediment type or partially filled by multiple sediments of different types. The top filled control volume is then treated as the bed floor and surpassed when it is overfilled or totally eroded. At the same time, a margin of empty control volumes is incorporated above the initial active cell to allow for morphological variation. Sediment types and their concentrations are set in suspension by storing individual concentrations for each control volume. Modelling multiple sediment types would normally require reformulating the conventional methods of sediment transport to include more equations for conservation of species. In this study introducing cumulative functions for the sediment concentration, sediment density, porosity, and other sediment variables, mitigates this complication. The resulting system consists of four equations for conservation of mass, momentum and species, as well an Exner-type equation for the bed. For entrainment and erosion, the empirical equations reported in [36] are considered together with modifications to allow for the discretised beds. To improve the accuracy in the erosion and deposition terms, each sediment is evaluated separately when considering bed level flux, and the proportions of sedimentary flux in the shallow water system are updated. The procedure leads to an accurate and fast model for both hydrodynamics and morphodynamics. Furthermore, the proposed model allows for several further functions to be incorporated into the system, including tracking the origin and transport of a particular type of sediment in the water flow. This is particularly useful for dam-break problems involving dangerous or contaminated sediments, such as tailings dam collapses investigated in [125].

Numerical solutions of the sediment transport models often present difficulties due to a combination of their non-linear form, the presence of the source terms, the coupling between the species conservation equation, and the equations governing the water flow [20]. Here, the main difficulty in the proposed model comes from the coupling terms involving derivatives of the unknown physical variables for the bed profile and sediment concentration. Due to the presence of these terms in the governing equations, a numerical method originally designed for solving shallow water flows over single-layer beds will lead to errors when applied separately to each bed layer. In the current work, the Eulerian-Lagrangian Finite Volume (ELFV) method, developed in [23], is implemented to solve the formulated system. The ELFV method avoids the solution of Riemann problems and it can be viewed as a predictor-corrector solver. The predictor step employs the Method of Characteristics (MoC) to reconstruct the numerical fluxes, whilst the

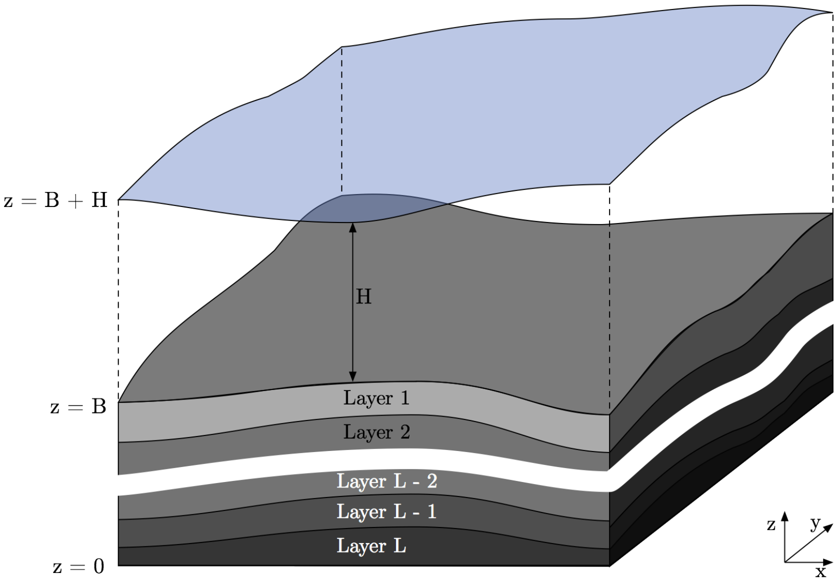

Figure 5.1: A two-dimensional system of a shallow water flow over a multilayered bed.

corrector step recovers the conservation equations in the finite volume framework. The Riemann problem is avoided by projecting the shallow water system in the local coordinates and using the MoC. In the first step, the newly formulated SWE system is integrated over an Eulerian control volume. In the predictor step, a non-conservative formulation of the SWE system is projected and integrated along the characteristic curves formed by the velocity of the flow. These non-conservative solutions are used to reconstruct the fluxes and solve the system integrated in the first step, which completes the corrector stage. The flux gradients and source terms are well-balanced and the method satisfies the C-property [23, 24].

Several numerical examples are presented to verify the ability of the proposed model to solve accurately the 2D shallow water flows over multilayer sedimentary beds. Prior to this, the simulations are compared to experimental data for test examples of dam-break flows over single-layer erodible beds. As no experimental data exists for multi-sediment experiments, new test cases are devised to test the abilities of the method. Four test cases are presented in this chapter: First, a one-dimensional (1D) dam-break problem is used to test for convergence in the discretisation of the flow in 2D and the bed in 3D. Then, a circular dam-break problem in 2D is tested. This is also used to evaluate other solvers and showcase the advantages of the one presented. Next, a large-scale partial dam-break problem is formulated and used to show the effects of sediment bed assumptions. Finally, experimental data from a smaller scale partial dam-break flow problem is used to assess the accuracy of the model and then showcase the effects of small changes in the sedimentary make-up of the bed. All these simulations are designed to assess the ability and illustrate the features of the proposed solver.

5.2 A model for shallow water flow over multi-sediment beds

As in [36], the governing equations used to formulate the model are in conservative form as below

$$
\begin{aligned}
\frac{\partial H}{\partial t}+\frac{\partial (Hu)}{\partial x}+\frac{\partial (Hv)}{\partial y} &= \frac{E-D}{1-\varPsi},\\
\frac{\partial (Hu)}{\partial t}+\frac{\partial}{\partial x}\left(Hu^2+\frac{1}{2}gH^2\right)+\frac{\partial}{\partial y}\Big(Huv\Big) &= -gH\frac{\partial B}{\partial x}-\frac{(\rho_s-\rho_w)gH^2}{2\rho}\frac{\partial c}{\partial x}+K_x,\\
\frac{\partial (Hv)}{\partial t}+\frac{\partial}{\partial x}\Big(Huv\Big)+\frac{\partial}{\partial y}\left(Hv^2+\frac{1}{2}gH^2\right) &= -gH\frac{\partial B}{\partial y}-\frac{(\rho_s-\rho_w)gH^2}{2\rho}\frac{\partial c}{\partial y}+K_y, \qquad (5.2.1)\\
\frac{\partial (Hc)}{\partial t}+\frac{\partial}{\partial x}\Big(Hcu\Big)+\frac{\partial}{\partial y}\Big(Hcv\Big) &= E-D,\\
\frac{\partial B}{\partial t} &= \frac{D-E}{1-\varPsi},
\end{aligned}
$$

where $H(t,x,y)$ is the water depth, $u(t,x,y)$ and $v(t,x,y)$ are the depth-averaged water velocities in the x and y-directions, $B(t,x,y)$ the bottom topography, $c(t,x,y)$ the averaged concentration of the suspended sediment, g the gravitational acceleration, $\varPsi$ the porosity, ρ_w the water density, and ρ_s the sediment density. In (5.2.1) E and D represent the total entrainment and deposition terms, respectively. In (5.2.1), the source terms K_x and K_y account for friction slopes and sediment reaction such that

$$
K_x=-gH\frac{n_m^2u\sqrt{u^2+v^2}}{H^{1/3}}-\frac{(\rho_0-\rho)(E-D)u}{\rho(1-\varPsi)}, \quad K_y=-gH\frac{n_m^2v\sqrt{u^2+v^2}}{H^{1/3}}-\frac{(\rho_0-\rho)(E-D)v}{\rho(1-\varPsi)},
$$

where n_m is the Manning roughness coefficient, $\rho(t,x,y)$ the density of the water-sediment flow, and ρ_0 the density of the saturated bed related to the sediment concentration and porosity by

$$
\rho=\rho_w(1-c)+\rho_s c, \qquad \rho_0=\rho_w\varPsi+\rho_s(1-\varPsi).
$$

It is easy to verify that the system (5.2.1) is hyperbolic with real and distinct eigenvalues, as in [20]

$$
\begin{array}{lllll}
\lambda_1=0, & \lambda_2=u, & \lambda_3=u, & \lambda_4=u-\sqrt{gH}, & \lambda_5=u+\sqrt{gH},\\
\mu_1=0, & \mu_2=v, & \mu_3=v, & \mu_4=v-\sqrt{gH}, & \mu_5=v+\sqrt{gH}.
\end{array} \qquad (5.2.2)
$$

Most of the research on equations (5.2.1) assumes that the suspended sediments and bed are homogeneous. However, for many applications in realistic sediment transport, the topography is formed with multiple soils that are often superposed in layers. The present work focuses on shallow water flows over multilayer beds, as illustrated in Figure 5.1. Thus, the bed topography B in equations (5.2.1) depends also on the vertical direction z, thus $B = B(t, x, y, z)$. Here, a system with multiple species of sediments ($\varrho = 1, 2, \ldots, N$) that can exist in a number of bed layers ($l = 1, 2, \ldots, L$) is considered, where N and L are the total number of sediment species and the total number of layers in the bed, respectively. Notice that two or more layers may contain the same sediment species and a layer may also contain multiple sediment species. In order to extend equations (5.2.1) to model sediment transport with multiple sediment types, the cumulative sediment concentration is used

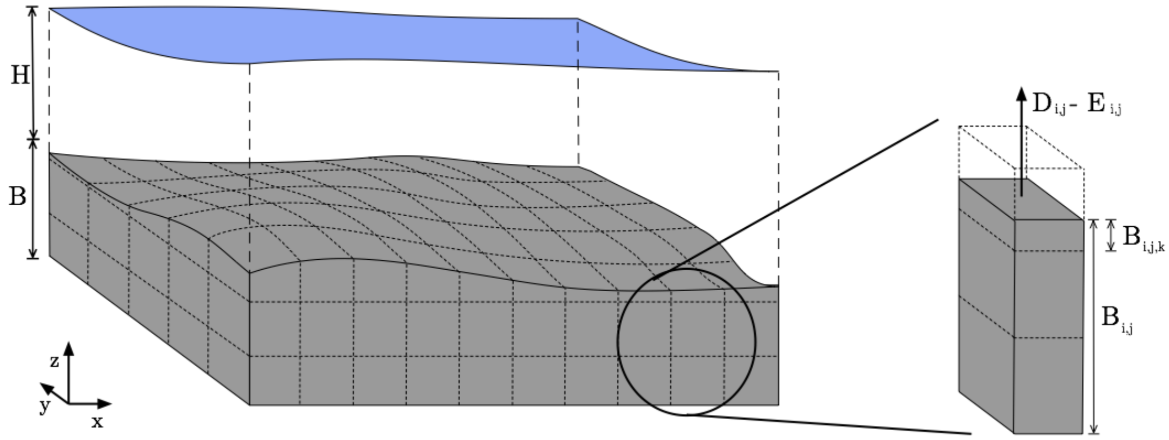

Figure 5.2: Vertical discretisation of a single-layer bed into 3D control volumes.

$$\overline{c} = \sum_{\varrho=1}^{N} c_{\varrho},$$

and the averaged sediment variables are defined as

$$\overline{\rho}_s = \sum_{\varrho=1}^{N} \frac{c_{\varrho}}{\overline{c}} \rho_{s,\varrho}, \qquad \overline{\rho} = \rho_w (1 - \overline{c}) + \sum_{\varrho=1}^{N} \frac{c_{\varrho}}{\overline{c}} \rho_{s,\varrho}, \qquad \overline{D} = \sum_{\varrho=1}^{N} \frac{c_{\varrho}}{\overline{c}} D_{\varrho}.$$

Hence, the bed-dependent variables are calculated using the weighted averaging procedure [177]

$$\overline{n}_m = \sum_{\varrho=1}^{N} \frac{b_{k,\varrho}}{B_k} n_{m,\varrho}, \qquad \overline{\Psi} = \sum_{\varrho=1}^{N} \frac{b_{k,\varrho}}{B_k} \Psi_{\varrho},$$

$$\overline{\rho}_0 = \rho_w (1 - \overline{\Psi}) + \sum_{\varrho=1}^{N} \frac{b_{k,\varrho}}{B_k} \rho_{\varrho} \Psi_{\varrho}, \qquad \overline{E} = \sum_{\varrho=1}^{N} \frac{b_{k,\varrho}}{B_k} E_{\varrho}.$$

Note that each control volume interacts only with its two neighbouring control volumes in the vertical direction. Erosion and deposition only occur in the active top control volume. Hence, the equations considered for modelling shallow water flows over multilayer beds are

$$\begin{aligned}
\frac{\partial H}{\partial t}+\frac{\partial(Hu)}{\partial x}+\frac{\partial(Hv)}{\partial y} &= \frac{\overline{E}-\overline{D}}{1-\overline{\Psi}},\\
\frac{\partial(Hu)}{\partial t}+\frac{\partial}{\partial x}\left(Hu^2+\frac{1}{2}gH^2\right)+\frac{\partial}{\partial y}\Big(Huv\Big) &= -gH\frac{\partial B}{\partial x}-\frac{(\overline{\rho_s}-\rho_w)gH^2}{2\overline{\rho}}\frac{\partial\overline{c}}{\partial x}+\overline{K}_x,\\
\frac{\partial(Hv)}{\partial t}+\frac{\partial}{\partial x}\Big(Huv\Big)+\frac{\partial}{\partial y}\left(Hv^2+\frac{1}{2}gH^2\right) &= -gH\frac{\partial B}{\partial y}-\frac{(\overline{\rho_s}-\rho_w)gH^2}{2\overline{\rho}}\frac{\partial\overline{c}}{\partial y}+\overline{K}_y, \qquad (5.2.3)\\
\frac{\partial(H\overline{c})}{\partial t}+\frac{\partial}{\partial x}\Big(H\overline{c}u\Big)+\frac{\partial}{\partial y}\Big(H\overline{c}v\Big) &= \overline{E}-\overline{D},\\
\frac{\partial B}{\partial t}+\frac{\partial\mathcal{G}(B)}{\partial z} &= \frac{\overline{D}-\overline{E}}{1-\overline{\Psi}},
\end{aligned}$$

where $\mathcal{G}(B)$ is a flux function which depends on the exchange terms between the bed control volumes, as formulated below in section 5.3. In (5.2.3),

$$\begin{aligned}
\overline{K}_x &= -gH\frac{\overline{n}_m^2u\sqrt{u^2+v^2}}{H^{1/3}}-\frac{(\overline{\rho_0}-\overline{\rho})(\overline{E}-\overline{D})u}{\overline{\rho}(1-\overline{\Psi})},\\
\overline{K}_y &= -gH\frac{\overline{n}_m^2v\sqrt{u^2+v^2}}{H^{1/3}}-\frac{(\overline{\rho_0}-\overline{\rho})(\overline{E}-\overline{D})v}{\overline{\rho}(1-\overline{\Psi})}.
\end{aligned}$$

To determine the entrainment and deposition rates, the semi-empirical relations reported in [36] are used

$$D_\varrho = w_{s,\varrho}\left(1-c_{B,\varrho}\right)^2 c_{B,\varrho},$$

where $c_{B,\varrho}$ is a coefficient larger than unity to ensure that the near-bed concentration does not exceed the value of $(1-\bar{\Psi})$. Here, the coefficient $c_{B,\varrho}$ is computed as in [38] by the relation

$$c_{B,\varrho} = \min\left(2,\frac{1-\overline{\Psi}}{c_\varrho}\right).$$

For the entrainment of sediments, the following empirical relation is employed

$$E_\varrho = \begin{cases} \varphi_\varrho\dfrac{\tau_\varrho-\tau_{cr,\varrho}}{H}\sqrt{u^2+v^2}d_\varrho^{-0.2}, & \text{if} \quad \tau_\varrho\geq\tau_{cr,\varrho},\\[2ex] 0, & \text{otherwise.}\end{cases}$$

Note that equations (5.2.3) can also be rewritten in a compact vector form as

$$\frac{\partial\mathbf{W}}{\partial t}+\frac{\partial\mathbf{F}(\mathbf{W})}{\partial x}+\frac{\partial\mathbf{G}(\mathbf{W})}{\partial y} = \mathbf{Q}(\mathbf{W})+\mathbf{R}(\mathbf{W}), \qquad (5.2.4)$$

where

$$\mathbf{W}=\begin{pmatrix} H \\ \\ Hu \\ \\ Hv \\ \\ H\bar{c} \\ \\ B \end{pmatrix}, \quad \mathbf{F}(\mathbf{W})=\begin{pmatrix} Hu \\ \\ Hu^2+\dfrac{1}{2}gH^2 \\ \\ Huv \\ \\ Hu\bar{c} \\ \\ 0 \end{pmatrix}, \quad \mathbf{G}(\mathbf{W})=\begin{pmatrix} Hv \\ \\ Huv \\ \\ Hv^2+\dfrac{1}{2}gH^2 \\ \\ Hv\bar{c} \\ \\ 0 \end{pmatrix},$$

$$\mathbf{Q}(\mathbf{W})=\begin{pmatrix} 0 \\ \\ -gH\dfrac{\partial B}{\partial x}-\dfrac{(\overline{\rho}_s-\overline{\rho}_w)}{2\overline{\rho}}gH^2\dfrac{\partial \bar{c}}{\partial x} \\ \\ -gH\dfrac{\partial B}{\partial y}-\dfrac{(\overline{\rho}_s-\overline{\rho}_w)}{2\overline{\rho}}gH^2\dfrac{\partial \bar{c}}{\partial y} \\ \\ 0 \\ \\ 0 \end{pmatrix}, \quad \mathbf{R}(\mathbf{W})=\begin{pmatrix} \dfrac{\overline{E}-\overline{D}}{1-\overline{\Psi}} \\ \\ \overline{K}_x \\ \\ \overline{K}_y \\ \\ \overline{E}-\overline{D} \\ \\ -\dfrac{\partial \mathcal{G}(B)}{\partial z}-\dfrac{\overline{E}-\overline{D}}{1-\overline{\Psi}} \end{pmatrix}.$$

It should be pointed out that since the flux function added in the bed is only differentiated with respect to z, the hyperbolic parts in the system (5.2.3) are not changed from those appearing in its conventional system (5.2.1). Therefore, the eigenvalues and eigenvectors associated with the system (5.2.4) are also given by the expressions in (5.2.2).

5.3 Exchange terms for multilayered beds

To formulate the exchange terms $\mathcal{G}(B)$ for multilayer beds in (5.2.3), the control volumes $[z_{k+1/2}, z_{k-1/2}]$ shown in Figure 5.2 are used. We begin with the Exner-type bed equation in system (5.2.3). We define the unbounded bed height change as

$$\mathcal{P}_{i,j}^n=\frac{\overline{E}_{i,j}^n-\overline{D}_{i,j}^n}{1-\overline{\Psi}_{i,j}}. \tag{5.3.5}$$

The vertical exchange terms for a homogeneous bed are defined by equation (3.3.9) (on page 66) as

$$\mathcal{G}^n_{k-1/2} = \begin{cases} \dfrac{\Delta z}{\Delta t}\left(B^n_k - \Delta z - \Delta t\dfrac{\overline{E}^n_k - \overline{D}^n_k}{1-\overline{(\Psi)}_k}\right), & \text{if} \quad B^n_k - \Delta t\dfrac{\overline{E}^n_k - \overline{D}^n_k}{1-\overline{(\Psi)}_k} > \Delta z, \\ \dfrac{\Delta z}{\Delta t}\left(-B^n_{k-1} + \Delta t\dfrac{\overline{E}^n_{k-1} - \overline{D}^n_{k-1}}{1-\overline{(\Psi)}_{k-1}}\right), & \text{if} \quad B^n_k - \Delta t\dfrac{\overline{E}^n_{k-1} - \overline{D}^n_{k-1}}{1-\overline{(\Psi)}_{k-1}} < 0, \\ 0, & \text{otherwise.} \end{cases} \tag{5.3.6}$$

The top control volume (or the active cell) is the one in contact with the fluid and is the only one which requires evaluation. In order to calculate the total bed height change we must first consider the separate erosion and deposition processes of each sediment type. This adds a fourth option as armouring must be considered where larger sediments can protect other sediments from erosion in the active cell. Thus, for the heterogeneous bed case there are four possible options:

i) **Volume growth:** erosion and deposition rates in the cell do not exceed the cell bounds. Though there maybe a change in bed height, it is small enough that the active cell does not change.

ii) **Volume depletion:** all the sediment is removed and the cell is entirely eroded. The cell below then becomes the active cell.

iii) **Volume overfill:** the cell is overfilled and the cell above becomes the active cell. During this time-step the original control volume is filled and the one above also starts to fill.

iv) **Volume armouring:** the cell holds out against total erosion. One or more sediment types remain in the active cell protecting the cell beneath it from being eroded.

These four options are shown in Figure 5.3. One of the two crucial aspects of this method is the correct choice of control volume size, as this will affect the bed formations created. One restriction on vertical discretisation is the size of the sediment: the cell must be able to accommodate the largest sediment fraction (often defined as d_{99}), thus

$$\Delta z \geq d_{99}.$$

However, as most sediment is computed with its average sediment particle size d_{50} which is approximately ten times smaller than d_{99} [121], we can use the relation.

$$\Delta z \geq 10 d_{50}. \tag{5.3.7}$$

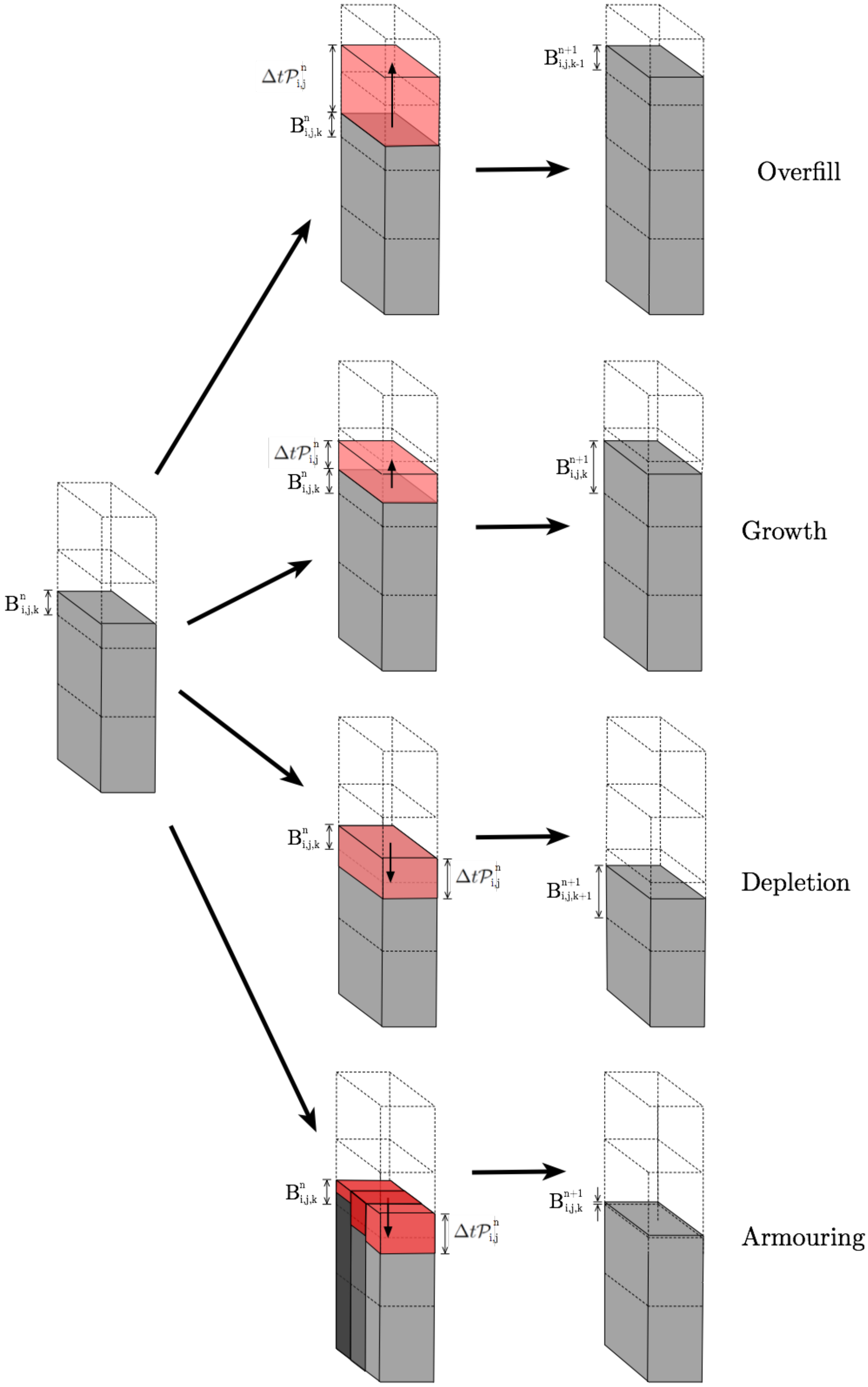

Figure 5.3: Illustration of the different evolutionary options in a control volume for shallow water flows over multilayer beds.

Consequently, the simulation should always be tested for convergence to ensure that the restrictions on discretisation do not affect the accuracy of the simulation. It should be noted that the bed cell height does not have to be uniform, if the situation arises where the bed description would be improved it is easy to implement a variable cell height. The other main consideration is the time-step which should not be restricted unnecessarily but must not allow the solver to skip over bed cells, thus

$$\Delta t < \frac{\Delta z}{\mathcal{P}^n}, \tag{5.3.8}$$

where $\mathcal{P}^n$ is defined in (5.3.5). These two constraints (5.3.7) and (5.3.8) allow for a reasonable Courant-Friedrichs-Lewy (CFL) condition to be chosen and, as beds nearly always develop far slower than fluid surfaces, have a minimal effect on the simulation.

5.4 The 2D Eulerian-Lagrangian finite volume method

To integrate the system (5.2.3), the method utilizes an operator splitting function, similar those used in first-order splitting [149, 172]. The presented method uses second-order splitting, proposed in [217]. To integrate equations (5.2.3) with respect to time, time is divided into subintervals $[t_n, t_{n+1}]$ with length $\Delta t = t_{n+1} - t_n$. The selected splitting method uses the following three stages:

Stage 1: Solve for $\mathbf{W}^*$

$$\begin{aligned} \frac{\partial \mathbf{W}^*}{\partial t} &= \mathbf{R}(\mathbf{W}^*), \qquad t \in [t_n, t_{n+1/2}], \\ \mathbf{W}^*(t_n) &= \mathbf{W}(t_n). \end{aligned} \tag{5.4.9}$$

Stage 2: Solve for $\mathbf{W}^{**}$

$$\begin{aligned} \frac{\partial \mathbf{W}^{**}}{\partial t} + \frac{\partial \mathbf{F}(\mathbf{W}^{**})}{\partial x} + \frac{\partial \mathbf{G}(\mathbf{W}^{**})}{\partial y} &= \mathbf{Q}(\mathbf{W}^{**}), \qquad t \in [t_n, t_{n+1}], \\ \mathbf{W}^{**}(t_n) &= \mathbf{W}^*(t_{n+1/2}). \end{aligned} \tag{5.4.10}$$

Stage 3: Solve for $\mathbf{W}^{***}$

$$\begin{aligned} \frac{\partial \mathbf{W}^{***}}{\partial t} &= \mathbf{R}(\mathbf{W}^{***}), \qquad t \in [t_{n+1/2}, t_{n+1}], \\ \mathbf{W}^{***}(t_{n+1/2}) &= \mathbf{W}^{**}(t_{n+1}). \end{aligned} \tag{5.4.11}$$

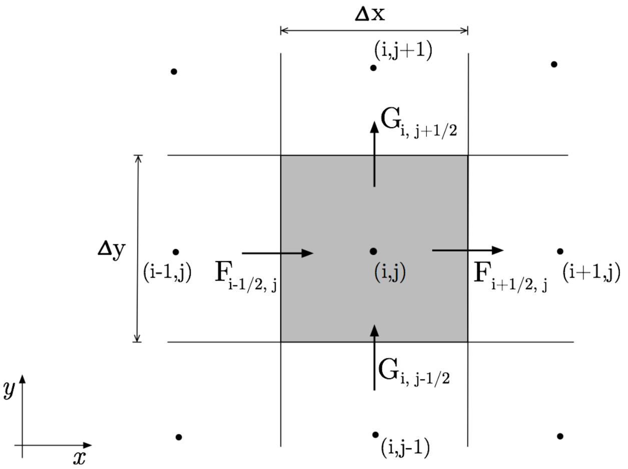

Figure 5.4: Control volume $V_{i,j}$ (shaded) used for the spatial discretisation.

Once a time-stepping scheme has been applied to the three stages above, the time integration of the system is complete. For the first and third steps, an explicit third-order Runge-Kutta method is utilised, as detailed in [161]. Thus time advances from time t_n to t_{n+1} by

$$\begin{aligned}
\mathcal{W}^{(1)} &= \mathbf{W}^n + \Delta t \mathbf{R}(\mathbf{W}^n), \\
\mathcal{W}^{(2)} &= \frac{3}{4}\mathbf{W}^n + \frac{1}{4}\mathcal{W}^{(1)} + \frac{1}{4}\Delta t \mathbf{R}(\mathcal{W}^{(1)}), \\
\mathbf{W}^{n+1} &= \frac{1}{3}\mathbf{W}^n + \frac{2}{3}\mathcal{W}^{(2)} + \frac{2}{3}\Delta t \mathbf{R}(\mathcal{W}^{(2)}).
\end{aligned} \tag{5.4.12}$$

Note the asterisks have been removed for ease of notation. Unfortunately, especially in complex flow situations, the solutions of the eigenvalues are non-trivial and can yield complex solutions. The model can therefore quickly lose the hyperbolic property and may yield Kelvin-Helmholtz instabilities. Consequently, a ELFV method is utilised that does not require the calculation of the eigenvalues.

5.4.1 The Eulerian step

The spatial domain is divided into control volumes $[x_{i-\frac{1}{2}}, x_{i+\frac{1}{2}}] \times [y_{j-\frac{1}{2}}, y_{j+\frac{1}{2}}]$ as shown in Figure 5.4. As detailed, the volumes are centred at (x_i, y_j) with uniform sizes Δx and Δy. The following notations are used

$$\mathbf{W}_{i\pm\frac{1}{2},j}(t) = \mathbf{W}(t, x_{i\pm\frac{1}{2}}, y_j), \qquad \mathbf{W}_{i,j\pm\frac{1}{2}}(t) = \mathbf{W}(t, x_i, y_{j\pm\frac{1}{2}}),$$

$$\text{and } \mathbf{W}_{i,j}(t) = \frac{1}{\Delta x}\frac{1}{\Delta y}\int_{x_{i-\frac{1}{2}}}^{x_{i+\frac{1}{2}}}\int_{y_{j-\frac{1}{2}}}^{y_{i+\frac{1}{2}}} \mathbf{W}(t, x, y)\, dydx, \tag{5.4.13}$$

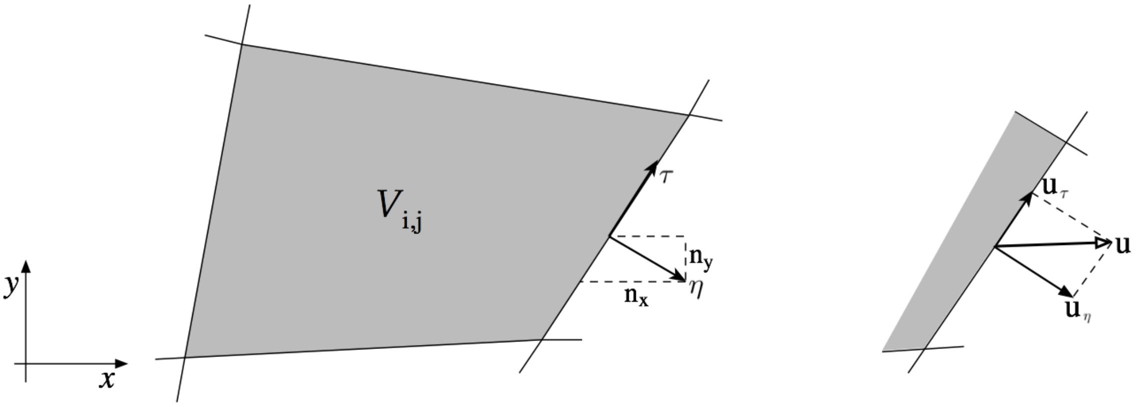

Figure 5.5: The projected velocities on the control volume $V_{i,j}$.

to denote the point-values and cell-average of the variable $\mathbf{W}$ at the gridpoint $(t, x_{i\pm\frac{1}{2}}, y_j)$, $(t, x_i, y_{j\pm\frac{1}{2}})$, and (t, x_i, y_j), respectively. By integrating equation (5.4.10) in space over the control volume $V_{i,j}$, as shown in Figure 5.4, the following semi-discrete equations are obtained

$$\frac{d\mathbf{W}_{i,j}}{dt} + \frac{\mathbf{F}_{i+1/2,j} - \mathbf{F}_{i-1/2,j}}{\Delta x} + \frac{\mathbf{G}_{i,j+1/2} - \mathbf{G}_{i,j-1/2}}{\Delta y} = \mathbf{Q}_{i,j},$$

where $\mathbf{F}_{i\pm1/2,j} = \mathbf{F}(\mathbf{W}_{i\pm1/2,j})$ and $\mathbf{G}_{i,j\pm1/2} = \mathbf{G}(\mathbf{W}_{i,j\pm1/2})$ are the numerical fluxes at the cell interfaces $(x_{i\pm1/2}, y_j$ and $(x_i, y_{i\pm1/2})$. By using divergence theorem to integrate (5.2.1) over the control volume V_{ij}we obtain

$$\begin{aligned}
\frac{\partial}{\partial t}\int_{V_{i,j}} H \; dV + \oint_{S_{i,j}} (Hu\mathbf{n}_x + Hv\mathbf{n}_y) \; d\sigma &= 0, \\
\frac{\partial}{\partial t}\int_{V_{i,j}} Hu \; dV + \oint_{S_{i,j}} \left(\left(Hu^2 + \frac{1}{2}gH^2\right)\mathbf{n}_x + Huv\mathbf{n}_y\right) d\sigma &= -gH\oint_{S_{i,j}} B\mathbf{n}_x \; d\sigma - \\
&\quad \oint_{S_{i,j}} \frac{(\bar{\rho}_s - \bar{\rho}_w)gh^2}{2\bar{\rho}}\bar{c}\mathbf{n}_x \; d\sigma, \\
\frac{\partial}{\partial t}\int_{V_{i,j}} Hv \; dV + \oint_{S_{i,j}} \left(\left(Hv^2 + \frac{1}{2}gH^2\right)\mathbf{n}_y + Huv\mathbf{n}_x\right) d\sigma &= -gH\oint_{S_{i,j}} B\mathbf{n}_y \; d\sigma - \\
&\quad \oint_{S_{i,j}} \frac{(\bar{\rho}_s - \bar{\rho}_w)gH^2}{2\bar{\rho}}\bar{c}\mathbf{n}_y \; d\sigma, \\
\frac{\partial}{\partial t}\int_{V_{i,j}} H\bar{c} \; dV + \oint_{S_{i,j}} (Hu\bar{c}\mathbf{n}_x + Hv\bar{c}\mathbf{n}_y) \; d\sigma &= 0, \\
\frac{\partial}{\partial t}\int_{V_{i,j}} B \; dV &= 0,
\end{aligned}$$

where $\boldsymbol{\eta} = (\mathbf{n}_x, \mathbf{n}_y)^T$ denotes the unit outward normal to the surface $S_{i,j}$ of the control volume V_{ij}. Using the local cell outward normal $\boldsymbol{\eta}$ and tangential $\boldsymbol{\tau} = \boldsymbol{\eta}^\perp$ depicted in Figure 5.5, the above equations can be projected as

$$\frac{\partial}{\partial t}\int_{V_{i,j}} H\ dV + \oint_{S_{i,j}} (H u_{\boldsymbol{\eta}})\ d\sigma = 0, \tag{5.4.14a}$$

$$\begin{aligned}\frac{\partial}{\partial t}\int_{V_{i,j}} Hu\ dV + \oint_{S_{i,j}} \left(Huu_{\boldsymbol{\eta}} + \frac{1}{2}gH^2\mathbf{n}_x\right) d\sigma &= -gH\oint_{S_{i,j}} B\mathbf{n}_x\ d\sigma - \\ &\quad \oint_{S_{i,j}} \frac{(\bar{\rho}_s - \bar{\rho}_w)gh^2}{2\bar{\rho}}\bar{c}\ d\sigma,\end{aligned} \tag{5.4.14b}$$

$$\begin{aligned}\frac{\partial}{\partial t}\int_{V_{i,j}} Hv\ dV + \oint_{S_{i,j}} \left(Hvu_{\boldsymbol{\eta}} + \frac{1}{2}gH^2\mathbf{n}_y\right) d\sigma &= -gH\oint_{S_{i,j}} B\mathbf{n}_y\ d\sigma - \\ &\quad \oint_{S_{i,j}} \frac{(\bar{\rho}_s - \bar{\rho}_w)gH^2}{2\bar{\rho}}\bar{c}\ d\sigma,\end{aligned} \tag{5.4.14c}$$

$$\frac{\partial}{\partial t}\int_{V_{i,j}} H\bar{c}\ dV + \oint_{S_{i,j}} (Hu_{\boldsymbol{\eta}}\bar{c})\ d\sigma = 0, \tag{5.4.14d}$$

$$\frac{\partial}{\partial t}\int_{V_{i,j}} B\ dV = 0, \tag{5.4.14e}$$

where the normal projected velocity $u_{\boldsymbol{\eta}} = u\mathbf{n}_x + v\mathbf{n}_y$ and the tangential projected velocity $u_{\boldsymbol{\tau}} = v\mathbf{n}_x - u\mathbf{n}_y$. In order to simplify the system (5.4.14), first equation (5.4.14b) multiplied by $\mathbf{n}_x$ is summed to the equation (5.4.14c) multiplied by $\mathbf{n}_y$, then equation (5.4.14b) multiplied by $\mathbf{n}_y$ is subtracted from the equation (5.4.14c) multiplied by $\mathbf{n}_x$. These operations result in

$$\begin{aligned}
\frac{\partial}{\partial t}\int_{V_{i,j}} H\ dV + \oint_{S_{i,j}} (Hu_{\boldsymbol{\eta}})\ d\sigma &= 0, \\
\frac{\partial}{\partial t}\int_{V_{i,j}} Hu_{\boldsymbol{\eta}}\ dV + \oint_{S_{i,j}} \left(Hu_{\boldsymbol{\eta}}u_{\boldsymbol{\eta}} + gH^2\mathbf{n}_{\boldsymbol{\eta}}\right)\ d\sigma &= -gH\oint_{S_{i,j}} \left(B\mathbf{n}_{\boldsymbol{\eta}} + \frac{(\bar{\rho}_s - \bar{\rho}_w)H}{2\bar{\rho}}\bar{c}\mathbf{n}_{\boldsymbol{\eta}}\right) d\sigma, \\
\frac{\partial}{\partial t}\int_{V_{i,j}} Hu_{\boldsymbol{\tau}}\ dV + \oint_{S_{i,j}} (Hu_{\boldsymbol{\eta}}u_{\boldsymbol{\tau}})\ d\sigma &= 0, \\
\frac{\partial}{\partial t}\int_{V_{i,j}} H\bar{c}\ dV + \oint_{S_{i,j}} (Hu_{\boldsymbol{\eta}}\bar{c})\ d\sigma &= 0, \\
\frac{\partial}{\partial t}\int_{V_{i,j}} B\ dV &= 0.
\end{aligned}$$

This system can be rewritten in a differential form as

$$\begin{aligned}
\frac{\partial H}{\partial t} + u_{\boldsymbol{\eta}}\frac{\partial H}{\partial \boldsymbol{\eta}} + H\frac{\partial u_{\boldsymbol{\eta}}}{\partial \boldsymbol{\eta}} &= 0, \\
\frac{\partial u_{\boldsymbol{\eta}}}{\partial t} + u_{\boldsymbol{\eta}}\frac{\partial u_{\boldsymbol{\eta}}}{\partial \boldsymbol{\eta}} + g\frac{\partial H}{\partial \boldsymbol{\eta}} &= -g\frac{\partial B}{\partial \boldsymbol{\eta}} - \frac{(\bar{\rho}_s - \bar{\rho}_w)gH}{2\bar{\rho}}\frac{\partial \bar{c}}{\partial \boldsymbol{\eta}}, \\
\frac{\partial u_{\boldsymbol{\tau}}}{\partial t} + u_{\boldsymbol{\eta}}\frac{\partial u_{\boldsymbol{\tau}}}{\partial \boldsymbol{\eta}} + u_{\boldsymbol{\tau}}\frac{\partial u_{\boldsymbol{\eta}}}{\partial \boldsymbol{\eta}} &= 0, \\
\frac{\partial \bar{c}}{\partial t} + u_{\boldsymbol{\eta}}\frac{\partial \bar{c}}{\partial \boldsymbol{\eta}} + \bar{c}\frac{\partial u_{\boldsymbol{\eta}}a}{\partial \boldsymbol{\eta}} &= 0,
\end{aligned}$$

and at this stage the bed Exner-type equation is neglected as it has no further bearing on the system. The system can also be reformulated in a non-conservative form as

$$\begin{aligned} \frac{DH}{Dt} + H\frac{\partial u_{\boldsymbol{\eta}}}{\partial \boldsymbol{\eta}} &= 0, \\ \frac{Du_{\boldsymbol{\eta}}}{Dt} + g\frac{\partial H}{\partial \boldsymbol{\eta}} &= -g\frac{\partial B}{\partial \boldsymbol{\eta}} - \frac{(\bar{\rho}_s - \bar{\rho}_w)gH}{2\bar{\rho}}\frac{\partial \bar{c}}{\partial \boldsymbol{\eta}}, \\ \frac{Du_{\boldsymbol{\tau}}}{Dt} + u_{\boldsymbol{\tau}}\frac{\partial u_{\boldsymbol{\eta}}}{\partial \boldsymbol{\eta}} &= 0, \\ \frac{D\bar{c}}{Dt} + \bar{c}\frac{\partial u_{\boldsymbol{\eta}}}{\partial \boldsymbol{\eta}} &= 0, \end{aligned} \tag{5.4.15}$$

where $\frac{D}{Dt}$ is the total material derivative defined as

$$\frac{D}{Dt} = \frac{\partial}{\partial t} + u_{\boldsymbol{\eta}}\frac{\partial}{\partial \boldsymbol{\eta}}.$$

System (5.4.15) can also be written as

$$\frac{D\mathbf{U}}{Dt} = \mathbf{S}(\mathbf{U}), \tag{5.4.16}$$

where

$$\mathbf{U} = \begin{pmatrix} H \\ u_{\boldsymbol{\eta}} \\ u_{\boldsymbol{\tau}} \\ \bar{c} \end{pmatrix}, \qquad \mathbf{S}(\mathbf{U}) = \begin{pmatrix} -H\frac{\partial u_{\boldsymbol{\eta}}}{\partial \boldsymbol{\eta}} \\ -g\frac{\partial H}{\partial \boldsymbol{\eta}} - g\frac{\partial B}{\partial \boldsymbol{\eta}} - \frac{(\bar{\rho}_s - \bar{\rho}_w)gH}{2\bar{\rho}}\frac{\partial \bar{c}}{\partial \boldsymbol{\eta}} \\ -u_{\boldsymbol{\tau}}\frac{\partial u_{\boldsymbol{\eta}}}{\partial \boldsymbol{\eta}} \\ -\bar{c}\frac{\partial u_{\boldsymbol{\eta}}}{\partial \boldsymbol{\eta}} \end{pmatrix}.$$

Note that the projection technique simplifies the 2D SWEs in (5.4.10) to the solution of an equivalent 1D system on each surface of the control volume $V_{i,j}$. A comparable procedure has been proposed by [24]. Note that the projected system implemented is only used to reconstruct the fluxes for the conservative ELFV method solution.

5.4.2 The Lagrangian step

As detailed in Chapter 4, the modified MoC is applied to the projected system in order to solve for the numerical fluxes $\mathbf{F}_{i\pm1/2,j}$ and $\mathbf{G}_{i,j\pm1/2}$. A regular grid is imposed at the next time-step and the flow trajectories are backtracked to the previous time levels, as with [144, 157]. The

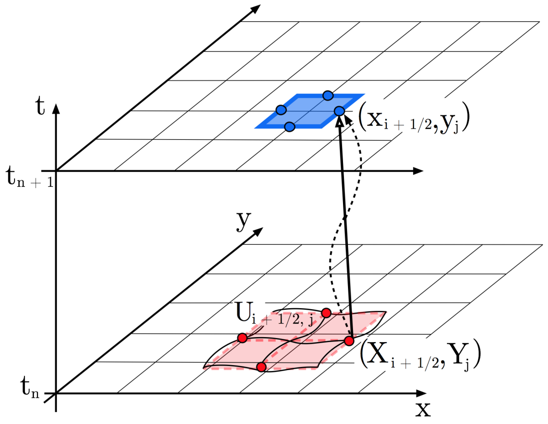

Figure 5.6: A sketch of the method of characteristics used to trace a water particle at gridpoint $(x_{i+1/2}, y_j)$ back through the time-step to $(X_{i+1/2}, Y_j)$, so that the intermediate solution $\widehat{\mathbf{U}}^n_{i+1/2,j}$ can be interpolated.

solutions for the characteristic foot are calculated using interpolation from the known grid at the prior time-step. Thus a solution can be found at gridpoint $(x_{i+1/2}, y_j)$: the characteristic curves $X_{i+1/2,j}(s)$ associated with the equations (5.4.15) are produced by solving the initial-value problems

$$\begin{aligned} \frac{dX_{i+1/2,j}(s)}{ds} &= u_{\boldsymbol{\eta}}\Big(s, X_{i+1/2,j}(s)\Big), \qquad s \in [t_n, t_{n+1}], \\ X_{i+1/2,j}(t_{n+1}) &= x_{i+1/2}, \end{aligned} \tag{5.4.17}$$

with equivalent initial-value problems for the characteristic curves $Y_{i,j+1/2}(s)$ related to the gridpoint $y_{i,j+1/2}$

$$\begin{aligned} \frac{dY_{i,j+1/2}(s)}{ds} &= u_{\boldsymbol{\eta}}\Big(s, Y_{i,j+1/2}(s)\Big), \qquad s \in [t_n, t_{n+1}], \\ Y_{i,j+1/2}(t_{n+1}) &= y_{j+1/2}. \end{aligned} \tag{5.4.18}$$

The curves are calculated by considering a particle travelling along them from one time-step to another. Therefore $(X_{i,i+1/2}(s), Y_j)$ and $(X_i, Y_{i,j+1/2}(s))$ are the departure points at time s of a particle that will arrive in the time t_{n+1}, at the gridpoints $(x_{i+1/2}, y_j)$ and $(x_i, y_{j+1/2})$ respectively, as shown in Figure 5.6. In the simulations, the third-order Runge-Kutta method (5.4.12) is used for the solution of the initial value problems (5.4.17) and (5.4.18). As the characteristic curves $X_{i+1/2,j}(t_n)$ and $Y_{i,j+1/2}(t_n)$ have no relation to the known grid at time s, once the departure points are known, the intermediate solutions $\mathbf{W}^n_{i+1/2,j}$ and $\mathbf{W}^n_{i,j+1/2}$ of a function $\mathbf{W}$ are reconstructed using

$$\mathbf{W}^n_{i+1/2,j} = \widehat{\mathbf{W}}^n_{i+1/2,j}, \qquad \mathbf{W}^n_{i,j+1/2} = \widehat{\mathbf{W}}^n_{i,j+1/2}, \tag{5.4.19}$$

where $\widehat{\mathbf{W}}^n_{i+1/2,j} = \mathbf{W}\left(t_n, X_{i+1/2,j}(t_n), Y_j\right)$ and $\widehat{\mathbf{W}}^n_{i,j+1/2} = \mathbf{W}\left(t_n, X_i, Y_{i,j+1/2}(t_n)\right)$ are the solutions at the departure points obtained by interpolation from the gridpoints of the control volume, see Figure 5.6. For example, a Lagrange-based interpolation polynomial can be formulated as

$$\widehat{\mathbf{W}}^n_{i+1/2,j} = \sum_{k,l} \mathcal{L}_{k,l}\left(X_{i+1/2,j}, Y_j\right) \mathbf{W}^n_{k,l}, \qquad \widehat{\mathbf{W}}^n_{i,j+1/2} = \sum_{k,l} \mathcal{L}_{k,l}\left(X_i, Y_{i,j+1/2}\right) \mathbf{W}^n_{k,l}, \tag{5.4.20}$$

with $\mathcal{L}_{k,l}$, that are Lagrange polynomials, defined as

$$\mathcal{L}_{k,l}(x,y) = \prod_{\substack{p=0\\ p\neq k}} \prod_{\substack{q=0\\ q\neq l}} \frac{x - x_p}{x_k - x_p} \frac{y - y_q}{y_l - y_q}.$$

Other high-order interpolation methods can also be used in (5.4.20). Assuming that the departure points $(X_{i+1/2}, Y_j)$ and $(Y_i, Y_{i,j+1/2})$ at time t_n are accurately approximated, the predictor stage in the Eulerian-Lagrangian method applied to the SWEs is defined by the solution of the system (5.4.16) as

$$\mathbf{U}^n_{i+1/2,j} = \widehat{\mathbf{U}}^n_{i+1/2,j} + \Delta t \mathbf{S}\left(\widehat{\mathbf{U}}^n_{i+1/2,j}\right). \tag{5.4.21}$$

Through a difference discretisation of the source terms of equations (5.4.21) we gain

$$\begin{aligned}
H^n_{i+1/2,j} &= \widehat{H}^n_{i+1/2,j} - \frac{\Delta t}{\Delta x} \widehat{H}^n_{i+1/2,j}\left((u_{\boldsymbol{\eta}})^n_{i+1,j} - (u_{\boldsymbol{\eta}})^n_{i,j}\right),\\
(u_{\boldsymbol{\eta}})^n_{i+1/2,j} &= (\widehat{u}_{\boldsymbol{\eta}})^n_{i+1/2,j} - g\frac{\Delta t}{\Delta x}\Big((H+B)^n_{i+1,j} - (H+B)^n_{i,j} + \\
&\qquad \frac{(\bar{\rho}_s - \bar{\rho}_w)}{2\bar{\rho}} \widehat{H}^n_{i+1/2,j}\left(\bar{c}^n_{i+1,j} - \bar{c}^n_{i,j}\right)\Big),\\
(u_{\boldsymbol{\tau}})^n_{i+1/2,j} &= (\widehat{u}_{\boldsymbol{\tau}})^n_{i+1/2,j} - \frac{\Delta t}{\Delta x}(\widehat{u}_{\boldsymbol{\tau}})^n_{i+1/2,j}\left((u_{\boldsymbol{\tau}})^n_{i+1,j} - (u_{\boldsymbol{\tau}})^n_{i,j}\right),\\
\bar{c}^n_{i+1/2,j} &= \widehat{\bar{c}}^n_{i+1/2,j} - \frac{\Delta t}{\Delta x}\widehat{\bar{c}}^n_{i+1/2,j}\left((u_{\boldsymbol{\eta}})^n_{i+1,j} - (u_{\boldsymbol{\eta}})^n_{i,j}\right),
\end{aligned}$$

where

$$\widehat{H}^n_{i+1/2,j} = H\left(t_n, X_{i+1/2}(t_n), y_j\right), \qquad (\widehat{u}_{\boldsymbol{\eta}})^n_{i+1/2,j} = u_{\boldsymbol{\eta}}\left(t_n, X_{i+1/2}(t_n), y_j\right),$$

$$(\widehat{u}_{\boldsymbol{\tau}})^n_{i+1/2,j} = u_{\boldsymbol{\tau}}\left(t_n, X_{i+1/2}(t_n), y_j\right), \qquad \widehat{\bar{c}}^n_{i+1/2,j} = \bar{c}\left(t_n, X_{i+1/2}(t_n), y_j\right).$$

The intermediate states in the y-direction $H^n_{i,j+1/2}$, $(u_{\boldsymbol{\eta}})^n_{i,j+1/2}$, and $(u_{\boldsymbol{\tau}})^n_{i,j+1/2}$ are calculated in the same way. When the projected states calculations are complete, the states $\mathbf{W}^n_{i\pm1/2,j}$ and $\mathbf{W}^n_{i,j\pm1/2}$ are determined by using $v = (u_{\boldsymbol{\tau}}, u_{\boldsymbol{\eta}}) \cdot \boldsymbol{\eta}$ and $u = (u_{\boldsymbol{\tau}}, u_{\boldsymbol{\eta}}) \cdot \boldsymbol{\tau}$. Using the concept of C-property, the discretisation of the source terms $\mathbf{Q}_{i,j}$ is carried so that the discretised source terms are well-balanced with the discretised flux gradients, for further explanation see [23]. A numerical scheme is said to satisfy the C-property for the equations (5.4.10) if the condition

$$B^n = B^{(0)}, \qquad H^n + B^n = cte_1, \qquad u^n = v^n = 0, \qquad \bar{E} = \bar{D} = 0, \qquad \bar{\rho} = cte_2, \tag{5.4.22}$$

is correct for flows at rest, and cte_1 and cte_2 are constants. Thus, the source terms are reconstructed such that the condition (5.4.22) is preserved. The predictor stage (5.4.16) provides the following useful relations at the interface $(x_{i\pm1/2,j}, y_j)$

$$H^n_{i+1/2,j} = \frac{H^n_{i,j} + H^n_{i+1,j}}{2}, \qquad \bar{c}^n_{i+1/2,j} = \frac{\bar{c}^n_{i,j} + \bar{c}^n_{i+1,j}}{2}. \tag{5.4.23}$$

By considering a flow at rest, the system (5.2.3) becomes

$$\frac{\partial}{\partial t}\begin{pmatrix} H \\ 0 \\ 0 \\ H\bar{c} \\ B \end{pmatrix} + \frac{\partial}{\partial x}\begin{pmatrix} 0 \\ \frac{1}{2}gH^2 \\ 0 \\ 0 \\ 0 \end{pmatrix} + \frac{\partial}{\partial x}\begin{pmatrix} 0 \\ 0 \\ \frac{1}{2}gH^2 \\ 0 \\ 0 \end{pmatrix} = \begin{pmatrix} 0 \\ -gH\dfrac{\partial B}{\partial x} \\ -gH\dfrac{\partial B}{\partial y} \\ 0 \\ 0 \end{pmatrix}.$$

Thus, the corrector stage reduces to

$$\begin{aligned} H^{n+1}_{i,j} &= H^n_{i,j}, \\ \frac{1}{2}g\frac{\Delta t}{\Delta x}\left(\left(H^n_{i+1/2,j}\right)^2 - \left(H^n_{i-1/2,j}\right)^2\right) &= \Delta t g\left(H\frac{\partial B}{\partial x}\right)^n_{i,j}, \\ \frac{1}{2}g\frac{\Delta t}{\Delta y}\left(\left(H^n_{i,j+1/2}\right)^2 - \left(H^n_{i,j-1/2}\right)^2\right) &= \Delta t g\left(H\frac{\partial B}{\partial x}\right)^n_{i,j}, \\ \left(H\bar{c}\right)^{n+1}_{i,j} &= \left(H\bar{c}\right)^n_{i,j}, \\ B^{n+1}_{i,j} &= B^n_{i,j}. \end{aligned} \tag{5.4.24}$$

By combining (5.4.23) and (5.4.24) it is possible to form

$$g\frac{1}{8\Delta x}\left(H^n_{i+1,j} + 2H^n_{i,j} + H^n_{i-1,j}\right)\left(H^n_{i+1,j} + H^n_{i-1,j}\right) = g\left(H\frac{\partial B}{\partial x}\right)^n_{i,j},$$

$$g\frac{1}{8\Delta y}\left(H^n_{i,j+1} + 2H^n_{i,j} + H^n_{i,j-1}\right)\left(H^n_{i,j+1} + H^n_{i,j-1}\right) = g\left(H\frac{\partial B}{\partial y}\right)^n_{i,j}.$$

As for a stationary solution where $H^n_{i+1,j} - H^n_{i-1,j} = B^n_{i+1,j} - B^n_{i-1,j}$ and $H^n_{i,j+1} - H^n_{i,j-1} = B^n_{i,j+1} - B^n_{i,j-1}$, the above equations become

$$\begin{aligned} \left(gH\frac{\partial B}{\partial x}\right)^n_{i,j} &= g\frac{H^n_{i+1/2,j} + H^n_{i-1/2,j}}{2}\frac{B^n_{i+1,j} - B^n_{i-1,j}}{2\Delta x}, \\ \left(gH\frac{\partial B}{\partial y}\right)^n_{i,j} &= g\frac{H^n_{i,j+1/2} + H^n_{i,j-1/2}}{2}\frac{B^n_{i,j+1} - B^n_{i,j-1}}{2\Delta y}, \end{aligned} \tag{5.4.25}$$

where the averaged solutions are defined by

$$H^n_{i+1/2,j} = \frac{H^n_{i+1,j} + H^n_{i,j}}{2}, \qquad H^n_{i,j+1/2} = \frac{H^n_{i,j+1} + H^n_{i,j}}{2}.$$

This allows for a well-balanced and conservative method. This procedure is implemented as shown in Figure 5.7.

5.5 Numerical results

Several test examples for shallow water flows over multilayer movable beds are presented in this section to ascertain the accuracy and adaptability of the proposed techniques. Dam-break flow problems are presented to illustrate the performance of the proposed numerical solver combined with the discretised bed to resolve non-homogeneous erodible sediment beds. Computational results for both single-layer and three-layer beds are presented, using the sediment characteristics listed in Table 3.1 (on page 77). These sediment parameters have been recommended in many experimental studies on sediment transport applications [151, 189, 207]. In these simulations, $\rho_w = 1000\ kg/m^3$, $g = 9.81\ m/s^2$, and $\nu = 1.2 \times 10^{-6}\ m^2/s$. In addition, the Courant number Cr = 0.7 is used to adjust the time-step Δt according to the stability condition

$$\Delta t = \text{Cr}\frac{\min(\Delta x, \Delta y)}{\max\limits_{k=1,\ldots,5}\left(|\lambda^n_k|, |\mu^n_k|\right)}, \tag{5.5.26}$$

where λ_k, μ_k $(k = 1, \ldots, 5)$ are the eigenvalues of the sediment transport system given in (5.2.2). It should be pointed out that the stability condition (5.5.26) accounts for the rate of vertical changes and ensures that the bed height never travels more than one control volume as long as the vertical discretisation step $\Delta z \leq \min(\Delta x, \Delta y)$.

5.5.1 Rectangular dam-break problem

In this class of flow problems, a dam-break problem is considered in a squared channel of length 20 m with a three-layer bed initially assumed to be flat. At time $t = 0\ s$, the flow is assumed to

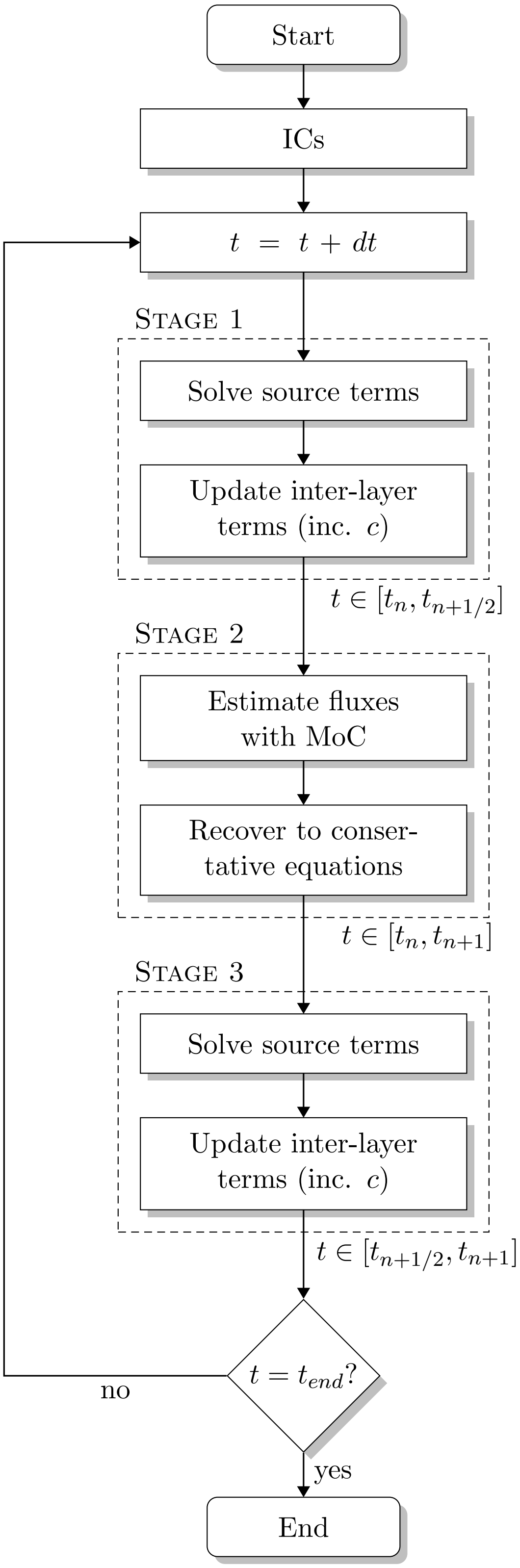

Figure 5.7: A flowchart demonstrating the stages in the proposed 2D Eulerian-Lagrangian procedure, including bed register is highlighted.

Table 5.1: CPU times, error in the entrained sediment, and error in the minimum values of the bed profile using different spatial and bed discretisation steps Δx, Δy, and Δz, for the test example of a rectangular dam-break over a three-layer bed.

		Lateral discretisation				
		$\Delta x = \Delta y =$ 0.8 m	$\Delta x = \Delta y =$ 0.4 m	$\Delta x = \Delta y =$ 0.2 m	$\Delta x = \Delta y =$ 0.1 m	$\Delta x = \Delta y =$ 0.05 m
Vertical discretisation	$\Delta z =$ 0.2 m	9.268 s	69.09 s	656.6 s	8381 s	21720 s
		7.68 %	6.84 %	7.17 %	7.58 %	7.63 %
		5.15 %	7.13 %	6.92 %	6.65 %	6.28 %
	$\Delta z =$ 0.1 m	8.539 s	69.47 s	656.5 s	8387 s	21650 s
		7.17 %	6.44 %	6.30 %	6.59 %	6.98 %
		5.32 %	7.19 %	6.98 %	6.69 %	6.38 %
	$\Delta z =$ 0.05 m	8.540 s	69.16 s	656.7 s	8388 s	25260 s
		2.36 %	1.58 %	1.50 %	1.99 %	2.56 %
		1.83 %	3.59 %	3.25 %	3.06 %	2.84 %
	$\Delta z =$ 0.025 m	8.530 s	69.10 s	657.3 s	8384 s	24180 s
		1.27 %	2.31 %	2.20 %	1.65 %	1.19 %
		0.79 %	0.38 %	0.21 %	0.10 %	0.29 %
	$\Delta z =$ 0.0125 m	10.84 s	74.03 s	664.7 s	8413 s	23110 s
		4.07 %	2.61 %	3.48 %	1.98 %	0.92 %
		2.50 %	1.08 %	0.54 %	0.26 %	0.08 %

be at rest and

$$H(0,x,y) = \begin{cases} 2\,m, & \text{if} \quad x \leq 0\,m, \\ \\ 0.2\,m, & \text{if} \quad x > 0\,m, \end{cases} \qquad \bar{c}(0,x,y) = 0.0001, \qquad u(0,x,y) = 0\,m/s,$$

$$v(0,x,y) = 0\,m/s, \qquad\qquad B(0,x,y) = 0\,m.$$

The depth of the bed is 0.6 m with three layers initially formed by

$$B(0,x,y,z) = \begin{cases} \text{Sand 1}, & \text{if} \quad -0.15\,m \ \leq z < \ 0\,m, \\ \\ \text{Sand 2}, & \text{if} \quad -0.25\,m \ \leq z < \ -0.15\,m, \\ \\ \text{Sand 3}, & \text{if} \quad -0.6\,m \ \leq z < \ -0.25\,m. \end{cases}$$

The sediment properties of Sand 1, Sand 2, and Sand 3 are listed in Table 3.1. This example is considered to perform a mesh convergence study for the proposed multilayer model using differ-

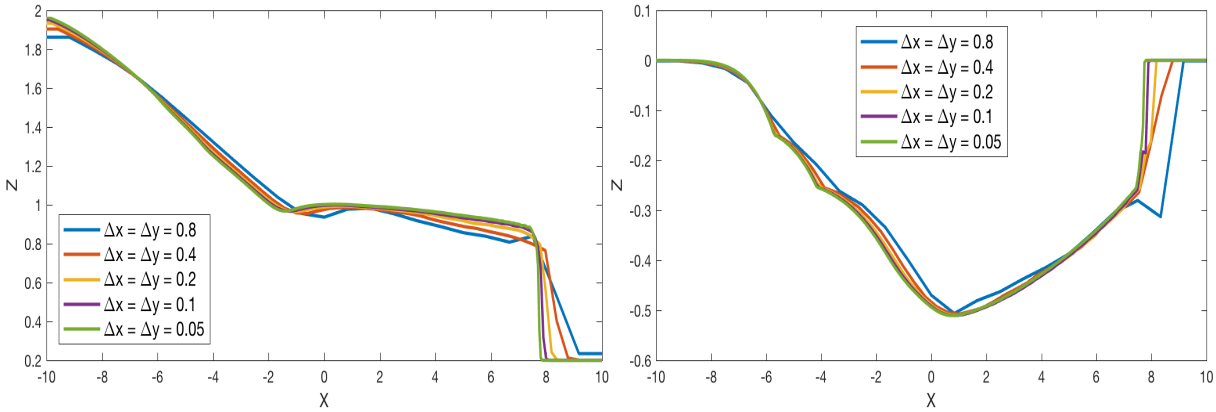

Figure 5.8: Water height (left) and bed profile (right) at $y = 0\ m$ obtained for the test example of a rectangular dam-break over a three-layer bed at time $t = 2\ s$ using different meshes.

ent number of control volumes in the spatial discretisation. Figure 5.8 depicts the computational results for the water height and bed profile obtained at time $t = 2\ s$, using $\Delta z = 0.1\ m$ and different values of $(\Delta x, \Delta y)$. It is clear from these results that refining the horizontal mesh leads to an increase in the accuracy of both water heights and bed profiles obtained using the ELFV method. In order to quantify the errors in these results, Table 5.1 summarises the errors in the entrained sediment, the errors in the bed profiles, and the computational times for different mesh discretisations of $(\Delta x, \Delta y, \Delta z)$. Here, a reference solution is computed using a fine discretisation with $\Delta x = \Delta y = 0.025\ m$ and $\Delta z = 0.001\ m$. The L^1-norm is used to compute the errors, and results are presented at the final time $t = 2\ s$. It is clear from the results presented in Table 5.1 that increasing the number of control volumes in the horizontal spatial discretisation yields an increase in the accuracy and also in the computational cost of the ELFV method for this test example. Using the coarse discretisation $(\Delta x = \Delta y = 0.8\ m,\ \Delta z = 0.2\ m)$, the computed errors for the water height and the bed profile are more pronounced than for the other discretisations. It should also be noted that, when compared to the lateral discretisation, the vertical discretisation has small effects on both the convergence and the efficiency of the proposed model. For instance, for a simulation using $(\Delta x = \Delta y = 0.4\ m,\ \Delta z = 0.1\ m)$ the computational time and the errors in the sediment concentration and the bed profile are $69.47\ s$, $6.44\ \%$, and $7.19\ \%$, respectively. By contrast, a discretisation of $(\Delta x = \Delta y = 0.1\ m,\ \Delta z = 0.025\ m)$ reduces the errors in the sediment concentration and the bed profile respectively to $1.65\ \%$ and $0.10\ \%$, which is a substantial step towards convergence. For this later simulation with $(\Delta x = \Delta y = 0.1\ m, \Delta z = 0.025\ m)$, the computational time increases to $8384\ s$. It is evident that a mesh convergence is achieved for this method, also that vertical bed discretisation has no effect on computational efficiency. For the considered flow and sediment conditions, a balance between convergence and efficiency in the ELFV method favours the vertical discretisation $\Delta z = 0.025\ m$.

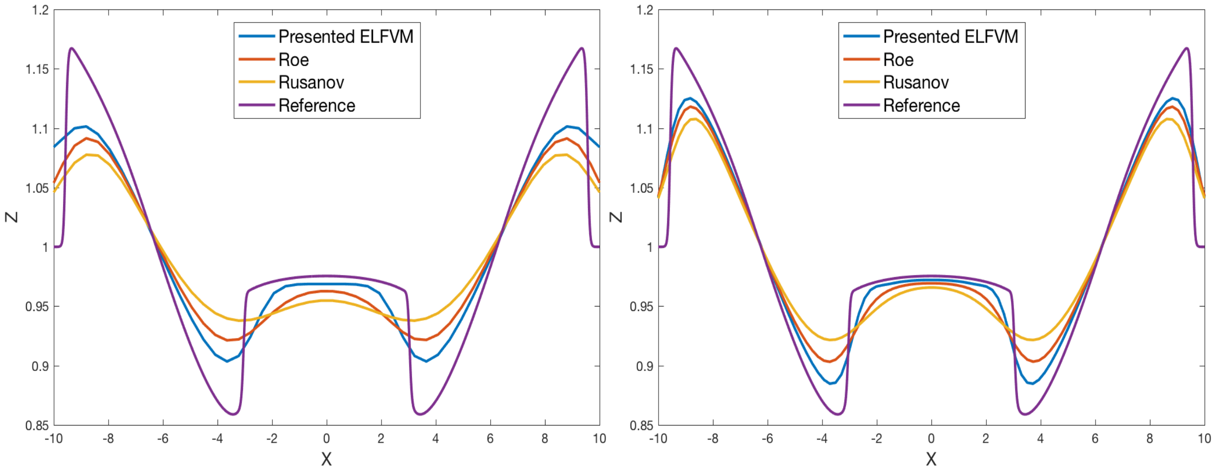

Figure 5.9: A comparison of cross-sections of the water height obtained using different solvers for the test example of a circular dam-break over a fixed single-layer bed at time $t = 2\ s$ using $\Delta x = \Delta y = 0.4$ (left) and $\Delta x = \Delta y = 0.2$ (right).

5.5.2 Circular dam-break problem

Next, test examples are considered for circular dam-break flows over erodible beds formed of single-layer and three-layer sediments. The circular dam-break problem is solved in a squared domain $[-10, 10] \times [-10, 10]$ with a flat bed, and is subject to the following initial conditions

$$H(0, x, y) = 1 + \ 2\left(1 - \tanh\left(10\left(\sqrt{0.4x^2 + 0.4y^2} - 1\right)\right)\right)\ m, \qquad B(0, x, y) = 0\ m,$$

$$u(0, x, y) = 0\ m/s, \qquad v(0, x, y) = 0\ m/s.$$

A similar problem has been considered in [106] for the standard circular dam-break problem over a fixed bed. Hence, as a first run for this class of problems, the same example is solved on a fixed bed and the results obtained using the ELFV method are compared to other well-established solvers. Here, a Riemann-based Roe solver and the Rusanov method are considered. Figure 5.9 presents the radial cross-sections of the water height at $y = 0$, using the considered methods at time $t = 2\ s$ on two meshes with 50×50 and 100×100 horizontal cells. For comparison, a reference solution obtained with the Roe scheme on a fine mesh with 500×500 is also included in this figure. It is clear from these results that the numerical diffusion is very pronounced in the solutions computed using the Rusanov scheme. This excessive numerical dissipation has been partially removed in the water heights using the Roe method, but the results obtained using the ELFV method remain the best. In terms of computational cost, the ELFV method is about 150 times faster than the Roe scheme for the same simulation, though it is slightly slower than the Godunov scheme (having just over double the run time). It also relies on a quadratic or linear interpolation in the Eulerian step, this comes with the respective in-accuracies and tendency to

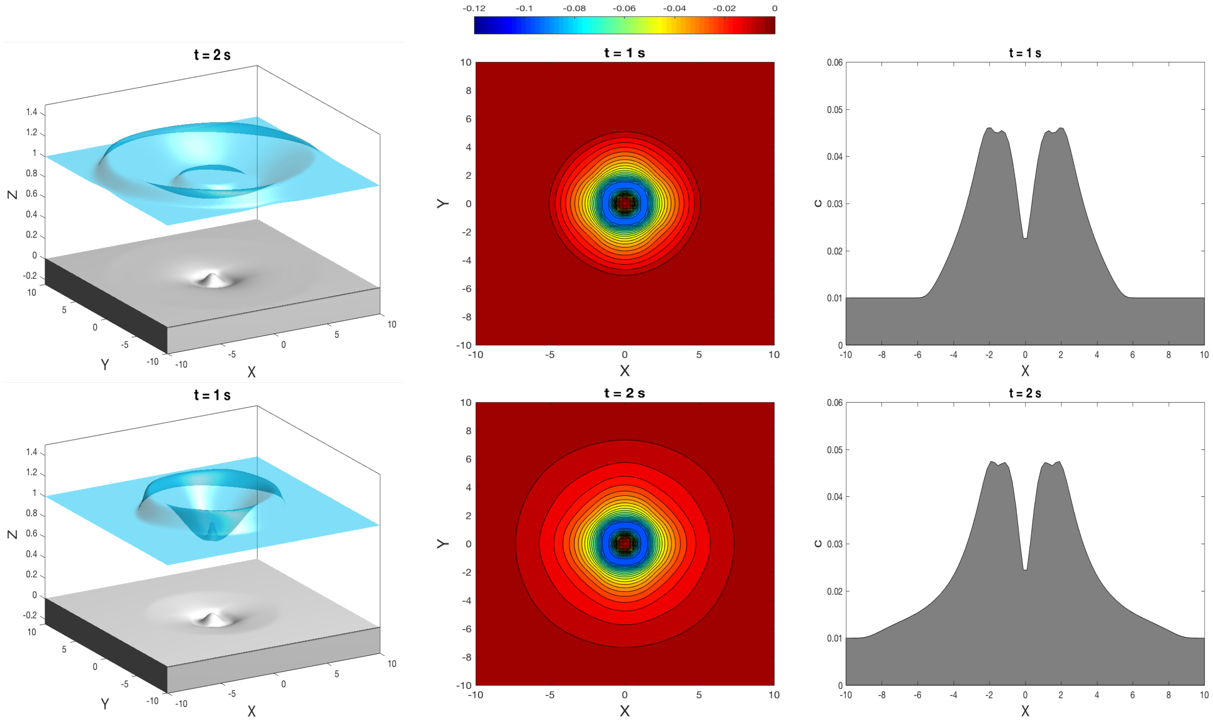

Figure 5.10: Circular dam-break over a single sediment bed: we display the water free-surface (left), bed surface (middle), and concentration profile at $y = 0\ m$ (right), at two different times $t = 1\ s$ and $2\ s$.

non TVD behaviour associated with both. For this test example, the ELFV method accurately solves the front propagation without generating non-physical oscillations or excessive numerical dissipation in the computed results.

The next step is to simulate a circular dam-break flow over an erodible bed. To this end, the same simulation is run over a single-layer bed of depth $0.25\ m$ and formed of Sand 2, the sediment properties of which are given in Table 3.1. The initial conditions are the same as the previous example and the sediment concentration is set to $c_1(0, x, y) = \bar{c}(0, x, y) = 0.01$. Figure 5.10 depicts the results obtained for the water height, bed, and sediment concentration obtained on a mesh with 100×100, at $t = 1\ s$ and $2\ s$. Here, only radial cross-sections at $y = 0$ of the sediment concentration are displayed in Figure 5.10. It is clear that allowing for a movable bed in circular dam-break flows results in a radial erosion of the bed. From the presented results, it is also clear that the water flows away from the central region as the rarefaction wave propagates outwards. Note that the ELFV method has accurately resolved this dam-break flow, and it preserves the radial symmetry (within the Cartesian grid) in all flow and sediment variables. To emphasis the effects of a multilayer bed on this dam-break problem, the same simulations are performed on a bed $0.25\ m$ deep and comprised of three layers as

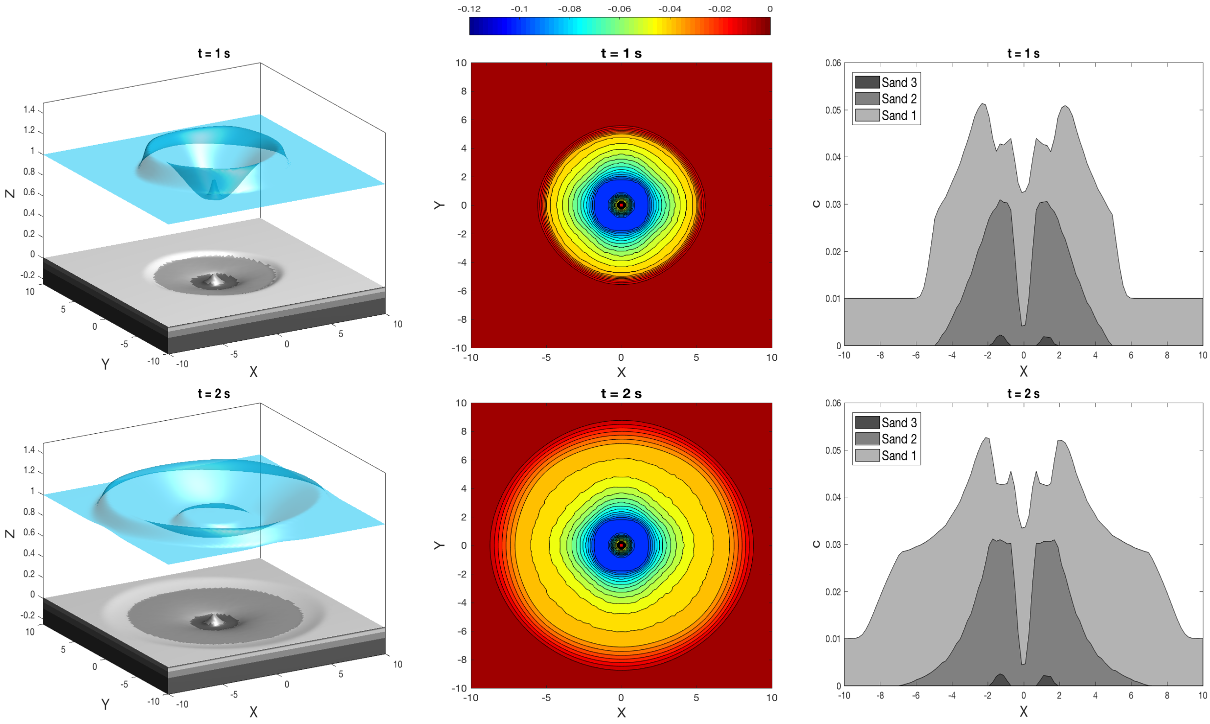

Figure 5.11: Circular dam-break over a three-layered sediment bed: we display the water free-surface (left), bed surface (middle), and concentration profile at $y = 0\ m$ (right), at two different times $t = 1\ s$ and $2\ s$.

$$B(0,x,y,z) = \begin{cases} \text{Sand } 1, & \text{if } -0.05\ m \leq z < \ \ 0\ m, \\ \text{Sand } 2, & \text{if } -0.1\ m \ \leq z < \ -0.05\ m, \\ \text{Sand } 3, & \text{if } -0.25\ m \leq z < \ -0.25\ m, \end{cases}$$

and the initial sediment concentrations are $\bar{c}(0,x,y) = c_1(0,x,y) = 0.01$. The sediment parameters for Sand 1, Sand 2, and Sand 3 are given in Table 3.1. Notice that, since the highly erodible Sand 1 is used in this test example, more scour is expected in the bed as well as a different concentration profile compared to the previous test example. The central bed peak should also be retained in this case, along with a bed that reflects the differences in erosion profiles of the multiple sedimentary sands. Figure 5.11 displays the water height, bed profile, and radial cross-section of the sediment concentrations obtained with a mesh of 100×100 gridpoints using vertical discretisation $\Delta z = 0.005\ m$ at $t = 1\ s$ and $2\ s$. Again, symmetry (within the constrains of a Cartesian grid) is obtained using the ELFV method for this dam-break problem over a three-layer sedimentary bed. Compared to the results obtained for the single-layer bed in Figure 5.10, the results for the three-layer bed in Figure 5.11 show a comparable quantity of scour, though the notable difference lies in the erosion rate for each simulation (compare the

c profiles in Figure 5.10 and Figure 5.11). For instance, it is noticeable that Sand 1, with its higher erosion rate, causes a greater net scour, whilst Sand 2 has a roughly constant sediment concentration rate from $t = 0.5\ s$ onwards. This implies that only the initial wave speed is large enough to cause the scour of Sand 2 in the bed. The computed results for this example of circular dam-break flows over erodible beds have demonstrated the ability of the ELFV method to handle multiple sediments in the beds. Here, the proposed system formulation combined with the ELFV method is able to resolve the erosion effects in multilayer sedimentary beds accurately, as well as capturing the multiple sediment concentrations, which are vital to the understanding of sediment transport in these types of dam-break problems.

5.5.3 Partial dam-break problem

The aim of these test examples is to investigate the effects of multiple sediment layers on partial dam-break flows over movable beds. The system (5.2.3) is solved in a 200 m long and 200 m wide flat reservoir with two different constant levels of water separated by a dam. At $t = 0\ s$ part of the dam breaks instantaneously. The dam is 4 m thick and the breach is assumed to be between $y = 90\ m$ and $y = 140\ m$. The initial conditions are

$$H(0,x,y) = \begin{cases} 5\ m, & \text{if } x \leq 100\ m, \\ 0.5\ m, & \text{if } x > 100\ m, \end{cases} \qquad B(0,x,y) = 0\ m \qquad \bar{c}(0,x,y) = c_1(0,x,y) = 0.0001,$$
$$u(0,x,y) = 0\ m/s, \qquad v(0,x,y) = 0\ m/s.$$

First, the problem is solved over a single-layer bed 6 m deep formed of Sand 2; see Table 3.1 for the sediment parameters associated with the bed. The water height, entrained sediment, and cross-sections of the sediment concentration at $y = 115\ m$ are presented in Figure 5.12 at $t = 3.6\ s$ and 7.2 s. Under these flow and sediment conditions, the results show that as the flow evolves downstream and the rarefaction wave propagates upstream, a deep scour hole is generated at the dam breach. These results are similar to others presented in [20]. As can be observed, the dam-break flow over the movable bed can build up a heavily concentrated wave-front. The bed mobility can strongly modify the water free-surface profiles and may have considerable implications for flood predictions. As in the previous simulations, an hydraulic jump in the water free-surface is initially formed around the dam site. It becomes less pronounced and propagates upstream over time, and eventually disappears. It is evident that the movable bed can be significantly scoured and the dimensions of the scour hole are of a similar order of magnitude to those of the water flow itself. Therefore, the rate of bed deformation is not

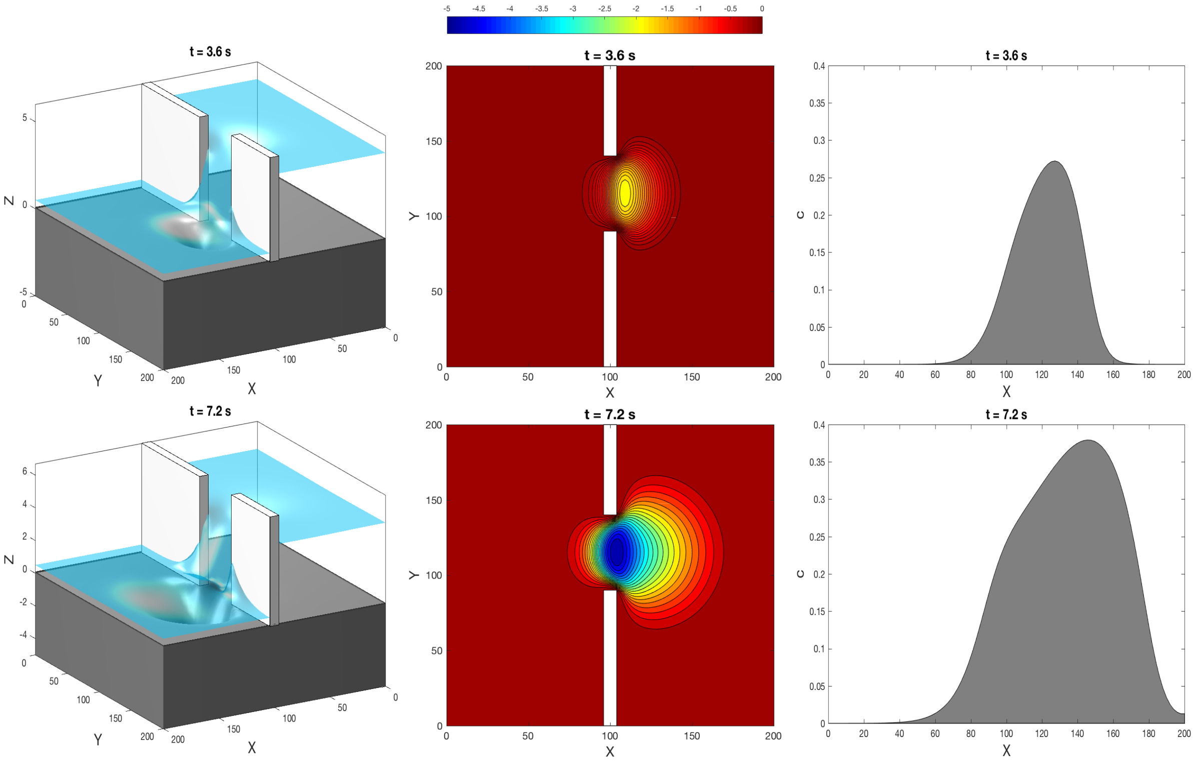

Figure 5.12: Partial dam-break over a single sediment bed: we display the water free-surface (left), bed surface (middle), and concentration profile at $y = 115\ m$ (right), at two different times $t = 3.6\ s$ and $7.2\ s$.

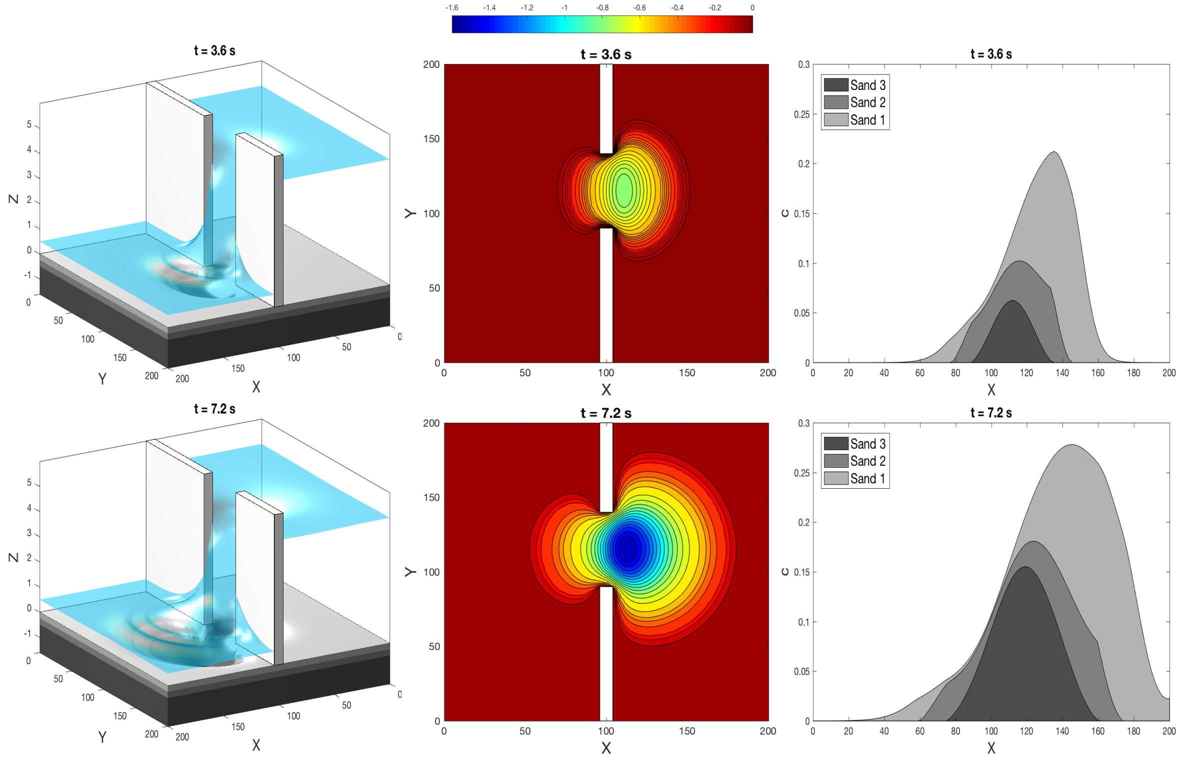

Figure 5.13: Partial dam-break over a three-layered sediment bed: we display the water free-surface (left), bed surface (middle), and concentration profile at $y = 115\ m$ (right), at two different times $t = 3.6\ s$ and $7.2\ s$.

negligible compared to the time-scale of the flow, characterising the need for coupled modelling of the strongly interacting flow-sediment-bed system. The presented results show that the proposed solver performs well for this dam-break problem since it is non-diffusive and no spurious oscillations have been detected.

The next concern in this test example is to demonstrate the capability of the proposed model in dealing with a multilayer bed for this partial dam-break problem. Here, the same simulations are considered on a 2 m deep bed formed with three layers

$$B(0,x,y,z) = \begin{cases} \text{Sand 1}, & \text{if} \quad -0.25\,m \ \le z < \ 0\,m, \\ \text{Sand 2}, & \text{if} \quad -0.5\,m \ \le z < \ -0.25\,m, \\ \text{Sand 3}, & \text{if} \quad -2.0\,m \ \le z < \ -0.5\,m, \end{cases}$$

and the initial sediment concentrations are $\bar{c}(0,x,y) = c_1(0,x,y) = 0.001$. The sediment parameters for Sand 1, Sand 2, and Sand 3 are given in Table 3.1. The three-layer sediment model provides good results and a clear difference in the bathymetry is detected, as shown in Figure 5.13, compared to Figure 5.12. This ability to handle multiple sediments allows analysis of erosion over a greater area, highlighting the more easily eroded Sand 1 while capturing the limitation on net erosion caused by the base layer (of less easily eroded Sand 3). As Sand 2 is an average of Sand 1 and Sand 3, it is possible to compare the results and note the differences. It is easy to see, as shown in Figure 5.12, the excess erosion caused by a single sediment assumption, which is a common problem in models that over simplify the sediment bed. It should also be noted that the discretisation of the bed adds no error, as the un-discretised and discretised homogeneous bed results are identical.

The differences between the three simulation types are further inspected in Table 5.2. In this table, three variables are presented. First, the total discharge measured as the quantity of water evacuated from the east side to the west side of the dam is presented. Second, the disturbed area, where the water height varies from the initial level owing to disturbance from the dam-break, is calculated. Third, the total suspended sediment, which is the volume taken up by the suspended sediments in the whole domain, is displayed. The total suspended sediment, is the volume of all entrained sediment in the domain. The table also provides a breakdown of these values at four intervals over the time period.

Erodible beds have a greater discharge than fixed beds (as shown in Table 5.2), even though they lose momentum by picking up sediments. This is due to the evolving bathymetry both in front and behind the dam-break, as more water is accelerated through the dam. The pertur-

Table 5.2: A comparison of the discharge volume, the area disturbed by the dam-break, and the volume of suspended sediment (for single and 3-layer simulations) for the three partial dam-break simulations at $t = 1.8\ s,\ 3.6\ s\ 5.4\ s$ and $7.2\ s$.

Simulation	Observed quantity	$t = 1.8\ s$	$t = 3.6\ s$	$t = 5.4\ s$	$t = 7.2\ s$
Fixed	Total discharge $[m^3]$	1788	3204	5012	6493
	Disturbed area [%]	4.69%	8.97%	14.71%	21.22%
Single layer	Total discharge $[m^3]$	1877	3589	5884	8488
	Total suspended sediment $[m^3]$	260	1435	3570	6312
	Disturbed area [%]	7.19%	13.42%	21.00%	29.62%
Three layer	Total discharge $[m^3]$	2005	3463	5058	6681
	Total suspended sediment $[m^3]$	413	1150	2203	3471
	Sand 1 [%]	66.8	61.3	58.2	56.3
	Sand 2 [%]	31.7	26.6	22.5	20.4
	Sand 3 [%]	1.6	12.1	19.3	23.2
	Disturbed area [%]	7.82%	14.78%	22.93%	32.10%

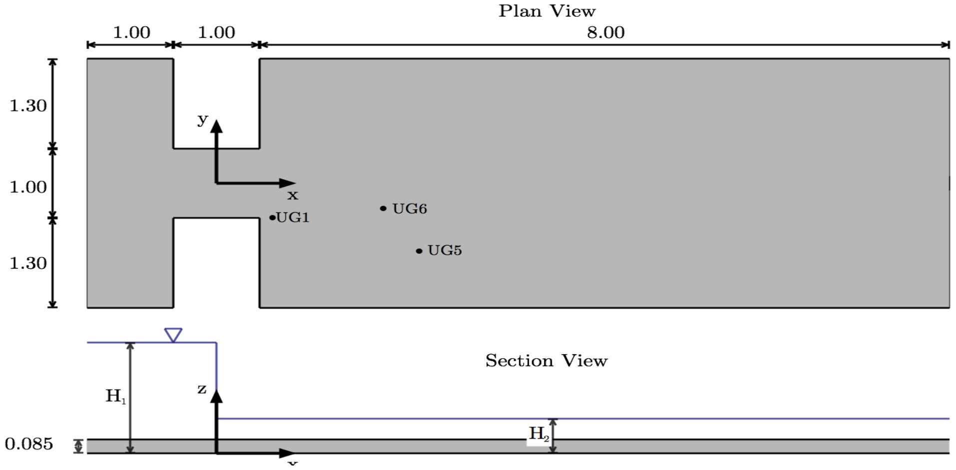

Figure 5.14: The domain of the Louvain experiment, showing the relative positions of the water height gauge points as reported in [165].

bation caused by the dam-break spreads over a far greater area than the fixed bed simulation. This is likely to be due to the diffusive effects of the sediment breaking down the wave-front. Table 5.2 also shows the evolution of sediment proportions for the three-layered erodible bed, it is interesting to see how they change over time as the various layers are uncovered.

5.5.4 Louvain partial dam-break experiment

This section models the experiment conducted at the Université Catholique de Louvain, as reported in [165]. The experiment consists of a 2D partial dam-break over a movable sediment bed consisting of Sediment 2, see Table 3.1 for the characteristics of this sediment. A variety of

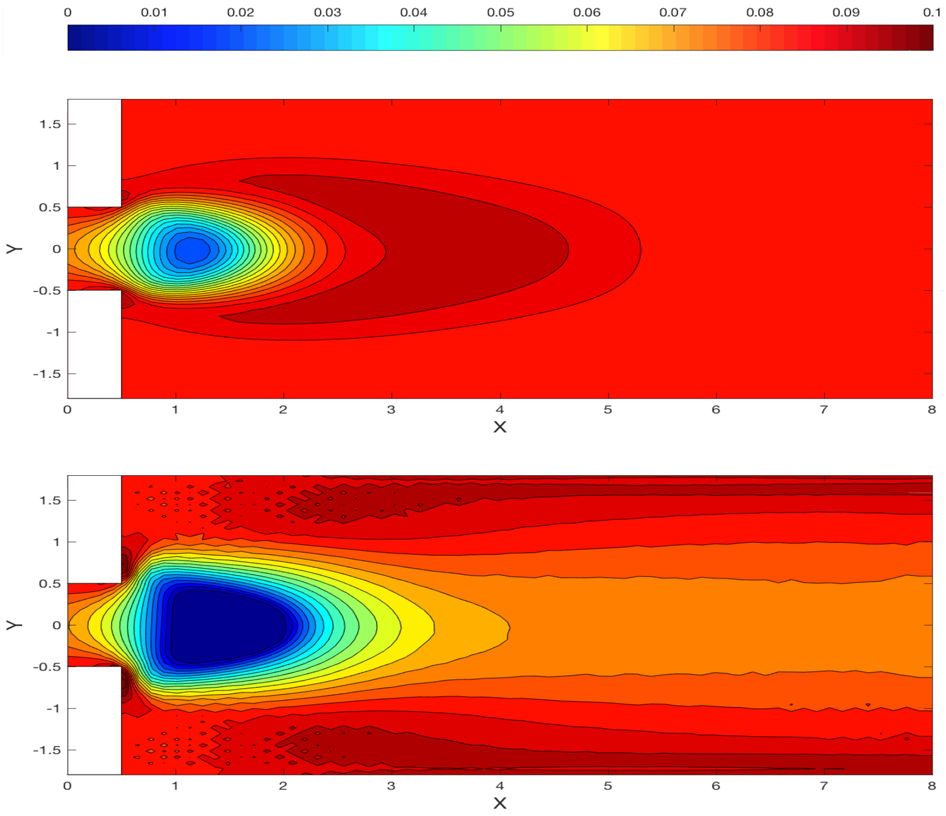

Figure 5.15: Bed surfaces at $t = 20\ s$ for the Louvain wet bed (top) and dry bed (bottom).

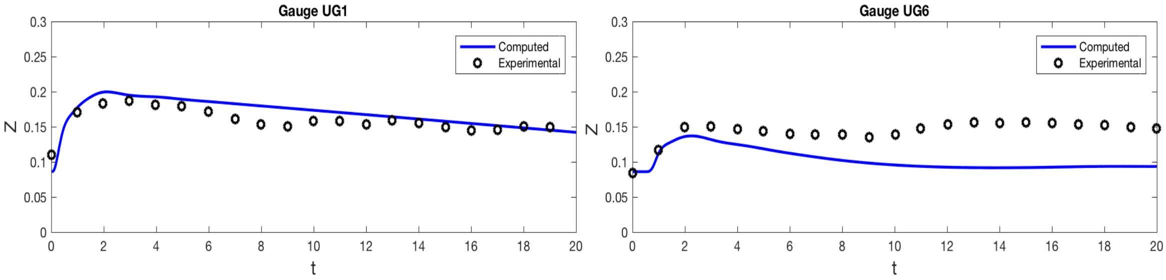

Figure 5.16: A comparison of water height results for the Louvain dry bed experiment and the presented model: gauge UG1 (left) and gauge UG6 (right)

measurements were taken and reported in [165], these included final bed height plots in 2D and water gauge heights at eight points. The experimental domain is shown in Figure 5.14 where all measurements are given in metres. Both wet and dry dam experiments are conducted to test the twelve computational models in [165]. The dry and wet cases had the following initial depth conditions:

- For Case 1 (dry bed): $H_1 = 0.47\ m,\ H_2 = 0.085\ m.$

- For Case 2 (wet bed): $H_1 = 0.51\ m,\ H_2 = 0.15\ m.$

For these water conditions the twelve well-developed models are used to run simulations using a variety of mesh sizes $(0.2-0.01\ m)$, centring around about $0.1\ m$. Data from two gauges is used in

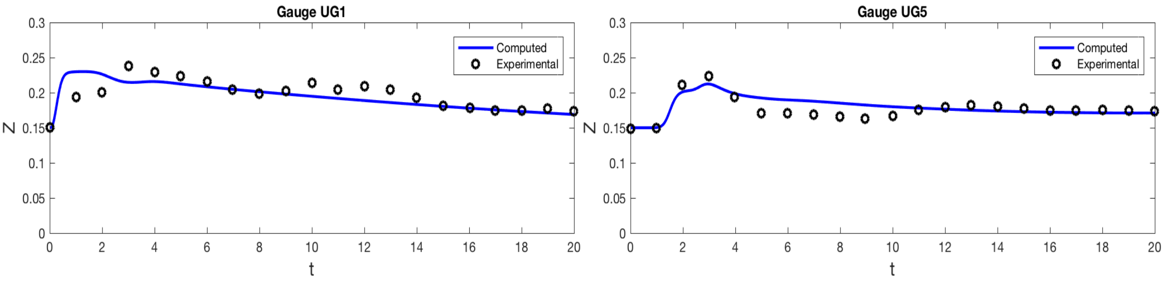

Figure 5.17: A comparison of water height results for the Louvain wet bed experiment and the presented model: gauge UG1 (left) and gauge UG5 (right).

both simulations as a benchmark. For Case 1, gauge UG1 is positioned at $(0.640\ m, -0.500\ m)$, and gauge UG6 is positioned at $(1.940\ m, -0.330\ m)$. For Case 2, gauge UG1 is positioned at $(0.640\ m, -0.500\ m)$, and gauge UG5 is positioned at $(2.340\ m, -0.990\ m)$.

As shown in Figure 5.15, the model over-predicts the scour caused by the dam-break in the dry bed experiment (as seen by the error in Gauge UG6), though a good result is gained for the prediction of the water heights initially at gauges UG1 & UG6, as seen in Figure 5.5.4. It should be noted that a discreteised bed has no effect on this simulation, as the results when compared to a undiscretised bed are identical. The loss of accuracy for gauge UG6, in Figure 5.5.4, is possibly due to the over erosion at that point as, if the bed height is assumed constant, a near true approximation is achieved. The wet bed results give a good agreement with the model presented, as shown in Figure 5.15: the scour is centred a little too far downstream and lacks lateral deposition, but it is still reasonably accurate as compared to other methods. The flow results, shown in Figure 5.17, on the other hand, have a strong likeness to the experimental data, which is a positive result for the presented method. The ELFV method appears to give a fast and accurate flow prediction. This model could be improved with a more sensitive sediment pick-up function giving a more accurate bed profile. As stated in the paper [165], previous models appear give either good flow or good bed predictions. Consequently, these results are encouraging as they demonstrate both reasonable bed results and good flow prediction. Now that a baseline result has been established, the bed profile is varied to see the effects of differing sediments. The bed in the laboratory experiment consisted of well-graded sediment of average diameter $1.61 \times 10^{-3}\ m$ (Sediment 2). In this simulation, two variants are added to the sediment mix by varying the sediment diameter d while keeping all other variables the same. Having created a bed using one third $d = 0.5 \times 10^{-3}\ m$ (Sediment 1), one third $d = 2 \times 10^{-3}\ m$ (Sediment 2), and one third $d = 1.61 \times 10^{-3}\ m$ (Sediment 3), the simulation is rerun with the same initial conditions. The aim is to show how a small variation in the sediment characteristics (for this case d), has a large effect on the sediment entrainment functions. As shown in Figure 5.18,

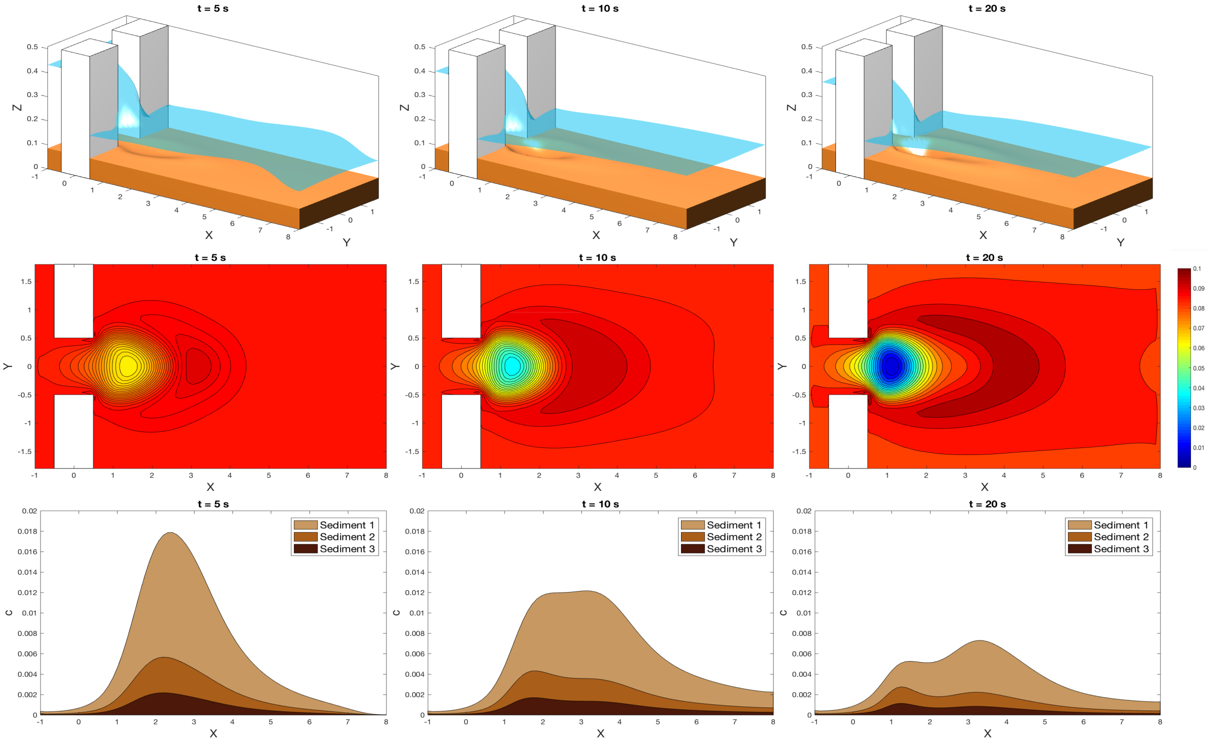

Figure 5.18: Louvain partial dam-break over a three-sediment mixed bed: we display the water free-surface (top), bed surface (middle), and concentration profile at $y = 0\ m$ (bottom), at two different times $t = 5\ s, 10\ s$ and $20\ s$.

greater net erosion is gained due to the smaller diameter sediment fraction, as well as more net deposition as compared to the single sediment result. It is interesting to note that the suspended sediment fractions are very dependent on the sediment mixtures. As the sediment is well-balanced and the erosion rates are comparable, there is no ripple formation or any other visible effect of armouring. With a more detailed study of the sediment used, it should be possible to represent the fractions more accurately by the sediment size. This simulation shows high levels of erosion but also an appreciable level of deposition, which is rare in simulations of this nature, especially with experimental data. The previous two simulations have shown how a small change to the sediment composition of the bed can cause a large difference in the final bed profile. The effects of armouring and the creation of ripples are demonstrated by modifying the bed. Therefore the erosion and deposition are no longer balanced and bed variation takes hold. Using the same sediment as the last simulation, it is arranged into three layers

$$B = \begin{cases} \text{Sediment 1} & \text{if} \quad 0.065\ m \le z < 0.085\ m, \\ \text{Sediment 2} & \text{if} \quad 0.035\ m \le z < 0.065\ m, \\ \text{Sediment 3} & \text{if} \quad 0\ m \le z < 0.035\ m. \end{cases}$$

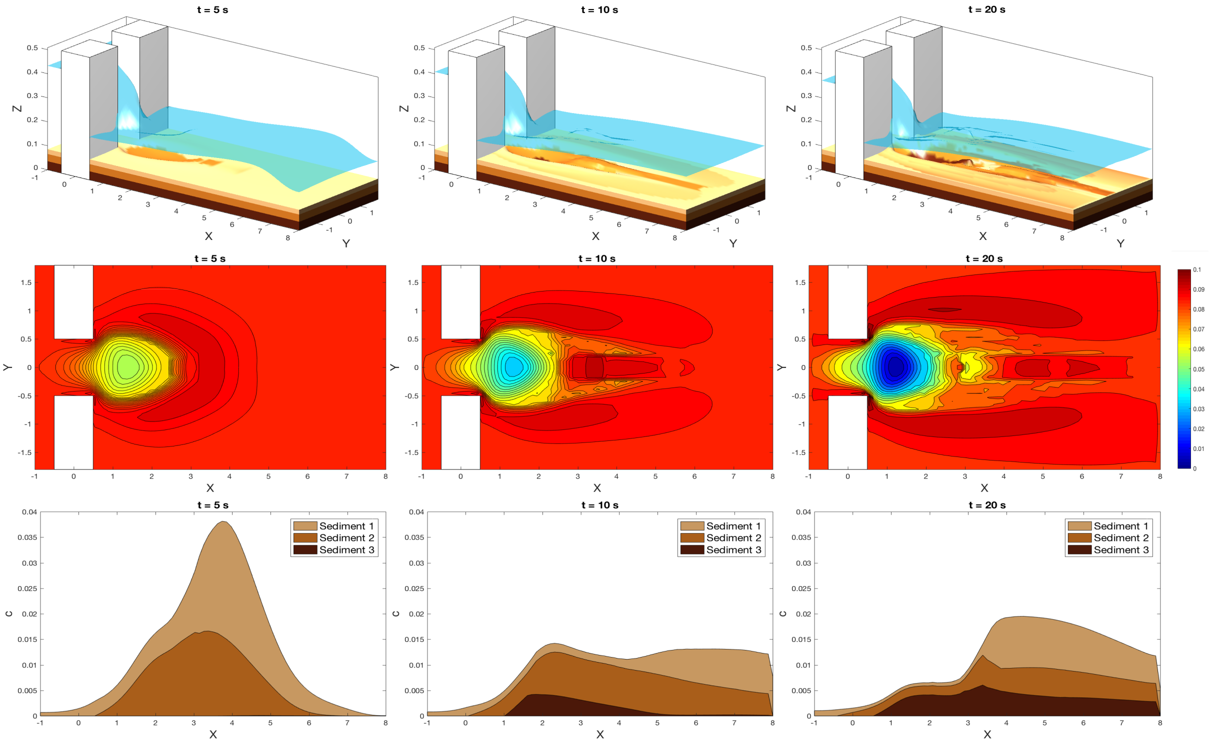

Figure 5.19: Louvain partial dam-break over a three-layered bed: we display the water free-surface (top), bed surface (middle), and concentration profile at $y = 0\ m$ (bottom), at two different times $t = 5\ s, 10\ s$ and $20\ s$.

As Figure 5.19 shows that the armouring occurs due to the unbalanced rates of erosion and deposition of the three sediment types and the finely tuned parameters of this simulation. It is interesting to note that the total rate of erosion is higher than in the previous simulations which could be attributed to the high initial rate of erosion of Sediment 1. As a consequence this creates a much more complex flow and bed profile.

5.6 Concluding remarks

A class of fast and accurate numerical models has been proposed for the modelling and simulation of two-dimensional shallow water flows over multi-sediment erodible beds. A hyperbolic system of five equations for balance laws with source terms is presented for coupled hydrodynamics, morphodynamics and suspended sediments. To close the system, a set of empirical equations for entrainment and deposition terms, along with flux terms for the mass exchange between the multiple layers in sedimentary beds, are proposed. A splitting approach is adopted to manage the complications arising from handling multiple sediments. This minimises computational expense, and it does not add further species conservation equations to the governing system. Although averaged variables have been used in the equations of suspended sediments, each sediment is still handled separately for erosion and deposition in the proposed model. A conservative vertical discretisation of the finite volume type is considered for the multilayer bed, to allow for different sediment properties forming the bed. This is combined with bed flux added to the Exner-type equation for bed height. This allows for any deficit or excess in entrained sediment (due to erosion or deposition) to be transferred to the cell beneath or above as appropriate.

For the numerical solution, a Eulerian-Lagrangian Finite Volume (ELFV) method is considered, which combines the advantages of a conservative finite volume method formulation and with the speed of the method of characteristics. The proposed method can be interpreted as a predictor-corrector procedure for which the numerical fluxes are reconstructed in the predictor stage, using the method of characteristics applied to the projected system in the local normal and tangential coordinates. The presented solver satisfies the conservation property and achieves excellent numerical balance between the gradient fluxes and the source terms for the coupled system. No Riemann-problem solvers are needed in the proposed method to compute the numerical fluxes; this greatly increases the efficiency of simulations as compared to conventional finite volume methods.

To examine the performance of the proposed models, a variety of two-dimensional shallow water flows are simulated over single and multi-sediment movable beds. First, a one-dimensional dam-break problem is considered, this example is used to show the convergence of the discretisation of the bed. Next, a circular dam-break problem is considered over a single and a multilayer bed; this example is used to compare the affects of bed composition. It is also used (over a fixed bed) to compare the proposed ELFV method with two other well established numerical solvers. The ELFV method is found to be highly accurate as well as more efficient than the other solvers considered. A partial dam-break problem is then simulated over three cases using: a fixed, a single sediment, and a three-layered bed. This simulation further highlights the importance of the correct modelling of the bed, as there is a wide variation in fluid discharge depending on the bed used. Finally, the proposed formulation is used to simulate a partial dam-break experiment; it is found to offer good results (as compared to similar models). This experiment is also varied upon to show the effects of bed assumptions with a mixed three sediment bed and a three-layered bed. The results obtained have exhibited accurate predictions of both the hydrodynamics and morphodynamics, with correct conservation properties and stable representations of the water free-surface response to the multilayer erodible beds. It can be concluded that both the model and method proposed offer notable advantages to this field.

Chapter 6

Modelling and simulation of multilayer shallow water flows in two space dimensions

This chapter examines a fast, efficient and conservative method for solving two-dimensional multilayer flows with mass exchange allowed between vertically superposed layers. The model considers the shallow water equations for each layer and combines them to create a formulation that offers stratified vertical velocities. These modelled layers can interact because exchange terms that facilitate the movement of mass and momentum between the layers are included in the formulation. The effects on the flow of non-flat bathymetry, forces acting on the free-surface (including accounting for wind) and body forces (such as the Coriolis effect), are also included in the model in order to demonstrate that it is able to handle all external forces and effects. To solve the model, a Eulerian-Lagrangian finite volume method is used. A projection finite volume method is used for the Eulerian stage, then the method of characteristics is employed to approximate the numerical fluxes for the Lagrangian stage. This method is fast and offers new insights for shallow water flow modelling, with vertically stratified velocities and new simulations (such as recirculation) available for the first time. The presented formulation shows good correlation against both benchmark tests and novel simulations. The model is also assessed against the three-dimensional incompressible Navier-Stokes equations, providing faster results with minimal differences in accuracy. To this end, a lake at rest, a one-dimensional dam-break flow, a circular dam-break flow, and recirculation flow problems are all considered to illustrate the features and advantages of the proposed method.

This chapter is organised into five sections: Section 6.1 outlines the problem to be tackled and provides an overview of the work conducted to remedy it. Section 6.2 formulates the model, incorporating the crucial mass exchange terms. The numerical method used to solve the system is detailed in Section 6.3. Section 6.4 presents the numerical results from benchmark testing and novel simulations. A summary of the work is given in Section 6.5.

6.1 Motivation and background to a multilayer approach to modelling shallow water flows

Incompressible Navier-Stokes equations have been widely used in the literature to simulate water flows including eddy diffusion and Coriolis forces, see for example [50, 137, 176]. However, for free-surface flows these models frequently become complicated due to the presence of moving boundaries with the flow domain and the hydrostatic pressure. Under certain assumptions these models can be replaced by the well-established Shallow Water Equations (SWEs). The depth-averaged nature of the SWEs produces an advantage in terms of simplification and therein computational expense. However, they estimate flow less accurately than the three-dimensional (3D) Navier-Stokes equations, especially when considering changing bathymetry. The aim of this chapter is to develop a third option that lies between the traditional two-dimensional (2D) SWEs and the 3D Navier-Stokes equations.

As shallow water models have been well developed, attention has shifted to the shortcomings of this type of modelling, namely the use of single velocity profile for the entire depth of the fluid. A notable area of recent development is the creation of multilayer non-hydrostatic models for wave dynamics, see [60, 143] among others. This work takes a different formulation route as we aim to develop sediment transfer in later chapters and therefore must have terms that can accommodate the properties required to handle sediment transport. This has been solved with the recent introduction of multilayer SWEs for geophysical flows. The first variety of these models dealt with immiscible shallow fluids, handling their basic interactions. These fluids were able to be modelled with unique characteristics in each layer, see for example [5, 29, 82]. The attractive attribute of this class of models is that they avoid the computationally expensive methods required to solve the 3D Navier-Stokes equations, at the same time as providing stratified flow velocities. This has led to the development of the second class of model where the same principal has been applied to a single fluid, see for example [11, 13, 70]. Both classes of multilayer model are strongly linked, but it is the second class of model that obtains a more accurate solution to classical SWE problems. Through key choices, such as the number of layers, the single fluid multilayer model can be related to the isopycnal coordinates that are often used when solving the Navier-Stokes equations. What makes these models unique is the use of modified finite volume schemes for hyperbolic systems, which were originally adapted for classical SWEs. For the single fluid models, the hypothesis of the shallowness of the flow is overcome by the shallowness of the individual layers and the hydrostatic characteristics of the flow. Thus, as the number of layers becomes sufficiently large, the model tends to the hydrostatic Navier-Stokes equations. This chapter develops a method in the second category that is able to handle fluid exchange as well as the complex inter-layer interactions. By considering any flow as a system of individual flow layers, it is possible to generate a more accurate view of the flow at various depths. This overcomes the depth-averaged velocity assumption and allows for more accurate bottom layer speed estimation which is crucial to sediment transport. The inclusion of mass exchange and varying bathymetry allows for an estimate (at the post processing stage) of vertical velocities.

A fast Eulerian-Lagrangian Finite Volume (ELFV) method is used in 2D form and it is reformulated for use in multilayer problems. This is achieved by using a predictor-corrector method: in the predictor stage the Method of Characteristics (MoC) is used to reconstruct the numerical fluxes, and then the corrector stage recovers the conservative equations; furthermore it is fast due to its simplicity and it is also conservative. This numerical method is crucial to the viability of the model, as it does not require the solution of the Riemann problem. Note that the model is very complex and the estimation of its eigenvalues make it impossible to solve using most conventional methods. This approach results in some new considerations, including the number of layers to be used and the variables for inter-layer forces. The number of layers used to describe the fluid is of great importance: too few threaten the vertical resolution of the model, and too many will increase the computational expense unnecessarily. The coefficients used for the momentum exchange terms are also vital. If the velocity difference between any given two layers is too large, the whole momentum exchange term can threaten the hyperbolic nature of the system and even cause Kelvin-Helmholtz type instabilities. The results from four problems are presented to verity the considered multilayer shallow water model with varying bathymetry and flow conditions. In these examples, the method is verified against a Navier-Stokes simulation of the benchmark for a dam-break simulation and a 2D lake at rest problem over non-flat bathymetry. The novel ability of the shallow water system to demonstrate wind-driven circulation is also shown in this work. To the best knowledge of the author, simulation of 2D multilayer SWEs with exchange terms is presented for the first time.

6.2 Formulation of a two-dimensional multilayer shallow water model

A fluid column in a 3D domain over a variable bed is modelled, as shown in Figure 6.1. Multilayer SWEs have been derived from the 3D hydrostatic incompressible Navier-Stokes equations with unknown free-surface by considering the vertical P_0-type discretisation of the horizontal velocity. This vertical discretisation defines a series of layers in the flow domain and the equa-

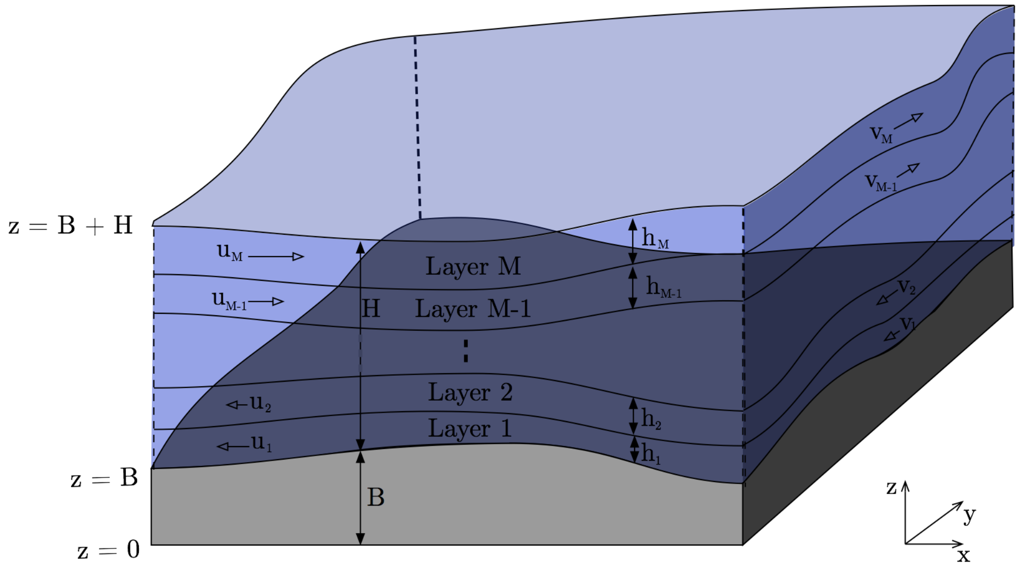

Figure 6.1: Sketch of the 2D fluid domain divided into M fluid layers.

tions are vertically integrated on each layer separately, compare [11, 13, 70] for more details on the steps used to derive these models. Here, we consider the 2D version of the model written in a conservative form as

$$\begin{aligned}
\frac{\partial h_\alpha}{\partial t} + \frac{\partial (h_\alpha u_\alpha)}{\partial x} + \frac{\partial (h_\alpha v_\alpha)}{\partial y} &= 0, \\
\frac{\partial (h_\alpha u_\alpha)}{\partial t} + \frac{\partial}{\partial x}\left(h_\alpha u_\alpha^2 + \frac{1}{2} g h_\alpha H\right) + \frac{\partial}{\partial y}\left(h_\alpha u_\alpha v_\alpha\right) &= -g h_\alpha \frac{\partial B}{\partial x} + \omega_c h_\alpha v_\alpha + F_\alpha, \qquad (6.2.1)\\
\frac{\partial (h_\alpha v_\alpha)}{\partial t} + \frac{\partial}{\partial x}\left(h_\alpha u_\alpha v_\alpha\right) + \frac{\partial}{\partial y}\left(h_\alpha v_\alpha^2 + \frac{1}{2} g h_\alpha H\right) &= -g h_\alpha \frac{\partial B}{\partial y} - \omega_c h_\alpha u_\alpha + G_\alpha,
\end{aligned}$$

where $h_\alpha(t, x, y)$ is the height of the αth layer, $u_\alpha(t, x, y)$ and $v_\alpha(t, x, y)$ are the depth-averaged velocities in the x and y-directions for the αth layer, g is the gravitational acceleration, ω_c is the Coriolis parameter resulting from rotation of the earth, and the bed height $B(t, x, y)$ is the topography of the basin. The water height of the whole flow system is denoted by $H(t, x, y)$ and l_α is the relative size of the αth layer, with

$$l_\alpha > 0, \qquad \sum_{\alpha=1}^{M} l_\alpha = 1.$$

The water height $h_\alpha(t, x, y)$ of the αth layer is defined as

$$h_\alpha = l_\alpha H, \qquad \alpha = 1, 2, \ldots M,$$

where M is the total number of layers in the flow domain, see Figure 6.1 for a simplified illustration of a multilayer shallow water flow system. In (6.2.1), the source term F_α is the external force in the x-direction acting on the αth layer and accounting for the friction and momentum exchange effects. Thus

$$F_\alpha = \mathcal{F}_\alpha^{(u)} + \mathcal{F}_\alpha^{(\nu)} + \mathcal{F}_\alpha^{(b)} + \mathcal{F}_\alpha^{(w)} + \mathcal{F}_\alpha^{(\mu)}, \qquad \alpha = 1, \ldots, M. \tag{6.2.2}$$

The external force in the y-direction G_α is accounted for similarly

$$G_\alpha = \mathcal{G}_\alpha^{(u)} + \mathcal{G}_\alpha^{(\nu)} + \mathcal{G}_\alpha^{(b)} + \mathcal{G}_\alpha^{(w)} + \mathcal{G}_\alpha^{(\mu)}, \qquad \alpha = 1, \ldots, M, \tag{6.2.3}$$

where:

- $\mathcal{F}_\alpha^{(u)}$ and $\mathcal{G}_\alpha^{(u)}$ estimate the momentum exchange between the layers
- $\mathcal{F}_\alpha^{(\nu)}$ and $\mathcal{G}_\alpha^{(\nu)}$ are due to the horizontal diffusion between layers
- $\mathcal{F}_\alpha^{(b)}$ and $\mathcal{G}_\alpha^{(b)}$ estimate the effects of bed friction on the system
- $\mathcal{F}_\alpha^{(w)}$ and $\mathcal{G}_\alpha^{(w)}$ add the effects of wind on the top layer to the system
- $\mathcal{F}_\alpha^{(\mu)}$ and $\mathcal{G}_\alpha^{(\mu)}$ are due to the effects of friction between the layers

For the sake of brevity, this section only details the force terms in the x-direction. Hence the x-direction momentum exchange term is defined as

$$\mathcal{F}_\alpha^{(u)} = u_{\alpha+1/2}\mathcal{E}_{\alpha+1/2}^x - u_{\alpha-1/2}\mathcal{E}_{\alpha-1/2}^x, \tag{6.2.4}$$

where the mass exchange terms $\mathcal{E}_{\alpha+1/2}^x$ are computed as

$$\mathcal{E}_{\alpha+1/2}^x = \begin{cases} 0, & \text{if} \quad \alpha = 0, \\ \displaystyle\sum_{\beta=1}^{\alpha} \left(\frac{\partial (h_\beta u_\beta)}{\partial x} - l_\beta \sum_{\gamma=1}^{M} \frac{\partial (h_\gamma u_\gamma)}{\partial x} \right), & \text{if} \quad \alpha = 1, \ldots, M-1, \\ 0, & \text{if} \quad \alpha = M, \end{cases}$$

and the interface velocity $u_{\alpha+1/2}$ in (6.2.4) is computed by a simple upwind method using the sign of the mass exchange term *i.e.*

$$u_{\alpha+1/2} = \begin{cases} u_\alpha, & \text{if} \quad \mathcal{E}_{\alpha+1/2}^x \geq 0, \\ u_{\alpha+1}, & \text{if} \quad \mathcal{E}_{\alpha+1/2}^x < 0. \end{cases}$$

The vertical kinematic eddy viscosity term $\mathcal{F}_\alpha^{(\mu)}$ takes into account the friction between neighbouring layers and it is defined as

$$\mathcal{F}_\alpha^{(\mu)} = \begin{cases} 2\nu \dfrac{u_2 - u_1}{(l_2 + l_1)\, H}, & \text{if} \quad \alpha = 1, \\[2ex] 2\nu \dfrac{u_{\alpha+1} - u_\alpha}{(l_{\alpha+1} + l_\alpha)\, H} - 2\nu \dfrac{u_\alpha - u_{\alpha-1}}{(l_\alpha + l_{\alpha-1})\, H}, & \text{if} \quad \alpha = 2, \dots, M-1, \\[2ex] -2\nu \dfrac{u_M - u_{M-1}}{(l_M + l_{M-1})\, H}, & \text{if} \quad \alpha = M, \end{cases}$$

where ν is the eddy viscosity. Note that a generalized derivation of the viscous tensor in multilayer SWEs has also been reported in [70]. The external friction terms in (6.2.2) are given by

$$\mathcal{F}_\alpha^{(b)} = \begin{cases} -\dfrac{\tau_{\mathrm{B}}^x}{\rho}, & \text{if} \quad \alpha = 1, \\[2ex] 0, & \text{if} \quad \alpha = 2, \dots, M, \end{cases} \qquad \mathcal{F}_\alpha^{(w)} = \begin{cases} 0, & \text{if} \quad \alpha = 1, \dots, M-1, \\[2ex] \dfrac{\tau_{wi}^x}{\rho}, & \text{if} \quad \alpha = M, \end{cases}$$

where ρ is the water density, and τ_{B}^x and τ_{wi}^x are respectively the bed shear stress and the shear of the blowing wind. These are defined by the water velocity and the wind velocity $U_{wi} = (U_{wi,x}, U_{wi,y})^T$ as

$$\tau_{\mathrm{B}}^x = \rho C_{\mathrm{B}} u_1 \sqrt{u_1^2 + v_1^2}, \qquad \tau_{wi}^x = \rho C_{wi} (U_{wi,x} - u_M) \sqrt{(U_{wi,x} - u_M)^2 + (U_{wi,y} - v_M)^2},$$

where C_{B} is the bed friction coefficient, which may either be set as a constant or estimated using the Manning equation as

$$C_{\mathrm{B}} = \frac{g n_m^2}{H^{1/3}}, \qquad C_{wi} = \frac{\sigma^2 \rho_a}{H},$$

where n_m is the Manning roughness coefficient of the bed, and the wind friction coefficient C_w is defined as in [159]. The wind stress coefficient is designated by σ, and ρ_a is the air density. The horizontal diffusion terms $\mathcal{F}_\alpha^{(\nu)}$ in (6.2.2) are defined as

$$\mathcal{F}_\alpha^{(\nu)} = \nu_H \frac{\partial}{\partial x} \left(h_\alpha \frac{\partial u_\alpha}{\partial x} \right) + \nu_H \frac{\partial}{\partial y} \left(h_\alpha \frac{\partial u_\alpha}{\partial y} \right), \qquad \alpha = 1, 2, \dots, M, \tag{6.2.5}$$

where ν_H is the horizontal viscosity coefficient. To aid in the manipulation of the equations (6.2.1), they are presented in compact vector form

$$\frac{\partial \mathbf{W}}{\partial t} + \frac{\partial \mathbf{F}(\mathbf{W})}{\partial x} + \frac{\partial \mathbf{G}(\mathbf{W})}{\partial y} = \mathbf{Q}(\mathbf{W}) + \mathbf{R}(\mathbf{W}), \tag{6.2.6}$$

where $\mathbf{W}$ is the vector of conserved variables, $\mathbf{F}(\mathbf{W})$ and $\mathbf{G}(\mathbf{W})$ are the vectors of the flux functions, $\mathbf{Q}(\mathbf{W})$ and $\mathbf{R}(\mathbf{W})$ are the vectors of the source terms, such that

$$\mathbf{W} = \begin{pmatrix} H \\ h_1u_1 \\ h_2u_2 \\ \vdots \\ h_Mu_M \\ h_1v_1 \\ h_2v_2 \\ \vdots \\ h_Mv_M \end{pmatrix}, \quad \mathbf{F}(\mathbf{W}) = \begin{pmatrix} \displaystyle\sum_{\alpha=1}^{M} h_\alpha u_\alpha \\ h_1u_1^2 + \frac{1}{2}gh_1H \\ h_2u_2^2 + \frac{1}{2}gh_2H \\ \vdots \\ h_Mu_M^2 + \frac{1}{2}gh_MH \\ h_1u_1v_1 \\ h_2u_2v_2 \\ \vdots \\ h_Mu_Mv_M \end{pmatrix}, \quad \mathbf{G}(\mathbf{W}) = \begin{pmatrix} \displaystyle\sum_{\alpha=1}^{M} h_\alpha v_\alpha \\ h_1u_1v_1 \\ h_2u_2v_2 \\ \vdots \\ h_Mu_Mv_M \\ h_1v_1^2 + \frac{1}{2}gh_1H \\ h_2v_2^2 + \frac{1}{2}gh_2H \\ \vdots \\ h_Mv_M^2 + \frac{1}{2}gh_MH \end{pmatrix},$$

$$\mathbf{Q}(\mathbf{W}) = \begin{pmatrix} 0 \\ -gh_1\dfrac{\partial B}{\partial x} + \omega_c h_1 v_1 \\ -gh_2\dfrac{\partial B}{\partial x} + \omega_c h_2 v_2 \\ \vdots \\ -gh_M\dfrac{\partial B}{\partial x} + \omega_c h_M v_M \\ -gh_1\dfrac{\partial B}{\partial y} - \omega_c h_1 u_1 \\ -gh_2\dfrac{\partial B}{\partial y} - \omega_c h_2 u_2 \\ \vdots \\ -gh_M\dfrac{\partial B}{\partial y} - \omega_c h_M u_M \end{pmatrix}, \quad \mathbf{R}(\mathbf{W}) = \begin{pmatrix} 0 \\ \mathcal{F}_1^{(u)} + \mathcal{F}_1^{(b)} + \mathcal{F}_1^{(w)} + \mathcal{F}_1^{(\mu)} + \mathcal{F}_1^{(\nu)} \\ \mathcal{F}_2^{(u)} + \mathcal{F}_2^{(b)} + \mathcal{F}_2^{(w)} + \mathcal{F}_2^{(\mu)} + \mathcal{F}_2^{(\nu)} \\ \vdots \\ \mathcal{F}_M^{(u)} + \mathcal{F}_M^{(b)} + \mathcal{F}_M^{(w)} + \mathcal{F}_M^{(\mu)} + \mathcal{F}_M^{(\nu)} \\ \mathcal{G}_1^{(u)} + \mathcal{G}_1^{(b)} + \mathcal{G}_1^{(w)} + \mathcal{G}_1^{(\mu)} + \mathcal{G}_1^{(\nu)} \\ \mathcal{G}_2^{(u)} + \mathcal{G}_2^{(b)} + \mathcal{G}_2^{(w)} + \mathcal{G}_2^{(\mu)} + \mathcal{G}_2^{(\nu)} \\ \vdots \\ \mathcal{G}_M^{(u)} + \mathcal{G}_M^{(b)} + \mathcal{G}_M^{(w)} + \mathcal{G}_M^{(\mu)} + \mathcal{G}_M^{(\nu)} \end{pmatrix}.$$

6.3 The Eulerian-Lagrangian method for multilayer flow

To solve the system (6.2.6) the method uses a second-order splitting, proposed in studies like [217]. To integrate with respect to time, the time interval is divided into sub-intervals $[t_n, t_{n+1}]$ with length $\Delta t = t_{n+1} - t_n$. The notation $\mathbf{W}^n$ is used to denote the value of a generic function $\mathbf{W}$ at time t_n. A splitting method as considered in (5.4.9) - (5.4.11) detailed on page 138 is implemented. In complex flow situations, the solutions of the eigenvalues are non-trivial and can yield complex results. Thus, the model can quickly become non-hyperbolic and even yield Kelvin-Helmholtz instabilities. Consequently, a Eulerian-Lagrangian method is utilized which does not require the calculation of the eigenvalues. The size of the time-step can be refined using the eigenvalues associated with the single-layer shallow water counterparts, defined by

$$\lambda_\alpha^\pm = u_\alpha \pm \sqrt{gH}, \qquad \mu_\alpha^\pm = v_\alpha \pm \sqrt{gH}, \qquad\qquad \alpha = 1, 2 \ldots, M. \tag{6.3.7}$$

The time-step estimation can be further improved by using the maximum wave speed for the multilayer shallow water system.

6.3.1 The Eulerian step

In order to discretise the stage (5.4.10) the spatial domain is divided into control volumes $V_{ij} = [x_{i-1/2,j}, x_{i+1/2,j}] \times [y_{i,j-1/2}, y_{i,j+1/2}]$ as shown in Figure 5.5. As detailed, the volumes V_{ij} are centred at $(x_{i,j}, y_{i,j})$ with uniform sizes Δx and Δy. We use the following notations

$$\mathbf{W}_{i\pm\frac{1}{2},j}(t) = \mathbf{W}(t, x_{i\pm\frac{1}{2}}, y_j), \qquad \mathbf{W}_{i,j\pm\frac{1}{2}}(t) = \mathbf{W}(t, x_i, y_{j\pm\frac{1}{2}}),$$

and

$$\mathbf{W}_{i,j}(t) = \frac{1}{\Delta x}\frac{1}{\Delta y}\int_{x_{i-\frac{1}{2}}}^{x_{i+\frac{1}{2}}}\int_{y_{j-\frac{1}{2}}}^{y_{i+\frac{1}{2}}} \mathbf{W}(t, x, y)\; dydx,$$

to denote the point-values and cell-average of the variable $\mathbf{W}$ at the gridpoint $(t, x_{i\pm\frac{1}{2}}, y_j)$, $(t, x_i, y_{j\pm\frac{1}{2}})$ and (t, x_i, y_j), respectively. By integrating the equation (5.4.10) in space over the control volume $V_{i,j}$ shown in Figure 5.5, the following semi-discrete equations are obtained

$$\frac{d\mathbf{W}_{i,j}}{dt} + \frac{\mathbf{F}_{i+1/2,j} - \mathbf{F}_{i-1/2,j}}{\Delta x} + \frac{\mathbf{G}_{i,j+1/2} - \mathbf{G}_{i,j-1/2}}{\Delta y} = \mathbf{Q}_{i,j}, \tag{6.3.8}$$

where $\mathbf{F}_{i\pm1/2,j} = \mathbf{F}(\mathbf{W}_{i\pm1/2,j})$ and $\mathbf{G}_{i,j\pm1/2} = \mathbf{G}(\mathbf{W}_{i,j\pm1/2})$ are the numerical fluxes at the cell interfaces $x = x_{i\pm1/2}$ and $y = y_{i\pm1/2}$. By using divergence theorem to integrate the control volume V_{ij}, the basic equations of the Finite Volume Method (FVM) are recovered thus

$$\begin{aligned}
\frac{\partial}{\partial t}\int_{V_{i,j}} H\,dV + \sum_{\alpha=1}^{M}\oint_{\mathcal{S}_{i,j}} \Big(h_\alpha u_\alpha \mathbf{n}_x + h_\alpha v_\alpha \mathbf{n}_y\Big)\,d\sigma &= 0,\\
\frac{\partial}{\partial t}\int_{V_{i,j}} h_\alpha u_\alpha\,dV + \oint_{\mathcal{S}_{i,j}} \left(\left(h_\alpha u_\alpha^2 + \frac{1}{2}gh_\alpha H\right)\mathbf{n}_x + h_\alpha u_\alpha v_\alpha \mathbf{n}_y\right)d\sigma &= -gh_\alpha \oint_{\mathcal{S}_{i,j}} B\mathbf{n}_x\,d\sigma +\\
&\qquad \int_{V_{i,j}} \omega_c h_\alpha v_\alpha\,dV,\\
\frac{\partial}{\partial t}\int_{V_{i,j}} h_\alpha v_\alpha\,dV + \oint_{\mathcal{S}_{i,j}} \left(h_\alpha u_\alpha v_\alpha \mathbf{n}_x + \left(h_\alpha v_\alpha^2 + \frac{1}{2}gh_\alpha H\right)\mathbf{n}_y\right)d\sigma &= -gh_\alpha \oint_{S_i} B\mathbf{n}_y\,d\sigma -\\
&\qquad \int_{V_{i,j}} \omega_c h_\alpha u_\alpha\,dV,
\end{aligned}$$

where $\boldsymbol{\eta} = (\mathbf{n}_x, \mathbf{n}_y)^T$ denotes the unit outward normal to the surface $\mathcal{S}_{i,j}$ of the control volume V_{ij}. Using the local cell outward normal $\boldsymbol{\eta}$ and tangential $\boldsymbol{\tau} = \boldsymbol{\eta}^\perp$ depicted in Figure 5.5 on page 140, the above equations can be projected as

$$\frac{\partial}{\partial t}\int_{V_{i,j}} H\,dV + \sum_{\alpha=1}^{M}\oint_{\mathcal{S}_{i,j}} h_\alpha u_{\alpha,\boldsymbol{\eta}}\,d\sigma = 0, \tag{6.3.9a}$$

$$\frac{\partial}{\partial t}\int_{V_{i,j}} h_\alpha u_\alpha\,dV + \oint_{\mathcal{S}_{i,j}} \left(h_\alpha u_\alpha u_{\alpha,\boldsymbol{\eta}} + \frac{1}{2}gh_\alpha H\mathbf{n}_x\right)d\sigma = -gh_\alpha \oint_{S_i} B\mathbf{n}_x\,d\sigma + \int_{V_{i,j}} \omega_c h_\alpha v_\alpha\,dV, \tag{6.3.9b}$$

$$\frac{\partial}{\partial t}\int_{V_{i,j}} h_\alpha v_\alpha\,dV + \oint_{\mathcal{S}_{i,j}} \left(h_\alpha v_\alpha u_{\alpha,\boldsymbol{\eta}} + \frac{1}{2}gh_\alpha H\mathbf{n}_y\right)d\sigma = -gh_\alpha \oint_{S_i} B\mathbf{n}_y\,d\sigma - \int_{V_{i,j}} \omega_c h_\alpha u_\alpha\,dV, \tag{6.3.9c}$$

where the normal projected velocity $u_{\alpha,\boldsymbol{\eta}} = u_\alpha \mathbf{n}_x + v_\alpha \mathbf{n}_y$ and the tangential projected velocity $u_{\alpha,\boldsymbol{\tau}} = v_\alpha \mathbf{n}_x - u_\alpha \mathbf{n}_y$. In order to simplify the system (6.3.9), first equation (6.3.9b) multiplied by $\mathbf{n}_x$ is summed to the equation (6.3.9c) multiplied by $\mathbf{n}_y$, then equation (6.3.9b) multiplied by $\mathbf{n}_y$ is subtracted from the equation (6.3.9c) multiplied by $\mathbf{n}_x$. These operations result in

$$\begin{aligned}
\frac{\partial}{\partial t}\int_{V_{i,j}} H\,dV + \sum_{\alpha=1}^{M}\oint_{\mathcal{S}_{i,j}} h_\alpha u_{\alpha,\boldsymbol{\eta}}\,d\sigma &= 0,\\
\frac{\partial}{\partial t}\int_{V_{i,j}} h_\alpha u_{\alpha,\boldsymbol{\eta}}\,dV + \oint_{\mathcal{S}_{i,j}} \left(h_\alpha u_{\alpha,\boldsymbol{\eta}} u_{\alpha,\boldsymbol{\eta}} + \frac{1}{2}gh_\alpha H\right)d\sigma &= -gl_\alpha H \oint_{S_i} B\,d\sigma + \int_{V_{i,j}} \omega_c h_\alpha u_{\alpha,\boldsymbol{\tau}}\,dV,\\
\frac{\partial}{\partial t}\int_{V_{i,j}} h_\alpha u_{\alpha,\boldsymbol{\tau}}\,dV + \oint_{\mathcal{S}_{i,j}} h_\alpha u_{\alpha,\boldsymbol{\tau}} u_{\alpha,\boldsymbol{\eta}}\,d\sigma &= -\int_{V_{i,j}} \omega_c h_\alpha u_{\alpha,\boldsymbol{\eta}}\,dV,
\end{aligned}$$

which can be rewritten in a differential form as

$$\begin{aligned}
\frac{\partial H}{\partial t}+\sum_{\alpha=1}^{M}\frac{\partial\left(h_\alpha u_{\alpha,\boldsymbol{\eta}}\right)}{\partial\boldsymbol{\eta}} &= 0,\\
\frac{\partial\left(h_\alpha u_{\alpha,\boldsymbol{\eta}}\right)}{\partial t}+\frac{\partial}{\partial\boldsymbol{\eta}}\left(h_\alpha u_{\alpha,\boldsymbol{\eta}}^2+\frac{1}{2}gh_\alpha H\right) &= -gh_\alpha\frac{\partial B}{\partial\boldsymbol{\eta}}-\omega_c h_\alpha u_{\alpha,\boldsymbol{\tau}},\\
\frac{\partial\left(h_\alpha u_{\alpha,\boldsymbol{\tau}}\right)}{\partial t}+\frac{\partial}{\partial\boldsymbol{\eta}}\left(h_\alpha u_{\alpha,\boldsymbol{\eta}}u_{\alpha,\boldsymbol{\tau}}\right) &= \omega_c h_\alpha u_{\alpha,\boldsymbol{\eta}}.
\end{aligned} \tag{6.3.10}$$

The system (6.3.10) can also be reformulated in a non-conservative form as

$$\begin{aligned}
\frac{D_0 H}{Dt}+\sum_{\alpha=1}^{M}h_\alpha\frac{\partial u_{\alpha,\boldsymbol{\eta}}}{\partial\boldsymbol{\eta}} &= 0,\\
\frac{D_\alpha u_{\alpha,\boldsymbol{\eta}}}{Dt}+g\frac{\partial H}{\partial\boldsymbol{\eta}} &= -g\frac{\partial B}{\partial\boldsymbol{\eta}}-\omega_c u_{\alpha,\boldsymbol{\tau}},\\
\frac{D_\alpha u_{\alpha,\boldsymbol{\tau}}}{Dt}+u_{\alpha,\boldsymbol{\tau}}\frac{\partial u_{\alpha,\boldsymbol{\eta}}}{\partial\boldsymbol{\eta}} &= \omega_c u_{\alpha,\boldsymbol{\eta}},
\end{aligned} \tag{6.3.11}$$

where $\frac{D_\zeta}{Dt}$ is the total material derivative defined as

$$\frac{D_\zeta}{Dt}=\frac{\partial}{\partial t}+U_\zeta\frac{\partial}{\partial\boldsymbol{\eta}},\qquad \zeta=0,1,\ldots,M,$$

with

$$U_\zeta=\begin{cases}\displaystyle\sum_{\alpha=1}^{M}l_\alpha u_{\alpha,\boldsymbol{\eta}}, & \text{if}\quad \zeta=0,\\[2ex] u_{\zeta,\boldsymbol{\eta}}, & \text{if}\quad \zeta=1,2,\ldots,M.\end{cases}$$

Notice that the above projection techniques simplify the solution of 2D SWEs (6.2.6) in the control volume $V_{i,j}$ to the solution of one-dimensional (1D) system (6.3.11) on each surface $\mathcal{S}_{i,j}$ of this control volume. A similar projection procedure has been proposed in [24] among others. It should be stressed that the projected system (6.3.11) is used in our approach only to reconstruct the numerical fluxes in the ELFV solution of the conservative system (6.2.6).

6.3.2 The Lagrangian step

The modified MoC is applied to the projected system (6.3.8) in order to solve for the numerical fluxes $\mathbf{F}_{i\pm1/2,j}$ and $\mathbf{G}_{i,j\pm1/2}$. A regular grid is imposed at the next time-step and the flow trajectories are backtracked to the previous time levels, as with [144,157]. The solutions for the characteristic foot are calculated using interpolation from the known grid at the prior time-step. Thus, a solution can be found for each layer ζ at the gridpoint $(x_{i+1/2},y_j)$. The characteristic curves $X_{\zeta,i+1/2}(s)$ associated with the equations (6.3.11) are produced by solving the initial-value problems

$$\begin{aligned} \frac{dX_{\zeta,i+1/2}(s)}{ds} &= U_\zeta\Big(s, X_{\zeta,i+1/2}(s), Y_j\Big), \qquad s \in [t_n, t_{n+1}], \\ X_{\zeta,i+1/2}(t_{n+1}) &= x_{\zeta,i+1/2}, \end{aligned} \tag{6.3.12}$$

with equivalent initial-value problems for the characteristic curves $Y_{\zeta,j+1/2}(s)$ related to the gridpoint $(x_i, y_{j+1/2})$, which may be expressed as

$$\begin{aligned} \frac{dY_{\zeta,j+1/2}(s)}{ds} &= U_{\zeta,}\Big(s, X_i, Y_{\zeta,j+1/2}(s)\Big), \qquad s \in [t_n, t_{n+1}], \\ Y_{\zeta,j+1/2}(t_{n+1}) &= y_{\zeta,j+1/2}. \end{aligned} \tag{6.3.13}$$

The curves are calculated by considering a particle travelling along them from one time-step to another. Therefore $(X_{\zeta,i+1/2}(s), Y_{\zeta,j})$ and $(X_{\zeta,i}, Y_{\zeta,j+1/2}(s))$ are the departure points at time s of a particle that will arrive in the time t_{n+1} at the gridpoint $(x_{i+1/2}, y_j)$ and $(x_i, y_{j+1/2})$ respectively, as shown in Figure 5.6. Once the characteristic curves $X_{\zeta,i+1/2}(t_n)$ and $Y_{\zeta,j+1/2}(t_n)$ are known for all layers, the intermediate solutions $\mathbf{W}^n_{i+1/2,j}$ and $\mathbf{W}^n_{i,j+1/2}$ of a function $\mathbf{W}$ are reconstructed using

$$\mathbf{W}^n_{i+1/2,j} = \widehat{\mathbf{W}}^n_{i+1/2,j}, \qquad \mathbf{W}^n_{i,j+1/2} = \widehat{\mathbf{W}}^n_{i,j+1/2}, \tag{6.3.14}$$

where $\widehat{\mathbf{W}}^n_{i+1/2,j}$ represents the combined solutions at the departure points obtained for each layer by interpolation from the gridpoints of the control volumes, see Figure 5.6. For example, a Lagrange-based interpolation polynomial can be formulated as

$$\widehat{\mathbf{W}}^n_{i+1/2,j} = \sum_{k,l} \mathcal{L}_{k,l}\left(X_{i+1/2}, Y_j\right) \mathbf{W}^n_{k,l}, \qquad \widehat{\mathbf{W}}^n_{i,j+1/2} = \sum_{k,l} \mathcal{L}_{k,l}\left(X_i, Y_{j+1/2}\right) \mathbf{W}^n_{k,l}, \tag{6.3.15}$$

where $\mathcal{L}_{k,l}$ are the Lagrange polynomials defined as

$$\mathcal{L}_{k,l}(x,y) = \prod_{\substack{p=0 \\ p\neq k}} \prod_{\substack{q=0 \\ q\neq l}} \frac{x - x_p}{x_k - x_p} \frac{y - y_q}{y_l - y_q}.$$

Other high-order interpolation methods can also be used in (6.3.15). Assuming that the departure points $(X_{\zeta,i+1/2}(t_n), Y_{\zeta,j})$ and $(X_{\zeta,i}, Y_{\zeta,j+1/2}(t_n))$ are accurately approximated, the predictor stage in the Eulerian-Lagrangian method applied to the multilayer SWEs is defined by the solution of the system (6.3.11) as

$$\begin{aligned}
H^n_{i+1/2,j} &= \widehat{H}^n_{i+1/2,j} - \frac{\Delta t}{\Delta x}\widehat{h}^n_{\alpha,i+1/2,j}\left((u_{\alpha,\boldsymbol{\eta}})^n_{i+1,j} - (u_{\alpha,\boldsymbol{\eta}})^n_{i,j}\right),\\
(u_{\alpha,\boldsymbol{\eta}})^n_{i+1/2,j} &= (\widehat{u}_{\alpha,\boldsymbol{\eta}})^n_{i+1/2,j} - g\frac{\Delta t}{\Delta x}\left((H+B)^n_{i+1,j} - (H+B)^n_{i,j}\right) - \Delta t\omega_c\left(\widehat{u}_{\alpha,\boldsymbol{\tau}}\right)^n_{i+1/2,j},\\
(u_{\alpha,\boldsymbol{\tau}})^n_{i+1/2,j} &= (\widehat{u}_{\alpha,\boldsymbol{\tau}})^n_{i+1/2,j} - \frac{\Delta t}{\Delta x}(\widehat{u}_{\alpha,\boldsymbol{\tau}})^n_{i+1/2,j}\left((u_{\alpha,\boldsymbol{\eta}})^n_{i+1,j} - (u_{\alpha,\boldsymbol{\eta}})^n_{i,j}\right) + \Delta t\omega_c\left(\widehat{u}_{\alpha,\boldsymbol{\eta}}\right)^n_{i+1/2,j},
\end{aligned} \tag{6.3.16}$$

where

$$\widehat{H}^n_{i+1/2,j} = H\left(t_n, X_{\alpha,i+1/2}(t_n), y_j\right), \qquad (\widehat{u}_{\alpha,\boldsymbol{\eta}})^n_{i+1/2,j} = u_{\alpha,\boldsymbol{\eta}}\left(t_n, X_{\alpha,i+1/2}(t_n), y_j\right),$$
$$(\widehat{u}_{\alpha,\boldsymbol{\tau}})^n_{i+1/2,j} = u_{\alpha,\boldsymbol{\tau}}\left(t_n, X_{\alpha,i+1/2}(t_n), y_j\right).$$

The intermediate states in the y-direction $H^n_{i,j+1/2}$, $(u_{\alpha,\boldsymbol{\eta}})^n_{i,j+1/2}$ and $(u_{\alpha,\boldsymbol{\tau}})^n_{i,j+1/2}$ are evaluated in the same manner. Once the projected states are calculated in the predictor stage (6.3.16), the states $\mathbf{W}^n_{i\pm1/2,j}$ and $\mathbf{W}^n_{i,j\pm1/2}$ are recovered by using the transformations $v_\alpha = (u_{\alpha,\boldsymbol{\tau}}, u_{\alpha,\boldsymbol{\eta}})\cdot\boldsymbol{\eta}$ and $u_\alpha = (u_{\alpha,\boldsymbol{\tau}}, u_{\alpha,\boldsymbol{\eta}})\cdot\boldsymbol{\tau}$. Finally, the discretisation of source terms $\mathbf{Q}_{i,j}$ in (6.3.8) is carried out such that they are well-balanced with the discretisation of flux gradients using the concept of C-property, see for example [12, 23, 24]. A numerical scheme is said to satisfy the C-property for the equations (6.2.6) if the condition

$$B^{(0)} = B^n, \qquad H^n + B = cte, \qquad u^n_\alpha = v^n_\alpha = 0, \qquad \alpha = 1, 2, \ldots, M, \tag{6.3.17}$$

is satisfied for stationary flows at rest and *cte* is a constant. Therefore, the treatment of source terms $\mathbf{Q}_{i,j}$ in (6.3.8) is reconstructed such that the condition (6.3.17) is preserved at the discretised level. Following the same steps as in [12, 24], and similar to that carried out in Chapter 5 (on page 138), the discretisation of the terms in (6.3.8) is carried out as

$$\begin{aligned}
\left(gh_\alpha\frac{\partial B}{\partial x}\right)^n_{i,j} &= g\frac{(h_\alpha)^n_{i+1/2,j} + (h_\alpha)^n_{i-1/2,j}}{2}\,\frac{B^n_{i+1,j} - B^n_{i-1,j}}{2\Delta x},\\
\left(gh_\alpha\frac{\partial B}{\partial y}\right)^n_{i,j} &= g\frac{(h_\alpha)^n_{i,j+1/2} + (h_\alpha)^n_{i,j-1/2}}{2}\,\frac{B^n_{i,j+1} - B^n_{i,j-1}}{2\Delta y},
\end{aligned}$$

where the averaged solutions are defined by

$$(h_\alpha)^n_{i+1/2,j} = \frac{(h_\alpha)^n_{i+1,j} + (h_\alpha)^n_{i,j}}{2}, \qquad (h_\alpha)^n_{i,j+1/2} = \frac{(h_\alpha)^n_{i,j+1} + (h_\alpha)^n_{i,j}}{2}.$$

This formulation employs the projection of the shallow water model into a local system for each layer.This procedure is implemented as shown in Figure 6.2.

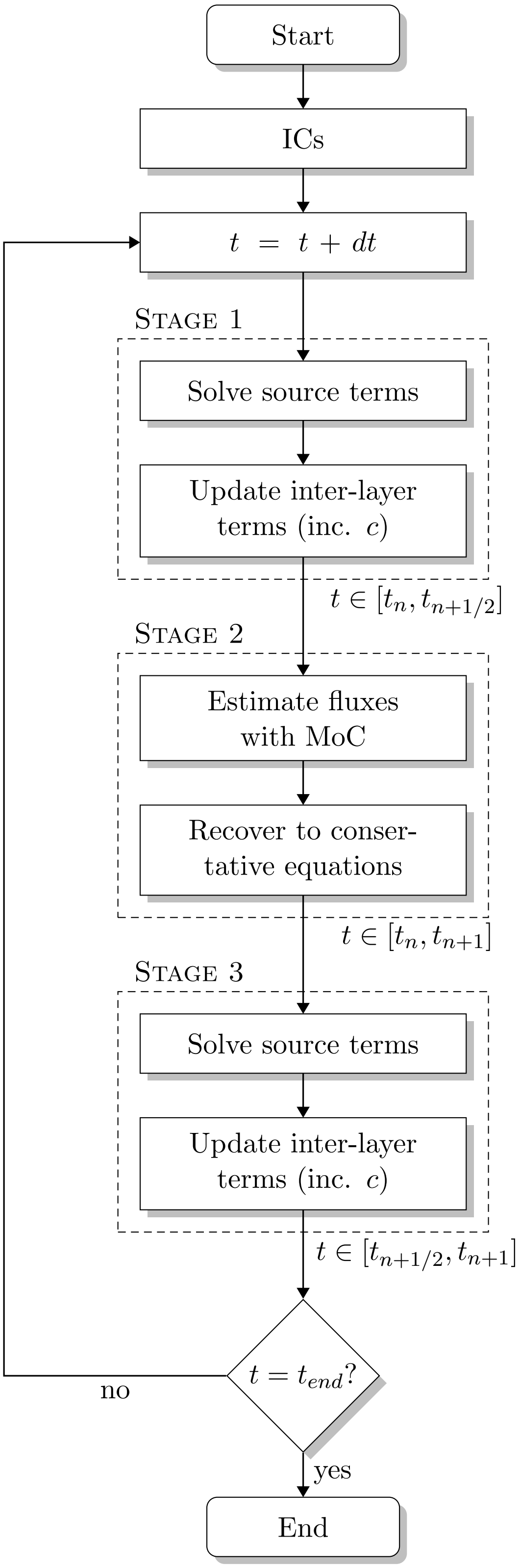

Figure 6.2: A flowchart demonstrating the stages in the proposed 2D Eulerian-Lagrangian procedure, including bed register is highlighted.

6.4 Numerical results

In this section, numerical results for several test problems in 2D multilayer shallow water flows are presented to check the accuracy and the performance of the proposed ELFV method. First, this study examines the conservation property of the method and then compares the obtained results for a dam-break problem to those using the 3D Navier-Stokes equations. A class of wind-driven recirculation problems in closed water domains are also solved, and the simulated velocity profiles are compared to those analytically calculated in [159]. In all the computations, the water heights h_α of the layers are defined using equal fractions such that

$$h_\alpha = l_\alpha H, \qquad \text{with} \qquad l_\alpha = \frac{1}{M}, \qquad \alpha = 1, \ldots, M.$$

In addition, a fixed Courant number Cr = 0.8 is used, the time-step Δt varies according to the stability condition

$$\Delta t = \mathrm{Cr} \frac{\min\left(\Delta x, \Delta y\right)}{\max\limits_{\alpha=1,\ldots,M} \left(|\lambda_\alpha^{\pm}|, |\ \mu_\alpha^{\pm}|\right)}.$$

In this chapter, the 3D velocity fields are generated from the 2D results using a similar post-processing procedure to that reported in [12, 13]. Hence, the vertical velocity w is recovered from the divergence-free condition

$$\frac{\partial u}{\partial x} + \frac{\partial v}{\partial y} + \frac{\partial w}{\partial z} = 0. \tag{6.4.18}$$

Integrating the equation (6.4.18) over a control volume yields

$$w_{\alpha+1,i,j}^{n} = w_{\alpha,i,j}^{n} + \Delta z \left(\frac{u_{\alpha,i+1/2,j}^{n} - u_{\alpha,i-1/2,j}^{n}}{\Delta x} + \frac{v_{\alpha,i,j-1/2}^{n} - v_{\alpha,i,j+1/2}^{n}}{\Delta y} \right), \tag{6.4.19}$$

where $\Delta z = \dfrac{h_{\alpha+1} + h_\alpha}{2}$. At bed-level, an impenetrable boundary condition is implemented. A similar procedure has also been used in [70] for 1D multilayer SWEs.

6.4.1 Lake at rest flow problem

Lake at rest flow has been introduced in [25] to check the well-balanced property of a FVM for single-layer 1D SWEs. In this example we reconstruct a similar test problem but use 2D shallow water flows instead. The idea relies on using the Kronecker tensor product of the 1D bed proposed in [25] in the x and y-direction. Hence, we solve the SWEs (6.2.1) with source

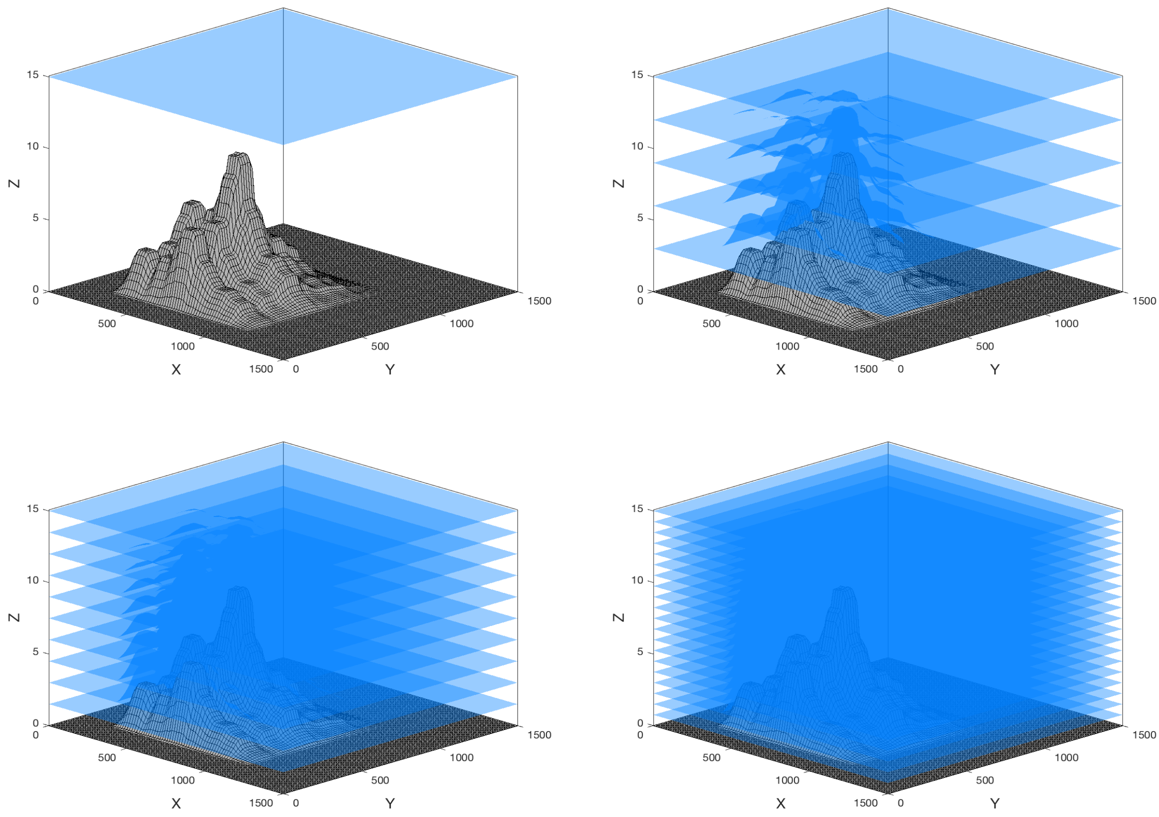

Figure 6.3: Water free-surface and interfaces for the multilayer flow at rest problem, at time $t = 10800\ s$ using different layers in the model.

terms associated with the bed only, *i.e.* $\omega_c = 0$ and $F_\alpha = G_\alpha = 0$ and the bed is defined as

$$B(x, y) = \frac{2}{7}\mathcal{B}(x) \otimes \mathcal{B}(y),$$

where $\mathcal{B}$ is the 1D bed defined in [25] and $\otimes$ is the Kronecker (or tensor) product of the two vectors

$$\underset{(m\times p)\times(n\times q)}{\boldsymbol{\mathcal{A}}} = \underset{m\times n}{\boldsymbol{\mathcal{C}}} \otimes \underset{p\times q}{\boldsymbol{\mathcal{D}}}$$

with elements defined by

$$c_{\alpha\beta} = a_{ij} b_{kl},$$

where

$$\alpha = p(i-1) + k, \qquad \beta = q(j-1) + l.$$

The problem is solved in a squared domain with a length of 1500 m and the results are presented at time $t = 10800\ s$, as in [25]. In practice, the total water free-surface must remain

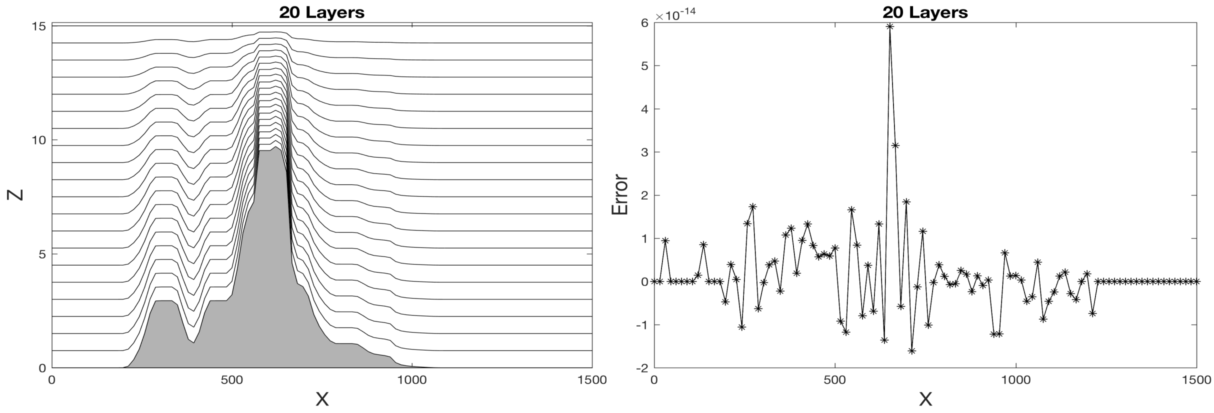

Figure 6.4: Cross-sections at time $t = 10800$ s along the main diagonal ($y = x$). The water free-surface and interfaces for the 20-layer flow problem at rest (left) and the associated error in the water free-surface (right).

constant and the water velocity should be zero at all times. However, many numerical methods fail to preserve these conditions at the discrete level. In Figure 6.3 we present the results obtained for water free-surface and interfaces using a mesh with 100 × 100 gridpoints and 5-layer, 10-layer, and 20-layer models. We also include results obtained using the conventional single-layer SWEs. As expected, the water free-surface remains constant along the simulations times for all considered models and no disturbances have been detected over the irregular 2D bed. In addition, increasing the number of layers in the model has not led to a deterioration of the response of the water free-surface in the lake. Figure 6.4 presents the cross-section along the main diagonal ($y = x$) of the results obtained for the 20-layer model, as well as the error in the water free-surface as a difference between the numerical and analytical solutions. It is clear from the results presented in Figure 6.4 that the ELFV method preserves the constant water free-surface and the errors are practically zero to the machine precision. This confirms that the proposed method is well-balanced and able accurately to resolve 2D multilayer shallow water flows over a non-flat bottom without relying on complex techniques to balance the discretisations of source terms and flux gradients.

6.4.2 Dam-break problem on a fixed bed

Dam-break problems have been mainly modelled using single-layer SWEs, but recently in [11,12] 1D multilayer shallow water formulations have been used to simulate a dam-break over a flat bottom. In this example we consider the 2D version of this problem in order to compare our results to those obtained using its 1D counterpart. Thus, we solve the multilayer shallow water system (6.2.1) in a flat rectangular channel of length 100 m and width 10 m subject to the following initial conditions

$$H(0,x,y)=\begin{cases}2\ m, & \text{if } x\leq 0\ m,\\ 1\ m, & \text{if } x>0\ m,\end{cases}\qquad B(0,x,y)=0\ m,\quad u(0,x,y,z)=v(0,x,y,z)=0\ m/s.$$

Wind effects and Coriolis forces are neglected in this test example and the same parameters as those used for the 1D case in [12, 13] are implemented. The viscosity coefficient $\nu = 0.01$, acceleration due to gravity $g = 2\ m/s^2$, and the friction coefficient $\kappa = 0.1$ are used, and the results are presented at time $t = 14\ s$. The results obtained for this problem, using the ELFV method, are also compared to those calculated with the 3D Navier-Stokes equations with free-surface conditions as published in [73].

Figure 6.5 presents the water free-surface and interfaces for the 5-layer, 10-layer and 20-layer models are compared to a 1-layer model, at time $t = 14$ using a mesh with 100×20 grid-points. This demonstrates the advantages of the multilayer model, as it is clear to see in 6.5 the multilayer models offer a huge advantage in flow fidelity. As in all dam-break problems, at $t = 0$ the dam breaks and the flow problem consists of a shock wave propagating downstream and a rarefaction wave propagating upstream. The proposed ELFV method captures these flow patterns without generating spurious oscillations around the shock. Under the considered dam-break conditions, it seems that the number of layers in the model has little effect on the flow features; compare the water free-surface profiles obtained for 5-layer and 20-layer models in Figure 6.5. To further emphasis these effects, we display in Figure 6.6 horizontal cross-sections of the water free-surface and water velocity at $y = 5$ for the 5-layer, 10-layer and 20-layer models. For comparison reasons we also include in Figure 6.6 the results obtained using the 1D counterparts. As can be seen from these results there is a difference between 2D results and their 1D counterparts. It seems that the 2D results are more diffusive than the 1D results at the rarefaction zone, but that at the shock zone the 2D results look sharper than their 1D counterparts. We observe the fluctuation at the hydraulic jump in the results presented in Figure 6.6 which has also been detected in the 3D results obtained using the full Navier-Stokes simulations in [12].

Following the same ideas reported in [12], in Figure 6.7 the results obtained using the presented 2D multilayer shallow water model are compared to those obtained using the 3D Navier-Stokes equations. In this figure, the velocity profiles at the location $(x = 8, y = 5)$ at time $t = 14\ s$ are presented for the 5-layer, 10-layer, and 20-layer models on a mesh with 100×20 gridpoints. In this comparison, the results obtained using the 1D multilayer shallow water model are included in this figure. It is clear from the results presented in Figure 6.7 that an increase in the number of layers in both 1D and 2D models produces an increase in the accuracy compared

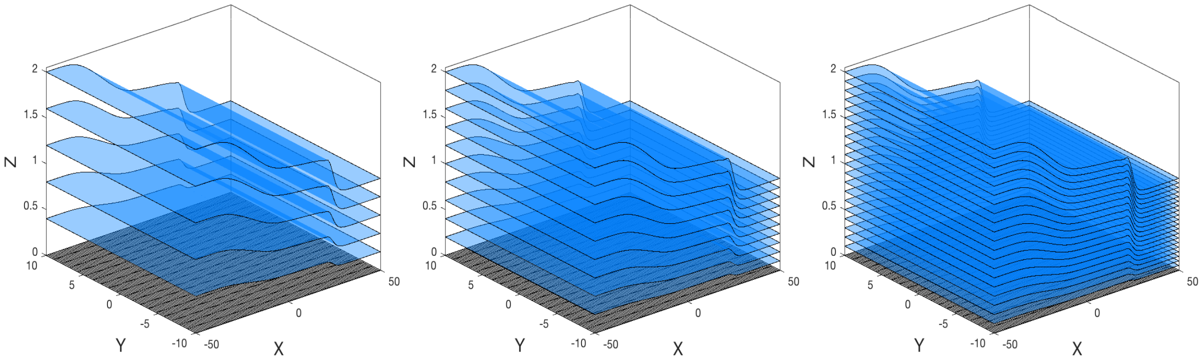

Figure 6.5: Water free-surface and interfaces for the multilayer dam-break problem on a flat bottom at time $t = 14\ s$ using a: 5-layer model (left), 10-layer model (middle), and 20-layer model (right).

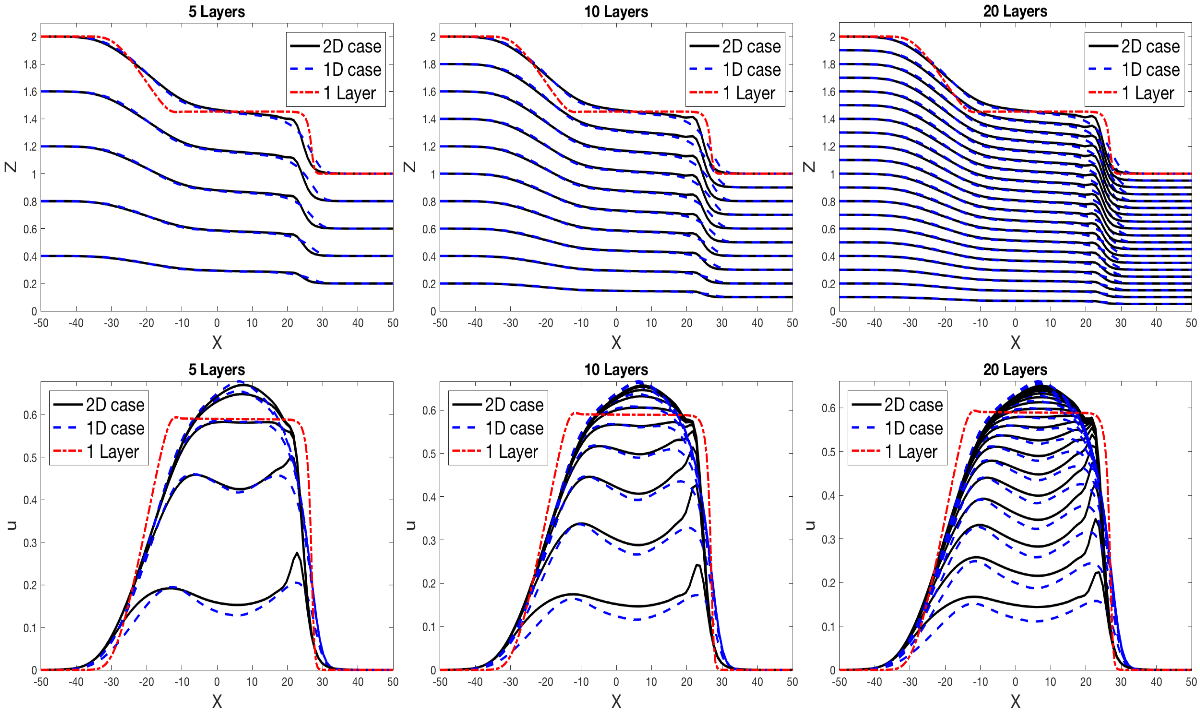

Figure 6.6: Horizontal cross-sections of the water free-surface (top) and water velocity (bottom) for the multilayer dam-break problem on a flat bottom at time $t = 14\ s$ using different numbers of layers in the model.

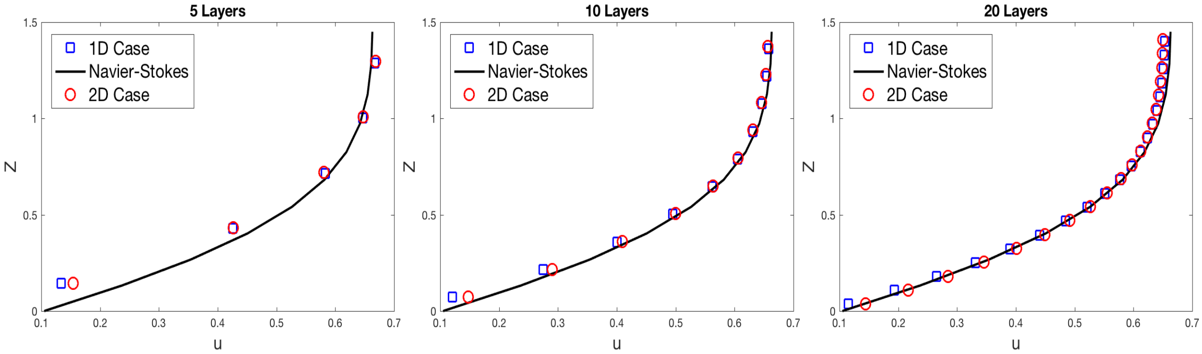

Figure 6.7: Water velocities in the z-dimension at $(x, y) = (8, 5)$ for the multilayer dam-break problem on a flat bottom at time $t = 14\ s$ using different numbers of layers in the model.

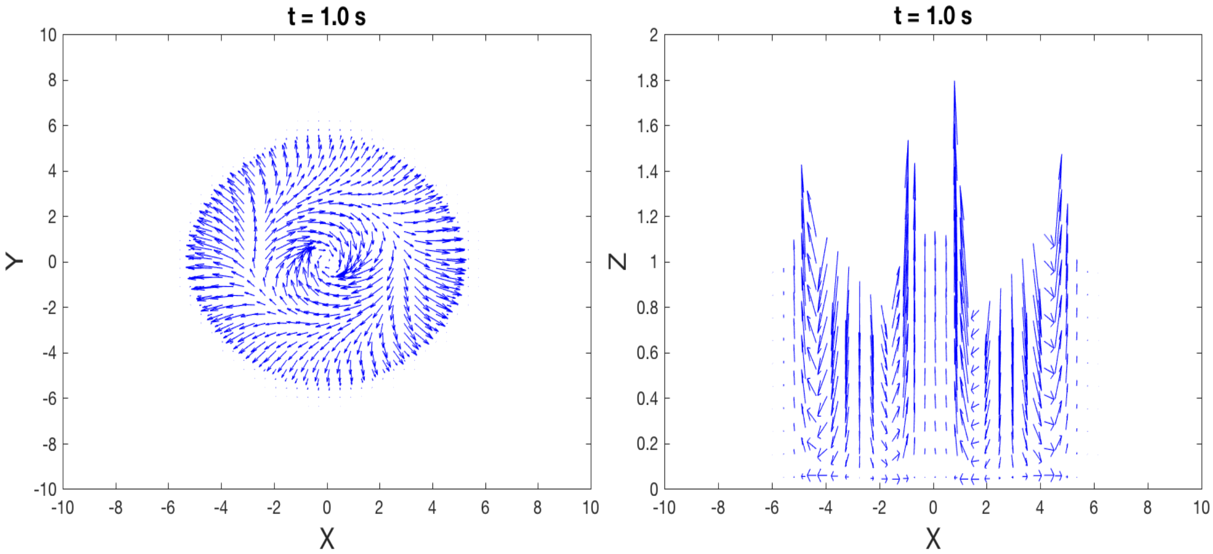

Figure 6.8: Lateral cross-section of the velocity field in the xy-plane at $z = 1\ m$ (left) and vertical cross-section of the velocity field in the xz-plane at $y = 0\ m$ for the multilayer circular dam-break on a flat bottom using 10-layers at $t = 1\ s$.

to the full 3D results. Under the considered flow conditions, the 2D results are slightly more accurate than those in 1D.

6.4.3 Circular dam-break problem

A multilayer circular dam-break problem in a squared domain $[-10, 10] \times [-10, 10]$ is considered. A similar problem has been considered in [106] for the standard single-layer circular dam-break problem. Here, the computational domain is discretised into 100×100 gridpoints and obtained results for water heights and velocity fields are presented for different instants. The domain is assumed to be flat, the viscosity of water is set to $\nu = 0.05\ m^2/s$, $\rho = 1025\ kg/m^3$, $g = 9.81\ m/s^2$, the Coriolis coefficient is $\omega_c = 1$, and the bed friction coefficient is set to $n_m = 0.001\ s/m^{1/3}$. Initially,

$$H(0, x, y) = 1 + \frac{1}{2}\left(1 - \tanh\left(\frac{\sqrt{ax^2 + by^2} - 1}{c}\right)\right)\ m, \qquad B(0, x, y) = 0\ m,$$
$$u(0, x, y) = 0\ m/s, \qquad v(0, x, y) = 0\ m/s,$$

where $a = \frac{5}{2}$, $b = \frac{5}{2}$ and $c = 0.1$. In Figure 6.8 we display the water heights and the velocity fields obtained using 10-layers at time $t = 0.1$, 0.4, 0.7 and $1\ s$. It is clear from the presented results that the water flows away from the deep central region as the rarefaction wave progresses outwards.

The Coriolis effect adds an extra rotational velocity to the results, though they remain

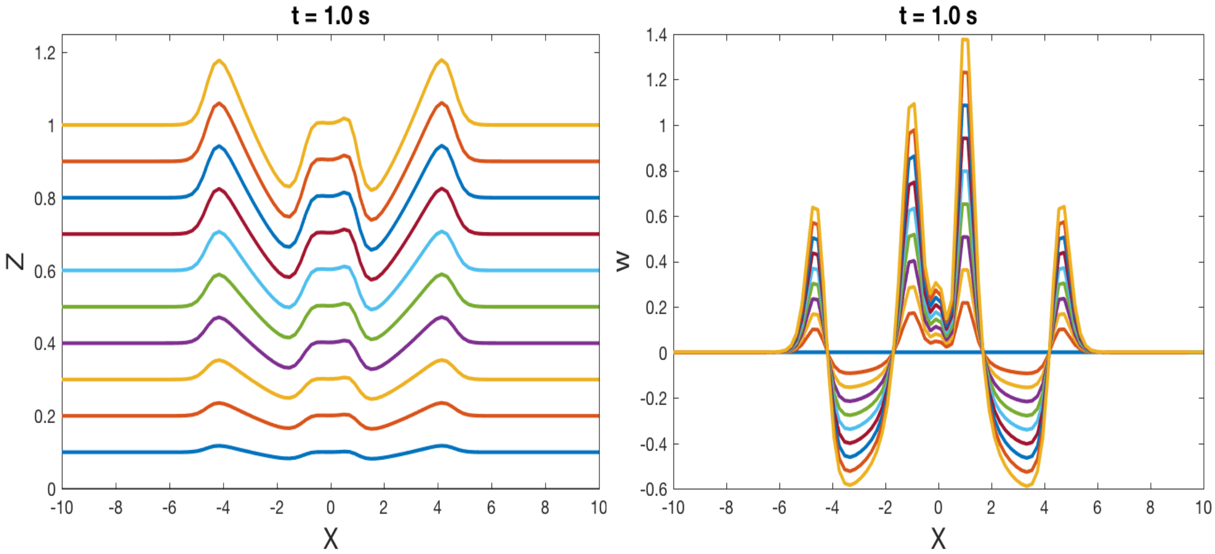

Figure 6.9: Vertical cross-sections at $y = 0\ m$ of water heights (left) and velocities (right) for the multilayer circular dam-break on a flat bottom using 10-layers at $t = 1\ s$.

symmetric, as well as retaining a strongly distinguishable wave-front which is to be expected. To emphasis the Coriolis effects on this dam-break problem, we present in Figure 6.8 the lateral and vertical cross-sections of the velocity fields at $z = 1\ m$ and $y = 0\ m$, respectively. The results are shown at the final simulation time $t = 1.0\ s$. The proposed method is able to accurately resolve the Coriolis effects and to capture the vertical velocities which are vital to the understanding of complex flows presented by this class of dam-break problems. Figure 6.9 further demonstrates the effects of the Coriolis term on this multilayer circular dam-break problem. Here we display the vertical cross-sections at $y = 0\ m$ of water heights and velocity profiles at time $t = 1\ s$. As can be seen, the symmetry is well preserved in the obtained water heights and mixing vertical velocities are also detected in the presented velocity profiles. Note that the velocity profiles in Figure 6.9 are not symmetric because of the Coriolis terms included in the multilayer model. Again the obtained results demonstrate the ability of the considered multilayer models to capture the vertical flow features without relying on the 3D free-surface flow equations. Next, attention is turned to multilayer circular dam-break problems on non-flat beds. To this end, the previous problem is solved over a non-flat bottom defined by

$$B(x,y) = \frac{1}{2}\mathcal{B}_x(x) \otimes \mathcal{B}_y(y),$$

where

$$\mathcal{B}_x(x) = \begin{cases} \sin\left(\frac{\pi}{4}x\right), & \text{if } -4\ m \le x < 4\ m, \\ 0, & \text{elsewhere}, \end{cases} \qquad \mathcal{B}_y(y) = \begin{cases} -\cos\left(\frac{\pi}{4}y\right), & \text{if } -2\ m \le y < 2\ m, \\ 0, & \text{elsewhere}. \end{cases}$$

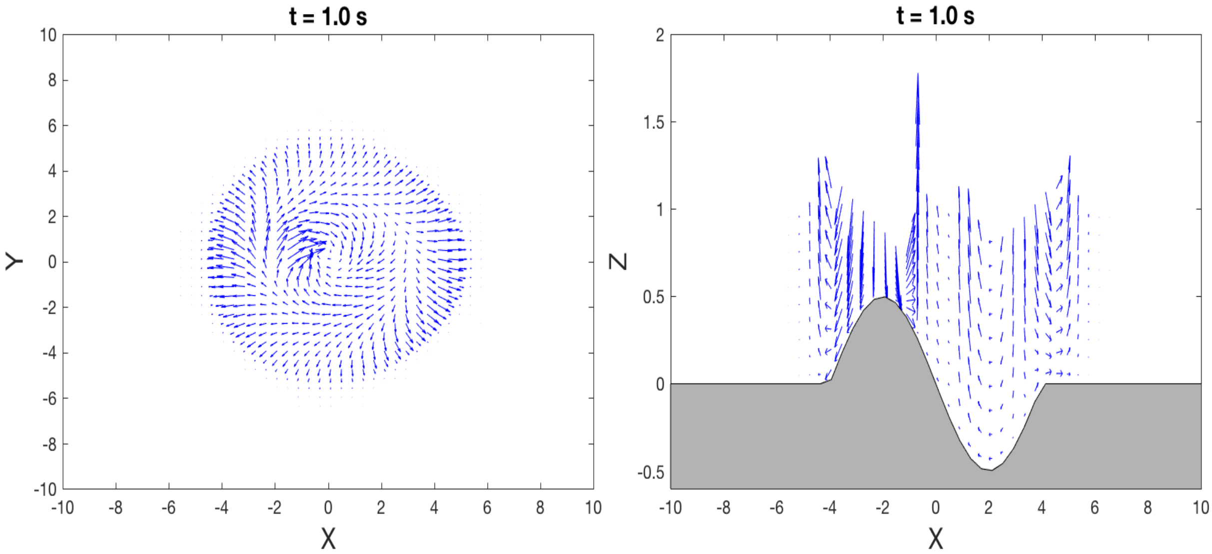

Figure 6.10: Lateral cross-section of the velocity field in the xy-plane at $z = 1\ m$ (left) and vertical cross-section of the velocity field in the xz-plane at $y = 0\ m$ for the multilayer circular dam-break on a non-flat bottom using 10-layers at $t = 1\ s$.

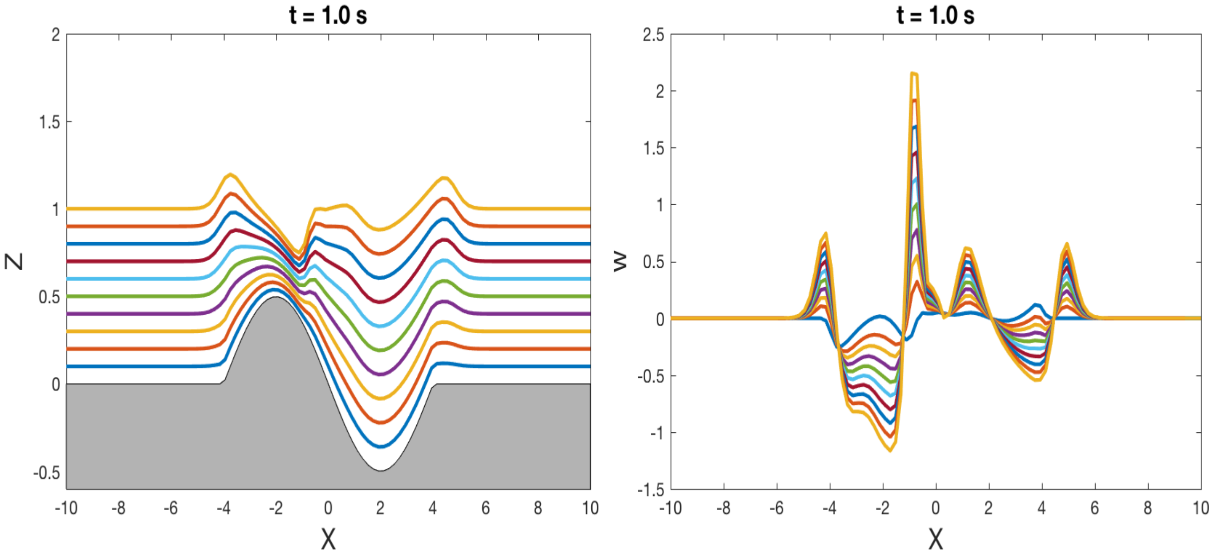

Figure 6.11: Vertical cross-sections at $y = 0\ m$ of water heights (left) and velocity plot (right) for the multilayer circular dam-break on a non-flat bottom using 10-layers at $t = 1\ s$.

The initial conditions and the flow parameters are the same as in the previous simulations. The capabilities of the proposed ELFV method to solve multilayer circular dam-break problems on a non-flat bed are evaluated here. Figure 6.10 exhibits the water heights and the velocity fields obtained using 10-layers at time 0.4 s and 1 s. Figure 6.10 displays the lateral and vertical cross-sections of the velocity fields at $z = 1\ m$ and $y = 0\ m$, respectively. The vertical cross-sections at $y = 0$ of water heights and velocity profiles at time $t = 1\ s$ are presented in Figure 6.11. Under the actual flow conditions, it is clear from the presented results that the non-flat bathymetry has direct effects on the flow structure. As the dam breaks over the bump, the

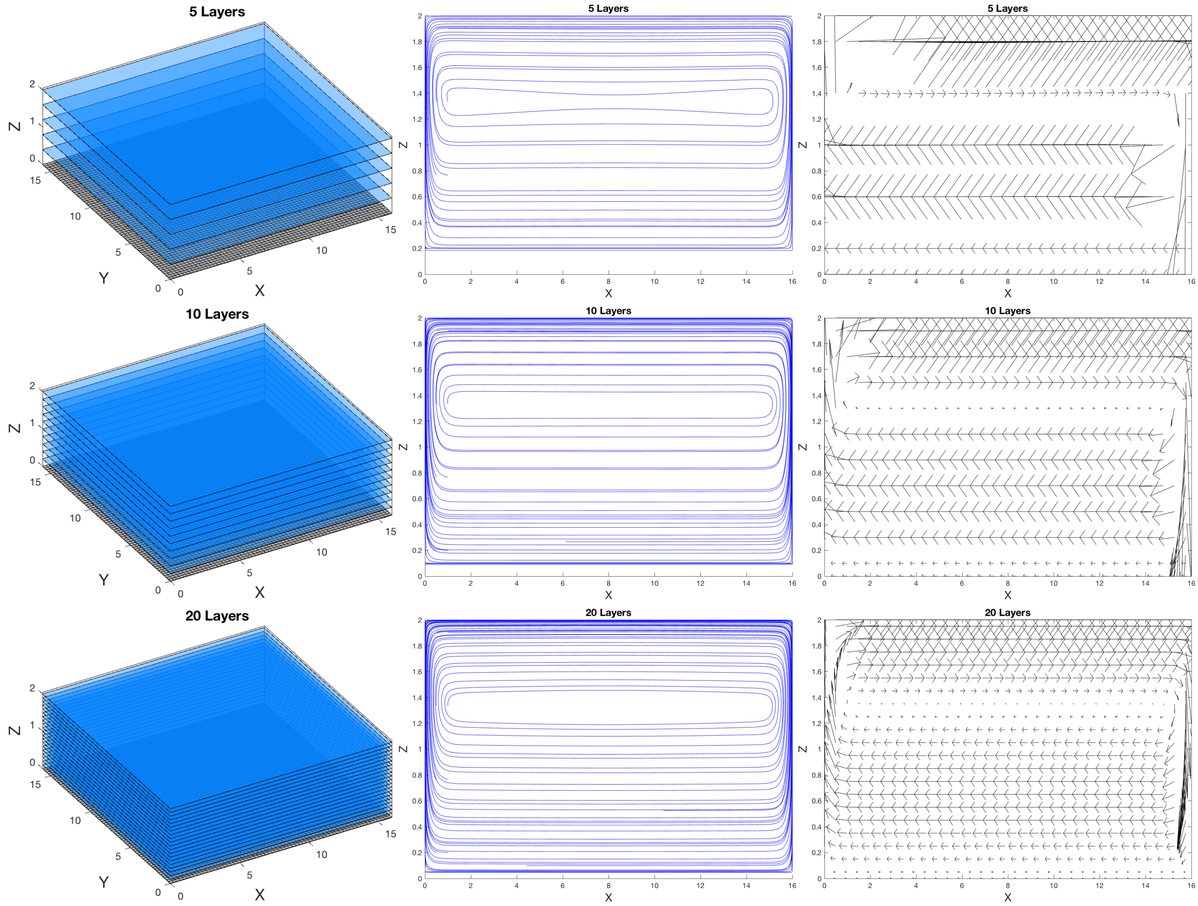

Figure 6.12: Water heights (left), streamlines at $y = 8.0\ m$ (middle), and velocity fields at $y = 8.0\ m$ (right) obtained for the wind circulation flow at time $t = 50\ s$ using a 5-layer model (top), a 10-layer model (middle), and a 20-layer model (bottom).

rarefaction wave progresses and both Coriolis and bathymetric terms change their behaviour. For example, when results in Figure 6.11 are compared to those in Figure 6.9 obtained for a flat bottom, it is easy to see the effect that the bathymetry has on the vertical velocity and the high level of variation caused. In addition, Figure 6.10 shows the asymmetry in the flow caused by the varying topography, though it is interesting to note that the rarefaction still progresses at the same speed over the non-flat bottom. The multilayer SWEs handle this complex flow problem well for both the flat and non-flat beds, and deliver new insights into vertical velocity for shallow water flows. The proposed ELFV method performs very satisfactorily for this flow problem, since it does not diffuse the moving fronts and no spurious oscillations have been detected near the steep gradients of the water heights in the computational domain.

6.4.4 Wind-driven recirculation flow

In this last test example we consider a flow problem for wind-driven circulations originally proposed in [159] and widely used to verify the results obtained from multilayer shallow water

Table 6.1: Values of the u $[\times 10^{-1}\ m/s]$ along the z-dimension at $(x, y) = (8\ m, 8\ m)$for the wind circulation flow with and without viscous terms using a 10-layer model at time $t = 50\ s$.

Layer	1	2	3	4	5	6	7	8	9	10
With	-0.006	-0.022	-0.030	-0.033	-0.029	-0.020	-0.003	0.19	0.48	0.83
Without	-0.003	-0.116	-0.116	-0.116	-0.116	-0.116	-0.116	-0.116	-0.116	0.920

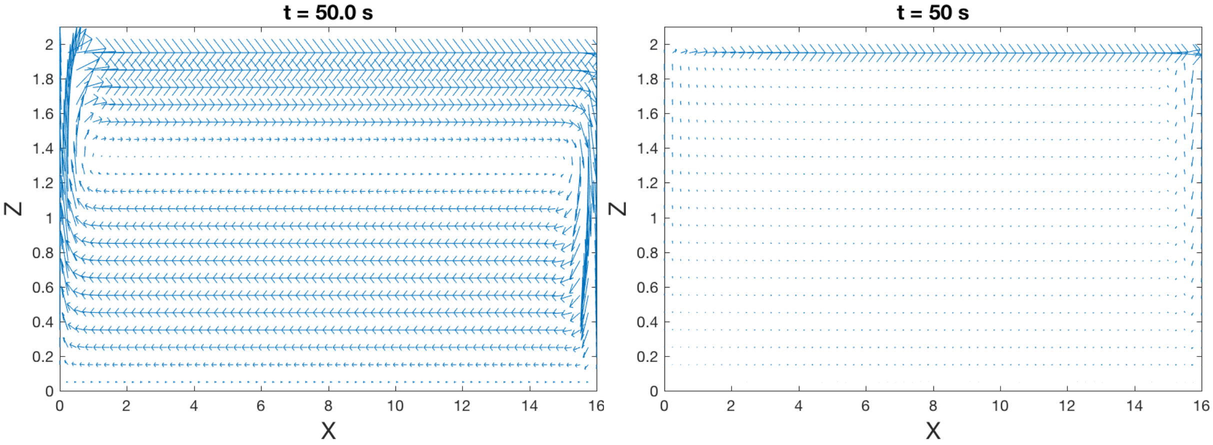

Figure 6.13: The velocity field in the xz-plane for the wind circulation flow using a 20-layer model with viscous terms (left) and without viscous terms (right) at time $t = 50\ s$.

models, see for instance [12,181]. Using the same flow parameters as in these references, we solve the multilayer SWEs (6.2.6) in a squared 2D domain, 16 m long, filled with 2 m of water, under a 2D wind blowing with an angle of 45° and a speed of $U_{wi} = 10\ m/s$, with slip walls. In our simulations, the Coriolis coefficient $\omega_c = 0$, the viscosity coefficient $\nu = 0.05\ m^2/s$, the Manning roughness coefficient $n_m = 0.001\ s/m^{1/3}$, the wind stress coefficient $\sigma = 0.0015\ N/m^2$, the water density $\rho = 1025\ kg/m^3$, the air density $\rho_a = 1.2\ kg/m^3$ and the gravity $g = 9.81\ m/s^2$. The bed is assumed to be flat, non-slip boundary conditions are used and we present results for water heights, streamlines and velocity fields at time $t = 50\ s$, using a mesh with 100×100 gridpoints.

Figure 6.12 presents the results obtained using 5-layer, 10-layer, and 20-layer models. The velocity plots show that the steady cavity flow within closed streamlines consists of a central inviscid core of nearly constant vorticity with viscous effects confined to thin shear layers near the walls. These plots also give a clear view of the overall flow pattern and the effect of the number of layers on the structure of the recirculating eddy in the cavity. As expected, a recirculation flow is generated in the computational domain and the proposed ELFV method resolves the flow features for this test example without relying on the computationally demanding 3D flow models. Next, this study examines the effect of the coupling terms in the multilayer model (6.2.1) on the flow structures for this test example. To this end, the method first provides a solution for

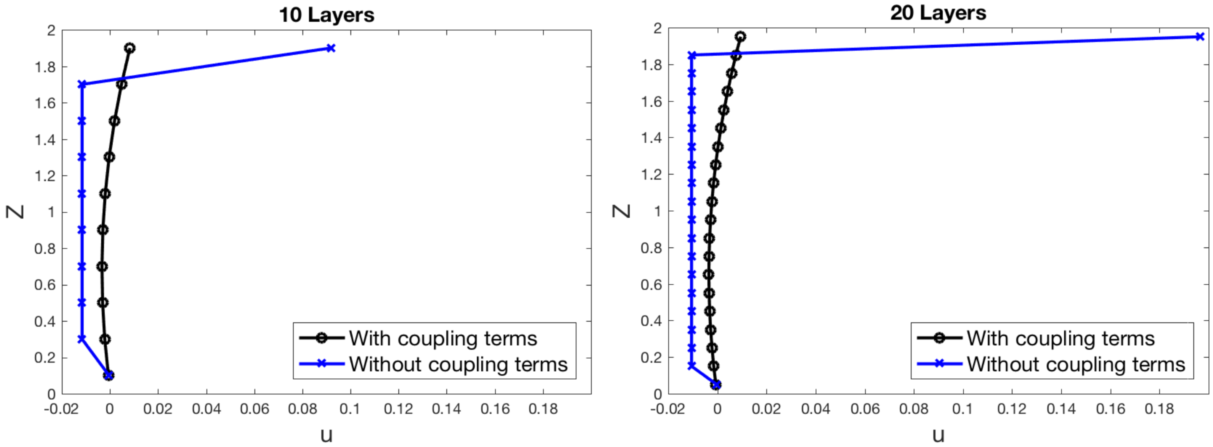

Figure 6.14: Water velocities in the z-dimension at $(x, y) = (8\ m, 8\ m)$ for the wind circulation flow with and without viscous terms using a 10-layer model (left) and a 20-layer model (right) at time $t = 50\ s$.

the system (6.2.1) without kinematic eddy viscous terms ($i.e.$ $\mathcal{F}_\alpha^{(u)} = \mathcal{F}_\alpha^{(\nu)} = \mathcal{G}_\alpha^{(u)} = \mathcal{G}_\alpha^{(\nu)} = 0$) and with the viscous terms. The obtained velocity fields in the xz-plane at fixed lateral location $y = 8\ m$ for both cases are shown in Figure 6.13. The effects of the kinematic eddy viscous terms in the multilayer SWEs can be clearly seen in these results. Observe the flow patterns at the domain walls and at the bed bottom in the results with and without kinematic eddy viscous terms in Figure 6.13. Accounting for kinematic eddy viscosity in the multilayer model intensifies the recirculation in the flow domain, and reproduces a well-developed eddy vortex in its centre which is not visible in the case of multilayer models without kinematic eddy viscous terms. The centre vortex counter-rotating eddies of a much weaker strength develop in the cavity for the simulation without viscous terms $\mathcal{F}_\alpha^{(u)} = \mathcal{F}_\alpha^{(\nu)} = \mathcal{G}_\alpha^{(u)} = \mathcal{G}_\alpha^{(\nu)} = 0$. Figure 6.14 presents the water velocities at the location $(x, y) = (8\ m, 8\ m)$ for the 10-layer and the 20-layer models, with and without viscous terms. The associated values for the velocity in the 10-layer figure are summarized in Table 6.1. It is clear from these values that simulations that do not include viscous terms overestimate the velocity of the flow, whereas, accounting for viscous terms in the simulations predicts more accurate flow velocities. The inclusion of these viscous terms is important for simulation of wind-driven recirculation using the multilayer SWEs.

6.5 Concluding remarks

A fast and fully conservative Eulerian-Lagrangian finite volume method is developed for the numerical solution of three-dimensional free-surface flows using two-dimensional multilayer shallow water equations. The governing system consists of a set of two-dimensional hydrostatic multilayer shallow water equations, with mass exchange including eddy viscosity and Coriolis forces on both flat and non-flat beds. Two stages are considered in the procedure to update the solution in time. In the first stage a projection finite volume of the system in local normal and tangential coordinates is used, whereas a method of characteristics is used in the second stage to approximate the numerical fluxes. A second-order splitting operator is also used to deal with the gradient and source terms in the system, and a third-order explicit Runge-Kutta scheme is implemented for the time integration process. This Eulerian-Lagrangian finite volume solver employs the modified method of characteristics in a finite volume discretisation of the multilayer two-dimensional shallow water system. The method offers the advantage of solving steady three-dimensional free-surface flows over non-flat bathymetry while only incurring errors of negligible magnitude. Thus, the presented scheme achieves excellent numerical balance between the discretisation of gradient fluxes and the source terms for this multilayer system. On the other hand, no Riemann-problem solvers are needed in the proposed method to compute the numerical fluxes.

To examine the performance of the proposed Eulerian-Lagrangian finite volume method and multilayer model we solved a wide application of two-dimensional multilayer shallow water equations under contrasting flow conditions. The well-balanced nature of the scheme is presented in the free-surface flow at rest over a non-flat bathymetry problem. Comparisons to three-dimensional results for incompressible hydrostatic Navier-Stokes equations have also been presented. The results obtained show detailed shock capture with high accuracy in smooth regions. There are also no non-physical oscillations in the regions of the shock which often hinder high order schemes of this nature.

Chapter 7

Modelling and simulation of multilayer turbulent shallow water flows over fixed beds

This chapter introduce a new model developed from the work in Chapter 6, combining the multilayer model formulated with the k-ϵ model for turbulence. The aim is to produce a novel multilayer turbulence formulation that bridges the gap between two-dimensional (2D) and three-dimensional (3D) models. The novel model allows for layers to affect each other through the transfer of mass, momentum and kinetic energy. It uses an efficient and conservative Eulerian-Lagrangian finite volume method to solve the multilayer system. This system is derived from the incompressible Navier-Stokes equations and it incorporates the k-ϵ model for turbulence in 2D shallow water flows. The inclusion of turbulence modelling increases the accuracy of the model and enables it to capture flow features that would otherwise be neglected. While many situations in which sediment transport is modelled do not require the inclusion of turbulence modelling, in some (such as dam-breaks, near shore regions and imposed structures in waterways) turbulence can play a significant role. This derivation is similar to previous models as studied in [14, 75], but is 2D and incorporates transfer terms between the layers. These transfer terms improve the accuracy of the model as the effects of complex and turbulent flow can now be transported through the layers. The model provides substantial advantages over the single layer formulation developed in [9, 68], as depth-stratified values for all variables are calculated. The numerical method uses the projection finite volume method for the Eulerian step and the method of characteristics to approximate the numerical fluxes for the Lagrangian stage. This creates a fast and easy to implement method that can handle the complex flows and topography if required. The method is compared to both conventional shallow water systems and to 3D Navier-Stokes simulations in a variety of benchmark and novel problems.

In order to demonstrate the accuracy of the model as well as its novel features, three problems are examined in this chapter: a backward step flow, a 3D recirculation problem, and a partial dam-break. Overall it can be seen that the model provides interesting and highly applicable results that add a new array of applications to shallow water equations.

This chapter has the following structure: Section 7.1 introduces the importance of simulating turbulence. The governing equations for both the fluid model and the empirical scour and deposition processes are derived in Section 7.2. In Section 7.3, the Eulerian-Lagrangian finite volume method is briefly described for the novel system. Numerical results are then presented in Section 7.4. Finally, concluding remarks are given in Section 7.5.

7.1 Introduction

One of the greatest problems with simulating water flow is accounting for turbulence, the unsteady and often violent movement of water. Many methods exist for modelling turbulent flows, from Direct Numerical Simulation [132] where every effective length scale is calculated, to Large Eddy Simulation [59]. However, all of these have individual drawbacks as well as advantages when applied to specific situations. This chapter bridges the gap between fully two-dimensional (2D) depth-averaged [9,68,114,212] and three-dimensional (3D) modelling [56,88], as the developed model can handle both types of simulations. The gap between the fully 3D and 2D models has becomes smaller through by the introduction of 2D (*i.e.* quasi-3D) multilayer models. It should be noted that two-layer models for fluid flow have been around for a while [194], though they were limited in their applications. In more recent times, models reported in [14, 70, 181] have been developed that are truly multilayer. Although some of these [5,29,40] are only able to deal with immiscible fluid layers, more recent models have been developed that can handle fluid mixing between layers [14, 70, 181]. It is to this later category that the presented model belongs. 3D turbulence modelling has been well developed, far more so than its 2D counterparts, and many methods have been proposed such as: Large Eddy Simulation [59], Reynolds-averaged Navier-Stokes (RaNS) [141], Mixing Length Model [44]. One of the best tools for this type of simulation is the Open source Field Operation And Manipulation (OpenFOAM) software[1]. It is not only an open-source but it also offers a wide variety of solvers that can handle most problems. OpenFOAM has been widely tested and validated [89, 145, 201] and is used in the current work to evaluate the presented model.

Turbulence modelling in shallow water flows is not new. Both the meshless model [9] and the Finite Volume Method (FVM) formulation in [68] use the popular k-ϵ method to study turbulence. Other turbulence models have been used in these kinds of shallow water simulations

---

[1] `https://www.openfoam.com/`

and good comparisons are discussed in [2,68,205], among others. The well established 2D Shallow Water Equation (SWE) formulations have two turbulent elements of note: the frictional source terms and the turbulent diffusion terms. The frictional terms compute the effects of the bed and boundaries (non-slip walls etc.) and quantify the vertical aspects of turbulent effects. The turbulent diffusion terms account for the effects of horizontal transfer of momentum (*i.e.* the turbulence in the x and y-dimensions). In order to solve the proposed model, the FVM is used to discretise the domain. One of the prominent difficulties with this method is that the first-order upwind discretisation dilutes the results with numerical diffusion. This can minimize the turbulent viscosity and make it hard to appreciate the turbulence field. This problem is avoided by utilizing a second-order method, the Eulerian-Lagrangian Finite Volume (ELFV) method.

This chapter formulates a multilayer shallow water approach to turbulence modelling using the k-ϵ model for the first time (to the best knowledge of the author). This includes exchange terms for turbulent energy k and dissipation rate ϵ between the layers as well as inter-layer friction forces that account for the turbulent energy produced between the fluid layers. This fully coupled model is solved using the ELFV method, avoiding the solution of the Riemann problem and allowing for a fast and accurate estimation of numerical fluxes. These flux estimations are then recovered to the conservative equations. Three problems are examined in this chapter: firstly the backward step flow problem, then a 3D recirculation problem, and finally a partial dam-break problem. The backward-step flow problem demonstrates the crucial nature of turbulence modelling, as turbulence effects are vital to the development of major flow features. This model is compared to experimental data to showcase its accuracy. Next, a recirculation problem in 3D is examined to show the crucial effects of exchange terms. This problem is adapted from the benchmark 2D recirculation problem and is compared to results from a 3D Navier-Stokes simulation to assess the ability of the presented model and method. Finally, a partial dam-break problem is considered and it is compared to 3D Navier-Stokes results. This problem is also used to demonstrate the effects of variable bathymetry on the model, and to show the gains in accuracy that are obtained from the use of more fluid layers.

The proposed model offers several advantages over other models widely used in this field. Compared to 3D models it is much faster and it is able to deal with evolving surfaces without re-meshing. The model also offers vertically stratified velocities, a feature which has a great advantage over 2D shallow water simulations. The inclusion of turbulence and exchange terms further improve the accuracy and ability of the model, as flow features that are normally neglected can be captured and the simulation of a new range of situations is made possible.

7.2 Modelling multilayer shallow water flows with turbulence

The 2D multilayer flow systems are usually obtained through the vertical integration of the 3D Navier-Stokes equations, accounting for the shallow water assumptions; compare [12–14] among others. The system includes terms for both external forces and mass exchange between the layers. Before we can derive the multilayer system, we must give a full description of the model to be depth-averaged. We begin with the incompressible RaNS equations

$$\frac{\partial(\rho u_i)}{\partial t} + \frac{\partial}{\partial x_j}\Big(\rho u_i u_j\Big) = -\frac{\partial p_s}{\partial x_i} - \frac{\partial}{\partial x_j}\Big(\rho u'_{av,i} u'_{av,j}\Big) + \frac{\partial \tau_{ij}}{\partial x_j} + \rho s_i, \tag{7.2.1}$$

where we have used the Cartesian tensor notation with $i, j = 1, 2, 3$ and coordinate directions $(x_1, x_2, x_3)^T = (x, y, z)^T$ and velocity components $(u_1, u_2, u_3)^T = (u, v, w)^T$. The Reynolds decomposition means that the instantaneous velocity u_i is split into mean $u_{av,i}$ and fluctuating parts u'_i such that $u_i = u'_i + u_{av,i}$. The Reynolds stress tensor is $\rho(u'_{av,i}u'_{av,j})$ and τ_{ij} is the mean deviatoric stress tensor. For water, which is a Newtonian fluid, the stress tensor τ_{ij} is

$$\tau_{ij} = \mu \left(\frac{\partial u_i}{\partial x_j} + \frac{\partial u_j}{\partial x_i} \right), \tag{7.2.2}$$

where μ is the dynamic viscosity of the fluid. Since the fluid is incompressible, the velocity field is divergence-free

$$\frac{\partial u_i}{\partial x_i} = 0.$$

The effects of turbulence on the momentum are part of the Reynolds stress terms. By comparing these forces to viscous stresses, it is possible to relate the deformation rate to the mean flow. For the fluctuating term, the Boussinesq equation relates

$$-\rho u'_{av,i} u'_{av,j} \quad = \quad \mu_t \left(\frac{\partial u_i}{\partial x_j} + \frac{\partial u_j}{\partial x_i} \right) - \frac{2}{3}\rho k \delta_{i3}, \tag{7.2.3}$$

in this relation μ_t is the dynamic eddy viscosity, which is a characteristic of the flow. The turbulent kinetic energy per unit volume is denoted as k. It should also be noted that $\mu_t \gg \mu$. The Kronecker delta is defined as

$$\delta_{ij} = \begin{cases} 0, & \text{if } \ i \neq j, \\ 1, & \text{if } i = j. \end{cases}$$

The latter term in equation (7.2.3) enables the quantification of normal stresses. Through the manipulation of equation (7.2.2) and equation (7.2.3) this latter term can be adsorbed by the pressure gradient term as $p_s = p + \frac{2}{3}k$. The external stress on the ij plane is defined as

$$\Sigma_{ij} = \nu\left(\frac{\partial u_i}{\partial x_j} + \frac{\partial u_j}{\partial x_i}\right).$$

The kinematic eddy viscosity is $\nu_t = \frac{\mu_t}{\rho}$ and the kinematic viscosity $\nu = \frac{\mu}{\rho}$. The source term for external body and surface forces $\mathbf{s} = (s_1, s_2, s_3)^T$ maybe expressed as

$$\mathbf{s} = \Sigma_T + \mathbf{f},$$

where $\mathbf{f}$ describes any external forces applied. The external tensor maybe written as

$$\Sigma_T = \begin{pmatrix} \Sigma_{xx} & \Sigma_{xy} & \Sigma_{xz} \\ \Sigma_{yx} & \Sigma_{yy} & \Sigma_{yz} \\ \Sigma_{zx} & \Sigma_{zy} & \Sigma_{zz} \end{pmatrix}.$$

We can write the incompressible Navier-Stokes equations (7.2.1) in the RaNS form as

$$\frac{\partial u_i}{\partial t} + \underbrace{u_j\frac{\partial u_i}{\partial x_j}}_{\text{Advective terms}} = -\frac{1}{\rho}\frac{\partial p}{\partial x_i} + \underbrace{\frac{\partial}{\partial x_j}\left(\left(\nu + \nu_t\right)\left(\frac{\partial u_i}{\partial x_j} + \frac{\partial u_j}{\partial x_i}\right)\right)}_{\text{Diffusive terms}} + \underbrace{s_i + \delta_{i3}g}_{\text{Source term}}. \tag{7.2.4}$$

The transport equation for turbulent kinetic energy k, as proposed in [108], is given by

$$\frac{\partial k}{\partial t} + \frac{\partial(u_i k)}{\partial x_i} = \frac{\partial}{\partial x_j}\left(\frac{\nu_t}{\sigma_k}\frac{\partial k}{\partial x_i}\right) + P_k - B_k - \epsilon, \tag{7.2.5}$$

where the production of turbulent kinetic energy is given by

$$P_k = \nu_t \frac{\partial u_i}{\partial x_j}\left(\frac{\partial u_i}{\partial x_j} + \frac{\partial u_j}{\partial x_i}\right),$$

and the loss of turbulent kinetic energy due to potential energy is defined as

$$B_k = \delta_{i3}\frac{\nu_t}{\sigma_c}N^2,$$

where N^2 is the Brunt-Vaisalla term or the buoyancy frequency. Further it is possible to relate

$$\nu_t = C_\mu \frac{k^2}{\epsilon}.$$

Table 7.1: The expanded coefficients used in the k-ϵ model suggested in [146, 205].

C_μ	$C_{\epsilon 1}$	$C_{\epsilon 2}$	$C_{\epsilon 3}$	$C_{\epsilon \Gamma}$	σ_k	σ_ϵ	σ_c
0.09	1.44	1.92	$\begin{cases} 1, & \text{if } B_k < 0, \\ 0, & \text{if } B_k > 0, \end{cases}$	1.8	0.5	1.3	1.8

This model relies on several empirical parameters $\left(C_\mu, C_{\epsilon 1}, C_{\epsilon 2}, C_{\epsilon 3}, \sigma_k, \sigma_\epsilon, \sigma_c, C_{\epsilon\Gamma}\right)$ which are given in Table 7.1. The transport equation for the second k-ϵ model equation is

$$\frac{\partial \epsilon}{\partial t} + \frac{\partial u_i \epsilon}{\partial x_i} = \frac{\partial}{\partial x_j}\left(\frac{\nu_t}{\sigma_\epsilon}\frac{\partial \epsilon}{\partial x_i}\right) + \frac{\epsilon}{k}\left(C_{\epsilon 1}\left(P_k + (1 - C_{\epsilon 3})B_k\right) - C_{\epsilon 2}\epsilon\right). \tag{7.2.6}$$

The five equations (7.2.4) - (7.2.6) create the system we consider to integrate over the layers. First, through the shallow water assumption (that vertical velocities are negligible *i.e.* $w = 0$), the third equation in (7.2.4) (where $i = 3$ and $j = 1, 2, 3$) reduces to the hydrostatic pressure assumption such that

$$\frac{\partial p}{\partial z} = -\rho g. \tag{7.2.7}$$

Next, we consider the conditions for both the water surface and the bed. The normals for these surfaces are

$$\mathbf{n}_{fs} = \frac{1}{\sqrt{\left(\frac{\partial \vartheta}{\partial x}\right)^2 + \left(\frac{\partial \vartheta}{\partial y}\right)^2 + 1}}\begin{pmatrix} -\frac{\partial \vartheta}{\partial x} \\ -\frac{\partial \vartheta}{\partial y} \\ 1 \end{pmatrix}, \quad \mathbf{n}_B = \frac{1}{\sqrt{\left(\frac{\partial B}{\partial x}\right)^2 + \left(\frac{\partial B}{\partial y}\right)^2 + 1}}\begin{pmatrix} -\frac{\partial B}{\partial x} \\ -\frac{\partial B}{\partial y} \\ 1 \end{pmatrix}.$$

The kinematic boundary condition at the water surface can be expressed as

$$\frac{\partial \vartheta}{\partial t} + u_{fs}\frac{\partial \vartheta}{\partial x} + v_{fs}\frac{\partial \vartheta}{\partial y} - w_{fs} = 0,$$

where u_{fs}, v_{fs}, and w_{fs} are the velocity components at the surface. Air viscosity is assumed negligible, therefore we can describe the stresses at the free boundary as

$$\Sigma_T \mathbf{n}_{fs} = -p^a \mathbf{n}_{fs} + \tau_{wi}\mathbf{t}_{fs},$$

where $p^a = p^a(t, x, y)$ is the atmospheric pressure function, and τ_{wi} is the wind stress coefficient. Thus we can relate

$$\mathbf{n}_{fs} \cdot \Sigma_T \mathbf{n}_{fs} = -p^a, \qquad \mathbf{t}_{fs} \cdot \Sigma_T \mathbf{n}_{fs} = \tau_{wi},$$

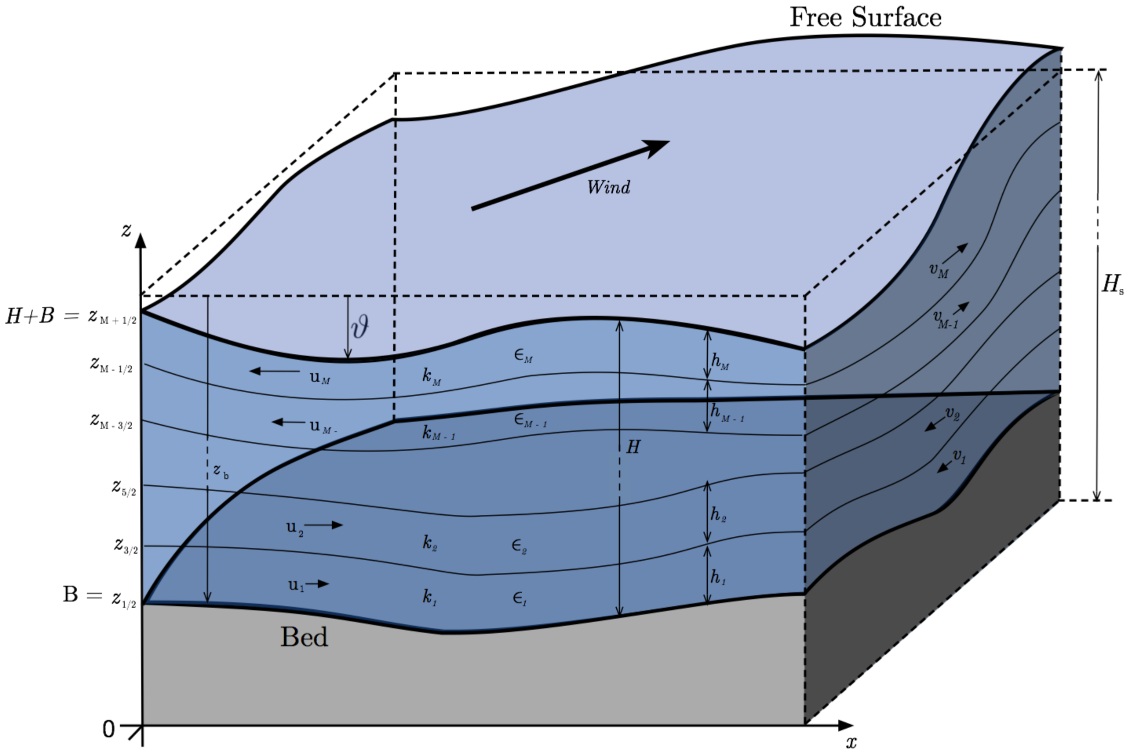

Figure 7.1: A sketch of the multilayer flow domain in 2D.

where $\mathbf{t}_{fs}$ is orthogonal to $\mathbf{n}_{fs}$. We consider a fixed impermeable bed thus

$$u_B \frac{\partial B}{\partial x} + v_B \frac{\partial B}{\partial y} - w_B = 0,$$

where u_B, v_B, and w_B are the velocity components at bed level. For the fluid stresses at the bed we consider a wall law in the form

$$\Sigma_T \cdot \mathbf{n}_B - \Big(\mathbf{n}_B \cdot \Sigma_T \cdot \mathbf{n}_B \Big) \cdot \mathbf{n}_B = \kappa(\mathbf{u}_B, H) \cdot \mathbf{u}_B.$$

If $\kappa(\mathbf{u}_B, H)$ is constant, then we recover the Navier friction condition detailed in [73]. Therefore the friction function κ may be represented by the laminar κ_l and the turbulent κ_t friction coefficients, thus

$$\kappa(\mathbf{u}_B, H) = \kappa_l + \kappa_t H \left| \mathbf{u}_B \right|.$$

By considering $\mathbf{t}_B$ as orthogonal to $\mathbf{n}_B$ we can obtain

$$\mathbf{t}_B \cdot \Sigma_T \cdot \mathbf{n}_B = \kappa \cdot \mathbf{u}_B \cdot \mathbf{t}_B, \qquad \text{and} \qquad \mathbf{u}_B \cdot \mathbf{n}_B = 0.$$

We now consider the system shown in Figure 7.1. We divide the domain into a number of layers each with height h_α such that

$$h_\alpha = l_\alpha H,$$

where the proportion l_α satisfies

$$l_\alpha \geq 0, \qquad \sum_{\alpha=1}^{M} l_\alpha = 1.$$

Note that the αth layer is bounded by $z_{\alpha+1/2}$ and $z_{\alpha-1/2}$. By applying Leibniz's rule [136] at the interface of $z_{\alpha+1/2}$, we gain exchange terms

$$\mathcal{E}_{\alpha+1/2} = w_{\alpha+1/2} - \frac{\partial z_{\alpha+1/2}}{\partial t} - u_{\alpha+1/2}\frac{\partial z_{\alpha+1/2}}{\partial x} - v_{\alpha+1/2}\frac{\partial z_{\alpha+1/2}}{\partial y}. \tag{7.2.8}$$

By applying the bed and free-surface boundary conditions we get

$$\mathcal{E}_{1/2} = 0, \qquad \mathcal{E}_{M+1/2} = 0, \tag{7.2.9}$$

where the velocity $\mathcal{E}_{\alpha+1/2}$ is orientated orthogonally to the layer interface. Since we divide the water flow into M layers of thickness h_α which lies between $[z_{\alpha-1/2}, z_{\alpha+1/2}]$ we describe the depth-averaged velocities and density as

$$\overline{u}_\alpha = \frac{1}{h_\alpha}\int_{z_{\alpha-1/2}}^{z_{\alpha+1/2}} u\ dz, \qquad \overline{v}_\alpha = \frac{1}{h_\alpha}\int_{z_{\alpha-1/2}}^{z_{\alpha+1/2}} v\ dz, \qquad \overline{\rho}_\alpha = \frac{1}{h_\alpha}\int_{z_{\alpha-1/2}}^{z_{\alpha+1/2}} \rho\ dz. \tag{7.2.10}$$

It is possible to obtain the continuity equation for the αth layer as

$$\begin{aligned} 0 &= \int_{z_{\alpha-1/2}}^{z_{\alpha+1/2}} \left(\frac{\partial u}{\partial x} + \frac{\partial v}{\partial y} + \frac{\partial w}{\partial z}\right) dz, \\ &= \frac{\partial}{\partial x}\int_{z_{\alpha-1/2}}^{z_{\alpha+1/2}} u\ dz + \frac{\partial}{\partial y}\int_{z_{\alpha-1/2}}^{z_{\alpha+1/2}} u\ dz - \left(u\frac{\partial z}{\partial x} + v\frac{\partial z}{\partial y}\right)\Bigg|_{z_{\alpha-1/2}}^{z_{\alpha+1/2}} - w_{\alpha-1/2} + w_{\alpha+1/2}. \end{aligned}$$

By summing (7.2.8) and (7.2.10) this equation becomes

$$\frac{\partial h_\alpha}{\partial t} + \frac{\partial(h_\alpha \bar{u}_\alpha)}{\partial x} + \frac{\partial(h_\alpha \bar{v}_\alpha)}{\partial y} = \mathcal{E}_{\alpha+1/2} - \mathcal{E}_{\alpha-1/2}. \tag{7.2.11}$$

In order to solve for $\mathcal{E}_{\alpha+1/2}$ we sum together all the layers between 1 and α (7.2.8) and apply the first relation of (7.2.9) and sum across the layers we obtain

$$\mathcal{E}_{\alpha+1/2} = \frac{\partial}{\partial t}\sum_{\beta=1}^{\alpha} h_\beta + \frac{\partial}{\partial x}\sum_{\beta=1}^{\alpha} h_\beta u_\beta + \frac{\partial}{\partial y}\sum_{\beta=1}^{\alpha} h_\beta v_\beta, \qquad \text{for } \alpha = 1, \ldots, M,$$

where $\beta \leq \alpha$. Through a similar process, but with all the layers between 1 and M, we obtain

$$\frac{\partial H}{\partial t} + \frac{\partial}{\partial x}\sum_{\alpha=1}^{M} h_\alpha u_\alpha + \frac{\partial}{\partial y}\sum_{\alpha=1}^{M} h_\alpha v_\alpha = 0, \qquad \alpha = 1, \dots, M. \tag{7.2.12}$$

Thus, by combining (7.2.12) with (7.2.8) and applying it to (7.2.11) we arrive at

$$\mathcal{E}_{\alpha+1/2} = \mathcal{E}^x_{\alpha+1/2} + \mathcal{E}^y_{\alpha+1/2} = \sum_{\beta=1}^{\alpha}\left(\frac{\partial h_\beta u_\beta}{\partial x} - l_\beta \sum_{\gamma=1}^{M}\left(\frac{\partial h_\gamma u_\gamma}{\partial x}\right)\right) + \sum_{\beta=1}^{\alpha}\left(\frac{\partial h_\beta v_\beta}{\partial y} - l_\beta \sum_{\gamma=1}^{M}\left(\frac{\partial h_\gamma v_\gamma}{\partial y}\right)\right).$$

Next, we consider the vertical integration of the u momentum equation in (7.2.4). Hence, starting with the non-differential terms, we utilize the relations in (7.2.10), (7.2.7) and Leibniz's rule to obtain

$$\begin{aligned}\int_{z_{\alpha-1/2}}^{z_{\alpha+1/2}}\left(\frac{\partial u}{\partial t} + \frac{1}{\rho}\frac{\partial p}{\partial x} + s_x\right) dz &= \frac{\partial(h_\alpha \overline{u}_\alpha)}{\partial t} - u\left.\frac{\partial z}{\partial t}\right|_{z_{\alpha-1/2}}^{z_{\alpha+1/2}} + \int_{z_{\alpha-1/2}}^{z_{\alpha+1/2}} \frac{\partial}{\partial x}\Big(g\Big(\partial\vartheta - B\Big)\Big) dz + h_\alpha s_{x,\alpha}, \\ &= \frac{\partial(h_\alpha \overline{u}_\alpha)}{\partial t} - u\left.\frac{\partial z}{\partial t}\right|_{z_{\alpha-1/2}}^{z_{\alpha+1/2}} + \frac{\partial}{\partial x}\left(\frac{1}{2} g H h_\alpha\right) - g h_\alpha \frac{\partial B}{\partial x} + h_\alpha s_{x,\alpha}.\end{aligned}$$

For the advection terms we obtain

$$\begin{aligned}\int_{z_{\alpha-1/2}}^{z_{\alpha+1/2}}\left(\frac{\partial u^2}{\partial x} + \frac{\partial uv}{\partial y} + \frac{\partial uw}{\partial z}\right) dz &= \frac{\partial}{\partial x}\int_{z_{\alpha-1/2}}^{z_{\alpha+1/2}} u^2 \, dz + \frac{\partial}{\partial y}\int_{z_{\alpha-1/2}}^{z_{\alpha+1/2}} uv \, dz + \\ & \quad u_{\alpha-1/2}\mathcal{E}^x_{\alpha-1/2} - u_{\alpha+1/2}\mathcal{E}^x_{\alpha+1/2},\end{aligned}$$

where the momentum exchange velocities $u_{\alpha+1/2}$ and $u_{\alpha-1/2}$ are defined by

$$u_{\alpha-1/2} = \begin{cases} \bar{u}_{\alpha-1}, & \text{if} \quad \mathcal{E}_{\alpha-1/2} \geq 0, \\ \bar{u}_\alpha, & \text{otherwise,} \end{cases} \qquad u_{\alpha+1/2} = \begin{cases} \bar{u}_{\alpha+1}, & \text{if} \quad \mathcal{E}_{\alpha+1/2} \leq 0, \\ \bar{u}_\alpha, & \text{otherwise,} \end{cases}$$

in which (7.2.8) has been utilised. As we already know that

$$h_\alpha \overline{u}_\alpha^2 = \int_{z_{\alpha-1/2}}^{z_{\alpha+1/2}} \left(2u\overline{u}_\alpha - \overline{u}_\alpha^2\right) dz,$$

it is possible to show that

$$\begin{aligned}\frac{\partial}{\partial x}\int_{z_{\alpha-1/2}}^{z_{\alpha+1/2}} u^2 \, dz &= \frac{\partial\big(h_\alpha \overline{u}_\alpha^2\big)}{\partial x} + \frac{\partial}{\partial x}\int_{z_{\alpha-1/2}}^{z_{\alpha+1/2}} \left(u - \overline{u}_\alpha\right)^2 dz, \\ &\approx \frac{\partial\big(h_\alpha \overline{u}_\alpha^2\big)}{\partial x},\end{aligned} \tag{7.2.13}$$

and that

$$\begin{aligned}\frac{\partial}{\partial y}\int_{z_{\alpha-1/2}}^{z_{\alpha+1/2}} uv\ dz &= \frac{\partial}{\partial y}\big(h_\alpha\overline{u}_\alpha\overline{v}_\alpha\big)+\frac{\partial}{\partial y}\int_{z_{\alpha-1/2}}^{z_{\alpha+1/2}}\big(u-\overline{u}_\alpha\big)\big(u-\overline{v}_\alpha\big)\ dz,\\ &\approx \frac{\partial}{\partial y}\big(h_\alpha\overline{u}_\alpha\overline{v}_\alpha\big). \end{aligned} \tag{7.2.14}$$

The latter terms of (7.2.13) and (7.2.14) are dispersion terms, which are a product of the error of the depth-averaged approximation. They are modelled as diffusion, and thus adsorbed into the horizontal diffusion terms used below through the inclusion of molecular diffusion term ν_{mol}. Next, we shall consider the integration of the viscous terms over the αth layer

$$\begin{aligned}\int_{z_{\alpha-1/2}}^{z_{\alpha+1/2}}\frac{\partial}{\partial x}\left(2(\nu+\nu_t)\frac{\partial u}{\partial x}\right)\ dz &= 2(\nu+\nu_t)\frac{\partial}{\partial x}\left(\frac{\partial}{\partial x}\int_{z_{\alpha-1/2}}^{z_{\alpha+1/2}} u\ dz - u\ \frac{\partial z}{\partial x}\bigg|_{z_{\alpha-1/2}}^{z_{\alpha+1/2}}\right) - \\ &\qquad (\nu+\nu_t)\ \frac{\partial u}{\partial x}\frac{\partial z}{\partial x}\bigg|_{z_{\alpha-1/2}}^{z_{\alpha+1/2}},\\ &\approx 2\nu_{h,\alpha}\left(\frac{\partial^2 h_\alpha\overline{u}_\alpha}{\partial x^2}-\frac{\partial}{\partial x}\left(u\ \frac{\partial z}{\partial x}\bigg|_{z_{\alpha-1/2}}^{z_{\alpha+1/2}}\right)-\frac{\partial u}{\partial x}\frac{\partial z}{\partial x}\bigg|_{z_{\alpha-1/2}}^{z_{\alpha+1/2}}\right).\end{aligned}$$

The horizontal viscosity $\nu_{h,\alpha}$ is the sum of three viscosity components $\nu_{h,\alpha}=\nu+\nu_{t,\alpha}+\nu_{mol}$, where ν is the dynamic viscosity, and ν_t is the turbulent diffusion term. The final step in deriving (7.2.15) is achieved by applying the shallow water assumptions to the internal fluid in the layer such that

$$u_{\alpha-1/2}\approx\overline{u}_\alpha,\qquad u_{\alpha+1/2}\approx\overline{u}_\alpha.$$

In addition, for a thin layer h_α we get

$$\frac{\partial z}{\partial x}\bigg|_{z_{\alpha-1/2}}^{z_{\alpha+1/2}}=\frac{\partial h_\alpha}{\partial x}.$$

This allows the momentum equation to be developed using the chain rule

$$\begin{aligned}\int_{z_{\alpha-1/2}}^{z_{\alpha+1/2}}\frac{\partial}{\partial y}\left((\nu+\nu_t)\left(\frac{\partial v}{\partial x}+\frac{\partial u}{\partial y}\right)\right)\ dz &= \nu_{h,\alpha}\frac{\partial}{\partial y}\left(\frac{\partial}{\partial x}\int_{z_{\alpha-1/2}}^{z_{\alpha+1/2}} v\ dz+\frac{\partial}{\partial y}\int_{z_{\alpha-1/2}}^{z_{\alpha+1/2}} u\ dz\right) - \\ &\qquad \nu_{h,\alpha}\frac{\partial}{\partial y}\left(u\ \frac{\partial z}{\partial x}\bigg|_{z_{\alpha-1/2}}^{z_{\alpha+1/2}} + v\ \frac{\partial z}{\partial x}\bigg|_{z_{\alpha-1/2}}^{z_{\alpha+1/2}}\right) - \nu_{h,\alpha}\left(\frac{\partial v}{\partial x}+\frac{\partial u}{\partial y}\right)\frac{\partial z}{\partial x}\bigg|_{z_{\alpha-1/2}}^{z_{\alpha+1/2}},\\ &\approx \nu_{h,\alpha}\left(\frac{\partial^2 h_\alpha\overline{v}_\alpha}{\partial y\partial x}+\frac{\partial^2 h_\alpha\overline{u}_\alpha}{\partial y^2}\right)-\nu_{h,\alpha}\left(\frac{\partial}{\partial y}\left(v\ \frac{\partial z}{\partial x}\bigg|_{z_{\alpha-1/2}}^{z_{\alpha+1/2}}+u\ \frac{\partial z}{\partial y}\bigg|_{z_{\alpha-1/2}}^{z_{\alpha+1/2}}\right)\right) - \\ &\qquad \nu_{h,\alpha}\left(\frac{\partial v}{\partial x}+\frac{\partial u}{\partial y}\right)\frac{\partial z}{\partial x}\bigg|_{z_{\alpha-1/2}}^{z_{\alpha+1/2}},\\ &\approx \frac{\partial}{\partial y}\left(h_\alpha\nu_{h,\alpha}\left(\frac{\partial\overline{v}_\alpha}{\partial x}+\frac{\partial\overline{u}_\alpha}{\partial y}\right)\right).\end{aligned}$$

For the diffusion term in the x-direction we obtain

$$\int_{z_{\alpha-1/2}}^{z_{\alpha+1/2}} \frac{\partial}{\partial x}\left(2(\nu+\nu_t)\frac{\partial u}{\partial x}\right)\, dz \;\approx\; 2\nu_{h,\alpha}\frac{\partial}{\partial x}\left(\frac{\partial h_\alpha \overline{u}_\alpha}{\partial x}\right).$$

For the diffusion term in the z-direction

$$\begin{aligned}
\int_{z_{\alpha-1/2}}^{z_{\alpha+1/2}} \frac{\partial}{\partial z}\left((\nu+\nu_t)\left(\frac{\partial w}{\partial x}+\frac{\partial u}{\partial z}\right)\right) dz &= \nu_{v,\alpha}\left(\frac{\partial w}{\partial x}+\frac{\partial u}{\partial z}\right)\Bigg|_{z_{\alpha-1/2}}^{z_{\alpha+1/2}} , \\
&\approx 2\nu_{v,\alpha}\frac{u_{\alpha+1}-u_\alpha}{h_{\alpha+1}+h_\alpha} - 2\nu_{v,\alpha}\frac{u_\alpha-u_{\alpha-1}}{h_\alpha+h_{\alpha-1}} ,
\end{aligned}$$

where $\nu_{v,\alpha}$ is the effective viscosity in the vertical dimension assumed to take into account vertical effects and it is selected as part of the turbulence model. Thus, we have

$$\begin{aligned}
\frac{\partial(h_\alpha\overline{u}_\alpha)}{\partial t} + \frac{\partial}{\partial x}\left(h_\alpha\overline{u}_\alpha^2+\frac{1}{2}gHh_\alpha\right) + \frac{\partial}{\partial y}\Big(h_\alpha\overline{u}_\alpha\overline{v}_\alpha\Big) &= -gh_\alpha\frac{\partial B}{\partial x} + \frac{\partial}{\partial y}\left(\nu_{h,\alpha}h_\alpha\left(\frac{\partial\overline{u}_\alpha}{\partial y}+\frac{\partial\overline{v}_\alpha}{\partial x}\right)\right) + \\
\frac{\partial}{\partial x}\left(2\nu_{h,\alpha}h_\alpha\frac{\partial\overline{u}_\alpha}{\partial x}\right) + 2\nu_{v,\alpha}\frac{\overline{u}_{\alpha+1}-\overline{u}_\alpha}{h_{\alpha+1}+h_\alpha} &- 2\nu_{v,\alpha}\frac{\overline{u}_\alpha-\overline{u}_{\alpha-1}}{h_\alpha+h_{\alpha-1}} + \overline{u}_{\alpha-1/2}\mathcal{E}^x_{\alpha-1/2} - \qquad (7.2.15) \\
&\overline{u}_{\alpha+1/2}\mathcal{E}^x_{\alpha+1/2} + h_\alpha\mathbf{s}_{x,\alpha}.
\end{aligned}$$

By applying the same treatment to the momentum equation in the y direction we obtain

$$\begin{aligned}
\frac{\partial(h_\alpha\overline{v}_\alpha)}{\partial t} + \frac{\partial}{\partial x}\Big(h_\alpha\overline{v}_\alpha\overline{u}_\alpha\Big) + \frac{\partial}{\partial y}\left(h_\alpha\overline{v}_\alpha^2+\frac{1}{2}gHh_\alpha\right) &= -gh_\alpha\frac{\partial B}{\partial y} + \frac{\partial}{\partial x}\left(\nu_{h,\alpha}h_\alpha\left(\frac{\partial\overline{u}_\alpha}{\partial y}+\frac{\partial\overline{v}_\alpha}{\partial x}\right)\right) + \\
\frac{\partial}{\partial y}\left(2\nu_{h,\alpha}h_\alpha\frac{\partial\overline{v}_\alpha}{\partial y}\right) + 2\nu_{v,\alpha}\frac{\overline{v}_{\alpha+1}-\overline{v}_\alpha}{h_{\alpha+1}+h_\alpha} &- 2\nu_{v,\alpha}\frac{\overline{v}_\alpha-\overline{v}_{\alpha-1}}{h_\alpha+h_{\alpha-1}} + \overline{v}_{\alpha-1/2}\mathcal{E}^y_{\alpha-1/2} - \qquad (7.2.16) \\
&\overline{v}_{\alpha+1/2}\mathcal{E}^y_{\alpha+1/2} + h_\alpha\mathbf{s}_{y,\alpha} .
\end{aligned}$$

Next, we depth-average the two species conservation equations of the k-ϵ model. First we quantify a depth-averaged value for turbulent energy $\overline{k}$ and its dispersion rate $\overline{\epsilon}$ in the αth layer bounded by $[z_{\alpha+1/2}, z_{\alpha-1/2}]$ such that

$$\overline{k}_\alpha = \frac{1}{h_\alpha}\int_{z_{\alpha-1/2}}^{z_{\alpha+1/2}} k\; dz, \qquad\qquad \overline{\epsilon}_\alpha = \frac{1}{h_\alpha}\int_{z_{\alpha-1/2}}^{z_{\alpha+1/2}} \epsilon\; dz.$$

The integration of the left hand side of (7.2.5) yields

$$\begin{aligned}
\int_{z_{\alpha-1/2}}^{z_{\alpha+1/2}}\left(\frac{\partial k}{\partial t}+u\frac{\partial k}{\partial x}+v\frac{\partial k}{\partial y}+w\frac{\partial k}{\partial z}\right) dz &= \frac{\partial(h_\alpha\overline{k}_\alpha)}{\partial t} + \frac{\partial}{\partial x}\Big(h_\alpha\overline{k}_\alpha\overline{u}_\alpha\Big) + \frac{\partial}{\partial y}\Big(h_\alpha\overline{k}_\alpha\overline{v}_\alpha\Big) + \\
&\mathcal{E}_{\alpha+1/2}\overline{k}_{\alpha+1/2} - \mathcal{E}_{\alpha+1/2}\overline{k}_{\alpha+1/2},
\end{aligned}$$

where

$$\bar{k}_{\alpha-1/2} = \begin{cases} \bar{k}_{\alpha-1}, & \text{if} \quad \mathcal{E}_{\alpha-1/2} \geq 0, \\ \\ \bar{k}_{\alpha}, & \text{otherwise.} \end{cases}$$

The dispersion terms produced by this integration

$$\int_{z_{\alpha-1/2}}^{z_{\alpha+1/2}} (k - \overline{k}_\alpha)(u - \overline{u}_\alpha)\ dz,$$

$$\int_{z_{\alpha-1/2}}^{z_{\alpha+1/2}} (k - \overline{k}_\alpha)(v - \overline{v}_\alpha)\ dz,$$

are handled in the same way as with the momentum terms, and are incorporated into the horizontal diffusion terms. The integration of the source terms may be written as

$$\begin{aligned}
\int_{z_{\alpha-1/2}}^{z_{\alpha+1/2}} \Big(P_k + B_k - \epsilon\Big)\ dz &= \int_{z_{\alpha-1/2}}^{z_{\alpha+1/2}} \frac{\partial u_i}{x_j}\left(\frac{\partial u_i}{\partial x_j} + \frac{\partial u_j}{\partial x_i}\right)\ dz + \int_{z_{\alpha-1/2}}^{z_{\alpha+1/2}} \frac{\nu_{v,\alpha}}{\sigma_c}\frac{g}{\rho}\frac{\partial \rho}{\partial z}\ dz + h_\alpha \overline{\epsilon}_\alpha, \\
&= \int_{z_{\alpha-1/2}}^{z_{\alpha+1/2}} \nu_t \left(2\left(\frac{\partial u}{\partial x}\right)^2 + 2\left(\frac{\partial v}{\partial y}\right)^2 + \left(\frac{\partial u}{\partial y} + \frac{\partial v}{\partial x}\right)^2 + \right. \\
&\qquad \left. 2\left(\frac{\partial w}{\partial z}\right)^2 + \left(\frac{\partial w}{\partial y} + \frac{\partial v}{\partial z}\right)^2 + \left(\frac{\partial w}{\partial x} + \frac{\partial u}{\partial z}\right)^2\right)\ dz + h_\alpha \overline{\epsilon}_\alpha, \\
&\approx h_\alpha \underbrace{\nu_t \left(2\left(\frac{\partial u}{\partial x}\right)^2 + 2\left(\frac{\partial v}{\partial y}\right)^2 + \left(\frac{\partial u}{\partial y} + \frac{\partial v}{\partial x}\right)^2\right)}_{\overline{P}_{\alpha,k}} + \\
&\qquad \nu_t \left(\frac{\partial v}{\partial z} + \frac{\partial u}{\partial z}\right)\Bigg|_{z_{\alpha-1/2}}^{z_{\alpha+1/2}} + h_\alpha \overline{\epsilon}_\alpha.
\end{aligned}$$

Here, we split the production of k term into three parts $\overline{P}_{k,\alpha}$, the horizontal production term and two layer interfaces production terms $\overline{P}_{k,\alpha+1/2}$, $\overline{P}_{k,\alpha-1/2}$. In order to derive $\overline{P}_{k,\alpha+1/2}$ and $\overline{P}_{k,\alpha-1/2}$ we use

$$\begin{aligned}
\overline{P}_{k,\alpha+1/2} + \overline{P}_{k,\alpha-1/2} &= \nu_t \left(\frac{\partial v}{\partial z} + \frac{\partial u}{\partial z}\right)\Bigg|_{z_{\alpha-1/2}}^{z_{\alpha+1/2}}, \\
&\approx \underbrace{\nu_v\Big((u_\alpha - u_{\alpha+1}) + (v_\alpha - v_{\alpha+1})\Big)}_{\overline{P}_{k,\alpha+1/2}} \underbrace{-\nu_v\Big((u_{\alpha-1} - u_\alpha) + (v_{\alpha-1} - v_\alpha)\Big)}_{\overline{P}_{k,\alpha-1/2}}.
\end{aligned}$$

The integration of the diffusion terms of (7.2.5) yields

$$\begin{aligned}
\int_{z_{\alpha-1/2}}^{z_{\alpha+1/2}} \left(\frac{\partial}{\partial x_i}\left(\frac{\nu_t}{\sigma_\epsilon}\frac{\partial k}{\partial x_i}\right)\right) dz \; = \; & \frac{\partial}{\partial x}\frac{\nu_t}{\sigma_\epsilon}\int_{z_{\alpha-1/2}}^{z_{\alpha+1/2}}\frac{\partial k}{\partial x}dz + \frac{\partial}{\partial y}\frac{\nu_t}{\sigma_\epsilon}\int_{z_{\alpha-1/2}}^{z_{\alpha+1/2}}\frac{\partial k}{\partial y}dz + \frac{\nu_t}{\sigma_\epsilon}\frac{\partial k}{\partial z}\bigg|_{z_{\alpha-1/2}}^{z_{\alpha+1/2}} - \\
& \frac{\nu_t}{\sigma_\epsilon}\frac{\partial k}{\partial x}\frac{\partial z}{\partial x}\bigg|_{z_{\alpha-1/2}}^{z_{\alpha+1/2}} - \frac{\nu_t}{\sigma_\epsilon}\frac{\partial k}{\partial y}\frac{\partial z}{\partial y}\bigg|_{z_{\alpha-1/2}}^{z_{\alpha+1/2}}, \\
= \; & \frac{\partial}{\partial x}\frac{\nu_t}{\sigma_\epsilon}\left(\frac{\partial h_\alpha \overline{k}_\alpha}{\partial x} + \frac{\nu_t}{\sigma_\epsilon}k\frac{\partial z}{\partial x}\bigg|_{z_{\alpha-1/2}}^{z_{\alpha+1/2}}\right) - \frac{\nu_t}{\sigma_\epsilon}\frac{\partial k}{\partial x}\frac{\partial z}{\partial x}\bigg|_{z_{\alpha-1/2}}^{z_{\alpha+1/2}} + \\
& \frac{\partial}{\partial y}\frac{\nu_t}{\sigma_\epsilon}\left(\frac{\partial h_\alpha \overline{k}_\alpha}{\partial y} + \frac{\nu_t}{\sigma_\epsilon}k\frac{\partial z}{\partial y}\bigg|_{z_{\alpha-1/2}}^{z_{\alpha+1/2}}\right) - \frac{\nu_t}{\sigma_\epsilon}\frac{\partial k}{\partial y}\frac{\partial z}{\partial y}\bigg|_{z_{\alpha-1/2}}^{z_{\alpha+1/2}} + \frac{\nu_t}{\sigma_\epsilon}\frac{\partial k}{\partial z}\bigg|_{z_{\alpha-1/2}}^{z_{\alpha+1/2}}, \\
\approx \; & \frac{\partial}{\partial x}\left(h_\alpha\frac{\nu_t}{\sigma_k}\frac{\partial \overline{k}_\alpha}{\partial x}\right) + \frac{\partial}{\partial y}\left(h_\alpha\frac{\nu_t}{\sigma_k}\frac{\partial \overline{k}_\alpha}{\partial y}\right).
\end{aligned}$$

As in [14,75], the vertical non-uniformities are neglected. This means the depth-averaged version of the k species conservation equation (7.2.5) is

$$\begin{aligned}
\frac{\partial (h_\alpha \overline{k}_\alpha)}{\partial t} + \frac{\partial}{\partial x}\left(h_\alpha \overline{k}_\alpha \bar{u}_\alpha\right) + \frac{\partial}{\partial y}\left(h_\alpha \overline{k}_\alpha \bar{v}_\alpha\right) \; = \; & \frac{\partial}{\partial x}\left(h_\alpha\frac{\nu_t}{\sigma_k}\frac{\partial \overline{k}_\alpha}{\partial x}\right) + \frac{\partial}{\partial y}\left(h_\alpha\frac{\nu_t}{\sigma_k}\frac{\partial \overline{k}_\alpha}{\partial y}\right) + \\
& \mathcal{E}_{\alpha+1/2}k_{\alpha+1/2} - \mathcal{E}_{\alpha-1/2}k_{\alpha-1/2} + h_\alpha \overline{P}_k + \overline{P}_{k,\alpha+1/2} - \overline{P}_{k,\alpha-1/2} - h_\alpha\bar{\epsilon}\,.
\end{aligned} \tag{7.2.17}$$

By applying the same steps to (7.2.6) we arrive at

$$\begin{aligned}
\frac{\partial (h_\alpha \bar{\epsilon}_\alpha)}{\partial t} + \frac{\partial}{\partial x}\left(h_\alpha \bar{\epsilon}_\alpha \bar{u}_\alpha\right) + \frac{\partial}{\partial y}\left(h_\alpha \bar{\epsilon}_\alpha \bar{v}_\alpha\right) \; = \; & \frac{\partial}{\partial x}\left(h_\alpha\frac{\nu_t}{\sigma_\epsilon}\frac{\partial \bar{\epsilon}_\alpha}{\partial x}\right) + \frac{\partial}{\partial y}\left(h_\alpha\frac{\nu_t}{\sigma_\epsilon}\frac{\partial \bar{\epsilon}_\alpha}{\partial y}\right) + \\
& \mathcal{E}_{\alpha+1/2}\epsilon_{\alpha+1/2} - \mathcal{E}_{\alpha+1/2}\epsilon_{\alpha+1/2} + \frac{h_\alpha\bar{\epsilon}}{\bar{k}}\left(C_{\epsilon 1}\overline{P}_{k,\alpha} - C_{\epsilon 2}\bar{\epsilon}\right) + \frac{\bar{\epsilon}C_{\epsilon 1}}{\bar{k}}\left(\overline{P}_{k,\alpha+1/2} - \overline{P}_{k,\alpha-1/2}\right).
\end{aligned} \tag{7.2.18}$$

7.2.1 Boundary conditions for the fluid column

Up to this point we have derived the governing equations for a single layer, now we must apply the boundary conditions at the bed and the free-surface. For the top layer M we use (7.2.8) to resolve the x and y-momentum conservation equations (7.2.15) and obtain

$$s_{x,M}h_M = \mathcal{F}_M^{(w)} = \frac{\tau_{wi}^x}{\rho}, \qquad\qquad s_{y,M}h_M = \mathcal{G}_M^{(w)} = \frac{\tau_{wi}^y}{\rho},$$

where the wind velocity is $U_{wi} = (U_{wi,x}, U_{wi,y})^T$, and

$$\tau_{wi}^x = \rho C_{wi}(U_{wi,x} - u_M)\sqrt{(U_{wi,x} - u_M)^2 + (U_{wi,y} - v_M)^2},$$

$$\tau^y_{wi} = \rho C_{wi}(U_{wi,y} - v_M)\sqrt{(U_{wi,x} - u_M)^2 + (U_{wi,y} - v_M)^2},$$

with the wind friction coefficient C_{wi} defined as [159]

$$C_{wi} = \frac{\sigma^2 \rho_a}{H},$$

where σ is the wind stress coefficient and ρ_a is the air density. Next, through the application of equation (7.2.8) to the k-ϵ equations we arrive at

$$\overline{P}_{k,M+1/2} = \nu_v \left(\frac{\partial v}{\partial z} + \frac{\partial u}{\partial z}\right)\bigg|_{z_{\alpha+1/2}} = \nu_v C_{wi}^{-1/2}\Big((\overline{u}_N - U_{wi,x})^2 + (\overline{v}_N - U_{wi,y})^2\Big).$$

Subsequently, for the bottom layer ($\alpha = 1$) it is possible to resolve (7.2.8) and the x and y-momentum source terms in the conservation equations (7.2.15) and (7.2.16), which yields (neglecting the turbulent part)

$$s_{x,1}h_1 = \mathcal{F}_1^{(b)} = \frac{\tau^x{}_{\mathrm{B}}}{\rho}, \qquad s_{y,1}h_1 = \mathcal{G}_1^{(b)} = \frac{\tau^y{}_{\mathrm{B}}}{\rho},$$

where the bed shear is defined as

$$\tau^x{}_{\mathrm{B}} = \rho C_{\mathrm{B}} \overline{u}_1 \sqrt{\overline{u}_1^2 + \overline{u}_1^2}\ , \qquad \tau^y{}_{\mathrm{B}} = \rho C_{\mathrm{B}} \overline{u}_2 \sqrt{\overline{u}_1^2 + \overline{v}_1^2}\ ,$$

where C_{B} is the bed friction coefficient, which may be either constant or estimated using the Manning equation as

$$C_{\mathrm{B}} = \frac{g n_m^2}{H^{1/3}},$$

where n_m is the Manning roughness coefficient of the bed. Next, through the application of the expression (7.2.8) to the k-ϵ equations it is possible to relate

$$\overline{P}_{k,1/2} = \nu_v \left(\frac{\partial v}{\partial z} + \frac{\partial u}{\partial z}\right)\bigg|_{z_{\alpha-1/2}}^{z_{\alpha+1/2}} = C_{\mathrm{B}}{}^{-1/2}\left(C_{\mathrm{B}}(\overline{u}_1^2 + \overline{v}_1^2)\right)^{3/2}.$$

As all velocities are now depth-averaged, the overline notation is dropped. The source term F_α is the external force in x-direction acting on the αth layer and accounting for the friction and momentum exchange effects. Thus

$$F_\alpha = \mathcal{F}_\alpha^{(u)} + \mathcal{F}_\alpha^{(b)} + \mathcal{F}_\alpha^{(w)} + \mathcal{F}_\alpha^{(\mu)}, \qquad \alpha = 1, 2, \ldots, M.$$

$$G_\alpha = \mathcal{G}_\alpha^{(u)} + \mathcal{G}_\alpha^{(b)} + \mathcal{G}_\alpha^{(w)} + \mathcal{G}_\alpha^{(\mu)}, \qquad \alpha = 1, 2, \ldots, M,$$

where G_α is the external force in the y-direction, and

- $\mathcal{F}_\alpha^{(u)}$ and $\mathcal{G}_\alpha^{(u)}$ estimate the momentum exchange between the layers
- $\mathcal{F}_\alpha^{(b)}$ and $\mathcal{G}_\alpha^{(b)}$ estimate the effects of bed friction on the system
- $\mathcal{F}_\alpha^{(w)}$ and $\mathcal{G}_\alpha^{(w)}$ add the effects of wind on the top layer to the system
- $\mathcal{F}_\alpha^{(\mu)}$ and $\mathcal{G}_\alpha^{(\mu)}$ are due to the effects of friction between the layers

For the sake of brevity, this section only details the force terms in the x-direction. The x-direction momentum exchange is defined as

$$\mathcal{F}_\alpha^{(u)} = u_{\alpha+1/2}\mathcal{E}_{\alpha+1/2}^x - u_{\alpha-1/2}\mathcal{E}_{\alpha-1/2}^x,$$

where the mass exchange terms $\mathcal{E}_{\alpha+1/2}^x$ are computed as

$$\mathcal{E}_{\zeta+1/2}^x = \begin{cases} 0, & \text{if} \quad \zeta = 0, \\ \sum_{\beta=1}^{\zeta} \left(\dfrac{\partial \left(h_\beta u_\beta\right)}{\partial x} - l_\beta \sum_{\gamma=1}^{M} \dfrac{\partial \left(h_\gamma u_\gamma\right)}{\partial x} \right), & \text{if} \quad \zeta = 1, 2, \ldots, M-1, \\ 0, & \text{if} \quad \zeta = M. \end{cases}$$

The vertical kinematic eddy viscosity term $\mathcal{F}_\alpha^{(\mu)}$ takes into account the friction between neighbouring layers and it is defined as

$$\mathcal{F}_\alpha^{(\mu)} = \begin{cases} 2\nu_{v,\alpha} \dfrac{u_2 - u_1}{\left(l_2 + l_1\right) H}, & \text{if} \quad \alpha = 1, \\ 2\nu_{v,\alpha} \dfrac{u_{\alpha+1} - u_\alpha}{\left(l_{\alpha+1} + l_\alpha\right) H} - 2\nu_{v,\alpha} \dfrac{u_\alpha - u_{\alpha-1}}{\left(l_\alpha + l_{\alpha-1}\right) H}, & \text{if} \quad \alpha = 2, 3, \ldots, M-1, \\ -2\nu_{v,\alpha} \dfrac{u_M - u_{M-1}}{\left(l_M + l_{M-1}\right) H}, & \text{if} \quad \alpha = M. \end{cases}$$

Note that, a generalized derivation of the viscous tensor in multilayer SWEs has also been reported in [70]. The external friction terms are given by

$$\mathcal{F}_\alpha^{(b)} = \begin{cases} -\dfrac{\tau_{\mathrm{B}}^x}{\rho}, & \text{if} \ \ \alpha = 1, \\ 0, & \text{if} \quad \alpha = 2, 3, \ldots, M, \end{cases}$$

$$\mathcal{F}_\alpha^{(w)} = \begin{cases} 0, & \text{if } \alpha = 1, 2, \ldots, M-1, \\ \\ \dfrac{\tau_w^x}{\rho}, & \text{if } \alpha = M. \end{cases}$$

We combine the source terms for k and ϵ such that

$$\begin{aligned} P_{h,\alpha} &= h_\alpha\Big(P_{k,\alpha} - \epsilon_\alpha\Big) + P_{k,\alpha+1/2} - P_{k,\alpha-1/2}, \\ P_{\epsilon,\alpha} &= \frac{h_\alpha \epsilon_\epsilon}{k}\left(C_{\epsilon 1} P_{k,\alpha} - C_{\epsilon 2}\epsilon_\alpha\right) + \frac{\epsilon_\alpha C_{\epsilon 1}}{k}\Big(P_{k,\alpha+1/2} - P_{k,\alpha-1/2}\Big). \end{aligned}$$

By combining equations (7.2.12), (7.2.15), (7.2.16), (7.2.17) and (7.2.18) we obtain

$$\frac{\partial H}{\partial t} + \sum_{\alpha=1}^{M} \frac{\partial}{\partial x}\big(h_\alpha u_\alpha\big) + \sum_{\alpha=1}^{M} \frac{\partial}{\partial y}\big(h_\alpha v_\alpha\big) = 0,$$

$$\begin{aligned} \frac{\partial\big(h_\alpha u_\alpha\big)}{\partial t} + \frac{\partial}{\partial x}\left(h_\alpha u_\alpha^2 + \frac{1}{2} g h_\alpha H\right) + \frac{\partial}{\partial y}\big(h_\alpha u_\alpha v_\alpha\big) &= \frac{\partial}{\partial y}\left(h_\alpha \nu_{h,\alpha}\left(\frac{\partial u_\alpha}{\partial y} + \frac{\partial v_\alpha}{\partial x}\right)\right) - g h_\alpha \frac{\partial B}{\partial x} + \\ & \quad \frac{\partial}{\partial x}\left(h_\alpha \nu_{h,\alpha}\frac{\partial u_\alpha}{\partial x}\right) + F_\alpha, \end{aligned}$$

$$\begin{aligned} \frac{\partial\big(h_\alpha v_\alpha\big)}{\partial t} + \frac{\partial}{\partial x}\big(h_\alpha u_\alpha v_\alpha\big) + \frac{\partial}{\partial y}\left(h_\alpha v_\alpha^2 + \frac{1}{2} g h_\alpha H\right) &= \frac{\partial}{\partial x}\left(h_\alpha \nu_{h,\alpha}\left(\frac{\partial u_\alpha}{\partial y} + \frac{\partial v_\alpha}{\partial x}\right)\right) - g h_\alpha \frac{\partial B}{\partial y} + \\ & \quad \frac{\partial}{\partial y}\left(h_\alpha \nu_{h,\alpha}\frac{\partial v_\alpha}{\partial y}\right) + G_\alpha, \end{aligned}$$

$$\begin{aligned} \frac{\partial\big(h_\alpha k_\alpha\big)}{\partial t} + \frac{\partial}{\partial x}\big(h_\alpha k_\alpha u_\alpha\big) + \frac{\partial}{\partial y}\big(h_\alpha k_\alpha v_\alpha\big) &= \frac{\partial}{\partial x}\left(\frac{h_\alpha \nu_{t,\alpha}}{\sigma_k}\frac{\partial k_\alpha}{\partial x}\right) + \frac{\partial}{\partial y}\left(\frac{h_\alpha \nu_{t,\alpha}}{\sigma_k}\frac{\partial k_\alpha}{\partial y}\right) + \\ & \quad P_{k,\alpha} - \mathcal{E}_{\alpha+1/2} k_{\alpha+1/2} + \mathcal{E}_{\alpha+1/2} k_{\alpha-1/2}, \end{aligned}$$

$$\begin{aligned} \frac{\partial\big(h_\alpha \epsilon_\alpha\big)}{\partial t} + \frac{\partial}{\partial x}\big(h_\alpha \epsilon_\alpha u_\alpha\big) + \frac{\partial}{\partial y}\big(h_\alpha \epsilon_\alpha v_\alpha\big) &= \frac{\partial}{\partial x}\left(\frac{h_\alpha \nu_{t,\alpha}}{\sigma_\epsilon}\frac{\partial \epsilon_\alpha}{\partial x}\right) + \frac{\partial}{\partial y}\left(\frac{h_\alpha \nu_{t,\alpha}}{\sigma_\epsilon}\frac{\partial \epsilon_\alpha}{\partial y}\right) + \\ & \quad P_{\epsilon,\alpha} - \mathcal{E}_{\alpha+1/2} \epsilon_{\alpha+1/2} + \mathcal{E}_{\alpha+1/2} \epsilon_{\alpha-1/2}. \end{aligned}$$

Note that this system can be rewritten in compact vector form as

$$\frac{\partial \mathbf{W}}{\partial t} + \frac{\partial \mathbf{F}(\mathbf{W})}{\partial x} + \frac{\partial \mathbf{G}(\mathbf{W})}{\partial y} = \frac{\partial \mathbf{D_x}(\mathbf{W})}{\partial x} + \frac{\partial \mathbf{D_y}(\mathbf{W})}{\partial y} + \mathbf{Q}(\mathbf{W}) + \mathbf{R}(\mathbf{W}), \tag{7.2.19}$$

$$\mathbf{W} = \begin{pmatrix} H \\ h_1 u_1 \\ h_2 u_2 \\ \vdots \\ h_M u_M \\ h_1 v_1 \\ h_2 v_2 \\ \vdots \\ h_M v_M \\ h_1 k_1 \\ h_2 k_2 \\ \vdots \\ h_M k_M \\ h_1 \epsilon_1 \\ h_2 \epsilon_2 \\ \vdots \\ h_M \epsilon_M \end{pmatrix}, \quad \mathbf{F}(\mathbf{W}) = \begin{pmatrix} \sum\limits_{\alpha=1}^{M} h_\alpha u_\alpha \\ h_1 u_1^2 + \dfrac{1}{2} g h_1 H \\ h_2 u_2^2 + \dfrac{1}{2} g h_2 H \\ \vdots \\ h_M u_M^2 + \dfrac{1}{2} g h_M H \\ h_1 u_1 v_1 \\ h_2 u_2 v_2 \\ \vdots \\ h_M u_M v_M \\ h_1 u_1 k_1 \\ h_2 u_2 k_2 \\ \vdots \\ h_M u_M k_M \\ h_1 u_1 \epsilon_1 \\ h_2 u_2 \epsilon_2 \\ \vdots \\ h_M u_M \epsilon_M \end{pmatrix}, \quad \mathbf{G}(\mathbf{W}) = \begin{pmatrix} \sum\limits_{\alpha=1}^{M} h_\alpha v_\alpha \\ h_1 u_1 v_1 \\ h_2 u_2 v_2 \\ \vdots \\ h_M u_M v_M \\ h_1 v_1^2 + \dfrac{1}{2} g h_1 H \\ h_2 v_2^2 + \dfrac{1}{2} g h_2 H \\ \vdots \\ h_M v_M^2 + \dfrac{1}{2} g h_M H \\ h_1 v_1 k_1 \\ h_2 v_2 k_2 \\ \vdots \\ h_M v_M k_M \\ h_1 v_1 \epsilon_1 \\ h_2 v_2 \epsilon_2 \\ \vdots \\ h_M v_M \epsilon_M \end{pmatrix} \quad \mathbf{Q}(\mathbf{W}) = \begin{pmatrix} 0 \\ -g h_1 \dfrac{\partial B}{\partial x} \\ -g h_2 \dfrac{\partial B}{\partial x} \\ \vdots \\ -g h_M \dfrac{\partial B}{\partial x} \\ -g h_1 \dfrac{\partial B}{\partial y} \\ -g h_2 \dfrac{\partial B}{\partial y} \\ \vdots \\ -g h_M \dfrac{\partial B}{\partial y} \\ 0 \\ 0 \\ \vdots \\ 0 \\ 0 \\ 0 \\ \vdots \\ 0 \end{pmatrix},$$

$$\mathbf{D_x}(\mathbf{W}) = \begin{pmatrix} 0 \\ 2h_1\nu_{h,1}\dfrac{\partial u_1}{\partial x} \\ 2h_2\nu_{h,2}\dfrac{\partial u_2}{\partial x} \\ \vdots \\ 2h_M\nu_{h,M}\dfrac{\partial u_M}{\partial x} \\ h_1\nu_{h,1}\left(\dfrac{\partial u_1}{\partial y}+\dfrac{\partial v_1}{\partial x}\right) \\ h_2\nu_{h,2}\left(\dfrac{\partial u_2}{\partial y}+\dfrac{\partial v_2}{\partial x}\right) \\ \vdots \\ h_M\nu_{h,M}\left(\dfrac{\partial u_M}{\partial y}+\dfrac{\partial v_M}{\partial x}\right) \\ \dfrac{h_1\nu_{t,1}}{\sigma_k}\dfrac{\partial k_1}{\partial x} \\ \dfrac{h_2\nu_{t,2}}{\sigma_k}\dfrac{\partial k_2}{\partial x} \\ \vdots \\ \dfrac{h_M\nu_{t,M}}{\sigma_k}\dfrac{\partial k_M}{\partial x} \\ \dfrac{h_1\nu_{t,1}}{\sigma_\epsilon}\dfrac{\partial \epsilon_1}{\partial x} \\ \dfrac{h_2\nu_{t,2}}{\sigma_\epsilon}\dfrac{\partial \epsilon_2}{\partial x} \\ \vdots \\ \dfrac{h_M\nu_{t,M}}{\sigma_\epsilon}\dfrac{\partial \epsilon_M}{\partial x} \end{pmatrix}, \qquad \mathbf{D_y}(\mathbf{W}) = \begin{pmatrix} 0 \\ h_1\nu_{h,1}\left(\dfrac{\partial u_1}{\partial y}+\dfrac{\partial v_1}{\partial x}\right) \\ h_2\nu_{h,2}\left(\dfrac{\partial u_2}{\partial y}+\dfrac{\partial v_2}{\partial x}\right) \\ \vdots \\ h_M\nu_{h,M}\left(\dfrac{\partial u_M}{\partial y}+\dfrac{\partial v_M}{\partial x}\right) \\ 2h_1\nu_{h,1}\dfrac{\partial v_1}{\partial y} \\ 2h_2\nu_{h,2}\dfrac{\partial v_2}{\partial y} \\ \vdots \\ 2h_M\nu_{h,M}\dfrac{\partial v_M}{\partial y} \\ \dfrac{h_1\nu_{t,1}}{\sigma_k}\dfrac{\partial k_1}{\partial y} \\ \dfrac{h_2\nu_{t,2}}{\sigma_k}\dfrac{\partial k_2}{\partial y} \\ \vdots \\ \dfrac{h_M\nu_{t,M}}{\sigma_k}\dfrac{\partial k_M}{\partial y} \\ \dfrac{h_1\nu_{t,1}}{\sigma_\epsilon}\dfrac{\partial \epsilon_1}{\partial y} \\ \dfrac{h_2\nu_{t,2}}{\sigma_\epsilon}\dfrac{\partial \epsilon_2}{\partial y} \\ \vdots \\ \dfrac{h_M\nu_{t,M}}{\sigma_\epsilon}\dfrac{\partial \epsilon_M}{\partial y} \end{pmatrix}, \qquad \mathbf{R}(\mathbf{W}) = \begin{pmatrix} 0 \\ F_1 \\ F_2 \\ \vdots \\ F_M \\ G_1 \\ G_2 \\ \vdots \\ G_M \\ P_{h,1} \\ P_{h,2} \\ \vdots \\ P_{h,M} \\ P_{\epsilon,1} \\ P_{\epsilon,2} \\ \vdots \\ P_{\epsilon,M} \end{pmatrix}.$$

7.2.2 Boundary conditions for turbulence simulations

The k-ϵ model presents a complex problem when it comes to boundary conditions as turbulent energy is created and dissipated at all solid boundaries. Calculating these rates accurately was the focus of studies reported in [115, 193, 203]. In this study, the commonly utilized approximations for boundary conditions are implemented as in [9]. Hence,

- **Boundary conditions on the walls:** In this work non-slip walls are used. It is assumed that each layer has an equivalent friction velocity, calculated using its mainstream velocity and its height above the bed

  $$\frac{\partial H}{\partial \mathbf{n}} = 0, \qquad u_\alpha = w_\alpha = 0, \qquad k_\alpha = \frac{\upsilon_\alpha^{*2}}{\sqrt{c_\mu}}, \qquad \epsilon_\alpha = \frac{\upsilon_\alpha^{*3}}{\kappa_{vK}\bar{s}},$$

  where κ_{vK} is the Von Karman constant ($\kappa_{vK} = 0.41$), $\bar{s}$ is the normal distance from the wall, and $\mathbf{n}$ is the normal direction from the boundary. The friction velocity υ_α^* is calculated as

  $$\upsilon_\alpha^* = \sqrt{\frac{c_\mu k_\alpha^2}{\epsilon_\alpha}|\nabla \mathbf{u} \cdot \mathbf{n}|}.$$

- **Boundary conditions at the inlet:** For the inlets it is assumed that the water height has a zero gradient across the boundary, the volume of flow is set through the manipulation of fluid velocity, and that other values can be calculated as

  $$k = 2.06655\upsilon_\alpha^{*2}, \qquad \epsilon_\alpha = 1.008687\frac{\epsilon_\gamma \upsilon_\alpha^{*3}}{h_\alpha},$$

  where $\epsilon_\gamma = 9.8$ for Reynolds numbers between 10^4 and 10^5 [9].

- **Boundary conditions at the outlet:** For the outlets it is assumed that the water height and velocities have zero gradient at the boundary, thus the boundary conditions can be expressed as

  $$\frac{\partial H}{\partial \mathbf{n}} = 0, \qquad \frac{\partial u_\alpha}{\partial \mathbf{n}} = 0, \qquad \frac{\partial v_\alpha}{\partial \mathbf{n}} = 0,$$

  this also leads to zero graident in the turbulence variables

  $$\frac{\partial k_\alpha}{\partial \mathbf{n}} = 0, \qquad \frac{\partial \epsilon_\alpha}{\partial \mathbf{n}} = 0.$$

It should be noted that other boundary conditions can easily be implemented but, for the flows under study, these are most suitable.

7.3 Eulerian-Lagrangian method for multilayer turbulent flows

In order to solve the presented system (7.2.19), a method of integration must be selected. In this case a second-order splitting method is used, as in the previous chapter. To achieve this, the time interval is divided into sub-intervals $[t_n, t_{n+1}]$, where $\Delta t = t_{n+1} - t_n$. The conserved variables $\mathbf{W}$ are written as $\mathbf{W}^n$ to denote their value at the time t_n. The operator splitting method is given in three stages:

Stage 1: Solve for $\mathbf{W}^*$

$$\begin{aligned} \frac{\partial \mathbf{W}^*}{\partial t} &= \frac{\partial \mathbf{D_x}(\mathbf{W}^*)}{\partial x} + \frac{\partial \mathbf{D_y}(\mathbf{W}^*)}{\partial y} + \mathbf{R}(\mathbf{W}^*), \qquad t \in [t_n, t_{n+1/2}], \\ \mathbf{W}^*(t_n) &= \mathbf{W}(t_n). \end{aligned} \tag{7.3.20}$$

Stage 2: Solve for $\mathbf{W}^{**}$

$$\begin{aligned} \frac{\partial \mathbf{W}^{**}}{\partial t} + \frac{\partial \mathbf{F}(\mathbf{W}^{**})}{\partial x} + \frac{\partial \mathbf{G}(\mathbf{W}^{**})}{\partial y} &= \mathbf{Q}(\mathbf{W}^{**}), \qquad t \in [t_n, t_{n+1}], \\ \mathbf{W}^{**}(t_n) &= \mathbf{W}^*(t_{n+1}). \end{aligned} \tag{7.3.21}$$

Stage 3: Solve for $\mathbf{W}^{***}$

$$\begin{aligned} \frac{\partial \mathbf{W}^{***}}{\partial t} &= \frac{\partial \mathbf{D_x}(\mathbf{W}^{***})}{\partial x} + \frac{\partial \mathbf{D_y}(\mathbf{W}^{***})}{\partial y} + \mathbf{R}(\mathbf{W}^{***}), \qquad t \in [t_{n+1/2}, t_{n+1}], \\ \mathbf{W}^{***}(t_{n+1/2}) &= \mathbf{W}^{**}(t_{n+1}). \end{aligned} \tag{7.3.22}$$

This method is straightforward and fast to implement. It also avoids the complication incurred from the source term $\mathbf{R}(\mathbf{W})$ when calculating fluxes and interpolating values. One problem faced in this method is the calculation of eigenvalues, as they are not trivial and can often become complex in certain flow cases. The proposed ELFV method does not need to compute the eigenvalues of the system. When determining the time-step, an equivalent single-layer shallow water system without turbulence is considered so that the Courant-Friedrichs-Lewy (CFL) condition is set correctly, as shown in [42, 76] this method is fast and stable. While it ignores the turbulent diffusion terms, as they are velocity reducing, the non-diffusive eigenvalues are an appropriate approximation. Here, the eigenvalues for each layer are defined as

$$\lambda_\alpha^\pm = u_\alpha \pm \sqrt{gH}, \qquad \mu_\alpha^\pm = v_\alpha \pm \sqrt{gH}, \qquad \alpha = 1, 2 \ldots, M.$$

Thus the time-step is adjusted for the maximum wave speed in the shallow water system.

7.3.1 The Eulerian step

In order to discretise the stage (7.3.21) the spatial domain is divided into control volumes $V_{ij} = [x_{i-\frac{1}{2}}, x_{i+\frac{1}{2}}] \times [y_{j-\frac{1}{2}}, y_{j+\frac{1}{2}}]$ as shown in Figure 5.4 (on page 139). As detailed, the volumes V_{ij} are centred at (x_i, y_j) with uniform sizes Δx and Δy. We use the following notations

$$\mathbf{W}_{i\pm\frac{1}{2},j}(t) = \mathbf{W}(t, x_{i\pm\frac{1}{2}}, y_j),$$

$$\mathbf{W}_{i,j\pm\frac{1}{2}}(t) = \mathbf{W}(t, x_i, y_{j\pm\frac{1}{2}}),$$

and

$$\mathbf{W}_{i,j}(t) = \frac{1}{\Delta x}\frac{1}{\Delta y}\int_{x_{i-\frac{1}{2}}}^{x_{i+\frac{1}{2}}}\int_{y_{j-\frac{1}{2}}}^{y_{i+\frac{1}{2}}} \mathbf{W}(t,x,y)\ dydx,$$

to denote the point-values and cell-average of the variable $\mathbf{W}$ at the gridpoint $(t, x_{i\pm\frac{1}{2}}, y_j)$, $(t, x_i, y_{j\pm\frac{1}{2}})$, and (t, x_i, y_j), respectively. By integrating the equation (7.3.21) in space over the control volume $V_{i,j}$ shown in Figure 5.4, the following semi-discrete equations are obtained

$$\frac{d\mathbf{W}_{i,j}}{dt} + \frac{\mathbf{F}_{i+1/2,j} - \mathbf{F}_{i-1/2,j}}{\Delta x} + \frac{\mathbf{G}_{i,j+1/2} - \mathbf{G}_{i,j-1/2}}{\Delta y} = \Delta t \mathbf{Q}_{i,j}, \tag{7.3.23}$$

where $\mathbf{F}_{i\pm1/2,j} = \mathbf{F}(\mathbf{W}_{i\pm1/2,j})$ and $\mathbf{G}_{i,j\pm1/2} = \mathbf{G}(\mathbf{W}_{i,j\pm1/2})$ are the numerical fluxes at the cell interfaces $x = x_{i\pm1/2}$ and $y = y_{i\pm1/2}$. By using divergence theorem to integrate the control volume V_{ij}, we obtain

$$\begin{aligned}
\frac{\partial}{\partial t}\int_{V_{i,j}} H\ dV + \sum_{\alpha=1}^{M}\oint_{\mathcal{S}_{i,j}} \left(l_\alpha H u_\alpha \mathbf{n}_x + l_\alpha H v_\alpha \mathbf{n}_y\right)\ d\sigma &= 0,\\
\frac{\partial}{\partial t}\int_{V_{i,j}} l_\alpha H u_\alpha\ dV + \oint_{\mathcal{S}_{i,j}} \left(\left(l_\alpha H u_\alpha^2 + \frac{1}{2} g l_\alpha H^2\right)\mathbf{n}_x + H u_\alpha v_\alpha \mathbf{n}_y\right) d\sigma &= -g l_\alpha H \oint_{\mathcal{S}_{i,j}} B \mathbf{n}_x\ d\sigma,\\
\frac{\partial}{\partial t}\int_{V_{i,j}} l_\alpha H v_\alpha\ dV + \oint_{\mathcal{S}_{i,j}} \left(H u_\alpha v_\alpha \mathbf{n}_x + \left(l_\alpha H v_\alpha^2 + \frac{1}{2} g l_\alpha H^2\right)\mathbf{n}_y\right) d\sigma &= -g l_\alpha H \oint_{S_i} B \mathbf{n}_y\ d\sigma,\\
\frac{\partial}{\partial t}\int_{V_{i,j}} h_\alpha k_\alpha\ dV + \oint_{\mathcal{S}_{i,j}} \left(h_\alpha k_\alpha u_\alpha\right)\mathbf{n}_x + \left(h_\alpha k_\alpha v_\alpha\right)\mathbf{n}_y\ d\sigma &= 0,\\
\frac{\partial}{\partial t}\int_{V_{i,j}} h_\alpha \epsilon_\alpha\ dV + \oint_{\mathcal{S}_{i,j}} \left(h_\alpha \epsilon_\alpha u_\alpha\right)\mathbf{n}_x + \left(h_\alpha \epsilon_\alpha v_\alpha\right)\mathbf{n}_y\ d\sigma &= 0,
\end{aligned}$$

where $\boldsymbol{\eta} = (\mathbf{n}_x, \mathbf{n}_y)^T$ denotes the unit outward normal to the surface $\mathcal{S}_{i,j}$ of the control volume V_{ij}. Using the local cell outward normal $\boldsymbol{\eta}$ and tangential $\boldsymbol{\tau} = \boldsymbol{\eta}^\perp$ depicted in Figure 5.5 (on page 140), the above equations can be projected as

$$\frac{\partial}{\partial t}\int_{V_{i,j}} H\, dV + \sum_{\alpha=1}^{M}\oint_{\mathcal{S}_{i,j}} l_\alpha H u_{\alpha,\boldsymbol{\eta}}\, d\sigma \;=\; 0, \tag{7.3.24a}$$

$$\frac{\partial}{\partial t}\int_{V_{i,j}} l_\alpha H u_\alpha\, dV + \oint_{\mathcal{S}_{i,j}} \left(l_\alpha H u_\alpha u_{\alpha,\boldsymbol{\eta}} + \frac{1}{2} g l_\alpha H^2 \mathbf{n}_x \right) d\sigma \;=\; -g l_\alpha H \oint_{S_i} B \mathbf{n}_x\, d\sigma, \tag{7.3.24b}$$

$$\frac{\partial}{\partial t}\int_{V_{i,j}} l_\alpha H v_\alpha\, dV + \oint_{\mathcal{S}_{i,j}} \left(l_\alpha H v_\alpha u_{\alpha,\boldsymbol{\eta}} + \frac{1}{2} g l_\alpha H^2 \mathbf{n}_y \right) d\sigma \;=\; -g l_\alpha H \oint_{S_i} B \mathbf{n}_y\, d\sigma, \tag{7.3.24c}$$

$$\frac{\partial}{\partial t}\int_{V_{i,j}} h_\alpha k_\alpha\, dV + \oint_{\mathcal{S}_{i,j}} h_\alpha k_\alpha u_{\alpha,\boldsymbol{\eta}}\, d\sigma \;=\; 0, \tag{7.3.24d}$$

$$\frac{\partial}{\partial t}\int_{V_{i,j}} h_\alpha \epsilon_\alpha\, dV + \oint_{\mathcal{S}_{i,j}} h_\alpha \epsilon_\alpha u_{\alpha,\boldsymbol{\eta}}\, d\sigma \;=\; 0, \tag{7.3.24e}$$

where the normal projected velocity $u_{\alpha,\boldsymbol{\eta}} = u_\alpha \mathbf{n}_x + v_\alpha \mathbf{n}_y$, and the tangential projected velocity $u_{\alpha,\boldsymbol{\tau}} = v_\alpha \mathbf{n}_x - u_\alpha \mathbf{n}_y$. In order to simplify the system (7.3.24) , first equation (7.3.24b) multiplied by $\mathbf{n}_x$ is summed to the equation (7.3.24c) multiplied by $\mathbf{n}_y$, then equation (7.3.24b) multiplied by $\mathbf{n}_y$ is subtracted from the equation (7.3.24c) multiplied by $\mathbf{n}_x$. These operations result in

$$\begin{aligned}
\frac{\partial}{\partial t}\int_{V_{i,j}} H\, dV + \sum_{\alpha=1}^{M}\oint_{\mathcal{S}_{i,j}} l_\alpha H u_{\alpha,\boldsymbol{\eta}}\, d\sigma &= 0,\\
\frac{\partial}{\partial t}\int_{V_{i,j}} l_\alpha H u_{\alpha,\boldsymbol{\eta}}\, dV + \oint_{\mathcal{S}_{i,j}} \left(l_\alpha H u_{\alpha,\boldsymbol{\eta}} u_{\alpha,\boldsymbol{\eta}} + \frac{1}{2} g l_\alpha H^2 \right) d\sigma &= -g l_\alpha H \oint_{S_{i,j}} B\, d\sigma,\\
\frac{\partial}{\partial t}\int_{V_{i,j}} l_\alpha H u_{\alpha,\boldsymbol{\tau}}\, dV + \oint_{\mathcal{S}_{i,j}} l_\alpha H u_{\alpha,\boldsymbol{\tau}} u_{\alpha,\boldsymbol{\eta}}\, d\sigma &= 0,\\
\frac{\partial}{\partial t}\int_{V_{i,j}} h_\alpha k_\alpha\, dV + \oint_{\mathcal{S}_{i,j}} h_\alpha k_\alpha u_{\alpha,\boldsymbol{\eta}}\, d\sigma &= 0,\\
\frac{\partial}{\partial t}\int_{V_{i,j}} h_\alpha \epsilon_\alpha\, dV + \oint_{\mathcal{S}_{i,j}} h_\alpha \epsilon_\alpha u_{\alpha,\boldsymbol{\eta}}\, d\sigma &= 0,
\end{aligned} \tag{7.3.25}$$

which can be rewritten in a differential form as

$$\begin{aligned}
\frac{\partial H}{\partial t} + \sum_{\alpha=1}^{M} \frac{\partial}{\partial \boldsymbol{\eta}} \left(l_\alpha H u_{\alpha,\boldsymbol{\eta}} \right) &= 0,\\
\frac{\partial}{\partial t} \left(l_\alpha H u_{\alpha,\boldsymbol{\eta}} \right) + \frac{\partial}{\partial \boldsymbol{\eta}} \left(l_\alpha H u_{\alpha,\boldsymbol{\eta}}^2 + \frac{1}{2} g l_\alpha H^2 \right) &= -g l_\alpha H \frac{\partial B}{\partial \boldsymbol{\eta}},\\
\frac{\partial}{\partial t} \left(l_\alpha H u_{\alpha,\boldsymbol{\tau}} \right) + \frac{\partial}{\partial \boldsymbol{\eta}} \left(l_\alpha H u_{\alpha,\boldsymbol{\eta}} u_{\alpha,\boldsymbol{\tau}} \right) &= 0,\\
\frac{\partial}{\partial t} \left(l_\alpha H k_\alpha \right) + \frac{\partial}{\partial \boldsymbol{\eta}} \left(l_\alpha H u_{\alpha,\boldsymbol{\eta}} k_\alpha \right) &= 0,\\
\frac{\partial}{\partial t} \left(l_\alpha H \epsilon_\alpha \right) + \frac{\partial}{\partial \boldsymbol{\eta}} \left(l_\alpha H u_{\alpha,\boldsymbol{\eta}} u_{\alpha,\boldsymbol{\tau}} \right) &= 0,
\end{aligned} \tag{7.3.26}$$

The system (7.3.26) can also be reformulated in a non-conservative form as

$$\begin{aligned}
\frac{D_0 H}{Dt} + \sum_{\alpha=1}^{M} l_\alpha H \frac{\partial u_{\alpha,\boldsymbol{\eta}}}{\partial \boldsymbol{\eta}} &= 0, \\
\frac{D_\alpha u_{\alpha,\boldsymbol{\eta}}}{Dt} + g \frac{\partial H}{\partial \boldsymbol{\eta}} &= -g \frac{\partial B}{\partial \boldsymbol{\eta}}, \\
\frac{D_\alpha u_{\alpha,\boldsymbol{\tau}}}{Dt} + u_{\alpha,\boldsymbol{\tau}} \frac{\partial u_{\alpha,\boldsymbol{\eta}}}{\partial \boldsymbol{\eta}} &= 0, \\
\frac{D_\alpha k_\alpha}{Dt} + k_\alpha \frac{\partial u_{\alpha,\boldsymbol{\eta}}}{\partial \boldsymbol{\eta}} &= 0, \\
\frac{D_\alpha \epsilon_\alpha}{Dt} + \epsilon_\alpha \frac{\partial u_{\alpha,\boldsymbol{\eta}}}{\partial \boldsymbol{\eta}} &= 0,
\end{aligned} \tag{7.3.27}$$

where $\frac{D_\zeta}{Dt}$ is the total material derivative defined as

$$\frac{D_\zeta}{Dt} = \frac{\partial}{\partial t} + U_\zeta \frac{\partial}{\partial \boldsymbol{\eta}}, \qquad \zeta = 0, 1, \ldots, M.$$

This method allows us to simplify the 2D system to a 1D system along each of the surfaces of the control volume $V_{i,j}$. It should be noted that the projected system is only used to reconstruct numerical fluxes; these are then used to solve the system in (7.3.21).

7.3.2 The Lagrangian step

The modified Method of Characteristics (MoC) is applied to the projected system (7.3.27) in order to solve for the numerical fluxes $\mathbf{F}_{i\pm1/2,j}$ and $\mathbf{G}_{i,j\pm1/2}$. A regular grid is imposed at the next time-step and the flow trajectories are backtracked to the previous time levels to establish the departure points, as with [144, 157]. Assuming that the departure points are accurately approximated, the predictor stage in the ELFV method applied to the multilayer SWEs is defined by the solution of the system (7.3.27) as

$$\begin{aligned}
H^n_{i+1/2,j} &= \widehat{H}^n_{\alpha,i+1/2,j} - \frac{\Delta t}{\Delta x} \widehat{h}^n_{i+1/2,j} \left((u_{\alpha,\boldsymbol{\eta}})^n_{i+1,j} - (u_{\alpha,\boldsymbol{\eta}})^n_{i,j} \right), \\
\left(u_{\alpha,\boldsymbol{\eta}} \right)^n_{i+1/2,j} &= \left(\widehat{u}_{\alpha,\boldsymbol{\eta}} \right)^n_{i+1/2,j} - g \frac{\Delta t}{\Delta x} \Big((h_\alpha + B)^n_{i+1,j} - (h_\alpha + B)^n_{i,j} \Big), \\
\left(u_{\alpha,\boldsymbol{\tau}} \right)^n_{i+1/2,j} &= \left(\widehat{u}_{\alpha,\boldsymbol{\tau}} \right)^n_{i+1/2,j} - \frac{\Delta t}{\Delta x} \left(\widehat{u}_{\alpha,\boldsymbol{\tau}} \right)^n_{i+1/2,j} \left((u_{\alpha,\boldsymbol{\eta}})^n_{i+1,j} - (u_{\alpha,\boldsymbol{\eta}})^n_{i,j} \right), \\
\left(k_\alpha \right)^n_{i+1/2,j} &= \left(\widehat{k}_\alpha \right)^n_{i+1/2,j} - \frac{\Delta t}{\Delta x} \left(\widehat{k}_\alpha \right)^n_{i+1/2,j} \left((u_{\alpha,\boldsymbol{\eta}})^n_{i+1,j} - (u_{\alpha,\boldsymbol{\eta}})^n_{i,j} \right), \\
\left(\epsilon_\alpha \right)^n_{i+1/2,j} &= \left(\widehat{\epsilon}_\alpha \right)^n_{i+1/2,j} - \frac{\Delta t}{\Delta x} \left(\widehat{\epsilon}_\alpha \right)^n_{i+1/2,j} \left((u_{\alpha,\boldsymbol{\eta}})^n_{i+1,j} - (u_{\alpha,\boldsymbol{\eta}})^n_{i,j} \right),
\end{aligned} \tag{7.3.28}$$

where

$$\widehat{H}^n_{i+1/2,j} = H\left(t_n, X_{\alpha,i+1/2}(t_n), y_j\right), \qquad \left(\widehat{u}_{\alpha,\boldsymbol{\eta}}\right)^n_{i+1/2,j} = u_{\alpha,\boldsymbol{\eta}}\left(t_n, X_{\alpha,i+1/2}(t_n), y_j\right),$$

$$\left(\widehat{u}_{\alpha,\boldsymbol{\tau}}\right)^n_{i+1/2,j} = u_{\alpha,\boldsymbol{\tau}}(t_n, X_{\alpha,i+1/2}(t_n), y_j), \qquad \left(\widehat{k}_{\alpha}\right)^n_{i+1/2,j} = k_\alpha\Big(t_n, X_{\alpha,i+1/2}(t_n), y_j\Big),$$

$$\left(\widehat{\epsilon}_{\alpha}\right)^n_{i+1/2,j} = \epsilon_\alpha\left(t_n, X_{\alpha,i+1/2}(t_n), y_j\right).$$

The intermediate states in the y-direction $H^n_{i,j+1/2}$, $(u_{\alpha,\boldsymbol{\eta}})^n_{i,j+1/2}$, $(u_{\alpha,\boldsymbol{\tau}})^n_{i,j+1/2}$, $(k_\alpha)^n_{i,j+1/2}$ and $(\epsilon_\alpha)^n_{i,j+1/2}$ are evaluated in the same manner. Once the projected states are calculated in the predictor stage (7.3.28), the states $\mathbf{W}^n_{i\pm1/2,j}$ and $\mathbf{W}^n_{i,j\pm1/2}$ are recovered by using the transformations $v_\alpha = (u_{\alpha,\boldsymbol{\tau}}, u_{\alpha,\boldsymbol{\eta}}) \cdot \boldsymbol{\eta}$ and $u_\alpha = (u_{\alpha,\boldsymbol{\tau}}, u_{\alpha,\boldsymbol{\eta}}) \cdot \boldsymbol{\tau}$.

Next, the discretisation of source terms $\mathbf{Q}_{i,j}$ in (7.3.23) is carried out in the same manner as in Chapter 6. The C-property, as used in Chapter 5, is designed specifically for SWE formulations. As this model includes turbulence we will assess the well-balanced property of the discretisation again using the lake at rest problem [115]. This means that the discretised source terms should satisfy

$$H + B = cte_1, \qquad u_\alpha = v_\alpha = 0, \qquad \rho_\alpha = cte_2, \tag{7.3.29}$$

where cte_1 and cte_2 are constants. As the velocities are set to zero there can be no turbulent kinetic energy thus

$$k_\alpha = 0, \qquad \varepsilon_\alpha = 0.$$

Therefore, the system reduces to

$$\mathbf{F}(\mathbf{W}) + \mathbf{G}(\mathbf{W}) = \mathbf{Q}(\mathbf{W}).$$

This enables us to perform a similar discretisation to Chapter 6, such that the discretised source terms are well-balanced with the discretised flux terms which gives

$$\begin{aligned} \left(g h_\alpha \frac{\partial B}{\partial x}\right)^n_{i,j} &= g\frac{(h_\alpha)^n_{i+1/2,j} + (h_\alpha)^n_{i-1/2,j}}{2}\frac{B^n_{i+1,j} - B^n_{i-1,j}}{2\Delta x}, \\ \left(g h_\alpha \frac{\partial B}{\partial y}\right)^n_{i,j} &= g\frac{(h_\alpha)^n_{i,j+1/2} + (h_\alpha)^n_{i,j-1/2}}{2}\frac{B^n_{i,j+1} - B^n_{i,j-1}}{2\Delta y}, \end{aligned} \tag{7.3.30}$$

where the averaged solutions are defined by

$$(h_\alpha)^n_{i+1/2,j} = \frac{(h_\alpha)^n_{i+1,j} + (h_\alpha)^n_{i-1,j}}{2},$$

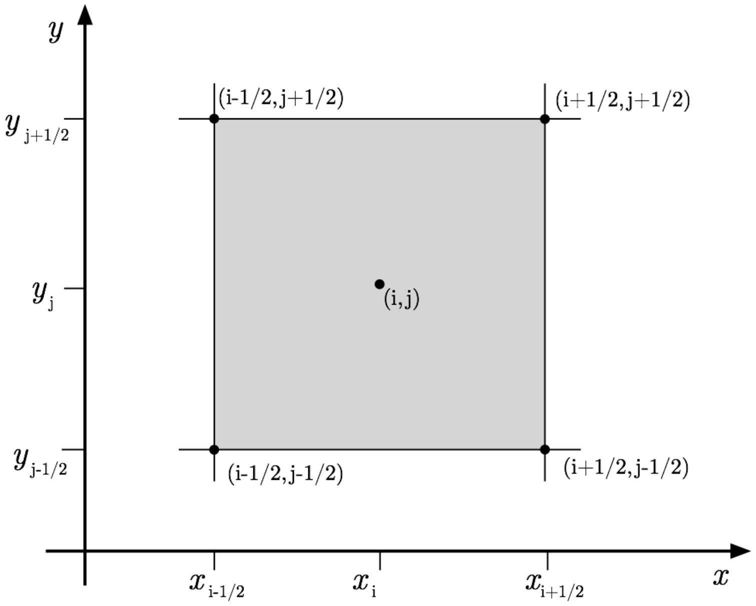

Figure 7.2: The staggered grid used for the space discretisation, showing control volume $V_{i,j}$.

$$(h_\alpha)^n_{i,j+1/2} = \frac{(h_\alpha)^n_{i,j+1} + (h_\alpha)^n_{i,j-1}}{2}.$$

It should be noted that the discretisation of source terms is achieved by projecting the original shallow water model into the local system where a dimension-by-dimension discretisation is used. Finally, we must consider the discretisation of the diffusion terms in steps (7.3.20) and (7.3.22). We begin with the staggered grid used in this method, shown in Figure 7.2, and consider the diffusion of some vector of variables $\mathbf{W}$ in a simple 2D manner such that

$$\nabla \cdot \Big(\boldsymbol{\mathcal{D}} \nabla \mathbf{W} \Big) = 0.$$

where $\boldsymbol{\mathcal{D}}(t, x, y, \mathbf{W})$ is a function of space time and $\mathbf{W}$ means that a linear approximation is not possible, therefore we employ the technique described in [178]. The space discretisation of this problem in a control volume such as $V_{i,j}$, as shown in Figure 7.2, when split into x and y components reads as

$$\left(\frac{\partial}{\partial x} \left(\boldsymbol{\mathcal{D}} \frac{\partial \mathbf{W}}{\partial x} \right) \right)_{i,j} := \frac{\boldsymbol{\mathcal{D}}_{i,j} + \boldsymbol{\mathcal{D}}_{i+1,j}}{2} \frac{\mathbf{W}_{i+1,j} - \mathbf{W}_{i,j}}{(\Delta x)^2} - \frac{\boldsymbol{\mathcal{D}}_{i-1,j} + \boldsymbol{\mathcal{D}}_{i,j}}{2} \frac{\mathbf{W}_{i,j} - \mathbf{W}_{i-1,j}}{(\Delta x)^2},$$

$$\left(\frac{\partial}{\partial y} \left(\boldsymbol{\mathcal{D}} \frac{\partial \mathbf{W}}{\partial y} \right) \right)_{i,j} := \frac{\boldsymbol{\mathcal{D}}_{i,j} + \boldsymbol{\mathcal{D}}_{i,j+1}}{2} \frac{\mathbf{W}_{i,j+1} - \mathbf{W}_{i,j}}{(\Delta y)^2} - \frac{\boldsymbol{\mathcal{D}}_{i,j-1} + \boldsymbol{\mathcal{D}}_{i,j}}{2} \frac{\mathbf{W}_{i,j} - \mathbf{W}_{i,j-1}}{(\Delta y)^2}.$$

This is then applied to all the diffusive terms in (7.2.19). This procedure is implemented as shown in Figure 7.3.

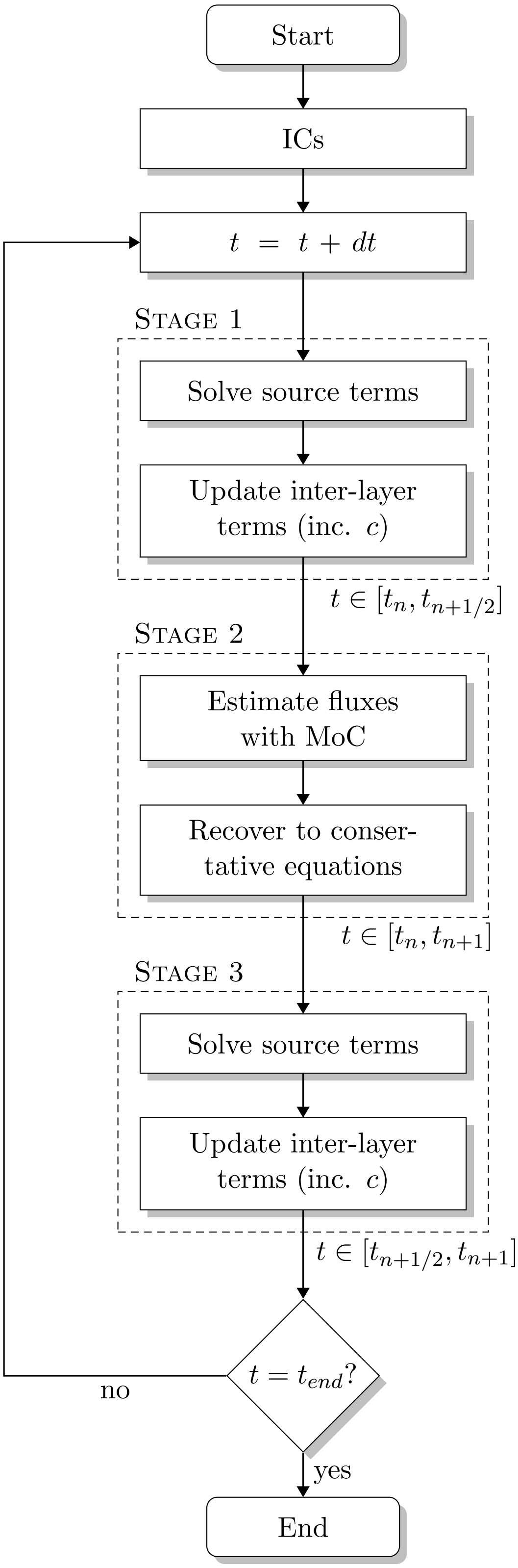

Figure 7.3: A flowchart demonstrating the stages in the proposed 2D Eulerian-Lagrangian procedure, including bed register is highlighted.

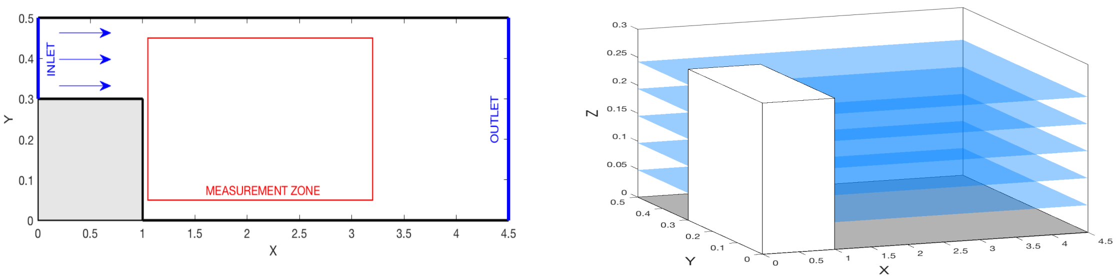

Figure 7.4: Configuration of the measurement zone and a 3D view of the backward-step flow problem domain.

7.4 Numerical results

The aim of this section is two-fold: to validate the presented model and to investigate its adaptability. The model is used to simulate three test cases. First the backward-step problem is used to evaluate the model. This problem is one of the few with experimental data that the model can be proved against and consequently provides an interesting benchmark, as in [9, 68]. It is theorized that the presented model will show some novel flow features due to its quasi-3D nature. Secondly, the model is tested against a 3D recirculation flow problem. Here, it is validated against a 3D simulation using the OpenFOAM software [200] in order to demonstrate its ability to capture complex 3D flow and k-ϵ solutions. The turbulence production coefficients are set to $C_w = 0.001$ and $C_B = 0.005$ as in [42, 46, 75, 182]. This test is similar in set-up to that used in [75]. Finally, the method is compared to a complex dam-break situation over both flat and variable topographies. This demonstrates the ability of the model to capture complex flows while simulating an evolving free-surface and varying bathymetry.

It should be noted that a Courant number of $\mathrm{Cr} = 0.7$ is implemented in all simulations and thus the time-step varies in the simulation according to the condition

$$\Delta t = \mathrm{Cr} \frac{\min\left(\Delta x, \Delta y\right)}{\max\limits_{\alpha=1,\dots,M}\left(|\lambda_\alpha^\pm|, |\ \mu_\alpha^\pm|\right)}.$$

A variety of data is presented to describe the flow. In order to achieve this, the vertical velocity w is calculated using the 2D results by implementing a similar post-processing method to that used [12, 13] and detailed in Chapter 6, see equation (6.4.19) on page 175.

7.4.1 Backward-step flow problem

The first problem addressed is the classical flow around a backward-step problem which creates a recirculation in the flow. The experimental data presented in [68] is used to assess the validity

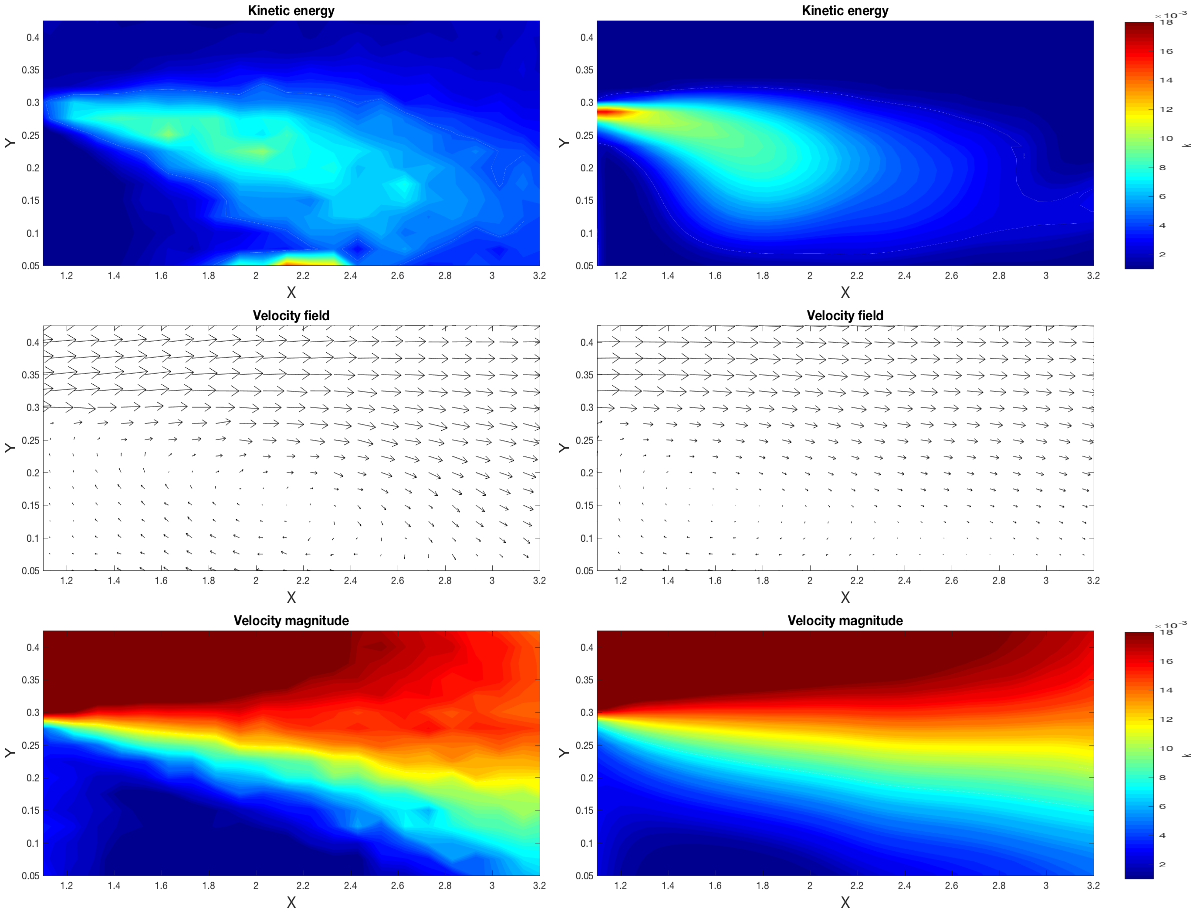

Figure 7.5: Comparison of the k energy (top), velocity (middle), and velocity magnitude (bottom) results in 2D between the experimental data (left) and the simulation data (right) form a 5-layer model.

of results. The domain is 4.5 m by 0.5 m, the step is 1 m by 0.297 m in size. The domain and the measurement zone are shown in Figure 7.4. The flow rate is 24.2×10^{-3} m^3/s and the water at rest has a height of 0.242 m. The Manning roughness coefficient is 0.01 $s/m^{1/3}$ and the eddy viscosity is set to 10^{-3} m^2/s. For this simulation, the inlet boundary condition is set using the flow rate, and the exit boundary condition is set at a water height of 0.242 m. Initial turbulence values of $k(0,x,y,z) = 0.1 \times 10^{-8}$ m^2/s^2 and $\epsilon(0,x,y,z) = 0.1 \times 10^{-8}$ m^2/s^2 are set across the domain. We have used 5-layers for this simulation, to mirror the course discretization used in similar simulations [9]. In which the steady state vertical velocity profile is measured and implemented at the boundary.

First, a comparison is drawn between the k in the xy-plane for the experimental and simulation results. As can be seen, in Figure 7.5 there is some variation between the experimental and the results from the model. A highly turbulent region is created just after the step in the simulation, this is likely to be due to the boundary conditions of the presented model being set to non-slip walls, as seen in other papers. This creates regions of high velocity deviation as

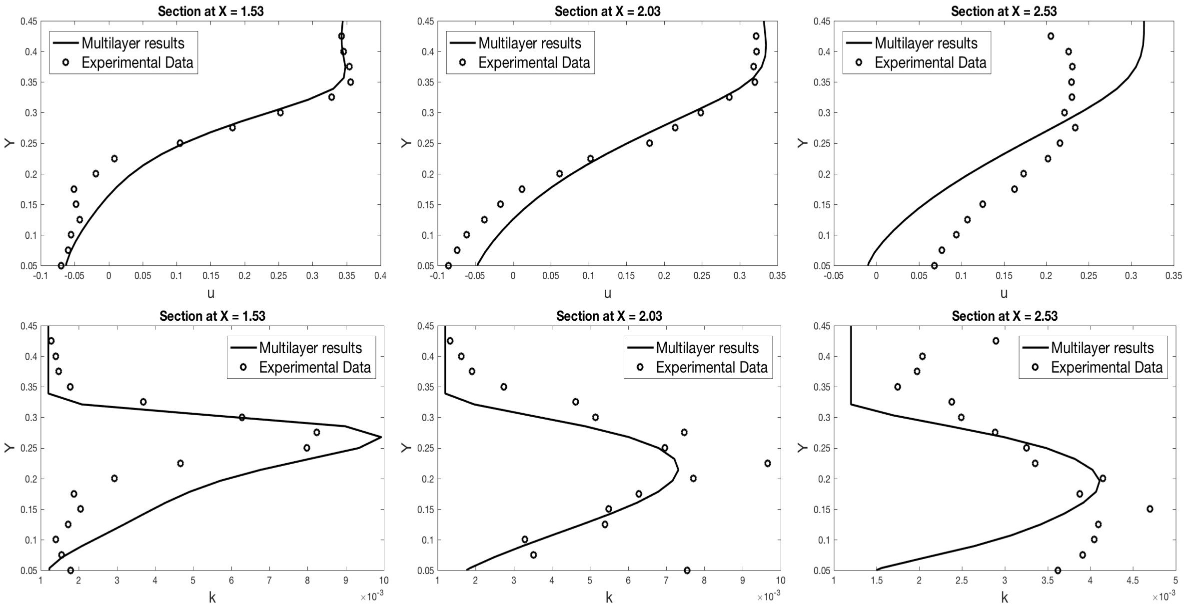

Figure 7.6: Comparison of the flow in terms of velocity u (top) and turbulent kinetic energy k (bottom) at three horizontal cross-sections: $x = 1.53\ m$, $x = 2.03\ m$ and $x = 2.53\ m$.

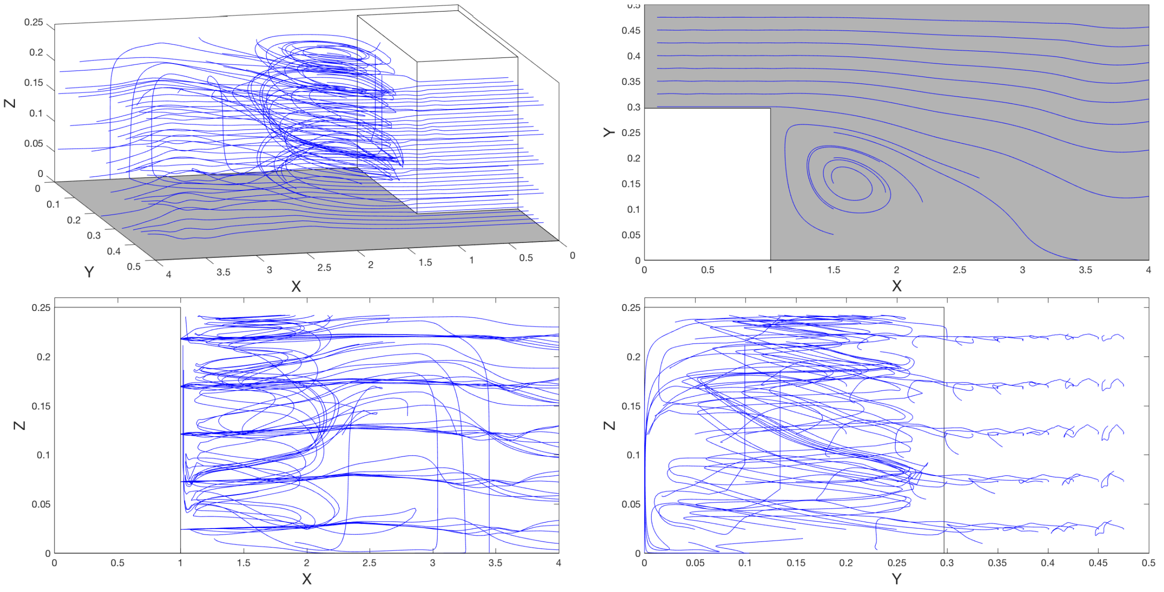

Figure 7.7: Streamlines obtained for backward step flow simulation in the domain view (top left), xy-plane view (top right), xz-plane view (bottom left) and zy-plane view (bottom right).

shown in Figure 7.5. Although the velocity field shown in Figure 7.5 shows a good agreement between the two flows, the magnitude of the recirculation is different, but crucially the feature is still captured. The shape of the area is correct, though the dissipation does not quite match as there is more natural variation in the flow. As the simulation is multilayer and the experimental measurements were taken on the top layer only, the top layer results are presented.

The velocity plots show a good agreement between the simulation and the experimental

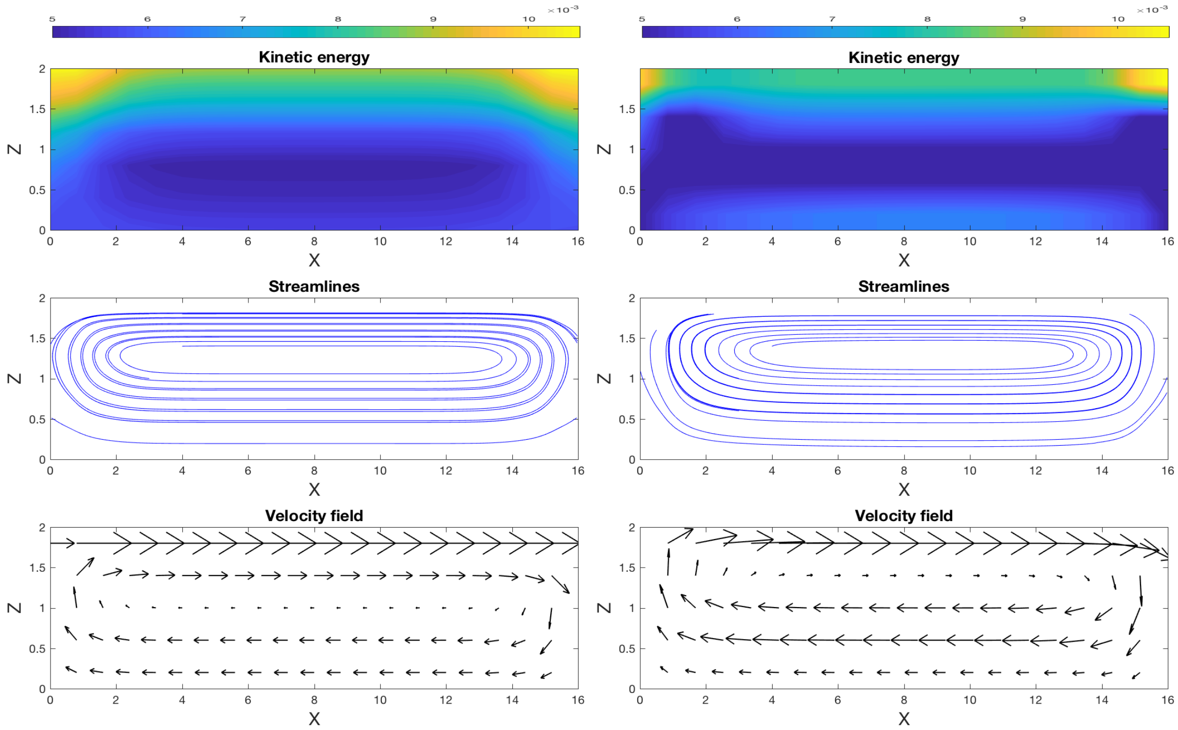

Figure 7.8: Cross-sections in the xz-plane of turbulent energy k (top), streamlines (middle) and velocity fields (bottom) at $y = 8\ m$, at $t = 50\ s$ OpenFOAM (left) and the multilayer model (right).

data. The centre of rotation is slightly further upstream compared to the experimental results, although the magnitude and distribution of the velocity is correct, as seen in Figure 7.5. This is further backed up by the three cross-sections presented in Figure 7.6. These cross-sections show a good agreement with the OpenFOAM data, though there is some degeneration, especially in terms of k when moving downstream. This is likely to be due to the development of the vortex, as although the flow evolves to the near steady state shown in the presented results, it fails to capture the localised deviations shown in the experimental results. This is in-line with the results presented in [9, 68] and appears to be a limitation of the k-ϵ when used with the mesh resolution proposed by those authors.

Finally, the main advantage that this model offers over the single layer model is shown in Figure 7.7: the ability to capture 3D flow effects. The figure depicts the changing flux and evolving vortex with a central point of revolution. This feature, novel to shallow water simulations of this type, shows the detailed and complex nature of the flow and how the method is able to capture the 3D effects of this problem. It goes further to demonstrate that the derived model is able to capture and account for the vertical velocity components even though they are not directly calculated in this model. This capturing of the key problem flow features is only possible with the inclusion of turbulence, which shows the crucial nature of turbulence modelling.

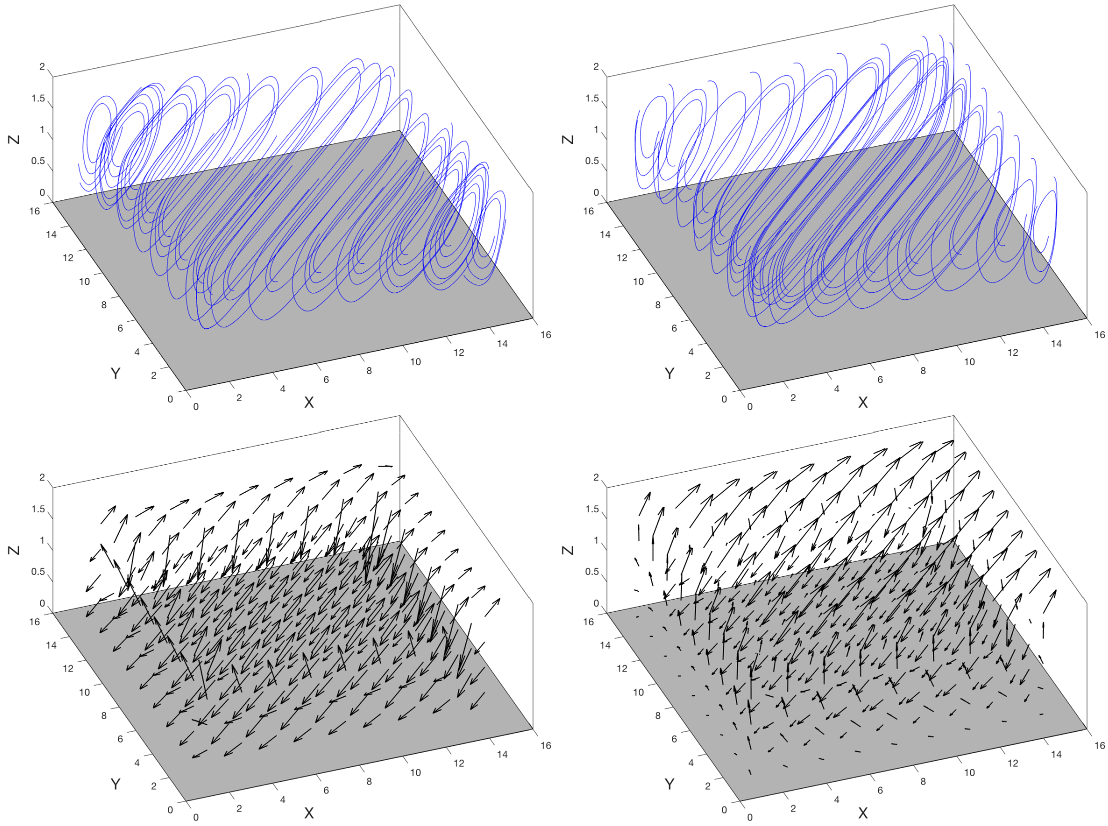

Figure 7.9: Streamlines (top) and velocity fields (bottom) of the recirculating flow at $t = 50\ s$ OpenFOAM (left) and the multilayer model (right).

7.4.2 Recirculation flow problem

Next, a vertical flow problem is considered in order to show the ability of the method to capture the 3D flow and the effects of including a k-ϵ model accurately. The OpenFOAM software is used to validate this model. In order to achieve this, the lid driven flow problem is modified to a 3D equivalent of wind driven flow[2]. Wind speed U_{wi} is set to 10 m/s at 45° to the x-dimension, the domain is altered to $16\ m \times 16\ m \times 2\ m$. The domain is discretised into control volumes of $\Delta x = \Delta y = 0.5\ m,\ \Delta z = 0.4\ m$. The flow is assumed to be at rest initially and can be described as

$$u(0,x,y,z) = 0\ m/s \qquad v(0,x,y,z) = 0\ m/s \qquad H(0,x,y) = 2\ m,$$
$$k(0,x,y,z) = 0.1 \times 10^{-8}\ m^2/s^2, \qquad \epsilon(0,x,y,z) = 0.1 \times 10^{-8}\ m^2/s^2.$$

The walls are modelled as non-slip and implemented with the above boundary conditions. Other variables are kept the same as the test example simulation. This coarse mesh highlights the

---

[2] `https://cfd.direct/openfoam/user-guide/v6-cavity/`

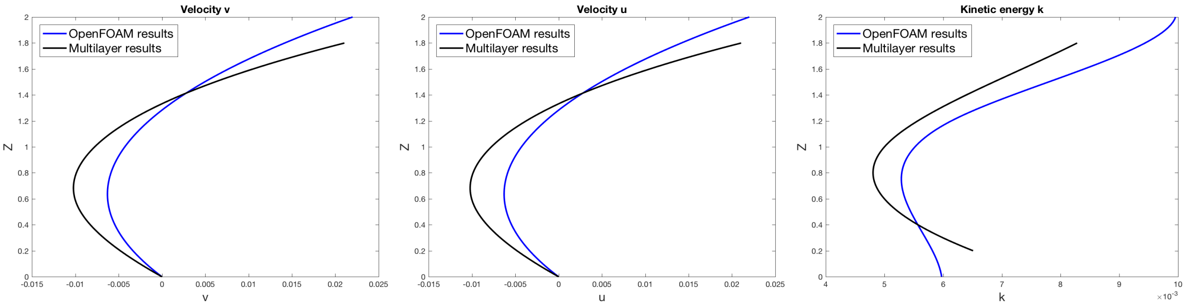

Figure 7.10: Comparison of the x and y-direction velocities and k along the vertical dimension at $x = 8\ m$, $y = 8\ m$ and $t = 50\ s$, between OpenFOAM and the multilayer model.

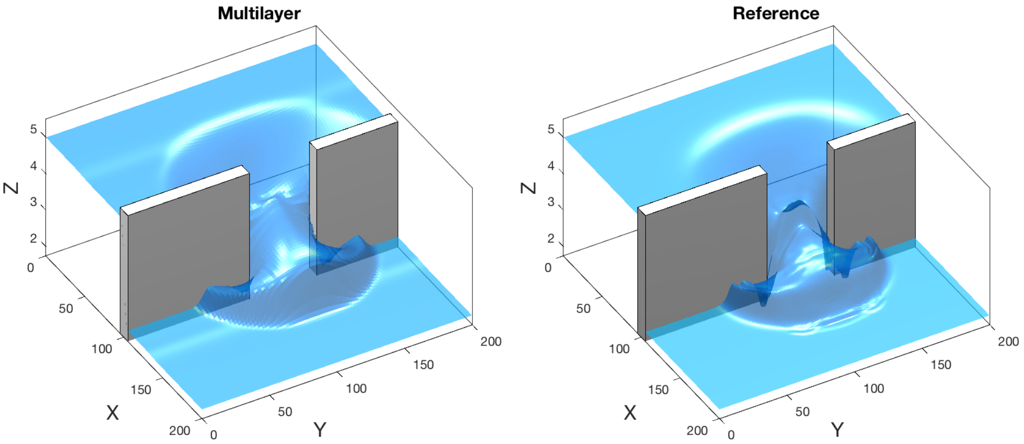

Figure 7.11: A comparison of wave forms at $t = 7.2\ s$ for the presented model (left) and reference solution (right).

flexibility of the system while remaining close to the wind-driven flow model used in the previous chapter and the well-documented lid-driven flow model in OpenFOAM software [200]. The simulation is designed to show the ability of the model to capture 3D flow and is allowed to run for 50 s.

Allowing for slight differences in the type of models, the streamlines shown in Figure 7.8 match the flow well. This is also born out in the Figure 7.8, which gives a cross-section of the turbulent kinetic energy and 2D streamlines. There is a minuscule deviation in flow direction shown in the streamlines but a larger variation in the flow turbulent energy, as the model does not take into account the variation in the vertical direction when calculating turbulent kinetic energy. Beyond this, the model is a good match showing the same formation of turbulent kinetic energy. Figure 7.10 shows the concurrence is between the two models.

The minor disparity between the two flows is likely to be due to the difference in free/restrictive surfaces used in the two solvers. The advantage of the proposed model is clear as it offers comparable accuracy, easier model formulation and is over five times faster to complete (requiring only 71.54 s as compared to 378.16 s).

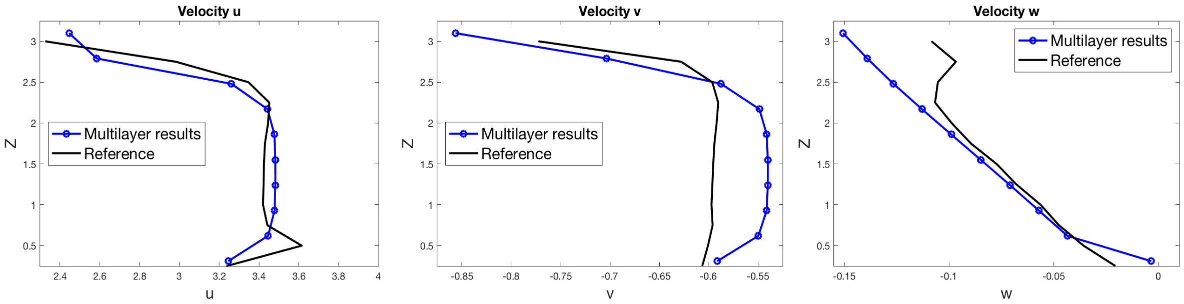

Figure 7.12: Comparison of velocities along the vertical dimension at $x = 115\ m,\ y = 100\ m$ at $t = 7.2\ s$, for the presented model and interFOAM

7.4.3 Partial dam-break flow problem

Finally, a partial dam-break problem is examined with and without a flat bed. First, a standard partial dam-break domain with a flat bed is considered and compared to OpenFOAM results, using the Volume of Fluid method (VoF) [200]. The aim of this step is to validate the model for this class of flow of problems. The domain is then modified by adding in a varying bathymetry, this demonstrates the ability of the model to handle even more complex flows. The effects of varying the number of layers are then evaluated.

The domain is 200 $m \times 200$ m with a 10 m wall (centred about $y = 100$ m) separating the domain into two halves. The water on the west side of the domain has a height of 5 m, and 2 m on the east side. A dam-break occurs between $x = 90$ m to $x = 140$ m at $t = 0$ s. The simulation is allowed to run for 7.2 s. The initial conditions are expressed as

$$u(0,x,y,z) = v(0,x,y,z) = 0\ m/s, \qquad k(0,x,y,z) = 0.1 \times 10^{-8}\ m^2/s^2,$$

$$\epsilon(0,x,y) = 0.1 \times 10^{-8}\ m^2/s^2, \qquad H(0,x,y) = \begin{cases} 5\ m, & \text{if } x \ \leq \ 100\ m, \\ 2\ m, & \text{if } x \ > \ 0\ m. \end{cases}$$

The domain is divided into 100×100 control volumes and 10 layers are used. The results are compared to an equivalent OpenFOAM simulation, using the interFOAM solver[3], where the domain is divided into $200 \times 200 \times 20$. The waveforms created by all both simulations are then compared in Figure 7.11.

There is a good convergence between the simulations, the reference solution waveform has the most pronounced wave-front and hydraulic jump. The presented simulation is slightly less accurate than the OpenFOAM method, this is likely to be due to the lack of z-dimension velocities. Beyond this, the solution has very similar features to the interFOAM solver, including

---

[3] `https://openfoamwiki.net/index.php/InterFoam`

Table 7.2: Errors in velocity and CPU times for the presented model, at points A $(115\ m, 75\ m)$, B $(115\ m, 100\ m)$ and C $(115\ m, 125\ m)$ at $t = 7.2\ s$.

	Velocity u		Velocity v		Velocity w		CPU
Point	L^∞-error	L^2-error	L^∞-error	L^2-error	L^∞-error	L^2-error	time $[s]$
A	7.994E-1	7.606E-1	4.149E-2	1.195E-2	2.881E-2	2.956E-3	30.01
B	3.793E-1	2.650E-1	5.619E-2	1.992E-2	8.052E-2	2.857E-2	
C	1.751E-1	7.780E-2	1.452E-0	5.981E-0	1.638E-1	8.556E-2	

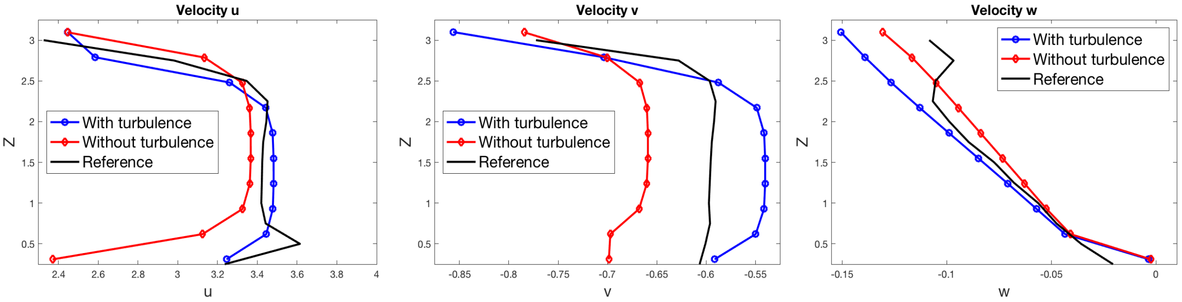

Figure 7.13: Comparison of velocities produced through the inclusion and exclusion of turbulence modelling along the vertical dimension at $x = 115\ m,\ y = 100\ m$ at $t = 7.2\ s$.

the presence of an hydraulic jump and the edge effects at the corners of the dam. It should also be noted that the interFOAM solver includes the effects of fluid-air interaction, therefore for the presented model the effects of wind have also been included. This effect is clearly seen in Figure 7.12, where the velocities of the three simulations are compared along a vertical axis located at $(115\ m, 100\ m)$. These three figures show that there is a very good realization of accurate flow in the presented model, as compared to the reference solution. It is interesting to see that an OpenFOAM simulation of similar discretisation has a similar level of error. This conclusion is supported by the data presented in Table 7.2, which shows a consistent image across the three points viewed: the level of accuracy in the OpenFOAM 3D simulation and the presented model are comparable. This is an encouraging result for the presented model and allows modification of the domain in the next simulation type. It is also worth comparing the CPU times. The presented model is over fifty times faster than the OpenFOAM simulation.

Now we consider the effects of the inclusion of the k-ϵ model in the presented formulation. The formulation should affect the maximum velocities and the discharge rate, as potential energy stored behind the dam will be converted to kinetic and turbulent energy. If the model does not include turbulent energy then a discrepancy should be visible in the results.

The results of the simulation without turbulence, with turbulence and the reference simulation are shown in Figure 7.13. It is interesting to note that the non-turbulent simulation under-estimates the mid body velocities in both the x and y-dimensions, while over-predicting

Table 7.3: Comparison of the discharge, disturbed area, maximum velocity and CPU times at four intervals (1.8 s, 3.6 s, 5.4 s, and 7.2 s) for a turbulent simulation (I) and a simulation without turbulence modelling (II).

Sim.	Time $[s]$	Discharge $[m^3]$	Disturbed area $[m^2]$	Max velocity $[m/s]$	CPU Time [s]
I	1.8	515.2	1893	3.599	11.35
	3.6	1685	3126	4.676	23.50
	5.4	2958	4277	5.019	34.33
	7.2	3731	5334	5.145	47.87
II	1.8	498.9	1375	3.537	9.472
	3.6	1600	2693	4.571	19.89
	5.4	2810	4277	4.927	30.69
	7.2	3545	5468	5.056	41.63

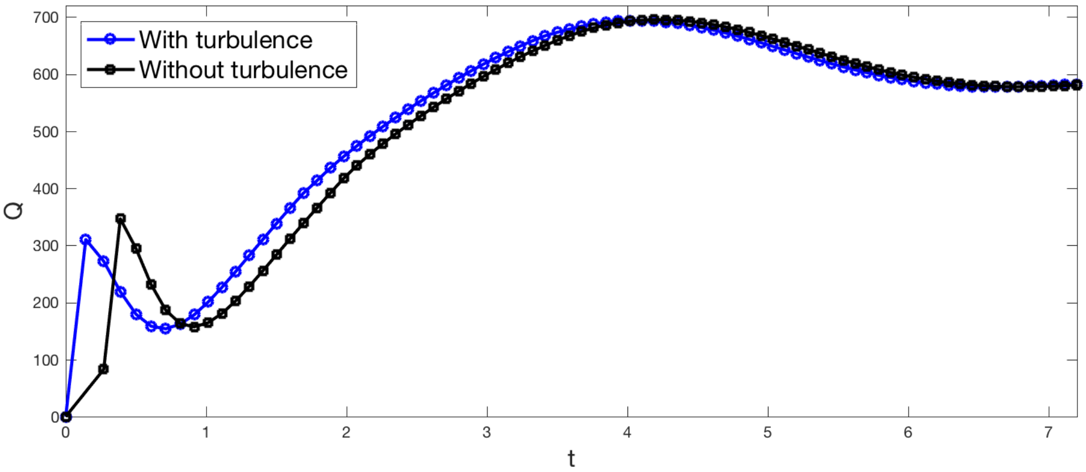

Figure 7.14: Comparison of volumetric discharge for partial dam-break simulations with and without turbulence modelling.

the vertical velocity. This difference presents an interesting change: as shown in Figure 7.14 the discharge profile for the two simulations varies widely, with the turbulent simulation accelerating the discharge much faster initially but settling to a similar rate further on. These differences will become crucial when considering sediment transport, as the changes in maximum velocity, as shown in Table 7.3, and the initial differences in volumetric flow rate Q will effect bed morphology. It is also worth noting that the computational expense for the turbulent simulation at 47.87 s compares to the laminar simulation at 41.63 s. This small discrepancy shows that the inclusion of the k-ϵ model has a minimal effect on the speed of the simulation. Next, the effects of the multilayer assumption in the system of equations is examined, specifically with regard to the effect that varying the number of layers has on the simulation. In order to do this an uneven bathymetry is introduced and the simulation is repeated with 2-layers, 5-layers , and 20-layers. The results are presented in Figure 7.17, and the velocities at the central point of the dam-break $(100\ m, 115\ m)$ are evaluated. In order to demonstrate the ability of the proposed method to

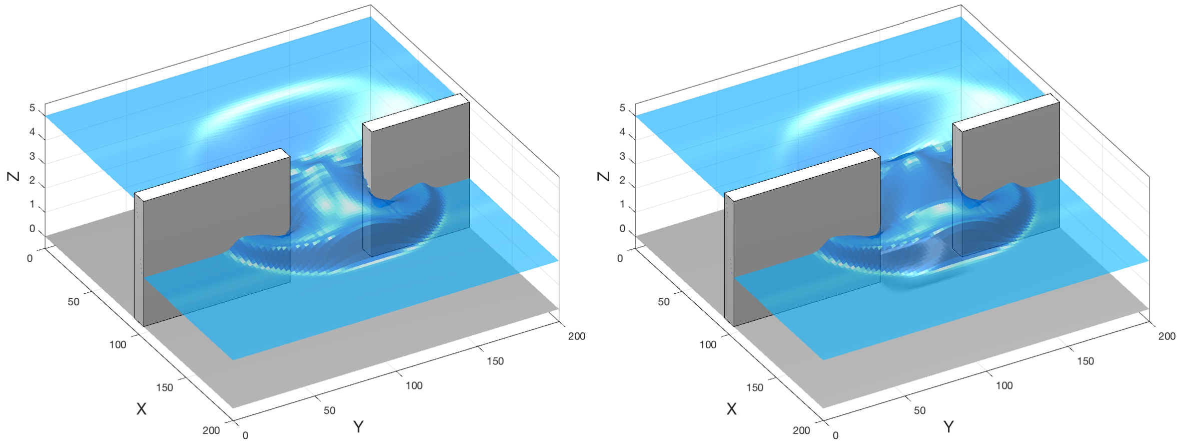

Figure 7.15: Comparison of partial dam-break flow at $t = 7.2\ s$ for the flat (left) and non-flat (right) bathymetry.

handle non-flat bathymetry, a partial dam-break over a dip is considered. This creates a more complex flow situation. The bed is varied with the following equation

$$B(x,y) = \frac{1}{2}\mathcal{B}_x(x) \otimes \mathcal{B}_y(y),$$

where

$$\mathcal{B}_x(x) = \begin{cases} \cos\left(\dfrac{\pi}{50}(x+85)\right), & \text{if } 90\ m \leq x < 140\ m, \\ 0, & \text{elsewhere,} \end{cases}$$

$$\mathcal{B}_y(y) = \begin{cases} \sin\left(\dfrac{\pi}{40}(y+120)\right), & \text{if } 80\ m \leq y < 120\ m, \\ 0, & \text{elsewhere.} \end{cases}$$

This creates a trench 0.5 m deep in the centre of the dam-break. The aim of this simulation is to show that the method can handle this uneven bathymetry and capture the crucial detail that separates this situation from the last. The two simulations are then compared to observe the differences captured. All parameters are kept the same, apart from the topography of the bed. The results are presented in Figure 7.15 and Figure 7.16 and, as is shown, there are small differences caused by the uneven bathymetry: the centre of the high speed portion of the wave is moved further from the dam-break and, while the velocity profile remains similar, there is a slight increase in the disturbed area and the maximum speed with the uneven bed. The dip itself helps to accelerate the discharge.

These small differences demonstrate that the method is even able to capture the fine detail that arises. Though these changes are small, it is important to note that when considering, for example, a movable bed (as we shall see in the next chapter) a huge difference in flow can be caused by even small changes in the wave speed. Thus the ability to account for small changes

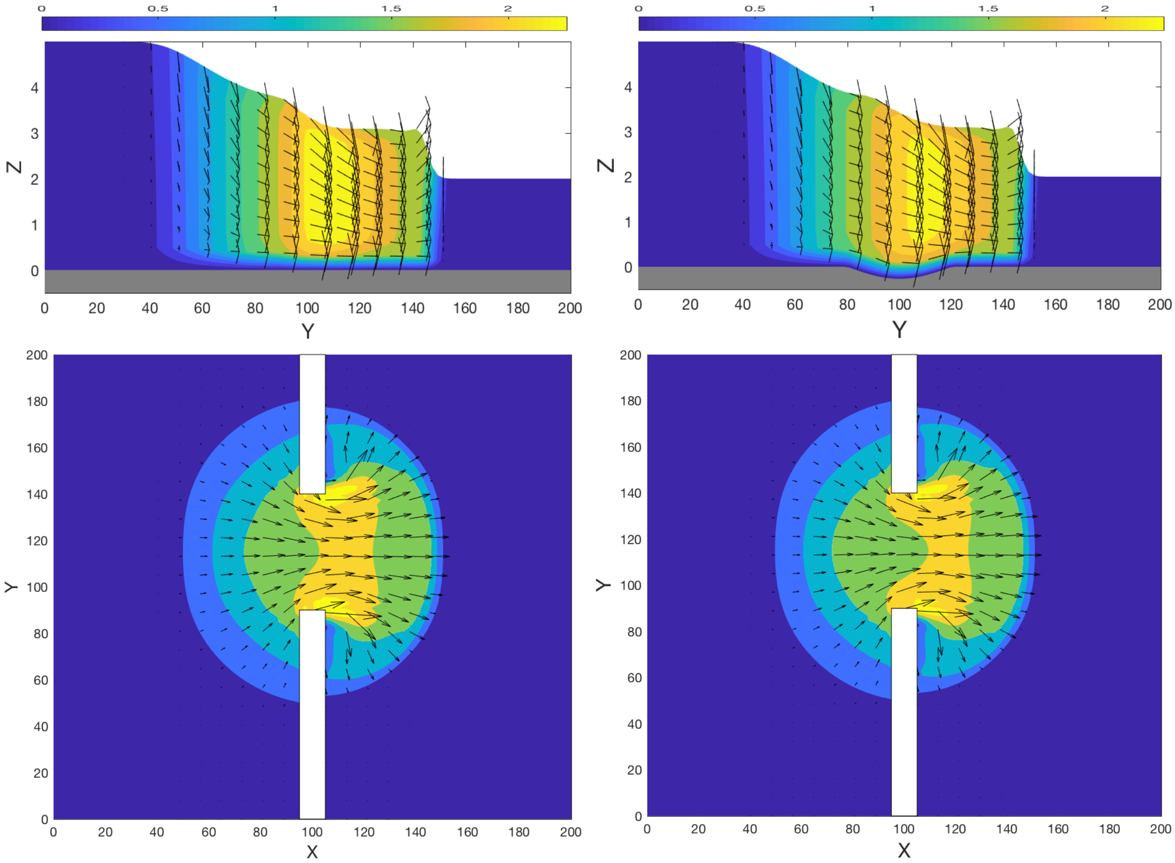

Figure 7.16: A comparison of velocity magnitudes in the yz-plane at $x = 115\ m$ (top) and in the xy-plane for top layer, at $t = 7.2\ s$ for the flat (left) and non-flat (right) bathymetry.

in flow caused by a movable bed is a crucial feature of this model.

As Figure 7.17 shows, there is a growing convergence when moving from 2 to 20-layers and a good agreement at 10-layers. This is further backed up by the results in Table 7.4 which show there is a very small variation between the number of layers in terms of area disturbed. More particularly, as the number of layers increases, the discharge drops. This implies that as the number of layers is increased, a greater resolution and correction for viscous effects is achieved. This implies that, as proposed in [14], if the number of layers becomes large enough, a truly 3D system is recovered; though as shown in Figure 7.17, an impractically large number is not required in order to approach a 3D system. The most significant effect is on maximum velocities which drop by over 10 % between the 2-layer and 20-layer simulation. This effect is small but will become important when modelling sediment transport, as even small fluctuations in velocity can have profound effects on bed and therefore flow patterns. This suggests that the number of layers used in the simulation does not affect the discharge profile or wave-form directly, but does impact the distribution of velocities therein. This is a useful result as it points to a convergence of a more precise vertical velocity distribution when using more layers.

Table 7.4: Comparison of the discharge, disturbed area, maximum velocity and CPU times at four intervals (1.8 s, 3.6 s, 5.4 s, and 7.2 s for the different number of layers).

Number of Layers	Time $[s]$	Discharge $[m^3]$	Disturbed area $[m^2]$	Max velocity $[m/s]$	CPU Time $[s]$
2	1.8	1623	3179	3.515	12.35
	3.6	2859	5012	4.848	23.50
	5.4	4018	6954	5.322	28.33
	7.2	5060	8575	5.556	30.87
5	1.8	1621	3179	3.516	7.580
	3.6	1850	5012	4.805	14.81
	5.4	3996	6954	5.236	22.18
	7.2	5015	8591	5.433	29.85
10	1.8	1620	3179	3.498	11.00
	3.6	2841	5012	4.706	22.91
	5.4	3972	6967	5.066	36.26
	7.2	4949	8611	5.209	47.61
20	1.8	1618	3179	3.499	27.63
	3.6	2827	5012	4.582	87.04
	5.4	3945	6987	4.845	133.4
	7.2	4876	8632	4.8921	154.7

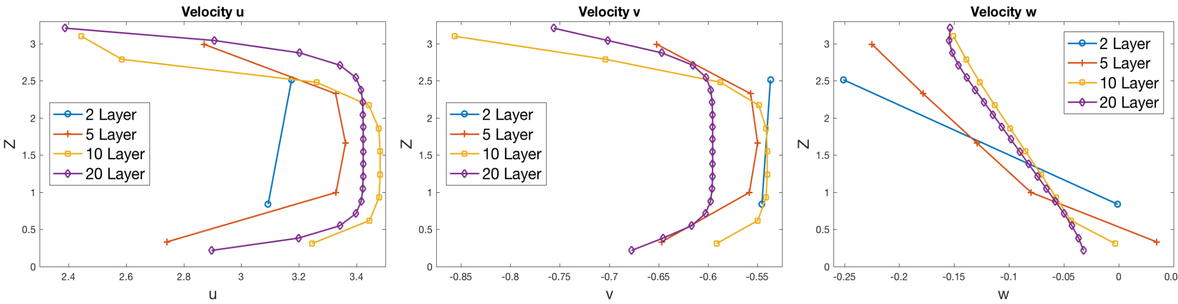

Figure 7.17: Comparison of velocities produced by varying the number of layers along the z-axis at $(x = 115\ m, y = 100\ m)$ at $t = 7.2\ s$.

7.5 Concluding remarks

In this chapter, a novel method for turbulence modelling is presented, where a multilayer two-dimensional shallow water model is coupled with the well established k-ϵ model for turbulence. This new model is derived from the Reynolds-averaged Navier-Stokes equations and includes some novel features. The derivation uses depth-averaged velocities and turbulent kinetic energy variables (k and ϵ) for each layer, so that vertically stratified results can be obtained. Crucial to this new formulation is the treatment of diffusive terms to incorporate inter-layer effects like momentum transfer and friction. For the first time, the same treatment is given to turbulence variables through their production terms, such that turbulent kinetic energy can be produced or lost due to the effects of the fluid layers around it. This model is novel in formulation and it provides new insight into complex shallow turbulent flows.

In order to solve this model, the Eulerian-Lagrangian finite volume method, is developed to include the effects of turbulent velocities in the Eulerian stage. Though these diffusive effects are generally small, it is important to include them to ensure a conservative method. The method of characteristics used in the Eulerian step to approximate fluxes that are then recovered to the conservative equations in the second step. As the Riemann problem is avoided, no eigenvalues (as needed by a standard Roe solver etc.) are calculated. Consequently the method provides stable second-order accurate results. These results are evaluated using three problems: the backward-step flow problem, the recirculation flow problem and a partial dam-break problem. The backward-step flow problem demonstrates the model is accurate and able to capture turbulent effects (namely the creation of a vortex). The model is validated for this example through the comparison with experimental data. Next a recirculation flow problem is considered, adapted from the OpenFOAM standard test to be a three-dimensional problem. This problem is compared to the OpenFOAM software, and used to demonstrate the ability of the model to capture vertical dimension effects and, through post processing, vertical velocities. Finally, a partial dam-break problem is considered, and is also compared to OpenFOAM to demonstrate the speed and accuracy of the presented model. The effects of turbulence modelling are examined as well, with a comparisons drawn between turbulent and non-turbulent simulations. It is interesting to note that the inclusion of the turbulence model only minimally increases the computational expense. The partial dam-break problem is also used to showcase the effects of the number of layers used in a simulation as well as the impacts of variable bathymetry. Though the number of layers and variable bathymetry have a small effect, as we have seen in terms of sediment transport, even minor variations in flow can cause large variations in bed morphology. These simulations show a good agreement and are a strong indicator that a two-dimensional multilayer shallow water system may be able to take on more complex flows in research and commercial exploitation in the future. Overall it provides interesting results that hold great promise for the development of sediment transport and other shallow water flow models.

Chapter 8

Modelling and simulation of turbulent multilayer shallow water flows over multi-sediment movable beds

The study detailed here combines the multilayer k-ϵ model presented in Chapter 7 with sediment transport (including multi-sediment tools). The aim is to develop an advanced multilayer sediment model capable of dealing with complex flows and bed situations. To the best knowledge of the author, this is the first time a two-dimensional multilayer model has been used for sediment transport with turbulence. The multilayer formulation allows for water, sediment, momentum, and turbulent energy exchange between layers. The aim of this work is to develop a fast and accurate model that overcomes some of the assumptions that limit the current sediment transport models widely used in the literature.

The formulation developed in this chapter is a seven-equation system which is solved by the multilayer Eulerian-Lagrangian finite volume method developed in previous chapters. The system builds on the five-equation model of the previous chapter by including the two sedimentary equations used in Chapter 5. The method used is fast, accurate and well-balanced, using similar steps to those detailed in Chapter 7. Furthermore, the method is easy to implement and can handle the complex flows and developing topography required. The method is used to simulate a series of benchmark and novel problems including: the lake at rest problem, the scour over an apron problem and a two-dimensional partial dam-break problem. The partial dam-break simulation is also further evolved to include vertically stratified and horizontally stratified layered beds. The merits of this model compared to the standard shallow water models over erodible beds are numerous. It has the ability to handle multiple sediments allowing for new levels of accuracy. Compared to standard shallow water models, it offers new features such as depth stratified results and turbulence effects. When compared to three-dimensional Navier-Stokes models, the method can obtain comparably accurate results with far smaller computational expense (as it does not require re-meshing like most three-dimensional Navier Stokes models). This final model demonstrates all these new and useful features, and has a robust nature which should improve the current trade-off between accuracy and cost for sediment transport simulations.

A basic introduction to the relevance of the problem is presented in Section 8.1. The governing equations for the model are given in Section 8.2.

The Eulerian-Lagrangian finite volume method used to solve the proposed model is briefly overviewed in Section 8.3. In Section 8.4, numerical results are compared to benchmark tests. Finally, conclusions are drawn in Section 8.5.

8.1 Overview of modelling turbulent flows over moveable beds

There are many methods for hydraulic modelling, from the three-dimensional (3D) Navier-Stokes models to the one-dimensional (1D) Shallow Water Equations (SWEs) and the Boussinesq equation; each is applicable to a certain situation. While the 3D Navier-Stokes equations are nearly universally applicable and are the most accurate, they are costly in terms of computation. Thus, any simplifications in the model design result in substantial computational savings. This chapter presents a two-dimensional (2D) multilayer shallow water model for use in solving 3D free-surface problems. The method is faster and simpler than 3D Navier-Stokes equations and utilises stratified horizontal velocities throughout, leading to significant gains in resolution over the standard 2D SWEs. The presented model is developed from [12] to include sediment transport methods.

Sediment transport can either be modelled statistically or deterministically [202]. This type of model uses empirical relations that have been well tested and developed from experimental data, combined with a deterministic approach to fluid modelling. Many different formulations exist for sediment pick-up functions; the most popular of these are Meyer-Peter and Muller [122], Grass [78], and van Rijn [186]. Research continues to be done to improve the empirical relations to this day [16, 213]. Recently, focus has turned to multi-sediment models (like the composite bed problem) where more than one sediment type is present and must be accounted for [69,196]. Some studies like [69] handle each sediment separately, while [196] takes a different approach and finds the optimal average for representing the sediments. In this chapter, a quasi-3D approach is used, where sediments are handled separately in the pick-up functions but as a single averaged mass in the water. This has the advantage of not expanding the governing equations whilst still treating the main characteristics of the sediments accurately.

Many 3D models exist for sediment transport, see [100, 116, 129, 219] among others. Most of these models solve variations on the Navier-Stokes equations coupled with a bed Exner equation. One of the most recently developed models is sedFOAM, which is an OpenFOAM sediment modelling tool that has been developed and repeatedly validated, see for example [49]. This has the advantage of being able to solve complex flow structures in 3D. However, these methods have the notable disadvantage of being highly computationally expensive, as the solution of the Navier-Stokes system is very complex and time demanding. Thus, any simplifications that can be made to the system are very valuable. One simplification is the use of the 2D SWE system, employed in conjunction with sediment transport equations. This has been widely developed in [4, 21, 58, 80, 104, 127] among others. Two methods for obtaining solutions exist: the first is an uncoupled approach, in which the bed Exner equation is solved as a latter step to the SWEs. This is a useful method for low shear, near steady-state situations where the time-scale of the bed evolution is much smaller than that of the flow. The second is the coupled approach where the bed equation is coupled with the SWEs; this approach is significantly more accurate and is used by almost all recent works, including [26, 77, 117, 166].

For the numerical solution of these models most use Roe-type solvers. This works by generating approximate Jacobian matrices for flux and requires the calculation of Roe average values and average wave-speed estimators. Consequently, the calculation of the eigenvalues of the Jacobian matrices is required. This is very computationally expensive and limits the adaptability of the models. These methods are further constrained by a lack of vertical velocity distributions, due to their depth-averaged assumption. The presented method overcomes this by using multiple 2D layers, so that the velocity can vary with depth as well as enabling exchange between the layers. The Eulerian-Lagrangian Finite Volume (ELFV) method is employed to mitigate the complications caused by the formulation of the model. The projection finite volume method is used for the Eulerian stage, and the method of characteristics for the Lagrangian stage. This method is well-balanced and conservative as well as exhibiting good speed advantages compared to 3D methods. In addition, the solution of the Riemann problem is avoided. As a result, the presented method and model are able to deal with hydrogeomorphic problems that would be impossible for many other models.

The gap between 2D and 3D models has recently been bridged by the introduction of multilayer models, though two-layer models for water flow have been developed for a while, see for instance [194]. More recently, models like those investigated in [14, 69, 181] which are capable of handling three or more layers have been developed. Some of these models [5, 29, 40] are constrained as they deal only with immiscible fluids. However, there is a second category of models in which mass exchange is allowed between the layers as in [14, 69, 181] and this is the category to which the model considered in the current study belongs.

Two problems are posed for this model: scour over an apron problem, a comparison to new experimental data for a 1D dam-break problem, and a partial dam-break problem. The scour over an apron problem tests the model for speed and accuracy compared to an equivalent 3D Navier Stokes formulation (the OpenFOAM solver sedFOAM). It should be noted that this is not the most advanced scour model and, as there are significant differences between the two models, only a partial comparison is possible. Nonetheless, the results gained are promising for the presented model. Finally, a run of partial dam-break simulations are considered. These are amongst the most complicated problems to model in sediment transport as they include vertically and horizontally stratified layered beds, which are difficult for many formulations to handle. Overall, the model demonstrates reliable and accurate results and illustrates all of the advances made during this project.

8.2 Model for multilayer turbulent flow over erodible beds

In this section, a short overview of the governing equations is given. The standard domain is discretised as shown in Figure 8.1. The fluid column is divided into multiple horizontal fluid layers, and the bed contains multiple layers of heterogeneous and homogeneous sediments. This means that there are concentrations of each sediment type in both the fluid and the bed to consider. As a starting point, the turbulent multilayer system in 2D is used, as detailed in Chapter 7. The flow is divided into M layers such that $\alpha = 1, \dots, M$. The αth layer is bounded by $z_{\alpha+1/2}$ and $z_{\alpha-1/2}$ and has a height h_α which is defined as

$$h_\alpha = l_\alpha H \ ,$$

where the proportion l_α also satisfies

$$l_\alpha \geq 0, \qquad \sum_{\alpha=1}^{M} l_\alpha = 1.$$

In this layer $(u_\alpha(t,x,y) \ v_\alpha(t,x,y) \ w_\alpha(t,x,y))^T$ are the velocity components in the $x, y,$ and z directions. Each layer also has values for turbulent kinetic energy $k_\alpha(t,x,y)$ and turbulent kinetic energy dissipation $\epsilon_\alpha(t,x,y)$. A bed containing L $(l = 1, \dots, L)$ number of discrete layers with N $(\varrho = 1, \dots, N)$ sediment types is also included in this model. A bed Exner-type equation for the bed height $B(t,x,y)$ and species conservation equations for the cumulative depth-averaged

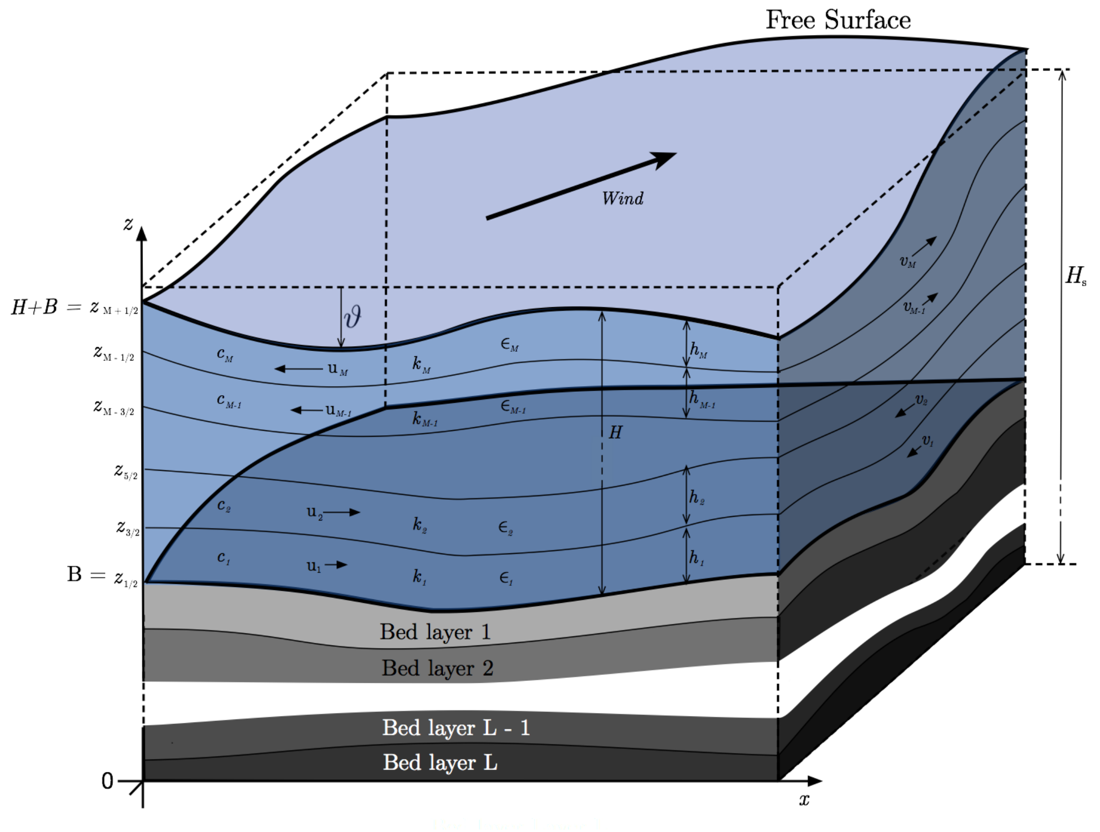

Figure 8.1: Illustration of a multilayer domain with a multilayer bed.

concentration of all sediments $\bar{c}_\alpha(t,x,y)$ in each layer are added to the formulation, where

$$\bar{c}_\alpha = \sum_{\varrho=1}^{N} c_{\alpha,\varrho},$$

and the averaged sediment variables are defined as

$$\overline{\rho}_{s,\alpha} = \sum_{\varrho=1}^{N} \frac{c_{\alpha,\varrho}}{\bar{c}_\alpha} \rho_{s,\varrho}, \qquad \overline{\rho}_\alpha = \rho_w (1 - \bar{c}_\alpha) + \sum_{\varrho=1}^{N} \frac{c_{\alpha,\varrho}}{\bar{c}_\alpha} \rho_{s,\varrho}, \tag{8.2.1}$$

Using the same method as Chapter 5, the bed is also discretised such that

$$\overline{\Psi} = \sum_{\varrho=1}^{N} \frac{b_{k,\varrho}}{B_k} (\Psi)_\varrho, \qquad \overline{\rho}_0 = \rho_w (1 - \overline{\Psi}) + \sum_{n=1}^{N} \frac{b_{k,\varrho}}{B_k} \rho_{s,\varrho} (\Psi)_\varrho.$$

The governing equations may be expressed in a conservative form as

$$\begin{aligned}
\frac{\partial H}{\partial t}+\sum_{\alpha=1}^{M}\frac{\partial(h_\alpha u_\alpha)}{\partial x}+\sum_{\alpha=1}^{M}\frac{\partial(h_\alpha v_\alpha)}{\partial y} &= \frac{\overline{E}_1-\overline{D}_1}{1-\Psi},\\
\frac{\partial(h_\alpha u_\alpha)}{\partial t}+\frac{\partial}{\partial x}\left(h_\alpha u_\alpha^2+\frac{1}{2}gh_\alpha H\right)+\frac{\partial}{\partial y}\left(h_\alpha u_\alpha v_\alpha\right) &= \frac{\partial}{\partial x}\left(h_\alpha \nu_{h,\alpha}\frac{\partial u_\alpha}{\partial x}\right)+\frac{\partial}{\partial y}\left(h_\alpha\nu_{h,\alpha}\left(\frac{\partial u_\alpha}{\partial y}+\frac{\partial v_\alpha}{\partial x}\right)\right)-\\
&\quad gh_\alpha\frac{\partial B}{\partial x}+\frac{(\overline{\rho}_{s,\alpha}-\rho_w)(h_\alpha)^2}{2\overline{\rho}_\alpha}\frac{\partial\overline{c}_\alpha}{\partial x}+F_\alpha,\\
\frac{\partial(h_\alpha v_\alpha)}{\partial t}+\frac{\partial}{\partial x}\left(h_\alpha u_\alpha v_\alpha\right)+\frac{\partial}{\partial y}\left(h_\alpha v_\alpha^2+\frac{1}{2}gh_\alpha H\right) &= \frac{\partial}{\partial x}\left(h_\alpha\nu_{h,\alpha}\left(\frac{\partial u_\alpha}{\partial y}+\frac{\partial v_\alpha}{\partial x}\right)\right)+\frac{\partial}{\partial y}\left(h_\alpha\nu_{h,\alpha}\frac{\partial v_\alpha}{\partial y}\right)-\\
&\quad gh_\alpha\frac{\partial B}{\partial y}-\frac{(\overline{\rho}_{s,\alpha}-\rho_w)g(h_\alpha)^2}{2\overline{\rho}_\alpha}\frac{\partial\overline{c}_\alpha}{\partial y}+G_\alpha,\\
\frac{\partial(h_\alpha\overline{c}_\alpha)}{\partial t}+\frac{\partial}{\partial x}\left(h_\alpha\overline{c}_\alpha u_\alpha\right)+\frac{\partial}{\partial y}\left(h_\alpha\overline{c}_\alpha v_\alpha\right) &= \frac{\partial}{\partial x}\left(h_\alpha\nu_{h,\alpha}\frac{\partial\overline{c}_\alpha}{\partial x}\right)+\frac{\partial}{\partial y}\left(h_\alpha\nu_{h,\alpha}\frac{\partial\overline{c}_\alpha}{\partial y}\right)+\mathcal{S}_{c,\alpha}\\
\frac{\partial(h_\alpha k_\alpha)}{\partial t}+\frac{\partial}{\partial x}\left(h_\alpha k_\alpha u_\alpha\right)+\frac{\partial}{\partial y}\left(h_\alpha k_\alpha v_\alpha\right) &= \frac{\partial}{\partial x}\left(\frac{h_\alpha\nu_{t,\alpha}}{\sigma_k}\frac{\partial k_\alpha}{\partial x}\right)+\frac{\partial}{\partial y}\left(\frac{h_\alpha\nu_t}{\sigma_k}\frac{\partial k_\alpha}{\partial y}\right)+P_{k,\alpha}-\\
&\quad k_{\alpha+\frac{1}{2}}\mathcal{E}_{\alpha+\frac{1}{2}}+k_{\alpha-\frac{1}{2}}\mathcal{E}_{\alpha-\frac{1}{2}},\\
\frac{\partial(h_\alpha\epsilon_\alpha)}{\partial t}+\frac{\partial}{\partial x}\left(h_\alpha\epsilon_\alpha u_\alpha\right)+\frac{\partial}{\partial y}\left(h_\alpha\epsilon_\alpha v_\alpha\right) &= \frac{\partial}{\partial x}\left(\frac{h_\alpha\nu_{t,\alpha}}{\sigma_\epsilon}\frac{\partial\epsilon_\alpha}{\partial x}\right)+\frac{\partial}{\partial y}\left(\frac{h_\alpha\nu_{t,\alpha}}{\sigma_\epsilon}\frac{\partial\epsilon_\alpha}{\partial y}\right)+P_{\epsilon,\alpha}-\\
&\quad \epsilon_{\alpha+\frac{1}{2}}\mathcal{E}_{\alpha+\frac{1}{2}}+\epsilon_{\alpha-\frac{1}{2}}\mathcal{E}_{\alpha-\frac{1}{2}},\\
\frac{\partial B}{\partial t}+\frac{\partial\mathcal{G}(B)}{\partial z} &= \frac{\overline{D}_1-\overline{E}_1}{1-\overline{\Psi}}.
\end{aligned}\tag{8.2.2}$$

The source/sink terms for k and ϵ are

$$\begin{aligned}
P_{h,\alpha} &= h_\alpha\Big(P_{k,\alpha}-\epsilon_\alpha\Big)+P_{k,\alpha+1/2}-P_{k,\alpha-1/2},\\
P_{\epsilon,\alpha} &= \frac{h_\alpha\epsilon_\epsilon}{k_\alpha}\Big(C_{\epsilon1}P_{k,\alpha}-C_{\epsilon2}\epsilon_\alpha\Big)+\frac{\epsilon_\alpha C_{\epsilon1}}{k_\alpha}\Big(P_{k,\alpha+1/2}-P_{k,\alpha-1/2}\Big),
\end{aligned}$$

where production of turbulent kinetic energy is defined as

$$P_{k,\alpha}=\nu_t\left(2\left(\frac{\partial u}{\partial x}\right)^2+2\left(\frac{\partial v}{\partial y}\right)^2+\left(\frac{\partial u}{\partial y}+\frac{\partial v}{\partial x}\right)^2\right),$$

where

$$P_{k,\alpha+1/2} = \begin{cases} {C_{\mathrm{B}}}^{-1/2}\left(C_{\mathrm{B}}(\overline{u}_1^2+\overline{v}_1^2)\right)^{3/2}, & \text{if } \alpha = 1, \\[2ex] \nu_v\big((u_\alpha - u_{\alpha+1}) + (v_\alpha - v_{\alpha+1})\big), & \text{if } \alpha = 2, \ldots, M-1, \\[2ex] \nu_v C_{wi}^{-1/2}\Big((\overline{u}_M - U_{wi,x})^2 + (\overline{v}_M - U_{wi,y})^2\Big), & \text{if } \alpha = M. \end{cases}$$

The source term for concentration $S_{c,\alpha}$ is defined as

$$\mathcal{S}_{c,\alpha} = \begin{cases} E_1 - D_1 + c_{1.5}\mathcal{E}_{1.5} - \varepsilon_c h_1 \left(\dfrac{\partial^2 c_{\Delta,3/2}}{\partial z^2}\right), & \text{if } \alpha = 1, \\[3ex] -c_{\alpha-1/2}\mathcal{E}_{\alpha-1/2} + c_{\alpha+1/2}\mathcal{E}_{\alpha+1/2} + \\ \qquad \varepsilon_c h_2 \left(\dfrac{\partial^2 c_{\Delta,\alpha-1/2}}{\partial z^2} - \dfrac{\partial^2 c_{\Delta,\alpha+1/2}}{\partial z^2}\right), & \text{if } \alpha = 2, \ldots, M-1, \\[3ex] -c_{M-\frac{1}{2}}\mathcal{E}_{M-\frac{1}{2}} + \varepsilon_c h_M \left(\dfrac{\partial^2 c_{\Delta,M-1/2}}{\partial z^2}\right), & \text{if } \alpha = M. \end{cases}$$

To determine the entrainment and deposition rates the semi-empirical relations reported in [36] are used

$$\overline{D}_\alpha = \begin{cases} \displaystyle\sum_{\varrho=1}^{N} \frac{c_{1,\varrho}}{\overline{c_1}}\big(w_{s,\varrho}\,(1-c_{B,\varrho})^2\, c_{B,\varrho}\big), & \text{if } \alpha = 1, \\[3ex] 0, & \text{otherwise,} \end{cases}$$

where

$$c_{B,\varrho} = c_{1,\varrho} \min\left(2, \left(\frac{c_{1,\varrho}}{1-\overline{\Psi}}\right)\right) .$$

For the entrainment of sediments, the following empirical relation is employed

$$\overline{E}_\alpha = \begin{cases} \displaystyle\sum_{\varrho=1}^{N} \frac{b_{k,\varrho}}{B_k}\varphi_\varrho \frac{\tau_\varrho - \tau_{cr,\varrho}}{H}\sqrt{u_\alpha^2 + v_\alpha^2}\, d_\varrho^{-0.2}, & \text{if } \ \tau_\varrho \geq \tau_{cr,\varrho} \text{ and } \alpha = 1, \\[3ex] 0, & \text{otherwise.} \end{cases}$$

This model relies on several empirical parameters for turbulence $(C_\mu, C_{\epsilon 1}, C_{\epsilon 2}, C_{\epsilon 3}, \sigma_k, \sigma_\epsilon, \sigma_c, C_{\epsilon\Gamma})$ and these are given in Table 7.1. The source term F_α is the external force in x-direction acting on the αth layer and accounting for the friction and momentum exchange effects. Thus

$$F_\alpha = \mathcal{F}_\alpha^{(u)} + F_\alpha^{(b)} + \mathcal{F}_\alpha^{(w)} + \mathcal{F}_\alpha^{(\mu)}, \qquad \alpha = 1, 2, \ldots, M. \tag{8.2.3}$$

The external force in the y-direction G_α is accounted for similarly as

$$G_\alpha = \mathcal{G}_\alpha^{(u)} + \mathcal{G}_\alpha^{(b)} + \mathcal{G}_\alpha^{(w)} + \mathcal{G}_\alpha^{(\mu)}, \qquad \alpha = 1, 2, \ldots, M. \tag{8.2.4}$$

Note that for (8.2.3) and (8.2.4):

- $\mathcal{F}_\alpha^{(u)}$ and $\mathcal{G}_\alpha^{(u)}$ estimate the momentum exchange between the layers
- $\mathcal{F}_\alpha^{(b)}$ and $\mathcal{G}_\alpha^{(b)}$ estimate the effects of bed friction on the system
- $\mathcal{F}_\alpha^{(w)}$ and $\mathcal{G}_\alpha^{(w)}$ add the effects of wind on the top layer to the system
- $\mathcal{F}_\alpha^{(\mu)}$ and $\mathcal{G}_\alpha^{(\mu)}$ are due to the effects of friction between the layers

For the sake of brevity, this section only details the force terms in the x-direction. The mass exhange term is split into two parts

$$\mathcal{E}_{\alpha+1/2}^{x} = \mathcal{E}_{\alpha+1/2}^{x} + \mathcal{E}_{\alpha+1/2}^{y}.$$

Therefore the x-direction momentum exchange is defined as

$$\mathcal{F}_\alpha^{(u)} = u_{\alpha+1/2}\mathcal{E}_{\alpha+1/2}^{x} - u_{\alpha-1/2}\mathcal{E}_{\alpha-1/2}^{x},$$

where the mass exchange terms $\mathcal{E}_{\alpha+1/2}^{x}$ are computed as

$$\mathcal{E}_{\alpha+1/2}^{x} = \begin{cases} 0, & \text{if} \quad \alpha = 0, \\ \displaystyle\sum_{\beta=1}^{\alpha} \left(\frac{\partial\left(h_\beta u_\beta\right)}{\partial x} - l_\beta \sum_{\gamma=1}^{M} \frac{\partial\left(h_\gamma u_\gamma\right)}{\partial x} \right), & \text{if} \quad \alpha = 1, 2, \ldots, M-1, \\ 0, & \text{if} \quad \alpha = M. \end{cases}$$

Furthermore, the interface velocities $u_{\alpha-1/2}$ and $u_{\alpha-1/2}$ and concentrations are calculated thus

$$u_{\alpha-1/2} = \begin{cases} u_{\alpha-1}, & \text{if} \quad \mathcal{E}_{\alpha-1/2}^{x} \geq 0, \\ u_\alpha, & \text{otherwise}. \end{cases} \qquad c_{\alpha-1/2} = \begin{cases} c_{\alpha-1}, & \text{if} \quad \mathcal{E}_{\alpha-1/2}^{x} \geq 0, \\ c_\alpha, & \text{otherwise}. \end{cases}$$

The vertical kinematic eddy viscosity term $\mathcal{F}_{\alpha}^{(\mu)}$ takes into account the friction between neighbouring layers and it is defined as

$$\mathcal{F}_{\alpha}^{(\mu)} = \begin{cases} 2\nu_{v,\alpha}\dfrac{u_2 - u_1}{(l_2 + l_1)\,H}, & \text{if} \quad \alpha = 1, \\[2ex] 2\nu_{v,\alpha}\dfrac{u_{\alpha+1} - u_{\alpha}}{(l_{\alpha+1} + l_{\alpha})\,H} - 2\nu_{v,\alpha}\dfrac{u_{\alpha} - u_{\alpha-1}}{(l_{\alpha} + l_{\alpha-1})\,H}, & \text{if} \quad \alpha = 2, 3, \ldots, M-1, \\[2ex] -2\nu_{v,\alpha}\dfrac{u_M - u_{M-1}}{(l_M + l_{M-1})\,H}, & \text{if} \quad \alpha = M, \end{cases}$$

where $\nu_{h,\alpha}$ is the horizontal eddy viscosity and $\nu_{v,\alpha}$ is the vertical eddy viscosity. Note that a generalized derivation of the viscous tensor in multilayer SWEs has also been reported in [70]. The external friction term for the bed in (8.2.3) is given by

$$\mathcal{F}_{\alpha}^{(b)} = \begin{cases} -\dfrac{\tau_{\mathrm{B}}^{x}}{\rho}, & \text{if} \quad \alpha = 1, \\[2ex] 0, & \text{if} \quad \alpha = 2, 3, \ldots, M. \end{cases}$$

The external stress due to wind term in (8.2.3) is calculated using

$$\mathcal{F}_{\alpha}^{(w)} = \begin{cases} 0, & \text{if} \quad \alpha = 1, 2, \ldots, M-1, \\[2ex] \dfrac{\tau_{wi}^{x}}{\rho}, & \text{if} \quad \alpha = M, \end{cases}$$

where ρ is the water density, and τ_{B}^{x} and τ_{wi}^{x} are respectively the bed shear stress and the shear of the blowing wind. These are defined by the water velocity in the top and bottom layers, and the wind velocity $U_{wi} = (U_{wi,x}, U_{wi,y})^T$ as

$$\tau_{\mathrm{B}}^{x} = \rho C_B u_1 \sqrt{u_1^2 + v_1^2}, \qquad \tau_{wi}^{x} = \rho C_{wi}(U_{wi,x} - u_M)\sqrt{(U_{wi,x} - u_M)^2 + (U_{wi,y} - v_M)^2},$$

where C_B is the bed friction coefficient, which may either be set as a constant or estimated using the Manning equation as

$$C_{\mathrm{B}} = \frac{g n_m^2}{H^{1/3}}, \qquad C_{wi} = \frac{\sigma^2 \rho_a}{H},$$

where n_m is the Manning roughness coefficient of the bed, and the wind friction coefficient C_{wi} is defined as [159]. The wind stress coefficient is designated by σ, and ρ_a is the air density. The system can also be rewritten in a compact vector form as

$$\frac{\partial \mathbf{W}}{\partial t} + \frac{\partial \mathbf{F}(\mathbf{W})}{\partial x} + \frac{\partial \mathbf{G}(\mathbf{W})}{\partial y} = \frac{\partial \mathbf{D_x}(\mathbf{W})}{\partial x} + \frac{\partial \mathbf{D_y}(\mathbf{W})}{\partial y} + \mathbf{Q}(\mathbf{W}) + \mathbf{R}(\mathbf{W}), \tag{8.2.5}$$

where

$$\mathbf{W} = \begin{pmatrix} H \\ h_1u_1 \\ h_2u_2 \\ \vdots \\ h_Mu_M \\ h_1v_1 \\ h_2v_2 \\ \vdots \\ h_Mv_M \\ h_1\bar{c}_1 \\ h_2\bar{c}_2 \\ \vdots \\ h_M\bar{c}_M \\ h_1k_1 \\ h_2k_2 \\ \vdots \\ h_Mk_M \\ h_1\epsilon_1 \\ h_2\epsilon_2 \\ \vdots \\ h_M\epsilon_M \\ B \end{pmatrix}, \quad \mathbf{F}(\mathbf{W}) = \begin{pmatrix} \displaystyle\sum_{\alpha=1}^{M} h_\alpha u_\alpha \\ h_1u_1^2 + \dfrac{1}{2}gh_1H \\ h_2u_2^2 + \dfrac{1}{2}gh_2H \\ \vdots \\ h_Mu_M^2 + \dfrac{1}{2}gh_MH \\ h_1u_1v_1 \\ h_2u_2v_2 \\ \vdots \\ h_Mu_Mv_M \\ h_1u_1\bar{c}_1 \\ h_2u_2\bar{c}_2 \\ \vdots \\ h_Mu_M\bar{c}_M \\ h_1u_1k_1 \\ h_2u_2k_2 \\ \vdots \\ h_Mu_Mk_M \\ h_1u_1\epsilon_1 \\ h_2u_2\epsilon_2 \\ \vdots \\ h_Mu_M\epsilon_M \\ 0 \end{pmatrix}, \quad \mathbf{G}(\mathbf{W}) = \begin{pmatrix} \displaystyle\sum_{\alpha=1}^{M} h_\alpha v_\alpha \\ h_1u_1v_1 \\ h_2u_2v_2 \\ \vdots \\ h_Mu_Mv_M \\ h_1v_1^2 + \dfrac{1}{2}gh_1H \\ h_2v_2^2 + \dfrac{1}{2}gh_2H \\ \vdots \\ h_Mv_M^2 + \dfrac{1}{2}gh_MH \\ h_1v_1\bar{c}_1 \\ h_2v_2\bar{c}_2 \\ \vdots \\ h_Mv_M\bar{c}_M \\ h_1v_1k_1 \\ h_2v_2k_2 \\ \vdots \\ h_Mv_Mk_M \\ h_1v_1\epsilon_1 \\ h_2v_2\epsilon_2 \\ \vdots \\ h_Mv_M\epsilon_M \\ 0 \end{pmatrix},$$

$$\mathbf{D_x}(\mathbf{W}) = \begin{pmatrix} 0 \\ 2h_1\nu_{h,1}\dfrac{\partial u_1}{\partial x} \\ 2h_2\nu_{h,2}\dfrac{\partial u_2}{\partial x} \\ \vdots \\ 2h_M\nu_{h,M})\dfrac{\partial u_M}{\partial x} \\ h_1\nu_{h,1}\left(\dfrac{\partial u_1}{\partial y} + \dfrac{\partial v_1}{\partial x}\right) \\ h_2\nu_{h,2}\left(\dfrac{\partial u_2}{\partial y} + \dfrac{\partial v_2}{\partial x}\right) \\ \vdots \\ h_M\nu_{h,M}\left(\dfrac{\partial u_M}{\partial y} + \dfrac{\partial v_M}{\partial x}\right) \\ h_1\nu_{h,1}\dfrac{\partial \bar{c}_1}{\partial x} \\ h_2\nu_{h,2}\dfrac{\partial \bar{c}_2}{\partial x} \\ \vdots \\ h_M\nu_{h,M}\dfrac{\partial \bar{c}_M}{\partial x} \\ \dfrac{h_1\nu_{t,1}}{\sigma_k}\dfrac{\partial k_1}{\partial x} \\ \dfrac{h_2\nu_{t,2}}{\sigma_k}\dfrac{\partial k_2}{\partial x} \\ \vdots \\ \dfrac{h_M\nu_{t,M}}{\sigma_k}\dfrac{\partial k_M}{\partial x} \\ \dfrac{h_1\nu_{t,1}}{\sigma_\varepsilon}\dfrac{\partial \varepsilon_1}{\partial x} \\ \dfrac{h_2\nu_{t,2}}{\sigma_\varepsilon}\dfrac{\partial \varepsilon_2}{\partial x} \\ \vdots \\ \dfrac{h_M\nu_{t,M}}{\sigma_\varepsilon}\dfrac{\partial \varepsilon_M}{\partial x} \\ 0 \end{pmatrix}, \qquad \mathbf{D_y}(\mathbf{W}) = \begin{pmatrix} 0 \\ h_1\nu_{h,1}\left(\dfrac{\partial u_1}{\partial y} + \dfrac{\partial v_1}{\partial x}\right) \\ h_2\nu_{h,2}\left(\dfrac{\partial u_2}{\partial y} + \dfrac{\partial v_2}{\partial x}\right) \\ \vdots \\ h_M\nu_{h,M}\left(\dfrac{\partial u_M}{\partial y} + \dfrac{\partial v_M}{\partial x}\right) \\ 2h_1\nu_{h,1}\dfrac{\partial v_1}{\partial y} \\ 2h_2\nu_{h,2}\dfrac{\partial v_2}{\partial y} \\ \vdots \\ 2h_M\nu_{h,M}\dfrac{\partial v_M}{\partial y} \\ h_1\nu_{h,1}\dfrac{\partial \bar{c}_1}{\partial y} \\ h_2\nu_{h,2}\dfrac{\partial \bar{c}_2}{\partial y} \\ \vdots \\ h_M\nu_{h,M}\dfrac{\partial \bar{c}_M}{\partial y} \\ \dfrac{h_1\nu_{t,1}}{\sigma_k}\dfrac{\partial k_1}{\partial y} \\ \dfrac{h_2\nu_{t,2}}{\sigma_k}\dfrac{\partial k_2}{\partial y} \\ \vdots \\ \dfrac{h_M\nu_{t,M}}{\sigma_k}\dfrac{\partial k_M}{\partial y} \\ \dfrac{h_1\nu_{t,1}}{\sigma_\varepsilon}\dfrac{\partial \varepsilon_1}{\partial y} \\ \dfrac{h_2\nu_{t,2}}{\sigma_\varepsilon}\dfrac{\partial \varepsilon_2}{\partial y} \\ \vdots \\ \dfrac{h_M\nu_{t,M}}{\sigma_\varepsilon}\dfrac{\partial \varepsilon_M}{\partial y} \\ 0 \end{pmatrix},$$

$$
\mathbf{Q}(\mathbf{W}) = \begin{pmatrix}
0 \\
\dfrac{(\bar{\rho}_{s,1}-\rho_w)g(h_1)^2}{2\bar{\rho}_1}\dfrac{\partial \bar{c}_1}{\partial x} - gh_1\dfrac{\partial B}{\partial x} \\
\dfrac{(\bar{\rho}_{s,2}-\rho_w)g(h_2)^2}{2\bar{\rho}_2}\dfrac{\partial \bar{c}_2}{\partial x} - gh_2\dfrac{\partial B}{\partial x} \\
\vdots \\
\dfrac{(\bar{\rho}_{s,M}-\rho_w)g(h_M)^2}{2\bar{\rho}_M}\dfrac{\partial \bar{c}_M}{\partial x} - gh_M\dfrac{\partial B}{\partial x} \\
\dfrac{(\bar{\rho}_{s,1}-\rho_w)g(h_1)^2}{2\bar{\rho}_1}\dfrac{\partial \bar{c}_1}{\partial y} - gh_1\dfrac{\partial B}{\partial y} \\
\dfrac{(\bar{\rho}_{s,2}-\rho_w)g(h_2)^2}{2\bar{\rho}_2}\dfrac{\partial \bar{c}_2}{\partial y} - gh_2\dfrac{\partial B}{\partial y} \\
\vdots \\
\dfrac{(\bar{\rho}_{s,\alpha}-\rho_w)g(h_M)^2}{2\bar{\rho}_M}\dfrac{\partial \bar{c}_M}{\partial y} - gh_M\dfrac{\partial B}{\partial y} \\
0 \\
0 \\
\vdots \\
0 \\
0 \\
0 \\
\vdots \\
0 \\
0 \\
0 \\
\vdots \\
0 \\
0
\end{pmatrix}, \quad
\mathbf{R}(\mathbf{W}) = \begin{pmatrix}
\dfrac{\overline{E}_1-\overline{D}_1}{1-\overline{\Psi}} \\
F_1 \\
F_2 \\
\vdots \\
F_M \\
G_1 \\
G_2 \\
\vdots \\
G_M \\
\mathcal{S}_{c,1} \\
\mathcal{S}_{c,2} \\
\vdots \\
\mathcal{S}_{c,M} \\
P_{h,1} \\
P_{h,2} \\
\vdots \\
P_{h,M} \\
P_{\epsilon,1} \\
P_{\epsilon,2} \\
\vdots \\
P_{\epsilon,M} \\
\dfrac{\partial \mathcal{G}(B)}{\partial z} + \dfrac{\overline{D}_1-\overline{E}_1}{1-\overline{\Psi}}
\end{pmatrix}.
$$

8.3 Eulerian Lagrangian method for multilayer sediment laden turbulent flows

In order to solve the presented system (8.2.5), a method of integration must be selected. In this case a second-order splitting method is chosen, as presented in [149, 172]. To achieve this, the time interval is divided into sub-intervals $[0, \ldots, t_n, t_{n+1}, \ldots]$, where $\Delta t = t_{n+1} - t_n$. Then the same splitting method as detailed in Section 7.3 of Chapter 7 (on page 206) is implemented, for the sake of brevity it is not detailed here. This method is computationally cheap and easy to implement. It also avoids the complications incurred from the source matrix $\mathbf{R}(\mathbf{W})$ when calculating fluxes and interpolating values. One problem faced in this method is the calculation of eigenvalues, as they are non-trivial and can often become complex in certain flow cases. If using a more standard Riemann solver (through exact or approximation techniques) in certain flow cases the simulation becomes vulnerable to Kelvin-Helmholtz instabilities at the interfaces of layers. Most solvers are unable to resolve this issue. However, the solver proposed in this study, utilizing an ELFV method, does not need to compute the eigenvalues in the solution of the system. When determining the time-step an equivalent single layer shallow water system is considered. This ensures that the Courant-Friedrichs-Lewy (CFL) condition is set safely, using equivalent eigenvalues (as in [42, 76]) to overestimate the wave speeds as

$$\lambda_\alpha^\pm = u_\alpha \pm \sqrt{gH}, \qquad \mu_\alpha^\pm = v_\alpha \pm \sqrt{gH}, \qquad \alpha = 1, 2 \ldots, M. \tag{8.3.6}$$

This overestimating approximation is used as the exact eigenvalues are complex and are more computationally expensive than this small overestimation (as we neglect the diffusive terms). Thus the time-step is adjusted for the maximum wave speed in the shallow water system, guaranteeing the stability of the simulation. This procedure is implemented as shown in Figure 8.2.

8.4 Numerical results

This section validates the presented model and demonstrates its adaptability. The model is used to simulate two test cases, both aiming to demonstrate a different facet of its abilities. The model is compared to the most advanced open-source sediment model: the fully 3D sedFOAM solver published by [49]. This aims to show the validity of the model and set a base line for it. Finally, the recently conceived composite bed problem is solved in a partial dam-break situation for the first time to the knowledge of the author. Both horizontally and vertically composite

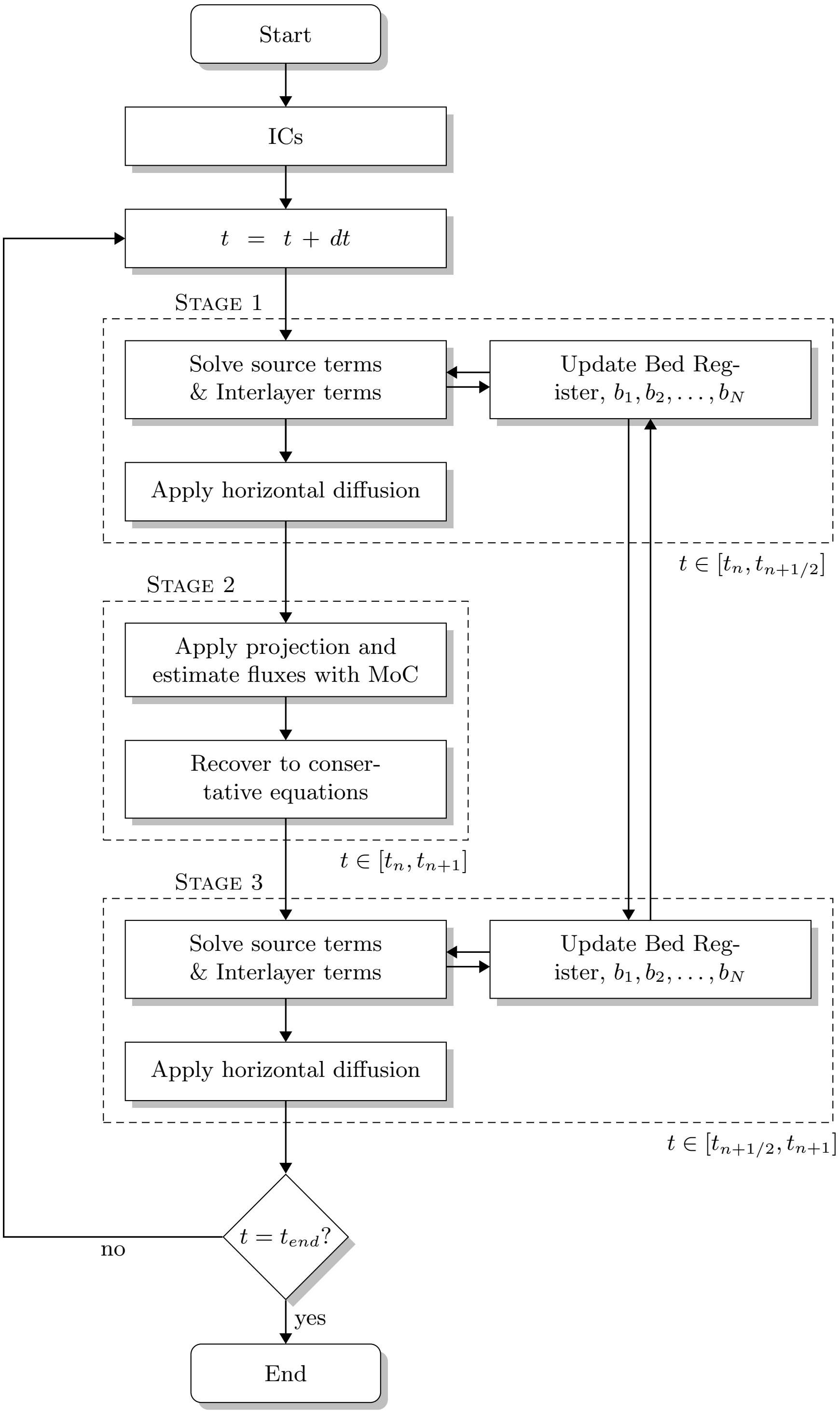

Figure 8.2: A flowchart demonstrating the stages in the proposed 2D Eulerian-Lagrangian procedure including the diffusion and bed register terms.

beds are considered. The goal of these tests is to show that the model is an effective method for quasi-3D modelling.

A Courant number of Cr = 0.7 is used in all the simulation runs. The vertical sediment diffusion coefficient $\varepsilon_c = 0.01\ m^2/s$. The turbulence production coefficients are set at $C_{wi} = 0.001$ and $C_B = 0.005$. The time-step Δt is adjusted using the CFL condition as

$$\Delta t = \mathrm{Cr}\frac{\min\left(\Delta x, \Delta y\right)}{\max\limits_{\alpha=1,\ldots,M}\left(\left|\lambda_\alpha^\pm\right|, \left|\ \mu_\alpha^\pm\right|\right)}.$$

It is also worth noting that linear interpolation is used in the predictor stage. In order to describe the 3D nature of the flow, the vertical velocities w are calculated using the post-processing techniques outlined in [14]. This is done using the same methods as the previous chapter.

8.4.1 Scour downstream of an apron problem

A well-established test for this type of simulation, known as the scour downstream of an apron problem, is used to compare the presented model with the OpenFOAM solver sedFOAM.
This problem is detailed in [10], and has also been used in the development of sedFOAM[1] [49]. The test requires a vertical distribution of velocities as well as accurate sediment handling. Although the domain reduces to a 2D problem, as one axis is in the vertical, it will test the 3D nature of the presented model. The domain is as shown in Figure 8.3. The initial conditions are

$$u(0,x,y,z) = \frac{1}{0.41}\ln\left(\frac{30z}{0.25d}\right), \quad v(0,x,y,z) = 0\ m/s, \quad k(0,x,y,z) = 0.1\times10^{-8}\ m^2/s^2,$$
$$\bar{c}(0,x,y,z) = 0.0001, \quad \epsilon(0,x,y,z) = 0.1\times10^{-8}\ m^2/s^3, \quad H(0,x,y) = 1\ m \quad B(0,x,y,z) = 0.$$

In this example, the sediment is Sediment 4 from Table 3.1. This domain is relatively basic in nature but it will require the k-ϵ model in order to develop its interesting flow features. The simulation is allowed to run for 10 s, with the aim of exhibiting the complex bed features developed from the initial bed height of 0 m, as shown in Figure 8.4.

The model demonstrates good agreement with the sedFOAM solver and shows a scour hole developing and shifting downstream. Figure 8.4 shows the concentration equilibrium and its movement from left to right. The model is very capable of developing and continuing a scour hole, though it is divergent from the sedFOAM model after 10 s, due to its free-surface nature. This shows that, as far as possible, the presented model is comparable to the sedFOAM

---

[1] `https://openfoamwiki.net/index.php/Contrib/sedfoam`

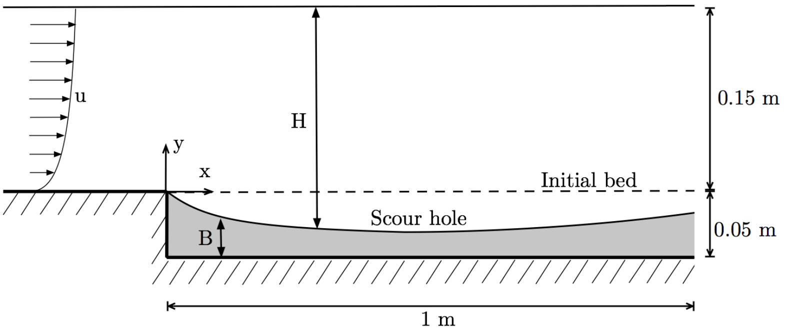

Figure 8.3: Configuration of the sour after an apron domain.

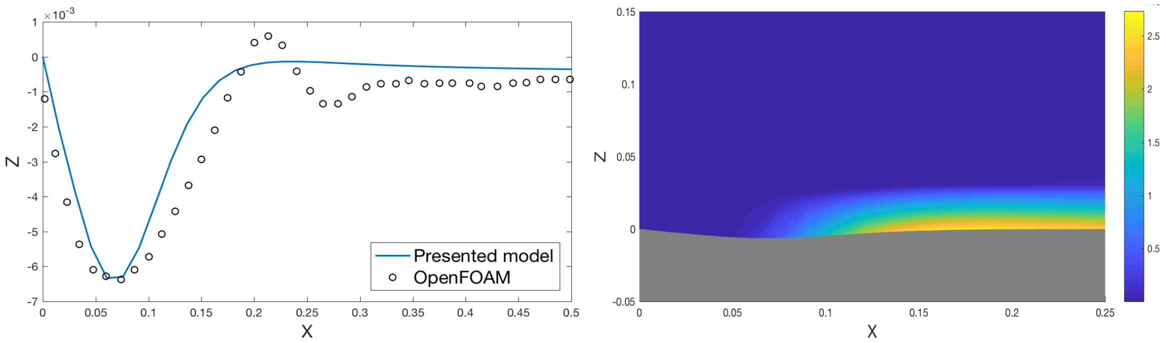

Figure 8.4: A comparison of the sour hole (left) and the concentration profile (right) at $t = 10\ s$.

solver. Nonetheless further development of either model would be required for a more complete comparison.

8.4.2 Partial dam-break flow problem

As Figure 8.5 shows, there is a steady evolution of the scour holes caused by the partial dam-break. The velocity profile demonstrates the crucial effects of the multilayer system, with a reduced bottom layer velocity. This is key as, especially in a complex flow situation like this one, the bottom layer flow must be correctly estimated if it is to initiate motion in the sediment. As can be seen in the concentration and velocity profiles, there is a varied vertical distribution of both. This demonstrates the key value of the multilayer nature of the model in this simulation. No turbulence data exists to compare to these results. The effects of turbulence modelling are visible in the diffusion of both velocity and concentration cross-sections shown in Figure 8.5. This simulation provides a good baseline for further tests.

Next, we introduce a vertical composite bed with three distinct layers of sediment. The domain is 200 m by 200 m and is divided into 200 × 200 cells, the simulation is run with 10 fluid layers. As each layer has different erosion and deposition characteristics, a more complex erosion profile is expected. The aim of this simulation is to demonstrate the abilities of the

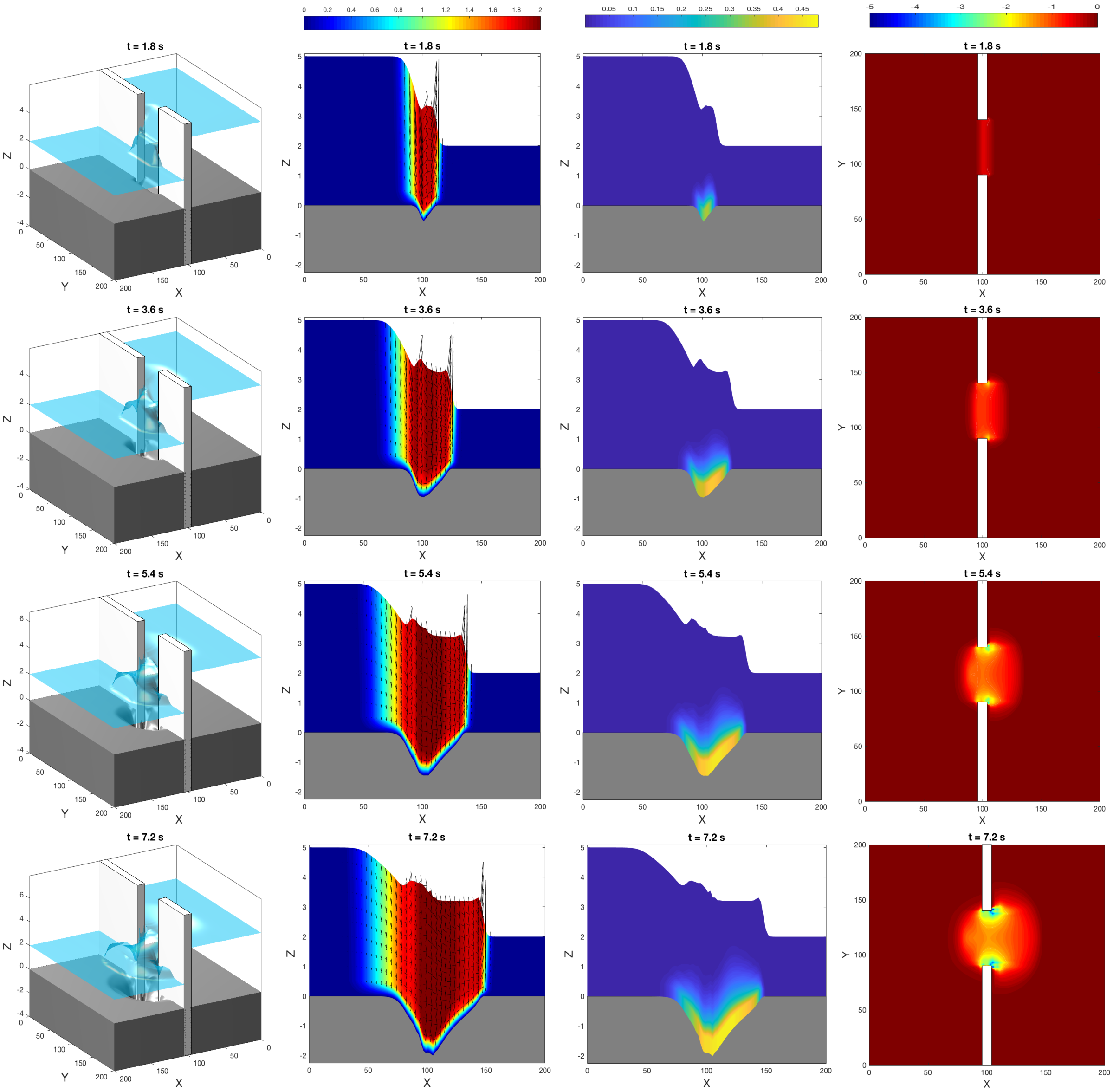

Figure 8.5: Results from the simulation of an partial dam-break over an homogeneous bed . From left to right: a 3D view of the domain, 2D cross-section velocity profile (at $y = 115\ m$), 2D cross-section concentration profile (at $y = 115\ m$), and a top view of the bed at $t = 1.8\ s$, $3.6\ s$, $5.4\ s$ and $7.2\ s$.

multi-sediment handling tools when combined with this model, as detailed in Section 8.2. The bed composition is such that

$$B = \begin{cases} \text{Sand 1,} & \text{if} \quad -0.25\,m \le z < 0\,m, \\ \text{Sand 2,} & \text{if} \quad -0.5\,m \le z < -0.25\,m, \\ \text{Sand 3,} & \text{if} \quad z < -0.25\,m. \end{cases}$$

All other simulation parameters remain identical to the previous run. As shown in Figure 8.6,

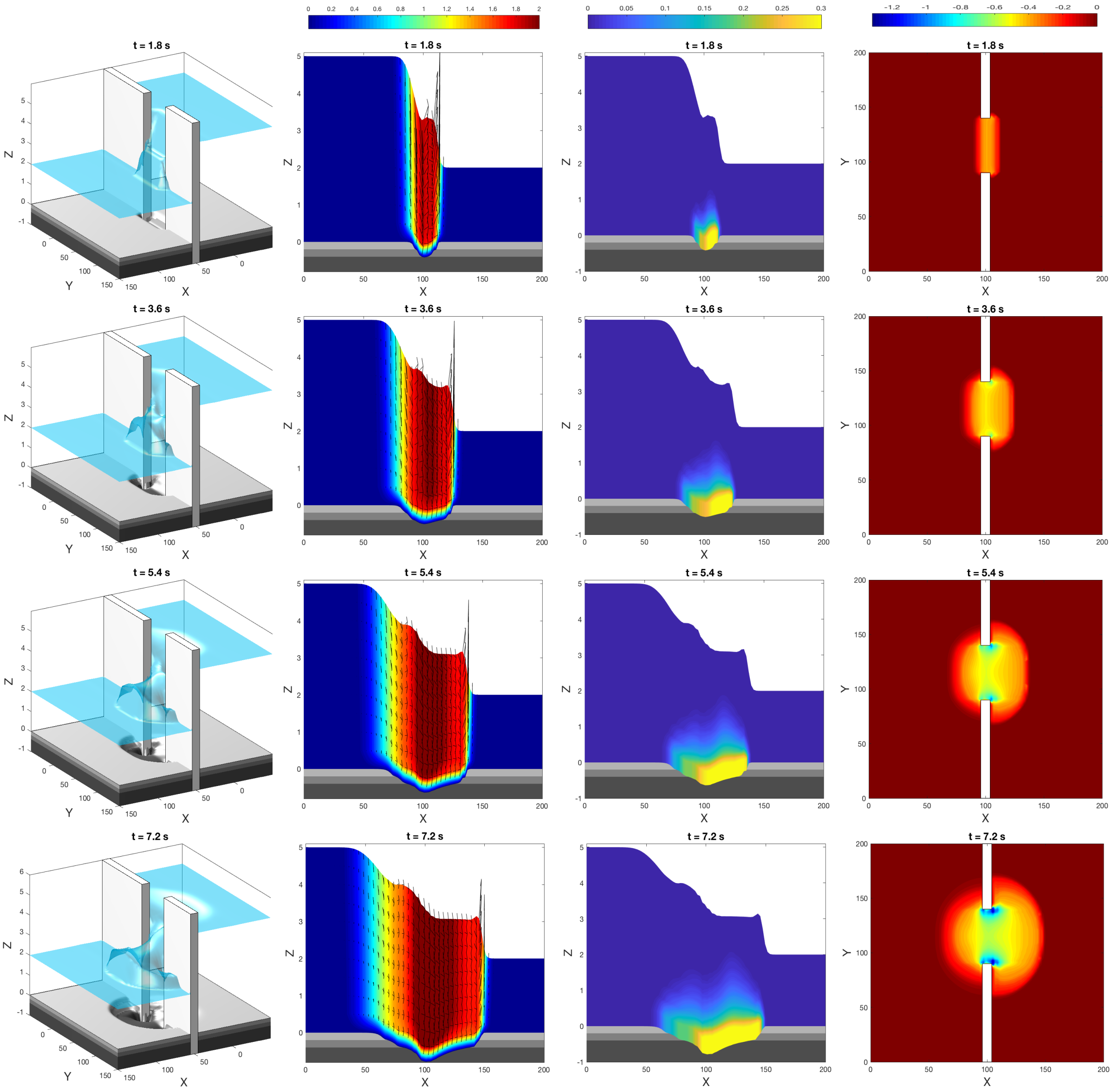

Figure 8.6: Results from the simulation of a partial dam-break over a horizontally composite bed, with the same plots as Figure 8.5.

the proposed model and numerical method easily handle this situation. The bed is complex in nature with its many inflection points, as shown in the concentration and velocity profiles, nonetheless this does not adversely affect the stability of the simulations. In fact, the simulation handles even the complex end of wall points, where deep scour holes are created. Figure 8.7 shows the expected evolution of sedimentary ratios, as each of the layers is eroded away. Compared to the previous simulation run there is a greater area of erosion, due to the prevalence of Sand 1. The depth of erosion is constrained by the less erodible Sand 3 in the base layer. Sand 2 could be used by other models as an approximation for these layers but, as shown in Figure 8.1, it is not an appropriate simplification. This text case has demonstrated the ability of the model not only to handle the complex flow situation of a partial dam-break, but also to capture the

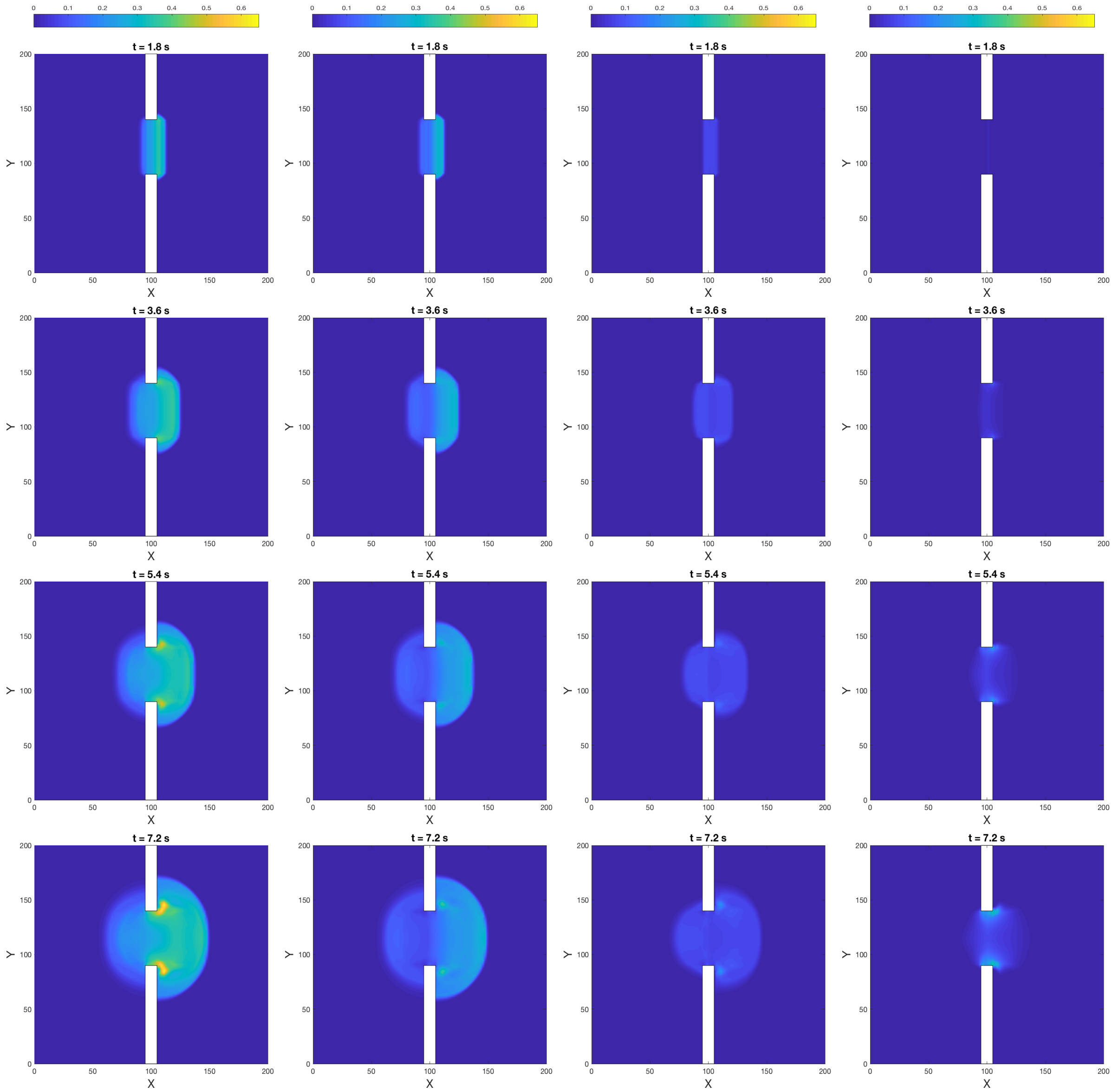

Figure 8.7: Results from the simulation of a partial dam break over a horizontal composite bed. From left to right: total concentration, Sand 1 concentration, Sand 2 concentration, and Sand 3 concentration at $t = 1.8\ s,\ 3.6\ s,\ 5.4\ s$ and $7.2\ s$.

complex topography (and the effect of that topography on the flow) of a multilayer bed. The multi-sediment nature of the domain with discretely layered beds would be impossible for a lot of models to solve, but the nature of the bed discretisation used in this model allows for it to be handled easily and efficiently. Overall, the test case lends validity and purpose to the model.

The final test considered is the partial dam-break over a horizontal composite bed, comprised

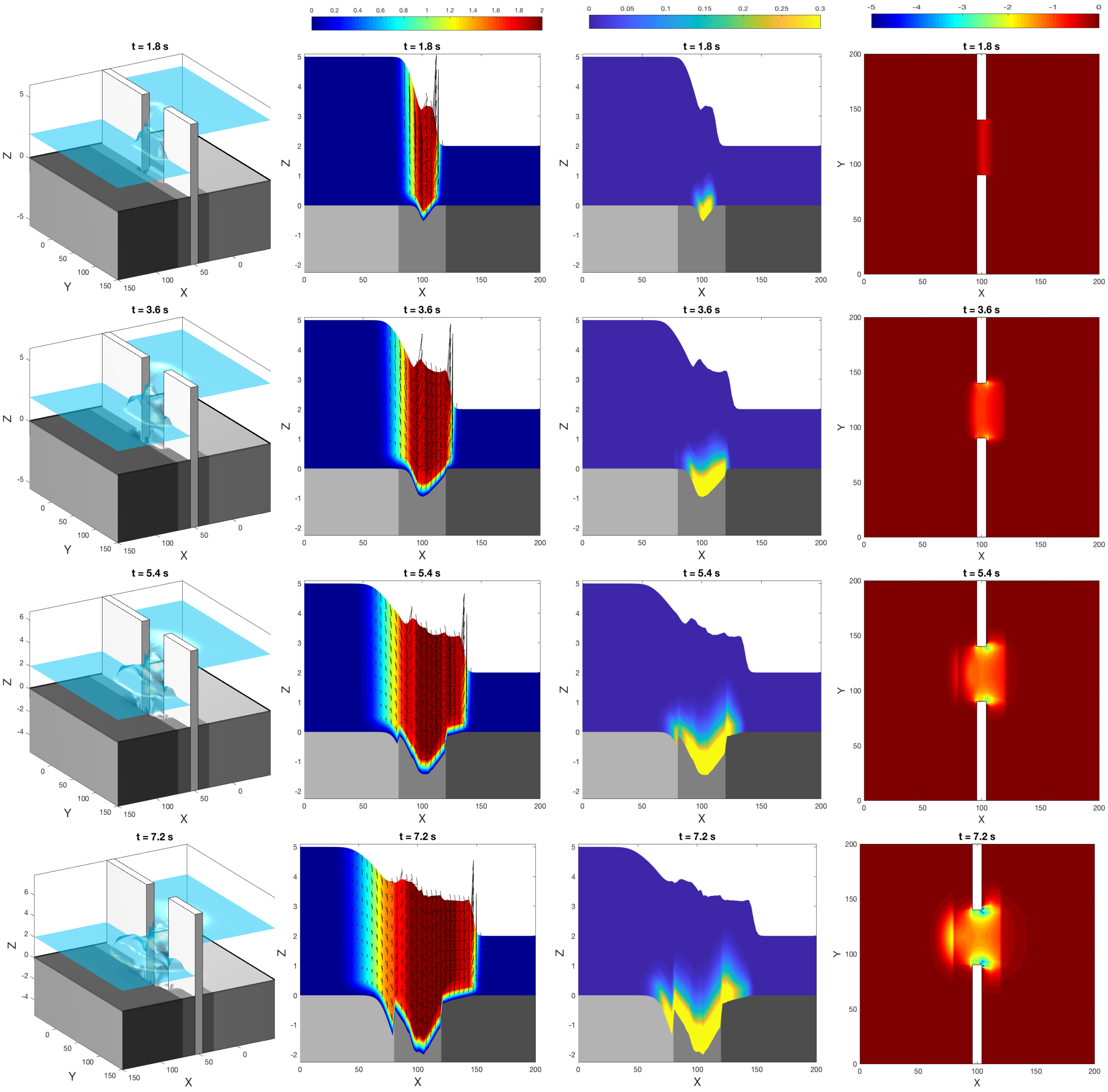

Figure 8.8: Results from the simulation of a partial dam-break over a vertically composite bed, with the same plot configuration as Figure 8.5.

of

$$B = \begin{cases} \text{Sand 1,} & \text{if} \quad \leq x < \ 85\ m, \\[2em] \text{Sand 2,} & \text{if} \quad 85\ m \ \leq x < \ 115\ m, \\[2em] \text{Sand 3,} & \text{if} \quad x < \ 115\ m. \end{cases}$$

This problem has an added level of difficulty owing to the horizontal step function in the sediment bed. It cannot be solved by any Exner-based system that relies on continuous sediment pick-up functions. The presented method does not have this problem, as the bed is discretised. This is still a very complex simulation, as the bed should evolve into an even more complex form than in the previous simulation.

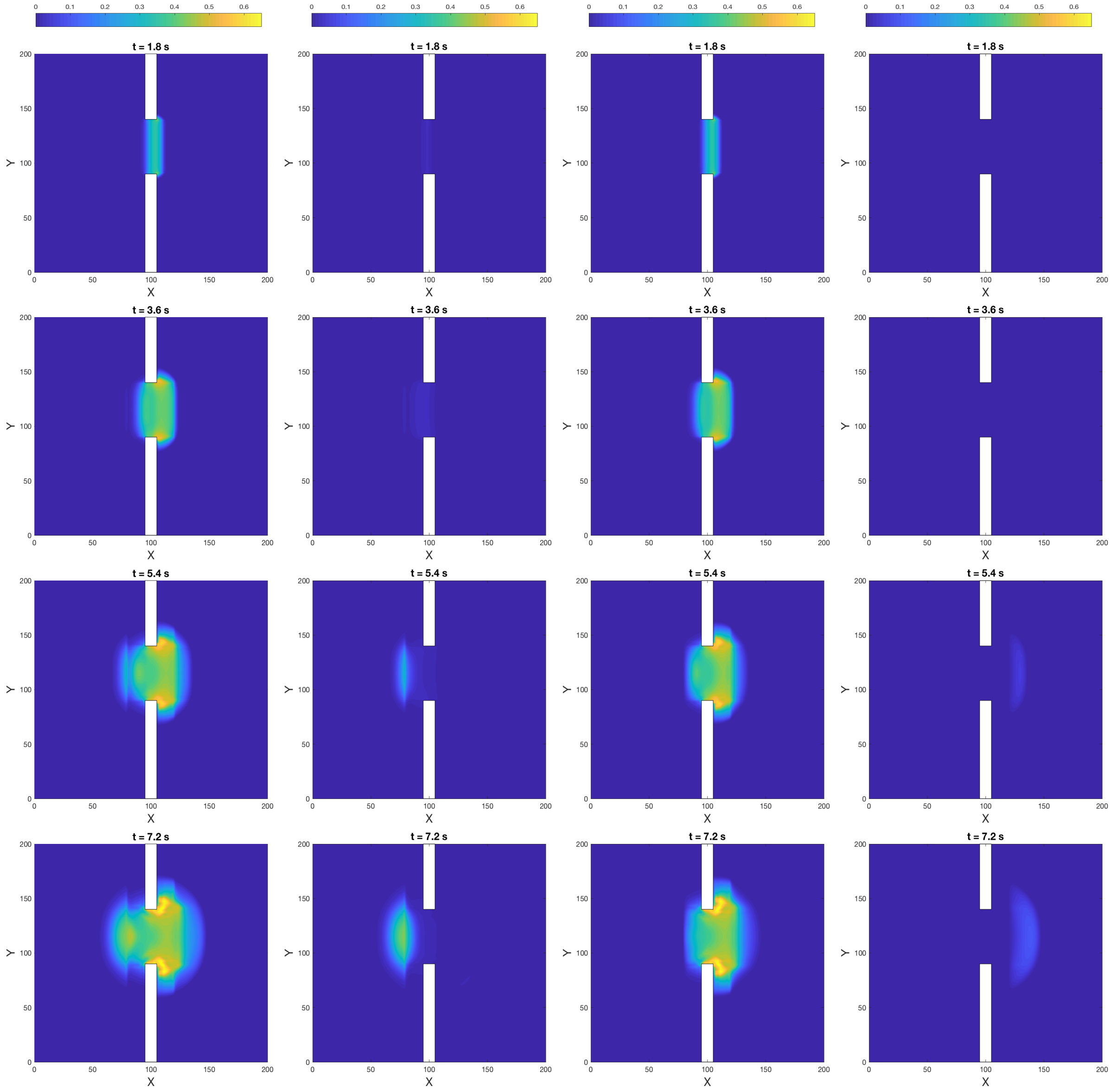

Figure 8.9: Results from the simulation of a partial dam-break over a the vertically composite bed, with the same plot configuration as Figure 8.7.

As shown in Figure 8.8, this simulation presents a very similar waveform to the single sediment bed simulation. This is largely due to the comparable quantity of erosion in the middle section, and is the crucial factor for accelerating the discharge through the dam. It is clear that the erosion profile is complex, causing ripples in the water surface and creating a very disrupted flow, especially when the accelerating water reaches the banks of Sand 1 and Sand 3. The developing concentration profiles are shown in Figure 8.9. This shows that, as the bottom velocities are very small, the majority of entrained sediment does not move from where it is sourced. This indicates how crucial the stratified velocities are when dealing with a situation of this type. When comparing the concentration amounts in Table 8.1 between simulations I, II, and III, it can be seen that although they all discharge similar quantities (5453 m^3, 5514 m^3,

Table 8.1: Comparison of the discharge volume, the area disturbed by the dam-break, total entrained sediment (by volume), the concentrations (by percentage) and CPU times for the three partial dam-break simulations: single sediment bed (simulation I), vertical composite bed (simulation II), and horizontal composite bed (simulation III).

Sim.	Time $[s]$	Discharge $[m^3]$	Disturbed area $[m^2]$	Entrained sed. $[m^3]$	Sand 1 c [%]	Sand 2 c [%]	Sand 3 c [%]	CPU Time $[s]$
I	1.8	1866	1286	262.5	100	0	0	42.32
	3.6	3263	2396	605.3	100	0	0	88.62
	5.4	5198	3824	1288	100	0	0	137.83
	7.2	7469	5453	1775	100	0	0	189.82
II	1.8	1897	1318	294.9	91.20	8.279	0.6402	42.57
	3.6	3049	2420	564.4	83.19	13.63	3.254	89.49
	5.4	4419	3865	953.7	78.04	16.00	6.014	139.04
	7.2	5895	5514	1429	74.83	17.04	8.161	186.18
III	1.8	1866	1286	262.9	58.81	41.26	0.1036	42.80
	3.6	3256	2396	600.3	33.31	66.35	0.4060	88.80
	5.4	4934	3824	1071	30.59	65.58	3.873	137.61
	7.2	6813	5428	1662	33.91	58.39	7.696	188.34

and 5428 m^3 respectively), the quantities of sediment vary more widely (1775 m^3, 1429 m^3, and 1662 m^3) at $t = 7.2$ s. This demonstrates that, although the first simulation I can be used as an approximation to II and III (as Sand 2 is roughly an average of Sands 1 and 3), the mapping of bed composition is a vital component. It is also worth noting the great variance between the last two simulations in terms of sediment concentrations. In simulation III the proportion of Sand 1 moves from 58.81 % at $t = 1.8$ s to only 33.91 % at $t = 7.2$ s, whereas simulation II has a more gradual concentration change of Sand 1, from 91.20 % at $t = 1.8$ s to only 74.83 % at $t = 7.2$ s. This is also demonstrated in Figure 8.7 and Figure 8.9. This sediment tracking showcases another useful feature of this method. As in many dam-break problems, like tailings dam failures, it is useful to know exactly which sediment is begin transported as certain sediments may be contaminated or naturally too high in one kind of chemical to be safe for release into the wider watercourse. Thus, this multi-sediment feature allows for not only a better description of the erosion process but also a better understanding of where each type of sediment ends up, as shown in Figure 8.9.

As Table 8.1 demonstrates, this multi-sediment method does not slow the simulation speed. It therefore adds accuracy to a model without any appreciable computational cost. The effects of all the elements of the model can be seen in this test case, as the inclusion of turbulence modelling allows for more descriptive results. The multilayer model gives new insight into the complex flow and velocity fields of this simulation, improving the accuracy of the eroded profile of the bed. Furthermore, the multi-sediment formulation allows for a much more accurate description of the bed through the inclusion of heterogeneous layers. This simulation run has demonstrated the ability of the method, not only to capture very complex flows over evolving bathymetry, but also to utilise multiple sediment methods.

8.5 Concluding remarks

This chapter presents a novel model for sediment transport that includes turbulence, a nearly three-dimensional (3D) formulation, and multi-sediment handling. It builds on previous multi-sediment work and the quasi-3D methods to create a two-dimensional shallow water model that is novel. Each layer has individual values for concentration, turbulence variables, and velocities, allowing for a good capture of 3D effects. This allows for vertically stratified velocities, concentrations and turbulence to be calculated for the first time. Using the novel derivation shown in Chapter 7, the model is able to account for interlayer forces for not only momentum and mass exchange but also for turbulence source functions. This provides a more accurate description of the flow than previous models developed in this work and the literature. Vertical velocity components are also post-processed from results, as they are accounted for in the model though the exchange terms. As no vertical velocity components are used during the simulation, the vertical distribution of sediment amongst the flow poses a problem. This problem is solved using the capacity driven sediment diffusion function found in Chapter 4.

A Eulerian-Lagrangian finite volume method is implemented which solves the multilayer system of equations and avoids the Riemann problem. Equivalent eigenvalues are used to approximate the time-step according to the Courant-Friedrichs-Lewy condition, providing stable second-order accurate results. This method of solution is found to be far faster whilst still offering comparable accuracy when compared to 3D Navier-Stokes solvers.

The model is tested for its well-balanced and conservative properties and it is found to have negligible errors, using the benchmark of a lake at rest. It is then compared, as far as possible, to the most advanced open-source sediment model, in the scour downstream of an apron problem. This simulation is hampered by the free-surface included in the presented model, though it shows promising results. It is also tested against the novel experimental data to assess its concentration distribution tools. In this test, it is found to have a very strong agreement with experimental data for a model of this type. This simulation is also used to assess the effects of the inclusion of turbulence modelling on the accuracy of the formulation. It is found that turbulence modelling slightly increases the precision of the model for this short-term simulation. It may be inferred that, for longer and more complex simulations, turbulence may play a crucial role in problems of this type. Finally, the model is used to compute a partial dam-break over a variety of bed compositions. A single-sediment, vertically layered heterogeneous bed and a horizontally layered heterogeneous bed were all simulated. These variations in bed composition created challenging flow and bed profiles, though the method was able to handle all the variations in the flow they presented. These problems have been solved for the first time to the knowledge of the author. This fully demonstrates the presented models multi-sediment handling tools and shows its ability to capture complex flow coupled to sediment transport on erodible beds. Overall, the model provides new abilities and insights for hydrogeomorphic simulations.

Chapter 9

Conclusions and recommendations

This thesis presents a detailed study on the development and validation of an improved class of shallow water models for sediment transport. This is achieved by augmenting existing models to include techniques for sediment handling, vertical sediment diffusion, and turbulence modelling for multilayer flow. The resulting model has been verified as robust and computationally cheap, achieving the goal of this thesis of improving the accuracy and accessibility of hydrogeomorphic simulations. This is important, as it provides both a modular platform upon which further advances can be based, as well as creating a current instrument for multilayer and multi-sediment shallow water modelling. A number of advances have been established in this thesis to tackle inaccuracies in shallow water sediment transport models, with each chapter investigating a different area as follows:

- Modelling and numerical simulation of shallow water flows over multi-sediment beds in one space dimension - Chapter 3
- Modelling and simulation of multilayer shallow water flows over erodible beds in one space dimension - Chapter 4
- Modelling and numerical simulation of shallow water flows over multi-sediment beds in two space dimensions - Chapter 5
- Modelling and simulation of multilayer shallow water flows in two space dimensions - Chapter 6
- Modelling and simulation of multilayer turbulent shallow water flows over fixed beds - Chapter 7

All these advances are then combined in Chapter 8 to develop the most complete model presented in this thesis. In order to develop a more evolved model, three major challenges needed to be addressed. The first to be tackled in this thesis is the assumption of homogeneity in sedimentary beds. As real-world beds are heterogeneous, this assumption leads to non-natural behaviour in most hydrogeomorphic models. The techniques developed here overcome this limitation without a notable increase in computational expense. They allow the modelling of heterogeneous beds, composite beds, and even sediment tracking in both one (1D) and two (2D) space dimensions. This work is presented in Chapter 3 for 1D, and is then expanded for 2D simulations in Chapter 5. Although there is currently no experimental data for composite beds (to the knowledge of the author), this model has been successfully tested against previous homogeneous bed situations. This developed technique is robust in both 1D and 2D and provides an improved tool for sediment transport modelling.

The second limitation challenged is the shallow water assumption of depth-averaged velocities. This is a weakness for most formulations, as sediment interactions are all velocity dependent and, without stratified vertical velocities, models struggle to map morphological evolution accurately. In Chapter 4, a novel 1D multilayer model for sediment transport is developed. A new capacity driven diffusion term is added to the existing inter-layer terms for sediment. The solution utilizes known sediment distribution curves to overcome the lack of simulated vertical forces. The multilayer model distinguishes itself in several situations, offering greater accuracy with vertically stratified results and minimal computational cost. The multilayer model is then developed into a 2D model without sediment transport in Chapter 6. The multilayer model is quasi-three-dimensional (3D) in nature, enabling it to assess increasingly complex flows. Vertically stratified velocities are calculated at a significant speed improvement compared to 3D Navier-Stokes simulations. In this chapter, the multilayer model is examined against various situations that test its well-balanced nature and its ability to capture 3D flow elements. This chapter produces a strong basis for future sediment transport models.

The final challenge, turbulence modelling in multilayer flows, is addressed in Chapter 7. A multilayer turbulence formulation of shallow water flows in 2D has yet to be addressed (to the knowledge of this author), but is a crucial component for the modelling of complex flows. To this end, the turbulence k-ϵ model is part of the formulation introduced in Chapter 6. This model is devised and developed to include interlayer exchange and the creation of turbulent energy. It is compared to both experimental data and OpenFOAM, a 3D Navier-Stokes solver. For the simulations presented, it is found not only to be faster than OpenFOAM, but also to have a comparable degree of accuracy. This chapter produces a useful feature that is integrated into the final model. In Chapter 8, the advancements from Chapters 3-7 are combined with the aim of simulating a novel problem the composite bed partial dam-break. The resulting model is capable of handling multiple sediments in multiple fluid layers whilst modelling turbulence. The final formulation is evaluated against various situations to confirm its adaptability and accuracy. It is ultimately used to model the composite bed partial dam-break, the first simulation of its type. Overall, this chapter demonstrates the ability of the model and showcases the advantages of each of the modular developments when applied to a complex situation.

A novel class of numerical methods has been developed to enable the advances in modelling of multilayer shallow water equations over movable multi-sediment beds. Initially, a non-homogeneous Riemann solver is used in Chapter 3 for simulations; this method is found to be highly accurate. Unfortunately, though this solver is well developed, it is unable to handle the multilayer fluid formulations proposed. Therefore attention is turned to a class of Eulerian-Lagrangian methods developed in this thesis. The Eulerian-Lagrangian Finite Volume (ELFV) method is based on predictor-corrector style solvers. This class of methods employs the method of characteristics to estimate the numerical fluxes, and then recovers them to the conservative equations in the corrector step. In Chapter 4, the ELFV method is used for a multilayer flow model. In this case the ELFV method avoids of the calculation of complex eigenvalues and vectors of the system, which prevent most solvers from being able to handle these types of multilayer models. In Chapter 5, this method is used for 2D problems through the use of a projection technique which reduces the reconstruction of the numerical fluxes at any boundary to a 1D problem, for which it works well. It is also developed for a multilayer model in 2D in Chapter 6. This method is found to be fast and accurate, it also enables more complex problems to be simulated using the shallow water equations through multilayer formulations. This is an important step towards the inclusion of turbulence modelling in the final model.

Chapter 8 combines together all the developments of the previous chapters and presents a final model for multilayer shallow water flow, including turbulence, over movable multi-sediment beds. As part of this study, a novel method for recording sediment distribution is designed and tested in the Engineering Department at Durham University. A novel experimental rig is devised and built, enabling high-speed, highly accurate images to be collected and evaluated. The novel aspect of this work is that the results are divided into cellular smaller images, which are then processed for their colour contents. Each image is first refined to remove any background pixels and to account for angle and lighting. The colour content of the image is then assessed, with sensible tuning undertaken to remove the complex effects of ripples and air content. This method allows the user accurately to assess the volume of sediment in a particular section of a fluid flow. This novel experimental technique provides a new avenue for testing and evaluating sediment transport models. The data gained from this example is used to test the model presented in Chapter 8, and it is the first time, to the best knowledge of the author, that vertically stratified sediment data has been used to assess the validity of a model of this class. The results are found to be consistent and it provides some benchmark validation for the final model.

For further works, the first area of development should be the multi-sediment model which could be developed to include differential transport rates for layers and sediment types. By having differential transport rates, the effects of sediment size and density could be taken into account more accurately. The work conducted in this thesis has been mainly focused on high-shear dam-break situations, as these are amongst the most pressing water management problems with the largest resource of literature and data to validate against. This work could be extended to look at longer-term simulations with constant water heights. Development of specific steady-state code could substantially accelerate these models. Another key feature for real-world simulations is wet-dry fronts. This will enable the model to be employed on a new range of real world problems. The addition of wet-dry fronts would greatly improve this model and should be a key priority for future work. Finally, this study has focused on various groups of experimental data, as sediment transport modelling is semi-empirical in its nature. Asymptotic analysis of this model would be of great worth in assessing its limitations. This is vital in order to fully exploit the potential of the model as a modular platform for hydrogeomorphic simulations.

Bibliography

[1] M. Abbott. *Computational hydraulics: Elements of the Theory of Free Surface Flows.* Fearon-Pitman Publishers, 1979.

[2] R. Abdellaoui, F. Benkhaldoun, I. Elmahi, and M. Seaid. A Finite Volume Method for Large-Eddy Simulation of Shallow Water Equations. *Finite Volumes for Complex Applications VII, Springer Proceedings in Mathematics & Statistics*, 78:741–748, 2014.

[3] K. Abderrezzak, A. Moran, E. Mosselman, J. Bouchard, H. Habersack, and D. Aelbrecht. A physical, movable-bed model for non-uniform sediment transport, fluvial erosion and bank failure in rivers. *Journal of Hydro-environment Research*, 8:95–114, 2013.

[4] K. Abderrezzak, A. Moran, P. Tassi, R. Ata, and J. Hervouet. Modelling river bank erosion using a 2D depth-averaged numerical model of flow and non-cohesive, non-uniform sediment transport. *Advances in Water Resources*, 93:75–88, 2015.

[5] R. Abgrall and S. Karni. Two-layer shallow water systems: A relaxation approach. *SIAM J. Sci. Comput.*, 31:1603–1627, 2009.

[6] R. Abgrall and C. Shu. *Handbook of Numerical Methods for Hyperbolic Problems.* Elsevier, 2016.

[7] H. Aksoy. *Challenges in Modelling Sediment Matters*, pages 61–81. Springer International Publishing, 2015.

[8] F. Alcrudo and F. Benkhaldoun. Exact solutions to the Riemann problem of the shallow water equations with a bottom step. *Computers & Fluids.*, 30:643–671, 2001.

[9] Y. Alhuri, F. Benkhaldoun, D. Ouazar, M. Seaid, and A. Taik. A meshless method for numerical simulation of depth-averaged turbulence flows using a k-ϵ model. *International Journal for Numerical Methods in Fluids*, 80:3–22, 2016.

[10] L. Amoudry and P. Liu. Two-dimensional, two-phase granular sediment transport model with applications to scouring downstream of an apron. *Coastal Engineering*, 56:693–702, 2009.

[11] E. Audusse. A multilayer Saint-Venant system: Derivation and numerical validation. *Discrete and Continuous Dynamical Systems, Ser. B.*, 5:189–214, 2005.

[12] E. Audusse, F. Benkhaldoun, S. Saida, M. Seaid, and P. Tassi. A fast finite volume solver for multi-layered shallow water flows with mass exchange. *Journal of Computational Physics*, 272:23–45, 2014.

[13] E. Audusse, M. Bristeau, M. Pelanti, and J. Sainte-Marie. Approximation of the hydrostatic Navier-Stokes system for density stratified flows by a multilayer model: Kinetic interpretation and numerical solution,. *J. Comput. Phys.*, 230:3453–3478, 2011.

[14] E. Audusse, M. Bristeau, B. Perthame, and J. Sainte-Marie. A multilayer Saint-Venant system with mass exchanges for Shallow Water flows. Derivation and Numerical Validation. *M2AN Math. Model. Numer. Anal.*, 45:169–200, 2009.

[15] B. Baldwin and H. Lomax, editors. *Thin-layer approximation and algebraic model for separated turbulent flows.* AIAA, 16th Aerospace Sciences Meeting, 1978.

[16] J. Barry, J. Buffington, and J. King. A general power equation for predicting bed load transport rates in gravel bed rivers. *Water Source Research*, 40, 2004.

[17] T. Barth, R. Herbin, and M. Ohlberger. *Finite Volume Methods: Foundation and Analysis*, pages 1–60. American Cancer Society, 2017.

[18] A. Bayram, M. Larson, H. C. Miller, and N. C. Kraus. Cross-shore distribution of longshore sediment transport: Comparison between predictive formulas and field measurements. *Coastal Eng*, 44:79–99, 2001.

[19] R. Beam and Warming R. An Implicit Finite-Difference Algorithm for Hyperbolic Systems in Conservation-Law Form. *Journal of Computational Physics*, 2:87–110, 1976.

[20] F. Benkhaldoun, I. Elmahi, S. Sari, and M. Seaid. An unstructured finite-volume method for coupled models of suspended sediment and bed load transport in shallow-water flows. *International Journal for Numerical Methods in Fluids*, 72:967 – 993, 2013.

[21] F. Benkhaldoun, S. Sahmim, and M. Seaid. A two-dimensional finite volume morphodynamic model on unstructured triangular grids. *International Journal of Numerical Methods in Fluids*, 63:1296–1327, 2010.

[22] F. Benkhaldoun, S. Sari, and M. Seaid. A flux-limiter method for dam-break flows over erodible sediment beds. *Applied Mathematical Modelling*, 36:4847–4861, 2012.

[23] F. Benkhaldoun, S. Sari, and M. Seaid. Projection finite volume method for shallow water flows. *Mathematics and Computers in Simulation*, 118:87–101, 2015.

[24] F. Benkhaldoun and M. Seaid. A simple finite volume method for the Shallow Water equations. *J. Comp. Applied Math.*, 234:58–72, 2010.

[25] A. Bermudez and M. Vázquez-Cendón. Upwind methods for hyperbolic conservation laws with source terms. *Computers & Fluids.*, 23:1049–1071, 1994.

[26] S. Bi, J. Zhou, N. Zhao, H. Zhang, and Y. Zhao, editors. *A finite volume model for dam-break floods with wet-dry fronts on non-uniform grids.* Twenty-second Euromicro International Conference on Parallel, Distributed, and Network-Based Processing, 2014.

[27] E. Bijker. Some considerations about scales for coastal models with movable bed. *Delft Hydraulics Laboratory*, 50:1–128, 1967.

[28] J. Boris and D. Book. Flux corrected transport. I. SHASTA, a fluid transport algorithm that works. *J. Comp. Physics.*, 11:38–69, 1973.

[29] F. Bouchut and T. Morales. An entropy satisfying scheme for two-layer shallow water equations with uncoupled treatment. *M2AN Math. Model. Numer. Anal.*, 42:683–698, 2008.

[30] R. Briganti, N. Dodd, D. Kelly, and Pokrajac D. An efficient and flexible solver for the simulation of morphodynamics of fast evolving flows on coarse sediment beaches. *International Journal for Numerical Methods in Fluids*, 69:859–877, 2011.

[31] M. Bristeau and J. Sainte-Marie. Derivation of a non-hydrostatic shallow water model; Comparison with Saint-Venant and Boussinesq systems. *Discrete Contin. Dyn. Syst. Ser.*, 10:733–759, 2008.

[32] W. Brownlie. Prediction of flow depth and sediment discharge in open channels. *Report Number KH-R-43A*, Keck Laboratory of Hydraulics and Water Resources, California Institute of Technology, 1981.

[33] B. Camenen and M. Larson. A General Formula for Noncohesive Suspended Sediment Transport. *Journal of Coastal Resource*, 24:615–627, 2008.

[34] F. Campbell and H. Bauder. A rating-curve method for determining silt-discharge of streams. *Eos Trans. Am. Geophys. Union*, 21:603–607, 1940.

[35] Z. Cao and P. Carling. Mathematical modelling of alluvial rivers: reality and myth. Part 1: General overview. *Water Maritime Engineering*, 154:207–220, 2002.

[36] Z. Cao and G. Pender. Numerical modelling of alluvial rivers subject to interactive sediment mining and feeding. *Advances in Water Resources*, 27:533–546, 2004.

[37] Z. Cao, G. Pender, and P. Carling. Shallow water hydrodynamic models for hyperconcentrated sediment-laden floods over erodible bed. *Advances in Water Resources*, 29:546–557, 2006.

[38] Z. Cao, G. Pender, S. Wallis, and P. Carling. Computational Dam-Break Hydraulics over Erodible Sediment Bed. *Journal of Hydraulic Engineering*, 67:149–152, 2004.

[39] H. Capart and D. Young. Formation of jump by the dam-break wave over a granular bed. *Journal of Fluid Mechanics*, 372:165 – 187, 1998.

[40] M. Castro, J. Macías, and C. Parés. A Q-scheme for a class of systems of coupled conservation laws with source term. Application to a two-layer 1D shallow water system. *M2AN Math. Model. Numer. Anal.*, 35:107–127, 2001.

[41] M. Castro Diaz, E. Fernadez-Nieto, and A. Ferreiro. Sediment transport models in Shallow Water equations and numerical approach by high order finite volume methods. *Computers and Fluids*, 37(3):299–316, 2008.

[42] L. Cea, J. Puertas, and M. Vazques-Cendon. Depth averaged modelling of turbulent shallow water flow with wet-dry fronts. *Arch. Comput. Methods Eng.*, 14:303–341.

[43] S. Chakravarthy and S. Osher, editors. *High resolution applications of the Osher upwind scheme for the Euler equations.* AIAA 6th Computational Fluid Dynamics Conference, AIAA, 1983.

[44] K. Chan and S. Sabatino. Validity tests of the mixing-length theory of deep convection. *Science*, 245:465–467, 1987.

[45] S. Chang. Simulation of bed-load dispersion process. *Journal of Hydraulic Engineering*, 128:331–342, 2002.

[46] Daoyi Chen and Gerhard H Jirka. Experimental study of plane turbulent wakes in a shallow water layer. *Fluid Dynamics Research*, 16:11–41.

[47] S.-C. Chen, C.-N. Yang, and C.-Y. Tsou. Bedform development and its effect on bed stabilization and sediment transport based on a flume experiment with non-uniform sediment. *International Journal of Sediment Research*, 2017.

[48] Y. Chen and S. Kim. Computations of turbulent flows using an extended k-ϵ turbulence closure model.

[49] Z. Cheng, T.-J. Hsu, and J. Calantoni. Sedfoam: A multi-dimensional Eulerian two-phase model for sediment transport and its application to momentary bed failure. *Coastal Engineering*, 119:32–50,, 2017.

[50] R. Codina. Numerical Solution of the Incompressible Navier–Stokes Equations with Coriolis Forces Based on the Discretization of the Total Time Derivative. *J. Comp. Physics.*, 148:467–496, 1999.

[51] C. Colebrook. Turbulent flow in pipes with particular reference to the transition region between the smooth and rough pipe laws. *J. Inst. Civ. Eng.*, 11:133–156, 1939.

[52] R. Courant, K. Friedrichs, and H. Lewy. On the Partial Difference Equations of Mathematical Physics. *AEC Research and Development Report*, 1928.

[53] R. Courant and D. Hilbert. *Methods of Mathematical Physics: Partial Differential Equations.* Wiley VCH, first edition, 1989.

[54] R. Courant, E. Isaacson, and M. Rees. On the Solution of Nonlinear Hyperbolic Differential Equations by Finite Differences. *Comm. Pure Appl. Math.*, 5:243–255, 1952.

[55] J. Cunge, F. Holly, and A. Verwey. Practical Aspects of Computation River Hydraulics. *Pitman Publishing Inc. Boston*, 2002.

[56] L. Davidson. *Fluid mechanics, turbulent flow and turbulence modeling.* Chalmers University of Technology, 2018.

[57] S. Davis. Simplified second-order Godunov-type methods. *SIAM J. Sci. Stat. Comput.*, 9:445–473, 1988.

[58] S. Dawei and F. Weibing. A Two-Dimensional Numerical Model of Suspended Sediment Transport Using in the Radial Sand Ridge Field. *International Conference on Mechatronic Science, Electric Engineering and Computer*, pages 826–830, 2011.

[59] J. Deardorff. A numerical study of three-dimensional turbulent channel flow at large Reynolds numbers. *Journal of Fluid Mechanics*, 41:453–480, 1970.

[60] M. Derakhti, J. Kirby, and G. Shi, F.and Ma. Wave breaking in the surf zone and deep-water in a non-hydrostatic rans model. part 1: Organized wave motions. *Ocean Modelling*, 107:125–138, 2016.

[61] M. du Boys. Etudes du règime du Rhône et de l'action exercée par les eaux sur un lit á fond de graviers indéfiniment affouillable. *Ann.Ponts Chaussees*, 5:141–195, 1879.

[62] J. Duan. Simulation of Flow and Mass Dispersion in Meandering Channels. *J. Hydraul. Eng. - ACSE*, 130:964–976, 2004.

[63] P. Dyke. Modeling Coastal and Offshore Processes. 2007.

[64] H. Einstein. Formulas for the Transportation of Bed Load. *Transactions of the American Society of Civil Engineers*, 107:561–573, 1949.

[65] F. Engelund and E. Hansen. A Monograph on Sediment Transport in Alluvial Streams. 1967.

[66] B. Engquist and S. Osher. One-sided Difference Approximations for Nonlinear Conservation Laws. *Math. Comp.*, 25:294–318, 1981.

[67] L. Euler. *Institutionum Calculi Integralis.* Lipsiae Et Berolini, 1768.

[68] J. Fe, F. Navarrina, J. Puertas, P. Vellando, and D. Ruiz. Experimental validation of two depth-averaged turbulence models. *International Journal for Numerical Methods in Fluids*, 60:177–202, 2009.

[69] E. Fernández-Nieto, E. Koné, T. Morales de Luna, and R. Burger. A multilayer shallow water system for polydisperse sedimentation. *Journal of Computational Physics*, 238:281–314, 2013.

[70] E. Fernández-Nieto, E. Koné, and Chacón T. A multilayer method for the hydrostatic Navier–Stokes equations: a particular weak solution. *J.Sci.Comput.*, 57:1–30.

[71] C. Field, V. Barros, T. Stocker, Q. Dahe, D. Dokken, K. Ebi, M. Mastrandrea, K. Mach, G-K. Plattner, and S. Allen et al. *Managing the Risks of Extreme Events and Disasters to Advance Climate Change Adaptation.* Intergovernmental Panel on Climate Change, 2017.

[72] P. Gastescu, W. Marszelewski, and P. Bretcan, editors. *History of building the main dams and reservoirs.* 2nd International Conference Water resources and wetlands., Romanian Limnogeographical Association.

[73] J. Gerbeau and B. Perthame. Derivation of viscous Saint-Venant system for laminar shallow water: Numerical validation. *Discrete and Continuous Dynamical Systems, Ser. B.*, 1:89–102, 2001.

[74] S. Godunov. A Difference Scheme for Numerical Solution of Discontinuous Solution of Hydrodynamic Equations. *Math.*, 47:271–306, 1959.

[75] E. Goede. *WAQUA/TRIWAQ : two- and three-dimensional shallow water flow model.* Rijkswaterstaat, 2016.

[76] L. Gomez. *An unstructured finite volume model for unsteady turbulent shallow water flow with wet–dry fronts, Numerical solver and experimental validation.* PhD thesis, Universidad de A Coruna, Departamento de Metodos Matematicos y de Representacion, 2005.

[77] R. Graham, editor. *Numerical Simulation of Local Scour with Free Surface and Automatic Mesh Deformation.* Examining the Confluence of Environmental and Water Concerns, IAHR, 2006.

[78] A. Grass. Sediment Transport by Waves and Currents. *SERC London Cent. Mar. Technol.*, (FL29), 1981.

[79] C. Grossmann, H.-G. Roos, and M. Stones. *Numerical Treatment of Partial Differential Equations.* Springer-Verlag Berlin Heidelberg, first edition, 2007.

[80] M. Guan, N. Wright, and P. Sleigh. A 2D process-based morphodynamic model for flooding by non-cohesive dyke breach. *Journal of Hydraulic Engineering*, 140, 2014.

[81] M. Guan, N. Wright, and P. Sleigh. Multimode morphodynamic model for sediment-laden flows and geomorphic impacts. *Journal of Hydraulic Engineering*, 141, 2015.

[82] J. Gula, V. Zeitlin, and F. Bouchut. Instabilities of buoyancy-driven coastal currents and their nonlinear evolution in the two-layer rotating shallow water model. Part 2. Active lower layer. *J. Fluid Mechanics.*, 665:209–237, 2010.

[83] J. Guo and P. Julien. Turbulent velocity profiles in sediment-laden flows. *J. of Hydraulic Research*, 39:11–23, 2001.

[84] M. Hajigholizadeh, A. Melesse, and H. Fuentes. Erosion and Sediment Transport Modelling in Shallow Waters: A Review on Approaches, Models and Applications. *International Journal of Environmental Research and Public Health*, 51:1–24, 2018.

[85] A. Harten, P. Lax, and B. van Leer. On Upstream Differencing and Godunov-Type Schemes for Hyperbolic Conservation Laws. *SIAM Rev.*, 1983:35–61, 1983.

[86] A. Harten and G. Zwas. Self-adjusting hybrid schemes for shock computations. *J. Comp. Physics.*, 9:568, 1972.

[87] E. Hayter and J. Gailani. *Fundamentals of Sediment Transport.* Springer New York, 2014.

[88] C. Hirsch and B. Tartinville. Reynolds-Averaged Navier-Stokes modelling for industrial applications and some challenging issues. *International Journal of Computational Fluid Dynamics*, 23:295–303, 2009.

[89] D. Hoang, V. van Steijn, L. Portela, M. Kreutzer, and C. Kleijn. Benchmark numerical simulations of segmented two-phase flows in microchannels using the volume of fluid method. *Computers and Fluids*, 86:28 – 36, 2013.

[90] P. Hu and Z. Cao. Fully coupled mathematical modeling of turbidity currents over erodible bed. *Advances in Water Resources*, 32:1–15, 2009.

[91] G. Huang. Time Lag between Economic Development and Flood Fatality. *Journal of Sustainable Development*, 5, 2012.

[92] S. Huang, Z. Sun, D. Xu, and S. Xia. Vertical distribution of sediment concentration. *Journal of Zhejiang University SCIENCE*, 9:1560–, 2008.

[93] A. Jakeman, I. Littlewood, and P. Whitehead. Computation of the Instantaneous Unit Hydrograph and Identifiable Component Flows with Application to Two Small Upland Catchments. *J. Hydrol.*, 117:275–300, 1990.

[94] A. Jha. *Sediment transport models for Shallow Water Equations.* PhD thesis, Loughborough University, Department of Civil and Building Engineering, 2012.

[95] N. Jinren and Q. Huapeng. Impact of River Realignment and Land Reclamation on Flood Control and Ecological Habitat in River-estuary-bay System. *Water International*, 26:206–214, 2001.

[96] J. Johnson. Distribution graphs of suspended-matter concentration. *Trans. Am. Soc. Civ. Eng.*, 108:941–956, 1943.

[97] B. Jongman, S. Hochrainer-Stigler, L. Feyen, J. Aerts, R. Mechler, W. Wouter Botzen, L. Bouwer, G. Pflug, R. Rojas, and P. Ward. Increasing stress on disaster-risk finance due to large floods. *Nature Climate Change*, 4:264–268, 2014.

[98] B. Jongman, E. Koks, T. Husby, and P. Ward. Increasing flood exposure in the Netherlands: Implications for risk financing. *Natural Hazards and Earth System Science*, 14:1245–1255, 2014.

[99] S. Jonkman, H. Voortman, W. Klerk, and S. Vuren. Developments in the management of flood defences and hydraulic infrastructure in the Netherlands. *Structure and Infrastructure Engineering*, 14:895–910, 2018.

[100] M. Keshtpoor, J. Puleo, F. Shi, and G. Ma. 3D numerical simulation of turbulence and sediment transport within a tidal inlet. *96*, 140:13–26, 2015.

[101] P. Kinnell. Applying the USLE-M within the agricultural non point source pollution model. *Environ. Model. Softw.*, 15:331–334, 2000.

[102] G. Kondolf et al. Sustainable sediment management in reservoirs and regulated rivers: Experiences from five continents. *Earth's Future*, 2:256 – 280, 2014.

[103] B. Koren. *A robust upwind discretisation method for advection, diffusion and source terms.* Numerical Methods for Advection–Diffusion Problems. Braunschweig: Viewweg, 1983.

[104] G. Kozyrakis. Numerical modeling of sediment transport applied to coastal morphodynamics. *Applied Numerical Mathematics*, 104:30–46, 2016.

[105] E. Kubatko and J. Westerink. Exact discontinuous solutions of Exner's bed evolution model: Simple theory for sediment bores. *Journal of Hydraulic Engineering*, 133, 2007.

[106] A. Kuo and L. Polvani. Nonlinear geostrophic adjustment, cyclone/anticyclone asymmetry, and potential vorticity rearrangement. *Phys. Fluids.*, 12:1087–1100, 2000.

[107] W. Kutta. *Beitrag zur näherungsweisen Integration totaler Differentialgleichungen.* B.G Teubner, 1901.

[108] B. Launder and D. Spalding. The Numerical Computation of Turbulent Flows. *Computer Methods in Applied Mechanics and Engineering*, 3:269–289, 1974.

[109] D. Laurence, J. Uribe, and S. Utyuzhnikov. A Robust Formulation of the v^2-f Model. *Flow Turbulence and Combustion*, 73:169–185, 2004.

[110] P. Lax. Weak solutions of nonlinear hyperbolic equations and their numerical approximation. *Comm. Pure Appl. Math.*, 7:159–193, 1954.

[111] P. Lax and B. Wendroff. Systems of Conservation Laws. *Comm. Pure Appl. Math.*, 13:217–237, 1960.

[112] R. LeVeque. *Numerical Methods for Conservation Laws*. Birkhäuser Basel, 1992.

[113] S. Li and C. Duffy. Fully coupled approach to modeling shallow water flow, sediment transport and bed evolution in rivers. *Water Resources Research*, 47:1–20, 2011.

[114] Q. Liang, K. Chen, J. Hou, Y. Xiong, G. Wang, and J. Qiang. Hydrodynamic modelling of flow impact on structures under extreme flow conditions. *Journal of Hydrodynamics*, 28:267–274, 2016.

[115] X. Liu. New Near-Wall Treatment for Suspended Sediment Transport Simulations with High-Reynolds Number (HRN) Turbulence Models. *J. Hydaul. Eng*, 140:333–339, 2014.

[116] X. Liu and A. Beljadid. A coupled numerical model for water flow, sediment transport and bed erosion. *Computers and Fluids*, 154:273–284, 2017.

[117] X. Liu, A. Mohammadian, and J. Sedano. A numerical model for three-dimensional shallow water flows with sharp gradients over mobile topography. *Computers and Fluids.*, 154:1–11, 2017.

[118] Q. Luo. A distributed surface flow model for watersheds with large water bodies and channel loops. *J. Hydrol.*, 337:172–186, 2007.

[119] R. Manning. On the flow of water in open channels and pipes. *Transactions of the Institution of Civil Engineers of Ireland*, 20:161–207, 1891.

[120] T. McCulloh. The effects of viscosity in hypervelocity impact cratering. *AIAA*.

[121] T. McCulloh. Mass Properties of Sedimentary Rocks and Gravimetric Effects of Petroleum and Natural-Gas Reservoirs. *United States Geological Survey*, 528-A, 1967. USGS Professional Paper.

[122] E. Meyer-Peter and R. Müller. Formulas for Bed-Load Transport. *Report on 2nd meeting on International Association on Hydraulic Structures Research*, pages 39–64, 1948.

[123] H. Mitasova, J. Hofierka, M. Zlocha, and L. Iverson. Modelling topographic potential for erosion and deposition using GIS. *Int. J. Geogr. Inf. Syst.*, 10:629–641, 1996.

[124] R. Morgan, D. Morgan, and H. Finney. A Predictive Model for the Assessment of Soil Erosion Risk. *J. Agric. Eng. Res.*, 30:245–253, 1984.

[125] N. Morgenstern. Report on Mount Polley Tailings Storage Facility Breach, January 2015. [Online; posted 30-January-2015].

[126] F. Moukalled, M. Mangani, and L. Darwish. *The Finite Volume Method in Computational Fluid Dynamics.* Springer International Publishing, first edition, 2015.

[127] J. Murillo and P. Garcia-Navarro. An Exner-based coupled model for two-dimensional transient flow over erodible bed. *Journal of Computational Physics*, 229:8704–8732, 2010.

[128] J. Murillo and P. Garcia-Navarro. Weak solutions for partial differential equations with source terms: Application to the shallow water equations. *J. Comput. Phys.*, 229:4327–4368, 2010.

[129] K. Naoto, F. Naoki, and M. Masafumi. Three-dimensional sediment transport processes on tsunami-induced topography changes in a harbor. *Earth, Planets and Space*, 64:787–797, 2012.

[130] United Nations. *Global Assessment Report on Disaster Risk Reduction.* United Nations International Strategy for Disaster Reduction, 2011.

[131] S. Neill, A. Elliott, and M. Hashemi. A model of inter-annual variability in beach levels. *Continental Shelf Research*, 28:1769–1781, 2008.

[132] S. Orszag. Analytical theories of turbulence. *Journal of Fluid Mechanics*, 41:363–386, 1970.

[133] T. Pahtz and O. Duran. Fluid forces or impacts: What governs the entrainment of soil particles in sediment transport mediated by a Newtonian fluid. *Phys. Rev. Fluids*, 2:074303, 2017.

[134] C. Paolo. *Sediment transport models for Shallow Water Equations.* PhD thesis, Universita Degli Studi di Pisa Facolta' di Ingegneria, 2012.

[135] D. Paphitis. Sediment movement under unidirectional flows: An assessment of empirical threshold curves. *Coastal Engineering*, 43:227–245, 2001.

[136] M. Protter and C. Morrey. *Differentiation under the Integral Sign.* New York: Springer.

[137] H. Qiu, R. An, L. Mei, and C. Xue. Two-step algorithms for the stationary incompressible Navier—Stokes equations with friction boundary conditions. *Applied Numerical Mathematics*, 120:97 – 114, 2017.

[138] J. Rahuel, F. Holly, J. Holly Chollet, and G. Yang. Modeling of Riverbed Evolution for Bedload Sediment Mixtures. *Journal of Hydraulic Engineering*, 115, 1989.

[139] J. Rahuel and F. Holly et al. Modeling of Riverbed Evolution for Bedload Sediment Mixtures. *J. of Hydr. Engrg*, 11:1521–1542, 2016.

[140] K. Rehman and Y. Cho. Bed Evolution under Rapidly Varying Flows by a New Method for Wave Speed Estimation. *Journal of Computational Physics*, 43:357–372, 2016.

[141] O. Reynolds. IV. On the dynamical theory of incompressible viscous fluids and the determination of the criterion. *Philosophical Transactions of the Royal Society of London A: Mathematical, Physical and Engineering Sciences*, 186:123–164, 1895.

[142] R. Richtmyer and K. Morton. *Difference Methods for Initial-value Problems.* Wiley-Interscience, 1967.

[143] D. Rijnsdorp, P. Smit, M. Zijlema, and A. Reniers. Efficient non-hydrostatic modelling of 3d wave-induced currents using a subgrid approach. *Ocean Modelling*, 116:118–133.

[144] A. Robert. A stable numerical integration scheme for the primitive meteorological equations. *Atmos. Ocean.*, 19:35–46, 1981.

[145] E. Robertson, V. Choudhury, S. Bhushan, and D. Walters. Validation of OpenFOAM numerical methods and turbulence models for incompressible bluff body flows. *Computers and Fluids*, 123:122 – 145, 2015.

[146] W. Rodi. *Turbulence models and their application in hydraulics - A state of the art review.* IAHR, 1980.

[147] P. Roe. Approximate Riemann solvers, parameter vectors and difference schemes. *J. Comp. Physics.*, 43:357–372, 1981.

[148] P. Roe. Some contributions to the modeling of discontinuous flows. *Lect. Notes Appl. Maths*, 22:163–193, 1985.

[149] D. Ropp and J. Shadi. Stability of Operator Splitting Methods for Systems with Indefinite Operators: Reaction-Diffusion Systems. *J. Comput. Physics*, 228:3508–3516, 2009.

[150] H. Rouse. Modern Conceptions of Mechanics of Fluid Turbulence. *Trans. ASCE*, 102:463–505, 1937.

[151] W. Rubey. Settling velocity of gravel, sand, and silt particles. *American Journal of Science*, 148:325–338, 1933.

[152] C. Runge. Ueber die numerische auflösung von differentialgleichungen. *Mathematische Annalen*, 46:167–178, 1895.

[153] S. Sahmim, F. Benkhaldoun, and F. Alcrudo. A Sign Matrix Based Scheme for Quasi-Hyperbolic Non-Homogeneous PDEs with an Analysis of the Convergence Stagnation Phenomenon. *Journal of Computational Physics*, 226:1753–1783, 2007.

[154] A. de Saint-Venant. Théorie du mouvement non permanent des eaux, avec application aux crues des rivières et a l'introduction de marées dans leurs lit. *Comptes Rendus des Séances de l'Académie des Sciences*, 73:147–154 and 237–240, 1871.

[155] L. Sanford. Modelling a dynamically varying mixed sediment bed with erosion, deposition, bioturbation, consolidation, and armoring. *Computers and Geosciences*, 34:1263–1283, 2006.

[156] P. Sayers. *Flood Risk: Planning, Design and Management of Flood Defence Infrastructure.* ICE Publishing, 2012.

[157] M. Seaid. On the Quasi-monotone Modified Method of Characteristics for Transport-diffusion Problems with Reactive Sources. *Comp. Methods in App. Math.*, 2:186–210, 2002.

[158] L.F. Shampine. Stability of explicit runge—kutta methods. *Computers & Mathematics with Applications*, 10(6):419–432.

[159] N. Shankar, H. Cheon, and S. Sankaranarayanan. Multilevel finite-difference model for three-dimensional hydrodynamic circulation. *Ocean Eng.*, 24:785–816, 1997.

[160] A. Shields. Anwendung der Ahnlichkeitsmechanik und der Turbulenzforschung auf die Geschiebebewegung. *Mitteilung der preussischen Versuchsanstalt fur Wasserbau und Schiffbau*, 26, 1936.

[161] C. Shu. Total Variation Diminishing Time Discretizations. *SIAM J. Sci. Stat. Comput.*, 9:1073–1084, 1988.

[162] G. Simpson and S. Castelltort. Coupled model of surface water flow, sediment transport and morphological evolution. *SIAM J. Numer. Anal.*, 21:1600–1614, 2006.

[163] V. Singh, A. Baniukiewicz, and V. Chen. An instantaneous unit sediment graph study for small upland watersheds. *Applied Modeling in Catchment Hydrology*, 1:534–554, 1982.

[164] H. Smaoui, F. Boughanim, and G. Chapalain. 1D vertical model for suspended sediment transport in turbulent tidal flow: Application to the English Channel. *Computers & Geosciences*, 33:1111–1129, 2007.

[165] S. Soares-Frazao and et al. Dam-break flows over mobile beds: Experiments and benchmark tests for numerical models. *Journal of Hydraulic Research*, 50:364–375, 2012.

[166] S. Soares-Frazao and Y. Zech. HLLC scheme with novel wave-speed estimators appropriate for two-dimensional shallow-water flow on erodible bed. *International Journal for Numerical Methods in Fluids*, 66:1019–1036, 2011.

[167] R. Soulsby. *Dynamics of Marine Sands. A Manual of Practical Applications.* Thomas Telford Publications, 1997.

[168] P. Spalart and S. Allmaras. A One-Equation Turbulence Model for Aerodynamic Flows. *La Recherche Aerospatiale*, 1:5–21, 1994.

[169] G. Stecca, A. Siviglia, and A. Blom. Mathematical analysis of the Saint–Venant–Hirano model for mixed–sediment morphodynamics. *Water Resources Research*, 50:7563–7589, 2014.

[170] J. Steele, K. Turekian, and S. Thorpe. *Encyclopedia of Ocean Sciences (Second Edition).* Academic Press, 2008.

[171] G. Stokes. On the Effect of the Internal Friction of Fluids on the Motion of Pendulum. *Transactions of the Cambridge Philosophical Society*, 9:8–106, 1851.

[172] G. Strang. On the construction and the comparison of difference schemes. *SIAM J. Numer. Anal.*, 5:506–517, 1968.

[173] A. Strickler, T. Roesgan, and W. Brownie. Contributions to the Question of a Velocity Formula and Roughness Data for Streams, Channels and Closed Pipelines. *W. M. Keck Lab of Hydraulics and Water Resources, California Institute of Technology, Pasadena*, 1923.

[174] P. Sweby. High Resolution Schemes using Flux Limiters for Hyperbolic Conservation Laws. *SIAM J. Num. Anal.*, 21:995–1011, 1984.

[175] W. Tan. *Shallow Water Hydrodynamics.* Elsevier Science, 1st edition, 1992.

[176] Q. Tang and Y. Huang. Stability and convergence analysis of a Crank-Nicolson Leap-Frog scheme for the unsteady incompressible Navier-Stokes equations. *Applied Numerical Mathematics*, 2017.

[177] K. Terzaghi, R. Peck, and G. Mersi. *Soil Mechanics in Engineering Practice.* John Wile and Sons Publishers, 1996.

[178] G. Thommes. Radiative heat transfer equations for glass cooling problems: Analysis and numerics. *Ph.D. Thesis, TU Darmstadt*, 2002.

[179] E. Toro. *Riemann Solvers and Numerical Methods for Fluid Dynamics.* Springer Verlag, 1999.

[180] E. Toro, M. Spruce, and W. Speares. Restoration of the contact surface in the HLL-Riemann solver. *Shock Waves*, 4:25–34, 1967.

[181] K. Tubbs and F. Tsai. Multilayer shallow water flow using lattice Boltzmann method with high performance computing. *Advances in Water Resources.*, 32:1767–1776, 2009.

[182] W. Uijttewaal and R. Booij. Effects of shallowness on the development of free-surface mixing layers. *Physics of Fluids*, 12(2):392–402.

[183] B. van Leer. Towards the ultimate conservative difference scheme. IV. A new approach to numerical convection. *J. Comp. Physics.*, 23:267–299, 1977.

[184] B. van Leer. On the Relation Between the Upwind-Differencing Schemes of Godunov, Engquist–Osher and Roe. *SIAM Journal on Scientific and Statistical Computing*, 5:1–20, 1984.

[185] L. van Rijn. Bed load transport: Part 2. *Journal of Hydraulic Division*, 110:1613–1641, 1984.

[186] L. van Rijn. Sediment pick-up functions. *Journal of Hydraulic Engineering*, 110:1494–1502, 1984.

[187] L. van Rijn. Sediment transport: Part 1. *Journal of Hydraulic Division*, 110:1431–1456, 1984.

[188] L. van Rijn. Suspended load transport: Part 3. *Journal of Hydraulic Division*, 110:1733–1754, 1984.

[189] L. van Rijn. Unified View of Sediment Transport by Currents and Waves. I : Initiation of Motion, Bed Roughness, and Bed-Load Transport. *Journal of Hydraulic Engineering*, 113:649–667, 2007.

[190] V. Vanoni. *Sedimentation Engineering.* American Society of Civil Engineers, classic edition, 2006.

[191] V. Vanoni and G. Nomicos. Resistance Properties of Sediment-Laden Streams. *Transactions of the American Society of Civil Engineers*, 125:1140–1167, 1960.

[192] K. Vercruysse, R. Grabowski, and R. Rickson. Suspended sediment transport dynamics in rivers: Multi-scale drivers of temporal variation. *Earth-Science Reviews*, 166:38–52, 2017.

[193] H. Versteeg and W. Malalasekera. *An Introduction to Computational Fluid Dynamics. The Finite Volume Method.* Addison-Wesley Longman: Harlow, 1995.

[194] C. Vreugdenhil. Two-Layer Shallow-Water Flow in Two Dimensions, a Numerical Study. *J. Comp. Physics.*, 33:169–184, 1979.

[195] H. Vuorinen, P. Juuti, and T. Katko. History of water and health from ancient civilizations to modern times. *Water Science and Technology: Water Supply*, 7, 2007.

[196] W. Wan Mohtar, Junaidi, S. Sharil, and M. Mukhlisin. Representative sediment sizes in predicting the bed-material load for nonuniform sediments. *International Journal of Sediment Research*, 31:79–86, 2016.

[197] S. Wang and W. Wu. River sedimentation and morphology - the state of the art and future development. *Proceedings of the Ninth International symposium on River Sedimentation*, pages 71–93, 2004.

[198] Y. Wang, Q. Liang, G. Kesserwani, and J. Hall. A 2D shallow flow model for practical dam-break simulations. *J Hydraul Res*, 49:307–316, 2011.

[199] Z. Wang, R. Fokkink, and A. Langerak. A dynamic-empirical model for estuarine morphology. In *Physics of Estuaries and Coastal Seas*, pages 279–286, Balkema, Rotterdam, 1998.

[200] H. Weller. *Open Foam: The Open Source CFD Toolbox.* OpenCFD Limited, 2018.

[201] H. Weller, G. Tabor, H. Jasak, and C. Fureby. A tensorial approach to computational continuum mechanics using object-oriented techniques. *Computers in Physics*, 12:620–631, 1998.

[202] W. White, H. Milli, and A. Crabbe. Sediment transport: An appraisal of available methods, it 119. Technical report, Hydraulics Research Station Wallingford, 1973.

[203] D. Wilcox. *Turbulence Modelling for CFD.* DCW Industries, Inc.: La Canada, CA,w, 2002.

[204] J. Williams and H. Berndt. Sediment Yield Prediction based on Watershed Hydrology. *Trans. Am. Soc. Agric. Eng.*, 20:1100–1104, 1977.

[205] W. Wu. Depth-averaged two-dimensional numerical modeling of unsteady flow and nonuniform sediment transport in open channels. *J. Hydraul. Eng. - ACSE*, 130:1013–1024, 2004.

[206] W. Wu and D. Vieira. *One-dimensional channel network model CCHE1D 2.0.* National Center for Computational Hydroscience and Engineering, 2002.

[207] W. Wu and S. Wang. Formulas for Sediment Porosity and Settling Velocity. *Journal of Hydraulic Engineering*, 132:858–862, 2006.

[208] W. Wu and S. Wang. One-Dimensional Modeling of Dam-Break Flow over Movable Beds. *J. Hydraul. Eng.*, 133:48–58, 2007.

[209] V. Yakhot, S.A. Orszag, S. Thangam, T. Gatski, and C. Speziale. Depth averaged modelling of turbulent shallow water flow with wet–dry fronts. *Physics of Fluids*, 4:1510–1520.

[210] T. Yoon and S. Kang. Finite volume model for two-dimensional shallow water flows on unstructured grids. *Journal of Hydraulic Engineering*, 23:678–688, 2004.

[211] R. Young, C. Onstad, D. Bosch, and W. Anderson. A nonpoint-source pollution model for evaluating agricultural watersheds. *J. Soil Water Conserv.*, 44:168–173, 1989.

[212] C. Yu and J. Duan. Two-dimensional depth-averaged finite volume model for unsteady turbulent flow. *Journal of Hydraulic Research*, 50:599–611, 2012.

[213] J. Zandenet et al. Suspended sediment transport around a large-scale laboratory breaker bar. *Coastal Engineering*, 125:51–69, 2017.

[214] T. Zang, C. Streett, and M. Hussaini. Spectral methods for CFD. Technical report, Institute for Computer Applications in Science and Engineering NASA, 1989.

[215] Q. Zhang, X. Zhou, J. Wang, and J. Guo. Wave-induced seabed response around an offshore pile foundation platform. *Ocean Engineering*, 130:567 – 582, 2017.

[216] W. Zhang, J. Yuan, J. Han, C. Huang, and M. Li. Impact of the Three Gorges Dam on sediment deposition and erosion in the middle Yangtze river: A case study of the Shashi Reach. *Hydrology Research*, 47:1–34, 2016.

[217] S. Zhao, J. Ovadia, X. Liu, Y. Zhang, and Q. Nie. Operator Splitting Implicit Integration Factor Methods for Stiff Reaction-Diffusion-Advection Systems. *J. Comput. Physics*, 230:5996–6009, 2011.

[218] G. Zhou. *Numerical simulations of physical discontinuities in single and multi-fluid flows for arbitrary Mach numbers.* PhD thesis, Chalmers Univ. of Tech., Goteborg, Sweden, 1995.

[219] T. Zi, M. Kumar, G. Kiely, C. Lewis, and J. Albertson. Simulating the spatio-temporal dynamics of soil erosion, deposition and yield using a couple sediment dynamics and 3D distributed hydrologic model. *Environmental Modelling and Software*, 83:310–325, 2016.

[220] O. Zienkiewicz, R. Taylor, and P. Nithiarasu. *The Finite Element Method for Fluid Dynamics.* Elsevier Ltd., seventh edition, 2014.